

2020

Drug Design and Development of Antivirals and Fluorescent Anion Transporters

Mohamed Metwaly

Follow this and additional works at: <https://ro.uow.edu.au/theses1>

University of Wollongong

Copyright Warning

You may print or download ONE copy of this document for the purpose of your own research or study. The University does not authorise you to copy, communicate or otherwise make available electronically to any other person any copyright material contained on this site.

You are reminded of the following: This work is copyright. Apart from any use permitted under the Copyright Act 1968, no part of this work may be reproduced by any process, nor may any other exclusive right be exercised, without the permission of the author. Copyright owners are entitled to take legal action against persons who infringe their copyright. A reproduction of material that is protected by copyright may be a copyright infringement. A court may impose penalties and award damages in relation to offences and infringements relating to copyright material.

Higher penalties may apply, and higher damages may be awarded, for offences and infringements involving the conversion of material into digital or electronic form.

Unless otherwise indicated, the views expressed in this thesis are those of the author and do not necessarily represent the views of the University of Wollongong.

Research Online is the open access institutional repository for the University of Wollongong. For further information contact the UOW Library: research-pubs@uow.edu.au



UNIVERSITY
OF WOLLONGONG
AUSTRALIA

Drug Design and Development of Antivirals and Fluorescent Anion Transporters

By

Mohamed Metwaly

BPharm, MPharm

Supervisors:

Paul Keller

Professor of Chemistry

School of Chemistry and Molecular Bioscience

University of Wollongong

Philip Gale

Professor of Chemistry and Head of School

School of Chemistry

The University of Sydney

This thesis is presented as part of the requirement for the conferral of the
degree:

Doctor of Philosophy

University of Wollongong

School of Chemistry and Molecular Bioscience

March 2020

Certification

I, Mohamed Metwaly, declare that this thesis submitted in fulfilment of the requirements for the conferral of the degree Doctor of Philosophy, from the University of Wollongong, is wholly my own work unless otherwise referenced or acknowledged. This document has not been submitted for qualifications at any other academic institution.

Mohamed Metwaly

March 2020

Declaration of authorship:

I agree with the contribution listed in Mohamed Metwaly's thesis.

	Chapters	Signature
Alessio Nocentini	7	
Anthony C. Willis	2	
Cecilia Lanzi	7	
Claudiu T. Supuran	7	
Dirk Jochmans	2,3,4	
Emanuele Masini	7	
Éthan Howe	5,6	
Hatem A. Abdel-Aziz	7	<i>Ha</i>
Johan Neyts	2,3,4	<i>JN</i>
Laura Lucarini	7	
Muhammad A. Alsherbiny	2,3	
Patrick M. McCosker	2	
Paul A. Keller	2,3,4,5,6,7	
Peter Canfield	3	
Philip A. Gale	3, 5, 6	
Silvia Bua	7	
Thomas S. Peat	7	
Timothy Clark	2	<i>TC</i>
Wagdy M. Eldehna	7	<i>WME</i>
William Lewis	3,5,6	<i>WL</i>
Xin Wu	5,6	<i>XW</i>

Acknowledgments

I am so thankful to anyone who helped me in any way during my PhD;

My mum and my dad for their unfailing faith, dedication, love, and support throughout my life.

Paul Keller for his guidance, encouragement, generous support, and for giving me the opportunity to work in his group.

Philip Gale for giving me the internship position to work in his group. Thanks for your guidance, help and support.

Ashraf Abdel-Megeed for his valuable suggestions and chemical insights. I would especially like to thank Patrick McCosker, Jayden Gaston and Nicholas Butler for the friendly work environment and the fun time. All past and present members of the Keller research group (UoW) and Philip Gale (U Syd) for help, suggestions, friendly environment and for the fun times.

Glennys O'Brien for continuous support and providing teaching opportunities that greatly helped me financially and for developing my academic career

Students and staff of the Schools of Chemistry at UoW and U Syd for making enjoyable working environments. Nick Proschogo and Ian Luck (U Syd), Alan Maccarone (UoW) and Wilford (UoW) for helping with the mass spectrometry and NMR problems.

UOW for providing the scholarship that made my study here possible.

My brothers, Mahmoud and Ahmed and my mother-in-law Nadia who were always there helping and supporting me. My beloved sons Anas and Amir for making me feel happy and satisfied during my intense PhD studies.

I would like to save the biggest thank you for my caring, loving and supportive wife, Radwa for her encouragement, help and support during my studies. Without you I would not complete this project or achieve half as much.

Table of Contents

Certification	i
Acknowledgments	ii
Table of Contents	iii
Abstract	ix
List of publications arising from this thesis (to date)	xiii
Context Statement	xvi
List of Abbreviations	xxv
List of Figures	xxviii
List of Tables	xxxv
List of Schemes	xxxvi

Chapter 1: Introduction

1.1 Biology, re-emergence and pathogenesis of chikungunya virus	1
1.1.1 Taxonomy of the chikungunya	1
1.1.2 Origin, re-emergence and spread of the virus	1
1.1.3 Virus lifecycle	3
1.1.4 Chikungunya fever (CHIKF)	4
1.1.5 Possible drug targets	5

1.2 Development of chemotherapeutics against chikungunya virus	8
1.2.1 Vaccines	8
1.2.2 Hits discovered by virtual screening	8
1.2.3 Anti-viral drugs inhibiting CHIKV	10
1.2.4 Genome-wide loss of function screen	11
1.2.5 Other inhibitors of the CHIKV	13
1.3 Thesis plan	15
1.3.1 Drug design and development cycle	15
1.3.2 Application to drug design cycle towards anti-CHIKV agents.	16
1.4 References	17

Chapter 2: Application of the hybridization concept towards anti-CHIKV agent

FOREWORD TO CHAPTER 2	21
2.1 Introduction	22
2.2 Results and discussion	24
2.3 Conclusions	33
2.4 Experimental section	33
2.4.1 Chemistry	33
2.4.2 Anti-viral assay	42
2.4.3 X-ray crystallographic data for compound 2.20	43
2.4.4 Computational methods	43
2.5 References	44

Chapter 3: Application of the bioisosterism and simplification concepts towards anti-CHIKV

FOREWORD TO CHAPTER 3	46
------------------------------	-----------

3.1 Introduction	47
3.2 Results and discussion	49
3.3 Conclusions	58
3.4 Experimental section	59
3.4.1 Chemistry	59
3.4.2 Biological evaluation	72
3.4.3 Computational studies	74
3.4.4 X-ray crystallography	76
3.5 References	78

Chapter 4: Structure-guided drug design targeting CHIKV

FOREWORD TO CHAPTER 4	81
4.1 Introduction	82
4.2 Results and discussion	85
4.3 Conclusions	89
4.4 Experimental section	90
4.4.1 Chemistry	90
4.4.2 Anti-viral assay	94
4.5 References	95

Chapter 5: Switchable anion transporters

FOREWORD TO CHAPTER 5	97
5.1 Introduction:	98
5.2 Results and discussion:	100
5.2.1 Chemistry	100
5.2.2 Binding in solution	105

5.2.3	Binding in solid state	107
5.2.4	Transport studies	108
5.2.5	Anion and cation selectivity	112
5.2.6	Reduction kinetic studies	113
5.2.7	Switchable time-dependant transport studies	119
5.3	Conclusions	123
5.4	Experimental Section	123
5.4.1	Chemistry	123
5.4.2	X-ray crystallography	129
5.4.3	¹ H NMR titration binding studies with TBACl	133
5.4.4	Anion transport studies:	133
5.4.4.1	Ion selective electrode (ISE) assays	133
5.4.4.2	General preparation for HPTS assays	135
5.4.4.3	Chloride vs anions selectivity assay	137
5.4.4.4	Calcein leakage assays	138
5.4.5	Reduction kinetic studies	138
5.4.6	Transport studies upon reduction of complexes 5.13, 5.14 5.16 and 5.17	142
5.5	References	143

Chapter 6: Fluorescent anion transporters

FOREWORD TO CHAPTER 6	147	
6.1 Introduction	148	
6.2 Results and discussion	150	
6.3 Conclusions	159	
6.4 Experimental section	159	
6.4.1	Chemistry	159
6.4.2	X-ray crystallography of compound 6.1	165
6.4.3	¹ H NMR titration binding studies with TBACl	165
6.4.4	Anion transport studies	166

6.4.4.1	Ion selective electrode (ISE) assays	166
6.4.4.2	General preparation for HPTS assays	168
6.5	References	170
Chapter 7: Carbonic anhydrase inhibitors		
	FOREWORD TO CHAPTER 7	172
7.1	Introduction	173
7.2	Results and discussion	175
7.2.1	Drug design and chemistry	175
7.2.2	Carbonic anhydrase inhibition	178
7.2.3	Protein X-ray crystallography	181
7.2.4	Anti-glaucoma activity (IOP lowering activity)	182
7.3	Conclusions	184
7.4	Experimental Protocol	184
7.4.1	Chemistry	184
7.4.2	Protein X-ray crystallography	196
7.4.3	CA Inhibition	197
7.4.4	Hypertensive rabbit IOP lowering studies	198
7.5	References	199
Chapter 8: Conclusions and Future Directions		
8.1	The search for anti-CHIKV lead compounds (Chapters 2-4)	201
8.1.1	Conclusions	201
8.1.2	Future directions	204
8.2	Fluorescent anion transporters (Chapters 5-6)	206
8.2.1	Conclusions	206
8.2.2	Future directions	206

8.3 Carbonic anhydrase inhibitors (Chapter 7)	207
8.3.1 Conclusions	207
8.3.2 Future directions	208
8.4 References	209
Appendices Table of Contents	210
<i>Appendix A: Supplementary Information to Chapter 2</i>	211
<i>Appendix B: Supplementary Information to Chapter 3</i>	228
<i>Appendix C: Supplementary Information to Chapter 4</i>	257
<i>Appendix D: Supplementary Information to Chapter 5</i>	264
<i>Appendix E: Supplementary Information to Chapter 6</i>	315
<i>Appendix F: Supplementary Information to Chapter 7</i>	343

Abstract

The application of medicinal chemistry drug design and development principles has been undertaken in the current thesis towards the development of antivirals, fluorescent anion transporters and carbonic anhydrase inhibitors.

Chikungunya viral infection is an increasing concern with no current treatments available beyond supportive measures. In the absence of detailed viral molecular information, phenotypic screening of compounds has provided leads for anti-chikungunya agents. **Chapter 2** discusses the application of hybridization of two fragments, namely pyrimidine and thiazolidine, with reported anti-CHIKV activity. Convergent and convenient regioselective synthesis of novel thiazolo[2,3-*a*]pyrimidine derivatives was accomplished using the one-pot reaction of 6-ethylthiouracil, bromoacetic acid, anhydrous sodium acetate, acetic anhydride, acetic acid and a suitable aldehyde. X-ray crystallographic studies reveal the presence of the *Z* configuration of only one regioisomer confirmed by computational studies as being the most likely isomer present. Anti-CHIKV activity evaluation showed the tailed thiazolopyrimidine (*Z*)-7-ethyl-2-((4'-methyl-[1,1'-biphenyl]-4-yl)methylene)-5*H*-thiazolo[3,2-*a*]pyrimidine-3,5(2*H*)-dione as a candidate for future development with $EC_{50} = 42 \mu\text{M}$, and $IC_{50} > 250 \mu\text{M}$ against the breast cancer cell line MCF-7 and the endothelial human sapiens cell line EA.hy926.

Chapter 3 reports the synthesis and chikungunya antiviral activity of 1-aryl-[1,2,4]triazolo[4,3-*a*]pyrimidin-5(1*H*)-ones as bioisosteres for the 5-ethyl-3-(3-isopropoxyphenyl)-3,6-dihydro-7*H*-[1,2,3]triazolo[4,5-*d*]pyrimidin-7-one related antiviral series. Importantly, this new scaffold features increased scope for

derivatisation, exhibits low cytotoxicity, is efficiently and scalably synthesised and is relatively inexpensive. Compound, 3-acetyl-5-ethyl-1-(3-isopropoxyphenyl)-[1,2,4]triazolo[4,3-*a*]pyrimidin-7(1*H*)-one **3.33**, being the 3-acetyl analogue of the prototype **3.1** emerged as having the most promising antiviral activity among the tested series **3.29-3.39** with EC₅₀ = 38 μM, and IC₅₀ > 300 μM against breast cancer cell lines, MCF-7 and MDA-MB-231 and normal cell line EA.hy926. Analysis of the bioactivities of several compounds including the related 2-anilino-pyrimidones using Density-Functional Theory (DFT) modelling provides insights into salient ligand-target interactions necessary for antiviral activity and allows for the drafting of a general pharmacophore

Chapter 4 discusses the development and derivatization of the hit compound NCI_37168 (3-hydroxy-*N*-(3-nitrophenyl)-2-naphthamide) discovered from virtual screening search using the NCI Diversity Set II database (1541 compounds). A small library of 3-hydroxy-*N*-(3-nitrophenyl)-2-naphthamides were synthesized and biologically evaluated for their anti-CHIKV activity. These compounds were toxic to Vero cells at the tested concentration (20 μg/mL). Further development and anti-CHIKV testing at lower concentration are planned be done to investigate their antiviral activity, while lowering their cytotoxic effect.

The second part of this dissertation was the development of fluorescent anion transporters for pharmacological evaluation. Anionophores are small organic molecules that facilitate anion transport across lipid bilayer membranes. **Chapter 5** discusses developing a method to switch on the anion transport function under specific conditions that would dramatically widen the scope of compounds. Therefore, they could be employed as potential therapeutics. This chapter presents the design, synthesis of fluorescent anion transporters and investigation of their

anion transporter and binding properties. Further, we developed four switchable complexes that are switched on in the presence of the physiologically reducing agent GSH and non-physiological reducing agents DTT and TCEP.

In **chapter 6**, a series of coumarin-based bisureas have been synthesised and their anion transport properties studied. The transporters function as highly potent HCl co-transport agents in lipid bilayer membranes. These compounds elicited a H⁺/Cl⁻ co-transport activity and a superior Cl⁻/NO₃⁻ exchange ability in ISE-based affinity than the previously reported fluorescent anion transporters. The fluorescence nature of these compounds will allow them to be localised within cells. A study of their potential cellular localisation, partitioning, and action using fluorescence imaging techniques is currently undergoing.

The third part of this thesis (**Chapter 7**) is the development of potent dual-tailed benzenesulfonamide inhibitors of human carbonic anhydrases implicated in glaucoma. The study investigated the *in vivo* profiling of their intraocular pressure lowering action. The design and synthesis of three dual-tailed sulfonamide series as carbonic anhydrase inhibitors are presented. All synthesized compounds were evaluated for their inhibitory action against pharmacologically relevant human (h) CAs isoforms (I, II, IV, and VII). The (*E*)-2-arylidene-3-oxo-*N*-(4-sulfamoylphenyl)butanamides emerged as the most potent CA inhibitors against the four tested isoforms with a significant selectivity to CA II, which is implicated in glaucoma (*K_i* values spanning the range 0.36 - 6.9 nM). X-ray crystallographic analysis of three compounds bound to CA II showed the validity of the adopted drug design strategy as specific moieties within the ligand structure interacted directly with the hydrophobic and hydrophilic halves of the CA II active site enhancing the inhibition efficiency. Compounds (*E*)-2-(4-chlorobenzylidene)-3-

xi

oxo-*N*-(4-sulfamoylphenyl)butanamide and (*E*)-2-(4-methoxybenzylidene)-3-oxo-*N*-(4-sulfamoylphenyl)butanamide showed significant anti-glaucoma efficacy when compared to the clinically used drug dorzolamide, presenting potential for the development of new therapeutic options against glaucoma.

List of publications arising from this thesis (to date)

a- Journal articles:

1. **Fares, M.;** McCosker, P. M.; Alsherbiny, M. A.; Willis, A. C.; Clark, T.; Neyts, J.; Jochmans, D.; Keller, P. A., Regioselective convergent synthesis of 2-arylidene thiazolo[3,2-*a*]pyrimidines as potential anti-chikungunya agents. *RSC Adv.* **2020**, 10, 5191-5195 (doi: 10.1039/D0RA00257G). Described in Chapter 2.
2. **Fares, M.;** Canfield, P.; Alsherbiny, M. A.; Lewis W.; Willis, A. C.; Li, C. G.; Neyts, J.; Jochmans, D.; Gale, P. A.; Keller, P. A., 1-Aryl-[1,2,4]triazolo[4,3-*a*]pyrimidines, a synthetically facile scaffold for chikungunya antiviral agents, reveals insights into the viral target-binding site. Submitted to *RSC Med. Chem.* Described in Chapter 3.
3. **Fares, M.;** Wu, X.; Soto-Cerrato, V.; Lewis W.; Keller, P. A.; Howe, E. N. W.; Pérez-Tomás, R.; Gale, P. A., Stimuli-responsive cycloaurated 'OFF-ON' switchable fluorescent anion transporters. *Angew. Chem.* 2020, (doi: 10.1002/anie.202006392 and 10.1002/ange.202006392). Described in Chapter 5.
4. **Fares, M.;** Wu, X.; Soto-Cerrato, V.; Lewis W.; Keller, P. A.; Pérez-Tomás, R.; Gale, P. A., Coumarin-bisurea hybrids as potent fluorescent transmembrane anion transporters. Prepared a communication for submission to *Chem. Comm.* Described in Chapter 6.
5. **Fares, M.;** Eldehna, W. M.; Bua, S.; Lanzi, C.; Lucarini, L.; Masini, E.; Peat, T. S.; Abdel-Aziz, H. A.; Nocentini, A.; Keller, P. A.; Supuran C. T., Discovery of potent dual-tailed benzenesulfonamide inhibitors of human carbonic anhydrases implicated in glaucoma and in vivo profiling of their intraocular

- pressure lowering action, *J. Med. Chem.* 2020 (doi: 10.1021/acs.jmedchem.9b02090). Described in Chapter 7.
6. **Fares, M.**; Abd El Hadi, S. R.; Eladwy, R. A.; Shoun A. A.; Abdel-Aziz, M. M.; Abdel-Aziz, H. A.; Keller, P. A., An improved synthesis of pyrido[2,3-*d*]pyrimidin-4(1*H*)-ones and their antimicrobial activity, *Org. Biomol. Chem.* **2018**, 16, 3389-3395 (doi: 10.1039/C8OB00627J).
 7. **Fares, M.**; Eladwy, R. A.; Nocentini, A.; Abd El Hadi, S. R.; Ghabbour, H. A.; Abdel-Megeed, A.; Eldehna, W. M.; Abdel-Aziz, H. A.; Supuran, C. T., Synthesis of bulky-tailed sulfonamides incorporating pyrido[2,3-*d*][1,2,4]triazolo[4,3-*a*]pyrimidin-1(5*H*)-yl) moieties and evaluation of their carbonic anhydrases I, II, IV and IX inhibitory effects. *Bioorg. Med. Chem.* **2017**, 25, 2210-2217 (doi: 10.1016/j.bmc.2017.02.037).

b- Conference Abstracts (presenter underlined)

Oral presentations:

1. **Fares, M.**; Willis, A. C.; Neyts, J.; Jochmans, D.; Keller, P. A., “Medicinal Chemistry Towards Anti-CHIKV Agents” UOW Annual Chemistry Conference 2017, Blue Mountains, Australia, 1st–3rd November **2017**.
Presentation awarded highly commended talk by a second-year PhD student.
2. **Fares, M.**; Willis, A. C.; Neyts, J.; Jochmans, D.; Keller, P. A., “Drug Design Development Targeting Chikungunya Virus” UOW Annual Chemistry Conference 2016, Blue Mountains, Australia, 2nd–4th November **2016**.
Presentation awarded highly commended talk by a first-year PhD student.

Oral presentations:

1. **Fares, M.:** Howe, E. N. W.; Wu, X.; Keller, A. P.; Gale, A. P., “Development of “Switch-on” Fluorescent Anionophores”, 14th International Symposium on Macrocyclic and Supramolecular Chemistry (ISMSC2019), Lecce, Italy, **2019**, 2nd June-6th June.

Context Statement

This thesis is presented as a compilation of manuscripts from published and unpublished work. The science is both multi-disciplinary and collaborative in nature. Chapters either stand separately or together to present the science achieved in the field of drug design and development of antivirals targeting chikungunya virus, anion transporters and carbonic anhydrase inhibitors. At the start of each chapter is a foreword with references added at the end of each chapter.

The outcomes of this dissertation are presented in **Chapters 2-7** with overarching conclusions and future directions in **Chapter 8**. Appendices are provided at the end of this thesis including NMR spectra of the synthesized compounds, Figures of NMR binding and anion transport studies, and protein X-ray crystallography data. From the beginning of the project it was thought that the anti-chikungunya virus project (**Chapters 1-4**) was challenging, and therefore a component of the dissertation plan was to investigate alternative topics. To this end, an internship at the University of Sydney was available in the fields of supramolecular chemistry and anion transporters. The outcomes from this internship are described in **Chapters 5 and 6**. Further, arising from an established collaboration in the design of carbonic anhydrase inhibitors, this dissertation also explored a new direction in this area (**Chapter 7**).

A detailed description of each topic follows:

A) Anti-chikungunya virus agents:

Chikungunya virus (CHIKV) (*alphavirus* genus, family *Togaviridae*) is one of the prevalent arboviruses that is implicated in high fever and severe persistent joint pain that may last for weeks to years. In the view of absence of anti-CHIKV and

the reported multiple re-emergent epidemic outbreaks of the CHIKV in the last 70 years, there is a pressing need to discover new anti-CHIKV agents. A literature review of the chikungunya virus biology and previous approaches used towards the development of anti-chikungunya agents is presented in **Chapter 1**.

In this dissertation, considerable efforts were directed towards the development of potential anti-CHIKV therapeutics *via* applying medicinal chemistry concepts (**Chapter 2** and **3**) and structure-based drug design approaches (**Chapter 4**).

Chapter 2 describes the application of the hybridization of existing CHIKV inhibitors towards the development of unprecedented anti-CHIKV agents. Molecular hybridization is fundamentally based on the fusion of two or more pharmacophoric moieties. Recently, hybridization of two or more bioactive fragments has emerged as a concept for the exploration of novel multitarget acting inhibitors as well as novel anti-CHIKV agents. This chapter discusses a molecular hybridization approach with the fusion of uracil and rhodanine pharmacophoric moieties and investigation of the biological activity against CHIKV. Uracil-rhodanine hybrids were synthesized using the state-of-art organic chemistry starting from 6-ethyl-2-thiouracil and by optimization of the multi-component collective reaction conditions *via* replacing chloroacetic acid with the more regioselective bromoacetic acid, lowering reaction temperature and changing the mode of addition. X-ray crystal structure analysis and computational studies showed that only one regioselective isomer formed with the *Z* configuration that is potentially stabilized by two intramolecular hydrogen bonds. The synthetic phase was followed by biological evaluation of the compounds as anti-CHIKV agents. The compounds demonstrated different percentages of viral replication inhibition at 20 $\mu\text{g}/\text{mL}^{-1}$ with (*Z*)-7-ethyl-2-((4'-methyl-[1,1'-biphenyl]-4-yl)methylene)-5*H*-thiazolo[3,2-
xvii

a]pyrimidine-3,5(2*H*)-dione showing the best activity with 58% inhibition of CHIKV replication. Anti-CHIKV activity evaluation showed the (*Z*)-7-ethyl-2-((4'-methyl-[1,1'-biphenyl]-4-yl)methylene)-5*H*-thiazolo[3,2-*a*]pyrimidine-3,5(2*H*)-dione as a promising lead compound for future development with EC₅₀ = 42 μM, with IC₅₀ > 250 μM against the breast cancer cell line MCF-7 and the endothelial human sapiens cell line EA.hy926. This compound is bearing *p*-methylbiphenyl tail functionality which might interact favourably with the target. This chapter is published in RSC Adv. 2020, 10, 5191-5195 (doi: 10.1039/D0RA00257G).

Chapter 3 discusses drug design and development of potential antiviral agents using synthetic modification including lead simplification and bioisosteric replacement. Using 6-ethyl-2-thiouracil as a starting material, two series of fused 1-aryl-[1,2,4]triazolo[4,3-*a*]pyrimidines and 2-anilinopyrimidines were designed and synthesized using the state-of-art organic chemistry. Single X-ray crystal structure of two target compounds confirmed the formation of the desired isomer. Tested compounds showed promising *in silico* pharmacokinetic properties calculation and drug likeness scores. Compounds [1,2,4]triazolo[4,3-*a*]pyrimidin-7(1*H*)-ones and 2-anilinopyrimidin-4(3*H*)-one were screened for their antiviral activities in a viral-cell based assay against chikungunya virus (Indian Ocean strain 899). The most active compounds were further tested for their cytotoxic activity against the normal cell line, EA.hy926, the endothelial human cell line, and two human breast cancer cell lines, namely, MCF-7 and MDA-MB-231. Whilst the series 2-anilinopyrimidines, proved to only exhibit weak anti-CHIKV activity, derivative 3-acetyl-5-ethyl-1-(3-isopropoxyphenyl)-[1,2,4]triazolo[4,3-*a*]pyrimidin-7(1*H*)-one emerged as the most active antiviral agent (EC₅₀ = 38 μM)

and the least cytotoxic with $IC_{50} > 300 \mu\text{M}$ against breast cancer cell lines, MCF-7 and MDA-MB-231 and normal cell line EA.hy926. Comparisons of the geometries and electrostatic potential-mapped surfaces (EPS) of the active CHIKV inhibitors has allowed for a consensus model for effective target binding. A manuscript based on the results from **Chapter 3** is in preparation for submission to RSC Med. Chem.

Chapter 4 presents the application of structure-based drug design concepts towards anti-CHIKV agents. *In silico* screening of the NCI Diversity set II database (1541 compounds) in our laboratory against three viral proteins, namely nsP2, nsP3 and envelope glycoproteins identified eleven potential inhibitors. The selected ligands were requested from Developmental Therapeutics Program Databases and Search Tools, National Cancer Institute, USA and were tested in Rega Institute, KU Leuven, Belgium for their anti-CHIKV activity. Three CHIKV agents were identified possessing naphthalene and quinoline scaffolds. A small library of molecules based on the naphthalene scaffold was synthesized and tested for its anti-CHIKV activity. The naphthalene scaffold showed considerable toxicity to Vero cells, which might impede the antiviral activity. Further development of the quinoline scaffold could be undertaken with planned iterative cycles of optimization.

B) Fluorescent anion transporters:

The transport of ions *via* phospholipid bilayer membranes is involved in diverse physiological functions including, neuroexcitation, muscle contraction, cell migration and proliferation, and maintaining cellular pH, membrane potential and cellular secretions. Channelopathies are a group of diseases characterised with ion-channel impairment, including cystic fibrosis, epilepsy and cancer. For example,

cystic fibrosis transmembrane regulator (CFTR) is a protein responsible for maintaining cellular chloride and bicarbonate levels and is implicated with cystic fibrosis, while impairment of sodium, potassium and T-type calcium channels is linked with epilepsy. Ionophores are transmembrane ion transporters that have been recognised for diverse applications in ion sensing, catalysis and in medicinal chemistry. Anionophores are a subclass of the ionophores that are capable of transporting anions and they demonstrated a cytotoxic effect against stem cancer cells by facilitating the transport of chloride and bicarbonate anions so changing cellular pH, causing cellular differentiation and death.

One of primary aims of this PhD work was to design and synthesise fluorescent anionophores and to investigate the mechanism of action of their cytotoxic effect in living cells. A literature review of the fluorescent anion transporters (**Chapters 5 and 6**) is included in the beginning of these chapters.

Chapter 5 describes the development of stimuli-responsive cycloaurated ‘OFF-ON’ switchable fluorescent anion transporters. Inspired by the high affinity of thiols, such as GSH, for gold, and by the reported efficient anion transport activity of 1,3-bis(benzimidazol-2-yl)benzenes, we designed and synthesized new switchable cycloaurated anion transporters that could be switched under physiological conditions such as high levels of GSH. Five 1,3-bis(benzimidazol-2-yl)benzenes anion transporters have been synthesized by condensation of dipicolinic acid or 2,6-pyridinedicarboxaldehyde and phenylenediamine derivative under acidic conditions. The structure of one derivative was confirmed by single crystal X-ray diffraction. These transporters have been shown to bind Cl^- in solution with moderate affinity in $\text{DMSO-}d_6/0.5\% \text{H}_2\text{O}$ and CD_3CN . A single

crystal of anionophore 2,6-bis(5(6)-(trifluoromethyl)-1*H*-benzo[*d*]imidazol-2-yl)pyridine with chloride ion was obtained for X-ray and interestingly showed that Cl⁻ is sandwiched between two molecules of the compound. Transporters 1,3-bis(benzimidazol-2-yl)benzenes were investigated for their chloride transport property *via* Cl⁻/NO₃⁻ exchange assay using a chloride ion selective electrode (ISE), cationophore coupled-KCl assay and 8-hydroxypyrene-1,3,6-trisulfonic acid (HPTS) assay. At the same concentration, they showed better transport properties when transporter loading volume increased from 10 μL to 40 μL. Transporter 2,6-bis(5(6)-(trifluoromethyl)-1*H*-benzo[*d*]imidazol-2-yl)pyridine was the most active with EC₅₀ = 0.42 mol%. A cationophore coupling assay, using valinomycin (Vln) or monensin (Mon) was used to investigate whether these compounds are functioning as Cl⁻ uniporter or H⁺/Cl⁻ symporter. Generally, these transporters can facilitate the transport of H⁺, Cl⁻ and NO₃⁻ in liposomal models. Four switchable cycloaurated complexes were constructed from the two most potent anion transporters. Single X-ray crystal structure of three cycloaurated complexes confirmed their structure. The switch-off the four gold III complexes demonstrated higher affinity to DTT, followed by GSH, while TCEP emerged as the weakest reducing agent. Finally transport studies showed that these switchable anion transporters are highly efficient and can be switched on by all tested reducing agents with different rates. DTT emerged as the most potent reducing agent followed by GSH and TCEP. This chapter is just accepted in *Angew. Chem.* 2020, (doi: 10.1002/anie.202006392 and 10.1002/ange.202006392) and describes the development stimuli-responsive cycloaurated 'OFF-ON' switchable fluorescent anion transporters.

Fluorescent labelling of the sub-cellular organelles has become an indispensable

tool of our understanding of the biological functions and it can shed the light on the mechanism of action at a cellular level. **Chapter 6** describes the development of efficient fluorescent anion transporters for biological evaluation. The development of these fluorescent anionophores was achieved by linking the bisureas-anion transporter moiety and the fluorescent 4-methylcoumarin. Four bisurea-coumarin transporters were prepared by nucleophilic addition of the 6,7-diamino-4-methylcoumarin with the corresponding aryl isocyanate in DCM or in absence of solvent. The structure of one derivative was confirmed by single crystal X-ray diffraction. The fluorescent anion receptors were tested for their anion binding properties in solution and elicited a relatively strong chloride binding affinity in DMSO-*d*₆/0.5%*H*₂O with $K_a = 81 - 177 \text{ M}^{-1}$.

The four receptors were investigated for their chloride transport properties across the lipid bilayer *via* liposome-based techniques using a chloride ion selective electrode (ISE), cationophore coupled-KCl assay and 8-hydroxypyrene-1,3,6-trisulfonic acid (HPTS) assay. These receptors showed a superior $\text{Cl}^-/\text{NO}_3^-$ exchange ability in ISE-based affinity and H^+/Cl^- co-transport activity than the previously reported fluorescent anion transporters. These transporters could be considered as better candidates for cellular fluorescent imaging. **Chapter 6** is a manuscript in preparation for submission to the journal *Chem. Comm.*

C) Design and synthesis of tailed carbonic anhydrase inhibitors:

Carbonic anhydrases (CAs, EC 4.2.1.1) constitute a superfamily of ubiquitous metalloenzymes which principally act as catalysts in the CO_2 hydration reaction. Abnormal expression of CAs is implicated in some diseases such as cancer, glaucoma and arthritis. A literature review of carbonic anhydrase inhibitors is

included at the beginning of **Chapter 7**.

Chapter 7 describes the design and synthesis of three series of dual-tailed sulphonamides CA inhibitors using accessible and low-cost starting materials including, sulfanilamide, acetyl acetone and ethyl acetoacetate. The newly synthesized compounds were evaluated for their inhibitory profiles against four carbonic anhydrase isoforms: hCA I, II, IV, and VII. The tested compounds showed selectivity to CA II and one series emerged as the most potent CA II inhibitors with low to sub nanomolar K_i values (0.36-6.9 nM). X-ray crystallographic studies of the compounds against CA II were performed to further understand and rationalize their strong CA II inhibitory profile. X-ray co-crystallographic analysis of the adducts of hCA II with three derivatives was achieved at resolutions of 1.32-1.67 Å. The X-ray crystallographic studies showed defined moieties within the ligand structures specifically interact with the hydrophobic and hydrophilic halves of the CA II active site. As CA II up-regulation is implicated with glaucoma, four of the most active CA II inhibitors (K_i values of 0.36-2.9 nM) were evaluated for their IOP lowering action against **DRZ** as the standard. Compound (*E*)-3-oxo-*N*-(4-sulfamoylphenyl)-2-(thiophen-2-ylmethylene)butanamide showed a comparable IOP lowering effect to DRZ (IOP reduction = 8.5 mmHg), while compounds (*E*)-2-(4-chlorobenzylidene)-3-oxo-*N*-(4-sulfamoylphenyl)butanamide and (*E*)-2-(4-methoxybenzylidene)-3-oxo-*N*-(4-sulfamoylphenyl)butanamide were more potent than DRZ with IOP reduction of 12.8 and 12.3 mmHg, respectively. Therefore, this study presents compounds (*E*)-2-(4-chlorobenzylidene)-3-oxo-*N*-(4-sulfamoylphenyl)butanamide and (*E*)-2-(4-methoxybenzylidene)-3-oxo-*N*-(4-sulfamoylphenyl)butanamide as promising candidates for the development of

therapeutic anti-glaucoma strategies. **Chapter 7** has been accepted to J. Med. Chem. (doi: 10.1021/acs.jmedchem.9b02090).

List of Abbreviations

^1H NMR	Proton nuclear magnetic resonance
^{13}C NMR	Carbon nuclear magnetic resonance
AAZ	Acetazolamide
ADP	Adenosine diphosphate
Ala	Alanine
APPI	Atmospheric pressure photoionization
BA	Binding affinity
BRZ	Brinzolamide
BSA	Bovine serum albumin
BST-2	Bone marrow stromal antigen 2
C	Capsid
CA	Carbonic anhydrase
CAG	Angle-closure glaucoma
CCCP	Carbonyl cyanide <i>m</i> -chlorophenyl hydrazone
CCDC	Cambridge crystallographic data centre
CDC	Cell division cycle
CDI	1,1'-Carbonyldiimidazole
CFTR	Cystic fibrosis transmembrane conductance regulator
CHIKF	Chikungunya fever
CHIKV	Chikungunya virus
CID	Compound ID
CLK	CDC-like kinase
$^c\log\text{P}$	Calculated log P
CPE	Cytopathic effect
DCM	Dichloromethane
DFT	Density functional theory
DIPEA	<i>N,N</i> -Diisopropylethylamine
DLS	Drug likeness scores
DMF	Dimethylformamide
DMSO	Dimethyl sulfoxide
DNA	Deoxyribonucleic acid
DRZ	Dorzolamide

DTT	Dithiothreitol
EC ₅₀	Half maximal effective concentration
ESI	Electrospray ionization
ESP	Electrostatic Potential
FBS	Foetal Bovine Serum
Gly	Glycine
GSH	Glutathione
GSSG	Glutathione disulfide
HCV	Hepatitis C
HEPES	4-(2-Hydroxyethyl)-1-piperazineethanesulfonic acid
His	Histidine
HIV	Human immunodeficiency viruses
HPTS	8-Hydroxypyrene-1,3,6-trisulfonic acid
HRMS	High resolution mass spectrometry
Hsp60	Heat shock protein 60
INF	Interferon
IOP	Intraocular pressure
KGlu	Potassium gluconate
LCMS	Liquid chromatography–mass spectrometry
LRMS	Low resolution mass spectra
MCR	Multi-component reaction
MEM	Minimum essential medium
MeOH	Methanol
Mon	Monensin
mRNA	Messenger ribonucleic acid
NADP	Nicotinamide adenine dinucleotide phosphate
NCDS	Australian national communicable diseases surveillance
NCI	National cancer institute
ND	Not determined
NHC	<i>N</i> -Heterocyclic carbene
NSAID	Non-steroidal anti-inflammatory drugs
nsPs	Non-structural proteins
NT	Not tested

OAG	Open angle glaucoma
PAINS	Pan-assay interference compounds
PDB	Protein data bank
PES	Potential Energy Surfaces
POPC	1-Palmitoyl-2-oleoyl-sn-glycero-3-phosphocholine
RNA	Ribonucleic acid
ROS	Reactive oxygen species
RTL	Relative to liposomes
SAR	Structure activity relationship
SCXRD	Single crystal X-ray diffraction
SR	Stacked rings
TBACl	Tetrabutylammonium chloride
TCEP	Tris(2-carboxyethyl)phosphine
TEACl	Tetraethylammonium chloride
THF	Tetrahydrofuran
TLC	Thin layer chromatography
TMS	Tetramethylsilane
TOFA	5-(Tetradecyloxy)furan-2-carboxylic acid
UOW	University of Wollongong
UPR	Unfolding protein response
Val	Valine
WHO	World health organization
Vln	Valinomycin

List of Figures

Chapter 1:

Figure 1.1: Schematic representation of arbovirus subclasses taxonomy.	1
Figure 1.2: Schematic diagram of alphavirus life cycle. Reproduced with permission from reference 4. ⁴	4
Figure 1.3: a) CHIKV nsP2 crystal structure (PDB id: 3TRK) b) The macrodomain (nsP3) of CHIKV (PDB id: 3GPG).	7
Figure 1.4: Structure of CHIKV nsP2 inhibitors identified by <i>in silico</i> studies.	9
Figure 1.5: Some known drugs inhibiting CHIKV replication.	11
Figure 1.6: Selected inhibitors of the CHIKV from the screening. CHIKV EC ₅₀ are in parenthesis.	12
Figure 1.7: Purines as of CHIKV inhibitors.	13
Figure 1.8: Selected CHIKV inhibitors with different scaffolds.	14
Figure 1.9: Iterative cycle of drug design and lead identification and optimization.	15

Chapter 2:

Figure 2.1: Examples of heterocyclic classes showing anti-CHIKV activity, including thiazolidineone 2.1 and 2.2 , pyrimidine 2.3 and pyrimidine fused rings 2.4 and 2.5-2.7 .	25
Figure 2.2: Design of the targeted uracil-rhodanine conjugates.	26
Figure 2.3: ¹ H NMR spectrum of the MCR product of the two regioisomers of 2.16 in a ratio of 1:5.	28
Figure 2.4: The four possible isomers that can be produced from the MCR reaction.	29
Figure 2.5: a) ORTEP diagram of compound 2.20 , b) Representation of stabilizing hydrogen bonds of the regioisomer ZA.	30
Figure 2.6: Proposed mechanism for the synthesis of isomers <i>Z</i> and <i>E</i> , the alcohol intermediate of interest (red) and the dehydration step (blue) are highlighted. Note the <i>Z</i> isomer is the product of the reaction in this example.	30
Figure 2.7: Structures of three alcohol intermediate conformers (C1 – C3) investigated. $\Delta_r G^0$ (298 K) energies calculated relative to the starting materials, Compound 2.13 and benzaldehyde, in kcal.mol ⁻¹ . All methods employed the aug-cc-pVDZ basis set.	31

Figure 2.8: Energy profile for the formation of compound **2.14(Z)** and **2.14(E)**, 33
calculated with DFT M06-2X/aug-cc-pVDZ. Divergent reaction pathways are
colour coded red for *E* formation and blue for *Z* formation. SR = stacked rings
conformer.

Chapter 3:

Figure 3.1: Application of medicinal chemistry concepts to current CHIKV 50
inhibitor MADTP-372 towards new potential anti-CHIKV agents. The assumed
core, including the explicit hydrogen, are highlighted green.

Figure 3.2: X-ray crystal structure of **3.15** (a, **3.20** (b and **3.24** (c. 52

Figure 3.3: ORTEP depictions of compounds **3.23** and **3.39** at 70% probability. 54

Figure 3.4: Structures and Density-Functional Theory (DFT) minimal 59
pharmacophore models of the [1,2,4]triazolo[4,3-*a*]pyrimidine (**3.53**), the
azahypoxanthine (**3.54**), the hypoxanthine (**3.55**) and the pyrimidone tautomers
(**3.56a-b**) showing the electrostatic potential mapped onto two different electron
isodensities to convey both the resolved atoms (middle row) and the diffuse
molecular surface as seen by the chemical environment (bottom row). Potential
H-bond interactions indicated by coloured arrows. The tautomers shown for **3.54**
and **3.55** calculated by DFT to represent 100% of the species *in vivo*. For the
pyrimidones **3.56**, the relative concentration of the two tautomers is shown.

Figure 3.5: a) Consensus picture of the minimal pharmacophore with inferred 60
important H-bond interactions indicated. For compounds like **3.54** and **3.55** R₂
could likely represent an H-bonded H₂O molecule. b) The DFT Potential Energy
Surfaces of **3.53** – **3.55** for the phenyl torsions as defined by the bold blue bonds
in (a).

Chapter 4:

Figure 4.1: Structure of the active potential leads. 88

Figure 4.2: Possible modification of NCI_37168 (**4.5**). 89

Chapter 5:

Figure 5.1: Schematic representation showing the design of switchable anion 102
transporters.

Figure 5.2: Reported GSH mediated activation and putative transporters **5.1-5.5**. 102

Figure 5.3: X-ray structure of anion transporter **5.2**. DMSO complex. 104

Figure 5.4: X-ray structure of complex **5.14**. 105

Figure 5.5: X-ray structure of anion complex **5.16**. 106

Figure 5.6: X-ray structure of anion transporter 5.17 .	107
Figure 5.7: Stack plot of ¹ H NMR spectroscopic titration of receptor 5.2 (1 mM) with TBACl in CD ₃ CN at 298 K.	108
Figure 5.8: Crystal structure of 5.2 with chloride complex.	109
Figure 5.9: a-c) schematic representation of ISE-based assays used to investigate the mechanism of anion transport of receptors 5.1-5.5 . d) Chloride efflux achieved by transporters 5.1-5.5 (1.0 mol%) (rtl) for transporters 5.1-5.4 and 0.8 mol% (rtl) for transporter 5.5 . e) Chloride efflux achieved by transporter 5.2 at 1.0 mol% (rtl) in the absence or presence of cationophores (monensin or valinomycin) monitored over a period of 5 min.	111
Figure 5.10: a-d) Schematic representation of the HPTS-based assays used in the current study e) H ⁺ /Cl ⁻ symport or OH ⁻ /Cl ⁻ antiport facilitated by compounds 5.1-5.5 (1.0 mol% (rtl)). f) Different conditions were applied to determine the effect of addition of the protonophore cccp at 0.5 mol% (as a measure of chloride uniport), oleic acid at 1 mol% (as a source of fatty acid) and BSA-treated lipid (to test if the transport is fatty acid dependent) on the rate of chloride transport of receptor 5.2 (1 mol%).	113
Figure 5.11: Observed fluorescence ratio response due to HCl influx in the presence of compounds 5.2 (1 mol%) into vesicles loaded with KCl (100 mM) and suspended in KCl, KBr, KI, KNO ₃ and KClO ₄ (100 mM). All external and internal solutions were buffered to pH 7 with HEPES (10 mM).	114
Figure 5.12: Chemical structure of tested compounds and the three reducing agents used in the current study.	115
Figure 5.13: Reduction of complexes 5.13 and 5.16 in organic solvent (DMSO) monitored by a) fluorescence and b) UV-Vis spectroscopies by thiols; namely GSH (reduced glutathione) and DTT (dithiothreitol), and TCEP (tris(2-carboxyethyl)phosphine hydrochloride). Fluorescence readings are averages of three replicates and UV-Vis readings are averages of two replicates, always with standard deviations less than 10%.	116
Figure 5.14: Reduction of complexes 5.14 and 5.17 in organic solvent (DMSO) monitored by a) fluorescence and b) UV-Vis spectroscopies by thiols; namely GSH (reduced glutathione) and DTT (dithiothreitol), and TCEP (tris(2-carboxyethyl)phosphine hydrochloride). Fluorescence readings are averages of three replicates and UV-Vis readings are averages of two replicates, always with standard deviations less than 10%.	117
Figure 5.15: Reduction of complexes 5.13 and 5.16 in liposomes monitored by	119

a) fluorescence and b) UV-Vis spectroscopies by thiols; namely GSH (reduced glutathione) and DTT (dithiothreitol), and TCEP (tris(2-carboxyethyl)phosphine hydrochloride). Fluorescence readings are averages of three replicates and UV-Vis readings are averages of two replicates, always with standard deviations less than 10%.

Figure 5.16: Reduction of complexes **5.14** and **5.17** in liposomes monitored by UV-Vis spectroscopy by thiols; namely GSH (reduced glutathione) and DTT (dithiothreitol), and TCEP (tris(2-carboxyethyl)phosphine hydrochloride). UV-Vis readings are averages of two replicates, always with standard deviations less than 10%. 120

Figure 5.17: Reduction of complexes **5.13** and **5.16** in GSH encapsulated liposomes. Fluorescence readings are averages of three replicates, always with standard deviations less than 10%. 120

Figure 5.18: Reduction of complexes **5.13**, **5.14**, **5.16** and **5.17** in GSH encapsulated liposomes. UV-Vis readings are averages of two replicates, always with standard deviations less than 10%. 121

Figure 5.19: KCl-KOH liposomal model used to assess the switchable-time dependent studies. POPC vesicles were loaded with KCl (100 mM), buffered to pH 7.0 with HEPES (10 mM). The test compound was added at 0 s and detergent was added at 200 s. 122

Figure 5.20. Observed fluorescence ratio response due to H^+/Cl^- symport or Cl^-/OH^- antiport upon reduction of complexes a) **5.13** and b) **5.14** (1 μM) by GSH (6 μM) using KCl-KOH assay from POPC vesicles loaded with KCl (100 mM), buffered to pH 7.0 with HEPES (10 mM) at different time intervals. The test complexes **5.13** and **5.14** (1 mol%) and KOH were added firstly, then GSH was added at 0 s. DMSO, GSH (3 mol%), parent anion transporters **5.2** and **5.3** and complex **5.13** and **5.14** (without addition of DTT) were used as controls. Detergent was added at 200 s. Ionophore concentrations are shown as ionophore to lipid molar ratios. Error bars represent SD from at least three repeats. 123

Figure 5.21. Observed fluorescence ratio response due to H^+/C^- symport or Cl^-/OH^- antiport upon reduction of complexes a) **5.16** and b) **5.17** (1 μM) by GSH (6 μM) using KCl-KOH assay from POPC vesicles loaded with KCl (100 mM), buffered to pH 7.0 with HEPES (10 mM) at different time intervals. The test complexes **5.16** and **5.17** (1 mol%) and KOH were added firstly, then GSH was added at 0 s. DMSO, GSH (3 mol%), parent anion transporters **5.2** and **5.3** and complex **5.16** and **5.17** (without addition of DTT) were used as controls. 124

Detergent was added at 200 s. Ionophore concentrations are shown as ionophore to lipid molar ratios. Error bars represent SD from at least three repeats.

Chapter 6:

- Figure 6.1:** Structure of designed fluorescent transporters **6.1-6.4.** 150
- Figure 6.2:** X-ray crystal structure of **6.1** a) ORTEP diagram showing 50% probability anisotropic displacement ellipsoids at 100 K. b) space-filling models. 153
- Figure 6.3:** Stack plot of the ^1H NMR spectrum of receptor **6.3** (2.0×10^{-3} M) upon titration with chloride (0-17 eq.) added as its tetrabutylammonium salt. 153
- Figure 6.4:** a-c) schematic representation of ISE-based assays used to investigate the mechanism of anion transport of receptors 1-4 a) $\text{Cl}^-/\text{NO}_3^-$ antiport, b) and c) cationophore coupled-KCl, valinomycin and monensin to measure the Cl^- uniport and M^+/Cl^- transport, respectively. 156
- Figure 6.5:** Chloride efflux achieved by transporters **6.1-6.4** (0.10 mol% for transporter **6.1** and 0.05 mol% for transporters **6.2-6.4**) from unilamellar POPC vesicles containing 489 mM KCl buffered to pH 7.2 with 5 mM potassium phosphate salts, suspended in 489 mM KNO_3 buffered to pH 7.2 with 5 mM phosphate salts. At the endpoint of each experiment (300 s), the detergent was added to lyse the vesicles and calibrate the electrode to 100% chloride efflux. Each point represents the average of at least two trials. 156
- Figure 6.6:** Chloride efflux achieved by transporter **6.3** at 0.05 mol% (rtl) in the absence or presence of cationophores (monensin or valinomycin) monitored over a period of 5 min. POPC vesicles are loaded with 300 mM KCl with 5 mM phosphate salts (pH 7.2) and suspended in a 300 mM potassium gluconate solution with 5 mM phosphate salts (pH 7.2). Electrogenic K^+ transport by valinomycin can only occur if it is balanced by electrogenic Cl^- transport by **6.3**. Electroneutral K^+/H^+ antiport by monensin can only occur if the pH gradient is dissipated by electroneutral H^+/Cl^- transport by **6.3**. 157
- Figure 6.7:** Schematic representation of the HPTS-based assays used in the current study a) H^+/Cl^- symport or OH^-/Cl^- antiport b) the presence of cccp (protonophore) to assess Cl^- uniport c) the presence of valinomycin to measure the proton flux d) the effect of fatty acid presence as a fuel on the transport. 158
- Figure 6.8:** H^+/Cl^- symport or OH^-/Cl^- antiport facilitated by compounds **6.1-6.4** (0.02 mol% (rtl) for transporter **6.1** and 0.002 mol% (rtl) for transporters **6.2-6.4**) from unilamellar POPC vesicles loaded with 100 mM KCl buffered to pH 7.0 with 10 mM HEPES buffer and 1 mM HPTS internal sensor. The vesicles were suspended in an external solution of 100 mM KCl buffered to pH 7.0 with 10 mM

HEPES buffer and a base pulse of KOH (25 μ L, 0.5 M) was added to generate a transmembrane pH gradient. At the endpoint of each experiment (200 s), the detergent was added to lyse the vesicles and collapse the pH gradient for calibration of HPTS fluorescence.

Figure 6.9: Using KCl-KOH assay from POPC vesicles loaded with KCl (100 mM), buffered to pH 7.0 with HEPES (10 mM), different conditions were applied including using BSA-treated lipid (to test if the transport is fatty acid dependent) addition of oleic acid at 1 mol% (as a source of fatty acid), addition of the protonophore CCCP at 1 mol% (to measure of chloride uniport solely), or addition of valinomycin at 0.05 mol% (as a measure of H⁺ flux), on the rate of chloride transport of receptor **6.3** (0.001 mol%). 157

Chapter 7:

Figure 7.1: Structures of clinically used CAIs and other inhibitors derived from sulfanilamide (**SA**). 175

Figure 7.2: Design of dual-tailed sulfonamides targeting hCAs. The molecular surface of hydrophobic and hydrophilic halves of the CA active site are coloured in red and blue, respectively. The Zn(II) ion is represented as an orange sphere (pdb 1CA2). 177

Figure 7.3: Active site view of the hCA II adduct with A) **7.10** (pdb 6UFB), B) **7.13** (pdb 6UFC) and C) **7.16** (pdb 6UFD). Hydrogen bonds are represented as black dashed lines. 183

Figure 7.4. Drop of intraocular pressure (Δ IOP, mmHg) versus time (min) in hypertonic saline-induced ocular hypertension in rabbits, treated with 50 μ L of 1% solution of compounds **7.11-7.13** and **7.16** and **DRZ** as the standard. Data are analyzed with 2way Anova followed by Bonferroni multiple comparison test. * $p < 0.05$ **7.11**, **7.16**, **DRZ** vs vehicle at 60' and **DRZ** vs vehicle at 120'; ** $p < 0.01$ **7.13** and vs vehicle at 60' and **7.16** vs vehicle at 120'; **** $p < 0.001$ **7.11** and **7.13** vs vehicle at 120'. 184

Chapter 8:

Figure 8.1: Summary of the application to medicinal chemistry concepts. 203

Figure 8.2: Structure-guided drug design workflow in this dissertation. 205

Figure 8.3: Structure of the active potential leads **4.1**, **4.5** and **4.11** and optimization of **4.5**. 206

Figure 8.4: Future development of the thiazolopyrimidine **2.23** and triazolopyrimidine **3.33**. 207

Figure 8.5: Future development of the switchable anion transporters 5.13, 5.14,	209
5.16 and 5.17.	
Figure 8.6: Drug design of the potent anti-glaucoma derivatives studied in the	210
current thesis.	
Figure 8.7: possible derivatization and development of the CA inhibitors.	211

List of Tables

Chapter 1:

Table 1.1: Target cells of CHIKV.	4
Table 1.2: The structures of some hit compounds identified by <i>in silico</i> studies against CHIKV proteins.	9

Chapter 2:

Table 2.1. The observed %inhibition of CHIKV activity of the novel compounds 2.14-2.26 .	34
--	----

Chapter 3:

Table 3.1: <i>In vitro</i> antiviral and cytotoxic activities of compounds 3.29-3.39 and 3.6-3.9 .	56
Table 3.2: Drug likeness calculations and Lipinski parameters of the compounds 3.29-3.39 and 3.6-3.9 .	57
Table 3.3: B3LYP-D3(BJ)/6-311++G(2d,p)-(water solvation) calculated free energies and relative concentrations at 37° C for tautomers of the minimal pharmacophores 3.54 , 3.54b , 3.55 , 3.55a , 3.56a-c .	77

Chapter 4:

Table 4.1: Results of the selected compounds of focused dockings on the nsP2, nsP3 and the glycoprotein envelope.	86
Table 4.2: <i>In vitro</i> antiviral and cytotoxic activities of compounds 4.14-4.20 .	91

Chapter 5:

Table 5.1: Binding properties of compounds 5.1-5.4 .	108
Table 5.2: Transport properties of compounds 5.1-5.5 .	111

Chapter 6:

Figure 6.3: Stack plot of the ¹ H NMR spectrum of receptor 6.3 (2.0 x 10 ⁻³ M) upon titration with chloride (0-17 eq.) added as its tetrabutylammonium salt.	154
Table 6.2: Transport and anion binding properties of compounds 6.1-6.4 .	155

Chapter 7:

Table 7.1: Inhibition data of compounds 7.9 , 7.10-7.16 , 7.17-7.24 and 7.26-7.30 against isoforms hCA I, II, IV and VII by a stopped-flow CO ₂ hydrase assay	180
---	-----

List of Schemes

Chapter 2:

Scheme 2.1: Reagents and conditions: i) NaOEt, C₂H₅OH, 6 h, reflux; ii) ClCH₂COOH, anhydrous CH₃COONa, (CH₃CO)₂, CH₃COOH, 4-chlorobenzaldehyde, reflux, 4 h. 27

Scheme 2.2: Reactions and conditions: i: BrCH₂COOH, anhydrous CH₃COONa, (CH₃CO)₂, CH₃COOH, 60 °C, 3 h; ii: benzaldehyde, anhydrous CH₃COONa, CH₃COOH, 60 °C, 2 h. iii) BrCH₂COOH, anhydrous CH₃COONa, (CH₃CO)₂, CH₃COOH, aldehyde, 60 °C, 4 h. 28

Chapter 3:

Scheme 3.1: Reagents and conditions: i) NaOEt, C₂H₅OH, 6 h, reflux; ii) NaOH, EtOH, CH₃I, 3 h, 50 °C; iii) corresponding aniline, pivalic acid, 130 °C. 51

Scheme 3.2: Reagents and conditions: i) SO₂Cl₂, 0 °C; ii) CH₃COONa/ 0 °C. 52

Scheme 3.3: Reagents and conditions: i) DIPEA, dioxane, 100 °C. 54

Chapter 4:

Scheme 4.1: Reagents and conditions i) 40 mol% PCl₃, xylene, 2 h, reflux ii) CDI, THF, 18 h, rt. 90

Chapter 5:

Scheme 5.1: Reagents and conditions: i) H₃PO₄, 200 °C, 6 h; ii) H₂SO₄/HNO₃ 3 h. 103

Scheme 5.2: Reagents and conditions: i) Na₂S₂O₅, EtOH, RT; ii) DMF, 120 °C, 4 h. 103

Scheme 5.3: Reagents and conditions: i) KAuCl₄, MeOH, NaOAc, reflux; ii) AgOTf, CH₃CN, reflux, 12 h in dark. 105

Chapter 6:

Scheme 6.1: Reagents and conditions: a) ethyl chloroformate/DEE; b) ethyl acetoacetate, 70% H₂SO₄; c) Al(NO₃)₃ · 9 H₂O, acetic anhydride.; d) Conc H₂SO₄, glacial acetic acid, reflux.; e) Sn/HCl, reflux.; f) suitable isocyanate, DCM, 45 °C, or Suitable isocyanate, 45 °C. 152

Chapter 7:

Scheme 7.1: Reagents and conditions: (a) neat reaction, reflux, 15 min; (b) MS 4 Å, piperidine, acetic acid, ethanol, RT, 8 h; (c) NaNO₂/HCl, 0 °C; (d) sodium acetate trihydrate, ethanol, 0 °C; (e) SO₂Cl₂, 0 °C, 1 h then RT for 4 h. 178

Chapter 1:

Introduction

1.1 Biology, re-emergence and pathogenesis of chikungunya virus

1.1.1 Taxonomy of the chikungunya

Arboviruses that mainly use arthropod vectors for transmission between hosts are known as arthropod-borne viruses.^{1, 2} They are classified into five distinctive classes: the three major classes are the *Flaviviridae*, *Bunyaviridae* or *Togaviridae* families, and the remaining two are members of the *Reoviridae* and *Orthomyxoviridae* families (Figure 1.1).³ Figure 1.1 shows some examples of the main five arbovirus families.

The *Togaviridae* family is subdivided into two genera, the *Alphavirus* genus and the *Rubivirus* genus, with the *Alphavirus* genus categorized fundamentally into seven serogroups of which 50% can cause diseases in humans.¹ Chikungunya virus (CHIKV) (*alphavirus* genus, family *Togaviridae*) is one of the prevalent tropical alphaviruses and is transmitted by the *Aedes* mosquito (Figure 1.1).⁴

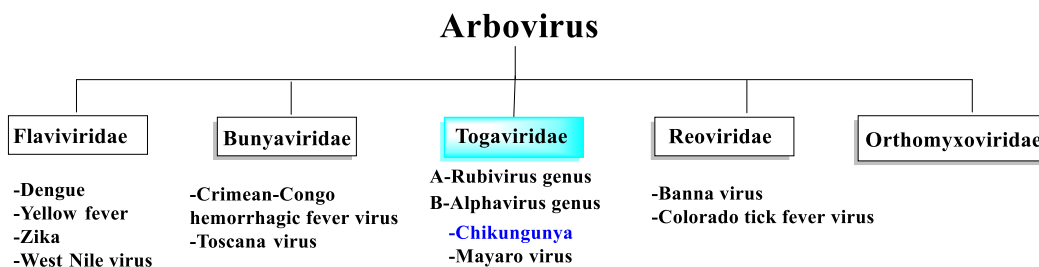


Figure 1.1. Schematic representation of arbovirus subclasses taxonomy.

1.1.2 Origin, re-emergence and spread of the virus

The name chikungunya is a Makonde (one of the ethnic Eastern Africa languages) word that means harsh joints pain, which are symptoms of pathogenesis of chikungunya virus.⁵ The virus was first discovered in 1952-1953 during an

outbreak in eastern Africa.⁵ Between the 1960s and 1970s, major outbreaks were documented in Southeast Asia and India⁶ and in the past sixty years, many intermittent outbreaks re-emerged in Africa and Asia.^{7,8}

There was no major re-emergence of chikungunya fever until the epidemic outbreak in Kenya in 2004, which resulted in considerable mortality and morbidity and infection spreading to neighboring areas.⁴ The spreading of the virus throughout Europe and the Americas arose from the number of adaptive mutations of the virus that allowed exploitation of a new vector (*Aedes albopictus*).⁹

After spreading in Africa and Asia, the virus continued to spread globally throughout Asia, Europe and regions of the Americas.¹⁰ Moreover, some countries in the Pacific have documented epidemics of chikungunya since 2013.¹¹ In late 2014, more than 150 deaths and 750,000 suspected cases were reported in both the north and south American continents, Latin America and Caribbean islands.¹¹ United States of America and Mexico have also documented new cases. In October 2014, there were 4 domestically acquired chikungunya infection patients diagnosed in Southern France.¹¹ In 2018, around 14,000 cases of CHIKV were reported in Sudan, with 95% in Kassala state.¹²

Between Jan-Dec 2019, 56 cases of the virus were diagnosed in Australia according to statistics from the Australian National Communicable Diseases Surveillance (NCDS) report.¹³ Zika and Dengue viruses are also arboviruses in the family *Flaviviridae* and share the same vectors with chikungunya virus.¹⁴ All are transmitted to the human through the bite of an infected *Aedes aegypti* or *Aedes albopictus* mosquito. The spread of these viruses may also trigger the re-emergence of chikungunya virus. During 2019, 1357 Dengue virus infection cases were

diagnosed and at least 13 cases with Zika Virus infection were reported in Australia during 2019 until the date of the report.¹³

1.1.3 Virus lifecycle

CHIKV is a small diameter (about 60–70 nm) positive strand RNA virus that attaches to the host cell by endocytosis in vesicles coated with clathrin (Figure 1.2).¹⁵⁻¹⁷ Under the acidic conditions of the endosome, a cascade of conformational changes of the viral envelope results in dissociation of the E2-E1 heterodimers to assemble the E1 homotrimers that catalyse the fusion to host cell membrane.¹⁸ The viral genome and the core are then delivered into the host cell. Translation of the viral m-RNA produces two precursors of non-structural proteins (nsPs) that are cleaved to non-structural proteins nsP1, nsP2, nsP3 and nsP4.¹⁹ These proteins form a replication complex that serves as the template for the synthesis of 26S subgenomic RNAs and genomic 49S (Figure 1.2).²⁰

The expression of the polyprotein precursor (C-pE2-6K-E1) is encoded in the positive strand of the 26S subgenomic RNA. Subsequently, serine protease in the Golgi complex catalyses the formation of the capsid (C), while the pE2 and E1 glycoproteins are produced by further processing.²¹ The pE2 and E1 are assembled in the Golgi and moved to the plasma membrane and further pE2 is processed into E2 and E3.²² The assembly of the viral cell is initiated in the cytoplasm, where the nucleocapsid is generated and contains 120 dimers of the C protein (Figure 1.2).²³ The assembled virion is formed by the binding of the viral nucleocapsid to the viral RNA and released from the host cell by budding (Figure 1.2).²⁴

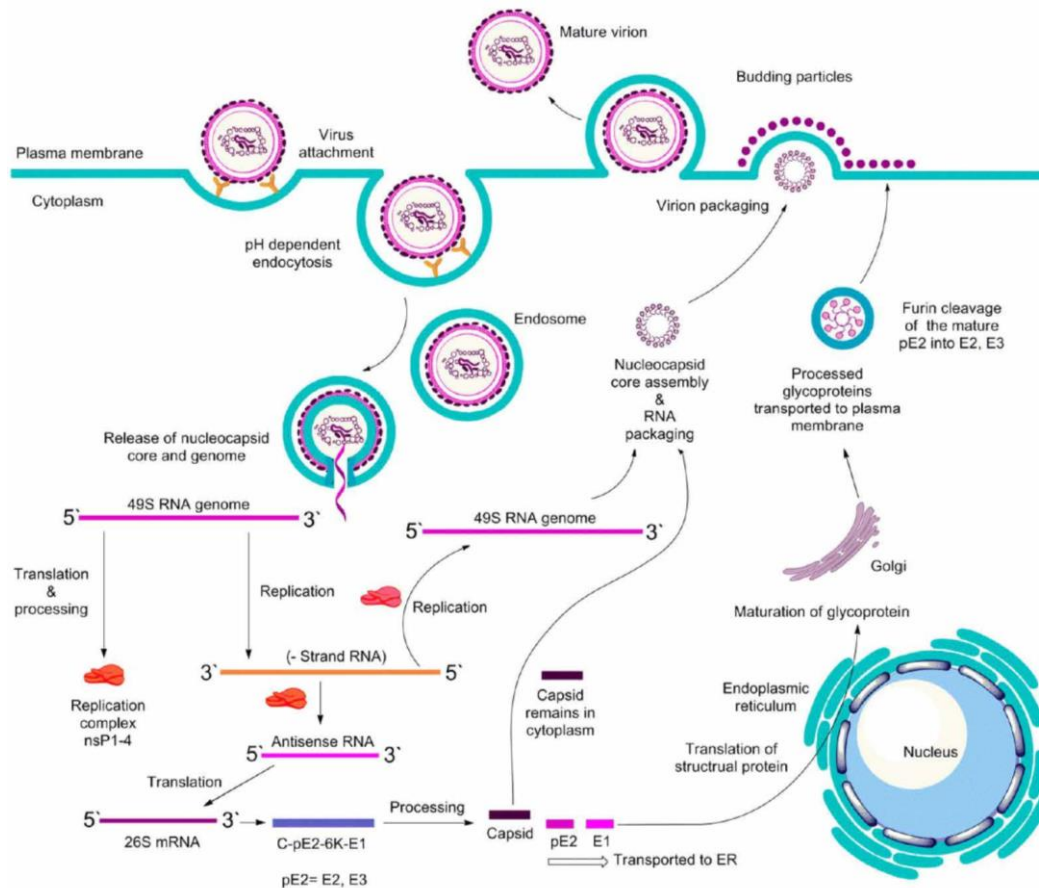


Figure 1.2: Schematic diagram of alphavirus life cycle. Reproduced with permission from reference 4.⁴

1.1.4 Chikungunya fever (CHIKF)

After an incubation period of about 2-4 days, symptoms start with the onset of high fever and severe persistent joint pain that may last for weeks to years.²⁴ Other symptoms of CHIKF include headache, vomiting, rash, myalgia (muscle pain), photophobia and maculopopular rash.^{4, 24, 25} Unlike other arbovirus infections, only around 15% of the patients may encounter “silent infections”. The acute phase of CHIKV infection may last from 1-10 days, while 30-40% of the cases might have recurrent joint pain that can last for years in some cases although this is not likely a result of chronic infection.²⁶ After infection, CHIKV disseminates through the blood stream, replicates in the fibroblasts of the skin, and can affect liver, muscles,

joints, lymphoid tissues (lymph nodes and spleen) and brain. The target cells in each organ are indicated in Table 1.1.²⁴

Table 1.1: Target cells of CHIKV.

	Brain	Joint	Lymphoid tissue	Muscle	Liver
Affected cells	Epithelial and Endothelial cells	Fibroblasts	Stromal cells and Macrophages	Satellite cells and Fibroblasts	Endothelial cells

1.1.5 Possible drug targets

There are multiple druggable targets of the CHIKV that can be categorized into six classes:

a) Structural proteins E1-E3: E1 and E2 CHIKV glycoproteins constitute the icosahedra shell and are involved in the attachment and interaction with the host cell.^{27, 28} The structural protein E3 prevents the earlier attachment of E1-E2 heterodimer with the cell membrane.²⁹ Many studies revealed the importance of 4 conserved amino acid residues in E1, namely Gly91, Val178, Ala226 and His230 to the membrane fusion.³⁰ Mutation of Gly91 or His230 is reported to diminish the attachment of E1 to the host cell.³⁰ Previous computational studies in our laboratory revealed the presence of druggable pockets in these structural proteins.³¹

b) Receptors for CHIKV entry: Viral receptors available as drug targets include prohibitin and glycosaminoglycan which both mediate the viral endocytosis.^{32,33} In addition, heat shock protein 60 (Hsp60) function in the viral cell fusion is not fully studied but could be another conceivable CHIKV antiviral targets.³² Furthermore, clathrin was reported to catalyse the

endocytosis dependent pH.³⁴ Therefore, inhibiting clathrin-mediated endocytosis might be an effective strategy to control viral entry and infection.

c) Non-structural protein 1 (nsP1): Studies on nsp1 revealed the multifunctional roles of this protein.³⁵ It is involved in capping and methylation of the newly formed viral genome as well as fusion with endosomes and lysosomes at the membrane cytoplasmic surface.³⁶ Moreover, it inhibits the bone marrow stromal antigen 2 (BST-2), therefore enhancing the virus attachment at the host cell membrane. BST-2 is induced by interferon (INF α) and it is one of the defensive mechanisms of the host cell.³⁷

d) Non-structural protein 2 (nsP2): The nonstructural protein nsP2 (Figure 1.3) is extensively studied as a possible drug target because of its multifunctionality with various enzymatic activity.^{4, 10} It is a virulence factor which represents a potential target for CHIKV inhibitors, due to its ability to cause a “transcriptional shutoff” (block cellular gene transcription) and impair the host cell defense mechanism.³⁸

The C-terminus of nsp2 contains the protease activity of the viral cell, specifically, cysteine carboxypeptidase activity (cleavage of protein substrates from the C termini) that enables the replication of the viral cell.³⁹ The mechanism of cysteine protease action is initialized by deprotonation of the thiol group of the cysteine residue by a basic amino acid most likely a histidine residue. Cysteines Cys1233 and Cys1290 and the four histidine residues, His1222, His1228, His1229 and His1236 could be associated in the deprotonation mechanism.⁴⁰

The nsp2 enzymatic activities within the N-terminus have been demonstrated. The N-terminal residues catalyse the first RNA capping *via* their

intrinsic RNA triphosphatase activity. Additionally, the N-terminus exhibits nucleotide triphosphatase activity that supplies the RNA helicase with energy.⁴¹

e) **Non-structural protein 3 (nsP3):** The X-ray structure of nsP3 consists of four asymmetric subunits, each composed of six-stranded β -sheets and four α -helices (Figure 1.3).⁴² nsP3 was proposed to promote CHIKV replication by interaction of the host heat shock protein 90 (HSP90).⁴³ The protein consists of an N-domain and C-domain; the N-domain is highly conserved while the C-domain is not.⁴⁴ The C-terminus function was investigated and has been implicated in RNA synthesis.⁴⁴ The N-terminus of nsP3 contains a macrodomain that modulates the metabolism of ADP-ribose and regulates the function in the cell. The alpha virus macrodomain has a positive charge at the pocket of the ADP-ribose, however, it has a negative charge away from the active site (which might interact with the RNA).⁴²

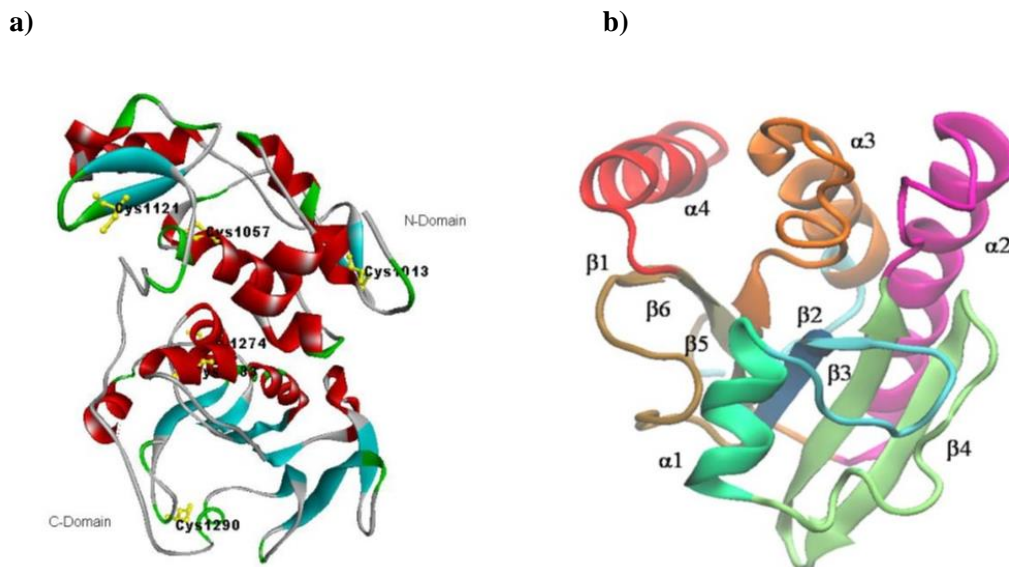


Figure 1.3: a) CHIKV nsP2 crystal structure (PDB id: 3TRK). Reproduced with permission from reference 4. b) The macrodomain (nsP3) of CHIKV (PDB id: 3GPG). Reproduced with permission from reference 42.

f) **Non-structural protein 4 (nsP4):** The exact functions of nsP4 remain ambiguous. A recent study stated that the *alphaviruses* nsP4 might downregulate the host cell unfolding protein response (UPR) by its RNA-dependent-RNA polymerase activity.⁴⁵ UPR is a defense mechanism of the host cell that inhibits the viral replication and protein synthesis.⁴⁶ Therefore, blocking the nsP4 will retain the normal immunological function of the UPR and control the viral infection by enhancing the innate immunity.

1.2 Development of chemotherapeutics against chikungunya virus

1.2.1 Vaccines

Different methods have been utilised to develop vaccines against CHIKV, including the use of inactivated vaccines, live attenuated or live vector virus, virus like particle vaccine, consensus-based DNA vaccine, recombinant subunit vaccines, passive immunization and plant derived vaccines.⁴⁷ Despite these attempts, only one candidate vaccine is in phase II clinical trials in humans.⁴⁸

1.2.2 Hits discovered by virtual screening

The exploitation of the X-ray structures of the CHIKV proteins in the virtual screening of libraries is a promising approach to develop new lead compounds against the chikungunya virus.^{7, 10, 49} *Alphavirus* nsP2 protein is considered an interesting and attractive antiviral drug target due to its crucial role in the replication of the viral cell. In this context, our group discovered NCI_217697 (**1.1**, Figure 1.4), NCI_61610 (**1.2**, Figure 1.3) and NCI_67436 (**1.3**, Figure 1.3) as nsP2 protease inhibitors identified by virtual screening of the NCI Diversity Set II

database.¹⁰ Agarwal *et. al.* reported CID_5808891 (**1.4**, Figure 1.3) as *in silico* nsP2 protease inhibitor (Figure 1.4).⁵⁰

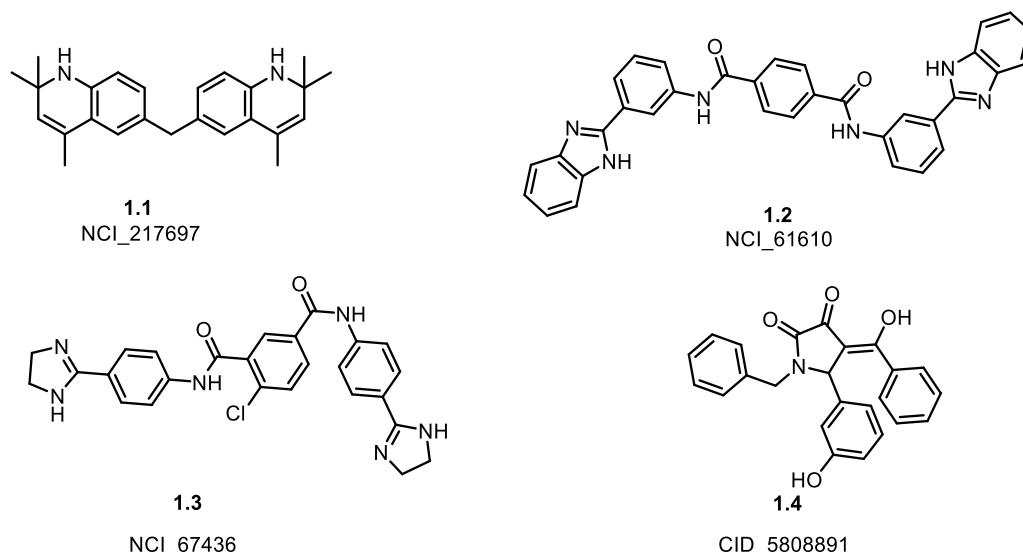
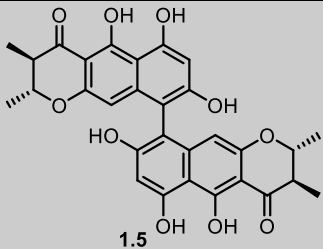
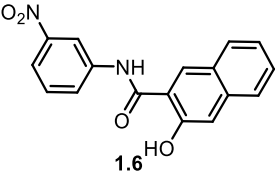
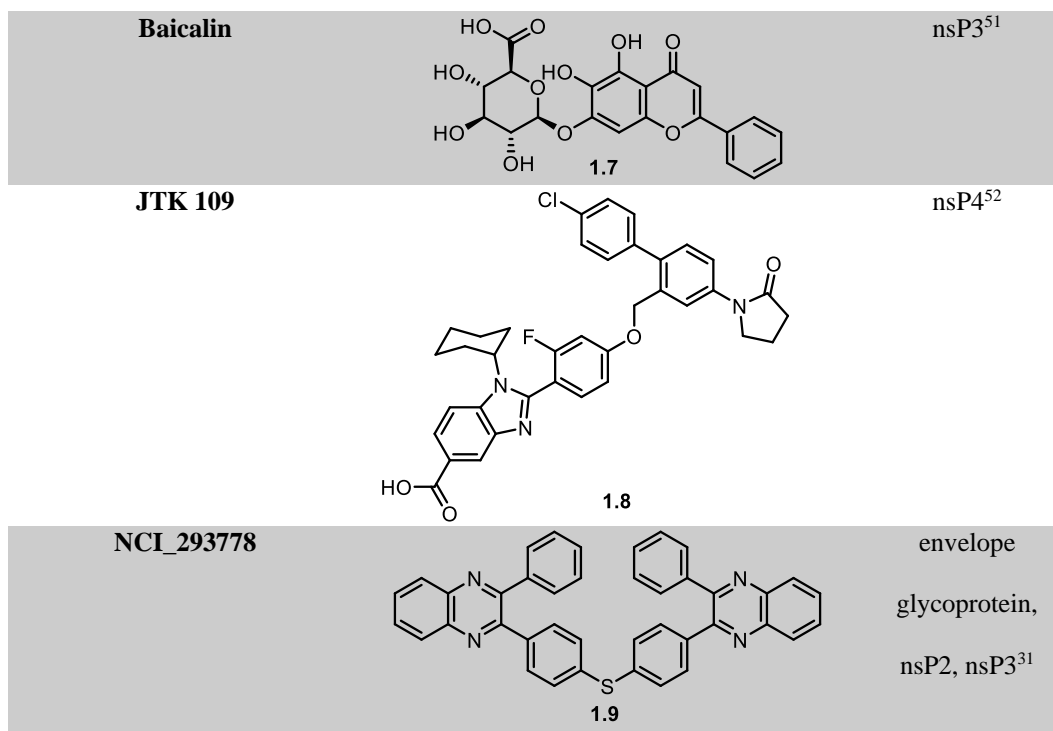


Figure 1.4: Structure of CHIKV nsP2 inhibitors identified by *in silico* studies.

In addition to nsP2, other computational studies performed on CHIKV proteins identified potential inhibitors for nsP3, nsP4 or/and the envelope glycoprotein (Table 1.2).

Table 1.2: The structures of some hit compounds identified by *in silico* studies against CHIKV proteins.

Compounds number or name	Structure	Target
NCI_345647		nsP3 ⁴²
NCI_37168		nsP3 ⁴²



1.2.3 Anti-viral drugs inhibiting CHIKV

The screening of known antiviral drugs against emerging viral infections is a strategy applied mainly when there is no effective chemotherapeutic agent available. Hence, *in vitro* whole cell phenotypic screening of a selection of known drugs revealed examples with anti CHIKV activity (Figure 1.5).^{17, 53-55}

The approved antimalarial drug, chloroquine (Figure 1.5, **1.10**) showed antiviral activity among different viruses including CHIKV,⁵⁶ possibly due to interaction with the endosomes eventually preventing viral fusion to the host cell.⁵⁷ However, it showed no significant activity in a small-scale double-blind placebo-controlled randomized trial.⁵⁸ Therefore, further studies are required to evaluate its effectiveness against the CHIKV.

The anti-viral agent ribavirin, (Figure 1.5, **1.11**) a triazole guanosine analogue, slowed the CHIKV replication in cell culture ($IC_{50} = 83.3$ mg/mL), but complete suppression of CHIKV particles was not observed (Figure 1.5, **1.11**).^{59,17}

Sofosbuvir, (Figure 1.5, **1.12**), is a uridine nucleoside prodrug approved for treatment of HCV in combination with other antiviral drugs.⁶⁰ Evaluation of the antiviral activity of sofosbuvir against CHIKV infection unveiled the potency and selectivity of sofosbuvir over ribavirin in human liver cells infected with CHIKV (Figure 1.5, **1.12**).⁶⁰ It also showed *in vivo* prevention of CHIKV-induced paw edema at a dose of 20 mg/kg/day and with decreased mortality in neonatal mice at doses of 40-80 mg/kg/day.⁶⁰ Arbidol, (Figure 1.5, **1.13**), ($IC_{50} = 12.2$ mg/mL) is an approved antiviral drug for treatment of acute respiratory tract infections that showed a broad spectrum antiviral activity and inhibited arthropod-borne flaviviruses and alphaviruses.^{61, 62} It inhibited CHIKV entry by targeting the E2 viral envelope protein, which is presumably involved in binding to host receptors.⁶³

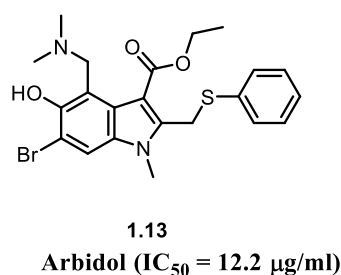
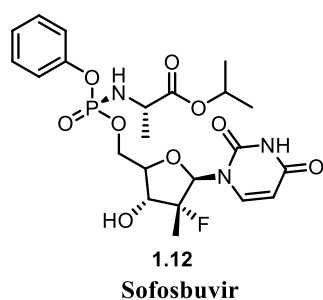
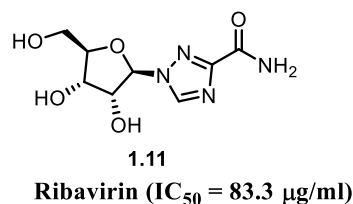
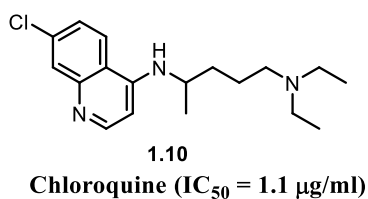


Figure 1.5: Some known drugs inhibiting CHIKV replication.

1.2.4 Genome-wide loss of function screen

A work by Karlas *et. al.* (2016) used a genome wide “loss of function screening” to identify druggable CHIKV targets.⁶⁴ Using a short interfering RNA genome wide screen, they identified 156 proviral and 41 antiviral host factors controlling the viral replication. The study revealed that 21 small molecule inhibitors have high

in vitro antiviral activity along with low toxicity. The screening focused on six proviral factors and pathways namely, i) fatty acid synthesis; ii) the vascular type H^+ ATPase (vATPase); iii) CDC-like kinase (CLK1); iv) fms related tyrosine kinase 4 (FLT4 or VEGFR3); v) calmodulin signalling; vi) the k (lysine) acetyltransferase 5. An example of some of these inhibitors that emerged are represented in Figure 1.6 (1.14 - 1.19). Interestingly, three identified inhibitors (TOFA 1.14 and pimozone 1.15, tivozanib 1.16) achieved prophylaxis against the viral infection in an *in vivo* mouse model.⁶⁴ Tivozanib 1.16, linifanib 1.18 and sorafenib 1.19 (Figure 1.6) are clinically approved tyrosine kinase inhibitors that elicited anti-CHIKV activity in this study.⁶⁴

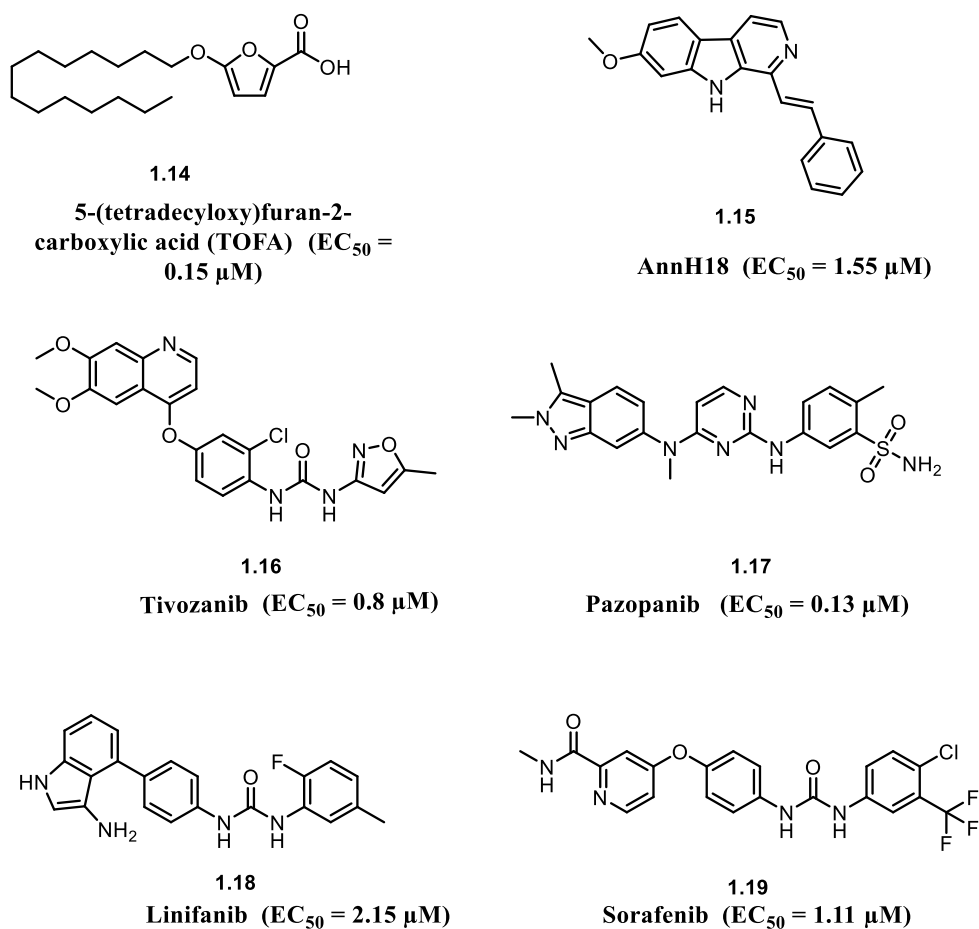


Figure 1.6: Selected CHIKV inhibitors from genome wide-loss of function screens. CHIKV EC_{50} are in parenthesis.

1.2.5 Other inhibitors of the CHIKV

The recent advances and growing knowledge about arboviruses expand our understanding of the CHIKV life cycle, pathogenesis and infection. Intensive research has led to the identification of new chemical scaffolds that might be potential anti CHIKV agents. In 2012, purine- β -lactam **1.20** and **1.21** and purine-amino propanol **1.22** (Figure 1.7) were screened against nine different viruses including CHIKV. The amino propanol derivative **1.22** ($EC_{50} = 11.51 \mu\text{M}$) showed relatively higher activity when compared to the purine- β -lactam. Therefore, the β -lactam is not essential for activity.⁶⁵

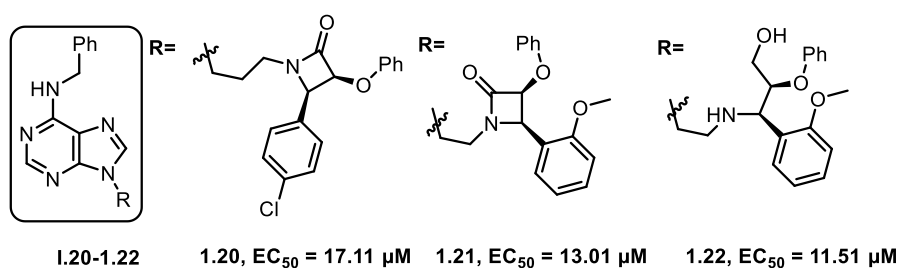


Figure 1.7: Purines as of CHIKV inhibitors.

In an effort to find new leads as CHIKV inhibitors, a random screening identified the [1,2,3]triazolo[4,5-*d*]pyrimidin-7(6*H*)ones as potential candidates.⁶⁶ Iterative optimization cycles led to the most potent compound (**1.23**, Figure 1.8) with $EC_{50} = 3 \mu\text{M}$ and a selectivity index greater than 600. The 3-isopropoxyphenyl triazolopyrimidine derivative (**1.23**, Figure 1.8) may be the first step in the process of development of a clinical drug candidate.⁶⁶ Rhodanine is a thiazolidin-4-one derivative presenting a promiscuous scaffold exhibiting broad antiviral activity against HCV, HIV-1 and chikungunya.⁶⁷ In a recent study, a series of rhodanine derivatives was tested for their anti CHIKV activity by cytopathic effect CPE

reduction assay. Among the tested compounds, the 2-methyl analogue (**1.24**, Figure 1.8) displayed excellent activity with submicromolar EC_{50} . The docking study showed good interaction points between the ligand and CHIKV nsp2 protease.⁶⁷

Non-steroidal anti-inflammatory drugs (NSAID) have been used to alleviate the symptoms of the CHIKF because of the lack of effective prevention or curing of the viral infection. Strikingly, NSAID can not only be used as anti-inflammatories, but also can be considered as antiviral agents.⁵⁹ Individually or in combination with ribavirin, mefenamic acid (anthranilic acid derivative) (**1.25**, Figure 1.8) inhibited the viral replication.⁵⁹ The estimated EC_{50} of the mefenamic acid alone was 13 μM , however the combination of mefenamic acid and ribavirin showed 3 μM inhibition. Ching *et al.* (2015) investigated the synthesis and structure-activity relationship of a class of thieno[3,2-*b*]pyrroles for their antiviral activities and identified trisubstituted thieno[3,2-*b*]pyrrole 5-carboxamide (**1.26**, Figure 1.8) as a potent and broad antiviral agent with limited cytotoxicity. It can effectively inhibit the expression of capsid, E2, nsP1 and nsP3 of the CHIKV.⁶⁸

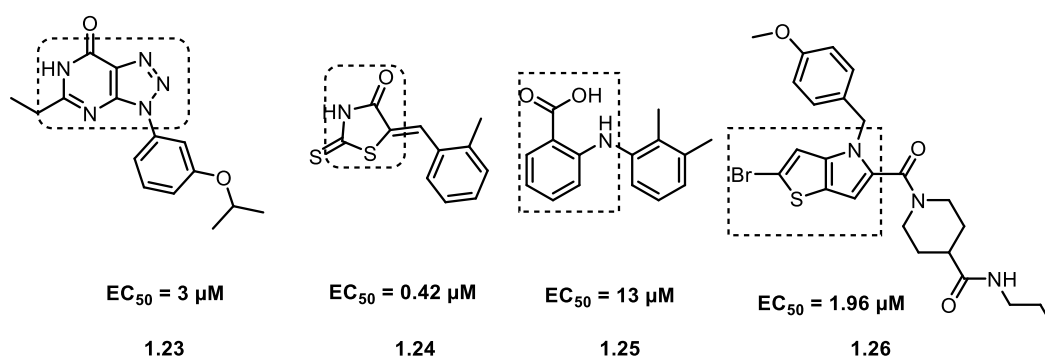


Figure 1.8: Selected CHIKV inhibitors with different scaffolds.

1.3 Thesis plan

1.3.1 Drug design and development cycle

Figure 1.9 shows the drug discovery cycles, where many of the current drug discovery strategies are relied on. Finding leads, for a certain disease, is the first milestone along the way to the introduction of new drug.⁶⁹

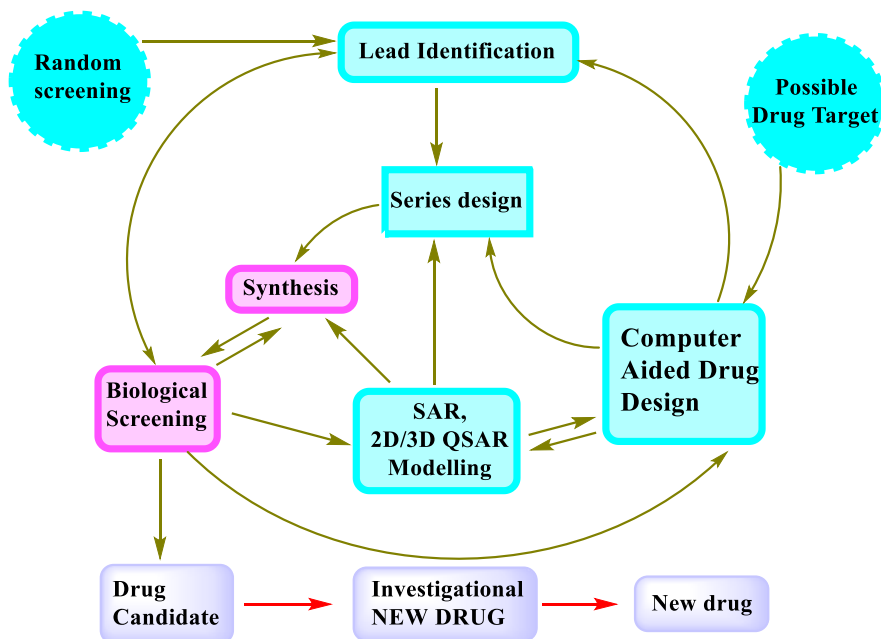


Figure 1.9: Iterative cycle of drug design and lead identification and optimization.

Lead identification is usually obtained by optimization of hits.^{70, 71} A hit is defined as an organic or inorganic molecule that maintains reproducible activity and selectivity in a relevant bioassay. Hit identification could be achieved by random screening of small molecules, including using high throughput screening and fragment-based drug design techniques, *in silico* screening, repurposing of known drugs and *de novo* synthesis.⁷² A lead could be defined as a hit with defined structure activity relationship.⁶⁹ The most challenging aspects in the lead identification include, drug like physicochemical properties, pharmacokinetics (absorption, distribution, metabolism and elimination) and toxicity.^{73, 74} Iterative

cycles of synthesis and biological screening would be performed for the potential lead molecules, followed by clinical trials of the promising compounds (Figure 1.9).⁶⁹

1.3.2 Application to drug design cycle towards anti-CHIKV agents

Strategies to discover antiviral agents have been described previously, however our limited knowledge about the virus impedes drug development and therefore the availability of a clinical anti-CHIKV drug.¹⁷

In this dissertation, one aim was to apply the basic concepts of medicinal chemistry such as hybridization (**Chapter 2**), simplification or bioisosterism (**Chapter 3**) of known inhibitors and the use of structure-guided drug design (**Chapter 4**) as steps in the discovery of unprecedented anti-CHIKV agents (Figure 1.9). The antiviral project design was aimed to follow the general drug design cycles (Figure 1.9).

1.4 References

1. Cleton, N.; Koopmans, M.; Reimerink, J.; Godeke, G. J.; Reusken, C. Come fly with me: Review of clinically important arboviruses for global travelers. *J. Clin. Virol.* **2012**, *55*, 191-203.
2. Huang, Y. S.; Higgs, S.; Vanlandingham, D. L. Arbovirus-mosquito vector-host interactions and the impact on transmission and disease pathogenesis of arboviruses. *Front. Microbiol.* **2019**, *10*, 1-14.
3. Jones, K. E.; Patel, N. G.; Levy, M. A.; Storeygard, A.; Balk, D.; Gittleman, J. L.; Daszak, P. Global trends in emerging infectious diseases. *Nature* **2008**, *451*, 990-993.
4. Rashad, A. A.; Mahalingam, S.; Keller, P. A. Chikungunya virus: Emerging targets and new opportunities for medicinal chemistry. *J. Med. Chem.* **2014**, *57*, 1147-1166.
5. Robinson, M. C. An epidemic of virus disease in southern province, tanganyika territory, in 1952-53. I. Clinical features. *Trans. R. Soc. Trop. Med. Hyg.* **1955**, *49*, 28-32.
6. Pulmanusahakul, R.; Roytrakul, S.; Auewarakul, P.; Smith, D. R. Chikungunya in southeast asia: Understanding the emergence and finding solutions. *Int. J. Infect. Dis.* **2011**, *15*, 671-676.
7. Abdelnabi, R.; Neyts, J.; Delang, L. Towards antivirals against chikungunya virus. *Antivir. Res.* **2015**, *121*, 59-68.
8. Kariuki Njenga, M.; Nderitu, L.; Ledermann, J. P.; Ndirangu, A.; Logue, C. H.; Kelly, C. H.; Sang, R.; Serگون, K.; Breiman, R.; Powers, A. M. Tracking epidemic chikungunya virus into the indian ocean from east africa. *J. Gen. Virol.* **2008**, *89*, 2754-2760.
9. Rudd, P. A.; Mahalingam, S. Fighting back against chikungunya. *Lancet Infect. Dis.* **2015**, *15*, 488-489.
10. Nguyen, P. T.; Yu, H.; Keller, P. A. Identification of chikungunya virus nsp2 protease inhibitors using structure-base approaches. *J. Mol. Graphics Modell.* **2015**, *57*, 1-8.
11. *Investing to overcome the global impact of neglected tropical diseases: Third who report on neglected diseases 2015*; 9241564865; World Health Organization: 2015.
12. *Chikungunya – sudan*; World Health Organization: 2018.
13. National notifiable diseases surveillance system - current cdna fortnightly report. <http://www.health.gov.au/cdnareport>
14. Lazear, H. M.; Diamond, M. S. Zika virus: New clinical syndromes and its emergence in the western hemisphere. *J. Virol.* **2016**, *90*, 4864-4875.
15. Singh, S. K.; Unni, S. K. Chikungunya virus: Host pathogen interaction. *Rev. Med. Virol.* **2011**, *21*, 78-88.
16. Jose, J.; Snyder, J. E.; Kuhn, R. J. A structural and functional perspective of alphavirus replication and assembly. *Future Microbiol.* **2009**, *4*, 837-856.
17. Perez-Perez, M. J.; Delang, L.; Ng, L. F. P.; Priego, E. M. Chikungunya virus drug discovery: Still a long way to go? *Expert Opin. Drug Discov.* **2019**, *14*, 855-866.
18. Sourisseau, M.; Schilte, C.; Casartelli, N.; Trouillet, C.; Guivel-Benhassine, F.; Rudnicka, D.; Sol-Foulon, N.; Le Roux, K.; Prevost, M. C.; Fsihi, H.; Frenkiel, M. P.; Blanchet, F.; Afonso, P. V.; Ceccaldi, P. E.; Ozden, S.; Gessain, A.; Schuffenecker, I.; Verhasselt, B.; Zamborlini, A.; Saib, A.; Rey, F. A.; Arenzana-Seisdedos, F.; Despres, P.; Michault, A.; Albert, M. L.; Schwartz, O. Characterization of reemerging chikungunya virus. *PLoS Pathog.* **2007**, *3*, e89.
19. Barton, D. J.; Sawicki, S. G.; Sawicki, D. L. Solubilization and immunoprecipitation of alphavirus replication complexes. *J. Virol.* **1991**, *65*, 1496-1506.
20. Shirako, Y.; Strauss, J. H. Regulation of sindbis virus rna replication: Uncleaved p123 and nsp4 function in minus-strand RNA synthesis, whereas cleaved products from p123 are required for efficient plus-strand rna synthesis. *J. Virol.* **1994**, *68*, 1874-1885.
21. Schilte, C.; Couderc, T.; Chretien, F.; Sourisseau, M.; Gangneux, N.; Guivel-Benhassine, F.; Kraxner, A.; Tschopp, J.; Higgs, S.; Michault, A.; Arenzana-Seisdedos, F.; Colonna, M.; Peduto, L.; Schwartz, O.; Lecuit, M.; Albert, M. L. Type i ifn controls chikungunya virus via its action on nonhematopoietic cells. *J. Exp. Med.* **2010**, *207*, 429-442.
22. Tang, B. L. The cell biology of chikungunya virus infection. *Cell. Microbiol.* **2012**, *14*, 1354-1363.
23. Perera, R.; Owen, K. E.; Tellinghuisen, T. L.; Gorbalenya, A. E.; Kuhn, R. J. Alphavirus nucleocapsid protein contains a putative coiled coil alpha-helix important for core assembly. *J. Virol.* **2001**, *75*, 1-10.
24. Schwartz, O.; Albert, M. L. Biology and pathogenesis of chikungunya virus. *Nat. Rev. Microbiol.* **2010**, *8*, 491-500.

25. Mahendradas, P.; Avadhani, K.; Shetty, R. Chikungunya and the eye: A review. *J. Ophthalmic Inflamm. Infect.* **2013**, *3*, 1-9.
26. Lemant, J.; Boisson, V.; Winer, A.; Thibault, L.; Andre, H.; Tixier, F.; Lemercier, M.; Antok, E.; Cresta, M. P.; Grivard, P.; Besnard, M.; Rollot, O.; Favier, F.; Huerre, M.; Campinos, J. L.; Michault, A. Serious acute chikungunya virus infection requiring intensive care during the reunion island outbreak in 2005-2006. *Crit. Care. Med.* **2008**, *36*, 2536-2541.
27. Smith, T. J.; Cheng, R. H.; Olson, N. H.; Peterson, P.; Chase, E.; Kuhn, R. J.; Baker, T. S. Putative receptor binding sites on alphaviruses as visualized by cryoelectron microscopy. *Proc. Natl. Acad. Sci. U. S. A.* **1995**, *92*, 10648-10652.
28. Ashbrook, A. W.; Burrack, K. S.; Silva, L. A.; Montgomery, S. A.; Heise, M. T.; Morrison, T. E.; Dermody, T. S. Residue 82 of the chikungunya virus e2 attachment protein modulates viral dissemination and arthritis in mice. *J. Virol.* **2014**, *88*, 12180-12192.
29. Li, L.; Jose, J.; Xiang, Y.; Kuhn, R. J.; Rossmann, M. G. Structural changes of envelope proteins during alphavirus fusion. *Nature* **2010**, *468*, 705-708.
30. Kielian, M.; Chanel-Vos, C.; Liao, M. Alphavirus entry and membrane fusion. *Viruses* **2010**, *2*, 796-825.
31. Nguyen, P. T. V. In silico drug discovery targeting chikungunya virus. University of Wollongong, 2015.
32. Wintachai, P.; Wikan, N.; Kuadkitkan, A.; Jaimipuk, T.; Ubol, S.; Pulmanasahakul, R.; Auewarakul, P.; Kasinrerak, W.; Weng, W. Y.; Panyasrivanit, M.; Paemanee, A.; Kittisenachai, S.; Roytrakul, S.; Smith, D. R. Identification of prohibitin as a chikungunya virus receptor protein. *J. Med. Virol.* **2012**, *84*, 1757-1770.
33. Silva, L. A.; Khomandiak, S.; Ashbrook, A. W.; Weller, R.; Heise, M. T.; Morrison, T. E.; Dermody, T. S. A single-amino-acid polymorphism in chikungunya virus e2 glycoprotein influences glycosaminoglycan utilization. *J. Virol.* **2014**, *88*, 2385-2397.
34. van Duijl-Richter, M. K.; Hoornweg, T. E.; Rodenhuis-Zybert, I. A.; Smit, J. M. Early events in chikungunya virus infection-from virus cell binding to membrane fusion. *Viruses* **2015**, *7*, 3647-3674.
35. Laakkonen, P.; Hyvonen, M.; Peranen, J.; Kaariainen, L. Expression of semliki forest virus nsp1-specific methyltransferase in insect cells and in escherichia coli. *J. Virol.* **1994**, *68*, 7418-7425.
36. Solignat, M.; Gay, B.; Higgs, S.; Briant, L.; Devaux, C. Replication cycle of chikungunya: A re-emerging arbovirus. *Virology* **2009**, *393*, 183-197.
37. Jones, P. H.; Maric, M.; Madison, M. N.; Maury, W.; Roller, R. J.; Okeoma, C. M. Bst-2/tetherin-mediated restriction of chikungunya (chikv) vlp budding is counteracted by chikv non-structural protein 1 (nsp1). *Virology* **2013**, *438*, 37-49.
38. Breakwell, L.; Dosenovic, P.; Karlsson Hedestam, G. B.; D'Amato, M.; Liljestrom, P.; Fazakerley, J.; McInerney, G. M. Semliki forest virus nonstructural protein 2 is involved in suppression of the type I interferon response. *J. Virol.* **2007**, *81*, 8677-8684.
39. Lulla, A.; Lulla, V.; Tints, K.; Ahola, T.; Merits, A. Molecular determinants of substrate specificity for semliki forest virus nonstructural protease. *J. Virol.* **2006**, *80*, 5413-5422.
40. Russo, A. T.; Malmstrom, R. D.; White, M. A.; Watowich, S. J. Structural basis for substrate specificity of alphavirus nsp2 proteases. *J. Mol. Graphics Modell.* **2010**, *29*, 46-53.
41. Karpe, Y. A.; Aher, P. P.; Lole, K. S. Ntpase and 5'-rna triphosphatase activities of chikungunya virus nsp2 protein. *PLoS One* **2011**, *6*, e22336.
42. Nguyen, P. T.; Yu, H.; Keller, P. A. Discovery of in silico hits targeting the nsp3 macro domain of chikungunya virus. *J. Mol. Model.* **2014**, *20*, 1-12.
43. Rathore, A. P.; Haystead, T.; Das, P. K.; Merits, A.; Ng, M. L.; Vasudevan, S. G. Chikungunya virus nsp3 & nsp4 interacts with hsp-90 to promote virus replication: Hsp-90 inhibitors reduce chikv infection and inflammation in vivo. *Antivir. Res.* **2014**, *103*, 7-16.
44. Malet, H.; Coutard, B.; Jamal, S.; Dutartre, H.; Papageorgiou, N.; Neuvonen, M.; Ahola, T.; Forrester, N.; Gould, E. A.; Lafitte, D.; Ferron, F.; Lescar, J.; Gorbalenya, A. E.; de Lamballerie, X.; Canard, B. The crystal structures of chikungunya and venezuelan equine encephalitis virus nsp3 macro domains define a conserved adenosine binding pocket. *J. Virol.* **2009**, *83*, 6534-6545.
45. Tardif, K. D.; Waris, G.; Siddiqui, A. Hepatitis c virus, er stress, and oxidative stress. *Trends Microbiol.* **2005**, *13*, 159-163.
46. Rathore, A. P.; Ng, M. L.; Vasudevan, S. G. Differential unfolded protein response during chikungunya and sindbis virus infection: Chikv nsp4 suppresses eif2alpha phosphorylation. *Virol. J.* **2013**, *10*, 1-15.
47. Morrison, T. E. Reemergence of chikungunya virus. *J. Virol.* **2014**, *88*, 11644-11647.

48. Chang, L. J.; Dowd, K. A.; Mendoza, F. H.; Saunders, J. G.; Sitar, S.; Plummer, S. H.; Yamshchikov, G.; Sarwar, U. N.; Hu, Z.; Enama, M. E.; Bailer, R. T.; Koup, R. A.; Schwartz, R. M.; Akahata, W.; Nabel, G. J.; Mascola, J. R.; Pierson, T. C.; Graham, B. S.; Ledgerwood, J. E.; Team, V. R. C. S. Safety and tolerability of chikungunya virus-like particle vaccine in healthy adults: A phase 1 dose-escalation trial. *Lancet* **2014**, 384, 2046-2052.
49. Subudhi, B.; Chattopadhyay, S.; Mishra, P.; Kumar, A. Current strategies for inhibition of chikungunya infection. *Viruses* **2018**, 10, 1-40.
50. Agarwal, T.; Asthana, S.; Bissoyi, A. Molecular modeling and docking study to elucidate novel chikungunya virus nsp2 protease inhibitors. *Indian J. Pharm. Sci.* **2015**, 77, 453-460.
51. Seyedi, S. S.; Shukri, M.; Hassandarvish, P.; Oo, A.; Muthu, S. E.; Abubakar, S.; Zandi, K. Computational approach towards exploring potential anti-chikungunya activity of selected flavonoids. *Sci. Rep.* **2016**, 6, 24027.
52. Kumar, S. P.; Kapopara, R. G.; Patni, M. I.; Pandya, H. A.; Jasrai, Y. T.; Patel, S. K. Exploring the polymerase activity of chikungunya viral non structural protein 4 (nsp4) using molecular modeling, epharmacophore and docking studies. *Int. J. Pharm. Life Sci.* **2012**, 3, 1752-1765.
53. Maheshwari, R. K.; Srikantan, V.; Bhartiya, D. Chloroquine enhances replication of semliki forest virus and encephalomyocarditis virus in mice. *J. Virol.* **1991**, 65, 992-995.
54. Ravichandran, R.; Manian, M. Ribavirin therapy for chikungunya arthritis. *J. Infect. Dev. Ctries.* **2008**, 2, 140-142.
55. Sweeney, M. J.; Hoffman, D. H.; Esterman, M. A. Metabolism and biochemistry of mycophenolic acid. *Cancer Res.* **1972**, 32, 1803-1809.
56. Khan, M.; Santhosh, S.; Tiwari, M.; Lakshmana Rao, P.; Parida, M. Assessment of in vitro prophylactic and therapeutic efficacy of chloroquine against chikungunya virus in vero cells. *J. Med. Virol.* **2010**, 82, 817-824.
57. Bernard, E.; Solignat, M.; Gay, B.; Chazal, N.; Higgs, S.; Devaux, C.; Briant, L. Endocytosis of chikungunya virus into mammalian cells: Role of clathrin and early endosomal compartments. *PLoS one* **2010**, 5, e11479.
58. Lamballerie, X. D.; Boisson, V.; Reynier, J.-C.; Enault, S.; Charrel, R. N.; Flahault, A.; Roques, P.; Grand, R. L. On chikungunya acute infection and chloroquine treatment. *Vector Borne Zoonotic Dis.* **2008**, 8, 837-840.
59. Rothan, H. A.; Bahrani, H.; Abdulrahman, A. Y.; Mohamed, Z.; Teoh, T. C.; Othman, S.; Rashid, N. N.; Rahman, N. A.; Yusof, R. Mefenamic acid in combination with ribavirin shows significant effects in reducing chikungunya virus infection in vitro and in vivo. *Antivir. Res.* **2016**, 127, 50-56.
60. Ferreira, A. C.; Reis, P. A.; de Freitas, C. S.; Sacramento, C. Q.; Villas Boas Hoelz, L.; Bastos, M. M.; Mattos, M.; Rocha, N.; Gomes de Azevedo Quintanilha, I.; da Silva Gouveia Pedrosa, C.; Rocha Quintino Souza, L.; Correia Loiola, E.; Trindade, P.; Rangel Vieira, Y.; Barbosa-Lima, G.; de Castro Faria Neto, H. C.; Boechat, N.; Rehen, S. K.; Bruning, K.; Bozza, F. A.; Bozza, P. T.; Souza, T. M. L. Beyond members of the flaviviridae family, sofosbuvir also inhibits chikungunya virus replication. *Antimicrob. Agents Chemother.* **2019**, 63, 1-15.
61. Boriskin, Y. S.; Leneva, I. A.; Pecheur, E. I.; Polyak, S. J. Arbidol: A broad-spectrum antiviral compound that blocks viral fusion. *Curr. Med. Chem.* **2008**, 15, 997-1005.
62. Haviernik, J.; Stefanik, M.; Fojtikova, M.; Kali, S.; Tordo, N.; Rudolf, I.; Hubalek, Z.; Eyer, L.; Ruzek, D. Arbidol (umifenovir): A broad-spectrum antiviral drug that inhibits medically important arthropod-borne flaviviruses. *Viruses* **2018**, 10, 1-8.
63. Delogu, I.; Pastorino, B.; Baronti, C.; Nougairede, A.; Bonnet, E.; de Lamballerie, X. In vitro antiviral activity of arbidol against chikungunya virus and characteristics of a selected resistant mutant. *Antivir. Res.* **2011**, 90, 99-107.
64. Karlas, A.; Berre, S.; Couderc, T.; Varjak, M.; Braun, P.; Meyer, M.; Gangneux, N.; Karo-Astover, L.; Weege, F.; Raftery, M.; Schonrich, G.; Klemm, U.; Wurzlbauer, A.; Bracher, F.; Merits, A.; Meyer, T. F.; Lecuit, M. A human genome-wide loss-of-function screen identifies effective chikungunya antiviral drugs. *Nat. Commun.* **2016**, 7, 1-14.
65. D'Hooghe, M.; Mollet, K.; De Vreese, R.; Jonckers, T. H.; Dams, G.; De Kimpe, N. Design, synthesis, and antiviral evaluation of purine-beta-lactam and purine-aminopropanol hybrids. *J. Med. Chem.* **2012**, 55, 5637-5641.
66. Gigante, A.; Canela, M. D.; Delang, L.; Priego, E. M.; Camarasa, M. J.; Querat, G.; Neyts, J.; Leyssen, P.; Perez-Perez, M. J. Identification of [1,2,3]triazolo[4,5-d]pyrimidin-7(6H)-ones as novel inhibitors of chikungunya virus replication. *J. Med. Chem.* **2014**, 57, 4000-4008.
67. Jadav, S. S.; Sinha, B. N.; Hilgenfeld, R.; Pastorino, B.; de Lamballerie, X.; Jayaprakash,

- V. Thiazolidone derivatives as inhibitors of chikungunya virus. *Eur. J. Med. Chem.* **2015**, 89, 172-178.
68. Ching, K. C.; Kam, Y. W.; Merits, A.; Ng, L. F.; Chai, C. L. Trisubstituted thieno[3,2-*b*]pyrrole 5-carboxamides as potent inhibitors of alphaviruses. *J. Med. Chem.* **2015**, 58, 9196-9213.
69. Bleicher, K. H.; Böhm, H.-J.; Müller, K.; Alanine, A. I. Hit and lead generation: Beyond high-throughput screening. *Nat. Rev. Drug Discov.* **2003**, 2, 369-378.
70. Baxter, A.; Cooper, A.; Kinchin, E.; Moakes, K.; Unitt, J.; Wallace, A. Hit-to-lead studies: The discovery of potent, orally bioavailable thiazolopyrimidine cxcr2 receptor antagonists. *Bioorg. Med. Chem. Lett.* **2006**, 16, 960-963.
71. Comess, K. M.; Schurdak, M. E. Affinity-based screening techniques for enhancing lead discovery. *Curr. Opin. Drug Discov. Devel.* **2004**, 7, 411-416.
72. Bohacek, R. S.; McMartin, C.; Guida, W. C. The art and practice of structure-based drug design: A molecular modeling perspective. *Med. Res. Rev.* **1996**, 16, 3-50.
73. Lipinski, C. A.; Lombardo, F.; Dominy, B. W.; Feeney, P. J. Experimental and computational approaches to estimate solubility and permeability in drug discovery and development settings. *Adv. Drug Deliv. Rev.* **1997**, 23, 3-25.
74. Bocci, G.; Carosati, E.; Vayer, P.; Arrault, A.; Lozano, S.; Cruciani, G. Adme-space: A new tool for medicinal chemists to explore adme properties. *Sci. Rep.* **2017**, 7, 1-13.

Chapter 2:

**Application of the hybridization
concept towards anti-CHIKV
agents**

FOREWORD TO CHAPTER 2

This chapter is published, in the *RSC Advances*, 2020, 10, 5191-5195 (impact factor 3.049) (doi: 10.1039/D0RA00257G). This paper describes the convergent and regioselective synthesis of thiazolo[3,2-*a*]pyrimidines as potential anti-chikungunya agents. Density functional theory (DFT) calculations were performed to investigate the observed preference for the *Z* isomer, using the widely applied M06-2X functional with a Dunning's aug-cc-pVDZ basis set. Appendix material pertaining to this chapter can be found in Appendix A (p. 211).

Contributions

Mohamed Fares	Compound design, performed the work and analysis, input into experimental design and prepared/edited the paper
Patrick M. McCosker	Performed and analysed DFT study
Timothy Clark	
Anthony C. Willis	Performed and solved the X-ray structure
Muhammad A. Alsherbiny	Performed the cytotoxicity assay.
Johan Neyts	Performed the antiviral evaluation
Dirk Jochmans	
Paul A. Keller	Oversight of the project, editing and proof-reading

2.1 Introduction

Arboviruses mainly use arthropod vectors for transmission between hosts and they are considered a growing global health threat.^{1, 2} This arises from the increasing number of international travellers, from 450 million in 1990 to nearly 1.4 billion in 2018, and consequently travel-related diseases incidence has increased significantly.³ Chikungunya virus (CHIKV) (*alphavirus* genus, family *Togaviridae*) is one of the prevalent tropical alphaviruses that is transmitted by the *Aedes* mosquitoes.^{4, 5} After an incubation period of 2-4 days, symptoms start with the onset of high fever and severe persistent joint pain that may last for weeks to years.^{6, 7} Other symptoms of chikungunya fever (CHIKF) include headache, vomiting, rash, myalgia (muscle pain), photophobia and maculopopular rash.^{6, 8} Unlike other arbovirus infections, around 15% of the patients may encounter “silent infections”.⁶

A variety of strategies have been applied to develop anti-CHIKV treatments, including vaccines, and for small molecule inhibitors, random screening, computer aided drug design, ligand-based drug design, high throughput screening and Genome-Wide loss of function screens.⁹⁻¹⁷ Non-steroidal anti-inflammatory drugs (NSAID) have been used to alleviate the symptoms of the CHIKF because of the lack of effective prevention or curing of the viral infection.¹⁸ However, so far there is no vaccine or approved medication to prevent or treat CHIKV infection.

The recent advances and growing knowledge about the arboviruses expand our understanding of the CHIKV life cycle, pathogenesis and infection.¹⁻⁶ Intensive research in the past 10 years has led to the identification of new chemical scaffolds that might be potential anti CHIKV agents. Rhodanin **2.1** is a thiazolidin-4-one derivative, presenting a scaffold that exhibited broad antiviral activity against

HCV, HIV-1 and chikungunya (**2.1**, Figure 2.1).¹⁹ A series of rhodanine derivatives was tested for their anti-CHIKV activity by a cytopathic effect (CPE) reduction assay (Figure 2.1). The 2-methyl analogue **2.2** emerged as the best compound and displayed excellent activity with submicromolar EC₅₀ (EC₅₀ = 0.42 μM) against CHIKV. A docking study also showed good interaction between the ligand and CHIKV nsp2 protease.¹⁹

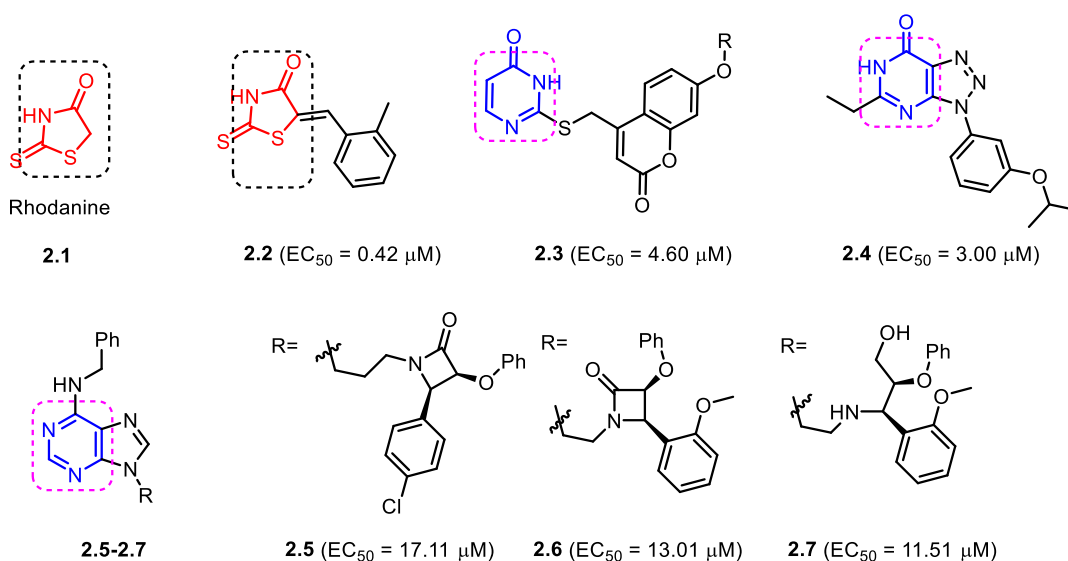


Figure 2.1: Examples of heterocyclic classes showing anti-CHIKV activity, including thiazolidineone **2.1** and **2.2**, pyrimidine **2.3** and pyrimidine fused rings **2.4** and **2.5-2.7**.

Among the main heterocycles that form the basis of small molecule inhibitors of CHIKV are the pyrimidine and fused pyrimidine rings, *e.g.* **2.3**, **2.4** and **2.5-2.7** (Figure 2.1).^{15, 20, 21} Recent reports indicated that hybridization between uracil-coumarin-arenes **2.3** resulted in the discovery of a novel anti-CHIKV scaffold that was found to impede CHIKV replication.²⁰ In an effort to find new leads as CHIKV inhibitors, a random screening identified the [1,2,3]triazolo[4,5-*d*]pyrimidin-7(6*H*)ones as potential candidates.²¹ Iterative optimization cycles led to the most potent compound **2.4** with EC₅₀ = 3 μM and a selectivity index greater than 600 (Figure 2.1).²¹ In 2012, purine-β-lactams **2.5** and **2.6** and purine-amino propanol

2.7 (Figure 2.1) conjugates were screened against nine different viruses including CHIKV. The amino propanol derivative **2.7** ($EC_{50} = 11.51-17.11 \mu\text{M}$) showed relatively higher activity when compared to the purine- β -lactam hybrids. Therefore, the β -lactam was not essential for activity.¹⁵

Recently, hybridization of two or more bioactive fragments has emerged as a concept for the exploration of novel multitarget acting inhibitors as well as novel anti CHIKV agents (Figure 2.2).^{15, 20, 22, 23} Therefore, in our ongoing efforts to discover new scaffolds for CHIKV infection, we investigated a molecular hybridization approach with the fusion of the uracil and the rhodanine pharmacophoric moieties (Figure 2.2).²²

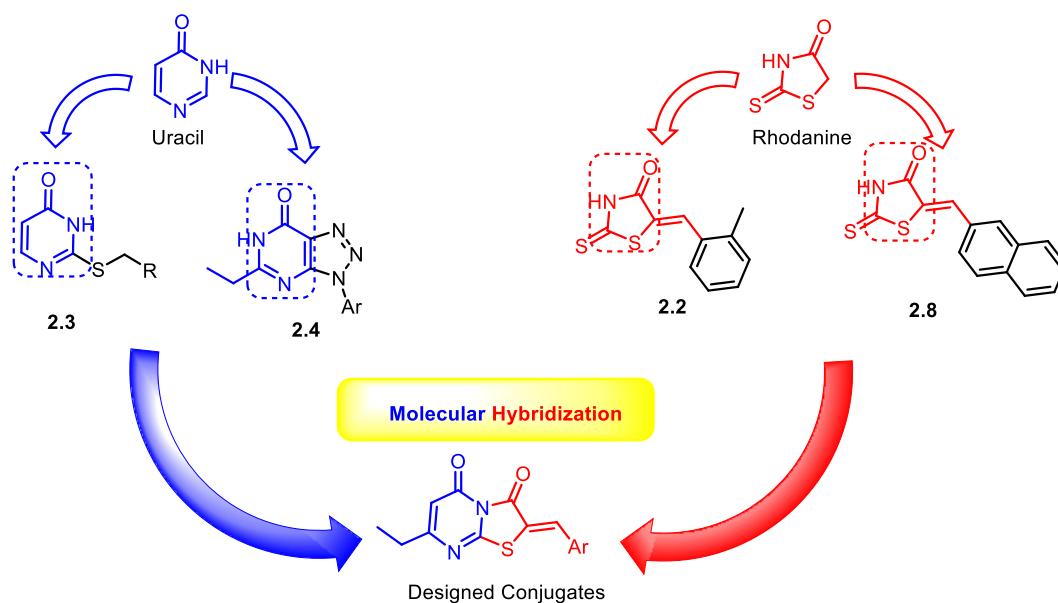
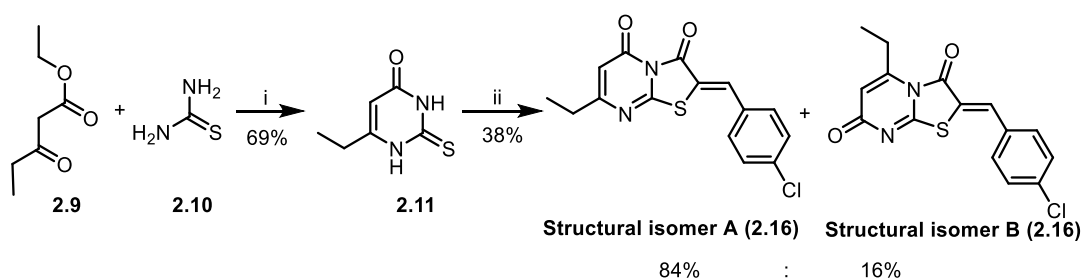


Figure 2.2: Design of the targeted Uracil-Rhodanine conjugates.

2.2 Results and discussion

The synthetic strategy started with the condensation of ethyl propionylacetate **2.9** and thiourea **2.10** to afford the known 6-ethyl-2-thiouracil **2.11** with 69% yield.²⁴

²⁵ Although the synthesis of the thiazolopyrimidine derivatives from the 6-ethyl-2-thiouracil substrate has not previously been reported, this multi-component reaction (MCR) was achieved using an analogous procedure²⁶⁻²⁹ by reacting **2.11** with the aldehyde, chloroacetic acid, sodium acetate anhydrous, acetic anhydride and acetic acid in one pot and at reflux for 4 h (Scheme 2.1).



Scheme 2.1: Reagents and conditions: i) NaOEt, C₂H₅OH, 6 h, reflux; ii) ClCH₂COOH, anhydrous CH₃COONa, (CH₃CO)₂, CH₃COOH, 4-chlorobenzaldehyde, reflux, 4 h.

These conditions consistently gave low yields and two configurational isomers (*e.g.* chlorobenzaldehyde **2.16** *E:Z* 16%:84%), the latter determined by analysis of the ¹H NMR spectrum (Figure 2.3) – attempts to separate the isomers by column chromatography failed.

Optimization of the reaction involved varying the mode of addition, replacement of the chloroacetic acid with bromoacetic acid, and lowering the reaction temperature. This aimed to favour the formation of the kinetic regioisomer (*Z*)-A, assumed to be the desired product, over the thermodynamic regioisomer (*Z*)-B (scheme 2.2), and resulted in the crystallization of only one regioisomer from the reaction mix (acetic acid) in each case. This may be due to lower regioselectivity of the chloroacetic acid compared to bromoacetic acid.

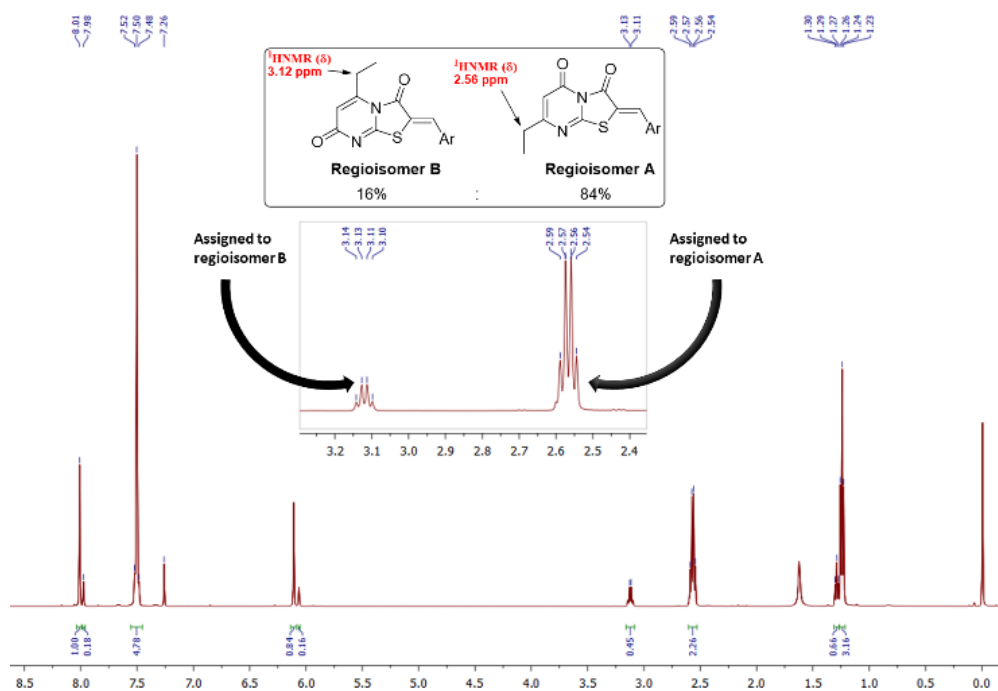
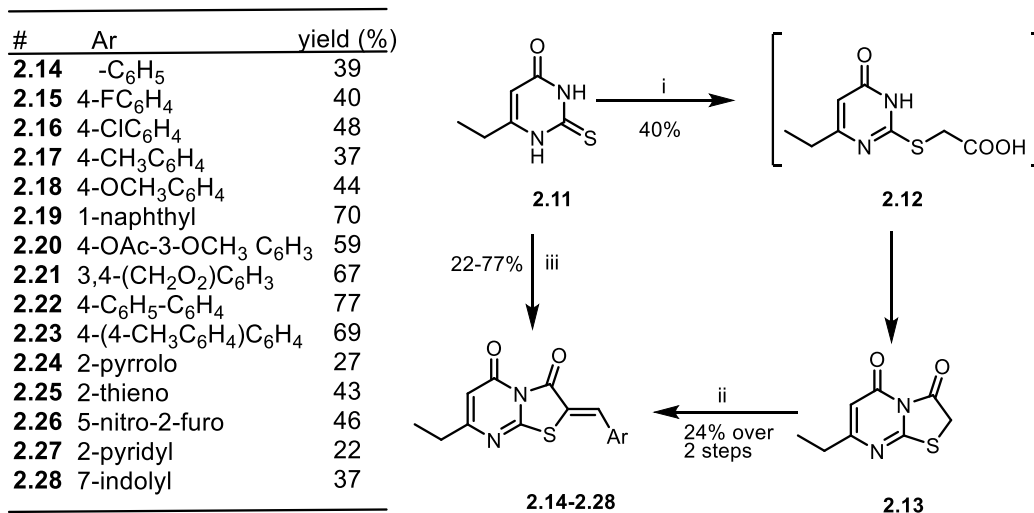


Figure 2.3: ^1H NMR spectrum of the MCR product of the two regioisomers of **2.16** in a ratio of 1:5.



Scheme 2.2: Reactions and conditions: i: BrCH₂COOH, anhydrous CH₃COONa, (CH₃CO)₂, CH₃COOH, 60 °C, 3 h; ii: Benzaldehyde, anhydrous CH₃COONa, CH₃COOH, 60 °C, 2 h. iii) BrCH₂COOH, anhydrous CH₃COONa, (CH₃CO)₂, CH₃COOH, aldehyde, 60 °C, 4 h.

From the convergent reaction conditions, four possible isomers can be formed: the *Z* or *E* configurations of structural isomers A or B – (*Z*)-A, (*E*)-A, (*Z*)-B and (*E*)-B

(Figure 2.4). Analysis of the ^1H NMR spectra showed a quartet at 2.48-2.57 ppm assigned to methylene hydrogens of the ethyl substituent – these were assigned to structural isomer A as a result of the adjacent carbonyl group and the sp^2 nitrogen atom (of the pyrimidine ring). The corresponding resonances of isomer B are expected to resonate more downfield (~ 3 ppm) as a result of the additional deshielding anisotropic effect of the adjacent carbonyl group of the thiazole ring.

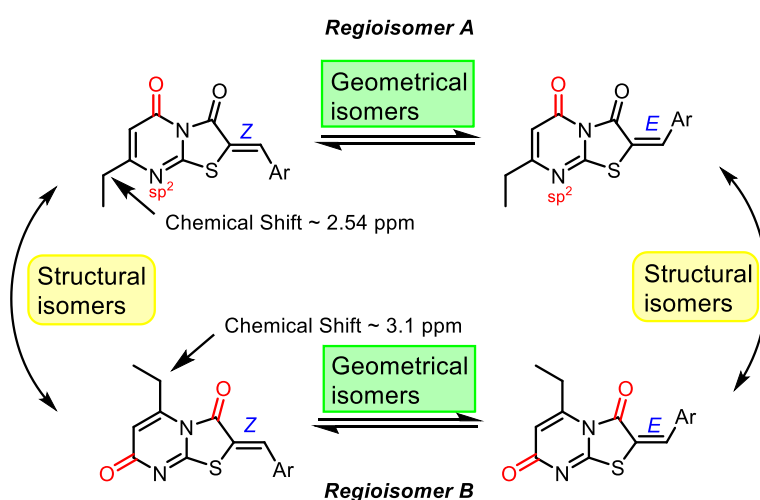


Figure 2.4: The four possible isomers that can be produced from the MCR reaction.

The *Z* absolute configuration of this class of molecules was confirmed by X-ray crystallographic analysis of derivative **2.20** (Figure 2.5). This illustrated the planarity of the thiazolopyrimidine rings with the aryl group, which may be attributed to two intramolecular hydrogen bonds. The *Z*-configuration is presumably stabilized by the two intramolecular hydrogen bonds between the arylidene H and the oxygen atom of the thiazole carbonyl group (HB1) and between the sulfur atom and the aryl hydrogen (HB2). The distance of both hydrogen bonds is 2.49 and 2.50 Å, for HB1 and HB2, respectively, and the angles are 102.81° and 132.94° for HB1 and HB2 respectively.

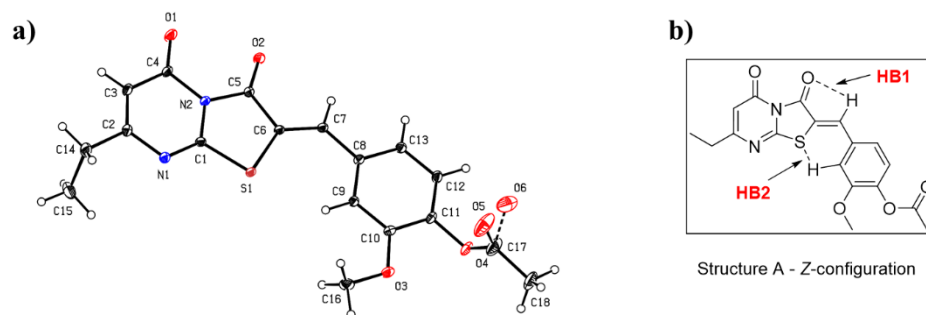


Figure 2.5: a) ORTEP diagram of compound **2.20**, b) Representation of stabilizing hydrogen bonds of the regioisomer **ZA**.

To investigate the observed preference for the *Z* isomer, density functional theory (DFT) calculations were performed using the widely applied M06-2X functional with a Dunning's aug-cc-pVDZ basis set. Compound **2.14** (Ar = C₆H₆) was selected for the theoretical study and all structures were optimised using acetic acid solvation modelling (SMD). Analysis of the proposed mechanism indicated a possible alcohol intermediate and dehydration step preceded the final *Z/E* isomer formation, and to keep the model simple, the calculations focussed on these molecules only, maintaining chirality where applicable (Figure 2.6).

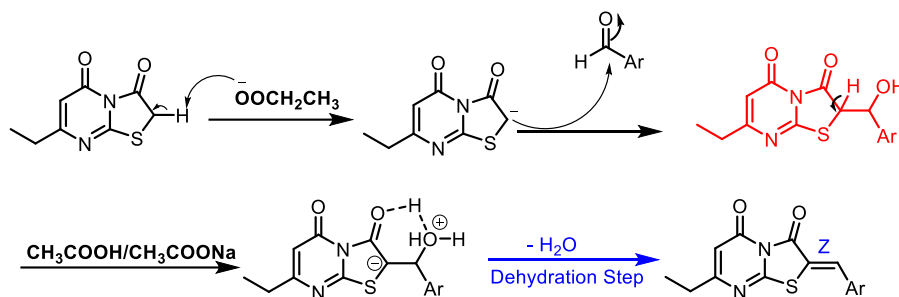


Figure 2.6: Proposed mechanism for the synthesis of isomers *Z* and *E*, the alcohol intermediate of interest (red) and the dehydration step (blue) are highlighted. Note the *Z* isomer is the product of the reaction in this example.

Conformer analysis of the alcohol intermediate indicated a Gibbs free energy of reaction ($\Delta_r G^0(298\text{K})$) range of +0.35 to -2.30 kcal.mol⁻¹ with the *Z* arranged **C1** being the lowest and the *E* arranged **C2** the highest energy conformers respectively

(Figure 2.7). Analysis of the optimised geometries gave no indication of hydrogen bond stabilisation for the alcohol, despite attempts at manually inputting the conformation. This indicated steric and geometric arrangement of the alcohol intermediate is more significant for the energy term.

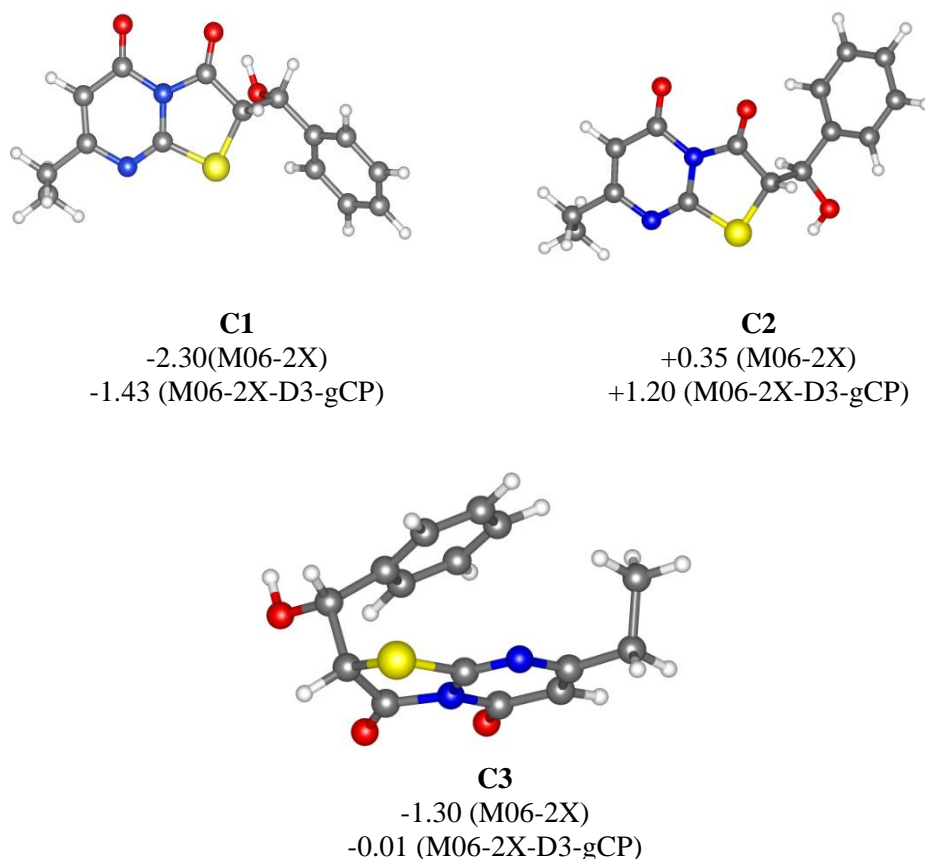


Figure 2.7: Structures of three alcohol intermediate conformers (**C1** – **C3**) investigated. $\Delta_r G^0$ (298 K) energies calculated relative to the starting materials, Compound **2.13** and benzaldehyde, in kcal.mol^{-1} . All methods employed the aug-cc-pVDZ basis set.

A stacked ring conformer (**C3**) was also observed with a favourable $\Delta_r G^0$ (298K) of $-1.30 \text{ kcal.mol}^{-1}$. To better account for this interaction, Grimmes dispersion (D3) and geometric counterpoise (gCP) corrections³⁰ were applied to the energy term, and the stacked **C3** was observed to increase by $+1.29 \text{ kcal.mol}^{-1}$, whereas **C1/C2** increased by $+0.87$ and $+0.85 \text{ kcal.mol}^{-1}$ respectively. The similar increase to the

energy term for **C1/C2** suggested there are no differences in dispersion effects to account for in these conformers. However, the greater energy change observed with **C3** was indicative the ring stacking is not a favourable intramolecular force. Based on the subtle differences in energies of the conformers, **C1** is the apparent favoured alcohol intermediate conformer, which is arranged to dehydrate to the *Z* isomer.

The transition states of the proposed dehydration reactions were calculated and the saddle point $\Delta_r G^0(298\text{K})$ were found to be +32.58 and +30.05 kcal.mol⁻¹ for the *E* **T1** and *Z* **T2** arranged transition states respectively (Figure 2.7). With the D3-gCP corrections $\Delta_r G^0(298\text{K})$ were +33.51 and +30.90 kcal.mol⁻¹ for **T1** and **T2** respectively. The similar increases in energy (+0.93 and +0.85 kcal.mol⁻¹) indicated negligible differences in dispersion force correction required when comparing **T1** and **T2**. What was particularly interesting to note, in contrast to the alcohol intermediate, is the preference of the water leaving hydrogen bound to the carbonyl. Despite attempts in manually positioning the water to leave adjacent to the sulfur, and in turn have H – S interaction, the transition state only converged to allow hydrogen bonding of the water with the thiazole carbonyl. Subsequently, it was proposed the principal factor dictating the favoured transition state is the arrangement of the aryl group, as the water has apparent preference for leaving *trans* to the sulfur, in favour of *Z* isomer formation. Subsequent calculation of the product (*E*)-**2.14** and (*Z*)-**2.14** isomers indicated $\Delta_r H^0(298\text{K})$ of -2.40 and -6.78 kcal.mol⁻¹ respectively, which indicates the *Z* isomer to be thermodynamically favoured, and D3-gCP corrections were in good agreement (Figure 2.8). Comparison of the calculated (*Z*)-**6** structure with the X-ray crystal structure of compound **2.14** indicated similar bond distances of H.B 1 = 2.43 Å and H.B 2 = 2.50 Å for the proposed intramolecular hydrogen bonds (Figure 2.5).

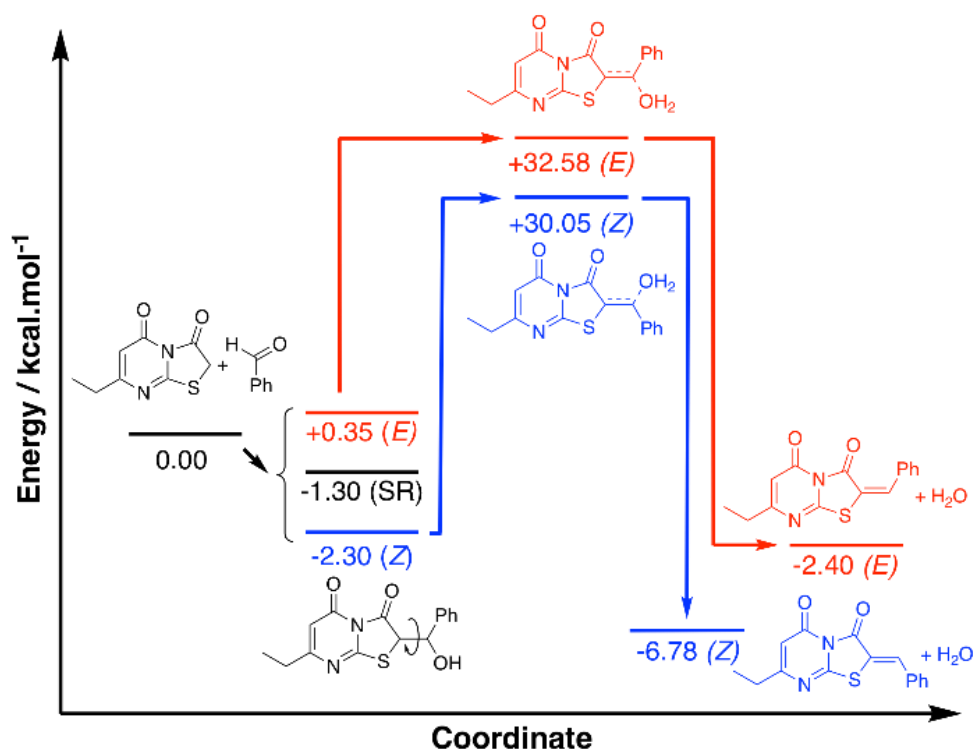


Figure 2.8: Energy profile for the formation of compound **2.14(Z)** and **2.14(E)**, calculated with DFT M06-2X/aug-cc-pVDZ. Divergent reaction pathways are colour coded red for *E* formation and blue for *Z* formation. SR = stacked rings conformer.

Likewise, the bond angles were in good agreement for H.B 1 and H.B 2 calculated at 101.34° and 127.70°, compared with 102.81° and 132.94° from the crystal structure, respectively. In conclusion, although the energy differences are small between the investigated reaction pathways, there is a consistent preference for the *Z* forming pathway at each step investigated and this result was reciprocated by D3-gCP energy corrections (Figure 2.8).

The compounds were screened for their antiviral activities in a viral-cell based assay against chikungunya virus (Indian Ocean strain 899) (Table 2.1). Based on the biological results, compounds **2.14-2.28** showed different percentages of viral replication inhibition at 20 µg/mL with (*Z*)-7-ethyl-2-((4'-methyl-[1,1'-biphenyl]-4-yl)methylene)-5*H*-thiazolo[3,2-*a*]pyrimidine-3,5(2*H*)-dione **2.23** showing the best activity with 58% inhibition of CHIKV replication. Derivatives **2.14**, **2.19** and

2.28 showed 19, 28 and 34% inhibition of viral replication, whilst rest of the compounds showed fair or no activity. However, thiazolidione **2.23** can be considered as a potential lead compound in our future iterative cycles of optimization. The compound emerged as the most promising antiviral among the tested series with $EC_{50} = 42 \mu\text{M}$, with $IC_{50} > 250 \mu\text{M}$ against the breast cancer cell line MCF-7 and the endothelial human sapiens cell line EA.hy926. Compound **2.23** is endowed with *p*-methylbiphenyl tail functionality which might interact favourably with the target. Our outlook will include optimization of compound **2.23** with the prime aim to find safe and effective anti-CHIKV agents.

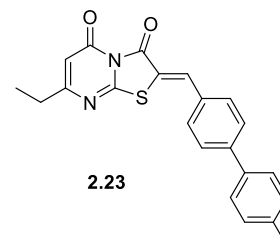
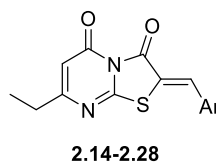


Table 2.1. The observed %inhibition of CHIKV activity of the novel compounds **2.14-2.26**.



Compound	Ar	% inhibition at 20 $\mu\text{g/mL}$	EC_{50} (μM)
2.14	-C ₆ H ₅	19	ND
2.15	4-FC ₆ H ₄	ND	ND
2.16	4-ClC ₆ H ₄	ND	ND
2.17	4-CH ₃ C ₆ H ₄	ND	ND
2.18	4-OCH ₃ C ₆ H ₄	4.3	ND
2.19	1-Naphthyl	29	ND
2.20	4-OAc-3-OCH ₃ C ₆ H ₃	5.5	ND
2.21	3,4-(OCH ₂ O)C ₆ H ₃	ND	ND
2.22	4-C ₆ H ₅ -C ₆ H ₄	5.0	ND
2.23	4(4-CH ₃ C ₆ H ₄)C ₆ H ₄	58	42
2.24	2-Pyrrolo	ND	ND
2.25	2-Thieno	5	ND
2.26	2-Nitro-2-furo	10	ND
2.27	2-Pyridyl	13	ND
2.28	7-Indolyl	34	ND

ND: not determined; EC_{50} : concentration of compound that inhibits virus-induced cell death with 50%.

2.3 Conclusions

In this chapter, we reported the convergent synthesis of a new series of 2-arylidene thiazolo[3,2-*a*]pyrimidines. Using simple synthons, namely 6-ethylthiouracil, bromoacetic acid and different aldehydes in a mixture of acetic acid/acetic anhydride and catalytic amount of anhydrous sodium acetate, a novel series of (*Z*)-7-ethyl-2-arylidene-5*H*-thiazolo[3,2-*a*]pyrimidine-3,5(2*H*)-diones was achieved. Optimization of the multi-component reaction conditions was achieved by replacing chloroacetic acid with the more regioselective bromoacetic acid, lowering reaction temperature and changing the mode of addition and we were able to prepare one isomer at each case. X-ray crystal structure of compound **2.20** shows that only one regioselective isomer formed with the *Z* configuration that is potentially stabilized by two intramolecular hydrogen bonds. Antiviral activity evaluation demonstrated the tailed thiazolodione **2.23** as a candidate for future development.

2.4 Experimental section

2.4.1 Chemistry

General methods and material

All reagents and solvents were purified and dried by standard techniques. Melting points were measured with a Stuart apparatus and were uncorrected. Reactions were monitored by TLC analysis using silica gel GF/UV 254. NMR spectra were recorded on Varian Gemini-300BB 500 MHz FT-NMR spectrometers (Varian Inc., Palo Alto, CA). ¹H spectra were run at 500 MHz and ¹³C spectra were run at 126 MHz, in deuterated dimethylsulfoxide (DMSO-*d*₆), (CD₃)₂CO and CDCl₃. Chemical shifts (δ_{H}) are reported relative to TMS as internal standard and coupling

constant (J) values are reported in Hertz. The abbreviations used are as follows: s, singlet; d, doublet; t, triplet; m, multiplet. Electrospray ionization (ESI single quadrupole) mass spectra have their ion mass to charge values (m/z) stated with their relative abundances as a percentage in parentheses. Peaks assigned to the molecular ion are denoted as $[M+H]^+$ or $[M+Na]^+$. Column chromatography was performed using silica gel 60 (0.063-0.200 mm). All reagents and solvents were purified and dried by standard techniques.

6-Ethyl-2-thioxo-2,3-dihydropyrimidin-4(1H)-one (2.11):

After preparing a sodium ethoxide solution by dissolving sodium (4.6 g, 0.1 mole) in absolute ethanol (150 mL), the thiourea **2.10** (3.8 g, 0.05 mole) was added with stirring till complete dissolution. The ethyl 3-oxopentanoate ester **2.9** (7.21 g, 0.05 mole) was then added and the reaction mixture was heated at reflux for 4 hours. After cooling the reaction mixture, water was added dropwise till complete dissolution of the formed white precipitate. Ice was added, and neutralization of the alkaline solution was accomplished using HCl (5 M). The reaction flask left overnight in the fridge and the formed white precipitate was filtered, washed thoroughly 3 times with water and 2 times with diethyl ether and dried to give **2.11** (5.38 g, 69%) as a white powder. In some cases, when glacial acetic acid was used instead of HCl as neutralizing agent, **2.11** was obtained as pink powder. m.p: 230 °C; ^1H NMR ($(\text{CD}_3)_2\text{SO}_2$) δ : 1.07 (t, $J = 7.5$ Hz, 3H, CH_3), 2.33 (q, $J = 7.5$ Hz, 2H, CH_2), 5.33 (s, 1H, pyridine-H), 12.30 (br s, 2H, 2 x -NH); ^{13}C NMR (CD_3OD): 13.4, 27.8, 103.9, 162.0, 165.8, 179.4; MS (ESI): 157 (20%, $\text{M}+\text{H}^+$), 179 (100%, $\text{M}+\text{Na}^+$).

7-Ethyl-5H-thiazolo[3,2-*a*]pyrimidine-3,5(2H)-dione (2.13):

A previously dried sodium acetate (82 mg, 1 mmol) was added to a suspension of 6-ethyl-2-thioxo-2,3-dihydropyrimidin-4(1*H*)-one **2.11** (156 mg, 1 mmol) and bromoacetic acid (153 mg, 1.1 mmol) in glacial acetic acid (2 mL) and acetic anhydride (1 mL). The reaction flask was heated gently at no more than 60 °C for 3 h. The formed precipitate was filtered while hot and washed thoroughly with water (3 x 10 mL) and diethyl ether (2 x 5 mL) and dried to afford **2.13** (79 mg, 40%) as a white solid. ¹H NMR ((CD₃)₂CO) δ: 1.19 (t, *J* = 7.5 Hz, 3H, CH₃), 2.49 (q, *J* = 7.5 Hz, 2H, CH₂), 4.02 (s, 2H, CH₂), 6.02 (s, 1H, pyridine-H); ¹³C NMR ((CD₃)₂CO): 11.5, 30.0, 32.4, 105.7, 147.3, 163.6, 169.0, 169.3; MS (ESI): 197 (25%, M+H)⁺, 219 (100%, M+Na)⁺; HRMS (ESI) calcd for C₈H₉N₂O₂S: 197.0381 found 197.0385.

General procedures for the synthesis of 2-aryl-7-ethyl-5H-thiazolo[3,2-*a*]pyrimidine-3,5(2H)-dione (2.14-2.28):

Method A: A previously dried sodium acetate (164 mg, 2 mmol) sample was added to a solution of 6-ethyl-2-thioxo-2,3-dihydropyrimidin-4(1*H*)-one **2.11** (156 mg, 1 mmol), corresponding aldehyde (1.1 mmol) and bromoacetic acid (153 mg, 1.1 mmol) in glacial acetic acid (2 mL) and acetic anhydride (1 mL). After gentle heating at no more than 60 °C, the reaction was monitored using TLC analysis till consumption of the starting material or until conversion was observed to stall. Heating was then discontinued, and the reaction mixture was filtered while hot and the residue washed with water (3 × 10 mL), and diethyl ether (2 × 10 mL) then dried to give the desired thiazolopyrimidine **2.14-2.28**.

Method B: A previously dried sodium acetate (82 mg, 1 mmol) was added to a suspension of 7-ethyl-5*H*-thiazolo[3,2-*a*]pyrimidine-3,5(2*H*)-dione (196 mg, 1 mmol) **2.13** in glacial acetic acid, and 1.1 mmol of the appropriate aldehyde was added and the mixture was gently heated at less than 60 °C. The reaction was monitored by TLC and the workup was similar to method A.

(*Z*)-2-benzylidene-7-ethyl-5*H*-thiazolo[3,2-*a*]pyrimidine-3,5(2*H*)-dione (2.14):

The compound was prepared according to method A (yield = 39%) and method B (yield = 24% over 2 steps); m.p: 170 °C; ¹H NMR (CDCl₃) δ: 1.24 (t, *J* = 7.5 Hz, 3H, CH₃), 2.54 (q, *J* = 7.5 Hz, 2H, CH₂), 6.10 (s, 1H, pyridine-H), 7.50-7.54 (m, 3H, ArH), 7.58 (d, *J* = 7.5 Hz, 2H, ArH), 8.07 (s, 1H, arylidene H); ¹³C NMR (CDCl₃): 11.7, 30.5, 108.9, 118.6, 129.6, 130.8, 131.4, 133.1, 137.4, 158.2, 158.9, 163.2, 168.4; MS (ESI): 285 (60%, M+H)⁺, 307 (100%, M+Na)⁺, 323 (70%, M+K)⁺; HRMS (ESI) calcd for C₁₅H₁₂N₂O₂SNa: 307.0502, found: 307.0517.

(*Z*)-7-ethyl-2-(4-fluorobenzylidene)-5*H*-thiazolo[3,2-*a*]pyrimidine-3,5(2*H*)-

dione (2.15): The compound was prepared according to method A (yield = 40%) m.p: 210 °C; ¹H NMR (CDCl₃) δ: 1.23 (t, *J* = 7.5 Hz, 3H, CH₃), 2.56 (q, *J* = 7.5 Hz, 2H, CH₂), 6.11 (s, 1H, pyridine-H), 7.21 (t, *J* = 8.5 Hz, 2H, Ar-H), 7.56 (dd, *J* = 8.5, 5.3 Hz, 2H, Ar-H), 8.01 (s, 1H, arylidene H); ¹³C NMR (CDCl₃) δ: 11.6, 30.3, 108.8, 116.8 (d, *J*²_{C-F} 21 Hz), 118.1, 129.3, 132.8 (d, *J*³_{C-F} 9 Hz), 135.9, 157.7, 158.7, 163.0, 163.0 (d, *J*¹_{C-F} 267 Hz), 168.3; MS (ESI): 303 (10%, M+H)⁺, 325 (65%, M+Na)⁺, 627 (100%, 2M+Na)⁺; HRMS (ESI) calcd for C₁₅H₁₂FN₂O₂S: 303.0618, found: 303.0604.

(Z)-2-(4-chlorobenzylidene)-7-ethyl-5H-thiazolo[3,2-a]pyrimidine-3,5(2H)-dione (2.16): The compound was prepared according to method A (yield = 48%); m.p: 184 °C; ¹H NMR (CDCl₃) δ: 1.23 (t, *J* = 7.5 Hz, 3H, CH₃), 2.55 (q, *J* = 7.5 Hz, 2H, CH₂), 6.12 (s, 1H, pyridine-H), 7.50 (m, 4H, ArH), 8.02 (s, 1H, arylidene H); ¹³C NMR (CDCl₃): 11.6, 30.4, 108.9, 119.1, 129.8, 131.4, 131.8, 135.7, 137.5, 157.6, 158.6, 162.9, 168.3; MS (ESI): 319 (20%, M+H)⁺, 341 (100%, M+Na)⁺, 357 (25%, M+K)⁺; HRMS (ESI) calcd for C₁₅H₁₁ClN₂O₂SNa: 319.0302 found: 319.0308.

(Z)-7-ethyl-2-(4-methylbenzylidene)-5H-thiazolo[3,2-a]pyrimidine-3,5(2H)-dione (2.17): The compound was prepared according to method A (yield = 37%) m.p: 180 °C; ¹H NMR (CDCl₃) δ: 1.24 (t, *J* = 7.5 Hz, 3H, CH₃), 2.42 (s, 3H, CH₃), 2.56 (q, *J* = 7.5 Hz, 2H, CH₂), 6.09 (s, 1H, pyridine-H), 7.31 (d, *J* = 8.0 Hz, 2H, Ar-H), 7.46 (d, *J* = 8.0 Hz, 2H, Ar-H), 8.04 (s, 1H, arylidene H); ¹³C NMR (CDCl₃) δ: 11.6, 21.7, 30.4, 108.7, 117.1, 130.2, 130.2, 130.9, 137.5, 142.4, 158.2, 158.8, 163.2, 168.2; MS (ESI): 299 (7%, M+H)⁺, 321 (35%, M+Na)⁺, 619 (100%, 2M+Na)⁺; HRMS (ESI) calcd for C₁₆H₁₄N₂O₂SNa: 321.0688, found: 321.0674.

(Z)-7-ethyl-2-(4-methoxybenzylidene)-5H-thiazolo[3,2-a]pyrimidine-3,5(2H)-dione (2.18): The compound was prepared according to method A (yield = 44%) m.p: 168 °C; ¹H NMR (CDCl₃) δ: 1.23 (t, *J* = 7.5 Hz, 3H, CH₃), 2.56 (q, *J* = 7.5 Hz, 2H, CH₂), 3.89 (s, 3H, OCH₃), 6.05-6.10 (m, 3H, pyridine-H + OCH₂O), 7.02 (d, *J* = 9.0 Hz, 2H, ArH), 7.53 (d, *J* = 9.0 Hz, 2H, ArH), 8.01 (s, 1H, arylidene H); ¹³C NMR (CDCl₃): 11.6, 30.3, 55.6, 108.5, 115.0, 115.1, 125.6, 132.9, 137.2, 158.3, 158.9, 162.2, 163.2, 168.2; MS (ESI): 315 (10%, M+H)⁺, 337 (25%,

$M+Na)^+$, 651 (100%, $2M+Na)^+$; HRMS (ESI) calcd for $C_{16}H_{14}N_2O_3SNa$: 337.0606
found: 337.0623.

(Z)-7-ethyl-2-(naphthalen-1-ylmethylene)-5H-thiazolo[3,2-*a*]pyrimidine-

3,5(2H)-dione (2.19): The compound was prepared according to method A (yield = 70%) m.p: 175 °C; 1H NMR ($CDCl_3$) δ : 1.24 (t, $J = 7.5$ Hz, 3H, CH_3), 2.56 (q, $J = 7.5$ Hz, 2H, CH_2), 6.26 (s, 1H, pyridine-H), 7.57-7.67 (m, 3H, Ar-H), 7.73 (d, $J = 7.0$ Hz, 1H, Ar-H), 7.92 (d, $J = 8.0$ Hz, 1H, Ar-H), 7.98 (d, $J = 8.0$ Hz, 1H, Ar-H), 8.14 (d, $J = 8.5$ Hz, 1H, Ar-H), 8.82 (s, 1H, arylidene H); ^{13}C NMR ($CDCl_3$) δ : 11.7, 30.5, 108.8, 121.6, 123.5, 125.4, 127.2 (2C), 127.9, 129.2, 130.3, 131.9, 132.1, 133.9, 134.4, 158.5, 159.0, 162.8, 168.4; MS (ESI): 335 (20%, $M+H)^+$, 691 (100%, $2M+Na)^+$; HRMS (ESI) calcd for $C_{19}H_{15}N_2O_2S$: 335.0849, found: 335.0854.

(Z)-4-((7-ethyl-3,5-dioxo-5H-thiazolo[3,2-*a*]pyrimidin-2(3H)-ylidene)methyl)-

2-methoxyphenyl acetate (2.20): The compound was prepared according to method A (yield = 59%) m.p: 208 °C; 1H NMR ($CDCl_3$) δ : 1.24 (t, $J = 7.5$ Hz, 3H, CH_3), 2.34 (s, 3H, $COCH_3$), 2.56 (q, $J = 7.5$ Hz, 2H, CH_2), 3.90 (s, 3H, OCH_3), 6.10 (s, 1H, pyridine-H), 7.13 (s, 1H, Ar-H), 7.18 (s, 2H, Ar-H), 8.01 (s, 1H, arylidene H); ^{13}C NMR ($CDCl_3$) δ : 11.0, 20.0, 29.8, 55.4, 108.2, 113.4, 117.9, 123.1, 123.3, 131.2, 135.9, 141.5, 151.2, 157.2, 158.0, 162.3, 167.6, 167.9; MS (ESI): 373 (15%, $M+H)^+$, 767 (100%, $2M+Na)^+$; HRMS (ESI) calcd for $C_{18}H_{17}N_2O_5S$: 373.0862, found: 373.0858.

(Z)-2-(benzo[*d*][1,3]dioxol-5-ylmethylene)-7-ethyl-5*H*-thiazolo[3,2-*a*]pyrimidine-3,5(2*H*)-dione (2.21): The compound was prepared according to method A (yield = 67%) m.p: 206 °C; ¹H NMR (CDCl₃) δ: 1.23 (t, *J* = 7.5 Hz, 3H, CH₃), 2.55 (q, *J* = 7.5 Hz, 2H, CH₂), 6.07-6.10 (m, 3H, pyridine-H + OCH₂O), 6.93 (d, *J* = 8.3 Hz, 1H, Ar-H), 7.02 (s, 1H, Ar-H), 7.12 (d, *J* = 8.3 Hz, 1H, Ar-H), 7.95 (s, 1H, arylidene H); ¹³C NMR (CDCl₃) δ: 11.7, 30.5, 120.3, 108.7, 109.4, 109.5, 115.9, 127.4, 127.8, 137.3, 148.9, 150.6, 158.2, 158.9, 163.2, 168.3; MS (ESI): 351 (70%, M+Na)⁺, 679 (100%, 2M+Na)⁺; HRMS (ESI) calcd for C₁₆H₁₂N₂O₄SNa: 351.0405, found: 351.0415.

(Z)-2-([1,1'-biphenyl]-4-ylmethylene)-7-ethyl-5*H*-thiazolo[3,2-*a*]pyrimidine-3,5(2*H*)-dione (2.22): The compound was prepared according to method A (yield = 77%) m.p: 172 °C; ¹H NMR (CDCl₃) δ: 1.23 (t, *J* = 7.5 Hz, 3H, CH₃), 2.55 (q, *J* = 7.5 Hz, 2H, CH₂), 6.08 (s, 1H, pyridine-H), 7.39-7.42 (m, 1H, ArH), 7.47 (t, *J* = 7.5 Hz, 2H, ArH), 7.62-7.64 (m, 4H, ArH), 7.74 (d, *J* = 8.0 Hz, 2H, ArH), 8.07 (s, 1H, arylidene H); ¹³C NMR (CDCl₃) δ: 11.7, 30.4, 108.8, 118.1, 127.2, 128.0, 128.5, 129.2, 131.4, 131.8, 136.9, 139.5, 144.0, 158.1, 158.8, 163.1, 168.3; MS (ESI): 383 (70%, M+Na)⁺, 743 (100%, 2M+Na)⁺; HRMS (ESI) calcd for C₂₁H₁₆N₂O₂SNa: 383.0837, found: 383.0830.

(Z)-7-ethyl-2-((4'-methyl-[1,1'-biphenyl]-4-yl)methylene)-5*H*-thiazolo[3,2-*a*]pyrimidine-3,5(2*H*)-dione (2.23): The compound was prepared according to method A (yield = 69%) m.p: 218 °C; ¹H NMR (CDCl₃) δ: 1.24 (t, *J* = 7.5 Hz, 3H, CH₃), 2.56 (q, *J* = 7.5 Hz, 2H, CH₂), 7.28 (d, *J* = 7.8 Hz, 2H, ArH), 7.54 (d, *J* = 7.8 Hz, 2H, ArH), 7.62 (d, *J* = 8.1 Hz, 2H, ArH), 7.73 (d, *J* = 8.1 Hz, 2H, ArH), 8.08

(s, 1H, arylidene H); ^{13}C NMR (CDCl_3) δ : 11.7, 21.3, 30.5, 108.8, 117.9, 127.1, 127.8, 129.9, 131.5, 131.6, 136.6, 137.0, 138.6, 144.1, 158.2, 158.9, 163.2, 168.3; MS (ESI): 375 (65%, $\text{M}+\text{H}^+$), 397 (75%, $\text{M}+\text{Na}^+$), 771 (100%, $2\text{M}+\text{Na}^+$); HRMS (ESI) calcd for $\text{C}_{22}\text{H}_{18}\text{N}_2\text{O}_2\text{SNa}$: 397.0996, found: 397.0987.

(Z)-2-((1H-pyrrol-2-yl)methylene)-7-ethyl-5H-thiazolo[3,2-a]pyrimidine-

3,5(2H)-dione (2.24): The compound was prepared according to method A (yield = 27%) m.p: 220 °C; ^1H NMR ($\text{DMSO}-d_6$) δ : 1.15 (t, $J = 7.5$ Hz, 3H, CH_3), 2.48 (q, $J = 7.5$ Hz, 2H, CH_2), 6.05 (s, 1H, pyridine-H), 6.44 (s, 1H, ArH), 6.66 (s, 1H, ArH), 7.32 (s, 1H, ArH), 7.89 (s, 1H, arylidene H), 11.86 (br s, 1H, NH); ^{13}C NMR ($\text{DMSO}-d_6$) δ : 12.3, 30.1, 108.6, 110.8, 113.5, 116.1, 126.1, 126.8, 128.0, 159.0, 159.3, 163.5, 167.9; MS (ESI): 274 (10%, $\text{M}+\text{H}^+$), 296 (40%, $\text{M}+\text{Na}^+$), 569 (15%, $2\text{M}+\text{Na}^+$); HRMS (ESI) calcd for $\text{C}_{13}\text{H}_{11}\text{N}_3\text{O}_2\text{SNa}$: 296.0484, found: 296.0470.

(Z)-7-ethyl-2-(thiophen-2-ylmethylene)-5H-thiazolo[3,2-a]pyrimidine-

3,5(2H)-dione (2.25): The compound was prepared according to method A (yield = 43%) m.p: 216 °C; ^1H NMR (CDCl_3) δ : 1.23 (t, $J = 7.5$ Hz, 3H, CH_3), 2.57 (q, $J = 7.5$ Hz, 2H, CH_2), 6.11 (s, 1H, pyridine-H), 7.24-7.26 (m, 1H, ArH), 7.51 (d, $J = 3.0$ Hz, 1H, ArH), 7.75 (d, $J = 5.0$ Hz, 1H, ArH), 8.01 (s, 1H, arylidene H); ^{13}C NMR (CDCl_3) δ : 11.6, 30.4, 108.8, 116.3, 129.1, 129.6, 133.3, 134.7, 137.7, 157.8, 158.9, 162.9, 168.3; MS (ESI): 291 (15%, $\text{M}+\text{H}^+$), 313 (75%, $\text{M}+\text{Na}^+$), 603 (100%, $2\text{M}+\text{Na}^+$); HRMS (ESI) calcd for $\text{C}_{13}\text{H}_{10}\text{N}_2\text{O}_2\text{S}_2\text{Na}$: 313.0081, found: 313.0071.

(Z)-7-ethyl-2-((5-nitrofuran-2-yl)methylene)-5H-thiazolo[3,2-a]pyrimidine-3,5(2H)-dione (2.26): The compound was prepared according to method A (yield = 46%) m.p: 202 °C; ¹H NMR (DMSO-*d*₆) δ: 1.14 (t, *J* = 7.5 Hz, 3H, CH₃), 2.48 (q, *J* = 7.5 Hz, 2H, CH₂), 6.14 (s, 1H, pyridine-H), 7.40 (d, *J* = 3.8 Hz, 1H, ArH), 7.84 (d, *J* = 3.8 Hz, 1H, Ar-H), 7.94 (s, 1H, arylidene H); ¹³C NMR (DMSO-*d*₆) δ: 11.5, 29.3, 108.5, 114.7, 118.6, 120.4, 123.7, 151.1, 152.8, 157.8, 158.3, 162.1, 167.2; MS (ESI): 320 (5%, M+H)⁺, 661 (100%, 2M+Na)⁺; HRMS (ESI) calcd for C₁₃H₁₀N₃O₅S: 320.0335, found: 320.0341.

(Z)-7-ethyl-2-(pyridin-2-ylmethylene)-5H-thiazolo[3,2-a]pyrimidine-3,5(2H)-dione (2.27): The compound was prepared according to method A (yield = 22%) m.p: 225 °C; ¹H NMR (CDCl₃) δ: 1.24 (t, *J* = 7.5 Hz, 3H, CH₃), 2.56 (q, *J* = 7.5 Hz, 2H, CH₂), 6.08 (s, 1H, pyrimidine H), 7.32 (dd, *J* = 7.4, 4.7 Hz, 1H), 7.59 (d, *J* = 7.7 Hz, 1H), 7.81 (dd, *J* = 7.4, 6.7 Hz, 1H), 7.98 (s, 1H, arylidene H), 8.78 (d, *J* = 4.7 Hz, 1H); ¹³C NMR (CDCl₃) δ: 11.6, 30.4, 108.5, 124.0, 124.3, 157.5, 132.0, 137.1, 149.2, 151.3, 159.1, 162.1, 163.5, 168.5; MS (ESI): 286 (5%, M+H)⁺, 308 (10%, M+Na)⁺; HRMS (ESI) calcd for C₁₄H₁₂N₃O₂S: 286.0649, found: 286.0650.

(Z)-2-((1H-indol-7-yl)methylene)-7-ethyl-5H-thiazolo[3,2-a]pyrimidine-3,5(2H)-dione (2.28): The compound was prepared according to method A (yield = 37%) m.p: 190 °C; ¹H NMR (CDCl₃) δ: 1.27 (t, *J* = 7.5 Hz, 3H, CH₃), 2.57 (q, *J* = 7.5 Hz, 2H, CH₂), 6.08 (s, 1H, pyrimidine H), 6.64 (s, 1H, ArH), 7.18 (t, *J* = 7.5 Hz, 1H, ArH), 7.34 (d, *J* = 7.5 Hz, 1H, ArH), 7.46 (s, 1H, ArH), 7.72 (d, *J* = 7.5 Hz, 1H, ArH), 8.78 (s, 1H, arylidene H), 9.67 (br s, 1H, NH); ¹³C NMR (CDCl₃) δ: 11.7, 30.4, 103.2, 108.4, 110.0, 117.2, 118.4, 119.9, 122.1, 125.0, 129.4, 133.4,

135.5, 158.8, 159.2, 163.5, 168.4; MS (ESI): 324 (30%, M+H)⁺, 346 (100%, M+Na)⁺; HRMS (ESI) calcd for C₁₇H₁₄N₃O₂S: 324.0799, found: 324.0807.

2.4.2 Anti-viral assay

CHIKV Indian Ocean strain 899 (Genbank FJ959103.1) was generously provided by Prof. S. Günther (Bernhard Nocht Institute for Tropical Medicine, Hamburg, Germany) (Panning M et al., *Emerging Infectious Diseases* 2008). BGM cells were maintained in cell growth medium composed of minimum essential medium (MEM Rega-3, Gibco, Belgium) supplemented with 10% Foetal Bovine Serum (FBS, Integro, The Netherlands), 1% L-glutamine (Gibco), and 1% sodium bicarbonate (Gibco). The antiviral assays were performed in virus growth medium which is the respective cell growth medium supplemented with 2% (instead of 10%) FBS. Cell cultures were maintained at 37 °C in an atmosphere of 5% CO₂ and 95-99% humidity. BGM cells were seeded in 96-well tissue culture plates (Becton Dickinson, Aalst, Belgium) at a density of 2.5 x 10⁴ cells/well in 100 µL assay medium and were allowed to adhere overnight. Next, a compound dilution series was prepared in the medium on top of the cells after which the cultures were infected with 0.001 MOI of CHIKV 899 inoculum in 100 µL assay medium. On day 5 post-infection (p.i.), the plates were processed using the MTS/PMS method as described by the manufacturer (Promega, The Netherlands). The 50% effective concentration (EC₅₀), which is defined as the compound concentration that is required to inhibit virus-induced cell death by 50%, was determined using logarithmic interpolation. All assay wells were checked microscopically for minor signs of virus induced CPE or possible alterations to the cell or monolayer morphology caused by the compound.

2.4.3 X-ray crystallographic data for compound 2.20

Crystal data. Compound **12**. C₁₈H₁₆N₂O₅S, $M = 372.40$, $T = 150$ K, Triclinic, $P\bar{1}$, $Z = 2$, $a = 7.8375$ (3), $b = 8.2458$ (3), $c = 14.5394$ (7) Å, $\alpha = 87.176$ (4)°, $\beta = 74.562$ (4)°, $\gamma = 73.335$ (4)°, $V = 867.31$ (7) Å³, $D_x = 1.426$ g cm⁻³, Cu $K\alpha$ radiation, $\lambda = 1.54184$ Å, 16946 reflections measured ($\theta = 6\text{--}74^\circ$), merged to 3491 unique data, $R = 0.034$ [for 3396 data with $I > 2\sigma(I)$], $R_w = 0.089$ [all data], $S = 1.00$

Structure determination of compound 2.20. Images were measured on an Agilent SuperNova diffractometer (Cu $K\alpha$ radiation, mirror monochromator, $\lambda = 1.54184$ Å) and data extracted using the CrysAlis PRO package.¹ Structure solution was by direct methods (SIR92).² The structure was refined using the CRYSTALS program package.³ CDCC 1968317.

2.4.4 Computational methods

Structures were built intuitively in Avogadro and initially optimized with Molecular Mechanics (Universal force field). These structures were used for subsequent DFT calculations utilizing Gaussian16 with initial optimization at B3LYP/def2SVP for minima structures and M06-2X/6-31G(d) for transition states. All final structures and thermodynamics were calculated with M06-2X/aug-cc-pVDZ and solvation in acetic acid modelled (SMD). Minima were confirmed by analysis of the normal modes. The transition states were confirmed saddle points by observation of one imaginary frequency with mode analysis indicating molecular displacement corresponding to the transition of interest. All structures energies were also corrected for dispersion (D3) and geometric counterpoise (gCP). Thermodynamic changes in the Gibbs free energy of reaction $\Delta_r G^0$ (298K) from the starting materials, compound **2.13** and benzaldehyde, were calculated as per

equation (E1), that is $\Delta_r G^0(298\text{K})$ for the product of interest is equal to the sum of electronic energy of the product – the sum of electronic energy for the starting materials, with all values having the free energy correction applied.

$$\Delta_r G^0(298\text{ K}) = \sum(\varepsilon_0 + G_{corr})_{products} - \sum(\varepsilon_0 + G_{corr})_{reactants}$$

2.5 References

1. Cifuentes Kottkamp, A.; De Jesus, E.; Grande, R.; Brown, J. A.; Jacobs, A. R.; Lim, J. K.; Stapleford, K. A. Atovaquone inhibits arbovirus replication through the depletion of intracellular nucleotides. *J. Virol.* **2019**, 93, 1-15.
2. Huang, Y. S.; Higgs, S.; Vanlandingham, D. L. Arbovirus-mosquito vector-host interactions and the impact on transmission and disease pathogenesis of arboviruses. *Front. Microbiol.* **2019**, 10, 1-14.
3. Vogels, C. B. F.; Ruckert, C.; Cavany, S. M.; Perkins, T. A.; Ebel, G. D.; Grubaugh, N. D. Arbovirus coinfection and co-transmission: A neglected public health concern? *PLOS Biol.* **2019**, 17, e3000130.
4. Rashad, A. A.; Mahalingam, S.; Keller, P. A. Chikungunya virus: Emerging targets and new opportunities for medicinal chemistry. *J. Med. Chem.* **2014**, 57, 1147-1166.
5. Matthews, B. J.; Dudchenko, O.; Kingan, S. B.; Koren, S.; Antoshechkin, I.; Crawford, J. E.; Glassford, W. J.; Herre, M.; Redmond, S. N.; Rose, N. H.; Weedall, G. D.; Wu, Y.; Batra, S. S.; Brito-Sierra, C. A.; Buckingham, S. D.; Campbell, C. L.; Chan, S.; Cox, E.; Evans, B. R.; Fansiri, T.; Filipovic, I.; Fontaine, A.; Gloria-Soria, A.; Hall, R.; Joardar, V. S.; Jones, A. K.; Kay, R. G. G.; Kodali, V. K.; Lee, J.; Lycett, G. J.; Mitchell, S. N.; Muehling, J.; Murphy, M. R.; Omer, A. D.; Partridge, F. A.; Peluso, P.; Aiden, A. P.; Ramasamy, V.; Rasic, G.; Roy, S.; Saavedra-Rodriguez, K.; Sharan, S.; Sharma, A.; Smith, M. L.; Turner, J.; Weakley, A. M.; Zhao, Z.; Akbari, O. S.; Black, W. C. t.; Cao, H.; Darby, A. C.; Hill, C. A.; Johnston, J. S.; Murphy, T. D.; Raikhel, A. S.; Sattelle, D. B.; Sharakhov, I. V.; White, B. J.; Zhao, L.; Aiden, E. L.; Mann, R. S.; Lambrechts, L.; Powell, J. R.; Sharakhova, M. V.; Tu, Z.; Robertson, H. M.; McBride, C. S.; Hastie, A. R.; Korlach, J.; Neafsey, D. E.; Phillippy, A. M.; Vossell, L. B. Improved reference genome of aedes aegypti informs arbovirus vector control. *Nature* **2018**, 563, 501-507.
6. Schwartz, O.; Albert, M. L. Biology and pathogenesis of chikungunya virus. *Nat. Rev. Microbiol.* **2010**, 8, 491-500.
7. Villero-Wolf, Y.; Mattar, S.; Puerta-Gonzalez, A.; Arrieta, G.; Muskus, C.; Hoyos, R.; Pinzon, H.; Pelaez-Carvajal, D. Genomic epidemiology of chikungunya virus in colombia reveals genetic variability of strains and multiple geographic introductions in outbreak, 2014. *Sci. Rep.* **2019**, 9, 9970.
8. Mahendradas, P.; Avadhani, K.; Shetty, R. Chikungunya and the eye: A review. *J. Ophthalmic Inflamm. Infect.* **2013**, 3, 1-9.
9. Chang, L. J.; Dowd, K. A.; Mendoza, F. H.; Saunders, J. G.; Sitar, S.; Plummer, S. H.; Yamshchikov, G.; Sarwar, U. N.; Hu, Z.; Enama, M. E.; Bailer, R. T.; Koup, R. A.; Schwartz, R. M.; Akahata, W.; Nabel, G. J.; Mascola, J. R.; Pierson, T. C.; Graham, B. S.; Ledgerwood, J. E.; Team, V. R. C. S. Safety and tolerability of chikungunya virus-like particle vaccine in healthy adults: A phase 1 dose-escalation trial. *Lancet* **2014**, 384, 2046-2052.
10. Agarwal, T.; Asthana, S.; Bissoyi, A. Molecular modeling and docking study to elucidate novel chikungunya virus nsp2 protease inhibitors. *Indian J. Pharm. Sci.* **2015**, 77, 453-460.
11. Nguyen, P. T.; Yu, H.; Keller, P. A. Discovery of in silico hits targeting the nsp3 macro domain of chikungunya virus. *J. Mol. Model.* **2014**, 20, 1-12.
12. Maheshwari, R. K.; Srikantan, V.; Bhartiya, D. Chloroquine enhances replication of semliki forest virus and encephalomyocarditis virus in mice. *J. Virol.* **1991**, 65, 992-995.
13. Nguyen, P. T.; Yu, H.; Keller, P. A. Identification of chikungunya virus nsp2 protease inhibitors using structure-base approaches. *J. Mol. Graphics Modell.* **2015**, 57, 1-8.
14. Karlas, A.; Berre, S.; Couderc, T.; Varjak, M.; Braun, P.; Meyer, M.; Gangneux, N.; Karo-Astover, L.; Weege, F.; Raftery, M.; Schonrich, G.; Klemm, U.; Wurzlbauer, A.; Bracher, F.;

- Merits, A.; Meyer, T. F.; Lecuit, M. A human genome-wide loss-of-function screen identifies effective chikungunya antiviral drugs. *Nat. Commun.* **2016**, *7*, 1-14.
15. D'Hooghe, M.; Mollet, K.; De Vreese, R.; Jonckers, T. H.; Dams, G.; De Kimpe, N. Design, synthesis, and antiviral evaluation of purine-beta-lactam and purine-aminopropanol hybrids. *J. Med. Chem.* **2012**, *55*, 5637-5641.
16. Feibelman, K. M.; Fuller, B. P.; Li, L.; LaBarbera, D. V.; Geiss, B. J. Identification of small molecule inhibitors of the chikungunya virus nsp1 RNA capping enzyme. *Antivir. Res.* **2018**, *154*, 124-131.
17. Gomez-SanJuan, A.; Gamo, A. M.; Delang, L.; Perez-Sanchez, A.; Amrun, S. N.; Abdelnabi, R.; Jacobs, S.; Priego, E. M.; Camarasa, M. J.; Jochmans, D.; Leyssen, P.; Ng, L. F. P.; Querat, G.; Neyts, J.; Perez-Perez, M. J. Inhibition of the replication of different strains of chikungunya virus by 3-aryl-[1,2,3]triazolo[4,5-*d*]pyrimidin-7(6*H*)-ones. *ACS Infect. Dis.* **2018**, *4*, 605-619.
18. Rothan, H. A.; Bahrani, H.; Abdulrahman, A. Y.; Mohamed, Z.; Teoh, T. C.; Othman, S.; Rashid, N. N.; Rahman, N. A.; Yusof, R. Mefenamic acid in combination with ribavirin shows significant effects in reducing chikungunya virus infection in vitro and in vivo. *Antivir. Res.* **2016**, *127*, 50-56.
19. Jadav, S. S.; Sinha, B. N.; Hilgenfeld, R.; Pastorino, B.; de Lamballerie, X.; Jayaprakash, V. Thiazolidone derivatives as inhibitors of chikungunya virus. *Eur. J. Med. Chem.* **2015**, *89*, 172-178.
20. Hwu, J. R.; Kapoor, M.; Tsay, S. C.; Lin, C. C.; Hwang, K. C.; Horng, J. C.; Chen, I. C.; Shieh, F. K.; Leyssen, P.; Neyts, J. Benzouracil-coumarin-arene conjugates as inhibiting agents for chikungunya virus. *Antivir. Res.* **2015**, *118*, 103-109.
21. Gigante, A.; Canela, M. D.; Delang, L.; Priego, E. M.; Camarasa, M. J.; Querat, G.; Neyts, J.; Leyssen, P.; Perez-Perez, M. J. Identification of [1,2,3]triazolo[4,5-*d*]pyrimidin-7(6*H*)-ones as novel inhibitors of chikungunya virus replication. *J. Med. Chem.* **2014**, *57*, 4000-4008.
22. Fares, M.; Eldehna, W. M.; Abou-Seri, S. M.; Abdel-Aziz, H. A.; Aly, M. H.; Tolba, M. F. Design, synthesis and in vitro antiproliferative activity of novel isatin-quinazoline hybrids. *Arch. Pharm.* **2015**, *348*, 144-154.
23. Hwu, J. R.; Huang, W. C.; Lin, S. Y.; Tan, K. T.; Hu, Y. C.; Shieh, F. K.; Bachurin, S. O.; Ustyugov, A.; Tsay, S. C. Chikungunya virus inhibition by synthetic coumarin-guanosine conjugates. *Eur. J. Med. Chem.* **2019**, *166*, 136-143.
24. Spengler, J. P.; Schunack, W. H₂-antihistaminics. 18. 5,6-alkyl-substituted 4-pyrimidinones with H₂-antihistaminic effects. *Arch. Pharm.* **1984**, *317*, 425-430.
25. Fares, M.; Abou-Seri, S. M.; Abdel-Aziz, H. A.; Abbas, S. E.; Youssef, M. M.; Eladwy, R. A. Synthesis and antitumor activity of pyrido [2,3-*d*]pyrimidine and pyrido[2,3-*d*] [1,2,4]triazolo[4,3-*a*]pyrimidine derivatives that induce apoptosis through G1 cell-cycle arrest. *Eur. J. Med. Chem.* **2014**, *83*, 155-166.
26. Mohamed, M. M.; Khalil, A. K.; Abbass, E. M.; El-Naggar, A. M. Design, synthesis of new pyrimidine derivatives as anticancer and antimicrobial agents. *Synth. Commun.* **2017**, *47*, 1441-1457.
27. Abdel-fattah, A.-S. M.; Negm, A. M.; Mustafa Gaafar, A. E. Reactions with 6-methyl-2-thiouracil synthesis of dipyrimidino [2, 1-*b*: 1', 2'-*c*] thiazine. A new ring system. *Phosphorus, Sulfur Silicon Relat. Elem.* **1992**, *72*, 145-156.
28. Hamouda, A. Synthesis of novel pyrimidines thiazolopyrimidines, triazolopyrimidines and pyrimidotriazines as potent antimicrobial agent. *Der Pharma Chem.* **2014**, *6*, 346-357.
29. Abdelghani, E.; Said, S. A.; Assy, M.; Hamid, A. M. A. Heterocyclization of thiouracil derivative: Synthesis of thiazolopyrimidines, tetrazolopyrimidines and triazolopyrimidines of potential biological activity. *J. Iran Chem. Soc.* **2015**, *12*, 1809-1817.
30. Kruse, H.; Grimme, S. A geometrical correction for the inter- and intra-molecular basis set superposition error in hartree-fock and density functional theory calculations for large systems. *J. Chem. Phys.* **2012**, *136*, 1-16.

Chapter 3:

**Application of the bioisosterism
and simplification concepts
towards anti-CHIKV**

FOREWORD TO CHAPTER 3

This chapter is a full research manuscript prepared for submission to the *RSC Medicinal Chemistry*. This chapter describes the synthesis of 1-aryl-[1,2,4]triazolo[4,3-*a*]pyrimidines and 2-anilinopyrimidines as potential chikungunya virus inhibitors. It also describes the preparation and characterisation of the key intermediates as well as the synthesis of target compounds. X-ray single crystal studies of three intermediates and two target compounds were performed and confirmed their structure. *In silico* pharmacokinetic and drug likeness modelling of target compounds were conducted, followed by biological evaluation. DFT calculations and analysis of ESP were performed and revealed new insights into the viral-target binding site.

Supporting information for this chapter can be found in Appendix B (p. 228).

Contributions

Mohamed Fares	Compound design, performed the work and analysis, input into experimental design and prepared/edited the paper
Peter Canfield	Performed and analysed the computational studies
Anthony C. Willis	Performed and solved the X-ray structures
William Lewis	
Muhammad A. Alsherbiny	Performed the cytotoxicity assay.
Johan Neyts	Performed the antiviral evaluation.
Dirk Jochmans	
Philip A. Gale	Editing and proof-reading.
Paul A. Keller	Oversight of the project, editing and proof-reading.

3.1 Introduction

Recent reports by the World Health Organization (WHO) on neglected tropical diseases underline the pressing need to discover new lead compounds to treat chikungunya virus (CHIKV) infection.^{1, 2} Strategies to discover antiviral agents have been described previously,^{3, 4} however our limited knowledge about the virus impedes drug development and therefore the availability of a clinical anti-CHIKV drug.

There is no vaccine or an approved drug for CHIKV-infection prophylaxis or treatment and current management is limited to supportive measures and includes non-steroidal anti-inflammatory drugs (NSAID) and corticosteroids to alleviate the symptoms of acute viremia.⁵ Strategies to discover anti-CHIKV agents include vaccine development, the development of small molecule drug-like ligands discovered through virtual screening, *in vitro* whole cell phenotypic screening, and genome-wide loss of function screens.⁶⁻¹³ Advances in anti-CHIKV drug discovery have been reviewed.^{3, 4, 14}

Amongst synthetic compounds, the triazolo[4,5-*d*]pyrimidin-7(6*H*)ones have emerged as promising and potent anti-CHIKV agents (Figure 3.1.)^{11, 12, 15} as exemplified by the optimised compound MADTP-372 (**3.1**) with a reported EC₅₀ (CHIKV) in the 0.75 – 2.6 μ M range.¹⁶ We note, however, that for **1** there is very limited scope for structural elaboration of the fused bicyclic core and, therefore, limited scope for improving the molecular design with the goal of an effective and commercial drug.

By applying robust medicinal chemistry strategies including bioisosteric substitution and simplification to **3.1** we devised two series of analogue scaffolds

as shown in Figure 3.1. with the prime aim of demonstrating their anti-CHIKV potential for future drug design and to provide insight into ligand-target interactions critical for activity.

Series A was arrived at through bioisosteric substitution freeing up ring position 3 for additional substitutional elaboration (R^2), and Series B through simplification to the conformationally more flexible 2-anilino pyrimidones. In both series we maintained the peripheral ethyl group adjacent to the ring nitrogen, the carbonyl group and unsubstituted intervening position as suggested by earlier structure activity studies.¹¹

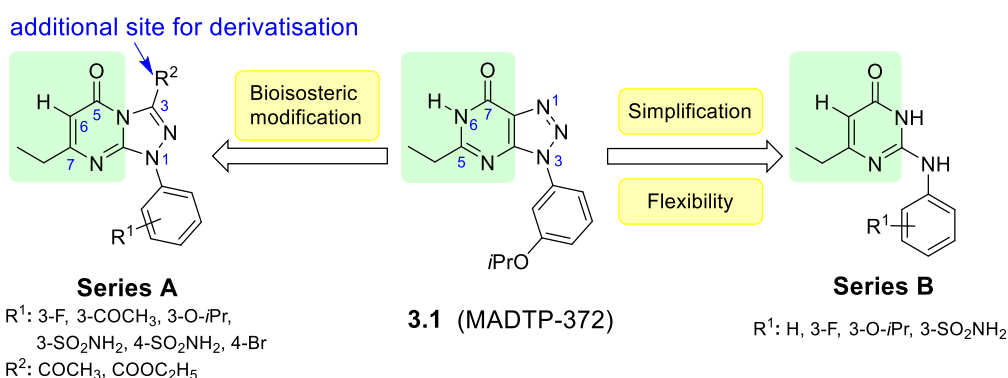
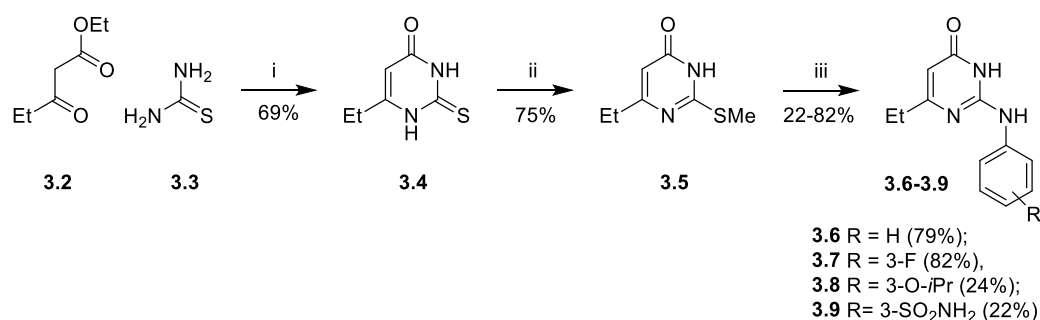


Figure 3.1: Application of medicinal chemistry concepts to current CHIKV inhibitor MADTP-372 towards new potential anti-CHIKV agents. The assumed core, including the explicit hydrogen, are highlighted green.

The selection of the simple acetyl and ethyl carboxylate groups for R^2 (Figure 3.1.) was principally to demonstrate the initial inclusion of scaffold functionality useful for further derivatisation. Different aryl substituents were selected including the 3-*iso*-propoxy of MADTP-372, the 3-acetyl group present in the parent compound used in the same study¹¹, the sulfonamide group considered an acetyl isostere with increased H-bond acceptor potential, the 3-fluoro and 4-bromo moieties.

3.2 Results and discussion

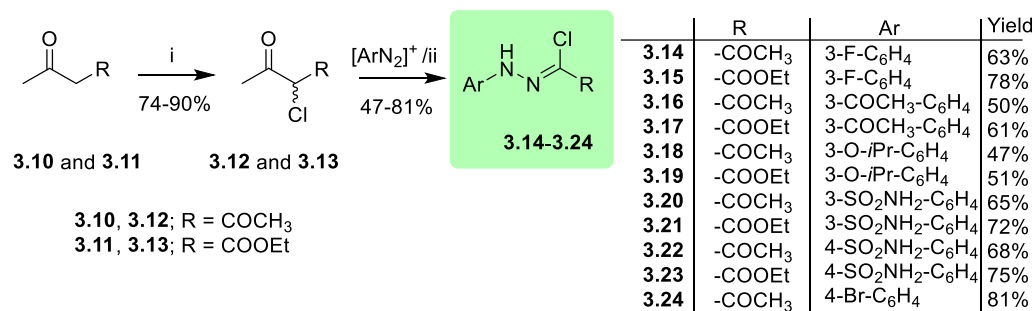
Syntheses of both series began with the construction of the thiouracil **3.4** achieved by the simple expedient of heating thiourea **3.3** at reflux with the β -keto ester **3.2** in the presence of sodium ethoxide in 69% yield (Scheme 3.1).¹⁷ The synthesis of the 2-anilinopyrimidine series **3.6-3.10** (Scheme 3.1) started with methylation of **3.4** with methyl iodide and sodium hydroxide as reported.¹⁸ The reaction between **3.5** and anilines was investigated using different conditions, including using a neat reaction, using catalytic amounts of bases or acids. The best reaction conditions were heating pivalic acid at reflux with *S*-methylthiouracil **3.5** and the corresponding aniline (Scheme 3.1).¹⁹ Applying these reaction conditions afforded the 2-anilinopyrimidine derivatives **3.6-3.9** in yields ranging from 22-82%.



Scheme 3.1: Reagents and conditions: i) NaOEt, C₂H₅OH, 6 h, reflux; ii) NaOH, EtOH, CH₃I, 3 h, 50 °C; iii) Corresponding aniline, pivalic acid, 130 °C.

Hydrazonoyl chlorides (highlighted in green in Scheme 3.2) are the main building blocks in this synthesis of these triazolo[4,3-*a*]pyrimidine derivatives and can be made via several routes from inexpensive and readily available precursors. Here we synthesised **3.14-3.24** starting with chlorination of the active methylene group of acetylacetone **3.10** and ethyl acetoacetate **3.11** using sulfuryl chloride as described by Alihn in 1878²⁰ (Scheme 3.2). Conventional coupling of the α -chloroacetyl

derivatives **3.12** and **3.13** (Scheme 3.2) with the readily prepared aryl diazonium salts afforded compounds **3.14-3.24** (Scheme 3.2) in yields ranging from 32-79%.²¹



Scheme 3.2: Reagents and conditions: i) SO₂Cl₂, 0 °C; ii) CH₃COONa/ 0 °C.

Analysis of the single crystal X-ray diffraction (Figure 3.2) of derivatives **3.15**, **3.20** and **3.24** confirmed the presence of the (Z) configuration (Figures 3.2).

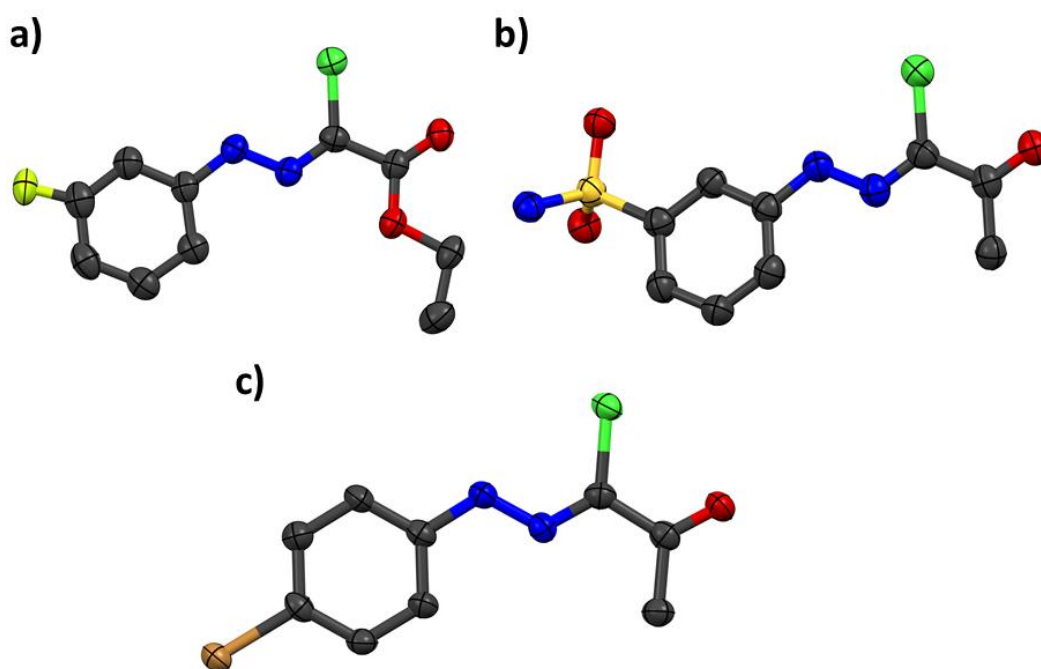
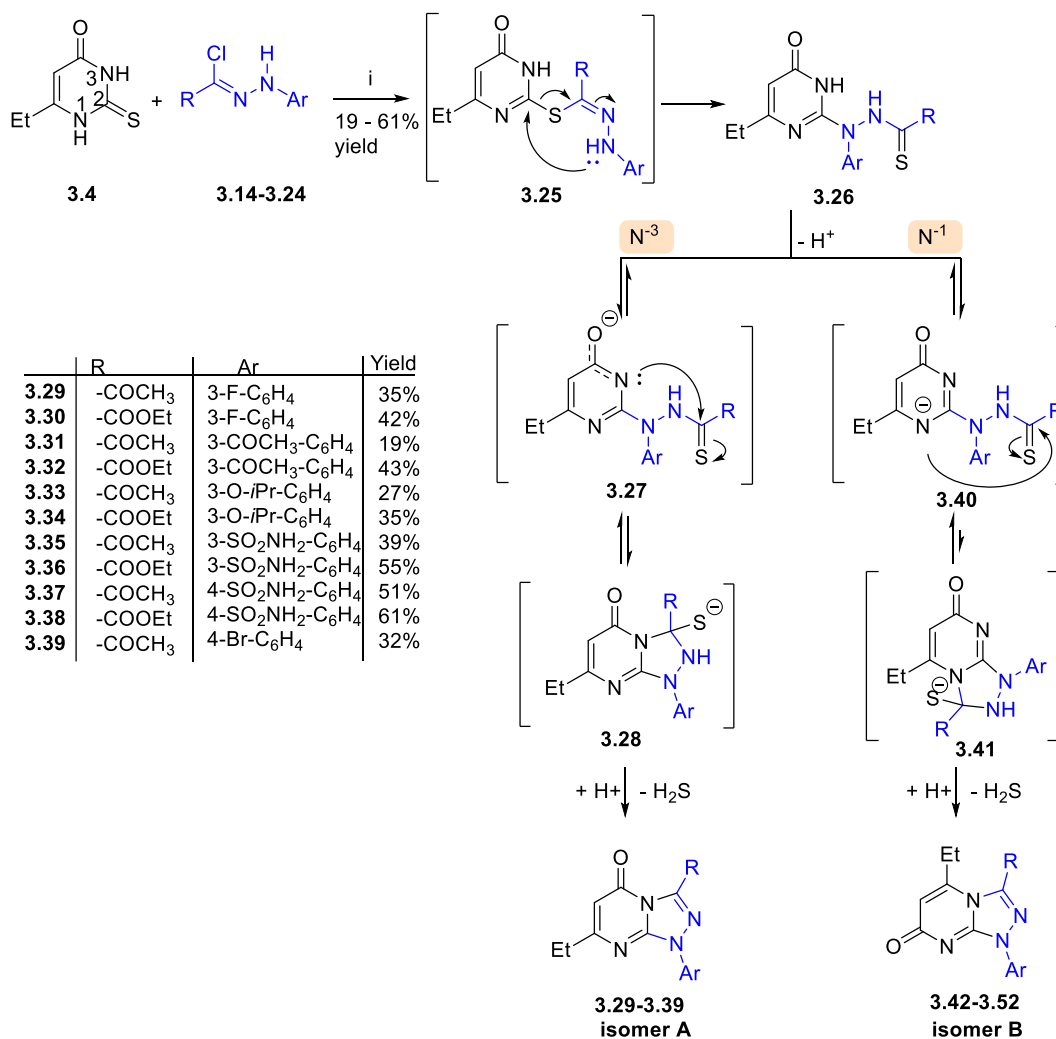


Figure 3.2: X-ray crystal structure of **3.15** (a), **3.20** (b) and **3.24** (c).

The reactions of the thiouracil derivatives and hydrazonoyl halides have been extensively studied (Scheme 3.3).²²⁻²⁴ Generally, the reaction proceeds *via* a 1,3-addition if the reacting heterocyclic thiones are protic nucleophiles, or a 1,3-dipolar cycloaddition pathway in the case that the heterocyclic thiones are dipolarophiles.²² A review of this reaction revealed an almost exclusive preference for product isomer **A** (**3.29-3.39**) over **B** (**3.42-3.52**) (Scheme 3.3).²² This suggests a reaction process through the cycloaddition of carbon-2 and nitrogen-3 (rather than nitrogen-1) of the thiouracil analogues with the hydrazonoyl chloride derivative in presence of base (Scheme 3.3).⁶⁷ The reaction mechanism was postulated to start with *S*-alkylation of the thiouracil derivative via a Japp-Klingmann reaction to afford the thiohydrazones **3.25**. In the presence of base, the nucleophilicity of the terminal hydrazone N increases and the compound undergoes Chapman-like rearrangement to give the corresponding thiohydrazide **3.26**. The latter thiohydrazide cyclized *in situ* to afford **A** or **B**.²² The use of the triethylamine in this reaction which was reported to be one of the best bases to use, resulted in low yields. Changing the base to DIPEA provided good reaction outcomes with good yields in short reaction times.

Analysis of ¹³C NMR spectra of compounds **3.29-3.39** (corresponds to isomer **A**) or **3.42-3.52** (corresponds to isomer **B**) showed resonances at 172 – 173 ppm and was assigned to the carbonyl of the pyrimidine ring which might indicate that isomer **B** was preferentially obtained as reported.²⁵ However, single crystal X-ray diffraction (SCXRD) of two compounds confirmed the presence of the other isomer (**3.32** and **3.39**, Fig. 2), required for the antiviral testing. X-ray analysis of compounds **3.32** and **3.39** showed the planarity of the fused bicyclic and the terminal aryl rings (Figure 3.3).



Scheme 3.3: Reagents and conditions: i) DIPEA, dioxane, 100 °C

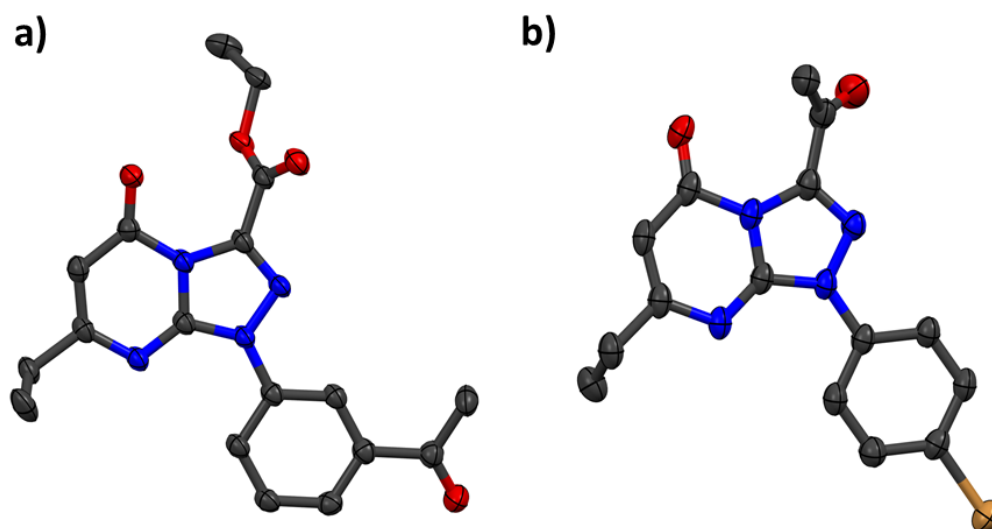


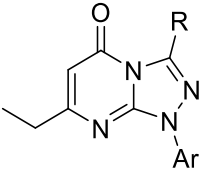
Figure 3.3: ORTEP depictions of compounds 3.23 and 3.39 at 70% probability.

In a typical example, analysis of the ^1H NMR spectrum of **3.29** revealed a triplet at 1.31 ppm and a quartet at 2.70 assigned to the CH_3 and CH_2 of the ethyl group, respectively and a resonance at 2.81 ppm assigned to the methyl of the acetyl group. The pyrimidine H was assigned to the singlet at δ 6.05 in the ^1H NMR spectrum. To the corresponding aryl hydrogens were assigned the triplet at 7.09 ppm, the doublet of doublet at 7.50 ppm, and the multiplet at 8.08-8.12 ppm. The ^{13}C NMR spectrum of the fluorine containing compound **3.29** showed a typical splitting pattern of the fluorine and carbon with coupling constants $J^1_{\text{C-F}} = 248$ Hz, at resonance 161.9 ppm, $J^2_{\text{C-F}} = 28$ Hz at resonance 108.1 ppm, $J^2_{\text{C-F}} = 21$ Hz at resonance 114.5, $J^3_{\text{C-F}} = 9$ Hz, at resonance 103.8, $J^3_{\text{C-F}} = 10$ Hz at resonance 137.8 and $J^4_{\text{C-F}} = 4$ Hz at resonance 115.9 ppm.

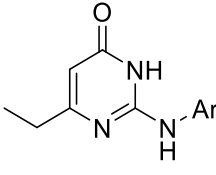
Compounds [1,2,4]triazolo[4,3-*a*]pyrimidin-7(1*H*)-ones **3.29-3.39** and 2-anilinopyrimidin-4(3*H*)-one **3.6-3.9** were screened for their antiviral activities in a viral-cell based assay against chikungunya virus (Indian Ocean strain 899) (Table 3.1). The most active compounds were further tested for their cytotoxic activity against the normal cell line, EA.hy926, the endothelial human cell line, and two human breast cancer cell lines, namely, MCF-7 and MDA-MB-231 (Table 3.1). Compound, 3-acetyl-5-ethyl-1-(3-isopropoxyphenyl)-[1,2,4]triazolo[4,3-*a*]pyrimidin-7(1*H*)-one **3.33**, being the 3-acetyl analogue of the prototype **3.1** emerged as having the most promising antiviral activity among the tested series **3.29-3.39** with $\text{EC}_{50} = 38$ μM , and $\text{IC}_{50} > 300$ μM against breast cancer cell lines, MCF-7 and MDA-MB-231 and normal cell line EA.hy926 (Table 3.1). The 3-acetylphenyl analogue **3.31** was approximately three times less active than **3.33** paralleling the activities of the 3-acetylphenyl analogue of **3.1**.¹¹ Of special interest was the finding that the only active ethyl carboxylate compound, **3.34**, as expected

featured the high activity 3-*iso*-propoxyphenyl group and exhibiting low antiviral activity, but also exhibited pronounced and consistent cytotoxicity across all cell lines. The sulfonamide derivatives **3.35-3.38** showed no antiviral activity, even at high concentrations (1% inhibition at 100 $\mu\text{g}/\text{mL}$ for **3.36**) (Table 3.1). Whilst all of the conformationally more flexible Series B compounds **3.6-3.9** demonstrated weak inhibition of viral replication, all exhibited an $\text{EC}_{50} > 200 \mu\text{M}$.

Table 3.1: *In vitro* antiviral and cytotoxic activities of compounds **3.29-3.39** and **3.6-3.9**.



3.29-3.39



3.6-3.9

	Ar	Anti-CHIKV activity			Cytotoxic activity		
		%inhibition	at [$\mu\text{g}/\text{mL}$]	EC_{50} (μM)	MCF 7 ^a	MDAM B231 ^a	Eahy 926 ^a
3.29	COCH ₃ 3-F-C ₆ H ₄	80	100	183	> 300	250	> 300
3.30	COOC ₂ H ₅ 3-F-C ₆ H ₄	9	100	>200	NT	NT	NT
3.31	COCH ₃ 3-(COCH ₃)-C ₆ H ₄	100	100	136	> 300	198	207
3.32	COOC ₂ H ₅ 3-(COCH ₃)-C ₆ H ₄	0	20	>200	NT	NT	NT
3.33	COCH ₃ 3-O- <i>i</i> Pr-C ₆ H ₄	69	20	38	> 300	> 300	> 300
3.34	COOC ₂ H ₅ 3-O- <i>i</i> Pr-C ₆ H ₄	90	75	100	68	65	73
3.35	COCH ₃ 3-SO ₂ NH ₂ -C ₆ H ₄	0	100	>200	NT	NT	NT
3.36	COOC ₂ H ₅ 3-SO ₂ NH ₂ -C ₆ H ₄	1	100	>200	NT	NT	NT
3.37	COCH ₃ 4-SO ₂ NH ₂ -C ₆ H ₄	2	20	>200	NT	NT	NT
3.38	COOC ₂ H ₅ 4-SO ₂ NH ₂ -C ₆ H ₄	2	100	>200	NT	NT	NT
3.39	COCH ₃ 4-Br-C ₆ H ₄	54	75	186	128	81	147
3.6	- -C ₆ H ₅	6	75	>200	NT	NT	NT
3.7	- 3-F-C ₆ H ₄	30	75	>200	NT	NT	NT
3.8	- 3-Pr ^{<i>t</i>} O-C ₆ H ₄	26	20	>200	NT	NT	NT
3.9	- 3-SO ₂ NH ₂ -C ₆ H ₄	0	75	>200	NT	NT	NT

NT: not tested, ^a Mean from three replicates, (errors were in the range $\pm 5-10\%$ of the reported values).

Drug Likeness Scores (DLS) were calculated using MolSoft²⁶ and are listed in Table 3.2. Drug candidates typically show positive DLS values, while non-drug candidates might elicit zero or negative DLS values. Whilst all tested compounds complied with Lipinski guidelines, only **3.33**, **3.34**, **3.37**, **3.39**, **3.6-3.9** received positive DLS ranging from 0.03 - 0.77, with the rest of the compounds showing zero or negative DLS.

Table 3.2: Drug likeness calculations and Lipinski parameters of the compounds **3.29-3.39** and **3.6-3.9**.

	M. Wt ^a	log P ^b	HB A ^c	HBD ^d	n violation ^e	Rule of 5	nrot ^f	TPSA ^g	%A BS ^h	DLS ⁱ
3.29	300	1.8	4	0	0	pass	3	69.3	85.1	0.00
3.30	330	2.6	5	0	0	pass	5	78.5	81.9	-0.05
3.31	324	1.3	5	0	0	pass	4	86.4	79.2	-0.37
3.32	354	2.1	6	0	0	pass	6	95.6	76.0	-0.45
3.33	340	2.4	5	0	0	pass	5	78.5	81.9	0.29
3.34	370	3.2	6	0	0	pass	7	87.7	78.7	0.29
3.35	361	0.4	7	2	0	pass	4	129.4	64.4	-0.39
3.36	391	1.2	8	2	0	pass	6	138.7	61.1	-0.42
3.37	361	0.4	7	2	0	pass	4	129.4	64.4	0.07
3.38	391	1.2	8	2	0	pass	6	138.7	61.1	-0.10
3.39	360	2.4	4	0	0	pass	3	69.3	85.1	0.03
3.6	215	1.9	2	2	0	pass	3	57.8	89.1	0.69
3.7	233	2.2	2	2	0	pass	3	57.8	89.1	0.41
3.8	273	2.7	3	2	0	pass	5	67.0	85.9	0.77
3.9	294	0.7	5	4	0	pass	4	118.0	68.3	0.27

^a Molecular weight. ^b Lipophilicity. ^c Number of hydrogen bond acceptors. ^d Number of hydrogen bond donors. ^e Number of violations. ^f Number of rotatable bonds. ^g Topological polar surface area. ^h Percentage absorption. ⁱ Drug-likeness model score.

In order to infer the nature of the ligand – target interactions important for binding and inhibition, a series of minimal pharmacophore models was developed using the closely comparable bioactivity results of compounds **3.53** and **3.56** (Figure 3.4)

along with **3.54** and **3.55** (pink-dashed box in Figure 3.4) for the 3-*iso*-propoxyphenyl analogues.¹¹ As we are unable to infer orientation of an asymmetric pendant aryl group due to free rotation it was modelled as a phenyl moiety. A methyl group on the bicyclic core is a suitable stand-in for substituents at that location.

All compounds were modelled using Density-Functional Theory (DFT) using the Gaussian16 package at the B3LYP-D3(BJ)/6-311G(2d,p) using implicit water solvation to reflect *in vivo* conditions. The possible tautomerism in **3.54** – **3.56** was examined with DFT calculated free energies indicating that for **3.54** and **3.55** only the single tautomer shown in each case is present in solution. For **3.56**, two of the three possible tautomers, **3.56a** and **3.56b**, would be present at 3% and 97% respectively.

The calculated Electrostatic Potential (ESP) was mapped onto two values of the electron isodensity and is shown in Figure 3.4. The large valued isodensity clearly resolves the atoms (middle row in Figure 3.4) whilst the lower value better reflects how the molecules are seen by the chemical environment, i.e. the ligand target. The closely similar molecular shapes of **3.53** – **3.56**, the very similar polarities of the π -systems and the comparable EC₅₀ values for **3.53** – **3.55** indicate that this comparative approach is valid for inferring the important ligand – target interactions. Both tautomers **3.56a-b** feature reversed polarity in contrast to **3.53** – **3.55** arising from the N-H groups. Not surprisingly, such a situation correlates with antiviral activity, but at levels higher than the bioassays could measure.

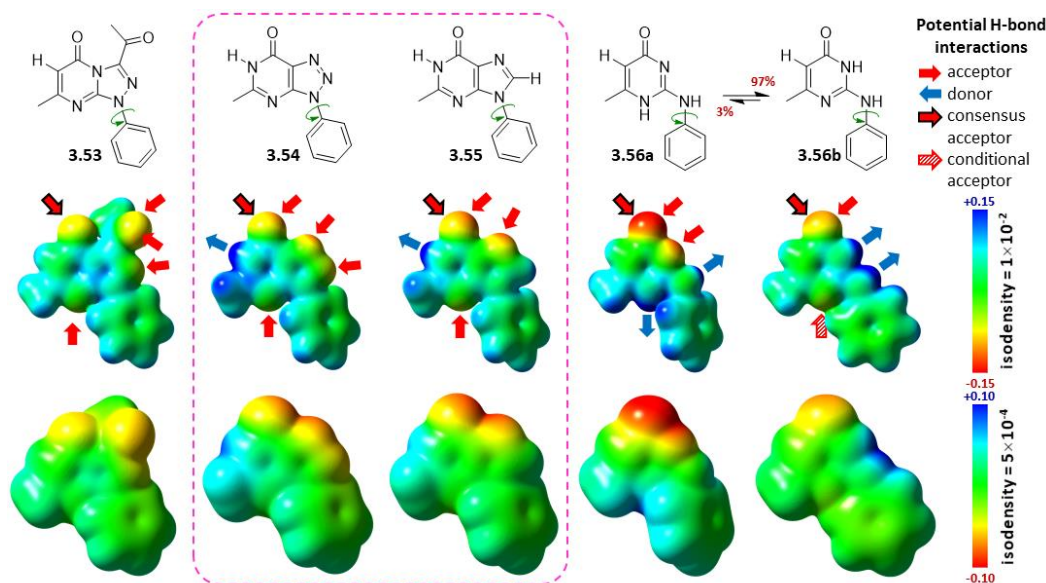


Figure 3.4: Structures and DFT minimal pharmacophore models of the [1,2,4]triazolo[4,3-*a*]pyrimidine (**3.53**), the azahypoxanthine (**3.54**), the hypoxanthine (**3.55**) and the pyrimidone tautomers (**3.56a-b**) showing the electrostatic potential mapped onto two different electron isodensities to convey both the resolved atoms (middle row) and the diffuse molecular surface as seen by the chemical environment (bottom row). Potential H-bond interactions indicated by coloured arrows. The tautomers shown for **3.54** and **3.55** calculated by DFT to represent 100% of the species *in vivo*. For the pyrimidones **3.56**, the relative concentration of the two tautomers is shown.

Figure 3.5 is the consensus model, principally arrived at through comparisons of steric and charge features of **3.53** – **3.55**. The H-bond acceptor facility at position 8 and the oxygen substituent at position 5 would both be expected to be important. Whilst no substituent can be tolerated at positions 2 and 6, there would seem to be a nebulous region of H-bond acceptor potential proximal to position 3. Since **3.33** is of comparable activity to **3.1** yet features greater steric bulk at position 3, we speculate that antivirals based on **3.54** and **3.55** interact with the target via a H₂O molecule H-bonded to the 5-membered ring imine nitrogen(s).

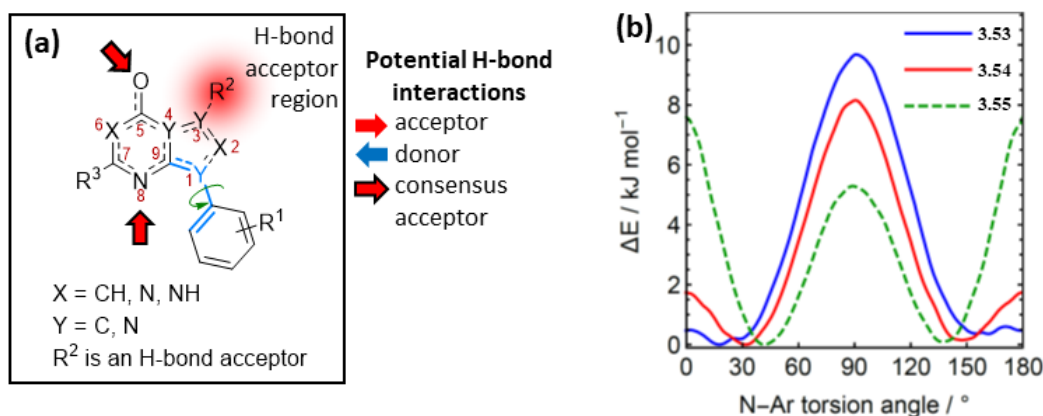


Figure 3.5: (a) Consensus picture of the minimal pharmacophore with inferred important H-bond interactions indicated. For compounds like **3.54** and **3.55** R² could likely represent an H-bonded H₂O molecule. (b) The DFT Potential Energy Surfaces of **3.53** – **3.55** for the phenyl torsions as defined by the bold blue bonds in (a).

Whilst the precise orientation of the aryl group is both unknown and cannot be inferred from our analysis, the calculated Potential Energy Surfaces (PES) for **3.53** – **3.55** as shown in Figure 3.5 does indicate the energetic penalty (with concomitant reduction in activity) for geometries deviating from the unconstrained equilibrium torsions. These predictions only apply to 2,6-unsubstituted phenyl groups.

3.3 Conclusions

Inspired by the reported anti-CHIKV activity of MADTP-372 (**3.1**), two series of compounds, the triazolopyrimidines **3.29-3.39** and anilinopyrimidines **3.6-3.9**, were designed, synthesised and bioassayed for anti-CHIKV activity and cytotoxicities. Whilst the series **3.6-3.9**, proved to only exhibit weak anti-CHIKV activity, **3.33**, the 3-acetyl analogue of **3.1** exhibited comparable anti-CHIKV activity and low cytotoxicity to **3.1**. The advantage of **3.33** over **3.1** is that the ability of the 3 position to accommodate substituents, these being accessed from easy to prepare hydrazonoyl chlorides, provides new and promising scope for improved drug design utilising this inexpensive scaffold. Comparisons of the geometries and

Electrostatic Potential-mapped surfaces of minimal pharmacophore models **3.53** – **3.56** of anti-CHIKV agents has allowed for a consensus model for effective target binding. These results place future research into anti-CHIKV agents in better standing.

3.4 Experimental section

3.4.1 Chemistry

General methods and material

All reagents and solvents were purified and dried by standard techniques. Melting points were measured and were uncorrected. Reactions were monitored by TLC analysis using silica gel GF/UV 254. NMR spectra were recorded on Varian Gemini-300BB 500 MHz FT-NMR spectrometers (Varian Inc., Palo Alto, CA). ¹H spectra were run at 500 MHz and ¹³C spectra were run at 126 MHz, in deuterated dimethylsulfoxide (DMSO-*d*₆), (CD₃)₂CO and CDCl₃. Chemical shifts (δ_{H}) are reported relative to TMS as internal standard and coupling constant (*J*) values are reported in Hertz. The abbreviations used are as follows: s, singlet; d, doublet; t, triplet; m, multiplet. Electrospray ionization (ESI single quadrupole) mass spectra have their ion mass to charge values (*m/z*) stated with their relative abundances as a percentage in parentheses. Peaks assigned to the molecular ion are denoted as [M+H] or [M+Na]. Column chromatography was performed using silica gel 60 (0.063-0.200 mm). Compounds **3.6-3.9** and **3.29-3.39** were $\geq 95\%$ pure. The purity was determined by HPLC analysis using a Shimadzu CLASS-VP LC10 analytical HPLC system equipped with a Photo Diode Array Detector and autosampler (100% H₂O/0.1% TFA \rightarrow 100% CH₃CN/0.1% TFA over 30 min).

6-Ethyl-2-thioxo-2,3-dihydropyrimidin-4(1H)-one (3.4):¹⁷

After preparing a sodium ethoxide solution by dissolving sodium (4.6 g, 0.1 mole) in absolute ethanol (150 mL), the thiourea (3.8 g, 0.05 mole) was added with stirring with complete dissolution. The ethyl 3-oxopentanoate ester **2** (7.21 g, 0.05 mole) was then added and the reaction mixture was heated at reflux for 4 hours. After cooling the reaction mixture, water was added dropwise until complete dissolution of the formed white precipitate. Ice was added, and neutralization of the alkaline solution was accomplished using HCl (5 M). The reaction flask was left overnight at 4 °C and the resulting white precipitate was filtered, washed with water (3 x 50 mL) and diethyl ether (2 x 30 mL) and dried to give **3** (5.38 g, 69%) as a white powder. m.p 230 °C; ¹H NMR (DMSO, δ): 1.07 (t, $J = 7.5$ Hz, 3H, CH_3), 2.33 (q, $J = 7.5$ Hz, 2H, CH_2), 5.33 (s, 1H, pyrimidine-H), 12.30 (br s, 2H, 2 x -NH); ¹³C NMR (CD₃OD, δ): 13.4, 27.8, 103.9, 162.0, 165.8, 179.4; MS (ESI⁺): 157 (20%, M+H)⁺, 179 (100%, M+Na)⁺.

6-Ethyl-2-(methylthio)pyrimidin-4(3H)-one (3.5): A mixture of 6-ethyl-2-thioxo-2,3-dihydropyrimidin-4(1H)-one **3** (156 mg, 1 mmol), sodium hydroxide (44 mg, 1.1 mmol) in water (1 mL) and ethanol (3 mL) were stirred for 30 min. Methyl iodide (142 mg, 1 mmol) was added dropwise to the slurry and the reaction mixture was gently heated at 50 °C with stirring for 3 h. The reaction mixture was allowed to cool to r.t and the resulting white solid was filtered out, washed with water (3 x 30 mL) and dried to give **4** (128 mg, 75%) as a white powder; ¹H NMR (CDCl₃, δ): 1.24 (t, $J = 7.5$ Hz, 3H, CH_3), 2.56 (q, $J = 7.5$ Hz, 2H, CH_2), 2.60 (s, 3H, SCH_3), 6.09 (s, 1H, pyrimidine-H), 9.32 (br. s, 1H, -NH); ¹³C NMR (CDCl₃, δ): 12.0, 13.2, 30.8, 106.7, 161.1, 165.9, 170.7; MS (ESI⁺): 171 (35%, M+H)⁺, 193

(100%, M+Na)⁺.

General procedure A for the preparation of 6-ethyl-2-(anilino)pyrimidin-4(3H)-ones (3.6-3.9):¹⁹ A mixture of 6-ethyl-2-(methylthio)pyrimidin-4(3H)-one **3.5** (170 mg, 1 mmol) and the corresponding aniline (1.2 mmol) in pivalic acid (9 volumes) was heated at 130 °C with stirring. Heating was maintained until the starting materials were fully consumed or until no further conversion was observed (as monitored by TLC analysis). The slurry was allowed to cool to 60-70 °C and hexanes (18 volumes) was added slowly with stirring and was further cooled to r.t. The resulting solid was filtered, washed with hexanes and dried.

6-Ethyl-2-(phenylamino)pyrimidin-4(3H)-one (3.6): The compound was prepared according to general method A (yield = 79%) as a white powder, m.p: 178-180 °C; HPLC purity 96.3%. ¹H NMR (CDCl₃, δ): 1.27 (t, *J* = 7.0 Hz, 3H, CH₃), 2.55 (q, *J* = 7.0 Hz, 2H, CH₂), 5.81 (s, 1H, pyrimidine-H), 7.05-7.13 (m, 1H, ArH), 7.36 (t, *J* = 8.0 Hz, 2H, ArH), 7.75 (d, *J* = 7.0 Hz, 2H, ArH), 9.50 (br. s, 1H, -NH), 11.62 (br. s, 1H, -NH); ¹³C NMR (CDCl₃, δ): 14.5, 31.4, 101.1, 120.2, 123.4, 129.1, 138.9, 151.7, 165.5, 173.9; MS (ESI⁺) *m/z* 216 (65%, M+H)⁺, MS (ESI⁻) *m/z* 214 (100%, M-H)⁻; HRMS (ESI⁺) calcd for C₁₂H₁₄N₃O: 216.1142 (M+H)⁺, found: 216.1137.

6-Ethyl-2-((3-fluorophenyl)amino)pyrimidin-4(3H)-one (3.7): The compound was prepared according to general method A (yield = 82%) as a buff powder, m.p: 198-200 °C; HPLC purity 98.1%. ¹H NMR (CDCl₃, δ): 1.26 (t, *J* = 7.0 Hz, 3H, CH₃), 2.56 (q, *J* = 7.0 Hz, 2H, CH₂), 5.83 (s, 1H, pyrimidine-H), 6.76-6.80 (m, 1H, ArH), 7.20-7.31 (m, 2H, ArH), 7.81 (d, *J* = 10.0 Hz, 1H, ArH), 9.45 (br. s, 1H, -

NH), 11.44 (br. s, 1H, -NH); ^{13}C NMR (CDCl_3 , δ): 12.2, 31.2, 101.4, 107.1 (d, $J^2_{\text{C-F}} = 26$ Hz), 109.7 (d, $J^2_{\text{C-F}} = 21$ Hz), 114.9, 129.9 (d, $J^3_{\text{C-F}} = 10$ Hz), 140.2 (d, $J^3_{\text{C-F}} = 11$ Hz), 151.0, 162.1 (d, $J^1_{\text{C-F}} = 248$ Hz), 165.1, 173.9; MS (ESI^+) m/z 234 (40%, M+H), MS (ESI^-) m/z 232 (100%, M-H) $^-$; HRMS (ESI^-) calcd for $\text{C}_{12}\text{H}_{11}\text{FN}_3\text{O}$: 232.0886 (M-H) $^-$, found: 232.0879.

6-Ethyl-2-((3-isopropoxyphenyl)amino)pyrimidin-4(3H)-one (3.8): The compound was prepared according to general method A (yield = 24%) as a green powder, m.p: 100-102 °C; HPLC purity 95.2%. ^1H NMR (CDCl_3 , δ): 1.27 (t, $J = 7.0$ Hz, 3H, CH_2CH_3), 1.38 (d, $J = 5.0$ Hz, 6H, 2CH_3), 2.55 (q, $J = 7.0$ Hz, 2H, CH_2CH_3), 4.45-4.59 (m, 1H, CH), 5.82 (s, 1H, pyrimidine-H), 6.63 (d, $J = 7.0$ Hz, 1H, ArH), 7.12 (d, $J = 8.0$ Hz, 1H, ArH), 7.22 (dd, $J = 7.0, 8.0$ Hz, 1H, ArH), 7.60 (s, 1H, ArH), 9.43 (br. s, 1H, -NH), 11.47 (br. s, 1H, -NH); ^{13}C NMR (CDCl_3 , δ): 12.2, 22.1, 31.2, 70.0, 101.0, 107.4, 111.2, 112.0, 129.6, 139.8, 151.4, 158.5, 165.2, 173.5; MS (ESI^+) m/z 274 (50%, M+H) $^+$, MS (ESI^-) m/z 272 (60%, M-H) $^-$; HRMS (ESI^-) calcd for $\text{C}_{15}\text{H}_{18}\text{N}_3\text{O}_2$: 272.1401 (M-H) $^-$, found: 272.1399.

3-((4-Ethyl-6-oxo-1,6-dihydropyrimidin-2-yl)amino)benzenesulfonamide

(3.9): The compound was prepared according to general method A (yield = 22%) as a buff powder, m.p: 203-205 °C; HPLC purity 95.6%. ^1H NMR (DMSO , δ): 1.17 (t, $J = 8.0$ Hz, 3H, CH_2CH_3), 2.44 (q, $J = 8.0$ Hz, 2H, CH_2CH_3), 5.78 (s, 1H, pyrimidine-H), 7.33 (br. s, 2H, $-\text{SO}_2\text{NH}_2$), 7.42-7.49 (m, 2H, ArH), 7.83 (d, $J = 7.0$ Hz, 1H, ArH), 8.26 (s, 1H, ArH), 9.18 (br. s, 1H, -NH), 11.79 (br. s, 1H, -NH); ^{13}C NMR (DMSO , δ): 12.6, 30.5, 101.2, 116.6, 119.5, 122.4, 129.7, 140.2, 145.1, 153.7, 164.9, 171.0; MS (ESI^-) m/z 293 (60%, M-H) $^-$, 587 (100%, 2M-H) $^-$; HRMS

(ESI⁻) calcd for C₁₂H₁₃N₄O₃S: 293.0711 (M-H)⁻, found: 293.0708.

General procedure B for preparation of hydrazoneyl chlorides (3.14-3.24):²⁷

The diazonium salt was prepared by slowly adding a cold sodium nitrite solution (0.7 g, 10 mmol) in deionized water (5 mL) to a cold solution of the appropriate arylamine (10 mmol) dissolved in hydrochloric acid (6 M, 6 mL). In a second beaker, sodium acetate trihydrate (4.1 g, 30 mmol) was added to a stirred solution of 3-chloro-2,4-pentanedione **3.12** (1.34 g, 10 mmol) or ethyl 2-chloro-3-oxobutanoate **3.13** (1.64 g, 10 mmol) in ethanol (100 mL) and the slurry was stirred for 15 min. The diazonium salt was added dropwise to the second beaker and the reaction was stirred for 2 h at 0-5 °C, then left for 8 h in a refrigerator (4 °C). The resulting solid was collected by filtration, washed thoroughly with water and dried. The crude product was crystallized from ethanol to give the corresponding hydrazoneyl chlorides **3.14-3.24**.

(Z)-N-(3-Fluorophenyl)-2-oxopropanehydrazoneyl chloride (3.14): The compound was prepared according to method B (yield = 63%) as yellow crystals, m.p: 155-157 °C. ¹H NMR (CDCl₃, δ): 2.58 (s, 3H, CH₃), 6.77 (td, *J* = 2.0, 8.5 Hz, 1H, ArH), 6.95 (dd, *J* = 1.0, 8.0 Hz, 1H, ArH), 7.02 (dt, *J* = 2.0, 10.0 Hz, 1H, ArH), 7.29-7.33 (m, 1H, ArH), 8.48 (br. s, 1H, NH); ¹³C NMR (CDCl₃, δ): 25.4, 101.9 (d, *J*_{C-F} = 28 Hz), 110.1 (d, *J*_{C-F} = 5 Hz), 110.2 (d, *J*_{C-F} = 14 Hz), 126.1, 130.9 (d, *J*_{C-F} = 9 Hz), 143.0 (d, *J*_{C-F} = 10 Hz), 162.8 (d, *J*_{C-F} = 246 Hz), 188.3; MS (ESI⁻) *m/z* 213 (100%, M-H)⁻, 249 (10%, M+Cl)⁻; HRMS (ESI⁺) calcd for C₉H₈ClFN₂ONa: 237.0218 (M+Na)⁺, found: 237.0207.

Ethyl (Z)-2-chloro-2-(2-(3-fluorophenyl)hydrazineylidene)acetate (3.15): The compound was prepared according to method B (yield = 78%) as yellow crystals, m.p: 110-112 °C. ¹H NMR (CDCl₃, δ): 1.44 (t, *J* = 7.5 Hz, 3H, CH₃), 4.43 (q, *J* = 7.5 Hz, 2H, CH₂), 6.76 (td, *J* = 2.0, 8.0 Hz, 1H, ArH), 6.97 (d, *J* = 8.0 Hz, 1H, ArH), 7.06 (d, *J* = 10.0 Hz, 1H, ArH), 7.28-7.33 (m, 1H, ArH), 8.38 (br. s, 1H, NH); ¹³C NMR (CDCl₃, δ): 14.2, 63.0, 102.0 (d, *J*²_{C-F} = 26 Hz), 109.7 (d, *J*²_{C-F} = 23 Hz), 110.0 (d, *J*⁴_{C-F} = 2 Hz), 117.1, 130.7 (d, *J*³_{C-F} = 9 Hz), 143.0 (d, *J*³_{C-F} = 10 Hz), 159.5, 162.8 (d, *J*¹_{C-F} = 246 Hz); MS (ESI⁻) *m/z* 243 (50%, M-H)⁻, 279 (15%, M+Cl)⁻; HRMS (ESI⁻) calcd for C₁₀H₉ClFN₂O₂: 243.0344 (M-H)⁻, found: 243.0337.

(Z)-N-(3-Acetylphenyl)-2-oxopropanehydrazonoyl chloride (3.16): The compound was prepared according to method B (yield = 50%) as a white powder, m.p: 160 -162 °C. ¹H NMR ((CD₃)₂CO, δ): 2.56 (s, 3H, CH₃), 2.59 (s, 3H, CH₃), 7.49 (t, *J* = 7.5 Hz, 1H, ArH), 7.68-7.72 (m, 2H, ArH), 8.02 (s, 1H, ArH), 10.01 (br. s, 1H, NH); ¹³C NMR ((CD₃)₂CO, δ): 24.6, 25.9, 114.1, 118.8, 122.7, 124.9, 129.8, 138.5, 143.0, 187.4, 196.7; MS (ESI⁻) *m/z* 237 (100%, M-H)⁻, 273 (20%, M+Cl)⁻; HRMS (ESI⁻) calcd for C₁₁H₁₀ClFN₂O₂: 237.0431 (M-H)⁻, found: 237.0431.

Ethyl (Z)-2-(2-(3-acetylphenyl)hydrazineylidene)-2-chloroacetate (3.17): The compound was prepared according to method B (yield = 61%) as yellow crystals, m.p: 142-144 °C. ¹H NMR ((CD₃)₂CO, δ): 1.36 (t, *J* = 7.0 Hz, 3H, -CH₂CH₃), 2.58 (s, 3H, COCH₃), 4.43 (q, *J* = 7.0 Hz, 2H, -CH₂CH₃), 7.49 (t, *J* = 7.5 Hz, 1H, ArH), 7.62-7.66 (m, 2H, ArH), 7.97 (s, 1H, ArH), 9.91 (br. s, 1H, NH); ¹³C NMR ((CD₃)₂CO, δ): 13.6, 25.9, 62.2, 113.9, 115.7, 118.7, 122.5, 129.7, 138.4, 143.2,

159.2, 196.7; MS (ESI⁻) m/z 267 (100%, M-H)⁻, 303 (20%, M+Cl)⁻; HRMS (ESI⁻) calcd for C₁₂H₁₂ClN₂O₃: 267.0528 (M-H)⁻, found: 267.0536.

(Z)-N-(3-Isopropoxyphenyl)-2-oxopropanehydrazonoyl chloride (3.18): The compound was prepared according to method B (yield = 47%) as red crystals, m.p: 80-82 °C. ¹H NMR (CDCl₃, δ): 1.37 (d, J = 6.0 Hz, 6H, 2CH₃), 2.57 (s, 3H, CH₃), 4.56-4.60 (m, 1H, CH), 6.62 (dd, J = 2.0, 8.0 Hz, 1H, ArH), 6.76 (dd, J = 1.0, 8.0 Hz, 1H, ArH), 6.82 (dd, J = 2.0, 2.0 Hz, 1H, ArH), 7.20-7.26 (m, 1H, ArH), 8.43 (br. s, 1H, NH); ¹³C NMR (CDCl₃, δ): 22.1, 25.3, 70.1, 102.6, 106.9, 110.6, 125.1, 130.5, 142.6, 159.2, 188.4; MS (ESI⁻) m/z 253 (15%, M-H)⁻; HRMS (ESI⁻) calcd for C₁₂H₁₄ClN₂O₂: 253.0749 (M-H)⁻, found: 253.0744.

Ethyl (Z)-2-chloro-2-(2-(3-isopropoxyphenyl)hydrazineylidene)acetate (3.19): The compound was prepared according to method B (yield = 51%) as brown needles, m.p: 67-69 °C. ¹H NMR (CDCl₃, δ): 1.34 (d, J = 7.0 Hz, 6H, 2CH₃, C10), 1.39 (t, J = 7.0 Hz, 3H, -CH₂CH₃), 4.37 (q, J = 7.0 Hz, 2H, -CH₂CH₃), 4.54-4.59 (m, 1H, CH), 6.57 (dd, J = 2.0, 8.0 Hz, 1H, ArH), 6.73 (d, J = 8.0 Hz, 1H, ArH), 6.82 (t, 2.0 Hz, 1H, ArH), 7.20 (dd, J = 8.0, 8.0 Hz, 1H, ArH), 8.31 (br. s, 1H, NH); ¹³C NMR (CDCl₃, δ): 14.4, 22.2, 62.9, 70.1, 102.5, 107.0, 110.5, 116.0, 130.4, 143.0, 159.2, 159.8; MS (ESI⁺) m/z 591 (70%, 2M+Na)⁺; MS (ESI⁻) m/z 283 (5%, M-H)⁻.

(Z)-2-Oxo-N-(3-sulfamoylphenyl)propanehydrazonoyl chloride (3.20): The compound was prepared according to method B (yield = 65%) as a yellow powder, m.p: 223-225 °C. ¹H NMR (DMSO, δ): 2.49 (s, 3H, CH₃), 7.39 (br. s, 2H, NH₂),

7.44 (d, $J = 7.0$ Hz, 1H, ArH), 7.51 (t, $J = 7.5$ Hz, 2H, ArH), 7.61 (dd, $J = 2.0, 7.5$ Hz, 1H, ArH), 7.89 (dd, $J = 2.0$ Hz, 2H, ArH), 10.90 (br. s, 1H, NH); ^{13}C NMR (DMSO, δ): 25.9, 112.3, 118.2, 120.0, 124.7, 130.5, 143.4, 145.8, 188.4; MS (ESI) m/z 274 (100%, M-H) $^-$; HRMS (ESI $^-$) calcd for $\text{C}_9\text{H}_9\text{ClN}_3\text{O}_3\text{S}$: 274.0050 (M-H) $^-$, found: 274.0053.

Ethyl (Z)-2-chloro-2-(2-(3-sulfamoylphenyl)hydrazineylidene)acetate (3.21):

The compound was prepared according to method B (yield = 72%) as an orange powder, m.p: 213-215 °C. ^1H NMR (DMSO, δ): 1.30 (t, $J = 7.0$ Hz, 3H, CH_3), 4.30 (q, $J = 7.0$ Hz, 2H, CH_2), 7.38 (br. s, 2H, NH_2), 7.44 (d, $J = 7.0$ Hz, 1H, ArH), 7.49-7.54 (m, 2H, ArH), 7.84 (s, 1H, ArH), 10.80 (br. s, 1H, NH); ^{13}C NMR (DMSO, δ): 14.6, 62.9, 112.0, 115.6, 118.0, 119.8, 130.5, 143.6, 145.7, 159.6; MS (ESI) m/z 304 (100%, M-H) $^-$, 340 (30%, M+Cl) $^-$; HRMS (ESI $^-$) calcd for $\text{C}_{10}\text{H}_{11}\text{ClN}_3\text{O}_4\text{S}$: 304.0160 (M-H) $^-$, found: 304.0159.

(Z)-2-Oxo-N-(4-sulfamoylphenyl)propanehydrazonoyl chloride (3.22):

The compound was prepared according to method B (yield = 68%) as a buff powder, m.p: 190-192 °C. ^1H NMR (DMSO, δ): 2.52 (s, 3H, CH_3), 7.24 (br. s, 2H, NH_2), 7.56 (d, $J = 9.0$ Hz, 2H, ArH), 7.78 (d, $J = 9.0$ Hz, 2H, ArH), 10.93 (br. s, 1H, NH); ^{13}C NMR (DMSO, δ): 25.5, 114.5, 124.6, 127.3, 137.7, 145.2, 188.1; MS (ESI) m/z 274 (100%, M-H) $^-$, 310 (15%, M+Cl) $^-$; HRMS (ESI $^-$) calcd for $\text{C}_9\text{H}_9\text{ClN}_3\text{O}_3\text{S}$: 274.0059 (M-H) $^-$, found: 274.0053.

Ethyl (Z)-2-chloro-2-(2-(4-sulfamoylphenyl)hydrazineylidene)acetate (3.23):

The compound was prepared according to method B (yield = 75%) as an orange

powder, m.p: 178-180 °C. ^1H NMR ($(\text{CD}_3)_2\text{CO}$, δ): 1.37 (t, $J = 7.0$ Hz, 3H, CH_3), 4.38 (q, $J = 7.0$ Hz, 2H, CH_2), 6.57 (br. s, 2H, NH_2), 7.51 (d, $J = 8.0$ Hz, 2H, ArH), 7.87 (d, $J = 8.0$ Hz, 2H, ArH), 10.03 (br. s, 1H, NH); ^{13}C NMR ($(\text{CD}_3)_2\text{CO}$, δ): 13.8, 62.0, 114.0, 117.1, 127.6, 137.8, 145.9, 159.5; MS (ESI $^-$) m/z 304 (100%, M-H); HRMS (ESI $^+$) calcd for $\text{C}_{10}\text{H}_{11}^{35}\text{ClN}_3\text{O}_4\text{S}$: 306.0315 (M+H) $^+$, found: 306.0316.

(Z)-N-(4-Bromophenyl)-2-oxopropanehydrazonoyl chloride (3.24):²⁸ The compound was prepared according to method B (yield = 81%) as a yellow needles, m.p: 154-156 °C. ^1H NMR (CDCl_3 , δ): 2.57 (s, 3H, CH_3), 7.12 (d, $J = 8.5$ Hz, 2H, ArH), 7.47 (d, $J = 8.5$ Hz, 2H, ArH), 8.42 (br. s, 1H, NH); ^{13}C NMR (CDCl_3 , δ): 25.3, 115.9, 116.0, 126.0, 132, 140.5, 188.2; MS (ESI $^-$) m/z 273 (100%, M-H, ^{79}Br).

General procedure C for preparation of target compounds (3.29-3.39)

To a mixture of 6-ethyl-2-thioxo-2,3-dihydropyrimidin-4(1*H*)-one **3.4** (156 mg, 1 mmol) and the corresponding hydrazonoyl chloride **3.14-3.24** (1 mmol) in dioxane (15.0 mL), DIPEA (174 μL , 1 mmol) was added. The reaction mixture was heated at reflux until the starting materials were fully consumed or until no further conversion was observed (monitored by TLC analysis). The solvent was removed under vacuum and the residue was triturated with methanol and the resulting precipitate filtered, taken up in EtOAc and washed with water (2 x 30 mL), brine (30 mL), dried (MgSO_4), filtered and concentrated then subjected to flash chromatography (methanol/dichloromethane, 1:10) to give **3.29-3.39**.

3-Acetyl-7-ethyl-1-(3-fluorophenyl)-[1,2,4]triazolo[4,3-*a*]pyrimidin-5(1*H*)-one (3.29): The compound was prepared according to method C (yield = 35%) as

a buff powder, m.p: 122-124 °C; HPLC purity 95.3%. ^1H NMR (CDCl_3 , δ): 1.31 (t, $J = 7.5$ Hz, 3H, CH_3), 2.70 (q, $J = 7.5$ Hz, 2H, CH_2), 2.81 (s, 3H, COCH_3), 6.05 (s, 1H, ArH), 7.09 (app t, $J = 8.0$ Hz, 1H, ArH), 7.50 (dd, $J = 8.0, 14.5$ Hz, 1H, ArH), 8.08-8.12 (m, 2H, ArH); ^{13}C NMR (CDCl_3 , δ): 12.7, 30.0, 31.4, 101.2, 108.1 (d, $J^2_{\text{C-F}} = 28$ Hz), 114.5 (d, $J^2_{\text{C-F}} = 21$ Hz), 115.9 (d, $J^4_{\text{C-F}} = 4$ Hz), 130.8 (d, $J^3_{\text{C-F}} = 9$ Hz), 137.8 (d, $J^3_{\text{C-F}} = 10$ Hz), 141.6, 147.8, 155.9, 161.9 (d, $J^1_{\text{C-F}} = 248$ Hz), 172.2, 186.6; MS (ESI $^+$) m/z 301 (80%, $\text{M}+\text{H}$) $^+$, 623 (100%, $2\text{M}+\text{Na}$) $^+$; HRMS (ESI $^+$) calcd for $\text{C}_{15}\text{H}_{14}\text{FN}_4\text{O}_2$: 301.1101 ($\text{M}+\text{H}$) $^+$, found: 301.1095.

Ethyl 7-ethyl-1-(3-fluorophenyl)-5-oxo-1,5-dihydro-[1,2,4]triazolo[4,3-*a*]pyrimidine-3-carboxylate (3.30): The compound was prepared according to general method C (yield = 42%) as a buff powder, m.p: 92-94 °C; HPLC purity 98.7%. ^1H NMR (CDCl_3 , δ): 1.31 (t, $J = 7.5$ Hz, 3H, CH_3), 1.46 (t, $J = 7.0$ Hz, 3H, CH_3), 2.69 (q, $J = 7.5$ Hz, 2H, CH_2), 4.58 (q, $J = 7.0$ Hz, 2H, CH_2), 6.05 (s, 1H, ArH), 7.07 (td, $J = 1.5, 8.0$ Hz, 1H, ArH), 7.49 (dd, $J = 8.0, 14.5$ Hz, 1H, ArH), 8.06-8.11 (m, 2H, ArH); ^{13}C NMR (CDCl_3 , δ): 12.8, 14.0, 31.5, 64.2, 100.7, 108.0 (d, $J^2_{\text{C-F}} = 28$ Hz), 114.4 (d, $J^2_{\text{C-F}} = 21$ Hz), 115.7 (d, $J^2_{\text{C-F}} = 3$ Hz), 130.8 (d, $J^3_{\text{C-F}} = 9$ Hz), 135.8, 137.7 (d, $J^3_{\text{C-F}} = 11$ Hz), 147.2, 155.6, 156.7, 161.8 (d, $J^2_{\text{C-F}} = 247$ Hz), 172.6; MS (ESI $^+$) m/z 331 (55%, $\text{M}+\text{H}$) $^+$, 683 (100%, $2\text{M}+\text{Na}$) $^+$; HRMS (ESI $^+$) calcd for $\text{C}_{16}\text{H}_{16}\text{FN}_4\text{O}_3$: 331.1218 ($\text{M}+\text{H}$) $^+$, found: 331.1206.

3-Acetyl-1-(3-acetylphenyl)-7-ethyl-[1,2,4]triazolo[4,3-*a*]pyrimidin-5(1*H*)-one (3.31): The compound was prepared according to general method C (yield = 19%) as an orange powder, m.p: 118-120 °C; HPLC purity 97.5%. ^1H NMR (CDCl_3 , δ): 1.32 (t, $J = 7.5$ Hz, 3H, CH_3), 2.68-2.71 (m, 5H, $\text{CH}_3 + \text{CH}_2$), 2.83 (s, 3H, COCH_3),

6.07 (s, 1H, ArH), 7.66 (app t, $J = 8.0$ Hz, 1H, ArH), 7.97 (d, $J = 8.0$ Hz, 1H, ArH), 8.47 (d, $J = 8.0$ Hz, 1H, ArH), 8.90 (s, 1H, ArH); ^{13}C NMR (CDCl_3 , δ): 12.6, 27.0, 30.0, 31.3, 101.2, 120.3, 124.7, 127.3, 129.9, 136.9, 138.1, 141.5, 147.8, 155.8, 172.1, 186.6, 197.1; MS (ESI⁺) m/z 325 (20%, $\text{M}+\text{H}$)⁺, 671 (100%, $2\text{M}+\text{Na}$)⁺; HRMS (ESI⁺) calcd for $\text{C}_{17}\text{H}_{17}\text{N}_4\text{O}_3$: 325.1293 ($\text{M}+\text{H}$)⁺, found: 325.1301.

Ethyl 1-(3-acetylphenyl)-7-ethyl-5-oxo-1,5-dihydro-[1,2,4]triazolo[4,3-*a*]pyrimidine-3-carboxylate (3.32): The compound was prepared according to general method C (yield = 43%) as a white powder, m.p: 120-122 °C; HPLC purity 99.5%. ^1H NMR (CDCl_3 , δ): 1.32 (t, $J = 7.5$ Hz, 3H, CH_3), 1.48 (t, $J = 7.5$ Hz, 3H, CH_3), 2.68-2.71 (m, 5H, $\text{CH}_3 + \text{CH}_2$), 4.59 (q, $J = 7.0$ Hz, 2H, CH_2), 6.03 (s, 1H, ArH), 7.64 (app t, $J = 8.0$ Hz, 1H, ArH), 7.97 (d, $J = 8.0$ Hz, 1H, ArH), 8.46 (d, $J = 8.0$ Hz, 1H, ArH), 8.90 (s, 1H, ArH); ^{13}C NMR (CDCl_3 , δ): 12.7, 14.1, 26.9, 31.5, 64.2, 100.7, 120.4, 124.6, 127.1, 129.9, 136.1, 137.2, 138.3, 147.4, 155.6, 156.7, 172.5, 197.0; MS (ESI⁺) m/z 355 (20%, $\text{M}+\text{H}$)⁺, 377 (90%, $\text{M}+\text{Na}$)⁺; HRMS (ESI⁺) calcd for $\text{C}_{18}\text{H}_{19}\text{N}_4\text{O}_4$: 355.1422 ($\text{M}+\text{H}$)⁺, found: 355.1406.

3-Acetyl-7-ethyl-1-(3-isopropoxyphenyl)-[1,2,4]triazolo[4,3-*a*]pyrimidin-5(1*H*)-one (3.33): The compound was prepared according to general method C (yield = 27%) as a buff powder, m.p: 88-90 °C; HPLC purity 96.5%. ^1H NMR (CDCl_3 , δ): 1.30 (t, $J = 7.5$ Hz, 3H, CH_3), 1.40 (d, $J = 5.5$ Hz, 6H, 2 x CH_3), 2.68 (q, $J = 7.5$ Hz, 2H, CH_2), 2.80 (s, 1H, 3H, CH_3), 4.62-4.64 (m, 1H, CH), 6.04 (s, 1H, ArH), 6.91 (d, $J = 7.5$ Hz, 1H, ArH), 7.40 (app t, $J = 7.5$ Hz, 1H, ArH), 7.73-7.79 (m, 1H, ArH), 7.84 (s, 1H, ArH); ^{13}C NMR (CDCl_3 , δ): 12.7, 22.1, 30.0, 31.4, 70.6, 100.8, 108.3, 112.7, 115.7, 130.3, 137.6, 141.3, 148.0, 156.1, 158.7, 172.2,

186.7; MS (ESI⁺) m/z 341 (60%, M+H)⁺, 703 (100%, 2M+Na)⁺; HRMS (ESI⁺) calcd for C₁₈H₂₁N₄O₃: 341.1611 (M+H)⁺, found: 341.1614.

Ethyl 7-ethyl-1-(3-isopropoxyphenyl)-5-oxo-1,5-dihydro-[1,2,4]triazolo[4,3-*a*]pyrimidine-3-carboxylate (3.34): The compound was prepared according to general method C (yield = 35%) as a buff powder, m.p: 95-97 °C; HPLC purity 98.3%. ¹H NMR (CDCl₃, δ): 1.30 (t, $J = 7.5$ Hz, 3H, CH₃), 1.38 (d, $J = 6.0$ Hz, 6H, 2CH₃), 1.46 (t, $J = 7.0$ Hz, 3H, CH₃), 2.67 (q, $J = 7.5$ Hz, 2H, CH₂), 4.57 (q, $J = 7.0$ Hz, 2H, CH₂), 4.60-4.65 (m, 1H, CH), 6.00 (s, 1H, ArH), 6.89 (d, $J = 8.0$ Hz, 1H, ArH), 7.39 (dd, $J = 8.0, 8.5$ Hz, 1H, ArH), 7.74 (d, $J = 8.5$ Hz, 1H, ArH), 7.82 (s, 1H, ArH); ¹³C NMR (CDCl₃, δ): 12.8, 14.1, 22.2, 31.6, 64.1, 70.5, 100.3, 108.0, 112.7, 115.8, 130.3, 135.7, 137.7, 147.4, 155.9, 157.0, 158.7, 172.7; MS (ESI⁺) m/z 371 (80%, M+H)⁺, 763 (100%, 2M+Na)⁺; HRMS (ESI⁺) calcd for C₁₉H₂₃N₄O₃: 371.1720 (M+H)⁺, found: 371.1719.

3-(3-Acetyl-7-ethyl-5-oxo-[1,2,4]triazolo[4,3-*a*]pyrimidin-1(5*H*)-yl)benzenesulfonamide (3.35): The compound was prepared according to general method C (yield = 39%) as a buff powder, m.p: 180-182 °C; HPLC purity 96.5 %. ¹H NMR ((CD₃)₂CO), δ: 1.30 (t, $J = 7.5$ Hz, 3H, CH₃), 2.68 (q, $J = 7.5$ Hz, 2H, CH₂), 2.77 (s, 1H, 3H, CH₃), 6.00 (s, 1H, ArH), 6.85 (br. s, 2H, NH₂), 7.82 (dd, $J = 8.0, 8.5$ Hz, 1H, ArH), 7.94 (d, $J = 8.0$ Hz, 1H, ArH), 8.61 (d, $J = 8.5$ Hz, 1H, ArH), 8.79 (s, 1H, ArH); ¹³C NMR ((CD₃)₂CO), δ: 12.2, 29.8, 31.0, 100.1, 118.1, 123.5, 124.7, 130.3, 137.5, 142.1, 145.8, 148.5, 155.9, 172.0, 188.0; MS (ESI⁺) m/z 362 (10%, M+H)⁺, 384 (15%, M+Na)⁺; HRMS (ESI⁺) calcd for C₁₅H₁₆N₅O₄S: 362.0917 (M+H)⁺, found: 362.0923.

Ethyl 7-ethyl-5-oxo-1-(3-sulfamoylphenyl)-1,5-dihydro-[1,2,4]triazolo[4,3-*a*]pyrimidine-3-carboxylate (3.36): The compound was prepared according to general method C (yield = 55%) as a pale yellow powder, m.p: 176-178 °C; HPLC purity 98.7%. ¹H NMR (DMSO, δ): 1.24 (t, $J = 7.5$ Hz, 3H, CH_3), 1.35 (t, $J = 7.0$ Hz, 3H, CH_3), 2.62 (q, $J = 7.5$ Hz, 2H, CH_2), 4.48 (q, $J = 7.0$ Hz, 2H, CH_2), 6.02 (s, 1H, ArH), 7.59 (br. s, 2H, NH₂), 7.81-7.86 (m, 2H, ArH), 8.42 (d, $J = 8.0$ Hz, 1H, ArH), 8.57 (s, 1H, ArH); ¹³C NMR (DMSO, δ): 12.9, 14.2, 31.0, 64.0, 100.0, 118.1, 123.8, 124.8, 130.8, 135.8, 137.0, 145.8, 148.2, 155.5, 157.0, 172.0; MS (ESI⁺) m/z 414 (35%, M+H)⁺, 805 (100%, 2M+Na)⁺; HRMS (ESI⁺) calcd for C₁₆H₁₇N₅O₅S: 414.0858 (M+Na)⁺, found: 414.0848.

4-(3-Acetyl-7-ethyl-5-oxo-[1,2,4]triazolo[4,3-*a*]pyrimidin-1(5H)-yl)benzenesulfonamide (3.37): The compound was prepared according to general method C (yield = 51%) as a buff powder, m.p: 162-164 °C; HPLC purity 96.3%. ¹H NMR (DMSO, δ): 1.25 (t, $J = 7.5$ Hz, 3H, CH_3), 2.65 (q, $J = 7.5$ Hz, 2H, CH_2), 2.72 (s, 1H, 3H, CH_3), 6.07 (s, 1H, ArH), 7.49 (br. s, 2H, NH₂), 8.05 (d, $J = 8.5$ Hz, 2H, ArH), 8.37 (d, $J = 8.5$ Hz, 2H, ArH); ¹³C NMR (DMSO, δ): 13.0, 30.6, 30.9, 100.5, 121.1, 127.6, 139.1, 141.9, 142.9, 148.4, 155.9, 171.8, 188.6; MS (ESI⁺) m/z 384 (10%, M+Na)⁺, 745 (15%, 2M+Na)⁺; HRMS (ESI⁺) calcd for C₁₅H₁₆N₅O₄S: 362.0912 (M+H)⁺, found: 362.0923.

Ethyl 7-ethyl-5-oxo-1-(4-sulfamoylphenyl)-1,5-dihydro-[1,2,4]triazolo[4,3-*a*]pyrimidine-3-carboxylate (3.38): The compound was prepared according to general method C (yield = 61%) as a pale yellow powder, m.p: 180-182 °C; HPLC purity 96.7%. ¹H NMR ((CD₃)₂CO), δ : 1.32 (t, $J = 7.5$ Hz, 3H, CH_3), 1.45 (t, $J =$

7.0 Hz, 3H, CH_3), 2.71 (q, $J = 7.5$ Hz, 2H, CH_2), 4.56 (q, $J = 7.0$ Hz, 2H, CH_2), 6.00 (s, 1H, ArH), 6.72 (br. s, 2H, NH_2), 8.13 (d, $J = 8.5$ Hz, 2H, ArH), 8.51 (d, $J = 8.5$ Hz, 2H, ArH); ^{13}C NMR ($(\text{CD}_3)_2\text{CO}$), δ : 12.1, 13.3, 30.9, 63.5, 99.8, 120.4, 127.4, 136.2, 139.5, 142.6, 148.0, 155.1, 156.7, 172.0; MS (ESI⁺) m/z 392 (5%, $\text{M}+\text{H}$)⁺, MS (ESI⁻) m/z 390 (100%, $\text{M}-\text{H}$)⁻; HRMS (ESI⁺) calcd for $\text{C}_{16}\text{H}_{18}\text{N}_5\text{O}_5\text{S}$: 392.1032 ($\text{M}+\text{H}$)⁺, found: 392.1029.

3-Acetyl-1-(4-bromophenyl)-7-ethyl-[1,2,4]triazolo[4,3-*a*]pyrimidin-5(1*H*)-

one (3.39): The compound was prepared according to general method C (yield = 32%) as a buff powder, m.p: 155-157 °C; HPLC purity 95.4%. ^1H NMR (CDCl_3 , δ): 1.30 (t, $J = 7.5$ Hz, 3H, CH_3), 2.68 (q, $J = 7.5$ Hz, 2H, CH_2), 2.81 (s, 3H, COCH_3), 6.05 (s, 1H, ArH), 7.66 (d, $J = 9.0$ Hz, 2H, ArH), 8.17 (d, $J = 9.0$ Hz, 2H, ArH); ^{13}C NMR (CDCl_3 , δ): 12.6, 29.9, 31.3, 100.9, 121.3, 122.0, 132.4, 135.6, 141.5, 147.6, 155.8, 172.1, 186.5; MS (ESI⁺) m/z 361 (10%, $\text{M}+\text{H}$, ^{79}Br)⁺, 363 (10%, $\text{M}+\text{H}$, ^{81}Br)⁺; HRMS (ESI⁺) calcd for $\text{C}_{15}\text{H}_{14}^{79}\text{BrN}_4\text{O}_2$: 361.0301 ($\text{M}+\text{H}$)⁺, found: 361.0300.

3.4.2 Biological evaluation

- Antiviral assay:²⁹

CHIKV Indian Ocean strain 899 (Genbank FJ959103.1) was generously provided by Prof. S. Günther (Bernhard Nocht Institute for Tropical Medicine, Hamburg, Germany) (Panning M et al., Emerging Infectious Diseases 2008). BGM cells were maintained in cell growth medium composed of minimum essential medium (MEM Rega-3, Gibco, Belgium) supplemented with 10% Foetal Bovine Serum (FBS, Integro, The Netherlands), 1% L-glutamine (Gibco), and 1% sodium bicarbonate (Gibco). The antiviral assays were performed in virus growth medium which is the

respective cell growth medium supplemented with 2% (instead of 10%) FBS. Cell cultures were maintained at 37 °C in an atmosphere of 5% CO₂ and 95-99% humidity. BGM cells were seeded in 96-well tissue culture plates (Becton Dickinson, Aalst, Belgium) at a density of 2.5 x 10⁴ cells/well in 100 µL assay medium and were allowed to adhere overnight. Next, a compound dilution series was prepared in the medium on top of the cells after which the cultures were infected with 0.001 MOI of CHIKV 899 inoculum in 100 µL assay medium. On day 5 post-infection (p.i.), the plates were processed using the MTS/PMS method as described by the manufacturer (Promega, The Netherlands). The 50% effective concentration (EC₅₀), which is defined as the compound concentration that is required to inhibit virus-induced cell death by 50%, was determined using logarithmic interpolation. All assay wells were checked microscopically for minor signs of virus induced CPE or possible alterations to the cell or monolayer morphology caused by the compound.

- **Cell viability assay:**

Exactly 100 µL of cells were cultured in 96 well-plates at a seeding density of 105 cells/mL. After 24 h, the cells were treated with the samples (dissolved in DMSO) and incubated for 72 h. Doxorubicin at 1 µM concentration was used as a positive control with 0.1% DMSO as a negative control for each plate. At the end of incubation period the culture media were aspirated followed by the addition of 100 µL of 0.1 mg/mL Alamar blue solution (resazurin, stock solution (1 mg/mL in a freshly prepared PBS), followed by 1:10 dilution with FBS free media) was added to each well. Absorbance at 570 nm and 600 nm was measured using a BMG LABTech FLUOstar OPTIMA plate reader (Mount Eliza, Victoria, Australia). The drugs were tested in triplicate with a negative control was taken as 100% cell

viability. Nonlinear regression and IC₅₀ calculations were performed with GraphPad Prism 7.0 (GraphPad Software, Inc., San Diego, CA).

3.4.3 Computational studies

All geometries and energies were calculated using the Gaussian16 package at the B3LYP-D3(BJ)/6-311++G(2d,p) level including implicit solvation (polarisable continuum model, solvent excluded surface and solvent-solute dispersion interaction included) using the standard parameters for water. Normal mode frequency analysis was performed on all ground state structures to confirm the nature of the energy stationary point and estimate free energies.

For tautomer distributions, the molar free energies (ΔG) of each tautomer (relative to that of the lowest) was calculated and isomer distributions derived using the Boltzmann factor:

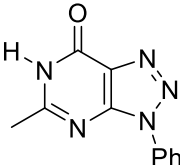
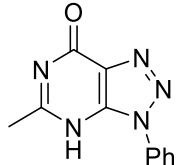
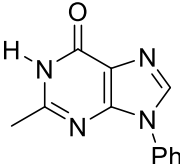
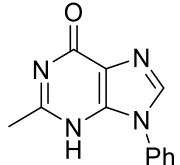
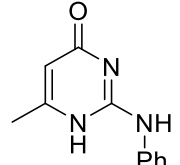
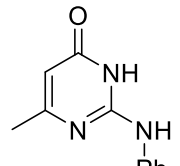
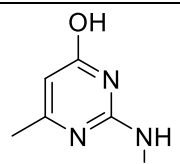
$$\frac{p_i}{p_0} = e^{\frac{-\Delta G}{RT}}$$

where R is the molar gas constant, T the temperature (37° C = 310.15 K). The results are shown in Table S1.

Electron density and Electrostatic Potential (ESP) cube files were calculated using the Gaussian cubegen utility. ESP mapped onto electron isodensities were generated using the GausView 6.0.16 application (Table 3.3).

Potential Energy Surfaces for the N-Ar torsion for **3.53**, **3.54** and **3.55** were calculated at the B3LYP-D3(BJ)/6-311G(2d,p) (Table 3.3) level including implicit solvation (continuum model, solvent excluded surface and solvent-solute dispersion interaction included) using the standard parameters for water. The torsional angle defined by the blue heavy bonds (9,1,a,b) shown below and scanned in 1° increments:

Table 3.3: B3LYP-D3(BJ)/6-311++G(2d,p)-(water solvation) calculated free energies and relative concentrations at 37° C for tautomers of the minimal pharmacophores **3.54**, **3.54b**, **3.55**, **3.55a**, **3.56a-c**.

Tautomer		G / Ha	$\Delta G / \text{kJ mol}^{-1}$	Relative conc.
3.54		-773.743900	[0]	[1]
3.54b		-773.728761	40	2.0×10^{-7}
3.55		-757.711628	[0]	[1]
3.55b		-757.695321	43	6.1×10^{-8}
3.56a		-665.434824	9	3.2×10^{-2}
3.56b		-665.438199	[0]	[1]
3.56c		-665.431651	17	1.3×10^{-3}

3.4.4 X-ray crystallography

- Single solid X-ray crystallographic data of 3.15

Crystal data. Compound **3.15**. $C_{10}H_{10}ClFN_2O_2$, $M = 244.65$, $T = 153$ K, Orthorhombic, $Z = 4$, $a = 4.590$ (1), $b = 9.619$ (2), $c = 25.879$ (4) Å, $V = 1142.6$ (4) Å³, $D_x = 1.422$ Mg m⁻³, synchrotron radiation, $\lambda = 0.710919$ Å, 4577 reflections measured ($\theta = 1.6$ – 29.1°), merged to 2330 unique data, $R = 0.040$ [for 2089 data with $I > 2\sigma(I)$], $R [F^2 > 2\sigma(F^2)] = 0.043$ [all data], $S = 0.99$

Structure determination of compound 3.15. Data was collected using Dectris Eiger 16M diffractometer with radiation source: MX1 Beamline Australian Synchrotron.³⁰ Structure solution was by direct methods (SIR92).³¹ The structure was refined using the CRYSTALS program package.³²

- Single solid X-ray crystallographic data of 3.20

Crystal data. Compound **3.20**. $C_{10}H_{10}ClFN_2O_2$, $M = 275.72$, $T = 153$ K, Orthorhombic, $Z = 8$, $a = 15.154$ (1), $b = 8.056$ (10), $c = 19.144$ (4) Å, $V = 2337$ (3) Å³, $D_x = 1.567$ Mg m⁻³, synchrotron radiation, $\lambda = 0.710919$ Å, 26664 reflections measured ($\theta = 2.1$ – 29.2°), merged to 2408 unique data, $R = 0.111$ [for 1625 data with $I > 2\sigma(I)$], $R [F^2 > 2\sigma(F^2)] = 0.060$ [all data], $S = 0.90$.

- *Structure determination of compound 3.20.* Data was collected using Dectris Eiger 16M diffractometer with radiation source: MX1 Beamline Australian Synchrotron.³⁰ Structure solution was by direct methods (SIR92).³¹ The structure was refined using the CRYSTALS program package.³²

- **Single solid X-ray crystallographic data of 3.24**

Crystal data. Compound **3.24**. $C_9H_8BrClN_2O$, $M = 275.53$, $T = 153$ K, Orthorhombic, $Z = 4$, $a = 8.821(6)$, $b = 25.123(15)$, $c = 4.560(4)$ Å, $V = 1010.5(13)$ Å³, $D_x = 1.811$ Mg m⁻³, synchrotron radiation, $\lambda = 0.710919$ Å, 12004 reflections measured ($\theta = 1.6$ – 29.0°), merged to 2334 unique data, $R = 0.093$ [for 2022 data with $I > 2\sigma(I)$], $R [F^2 > 2\sigma(F^2)] = 0.046$ [all data], $S = 1.01$.

Structure determination of compound 3.24. Data was collected using Dectris Eiger 16M diffractometer with radiation source: MX1 Beamline Australian Synchrotron.³⁰ Structure solution was by direct methods (SIR92).³¹ The structure was refined using the CRYSTALS program package.³²

- **Single solid X-ray crystallographic data of 3.23**

Crystal data. For compound **3.23** $C_{18}H_{18}N_4O_4$ ($M = 354.36$ g/mol): monoclinic, space group $P2_1/n$ (no. 14), $a = 16.2162(9)$ Å, $b = 5.5670(3)$ Å, $c = 19.1376(13)$ Å, $\beta = 96.256(6)^\circ$, $V = 1717.37(19)$ Å³, $Z = 4$, $T = 100(2)$ K, $\mu(\text{CuK}\alpha) = 0.824$ mm⁻¹, $D_{\text{calc}} = 1.371$ g/cm³, 11249 reflections measured ($7.564^\circ \leq 2\theta \leq 145.012^\circ$), 3326 unique ($R_{\text{int}} = 0.0503$, $R_{\text{sigma}} = 0.0396$) which were used in all calculations. The final R_1 was 0.0575 ($I > 2\sigma(I)$) and wR_2 was 0.1665 (all data).

Structure determination of compound 3.23: Data was collected using SuperNova, Dual, Cu at home/near, Atlas diffractometer. Using Olex2³³, the structure was solved with the olex2.solve³⁴ structure solution program using Charge Flipping and refined with the ShelX³⁵ refinement package using Least Squares Minimization.

- **Single solid X-ray crystallographic data of 3.39**

Crystal data. Compound **3.39**. C₁₅H₁₃BrN₄O₂, $M = 361.20$, $T = 153$ K, Monoclinic, $Z = 4$, $a = 4.668$ (1), $b = 21.780$ (2), $c = 14.348$ (2) Å, $\beta = 93.379$ (6)°, $V = 1456.2$ (5) Å³, $D_x = 1.647$ Mg m⁻³, synchrotron radiation, $\lambda = 0.710919$ Å, 19044 reflections measured ($\theta = 1.7$ – 29.2°), merged to 2876 unique data, $R = 0.053$ [for 2544 data with $I > 2\sigma(I)$], $R [F^2 > 2\sigma(F^2)] = 0.031$ [all data], $S = 0.99$.

Structure determination of compound 3.39. Data was collected using Dectris Eiger 16M diffractometer with radiation source: MX1 Beamline Australian Synchrotron.³⁰ Structure solution was by direct methods (SIR92).³¹ The structure was refined using the CRYSTALS program package.³²

3.5 References

1. *Investing to overcome the global impact of neglected tropical diseases: Third WHO report on neglected diseases 2015*; 9241564865; World Health Organization: 2015.
2. *Chikungunya – sudan*; World Health Organization: 2018.
3. Rashad, A. A.; Mahalingam, S.; Keller, P. A. Chikungunya virus: Emerging targets and new opportunities for medicinal chemistry. *J. Med. Chem.* **2014**, *57*, 1147-1166.
4. Perez-Perez, M. J.; Delang, L.; Ng, L. F. P.; Priego, E. M. Chikungunya virus drug discovery: Still a long way to go? *Expert Opin. Drug Discov.* **2019**, *14*, 855-866.
5. Rothan, H. A.; Bahrani, H.; Abdulrahman, A. Y.; Mohamed, Z.; Teoh, T. C.; Othman, S.; Rashid, N. N.; Rahman, N. A.; Yusof, R. Mefenamic acid in combination with ribavirin shows significant effects in reducing chikungunya virus infection in vitro and in vivo. *Antivir. Res.* **2016**, *127*, 50-56.
6. Nguyen, P. T.; Yu, H.; Keller, P. A. Discovery of in silico hits targeting the nsp3 macro domain of chikungunya virus. *J. Mol. Model.* **2014**, *20*, 1-12.
7. Nguyen, P. T.; Yu, H.; Keller, P. A. Identification of chikungunya virus nsp2 protease inhibitors using structure-based approaches. *J. Mol. Graphics Modell.* **2015**, *57*, 1-8.
8. Maheshwari, R. K.; Srikantan, V.; Bhartiya, D. Chloroquine enhances replication of semliki forest virus and encephalomyocarditis virus in mice. *J. Virol.* **1991**, *65*, 992-995.
9. Ravichandran, R.; Manian, M. Ribavirin therapy for chikungunya arthritis. *J. Infect. Dev. Ctries.* **2008**, *2*, 140-142.
10. Kaur, P.; Thiruchelvan, M.; Lee, R. C.; Chen, H.; Chen, K. C.; Ng, M. L.; Chu, J. J. Inhibition of chikungunya virus replication by harringtonine, a novel antiviral that suppresses viral protein expression. *Antimicrob. Agents Chemother.* **2013**, *57*, 155-167.
11. Gigante, A.; Canela, M. D.; Delang, L.; Priego, E. M.; Camarasa, M. J.; Querat, G.; Neyts, J.; Leyssen, P.; Perez-Perez, M. J. Identification of [1,2,3]triazolo[4,5-*d*]pyrimidin-7(6*H*)-ones as novel inhibitors of chikungunya virus replication. *J. Med. Chem.* **2014**, *57*, 4000-4008.
12. Gigante, A.; Gomez-SanJuan, A.; Delang, L.; Li, C.; Bueno, O.; Gamo, A. M.; Priego,

- E. M.; Camarasa, M. J.; Jochmans, D.; Leyssen, P.; Decroly, E.; Coutard, B.; Querat, G.; Neyts, J.; Perez-Perez, M. J. Antiviral activity of [1,2,3]triazolo[4,5-*d*]pyrimidin-7(6*H*)-ones against chikungunya virus targeting the viral capping nsp1. *Antivir. Res.* **2017**, *144*, 216-222.
13. Karlas, A.; Berre, S.; Couderc, T.; Varjak, M.; Braun, P.; Meyer, M.; Gangneux, N.; Karo-Astover, L.; Weege, F.; Raftery, M.; Schonrich, G.; Klemm, U.; Wurzlbauer, A.; Bracher, F.; Merits, A.; Meyer, T. F.; Lecuit, M. A human genome-wide loss-of-function screen identifies effective chikungunya antiviral drugs. *Nat. Commun.* **2016**, *7*, 1-14.
14. Powers, A. M. Vaccine and therapeutic options to control chikungunya virus. *Clin. Microbiol. Rev.* **2018**, *31*, 1-29.
15. D'Hooghe, M.; Mollet, K.; De Vreese, R.; Jonckers, T. H.; Dams, G.; De Kimpe, N. Design, synthesis, and antiviral evaluation of purine-beta-lactam and purine-aminopropanol hybrids. *J. Med. Chem.* **2012**, *55*, 5637-5641.
16. Delang, L.; Li, C.; Tas, A.; Quérat, G.; Albulescu, I.; De Burghgraeve, T.; Guerrero, N. S.; Gigante, A.; Piorkowski, G.; Decroly, E. The viral capping enzyme nsp1: A novel target for the inhibition of chikungunya virus infection. *Sci. Rep.* **2016**, *6*, 31819.
17. Fares, M.; Abd El Hadi, S. R.; Eladwy, R. A.; Shoun, A. A.; Abdel-Aziz, M. M.; Eldehna, W. M.; Abdel-Aziz, H. A.; Keller, P. A. An improved synthesis of pyrido[2,3-*d*]pyrimidin-4(1*H*)-ones and their antimicrobial activity. *Org. Biomol. Chem.* **2018**, *16*, 3389-3395.
18. Kusturin, C.; Liebeskind, L. S.; Rahman, H.; Sample, K.; Schweitzer, B.; Srogl, J.; Neumann, W. L. Switchable catalysis: Modular synthesis of functionalized pyrimidinones via selective sulfide and halide cross-coupling chemistry. *Org. Lett.* **2003**, *5*, 4349-4352.
19. Maddess, M. L.; Carter, R. Snar reactions of 2-methylthio-4-pyrimidinones in pivalic acid: Access to functionalized pyrimidinones and pyrimidines. *Synthesis* **2012**, *44*, 1109-1118.
20. R, W. 3-methylcoumarone. *Org. Syn.* **1953**, *33*, 43-43.
21. Farghaly, T. A.; Hassaneen, H. M. Synthesis of pyrido[2,3-*d*][1,2,4]triazolo[4,3-*a*]pyrimidin-5-ones as potential antimicrobial agents. *Arch. Pharmacol. Res.* **2013**, *36*, 564-72.
22. Shawali, A. S.; Farghaly, T. A. Reactions of hydrazonoyl halides with heterocyclic thiones. Convenient methodology for heteroannulation, synthesis of spiroheterocycles and heterocyclic ring transformation. *Arkivoc* **2008**, *1*, 18-64.
23. Fares, M.; Abou-Seri, S. M.; Abdel-Aziz, H. A.; Abbas, S. E.; Youssef, M. M.; Eladwy, R. A. Synthesis and antitumor activity of pyrido [2,3-*d*]pyrimidine and pyrido[2,3-*d*] [1,2,4]triazolo[4,3-*a*]pyrimidine derivatives that induce apoptosis through G1 cell-cycle arrest. *Eur. J. Med. Chem.* **2014**, *83*, 155-166.
24. Shawali, A. S.; Abdallah, M. A.; Zayed, M. M. A convenient one-pot synthesis and antimicrobial activity of pyrimido [1, 2-*b*][1, 2, 4, 5] tetrazines. *J. Heterocycl. Chem.* **2002**, *39*, 45-49.
25. Mosselhi, M. A. A convenient synthesis of novelderivatives of pyrido [2, 3-*d*][1, 2, 4] triazolo [4, 3-*a*] pyrimidine-5, 6-dione. *Monatsh. Chem.* **2002**, *133*, 1297-1304.
26. Molsoft, L. Drug-likeness and molecular property prediction. <http://molsoft.com/mprop/>.
27. Abdel-Aziz, H. A.; Eldehna, W. M.; Fares, M.; Elsaman, T.; Abdel-Aziz, M. M.; Soliman, D. H. Synthesis, in vitro and in silico studies of some novel 5-nitrofurano-2-yl hydrazones as antimicrobial and antitubercular agents. *Biol. Pharm. Bull.* **2015**, *38*, 1617-1630.
28. Edrees, M. M.; Melha, S. A.; Saad, A. M.; Kheder, N. A.; Gomha, S. M.; Muhammad, Z. A. Eco-friendly synthesis, characterization and biological evaluation of some novel pyrazolines containing thiazole moiety as potential anticancer and antimicrobial agents. *Molecules* **2018**, *23*.
29. Ahmed, S. A.; Gogal, R. M., Jr.; Walsh, J. E. A new rapid and simple non-radioactive assay to monitor and determine the proliferation of lymphocytes: An alternative to [3H]thymidine incorporation assay. *J. Immunol. Methods* **1994**, *170*, 211-24.
30. Kabsch, W. Xds. *Acta Crystallogr. Sect. D. Struc. Biol.* **2010**, *66*, 125-32.
31. Altomare, A.; Casciarano, G.; Giacovazzo, C.; Guagliardi, A.; Burla, M.; Polidori, G. t.; Camalli, M. Sirpow. 92—a program for automatic solution of crystal structures by direct methods optimized for powder data. *J. Appl. Crystallogr.* **1994**, *27*, 435-436.
32. Betteridge, P. W.; Carruthers, J. R.; Cooper, R. I.; Prout, K.; Watkin, D. J. Crystals version 12: Software for guided crystal structure analysis. *J. Appl. Crystallogr.* **2003**, *36*, 1487-1487.
33. Dolomanov, O. V.; Bourhis, L. J.; Gildea, R. J.; Howard, J. A.; Puschmann, H. Olex2: A complete structure solution, refinement and analysis program. *J. Appl. Crystallogr.* **2009**, *42*, 339-341.
34. Bourhis, L. J.; Dolomanov, O. V.; Gildea, R. J.; Howard, J. A.; Puschmann, H. The

anatomy of a comprehensive constrained, restrained refinement program for the modern computing environment—olex2 dissected. *Acta Crystallogr. Sect. A: Found. Adv.* **2015**, 71, 59-75.

35. Sheldrick, G. M. Crystal structure refinement with shelxl. *Acta Crystallogr. Sect. C: Struct. Chem.* **2015**, 71, 3-8.

Chapter 4:

**Structure-guided drug design
targeting CHIKV**

FOREWORD TO CHAPTER 4

This chapter describes application of structure-guided design approaches in the development of new anti-CHIKV agent. Herein, the biological evaluation of the active hits discovered by *in silico* screening is described. This chapter reports three potential CHIKV inhibitors discovered from the antiviral screening. It also describes the synthesis of a small library of the naphthamide derivative. However, more studies need to be performed, including biological testing of the naphthamide library at lower concentration and also development of the quinoline and the spirobi[cyclopenta[*b*]naphthalene]dione scaffolds. NMR data of the synthesized compounds from this chapter can be found in Appendix C (p. 257).

4.1 Introduction

Chikungunya virus (CHIKV) is an arbovirus that is transmitted mainly by female *Aedes aegypti* or *Aedes albopictus* mosquito and is accompanied with abrupt onset of fever and debilitating acute and chronic joints pain in humans.¹ In 1952 symptoms of the CHIKV infection were reported for the first time after an outbreak in eastern Africa.² Many intermittent outbreaks re-emerged in Africa and Asia in the past sixty years.³⁻⁵ There was no major re-emergence of chikungunya fever until the epidemic outbreak in Kenya in 2004.¹ This epidemic CHIKV fever resulted in considerable mortality and morbidity and unfortunately, the infection spread to neighbouring areas.⁶

The wider spreading of the virus throughout Europe and Americas was due to number of adaptive mutations of the virus that allowed for exploitation a new vector (*Aedes albopictus*).⁷ In 2013, CHIKV infection has been reported on the Caribbean island of Saint Martin and spread to another 22 countries in Caribbean and America in less than a year. In 2018, around 14,000 cases of CHIKV were reported in Sudan, with 95% in Kassala state.^{9, 10} More than 55 countries have reported the CHIKV infection so far and the virus was classified by US National Institute of Allergy and Infectious Diseases (NIAID) as a category C priority pathogen; this category includes reemerging pathogens that could be used for mass dissemination.¹

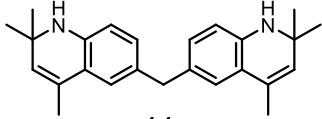
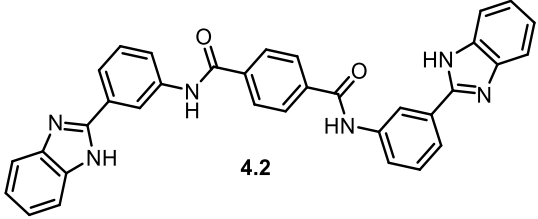
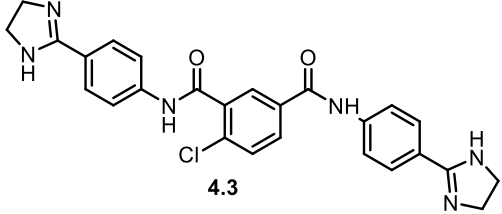
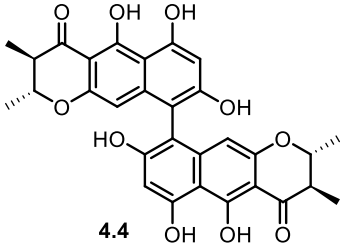
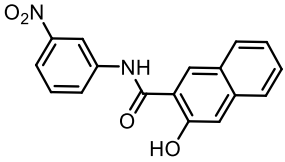
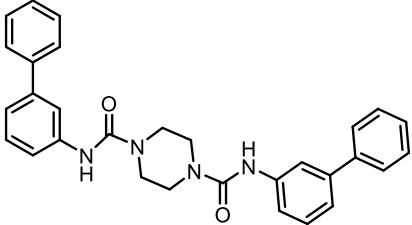
So, far, there is no vaccine or an approved drug to treat, cure or prevent the CHIKV infection. Current management of the CHIKV infection includes non-steroidal anti-inflammatory drugs (NSAID) to alleviate the symptoms of CHIKV and corticosteroids as anti-inflammatory in chronic CHIKV infection.¹¹ Efforts have been made to discover clinical anti-CHIKV agents by many research groups. This

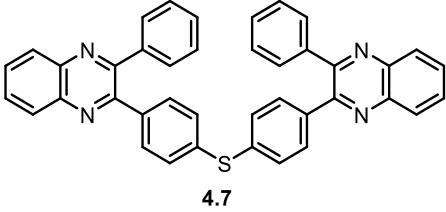
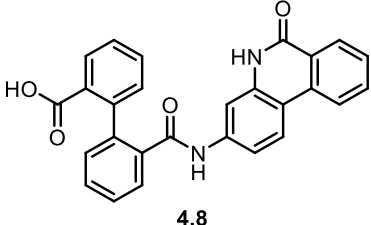
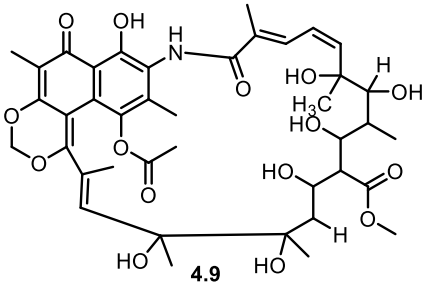
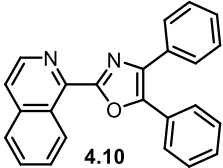
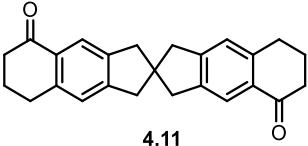
includes vaccine development, virtual screening, *in vitro* whole cell phenotypic screening and genome-wide loss of function screens.^{6, 12-18} Recent advances in CHIKV drug discovery have been recently reviewed.^{1, 19, 20}

In 2010, crystal structure of the virus genome was fully elucidated offering an important step for anti-CHIKV *in-silico* drug discovery.¹ A computational study in our research group has led to identification of potential CHIKV inhibitors,^{6, 12, 21} using *in silico* tools to elucidate possible interactions of small molecule inhibitors with the viral protein. Molecular docking, virtual screening, molecular dynamic (MD) simulation and binding free energy calculations were computational strategies used to identify novel CHIKV inhibitors from the NCI Diversity Set II database (1541 compounds). The study investigated nsP2 proteases and the nsP3 macrodomain, in addition to the envelope glycoprotein complexes responsible for virus entry and attachment as targets for potential inhibitors.²¹

Table 4.1 presents the outcomes of the above study showing the compounds and their binding activity. Analysis of the docking experiments showed the different interactions between the ligands and the viral targets.²¹ Two promiscuous compounds were reported interacting with all the tested viral components, namely, the benzimidazole derivative, NCI_61610 and the quinoxaline derivative, NCI_293778 (**1.9**).²¹ Among the investigated compounds, NCI_25457 **1.30**, NCI_37553 **1.27**, and NCI_127133 **1.28**, showed good interaction with two of the three target proteins and glycoproteins (Table 4.1).²¹

Table 4.1: Results of the selected compounds of focused dockings on the nsP2, nsP3 and the glycoprotein envelope.

NCI #	Chemical Structure	Target	BA* Kcal/mol
217697	 4.1	nsP2	-9.2
61610	 4.2	nsP2	-10.6
		nsP3	-11.1
67436	 4.3	E glyp	-12.2
		nsP2	-15.5
345647	 4.4	nsP3	-10.9
37168	 4.5	nsP3	-10.0
37553	 4.6	nsP2	-9.6
		E glyp	-11.7

293778		nsP2 (-9.8) – nsP3 -9.4 E glyp -13.2
127133		nsP2 -8.8 nsP3 -8.3
156219		E glyp -11.1
25457		nsP2 -9.0 nsP3 -10.8
670283		nsP3 -10.6

*BA: Binding Affinity

4.2 Results and discussion

In this dissertation, the eleven compounds (Table 4.1) which were discovered by docking-based virtual screening and molecular dynamic simulation were selected for biological investigation for their anti CHIKV activity. The selected ligands were requested from Developmental Therapeutics Program Databases and Search

Tools, National Cancer Institute, USA and were tested in Rega Institute, KU Leuven, Belgium for their anti-CHIKV activity.

Three compounds, out of the tested eleven compounds, showed antiviral activities, the quinoline derivative **4.1** ($EC_{50} = 6.8 \mu\text{g/mL}$ and $EC_{90} = 12.0 \mu\text{g/mL}$) and the naphthalene derivatives **4.5** ($EC_{50} = 0.8 \mu\text{g/mL}$) and **4.11** ($11.5 \mu\text{g/mL}$) (Figure 4.1). We chose compound **4.5** for the next cycle of optimization because of availability of the starting materials and ease of synthesis.

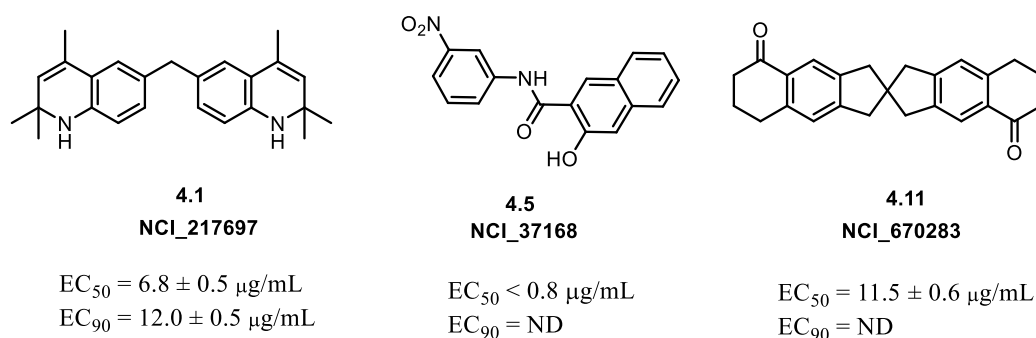


Figure 4.1: Structure of the active potential leads.

To further gain insights into the structure activity relationship of NCI_37168 (**4.5**), possible modifications were postulated including changing the aniline substitution and spacer between the amide group nitrogen and aryl side chain and also investigate the effect of the presence of naphthalene hydroxyl group (Figure 4.2). Firstly, the effect of the presence of hydroxyl moiety in the parent molecule **4.5** was investigated **4.14**.

Then, aniline substitution with different groups was suggested to explore the structure activity relationship (**4.15-4.17**), while adding a spacer (1 carbon) between the amino group and the aryl side chain was supposed to increase the flexibility that can possibly add more points of interaction with the receptor (**4.19**

and 4.20).

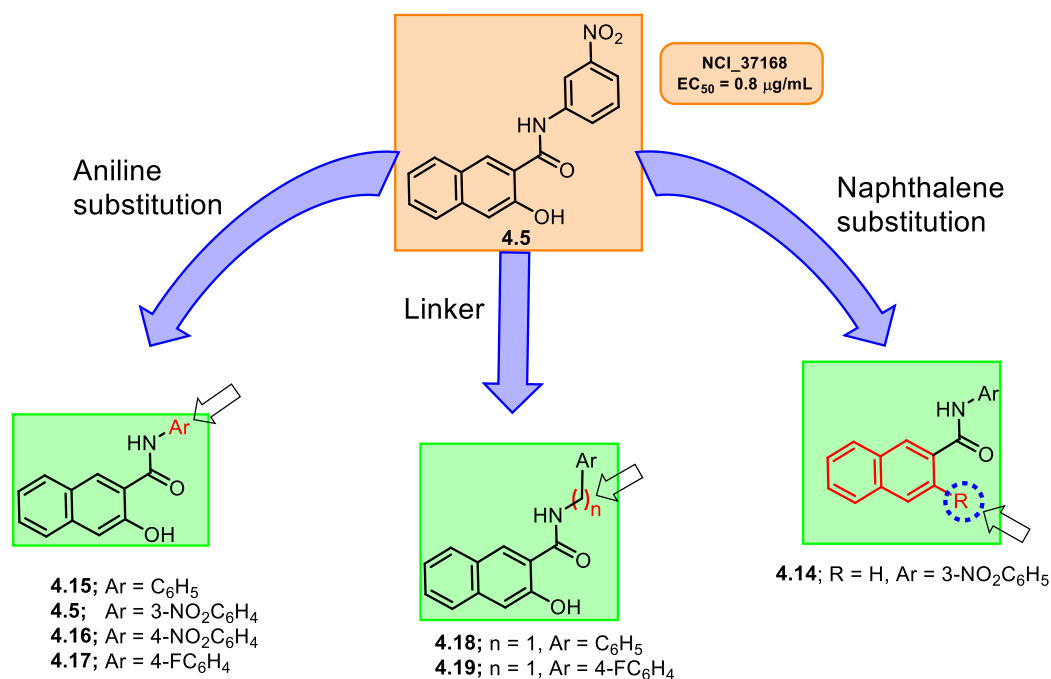
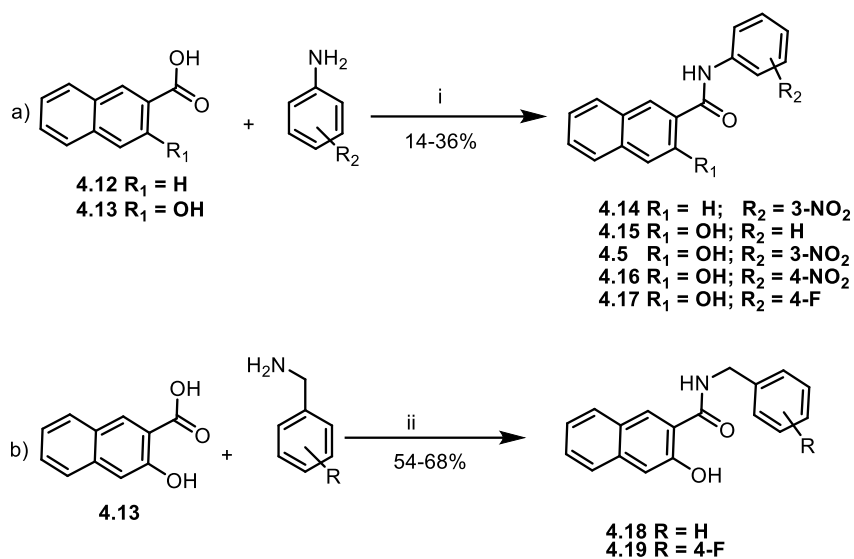


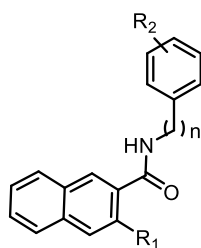
Figure 4.2: Possible modification of NCI_37168 (**4.5**).

Compounds **4.18** and **4.19** were prepared by the standard amide bond formation using CDI in THF (yields 45 and 50%, respectively).²² It is worthy to note that the CDI coupling procedure failed to prepare 3-hydroxy-*N*-aryl-2-naphthamides compounds **4.5** and **4.14-4.17** presumably due to formation of the ester side product. The required compounds **4.14-4.17** were prepared using PCl₃ promoted coupling of 2-naphthoic acid **4.12** or 3-hydroxy-2-naphthoic acid **4.13**, corresponding anilines and catalytic amounts of PCl₃ (40 mol%) in xylene and heating at reflux gave yields 14-32% (Scheme 4.1).²²



Scheme 4.1: Reagents and conditions i) 40 mol% PCl_3 , xylene, 2 h, reflux ii) CDI, THF, 18 h, rt.

The synthesized compounds were investigated for their biological activity against CHIKV and showed considerable toxic effect to the Vero cells, which impedes detection of their antiviral activity (Table 4.2). Although some compounds showed antiviral activity such as **4.5**, **4.15** and **4.16**, however toxicity of these compounds might impede further development of the naphthalene scaffold **4.5**. Antiviral testing of these inhibitors at lower concentration could be done to investigate their antiviral activity, while lowering their toxic effect. It is worthy to note that another study could investigate the development of the quinoline scaffold **4.1** and exploring the potential antiviral activity of this scaffold.

Table 4.2: *In vitro* antiviral and cytotoxic activities of compounds **4.14-4.20**.

Cpd number	R ₁	R ₂	n	CHIKV [20] $\mu\text{g/mL}$	at	Toxicity IC ₅₀ $\mu\text{g/mL}$
4.14	H	3-NO ₂	0	3		NT
4.15	OH	H	0	25		NT
4.5	OH	3-NO ₂	0	49		1.74
4.16	OH	4-NO ₂	0	27		<0.4
4.17	OH	4-F	0	13		NT
4.18	OH	H	1	0		NT
4.19	OH	4-F	1	0		NT

NT: not tested

4.3 Conclusions

A virtual screening search using NCI Diversity Set II database (1541 compounds) was performed against three CHIKV targets, namely nsP2, nsP3 and the envelope glycoprotein. Eleven hits were identified and tested for their anti-CHIKV activity in a cell-based assay and three hits, with naphthalene and quinoline scaffolds, showed promising anti-CHIKV. A facile and applicable synthesis of a small library **4.14-4.19** of the naphthamide hit **4.5** and their characterization were reported. Antiviral testing of these inhibitors at lower concentration will be done to investigate their antiviral activity, while lowering their toxic effect.

4.4 Experimental section

4.4.1 Chemistry

General

Electrospray ionisation mass spectra (ESI-MS) were recorded on a Shimadzu LCMS 2010 EV spectrometer and are reported as ion mass to charge ratio (m/z) with their abundance as a percentage. Solvents used were analytical reagent grade. Reactions were monitored by TLC analysis using silica gel GF/UV 254. NMR spectra were recorded on Bruker Avance III HD 500 or 400 MHz NMR spectrometers with spectra run at 400 and 500 MHz and ^{13}C spectra at 100 and 125 MHz, in deuterated chloroform or dimethylsulfoxide ($\text{DMSO-}d_6$). Chemical shifts (δ_{H}) are reported relative to TMS as an internal standard and coupling constant (J) values are reported in Hertz. Abbreviations used are: s, singlet; d, doublet; t, triplet; m, multiplet. All reagents and solvents were purified and dried by standard techniques.

General method A:

A solution of 2-naphthoic acid **4.12** (182 mg, 1.06 mmol) or 3-hydroxy-2-naphthoic acid **4.13** (200 mg, 1.06 mmol) in xylene (6 mL) and the corresponding aniline (1.17 mmol) was heated at reflux. PCl_3 (40.0 μL , 0.424 mmol) was added slowly and heat was maintained till HCl evolution had ceased (ca. 1 h). The reaction mixture was cooled down and water was added to decompose excess PCl_3 . The resulting precipitate was filtered, washed with petroleum spirit (2 x 10 mL) and recrystallized from THF and water (3:1, 20 mL) with a few drops of methanol.

General method B:

A solution of 3-hydroxy-2-naphthoic acid **4.13** (109 mg, 0.58 mmol), CDI (197 mg, 1.22 mmol), in THF (4 mL) was stirred at r.t. overnight. The reaction mixture was cooled to 0 °C and the corresponding benzylamine (1.16 mmol) in THF (4 mL) was added dropwise. The reaction was stirred at room temperature for 18 h, concentrated *in vacuo* and subjected to flash chromatography (MeOH 5%/ DCM 95%) to give compounds **4.19** and **4.20**.

***N*-(3-Nitrophenyl)-2-naphthamide (4.14)²²**

Using general procedure A, **4.12** and 3-nitroaniline (98.4 mg, 0.697 mmol), compound **4.14** (140 mg, 45%) was isolated as a white solid; m.p: 162-164 °C. ¹H NMR (500 MHz, DMSO) δ: 7.71-7.64 (m, 3H, ArH), 8.13-7.98 (m, 5H, ArH), 8.27 (dd, 1H, *J* = 8.2, 1.2 Hz, ArH), 8.65 (s, 1H, ArH), 8.86 (s, 1H, ArH), 10.89 (s, 1H, NH); ¹³C NMR (126 MHz, DMSO) δ: 114.8, 118.6, 124.8, 126.7, 127.5, 128.2, 128.6, 128.7, 128.8, 129.5, 130.6, 132.0, 132.5, 135.0, 141.0, 148.4, 166.6; ESI-MS *m/z* 315 (53%, [M+Na]⁺), 291 (100%, [M-H]⁻).

3-Hydroxy-*N*-phenyl-2-naphthamide (4.15)²³

Using general procedure A, **4.13** and aniline (106 μL, 1.17 mmol), compound **4.15** (91 mg, 32%) was isolated as a red crystals; m.p: 244-246 °C. ¹H NMR (500 MHz, DMSO) δ: 7.23-7.19 (m, 1H, ArH), 7.39 (s, 1H, ArH), 7.47-7.41 (m, 3H, ArH), 7.59-7.56 (m, 1H, ArH), 7.83-7.81 (m, 3H, ArH), 7.99 (d, 1H, *J* = 8.1 Hz, ArH), 8.56 (s, 1H, ArH), 10.65 (s, 1H, NH), 11.40 (s, 1H, OH); ¹³C NMR (126 MHz, DMSO) δ: 111.0, 121.0, 122.3, 124.3, 124.6, 126.3, 127.4, 128.6, 129.2, 129.3, 130.9, 136.2, 138.9, 154.2, 166.1; ESI-MS *m/z* 286 (100%, [M+Na]⁺), 262 (100%,

[M-H]⁻).

3-Hydroxy-*N*-(3-nitrophenyl)-2-naphthamide (4.5) ²³

Using general procedure A, **4.13** and 3-nitroaniline (162 mg, 1.17 mmol), compound **4.16** (46 mg, 14%) was isolated as a yellow solid; m.p: 248-250 °C. ¹H NMR (500 MHz, DMSO) δ: 7.35 (s, 1H, ArH), 7.39-7.36 (m, 1H, ArH), 7.53 (app t, 1H, *J* = 7.5 Hz, ArH), 7.69 (app t, 1H, *J* = 8.2 Hz, ArH), 7.78 (d, 1H, *J* = 8.3 Hz, ArH), 7.95 (d, 1H, *J* = 8.2 Hz, ArH), 8.00 (dd, 1H, *J* = 8.2, 2.1 Hz, ArH), 8.12 (d, 1H, *J* = 8.8 Hz, ArH), 8.45 (s, 1H, ArH), 8.84 (s, 1H, ArH), 10.94 (s, 1H, NH), 11.09 (s, 1H, OH); ¹³C NMR (126 MHz, DMSO) δ: 111.0, 114.8, 118.9, 123.0, 124.3, 126.3, 126.7, 127.3, 128.7, 129.2, 130.7, 131.0, 136.2, 140.3, 148.5, 153.8, 166.6; ESI-MS *m/z* 331 (100%, [M+Na]⁺), 307 (100%, [M-H]⁻).

3-Hydroxy-*N*-(4-nitrophenyl)-2-naphthamide (4.16) ²³

Using general procedure A, **4.13** and 4-nitroaniline (162 mg, 1.17 mmol), compound **4.17** (47 mg, 15%) was isolated as a green solid; m.p: 262-264 °C. ¹H NMR (500 MHz, DMSO) δ: 7.44-7.40 (m, 2H, ArH), 7.57 (app t, 1H, *J* = 7.5 Hz, ArH), 7.83 (d, 1H, *J* = 8.3 Hz, ArH), 8.00 (d, 1H, *J* = 8.4 Hz, ArH), 8.10 (d, 2H, *J* = 9.1 Hz, ArH), 8.35 (d, 2H, *J* = 9.1 Hz, ArH), 8.46 (s, 1H, ArH), 11.21-11.08 (m, 2H, OH/NH); ¹³C NMR (126 MHz, DMSO) δ: 110.9, 120.3, 123.6, 124.3, 125.5, 126.3, 127.4, 128.7, 129.2, 131.2, 136.2, 143.1, 145.4, 153.4, 166.4; ESI-MS *m/z* 307 (100%, [M-H]⁻).

3-Hydroxy-*N*-(4-fluorophenyl)-2-naphthamide (4.17) ²⁴

Using general procedure A, **4.13** and 4-fluoroaniline (110 μL, 1.17 mmol), compound **4.18** (52 mg, 17%) was isolated as a pale green solid; m.p: 266-286 °C.

^1H NMR (500 MHz, DMSO) δ : 7.24 (app t, 2H, $J = 8.5$ Hz, ArH), 7.38-7.34 (m, 2H, ArH), 7.52 (app t, 1H, $J = 7.3$ Hz, ArH), 7.80-7.77 (m, 3H, ArH), 7.93 (d, 1H, $J = 7.9$ Hz, ArH), 8.50 (s, 1H, ArH), 10.64 (s, 1H, NH), 11.30 (s, 1H, OH); ^{13}C NMR (126 MHz, DMSO) δ : 111.0, 115.9 (d, $^2J_{\text{CF}} = 22$ Hz), 122.2, 122.9 (d, $^3J_{\text{CF}} = 7.9$ Hz), 124.2, 126.8, 127.3, 128.6, 129.2, 130.8, 135.3, 136.3, 154.3, 159.0 (d, $^1J_{\text{CF}} = 241$ Hz), 166.2; ESI-MS m/z 304 (100%, $[\text{M}+\text{Na}]^+$), 280 (100%, $[\text{M}-\text{H}]^-$).

***N*-Benzyl-3-hydroxy-2-naphthamide (4.18)** ²³

Using general procedure B and benzyl aniline (124 mg, 1.16 mmol), compound **4.19** (72 mg, 45%) was isolated as white crystals; m.p: 168-170 °C. ^1H NMR (500 MHz, DMSO): 4.59 (d, 2H, $J = 5.8$ Hz, CH_2), 7.29-7.26 (m, 2H, ArH), 7.41-7.34 (m, 5H, ArH), 7.51 (ddd, 1H, $J = 8.2, 6.8, 1.2$ Hz, ArH), 7.75 (d, 1H, $J = 8.2$ Hz, ArH), 7.86 (d, 1H, $J = 8.1$ Hz, ArH), 8.56 (s, 1H, ArH), 9.53 (1H, $J = 5.7$ Hz, NH), 11.98 (s, 1H, OH); ^{13}C NMR (126 MHz, DMSO) δ : 43.1, 111.2, 119.1, 124.2, 126.3, 127.1, 127.4, 127.9, 128.7, 128.9, 129.2, 130.1, 136.5, 139.4, 155.8, 168.4; ESI-MS m/z 300 (100%, $[\text{M}+\text{Na}]^+$), 276 (100%, $[\text{M}-\text{H}]^-$).

***N*-4-Fluorobenzyl-3-hydroxy-2-naphthamide (4.19)** ²³

Using general procedure B and benzyl aniline (145 mg, 1.16 mmol) compound **4.20** (86 mg, 50%) was isolated as white powder; m.p: 188-190 °C. ^1H NMR (500 MHz, DMSO): 4.68 (d, 2H, $J = 5.2$ Hz, CH_2), 6.81 (s, 1H, ArH), 7.08 (t, $J = 8.0$ Hz, 2H, ArH), 7.29-7.50 (m, 5H, ArH), 7.67-7.72 (m, 2H, ArH), 7.94 (1H, $J = 5.7$ Hz, NH), 11.65 (s, 1H, OH); ^{13}C NMR (126 MHz, CDCl_3) δ : 43.3, 110.0, 112.5, 115.8 (d, $^2J_{\text{CF}} = 22$ Hz), 116.8, 124.0, 126.3, 126.7, 128.5, 128.6, 129.7 (d, $^3J_{\text{CF}} = 8$ Hz), 133.2, 137.2, 156.7, 161.8 (d, $^1J_{\text{CF}} = 241$ Hz), 169.7; ESI-MS m/z 318 (100%,

[M+Na]⁺, 294 (100%, [M-H]⁻). HRMS (ESI⁻) calcd for C₁₈H₁₃FNO₂: 294.0927 (M-H)⁻, found: 294.0930.

4.4.2 Anti-viral assay

CHIKV Indian Ocean strain 899 (Genbank FJ959103.1) was generously provided by Prof. S. Günther (Bernhard Nocht Institute for Tropical Medicine, Hamburg, Germany) (Panning M et al., *Emerging Infectious Diseases* 2008). BGM cells were maintained in cell growth medium composed of minimum essential medium (MEM Rega-3, Gibco, Belgium) supplemented with 10% Foetal Bovine Serum (FBS, Integro, The Netherlands), 1% L-glutamine (Gibco), and 1% sodium bicarbonate (Gibco). The antiviral assays were performed in virus growth medium which is the respective cell growth medium supplemented with 2% (instead of 10%) FBS. Cell cultures were maintained at 37 °C in an atmosphere of 5% CO₂ and 95-99% humidity. BGM cells were seeded in 96-well tissue culture plates (Becton Dickinson, Aalst, Belgium) at a density of 2.5 x 10⁴ cells/well in 100 µL assay medium and were allowed to adhere overnight. Next, a compound dilution series was prepared in the medium on top of the cells after which the cultures were infected with 0.001 MOI of CHIKV 899 inoculum in 100 µL assay medium. On day 5 post-infection (p.i.), the plates were processed using the MTS/PMS method as described by the manufacturer (Promega, The Netherlands). The 50% effective concentration (EC₅₀), which is defined as the compound concentration that is required to inhibit virus-induced cell death by 50%, was determined using logarithmic interpolation. All assay wells were checked microscopically for minor signs of virus induced CPE or possible alterations to the cell or monolayer

morphology caused by the compound.

4.5 References

1. Rashad, A. A.; Mahalingam, S.; Keller, P. A. Chikungunya virus: Emerging targets and new opportunities for medicinal chemistry. *J. Med. Chem.* **2014**, *57*, 1147-1166.
2. Robinson, M. C. An epidemic of virus disease in southern province, tanganyika territory, in 1952-53. I. Clinical features. *Trans. R. Soc. Trop. Med. Hyg.* **1955**, *49*, 28-32.
3. Pulmanusahakul, R.; Roytrakul, S.; Auewarakul, P.; Smith, D. R. Chikungunya in southeast asia: Understanding the emergence and finding solutions. *Int. J. Infect. Dis.* **2011**, *15*, 671-676.
4. Kariuki Njenga, M.; Nderitu, L.; Ledermann, J. P.; Ndirangu, A.; Logue, C. H.; Kelly, C. H.; Sang, R.; Sergon, K.; Breiman, R.; Powers, A. M. Tracking epidemic chikungunya virus into the indian ocean from east africa. *J. Gen. Virol.* **2008**, *89*, 2754-2760.
5. Abdelnabi, R.; Neyts, J.; Delang, L. Towards antivirals against chikungunya virus. *Antivir. Res.* **2015**, *121*, 59-68.
6. Nguyen, P. T.; Yu, H.; Keller, P. A. Identification of chikungunya virus nsp2 protease inhibitors using structure-base approaches. *J. Mol. Graphics Modell.* **2015**, *57*, 1-8.
7. Rudd, P. A.; Mahalingam, S. Fighting back against chikungunya. *Lancet Infect. Dis.* **2015**, *15*, 488-489.
8. *Investing to overcome the global impact of neglected tropical diseases: Third who report on neglected diseases 2015*; 9241564865; World Health Organization: 2015.
9. *Chikungunya – sudan*; World Health Organization: 2018.
10. Lazear, H. M.; Diamond, M. S. Zika virus: New clinical syndromes and its emergence in the western hemisphere. *J. Virol.* **2016**, *90*, 4864-4875.
11. Rothan, H. A.; Bahrani, H.; Abdulrahman, A. Y.; Mohamed, Z.; Teoh, T. C.; Othman, S.; Rashid, N. N.; Rahman, N. A.; Yusof, R. Mefenamic acid in combination with ribavirin shows significant effects in reducing chikungunya virus infection in vitro and in vivo. *Antivir. Res.* **2016**, *127*, 50-56.
12. Nguyen, P. T.; Yu, H.; Keller, P. A. Discovery of in silico hits targeting the nsp3 macro domain of chikungunya virus. *J. Mol. Model.* **2014**, *20*, 1-12.
13. Maheshwari, R. K.; Srikantan, V.; Bhartiya, D. Chloroquine enhances replication of semliki forest virus and encephalomyocarditis virus in mice. *J. Virol.* **1991**, *65*, 992-995.
14. Ravichandran, R.; Manian, M. Ribavirin therapy for chikungunya arthritis. *J. Infect. Dev. Ctries.* **2008**, *2*, 140-142.
15. Kaur, P.; Thiruchelvan, M.; Lee, R. C.; Chen, H.; Chen, K. C.; Ng, M. L.; Chu, J. J. Inhibition of chikungunya virus replication by harringtonine, a novel antiviral that suppresses viral protein expression. *Antimicrob. Agents Chemother.* **2013**, *57*, 155-167.
16. Gigante, A.; Canela, M. D.; Delang, L.; Priego, E. M.; Camarasa, M. J.; Querat, G.; Neyts, J.; Leyssen, P.; Perez-Perez, M. J. Identification of [1,2,3]triazolo[4,5-d]pyrimidin-7(6H)-ones as novel inhibitors of chikungunya virus replication. *J. Med. Chem.* **2014**, *57*, 4000-4008.
17. Gigante, A.; Gomez-SanJuan, A.; Delang, L.; Li, C.; Bueno, O.; Gamo, A. M.; Priego, E. M.; Camarasa, M. J.; Jochmans, D.; Leyssen, P.; Decroly, E.; Coutard, B.; Querat, G.; Neyts, J.; Perez-Perez, M. J. Antiviral activity of [1,2,3]triazolo[4,5-d]pyrimidin-7(6H)-ones against chikungunya virus targeting the viral capping nsp1. *Antivir. Res.* **2017**, *144*, 216-222.
18. Karlas, A.; Berre, S.; Couderc, T.; Varjak, M.; Braun, P.; Meyer, M.; Gangneux, N.; Karo-Astover, L.; Weege, F.; Raftery, M.; Schonrich, G.; Klemm, U.; Wurzlbauer, A.; Bracher, F.; Merits, A.; Meyer, T. F.; Lecuit, M. A human genome-wide loss-of-function screen identifies effective chikungunya antiviral drugs. *Nat. Commun.* **2016**, *7*, 1-14.
19. Perez-Perez, M. J.; Delang, L.; Ng, L. F. P.; Priego, E. M. Chikungunya virus drug discovery: Still a long way to go? *Expert Opin. Drug Discov.* **2019**, *14*, 855-866.
20. Powers, A. M. Vaccine and therapeutic options to control chikungunya virus. *Clin. Microbiol. Rev.* **2018**, *31*, 1-29.
21. Nguyen, P. T. V. In silico drug discovery targeting chikungunya virus. University of Wollongong, 2015.
22. Vaillancourt, V. A.; Cudahy, M. M.; Staley, S. A.; Brideau, R. J.; Conrad, S. J.; Knechtel, M. L.; Oien, N. L.; Wieber, J. L.; Yagi, Y.; Wathen, M. W. Naphthalene carboxamides as inhibitors

- of human cytomegalovirus DNA polymerase. *Bioorg. Med. Chem. Lett.* **2000**, 10, 2079-2081.
23. Vaillancourt, V. A.; Cudahy, M. M.; Staley, S. A.; Brideau, R. J.; Conrad, S. J.; Knechtel, M. L.; Oien, N. L.; Wieber, J. L.; Yagi, Y.; Wathen, M. W. Naphthalene carboxamides as inhibitors of human cytomegalovirus DNA polymerase. *Bioorg. Med. Chem. Lett.* **2000**, 10, 2079-81.
24. Li, B. X.; Yamanaka, K.; Xiao, X. Structure–activity relationship studies of naphthol as e and its derivatives as anticancer agents by inhibiting creb-mediated gene transcription. *Bioorg. Med. Chem.* **2012**, 20, 6811-6820.

Chapter 5:

Switchable anion transporters

FOREWORD TO CHAPTER 5

This chapter is a full research manuscript is accepted to *Angewandte Chemie*, 2020 (doi: 10.1002/anie.202006392 and 10.1002/ange.202006392, impact factor 12.257). This manuscript describes the development stimuli-responsive cycloaurated ‘OFF-ON’ switchable fluorescent anion transporters. Herein, we report the synthesis and characterization of five anion transporters based on 1,3-bis(benzimidazol-2-yl)pyrimidine scaffold. We also developed four putative anion transporters that are switched-on in the presence of GSH, which is found in a higher concentration in cancer cells. It also describes full transport and binding properties of the free receptors and extensive reduction kinetic studies of the switchable cycloaurated complexes under different conditions, including in DMSO, external addition in liposomes and in GSH-encapsulated liposomes.

Supporting information for this chapter can be found in Appendix D (p. 264).

Contributions

Mohamed Fares	Performed the synthesis, the anion transport studies and analysis, binding studies and reduction kinetics. Input into experimental design, analysed the data and prepared/edited the paper.
Xin Wu	Compound design.
Ethan Howe	Design of transport and reduction kinetics studies experiments
William Lewis	Performed and solved the X-ray structures
Paul A. Keller	Editing and proof-reading.
Philip A. Gale	Oversight of the project, editing and proof-reading.

5.1 Introduction

Biomimetic stimuli-responsive systems activated under particular physical, chemical or biological conditions have recently gained increasing attention and represent a promising therapeutic approach due to their selective and controllable action.¹⁻⁴ These smart systems can be switched on under specific conditions, including in the presence of certain proteins, redox states or chemical signals (such as changes in pH).⁵ In the field of anion recognition, pH-responsive, redox-switchable and photophysical controllable anion receptors have been developed.⁵⁻¹⁰ These switchable anion receptors have been recognised for diverse applications including ion sensing, catalysis and can be used as potential drug candidates in medicinal chemistry.¹¹⁻¹³

Transmembrane ion transport is a fundamental biological process and is involved in diverse physiological functions including, neuroexcitation, muscle contraction, cell migration and proliferation, and maintaining cellular pH, membrane potential and cellular secretions.¹⁴ Channelopathies are a group of diseases characterised by impaired ion channel function, including cystic fibrosis, epilepsy and cancer.¹⁵⁻¹⁷ Anionophores are small molecules that are capable of transporting anions and they demonstrated cytotoxic effects against stem cancer cells by facilitating the transport of chloride and bicarbonate anions so changing the cellular pH, causing cellular differentiation and death.^{13, 18-20}

A recent mechanistic study of cancer death showed that the induction of apoptosis and inhibition of autophagy by particular anion transporters are due to the cellular osmotic stress which is caused by increasing cellular ion concentration.²¹ This promotes the generation of reactive oxygen species (ROS) and activates a caspase-

dependent apoptosis. Two of the tested transporters induced cellular osmotic stress, by increasing the intracellular Ca^{+2} concentration and lysosomal pH (as a result of a decrease in the lysosomal chloride ion concentration), leading eventually to autophagy disruption.²¹

Glutathione (GSH), is a tripeptide and forms with glutathione disulfide (GSSG) a redox complex that keeps the cellular oxidative properties under normal physiological conditions.²² Many diseases such as diabetes, neurodegenerative disorders and cancer are implicated with high levels of GSH. Redox state environment in cancer cells is greatly dictated by the NADPH (NADPH, NADP^+) and GSH (GSH, GSSG) redox systems.^{23, 24} In normal cells, GSH intracellular concentration was reported to be 10 mM, while the extracellular concentration was ranged from 2 to 20 μM .²⁵ However, previous reports stated that there was a four-fold increase in GSH concentration in cancer cells, compared to normal cells and even higher in multi-resistant tumour cells.^{26, 27} These findings inspired the development of stimuli-responsive systems targeting high GSH levels and these systems have been widely used in contemporary drug delivery approaches.²⁸⁻³² Recently, Akhtar et al. developed water soluble GSH-responsive anion transporters with potential activity to treat cystic fibrosis.³³ However, GSH content in cystic fibrosis cells is lower than normal cells presumably due to the abnormal extracellular GSH transport ability of CFTR proteins, limiting the application of these molecules as potential treatment.^{33, 34}

Inspired by the high affinity of thiols, such as GSH, for gold and prompted by the reported efficient anion transport activity of 1,3-bis(benzimidazol-2-yl)benzenes, we designed and synthesized new switchable cycloaurated anion transporters based

on the structurally related 1,3-bis(benzimidazol-2-yl)pyrimidine (BisBzImPy) (Figure 5.1).

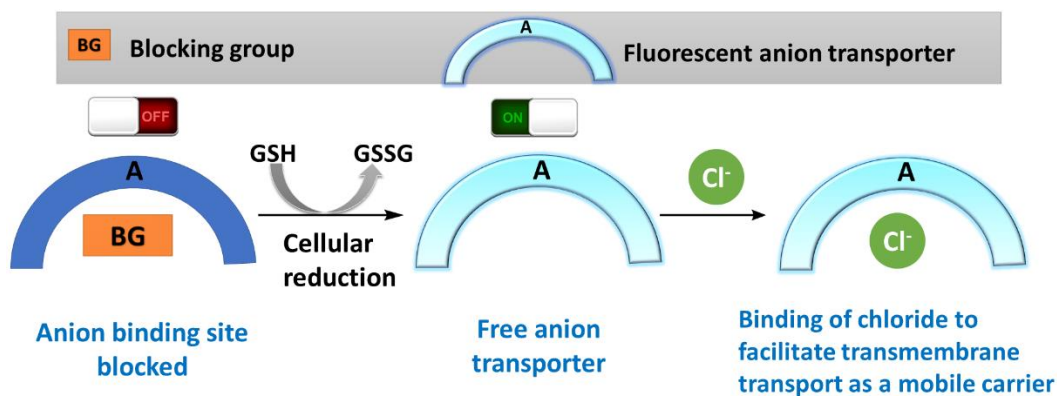


Figure 5.1: Schematic representation showing the design of switchable anion transporters.

Blocking groups, such as chloride or *N*-heterocyclic carbene (NHC) were used to afford the switchable complexes (Figure 5.2).^{32, 35-37} These complexes were designed to be reduced by GSH as a stimulus to liberate the fluorescent anion transporters that can bind to chloride and facilitate transmembrane transport (Figure 5.2).

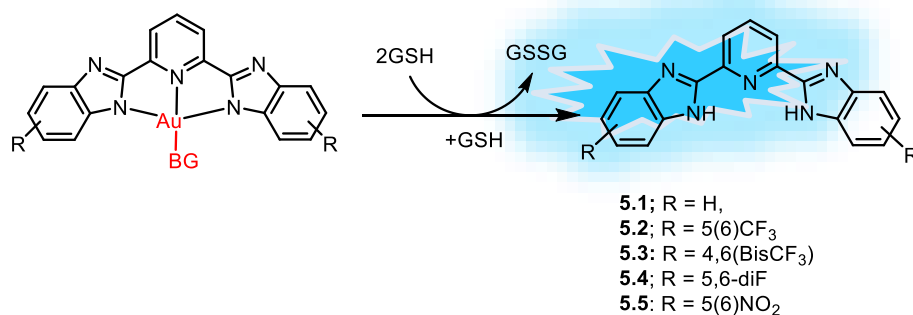


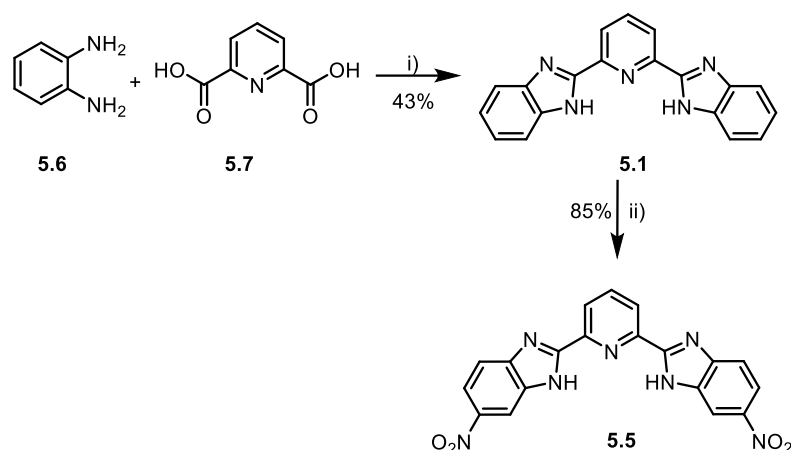
Figure 5.2: Reported GSH mediated activation and putative transporters **5.1-5.5**³⁸

5.2 Results and discussion

5.2.1 Chemistry

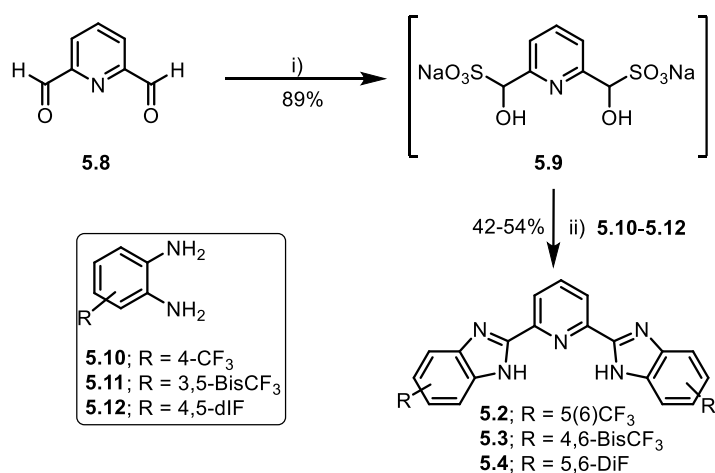
Unsubstituted BisBzImPy **5.1** was synthesized by condensation of *o*-

phenylenediamine with dipicolinic acid in phosphoric acid at 200 °C for 6 h (Scheme 5.1).^{39, 40} Dinitro BisBzImPy derivative **5.5** was prepared by nitration of **5.1** and showed low solubility in most solvents.⁴⁰



Scheme 5.1: Reagents and conditions: i) H₃PO₄, 200 °C, 6 h; ii) H₂SO₄/HNO₃ 3 h.

Attempts to synthesize ditrifluoromethyl BisBzImPy derivative **5.2** using the same procedure failed may be due to the deactivating effect of the trifluoromethyl, bistrifluoromethyl and difluoro groups that would make the amino groups in the arylidene diamines less nucleophilic.



Scheme 5.2: Reagents and conditions: i) NaS₂O₅, EtOH, RT; ii) DMF, 120 °C, 4 h.

BisBzImPy derivatives **5.2-5.4** were obtained in 42-54% yields by adopting an alternative procedure using sodium metabisulfite and 2,6-pyridinedicarboxaldehyde (Scheme 5.2).⁴¹ The structure of **5.2** was confirmed by X-ray diffraction analysis (Figure 5.3) which showed that transporter **5.2** formed a 1:1 complex with DMSO *via* two hydrogen bonds with nitrogen atoms of benzimidazole (NH- -O distances of 1.991 Å and 2.018 Å and NH- -O bond angles of 169.21° and 170.77°).

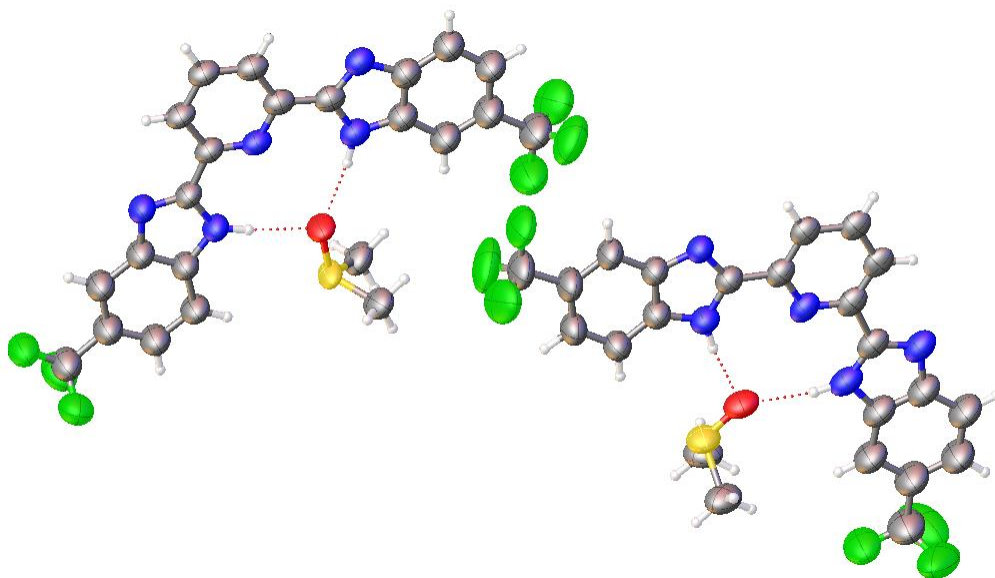
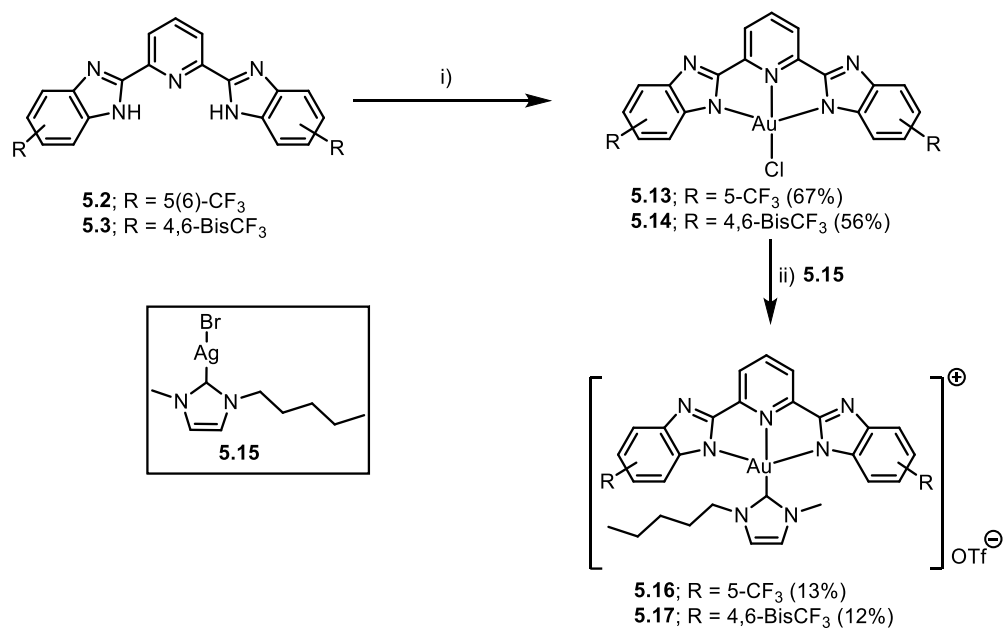


Figure 5.3: X-ray structure of anion transporter **5.2**. DMSO complex.

Gold chloride derivatives **5.13** and **5.14** were readily prepared by heating at reflux BisBzImPy derivatives **5.2** and **5.3**, respectively, with KAuCl₄ and anhydrous sodium acetate in methanol for 3 h (Scheme 5.3).³⁸ The structure of **5.14** was determined by single X-ray crystallography (Figure 5.4) and showed a heptacyclic flat planar gold chloride complex. The bond lengths between Au(III) and nitrogen atoms of benzimidazole and pyridine rings were 1.98-1.99 Å. The angle between the nitrogen atom of pyridine, Au(III) and nitrogen atoms of benzimidazole

(N[^]Au[^]N) were 79.24° and 80.23°, while the angle between chloride, Au^{III}, and nitrogen atoms of benzimidazole were (Cl[^]Au[^]N) 100.02° and 100.45°.



Scheme 5.3: Reagents and conditions: i) KAuCl₄, MeOH, NaOAc, reflux; ii) AgOTf, CH₃CN, reflux, 12 h in dark.

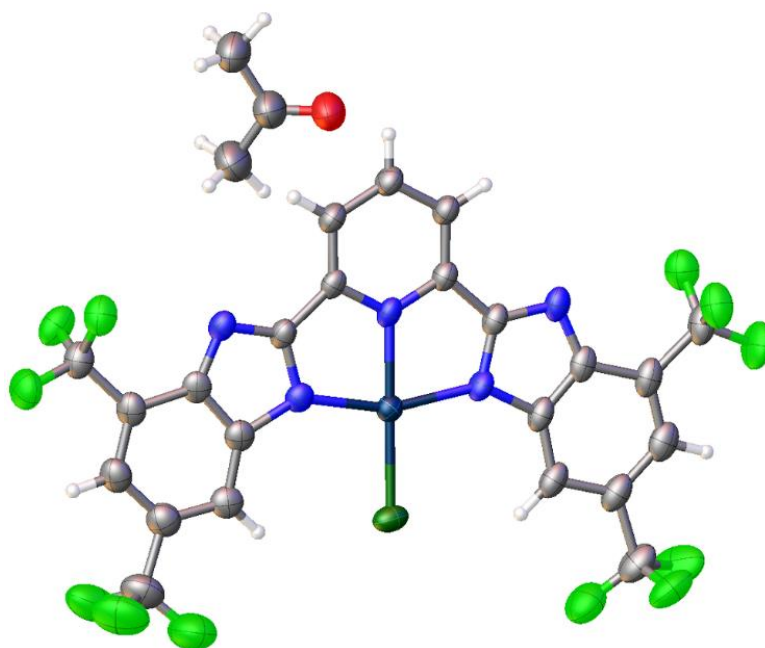


Figure 5.4: X-ray structure of complex **5.14**.

Reaction of **5.13** and **5.14** with NHC **5.15**, silver triflate in acetonitrile in the absence of light gave complexes **5.16** and **5.17** in 13% and 12% yields, respectively

(Scheme 5.3).³⁸

The X-ray crystal structure of the Au(III) complex **5.16** and **5.17** (Figures 5.5 and 5.6) revealed that the NHC plane is almost perpendicular to the BizBzImPy plane with a torsion angle of 73.79° and 81.23° and for complexes **5.16** and **5.17**, respectively (Figures 5.5 and 5.6). The bond length between Au(III) and nitrogen atoms of benzimidazole and pyridine rings were 2.007-2.015 Å for complex **5.16** and 1.988-2.009 Å for complex **5.17**, slightly longer than in complex **5.14**.

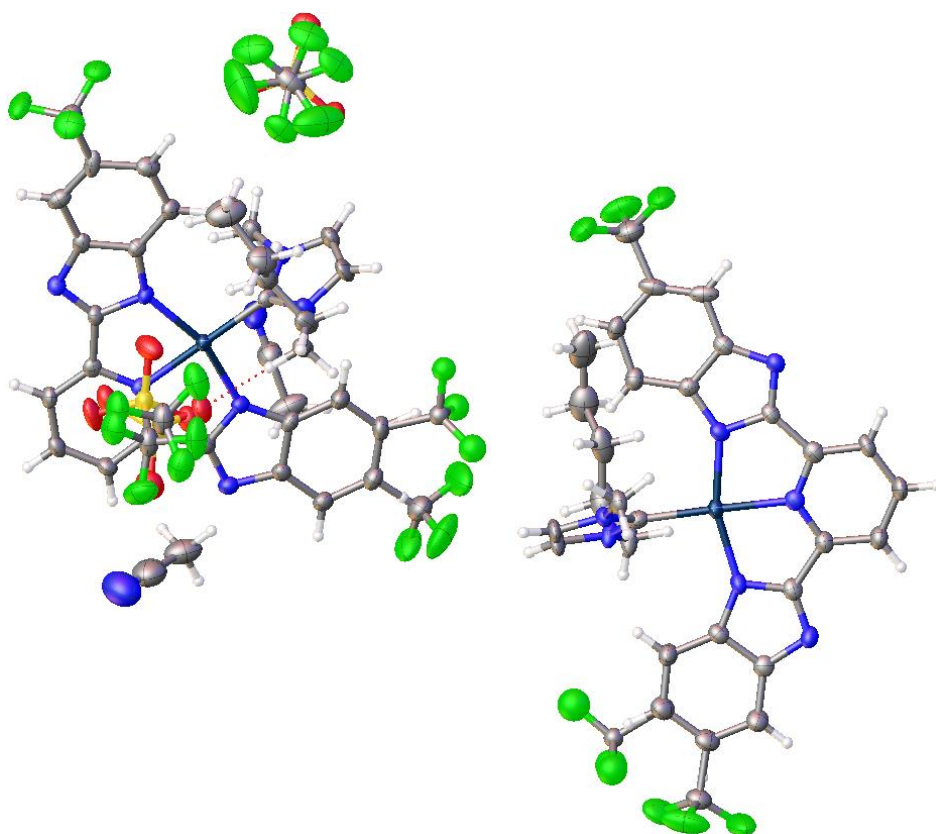


Figure 5.5: X-ray structure of anion complex **5.16**.

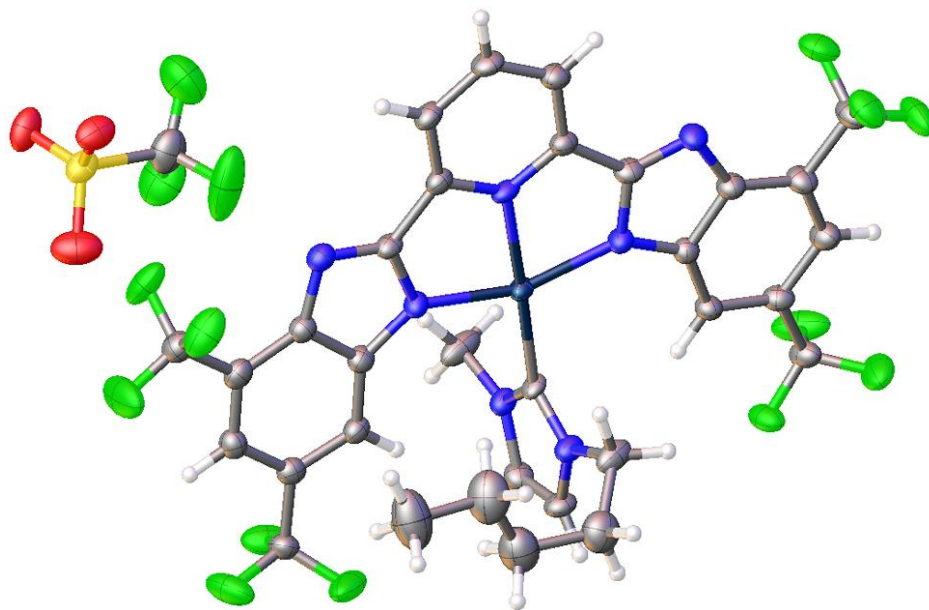


Figure 5.6: X-ray structure of anion transporter **5.17**.

5.2.2 Binding in solution

To gain a better understanding of the anionophoric properties of the compounds, NMR chloride binding studies were performed in DMSO-*d*₆/0.5% H₂O and CD₃CN with TBACl. Data were fitted globally to the 1:1 or 2:1 (host: guest) for transporters **5.1-5.4**, while transporter **5.5** was omitted from this study due to its low solubility (Table 5.1, Figures 5.7, Figures D1-D8).

In DMSO, anionophores **5.1-5.4** were fitted to the 1:1 binding model giving K_a ranging from 63 to 132 M⁻¹. Transporters **5.1**, **5.3** and **5.4** were fitted also to 2:1 model giving greater K_{21} values than K_{11} . These findings show that transporters **5.1**, **5.3** and **5.4** might adopt different binding modes in DMSO. NMR anion binding titration studies in CD₃CN showed that anion transporters **5.1** and **5.2** adopt the 1:1 binding mode and interestingly transporters **5.3** and **5.4** prefer the 2:1 sandwich mode (Table 5.1) (Figures 5.7).

Table 5.1: Binding properties of compounds 5.1–5.4.

		5.1	5.2	5.3	5.4
DMSO	1:1 (K_a)	92	77	132	63
	covfit ^[a]	1.1×10^{-2}	2.3×10^{-4}	2.0×10^{-3}	3.0×10^{-4}
	2:1 (K_a)	K_{11} : 40; K_{21} : 2.5×10^2	-	K_{11} : 40; K_{21} : 2.6×10	K_{11} : 75; K_{21} : 89
	β_{21} ^[b]	1.0×10^5	-	1.0×10^4	6.7×10^3
	covfit	4.0×10^{-3}	-	1.5×10^{-3}	2.0×10^{-4}
CD ₃ CN	1:1 (K_a)	4.6×10^3	1.2×10^4	-	-
	covfit ^[a]	9.4×10^{-4}	2.5×10^{-4}	-	-
	2:1 (K_a)	-	-	K_{11} and K_{21} : 2.0×10^3	K_{11} : 0.69; K_{21} : 8.2×10^6
	β_{21} ^[b]	-	-	4.4×10^6	5.5×10^6
	covfit	-	-	2.9×10^{-4}	5.2×10^{-3}

[a] The covariance of the fit (covfit) is calculated by dividing the covariance of the residual (experimental data – calculated data) with the covariance of the experimental data. [b] The association constant (β_{21}) for the 2:1 host:guest complex calculated by multiplying K_{11} and K_{21} . nd: not determined.

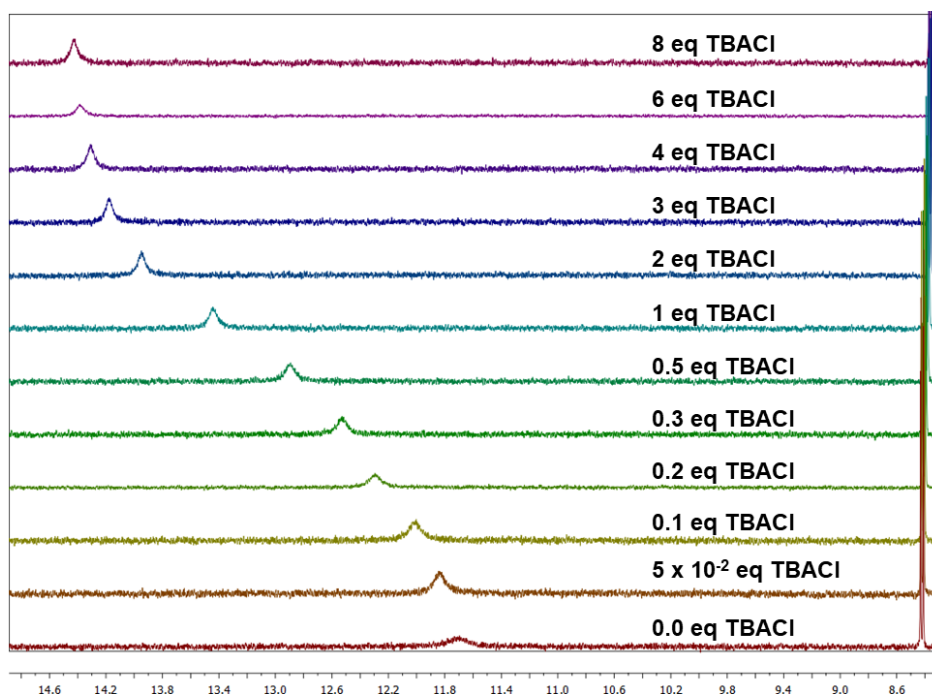


Figure 5.7: Stack plot of ¹H NMR spectroscopic titration of receptor 5.2 (1 mM) with TBACl in CD₃CN at 298 K.

5.2.3 Binding in solid state

A single crystal of anionophore **5.2** with chloride ion was obtained for X-ray crystallographic diffraction by vapor diffusion of Et₂O into a CH₃CN solution of transporter **5.2** and two equivalents of TEACl (Figure 5.8). Interestingly, Cl⁻ is sandwiched between two molecules of compound **5.2**, where it forms two hydrogen bonds with imidazole NHs, with NH... Cl⁻ distances of 2.41 and 2.63 Å, and one hydrogen bond with a water molecule with an OH...Cl⁻ distance of 2.29 Å (Figure 5.8).

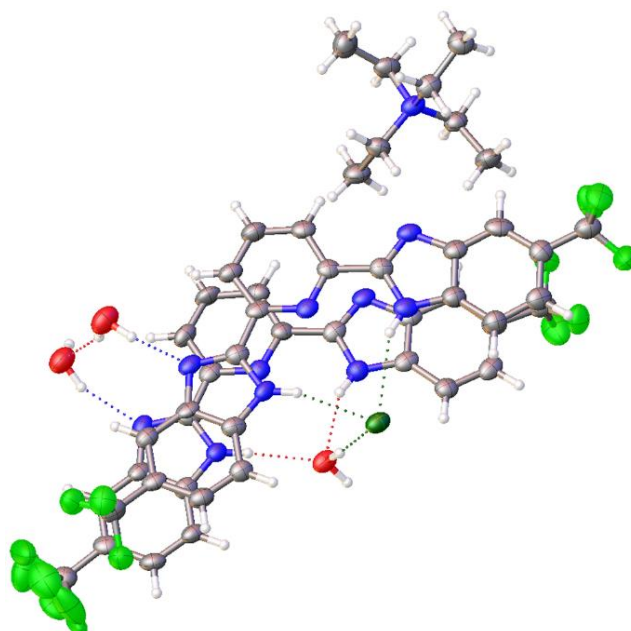


Figure 5.8: Crystal structure of **5.2** with chloride complex.

This water molecule connects the chloride anion and the second transporter molecule by acting as a hydrogen bond donor and an acceptor. It forms five hydrogen bonds including two with imidazole NHs of the bottom compound **5.2**, one with imidazole NH of the top compound **5.2**, one with the pyridine N and the one mentioned earlier with chloride, with distances ranging from 2.29 to 3.54 Å. The sandwich complex is further stabilized by another water molecule, which forms hydrogen bonds with both molecules of **5.2** (Figure 5.8).

5.2.4 Transport studies

Transporters **5.1-5.5** were investigated for their chloride transport property *via* Cl/NO₃ exchange assay using a chloride ion selective electrode (ISE) (Figure 5.9, Table 5.2). Briefly, 1-palmitoyl-2-oleoyl-*sn*-glycero-3-phosphocholine (POPC) unilamellar liposomes were prepared with diameter 200 nm and loaded with 489 mM KCl, buffered to pH = 7.2 and suspended in 489 mM KNO₃ solution which is buffered to pH = 7.2. The chloride efflux which is considered as indication of Cl⁻/NO₃⁻ exchange process, was monitored using chloride ion selective electrode upon addition of DMSO solution of transporters **5.1-5.5** to the prepared liposomes.⁴² At the same concentration, compounds **5.1-5.5** showed better transport properties when transporter loading volume increased from 10 μL to 40 μL, presumably due to better deliverability in a higher volume of DMSO. Chloride efflux at different concentrations of tested compounds (expressed as mol% with respect to lipid concentration (rtl)) was measured to obtain Hill plots and to calculate EC₅₀ (defined as the concentration required to achieve 50% the chloride efflux at 270 s) and Hill coefficient (n). Hill coefficient indicates the stoichiometry of the formed complex during the anion transport across the lipid bilayer, while EC₅₀ is used as a measure of anion transporter potency.

Compounds **5.1** and **5.5** were excluded from Hill plot analysis due to low potency of compound **5.1** and solubility limitation of transporter **5.5**. Among tested anionophores **5.2-5.4**, transporter **5.2** was the most active with EC₅₀ = 0.42 mol%, followed by transporters **5.3** and **5.4** (EC₅₀ = 0.49 and 0.58 mol% (rtl), respectively) (Figure 5.9a and 5.9d, Table 5.2). Cationophore coupling assay, using valinomycin (Vln) or monensin (Mon) was used to investigate the mechanism of anion transport of the novel transporters.

Table 5.2: Transport properties of compounds 5.1–5.5.

	1	2	3	4	5
cLog P ^[a]	4.0	4.4	5.0	4.0	3.8
KCl (EC₅₀, mol%) ^[b]	4.8	1.0 x 10 ⁻¹	9.4 x 10 ⁻²	2.3 x 10 ⁻¹	6.1 x 10 ⁻²
n ^[c]	2.2	1.3	0.7	1.2	0.9
KGlu (EC₅₀, mol%) ^[d]	2.3	2.3 x 10 ⁻²	3.5 x 10 ⁻³	4.4 x 10 ⁻²	3.8 x 10 ⁻²
n ^[c]	1.4	1.2	1.2	1.0	1.0
Cl/NO₃ (EC₅₀, mol%) ^[e]	nd	0.42	0.49	0.58	nd
n ^[c]	nd	1.4	0.9	1.4	nd

[a] clog P values calculated using VCCLab. [b] EC₅₀ from the KCl assay measuring H⁺/Cl⁻ symport. [c] Hill coefficient as an indicator of the stoichiometry the complex mediating transport. [d] EC₅₀ from the KGlu assay measuring Cl⁻ uniport. [e] EC₅₀ from the Cl/NO₃ exchange assay. Nd: not determined.

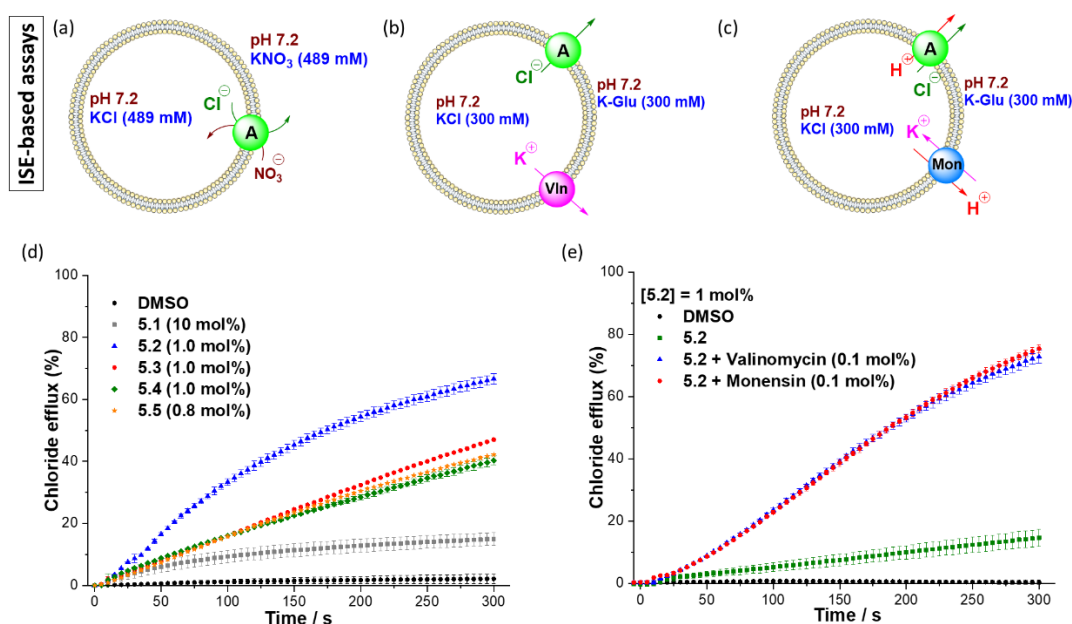


Figure 5.9: a-c) Schematic representation of ISE-based assays used to investigate the mechanism of anion transport of receptors 5.1–5.5. a) Cl⁻/NO₃⁻ antiport, b) and c) cationophore coupled-KCl, valinomycin and monensin to measure the Cl⁻ uniport and M⁺/Cl⁺ transport, respectively. d) Chloride efflux achieved by transporters 5.1–5.5 (1.0 mol%, rtl) for transporters 5.1–5.4 and 0.8 mol% (rtl) for transporter 5.5 from unilamellar POPC vesicles containing 489 mM KCl buffered to pH 7.2 with 5 mM potassium phosphate salts, suspended in 489 mM KNO₃ buffered to pH 7.2 with 5 mM phosphate salts. e) Chloride efflux achieved by transporter 5.2 at 1.0 mol% (rtl) in the absence or presence of cationophores (monensin or valinomycin) monitored over a period of 5 min.

Such assays are used to determine the activities of Cl⁻ uniport (coupling with valinomycin) and H⁺/Cl⁻ symport (coupling with monensin) (Figure 5.9b-c and 5.9e).⁴² Compounds **5.1-5.5** were capable of both Cl⁻ uniport and H⁺/Cl⁻ symport (Figure 5.9e).

BisBzImPy derivatives **5.1-5.5** were investigated for their potential anion transport properties using 8-hydroxypyrene-1,3,6-trisulfonic acid (HPTS) assay (Table 5.2 and Figure 5.10).⁴² The HPTS-KCl assays measures the activity of anion transporters in facilitating H⁺/Cl⁻ cotransport leading to the dissipation of pH gradients. The unsubstituted BisBzImPy **5.1** emerged as the lowest activity transporter in HPTS-KCl (HCl symport, Figure 5.10a) assay with an EC₅₀ = 4.8 mol% (Table 5.2). Grafting electron withdrawing groups such as bistrifluoromethyl, tetratrifluoromethyl, tetrafluoro or dinitro in the phenyl of benzimidazole rings (**5.2-5.5**) increased the ability to facilitate H⁺/Cl⁻ symport, with EC₅₀ values of these compounds ranging from (2.3 x 10⁻¹) - (6.1 x 10⁻²) mol%, rtl, (Figure 5.10e, Table 5.2). The activity decreased in the order of **5.5** > **5.3** > **5.2** > **5.4**.

To further investigate the intrinsic ability of transporters **5.1-5.5** to transport only chloride ion, the same assay was employed at 1 mol% transporter (mol% relative to lipid concentration, rtl) and using the protonophore carbonyl cyanide m-chlorophenyl hydrazone (CCCP) as an efficient proton transporter (Figure 5.10b). If H⁺ transport is the rate determining step of HCl symport, CCCP will improve transport and accelerate the pH dissipation (Figure 5.10f, Figures D14-D18, appendix D).⁴² Anionophores **5.1-5.5** transport properties demonstrated no CCCP dependence indicating effective H⁺ transport by these compounds.

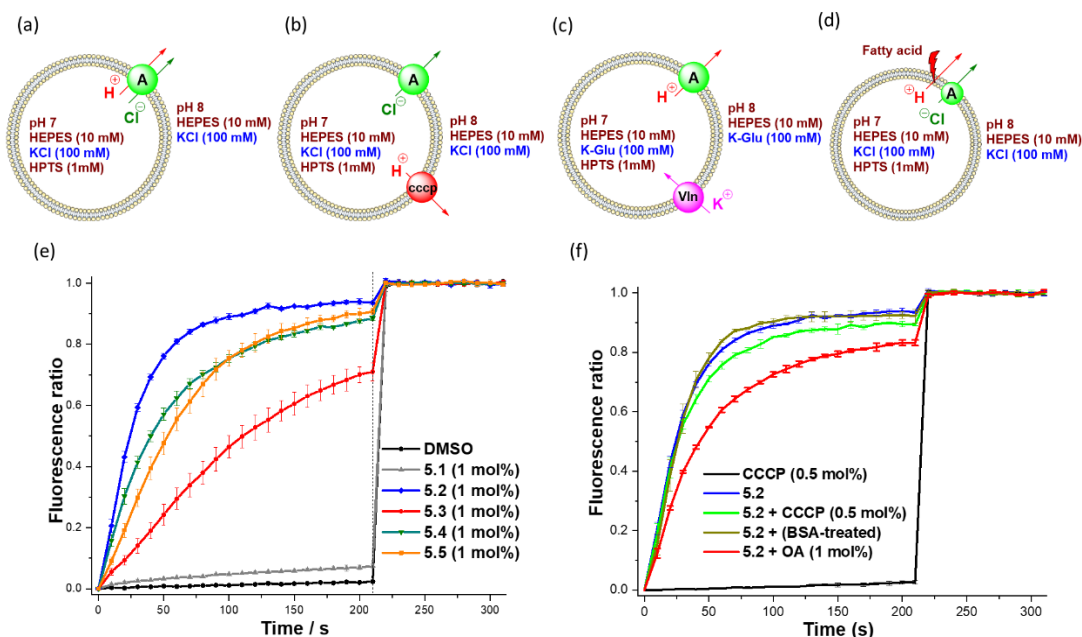


Figure 5.10: **a-d**) Schematic representation of the HPTS-based assays used in the current study **(a)** H^+/Cl^- symport or OH^-/Cl^- antiport **(b)** the presence of cccp (protonophore) to assess Cl^- uniport **(c)** the presence of valinomycin to measure the proton flux **(d)** the effect of fatty acid presence as a fuel on the transport. **(e)** H^+/Cl^- symport or OH^-/Cl^- antiport facilitated by compounds **5.1-5.5** (1.0 mol% (rtl)) from unilamellar POPC vesicles loaded with 100 mM KCl buffered to pH 7.0 with 10 mM HEPES buffer and 1 mM HPTS internal sensor. **(f)** Using KCl-KOH assay from POPC vesicles loaded with KCl (100 mM), buffered to pH 7.0 with HEPES (10 mM), different conditions were applied to determine the effect of addition of the protonophore cccp at 0.5 mol% (as a measure of Cl^- uniport), oleic acid at 1 mol% (as a source of fatty acid) and BSA-treated lipid (to test if the transport is fatty acid dependent) on the rate of chloride transport of receptor **5.2** (1 mol%).

We next examined the abilities of transporters **5.1-5.5** to transport only H^+ using the H^+ transport assay by replacing potassium chloride with potassium gluconate (KGlu) (Figure 5.10c) and using valinomycin to facilitate K^+ transport and dissipate the membrane potential generated by H^+ transport.⁴² Gluconate is a relatively large hydrophilic anion that can be considered lipid bilayer impermeable⁴². Apart from the unsubstituted BisBzImPy **5.1** ($\text{EC}_{50} = 2.3$ mol%), tested compounds **5.2-5.5** showed a remarkable protonophoric affinity with EC_{50} spanning from $(4.4 \times 10^{-2}) - (3.5 \times 10^{-3})$ mol%, rtl, (Table 5.2). These values are lower than the EC_{50} for H^+/Cl^- symport, indicating faster H^+ transport than Cl^- transport.

The activity of transporters **5.2-5.5** as protonophores decreased in the order of **5.3** > **5.2** > **5.5** > **5.4** (Table 5.2). To further investigate the potential interaction between

fatty acids and the tested anion transporters **5.1-5.5**, oleic acid (1 mol%) or BSA treated liposomes (to remove fatty acids) were used (Figure 5.10f). It was reported that some transporters could transport H^+ indirectly by facilitating the transmembrane flip-flop of deprotonated fatty acids.^{42, 43} The transport activity in KCl and KGlu assays were not affected by addition or removal of fatty acids, which indicate that H^+ transport by **5.1-5.5** is fatty acid-independent and presumably occurs via deprotonation of the NH groups. A liposomal leakage experiment performed using self-quenching calcein confirm the absence of non-specific membrane leakage.⁴³

5.2.5 Anion and cation selectivity

A selectivity assay has demonstrated preferential transport of more lipophilic anions including Br^- , I^- , NO_3^- , and ClO_4^- over Cl^- for all anionophores **5.1-5.5** (Figures D29-D33, appendix D). Identical transport rates were found when the K^+ in the HPTS assay was replaced with Na^+ (Figures D34 and D35, appendix D) consistent with the lack of metal ion transport.

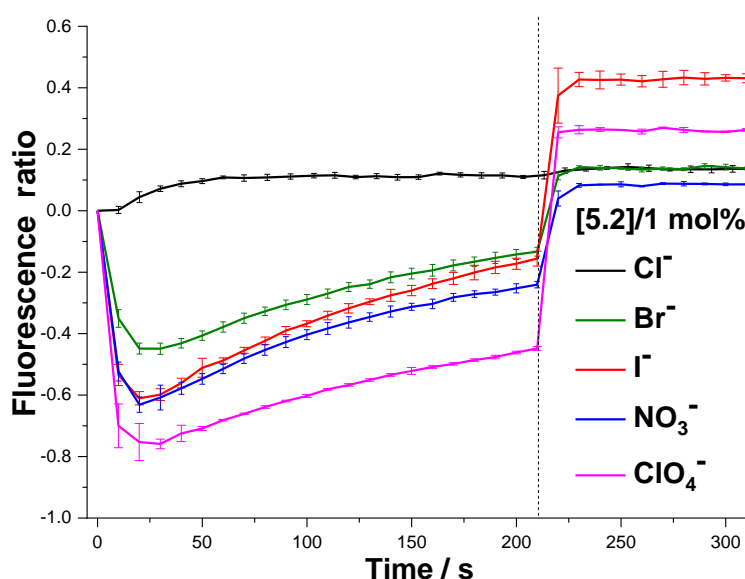


Figure 5.11: Observed fluorescence ratio response due to HCl influx in the presence of compounds **5.2** (1 mol%) into vesicles loaded with KCl (100 mM) and suspended in KCl, KBr, KI, KNO_3 and $KClO_4$ (100 mM). All external and internal solutions were buffered to pH 7 with HEPES (10 mM).

5.2.6 Reduction kinetic studies

We exploited the fluorescence and anion transport properties of transporters **5.2** and **5.3** and examined the corresponding gold complexes **5.13**, **5.14**, **5.16** and **5.17** (complexes **5.13** and **5.16** for transporter **5.2**, while complexes **5.14** and **5.17** for transporter **5.3**) against the effect of the physiological reducing agent GSH **5.18** and the non-physiological reducing agents DTT **5.19** and TCEP **5.20** (Figure 5.12).

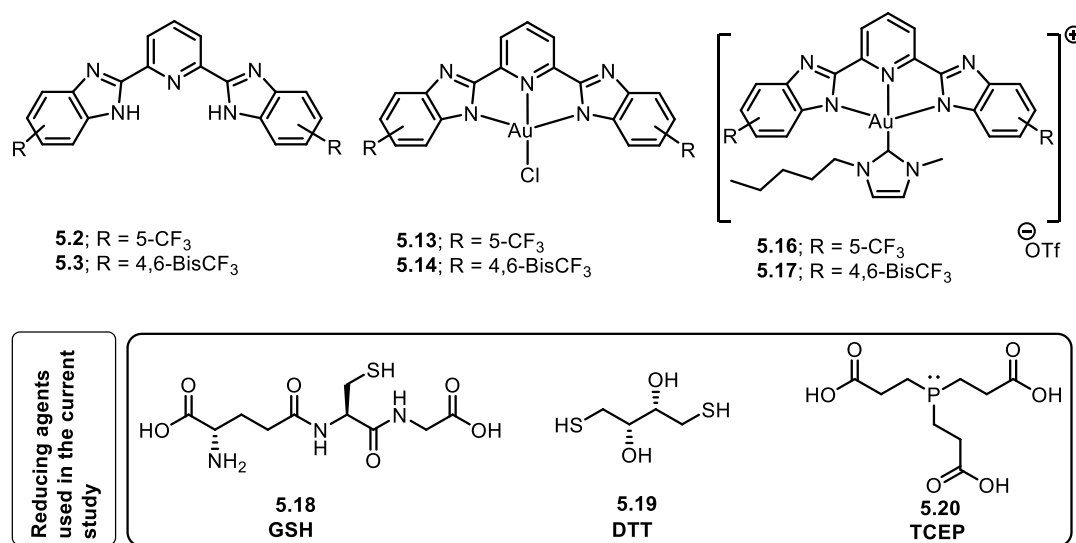


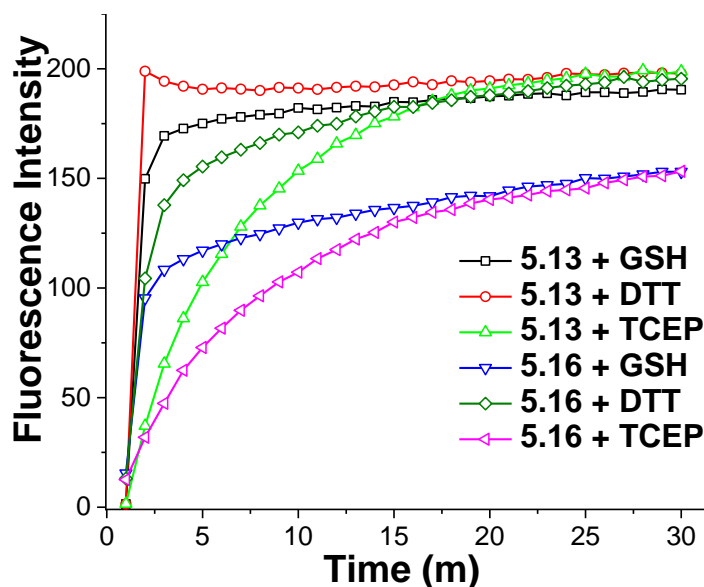
Figure 5.12: Chemical structure of tested compounds and the three reducing agents used in the current study.

Time-dependent reduction kinetics of these complexes were examined under different conditions, including external addition of the reducing agent in organic solvent (DMSO) and in liposomes (Figure 5.13-5.16). Also, encapsulation of GSH in liposomes was performed to mimic the cellular physiological conditions (Figure 5.17). UV-Vis and fluorescence spectroscopies were used to detect the change in the absorbance or fluorescence intensity upon reduction of complexes with GSH **5.18**, DTT **5.19** and TCEP **5.20**. GSH was tested at molar ratio 6:1, while TCEP and DTT were used at molar ratio 3:1, with respect to tested compound.

In DMSO, complexes **5.13**, **5.14**, **5.16** and **5.17** showed higher affinity to thiols

(GSH **5.18** and DTT **5.19**) over TCEP. As indicated from fluorescence and UV-Vis spectra, the reaction between complexes **5.13**, **5.14**, **5.16** and **5.17** and the reducing agent is fast, and it took only few seconds to 20 minutes to reach a plateau in both absorbance and fluorescence studies (Figures 5.13 and 5.14).

a)



b)

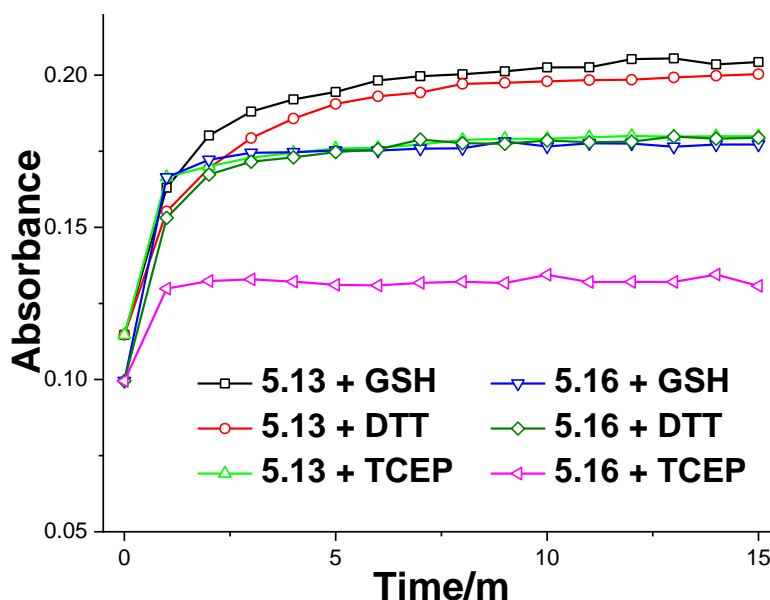


Figure 5.13: Reduction by thiols; namely GSH (reduced glutathione) and DTT (dithiothreitol), and TCEP (tris(2-carboxyethyl)phosphine hydrochloride) of complexes **5.13** and **5.16** in organic solvent (DMSO) monitored by a) fluorescence and b) UV-Vis spectroscopies. Fluorescence readings are averages of three replicates and UV-Vis readings are averages of two replicates, always with standard deviations less than 10%.

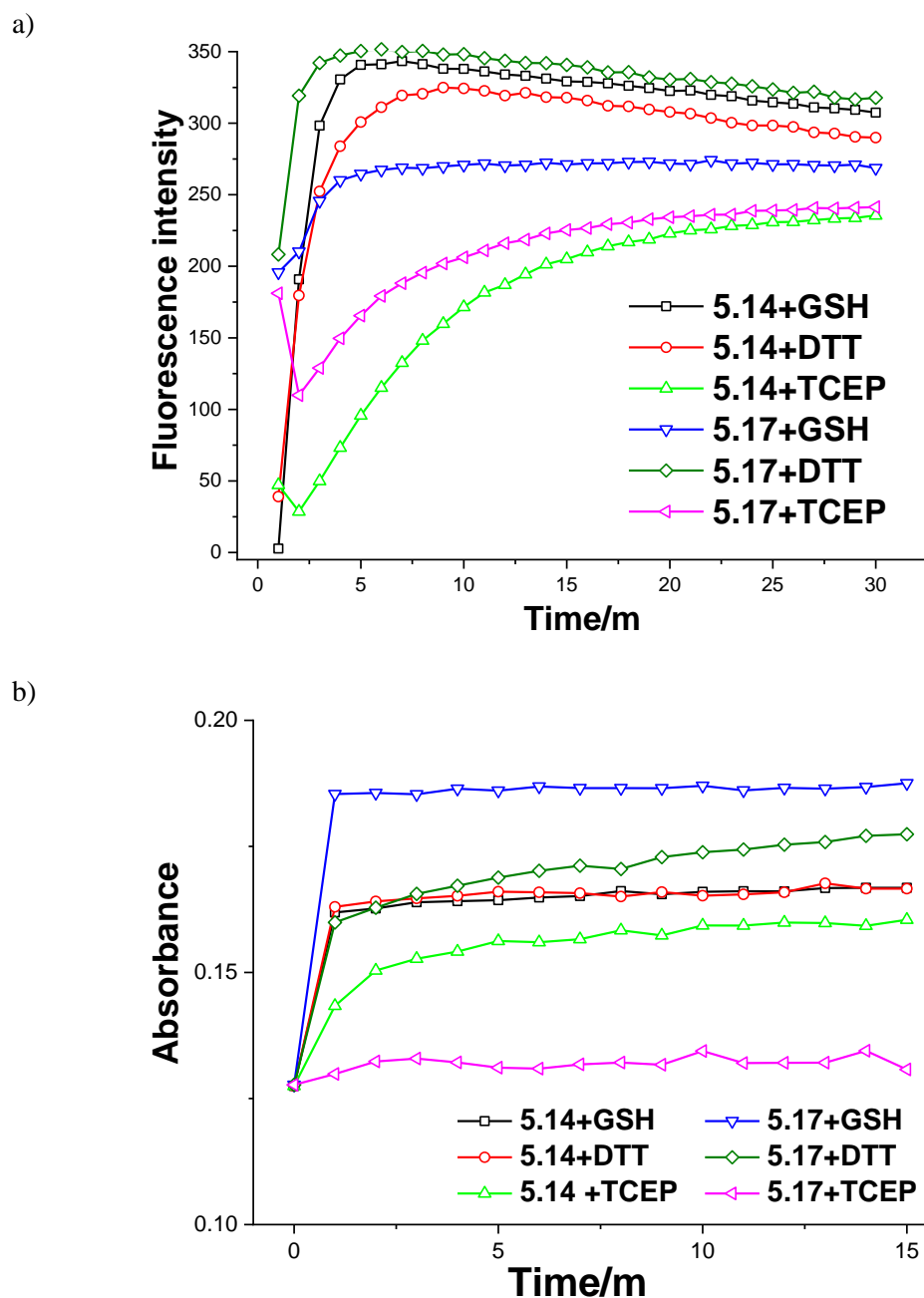


Figure 5.14: Reduction by thiols; namely GSH (reduced glutathione) and DTT (dithiothreitol), and TCEP (tris(2-carboxyethyl)phosphine hydrochloride) of complexes **5.14** and **5.17** in organic solvent (DMSO) monitored by a) fluorescence and b) UV-Vis spectroscopies. Fluorescence readings are averages of three replicates and UV-Vis readings are averages of two replicates, always with standard deviations less than 10%.

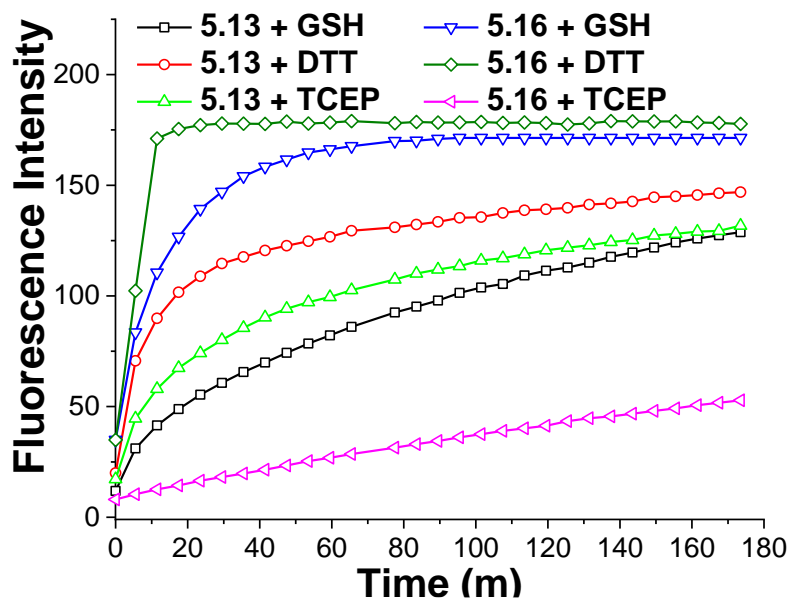
Moving to the liposome model, with external addition of the reducing agent, affinities of the gold-NHC complexes **5.16** and **5.17** to the tested reducing agents were much higher than their corresponding gold chloride complexes **5.13** and **5.14**, respectively (Figures 5.15 and 5.16). DTT emerged as the most powerful reducing

agent in liposomes. NHC-gold complexes **5.16** and **5.17** responded rapidly to DTT with prompt increase in the UV-Vis absorption spectra and reach a plateau after 1-2 minutes. Complex **5.14** showed a stronger response to DTT than complex **5.13** with a gradual increase in absorbance and reached a plateau in 30 minutes, while the reduction of complex **5.13** took 3 h to reach a plateau.

Monitoring the reduction kinetics of compounds **5.13** and **5.16** by fluorescence spectroscopy showed similar pattern as seen in the UV-Vis studies. Surprisingly, complexes **5.14** and **5.17** reduction kinetics could not be chased by fluorescence spectroscopy as the fluorescence intensity of the parent anion transporter **5.3** was diminished in the liposome model. GSH and TCEP showed a comparable reduction activity towards Au(III) chloride complexes **5.13** and **5.14** and it took less than 3 h for a complete reduction and a stable fluorescence or absorbance reading (Figures 5.15 and 5.16).

GSH achieved fast reduction of NHC gold complexes **5.16** and **5.17** and reach a plateau in 5 minutes as illustrated by UV-Vis spectroscopy. However, compound **5.16** showed a gradual increase in fluorescence in response to GSH and took 60 minutes to reach the highest fluorescence intensity. This may be attributed to encapsulation of the formed free transporter in the membrane bilayer. TCEP demonstrated the lowest reduction affinity to complexes **5.16** and **5.17** and it took more than 3 h for complex **5.16** and 1 h for complex **5.17** to reach a plateau (Figures 5.15 and 5.16).

a)



b)

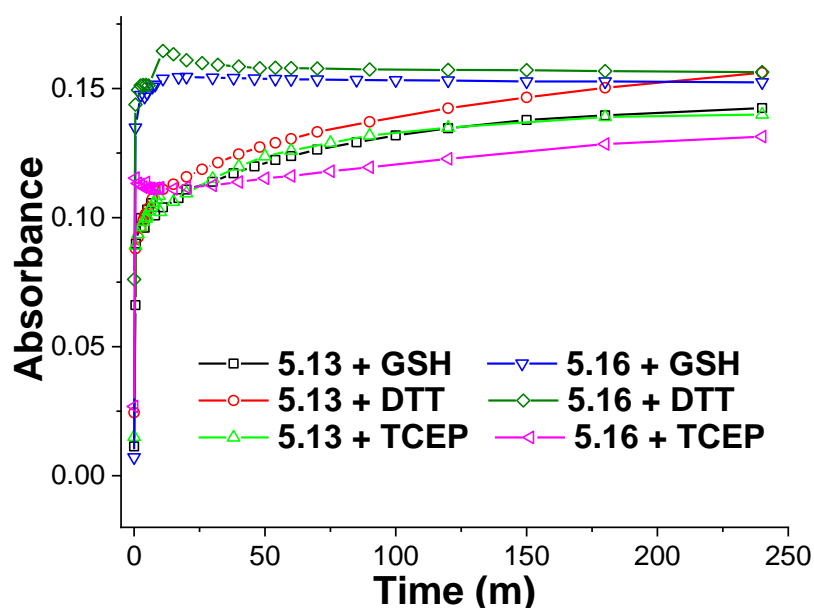


Figure 5.15: Reduction by thiols; namely GSH (reduced glutathione) and DTT (dithiothreitol), and TCEP (tris(2-carboxyethyl)phosphine hydrochloride) of complexes **5.13** and **5.16** in liposomes monitored by a) fluorescence and b) UV-Vis spectroscopies. Fluorescence readings are averages of three replicates and UV-Vis readings are averages of two replicates, always with standard deviations less than 10%.

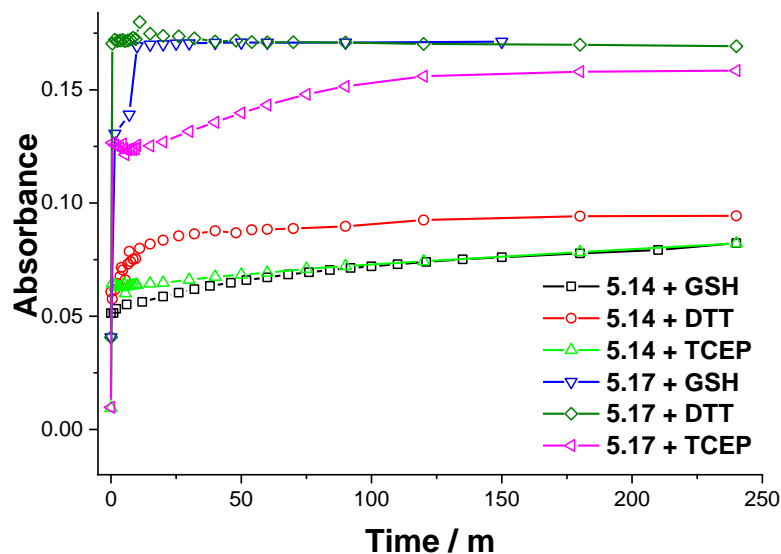


Figure 5.16: Reduction by thiols; namely GSH (reduced glutathione) and DTT (dithiothreitol), and TCEP (tris(2-carboxyethyl)phosphine hydrochloride) of complexes **5.14** and **5.17** in liposomes monitored by UV-Vis spectroscopy. UV-Vis readings are averages of two replicates, always with standard deviations less than 10%.

In order to mimic the physiological conditions, the reduction kinetics of complexes **5.13**, **5.14**, **5.16** and **5.17** in GSH-encapsulated liposomes were investigated (Figures 5.17 and 5.18). In a similar pattern to the liposome model, complexes **5.16** and **5.17** showed a fast reaction with GSH and reach a plateau in 10 minutes as illustrated from UV-Vis spectra, while complexes **5.13** and showed weaker responses than complexes **5.16** and **5.17**.

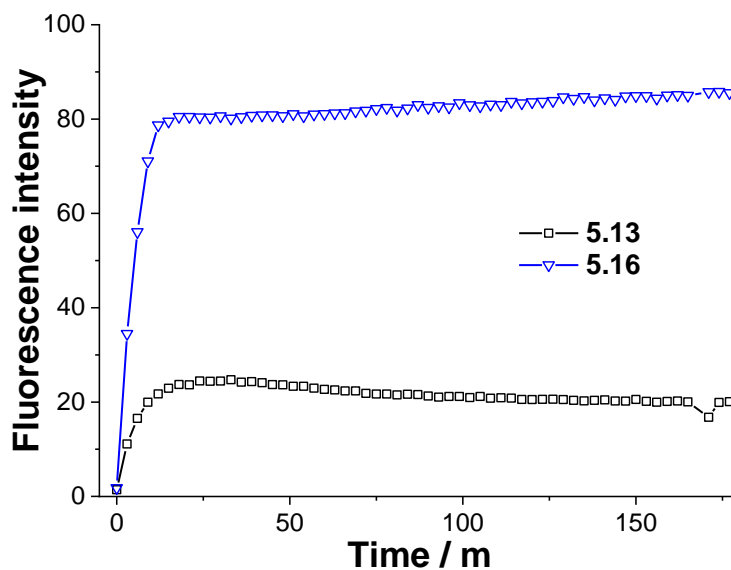


Figure 5.17: Reduction of **5.13** and **5.16** in GSH encapsulated liposomes. Fluorescence readings are averages of three replicates, always with standard deviations less than 10%.

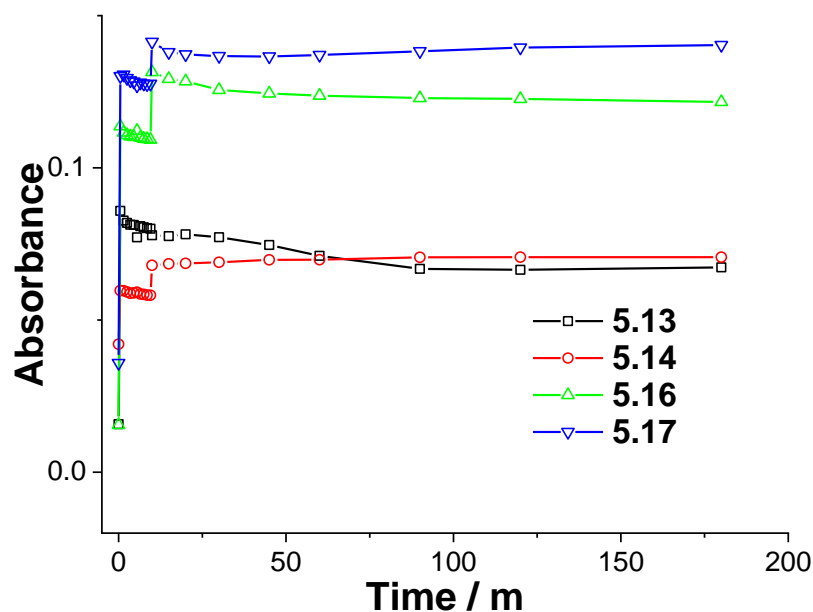


Figure 5.18: Reduction of complexes **5.13**, **5.14**, **5.16** and **5.17** in GSH encapsulated liposomes. UV-Vis readings are averages of two replicates, always with standard deviations less than 10%.

Generally, fluorescence and absorbance intensities of complexes **5.13**, **5.14**, **5.16** and **5.17** changed over time upon addition of the reducing agents under all conditions, but with different rates.

5.2.7 Switchable time-dependant transport studies

Time-dependent transport studies of complexes **5.13**, **5.14**, **5.16** and **5.17** were performed in HPTS-KCl liposome (HCl symport, Figure 5.19) against the three-reducing agents at 1 mol% (rtl) of receptors **5.2-5.3** and complexes **5.13**, **5.14**, **5.16** and **5.17**. Complexes **5.13** and **5.16** (without addition of the reducing agent) showed low anion transport activities at 1 mol% (Figures 5.20 and 5.21, Figures D50-D57 appendix D).

Interestingly, complexes **5.14** and **5.17** showed 35% and 36% efflux respectively at 1 mol% (rtl) (Figures 5.20 and 5.21), indicating that Au (III)-mediated chloride transport across phospholipid membranes.⁴⁴

As evidenced by kinetic studies, DTT is the most potent reducing agent among all tested complexes **5.13**, **5.14**, **5.16** and **5.17**, followed by GSH and TCEP showed the slowest reduction rate.

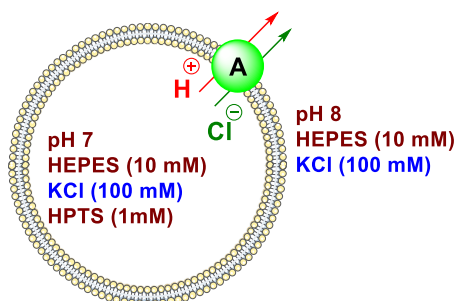


Figure 5.19: KCl-KOH liposomal model used to assess the switchable-time dependent studies. POPC vesicles were loaded with KCl (100 mM), buffered to pH 7.0 with HEPES (10 mM). The test compound was added at 0 s and detergent was added at 200 s.

Complex **5.13** showed the same chloride efflux as the parent anion transporter **5.2** after mixing with the reducing agents for 3 h (Figure 5.20a). Incubation of complex **5.14** with GSH and TCEP for 30 minutes demonstrated a similar chloride efflux rate to that of the parent anion transporter **5.3**, however, incubation with DTT for 30 minutes led to a faster chloride efflux than the parent compound **5.3** (Figure 20b, Figures D52 and D53, appendix D). This is presumably due to anion transport activity of complex **5.14** itself. Also, reacting complex **5.14** with all reducing agents for 3 hours gave a higher chloride efflux than anion transporter **5.3** at 1 mol%. Incubation of complex **5.16** with DTT or GSH for 5 minutes showed 100% and ~90% chloride efflux, respectively, in comparison with the parent transporter **5.2**, while incubation for 20 minutes reach 100% for both reductants (Figure 5.21a). Incubation of DTT, GSH or TCEP with complex **5.17** showed higher chloride efflux (with GSH and DTT) and similar chloride efflux (with TCEP) in comparison to the parent transporter **5.3** (Figure 5.21b).

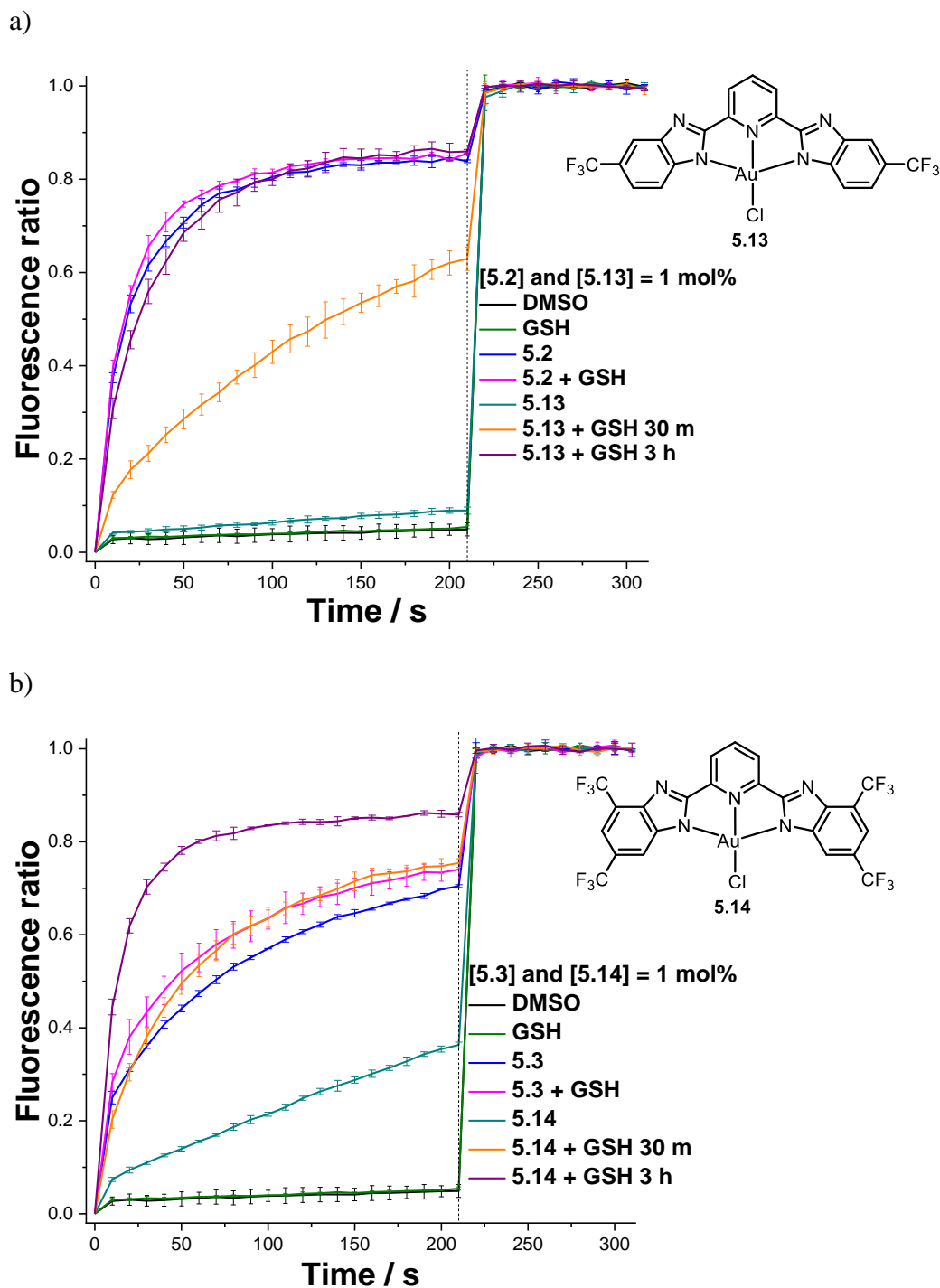


Figure 5.20. Observed fluorescence ratio response due to H^+/Cl^- symport or Cl^-/OH^- antiport upon reduction of complexes a) **5.13** and b) **5.14** ($1 \mu\text{M}$) by GSH ($6 \mu\text{M}$) using KCl-KOH assay from POPC vesicles loaded with KCl (100 mM), buffered to pH 7.0 with HEPES (10 mM) at different time intervals. The test complexes **5.13** and **5.14** ($1 \text{ mol}\%$) and KOH were added firstly, then GSH was added at 0 s. DMSO, GSH ($3 \text{ mol}\%$), parent anion transporters **5.2** and **5.3** and complex **5.13** and **5.14** (without addition of DTT) were used as controls. Detergent was added at 200 s. Ionophore concentrations are shown as ionophore to lipid molar ratios. Error bars represent SD from at least three repeats.

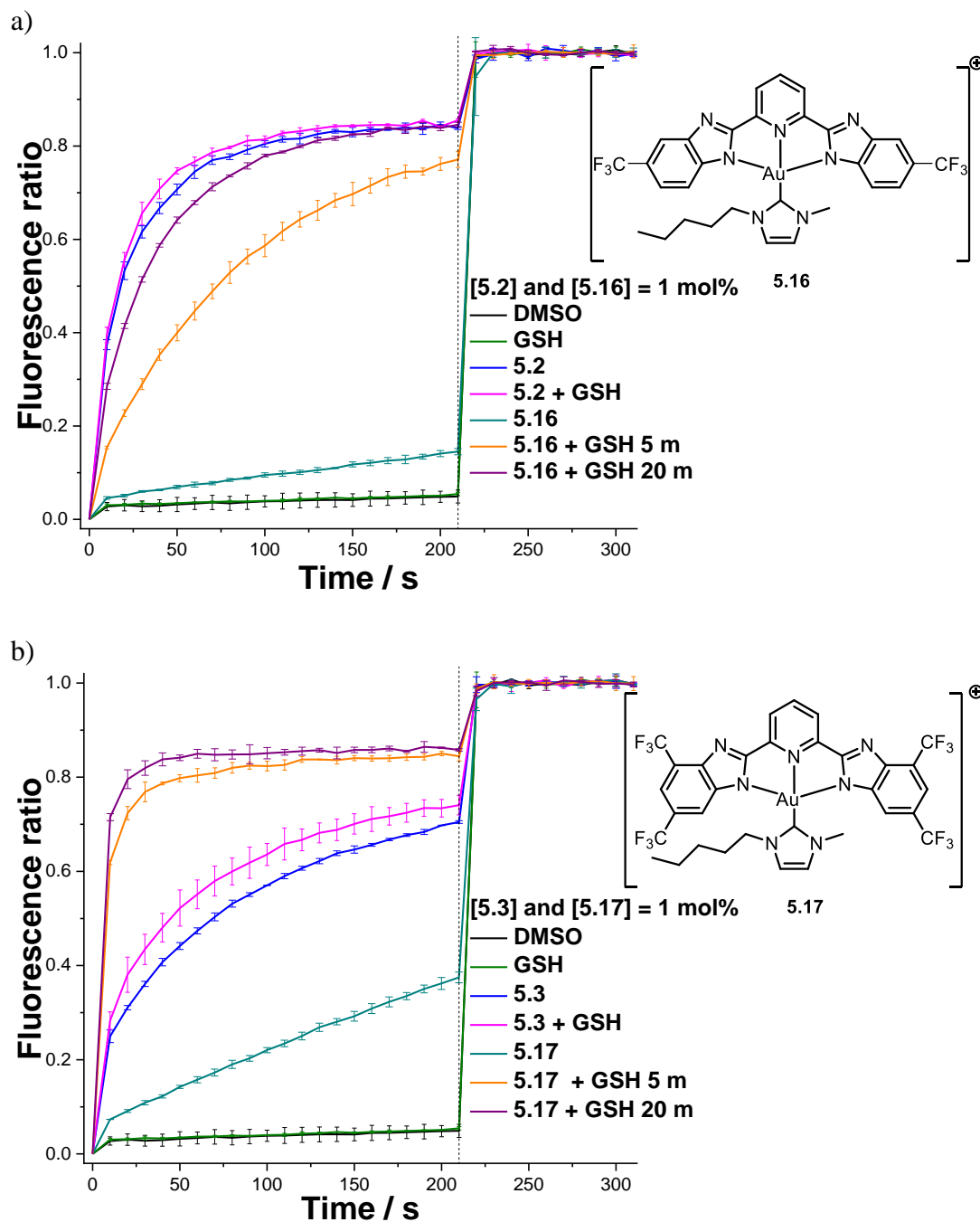


Figure 5.21. Observed fluorescence ratio response due to H^+/Cl^- symport or Cl^-/OH^- antiport upon reduction of complexes a) **5.16** and b) **5.17** ($1 \mu\text{M}$) by GSH ($6 \mu\text{M}$) using KCl-KOH assay from POPC vesicles loaded with KCl (100 mM), buffered to pH 7.0 with HEPES (10 mM) at different time intervals. The test complexes **5.16** and **5.17** ($1 \text{ mol}\%$) and KOH were added firstly, then GSH was added at 0 s. DMSO, GSH ($3 \text{ mol}\%$), parent anion transporters **5.2** and **5.3** and complex **5.16** and **5.17** (without addition of DTT) were used as controls. Detergent was added at 200 s. Ionophore concentrations are shown as ionophore to lipid molar ratios. Error bars represent SD from at least three repeats.

5.3 Conclusions

We present herein stimuli-responsive gold complexes as efficient switchable anion transporters that can be reduced to release active anion transporters by a set of reducing agents, including the physiologically predominant GSH. Five BisBzImPy anion transporters **5.1-5.5** have been synthesized and they have been shown to bind Cl^- with moderate affinity in $\text{DMSO-}d_6/0.5\%\text{H}_2\text{O}$ and CD_3CN and facilitate the transport of H^+ , Cl^- and NO_3^- in liposomal models. Switchable cycloaurated complexes **5.13**, **5.14**, **5.16** and **5.17** were constructed from the two most potent anion transporters **5.2** and **5.3**. The switch-off complexes **5.13**, **5.14**, **5.16** and **5.17** demonstrated higher affinity to DTT, followed by GSH, while TCEP emerged as the weakest reducing agent. Finally transport studies showed that these switchable anion transporters **5.13**, **5.14**, **5.16** and **5.17** are highly efficient and can be switched on by all tested reducing agents with different rates. DTT emerged as the most potent reducing agent followed by GSH and TCEP. A remarkably rapid reduction of Au(III) centre was found for complex **5.17** upon treatment with GSH leading to complete release of the active anion transporter within 5 min.

5.4 Experimental Section

5.4.1 Chemistry

General methods and material

All reagents and solvents were purified and dried by standard techniques. Reactions were monitored by TLC analysis using silica gel GF/UV 254. NMR spectra were recorded on Bruker 400 MHz FT-NMR spectrometer and Varian Gemini-300BB 300 MHz FT-NMR spectrometers (Varian Inc., Palo Alto, CA). ^1H spectra were

run at 300 and 400 MHz and ^{13}C spectra were run at 75 and 101 MHz, in the stated solvent. Chemical shifts (δ_{H}) are reported relative to TMS as internal standard and coupling constant (J) values are reported in Hertz. The abbreviations used are as follows: s, singlet; d, doublet; t, triplet; m, multiplet. Electrospray ionization (ESI single quadrupole) mass spectra have their ion mass to charge values (m/z) stated with their relative abundances as a percentage in parentheses. Peaks assigned to the molecular ion are denoted as $[\text{M}+\text{H}]^+$ or $[\text{M}+\text{Na}]^+$. Column chromatography was performed using silica gel 60 (0.063-0.200 mm). Low resolution mass spectra (LRMS) and high-resolution mass spectra (HRMS) were recorded using positive/negative ion electrospray ionization (ESI) and atmospheric pressure photoionization (APPI) on Bruker amaZon SL mass spectrometer and Bruker Solarix 2xR 7T Fourier transform ion cyclotron resonance mass spectrometer (FTICR). UV-Vis kinetic studies were performed on an Agilent Cary 4000 UV-Vis absorption spectrometer equipped with a magnetic stirrer and a temperature controller. Synthesis of 2,6-bis(1*H*-benzo[*d*]imidazol-2-yl)pyridine **5.1**, 2,6-bis(5-nitro-1*H*-benzo[*d*]imidazol-2-yl)pyridine **5.5** and Ag *N*-heterocyclic carbene (NHC) derivatives **5.15** were attempted according to literature.^{40, 45, 46}

2,6-Bis(1*H*-benzo[*d*]imidazol-2-yl)pyridine (5.1): ^{39, 40} Dipicolinic acid (pyridine-2,6-dicarboxylic acid) (1.67 g, 10 mmol) and *o*-phenylenediamine (2.38, 22 mmol) were suspended in orthophosphoric acid (30 mL) at 200 °C for 6 h. After cooling, the reaction melt was poured in 500 mL of cold water and vigorous stirring was applied. The blue-green precipitate was filtered out and then stirred with hot 10% aqueous sodium carbonate for 10 min. The formed solid was collected by filtration and crystallized from methanol to give **5.1** (1.35 g, 43%); as a white

powder ^1H NMR (400 MHz, DMSO, d_6) δ : 7.23-7.36 (m, 4H, ArH), 7.77 (dd, J = 8.0, 24.0 Hz, 4H, Ar-H), 8.18 (t, J = 8.0 Hz, 1H, Ar-H), 8.36 (d, J = 8.0 Hz, 2H, Ar-H), 13.10 (br s, 2H, 2 x -NH); ^{13}C NMR (101 MHz, DMSO, d_6) δ : 112.3, 120.2, 121.8, 122.7, 124.2, 134.9, 139.7, 144.6, 148.3, 151.0. HRMS (ESI⁺) calcd for $\text{C}_{19}\text{H}_{13}\text{N}_5\text{Na}$ (M+Na)⁺: m/z 334.1063, found 334.1061.

General procedure A of synthesis of anion transporters 5.2-5.4⁴¹

Step 1. To a suspension of pyridine-2,6-dicarbaldehyde (270 mg, 2 mmol) in ethanol (7 mL), was slowly added a solution of sodium metabisulfite (213 mg, 1.1 mmol) in water (1 mL). The mixture was stirred vigorously at room temperature and ethanol (10 mL) was added. The reaction flask was left overnight at 0 °C and the resulting pink precipitate was filtered and dried to give the aldehyde adduct (611 mg, 89%) as a pink powder. The aldehyde adduct was used without further purification.

Step 2.

A mixture of aldehyde adducts (342 mg, 1 mmol) and the appropriate phenylene diamine (2 mmol) in dry DMF (1 mL) was heated at 120 °C for 4 h. The mixture was cooled overnight and poured on brine solution and left to stir overnight. The resulting solid filtered, washed with water (3 x 10 mL), dried and recrystallized from ethanol to give anion transporter **2-4**.

2,6-Bis(5(6)-(trifluoromethyl)-1H-benzo[*d*]imidazol-2-yl)pyridine (5.2): Using general procedure A and 4-(trifluoromethyl)benzene-1,2-diamine (352 mg, 2 mmol), anion transporter **5.2** (482 mg, 54%) was obtained as a white solid; m.p:

285-287 °C. ^1H NMR (400 MHz, CD_3CN) δ : 7.39 (dd, $J = 1.0, 9.0$ Hz, 2H, Ar-H), 7.54 (d, $J = 8.0$ Hz, 2H, Ar-H), 7.72 (t, $J = 8.0$ Hz, 1H, Ar-H), 7.77-7.83 (m, 2H, ArH), 8.02 (d, $J = 8.0$ Hz, 2H, Ar-H); ^{13}C NMR (101 MHz, CD_3CN) δ : 118.1, 120.6, 121.9, 123.1, 124.6, 125.0 (d, $J_{\text{C-F}} = 31$ Hz), 127.3, 130.0, 139.5, 147.9, 153.2. HRMS (ESI⁺) calcd for $\text{C}_{21}\text{H}_{11}\text{F}_6\text{N}_5\text{Na}$ ($\text{M}+\text{Na}$)⁺: m/z 470.0811, found 470.0809.

2,6-Bis(4,6(3,5)-bis(trifluoromethyl)-1H-benzo[d]imidazol-2-yl)pyridine (5.3):

Using general procedure A and 4-(trifluoromethyl)benzene-1,2-diamine (488 mg, 2 mmol), anion transporter **5.3** (495 mg, 42%) was obtained as a white solid; m.p: 290-291 °C. ^1H NMR (300 Hz, CD_3CN) δ : 7.78-7.90 (m, 2H, ArH), 8.13 (t, $J = 8.0$ Hz, 1H, Ar-H), 8.18-8.25 (m, 2H, ArH), 8.40 (d, $J = 8.0$ Hz, 2H, Ar-H); ^{13}C NMR (126 Hz, $(\text{CD}_3)_2\text{CO}$) δ : 113.6, 113.8, 116.2, 117.8, 120.9, 121.2, 121.5, 122.5, 123.7, 123.8, 124.0, 124.1, 124.4, 124.6, 125.3, 126.8, 132.7, 135.6, 139.3, 143.1, 145.6, 147.3, 154.2, 154.5; ^{19}F (471 Hz, $(\text{CD}_3)_2\text{CO}$) δ : -61.63. HRMS (ESI⁺) calcd for $\text{C}_{23}\text{H}_9\text{F}_{12}\text{N}_5\text{Na}$ ($\text{M}+\text{Na}$)⁺: m/z 606.0559, found 606.0559.

2,6-Bis(5,6-difluoro-1H-benzo[d]imidazol-2-yl)pyridine (5.4)

Using general procedure A and 4-(trifluoromethyl)benzene-1,2-diamine (288 mg, 2 mmol), anion transporter **5.4** (390 mg, 51%) was obtained as a violet solid; m.p: > 300 °C. ^1H NMR (300 Hz, DMSO, d_6) δ : 7.75-7.85 (m, 4H, ArH), 8.18 (t, $J = 7.0$ Hz, 1H, Ar-H), 8.30 (d, $J = 7.0$ Hz, 2H, Ar-H); ^{13}C NMR (75 Hz, DMSO, d_6): 122.0, 139.9, 146.2, 147.7, 149.4, 152.8. HRMS (ESI⁺) calcd for $\text{C}_{19}\text{H}_{10}\text{F}_4\text{N}_5$ ($\text{M}+\text{H}$)⁺: m/z 384.0867, found 384.0864.

2,6-Bis(6-nitro-1*H*-benzo[*d*]imidazol-2-yl)pyridine (5.5):⁴⁵

Compound **5.1** (311 mg, 1 mmol) was dissolved in concentrated H₂SO₄ (1 mL) and was cooled in an ice-water mixture. A mixture of 1:1 HNO₃/H₂SO₄ (0.25 mL) was added dropwise and the reaction suspension was stirred for 3 h, poured into ice water (10 mL) and neutralized with 20% NaOH. The resulting solid was filtered and washed with water (2 x 10 mL) to give **5.5** (310 mg, 77%) as pale-yellow powder. ¹H NMR (500 Hz, pyridine, *d*₅) δ: 7.70-7.85 (m, 4H, Ar-H), 8.06 (t, 1H, *J* = 7.5 Hz, Ar-H), 8.27 (dd, 2H, *J* = 2.0, 9.0 Hz, Ar-H), 8.65 (d, 2H, *J* = 7.5 Hz, Ar-H); ¹³C NMR (126 Hz, pyridine, *d*₅) δ: 118.8, 122.9, 134.9, 135.7, 138.9, 139.1, 144.0, 148.1, 149.2, 155.2; HRMS (ESI⁺) calcd for C₁₉H₁₂N₇O₄ (M+H)⁺: *m/z* 402.0945, found 402.0951.

General procedure B for synthesis of complexes 5.13 and 5.14³⁸

Dry methanol (25 mL) was added a mixture of anion receptor **5.2** (224 mg, 0.50 mmol) or anion receptor **5.3** (292 mg, 0.50 mmol), dried sodium acetate (325 mg, 3.97 mmol) and KAuCl₄ (284 mg, 0.75 mmol) and was heated at reflux for 3 h. The resulting solid was filtered and washed with methanol (2 x 10 mL) and diethyl ether (3 x 10 mL) and dried to give complex **5.13** (352 mg, 67%) and **5.14** (455 mg, 56%) as yellow powders.

Characterisation of complex 5.13: Using general procedure B and anion receptor **5.2**, complex **5.13** (352 mg, 67%) was obtained as a yellow solid; m.p.: > 300 °C. ¹H NMR (500 Hz, DMSO, *d*₆) δ: 7.56 (td, *J* = 2.0, 7.0 Hz, 1H, Ar-H), 7.70 (dd, *J* = 2.0, 9.0 Hz, 1H, Ar-H), 7.95-7.98 (m, 1H, Ar-H), 8.14 (s, 1H, Ar-H), 8.23 (t, *J* = 8.0 Hz, 1H, Ar-H), 8.33-8.40 (m, 3H, Ar-H), 8.61-8.66 (m, 1H, Ar-H); ¹³C NMR

(126 Hz, DMSO, d_6) δ : 111.1, 114.8, 118.7, 119.5, 122.2, 123.4, 123.5, 124.0, 142.2, 126.1, 140.0, 142.4, 142.8, 145.3, 146.7, 146.8, 147.6, 160.4, 160.8; ^{19}F (471 Hz, DMSO) δ : -59.62, -59.26. HRMS (APPI) calcd for $\text{C}_{21}\text{H}_9\text{AuClF}_6\text{N}_5(\text{M})^+$: m/z 677.0111, found 677.0107.

Characterisation of complex 5.14: Using general procedure B and anion receptor **5.3**, complex **5.14** (455 mg, 56%) was obtained as a yellow solid; m.p: > 300 °C. ^1H NMR (500 Hz, $(\text{CD}_3)_2\text{CO}$) δ : 7.75 (s, 2H, Ar-H), 8.41 (d, $J = 5.0$ Hz, 2H, Ar-H), 8.58 (s, 2H, Ar-H), 8.73 (t, $J = 8.0$ Hz, 1H, Ar-H); ^{13}C NMR (126 Hz, $(\text{CD}_3)_2\text{CO}$) δ : 115.3 (d, $J^1_{\text{C-F}} = 200$ Hz), 120.8, 122.1 (d, $J^2_{\text{C-F}} = 16$ Hz), 122.9, 124.4 (d, $J^3_{\text{C-F}} = 8$ Hz), 125.1, 125.7 (d, $J^1_{\text{C-F}} = 200$ Hz), 125.9 (d, $J^2_{\text{C-F}} = 33$ Hz), 127.3, 141.1, 141.7, 147.0, 147.8, 161.8. ^{19}F (471 Hz, $(\text{CD}_3)_2\text{CO}$) δ : -61.92. HRMS (APCI) calcd for $\text{C}_{23}\text{H}_7\text{AuClF}_{12}\text{N}_5(\text{M})^+$: m/z 812.9859, found 812.9898.

General procedure C of complexes 8 and 9³⁸

Previously dried silver triflate (46 mg, 0.18 mmol) was added to a suspension of (1-methyl-3-pentyl-1,3-dihydro-2*H*-imidazol-2-ylidene)silver(I) bromide (60 mg, 0.18 mmol) **5.15** and complex **5.13** (100 mg, 0.15 mmol) or complex **5.14** (120 mg, 0.15 mmol) in acetonitrile (15 mL). After holding the reaction mixture in the dark at reflux for 12 h, it was cooled, filtered and purified by cycles of crystallization of diethyl ether diffusion in an acetonitrile solution of the product.

Characterisation of complex 5.16

Using general procedure C, complex **5.16** (18 mg, 13%); was obtained as a yellow solid; m.p: > 237-239 °C. ^1H NMR (300 MHz, CD_3CN) δ : 0.51 (t, $J = 7.0$ Hz, 3H,

CH₃), 0.98-1.05 (m, 2H, CH₂), 1.13-1.18 (m, 2H, CH₂), 1.71-1.80 (m, 2H, CH₂), 4.05 (s, 3H, CH₃), 4.36-4.41 (m, 2H, CH₂), 6.12-6.15 (m, 2H, Ar-H), 7.53-7.62 (m, 2H, Ar-H), 7.93-8.03 (m, 2H, Ar-H), 8.22 (s, 1H, Ar-H), 8.39 (d, $J = 8.0$ Hz, 2H, Ar-H), 8.64 (t, $J = 8.0$ Hz, 1H, Ar-H); ¹³C NMR (101 MHz, CD₃CN) δ : 12.6, 21.6, 27.8, 30.1, 38.4, 51.6, 108.8, 112.5, 112.7, 119.1, 122.4, 122.9, 125.5, 126.9, 138.3, 141.2, 142.3, 147.2, 147.2, 147.5, 161.6; HRMS (APPI) calcd for C₃₀H₂₅AuF₆N₇⁺ (M - OTf)⁺: m/z 794.1736, found 794.1737.

Characterisation of complex 5.17

Using general procedure C, complex **5.17** (20 mg, 12%); was obtained as a yellow solid; m.p.: > 231-233 °C. ¹H NMR (300 MHz, (CD₃)₂CO) δ : 0.39 (t, $J = 7.0$ Hz, 3H, CH₃), 0.85-1.03 (m, 2H, CH₂), 1.04-1.11 (m, 2H, CH₂), 1.72-1.79 (m, 2H, CH₂), 4.26 (s, 3H, CH₃), 4.63 (t, $J = 7.0$ Hz, 2H, CH₃), 6.45 (s, 2H, Ar-H), 7.77 (s, 1H, Ar-H), 7.88 (s, 1H, Ar-H), 8.37 (d, $J = 2.0$ Hz, 2H, Ar-H), 8.42 (d, $J = 2.0$ Hz, 2H, Ar-H), 8.51 (d, $J = 8.0$ Hz, 2H, Ar-H), 8.75 (t, $J = 8.0$ Hz, 1H, Ar-H); ¹³C NMR (75 MHz, (CD₃)₂CO) δ : 12.6, 21.7, 27.9, 30.4, 38.5, 51.8, 113.0, 116.8, 119.8, 119.9, 120.5, 122.1, 122.8 (q, ² $J_{C,F} = 34$ Hz), 124.2, 124.5 (q, ¹ $J_{C,F} = 209$ Hz), 127.6, 131.9, 139.8, 141.5, 147.4, 147.6, 163.9; HRMS (APPI) calcd for C₃₂H₂₃AuF₁₂N₇⁺ (M - OTf)⁺: m/z 930.1484, found 930.1486.

5.4.2 X-ray crystallography

X-ray of transporter (5.2)

Single crystals of transporter **5.2** (C₂₃H₁₇N₅OF₆S) were obtained by slow diffusion of DMSO solution of **5.2**. A suitable crystal was selected and in Paratone on a micromount on a SuperNova, Dual, Cu at home/near, Atlas diffractometer. The

crystal was kept at 100 K during data collection. Using Olex2⁴⁷, the structure was solved with the ShelXS⁴⁸ structure solution program using Direct Methods and refined with the ShelXL⁴⁹ refinement package using Least Squares minimization.

Crystal Data for C₂₃H₁₇N₅O₆S ($M = 525.47$ g/mol): orthorhombic, space group Pmc2₁ (no. 26), $a = 6.841(2)$ Å, $b = 17.047(3)$ Å, $c = 19.783(4)$ Å, $V = 2307.1(10)$ Å³, $Z = 4$, $T = 100(2)$ K, $\mu(\text{Cu K}\alpha) = 1.943$ mm⁻¹, $D_{\text{calc}} = 1.513$ g/cm³, 3102 reflections measured ($8.94^\circ \leq 2\Theta \leq 147.086^\circ$), 3102 unique ($R_{\text{sigma}} = 0.0551$) which were used in all calculations. The final R_1 was 0.1265 ($I > 2\sigma(I)$) and wR_2 was 0.3804 (all data).

X-ray of complex (5.14)

Single crystals of complex **5.14** (C₂₆H₁₃AuClF₁₂N₅O) were obtained by slow diffusion of acetone solution of **5.14**. A suitable crystal was selected and in Paratone on a micromount on a SuperNova, Dual, Cu at home/near, Atlas diffractometer. The crystal was kept at 100 K during data collection. Using Olex2⁴⁷, the structure was solved with the ShelXS⁴⁸ structure solution program using Direct Methods and refined with the ShelXL⁴⁹ refinement package using Least Squares minimization.

Crystal Data for C₂₆H₁₃AuClF₁₂N₅O ($M = 871.83$ g/mol): orthorhombic, space group P2₁2₁2₁ (no. 19), $a = 4.9760(2)$ Å, $b = 18.4846(6)$ Å, $c = 29.9692(9)$ Å, $V = 2756.57(16)$ Å³, $Z = 4$, $T = 100(2)$ K, $\mu(\text{CuK}\alpha) = 11.990$ mm⁻¹, $D_{\text{calc}} = 2.101$ g/cm³, 10634 reflections measured ($9.57^\circ \leq 2\Theta \leq 146.43^\circ$), 5220 unique ($R_{\text{int}} = 0.0665$, $R_{\text{sigma}} = 0.0718$) which were used in all calculations. The final R_1 was 0.0895 ($I > 2\sigma(I)$) and wR_2 was 0.2353 (all data).

X-ray of transporter **5.16**

Single crystals of transporter **5.16** ($C_{33}H_{28}AuF_9N_8O_3S$) were crystallized by a mixture of acetonitrile and diethyl ether solution of **5.16**. A suitable crystal was selected and in Paratone on a micromount on a SuperNova, Dual, Cu at home/near, Atlas diffractometer. The crystal was kept at 100 K during data collection. Using Olex2⁴⁷, the structure was solved with the ShelXS⁴⁸ structure solution program using Direct Methods and refined with the ShelXL⁴⁹ refinement package using Least Squares minimization.

Crystal Data for $C_{33}H_{28}AuF_9N_8O_3S$ ($M = 984.66$ g/mol): monoclinic, space group $P2_1/n$ (no. 14), $a = 15.51220(20)$ Å, $b = 16.2596(2)$ Å, $c = 28.5690(3)$ Å, $\beta = 95.2011(11)^\circ$, $V = 7176.06(16)$ Å³, $Z = 8$, $T = 100(2)$ K, $\mu(\text{Cu K}\alpha) = 9.101$ mm⁻¹, $D_{\text{calc}} = 1.823$ g/cm³, 12657 reflections measured ($7.894^\circ \leq 2\theta \leq 133.198^\circ$), 12657 unique ($R_{\text{int}} = ?$, $R_{\text{sigma}} = 0.0511$) which were used in all calculations. The final R_1 was 0.0380 ($I > 2\sigma(I)$) and wR_2 was 0.0907 (all data).

X-ray of complex **5.17**

Single crystals of complex **5.17** were obtained by slow diffusion vapour diffusion of Et₂O into an acetone solution of **5.17**. A suitable crystal was selected and in Paratone on a micromount on a SuperNova, Dual, Cu at home/near, Atlas diffractometer. The crystal was kept at 100 K during data collection. Using Olex2⁴⁷, the structure was solved with the ShelXS⁴⁸ structure solution program using Direct Methods and refined with the ShelXL⁴⁹ refinement package using Least Squares minimization.

Crystal Data for $C_{36}H_{29}N_7O_4F_{15}SAu$ ($M = 1137.69$ g/mol): triclinic, space group P-1 (no. 2), $a = 11.2877(3)$ Å, $b = 14.0974(3)$ Å, $c = 14.9642(4)$ Å, $\alpha = 109.821(2)^\circ$, $\beta = 107.118(2)^\circ$, $\gamma = 102.3303(19)^\circ$, $V = 2006.66(9)$ Å³, $Z = 2$, $T = 100(2)$ K, $\mu(\text{CuK}\alpha) = 8.474$ mm⁻¹, $D_{\text{calc}} = 1.883$ g/cm³, 14400 reflections measured ($6.848^\circ \leq 2\Theta \leq 145.304^\circ$), 7742 unique ($R_{\text{int}} = 0.0278$, $R_{\text{sigma}} = 0.0382$) which were used in all calculations. The final R_1 was 0.0337 ($I > 2\sigma(I)$) and wR_2 was 0.0859 (all data).

X-ray of 5.2.TEACl complex

Single crystals of transporter **5.2** and chloride ion were obtained by slow diffusion vapour diffusion of Et₂O into acetonitrile solution of **5.2** and two equivalents of TEACl. A suitable crystal was selected and in Paratone on a micromount on a SuperNova, Dual, Cu at home/near, Atlas diffractometer. The crystal was kept at 100 K during data collection. Using Olex2⁴⁷, the structure was solved with the ShelXS⁴⁸ structure solution program using Direct Methods and refined with the ShelXL⁴⁹ refinement package using Least Squares minimization.

Crystal Data for $C_{50}H_{48}ClF_{12}N_{11}O_3$ ($M = 1114.44$ g/mol): triclinic, space group P-1 (no. 2), $a = 11.3690(16)$ Å, $b = 11.800(2)$ Å, $c = 19.141(3)$ Å, $\alpha = 100.941(16)^\circ$, $\beta = 90.546(14)^\circ$, $\gamma = 104.405(14)^\circ$, $V = 2437.5(7)$ Å³, $Z = 2$, $T = 100(2)$ K, $\mu(\text{CuK}\alpha) = 1.605$ mm⁻¹, $D_{\text{calc}} = 1.518$ g/cm³, 19563 reflections measured ($7.892^\circ \leq 2\Theta \leq 147.71^\circ$), 9489 unique ($R_{\text{int}} = 0.1261$, $R_{\text{sigma}} = 0.1672$) which were used in all calculations. The final R_1 was 0.1404 ($I > 2\sigma(I)$) and wR_2 was 0.4052 (all data).

5.4.3 ^1H NMR titration binding studies with TBACl

Proton NMR titration binding studies were performed on Bruker 400 MHz FT-NMR spectrometer at 298 K. Solution of receptors **5.1-5.4** in DMSO- d_6 /0.5% H₂O or acetonitrile were prepared in 2 mM and 1 mM concentrations, respectively. The guest anion, tetra-*n*-butylammonium (TBA) chloride, was prepared with the same receptor solution, to ensure the overall receptor concentration stays constant whilst the guest anion concentration changes. Using small aliquots of the guest salt, the receptor solution was titrated, and after each addition, chemical shifts were reported in ppm in reference to residual solvent peaks. The isotherm based on the NH and CH chemical shifts were globally fitted using the online fitting program Bindfit.⁵⁰

5.4.4 Anion transport studies:

5.4.4.1 Ion selective electrode (ISE) assays

a- Cl/NO₃ exchange assay:

Unilamellar vesicles were prepared as reported.⁵¹⁻⁵³ Briefly, ~ 30 mg of POPC (1-palmitoyl-2-oleoylphosphatidylcholine) was dissolved in 1 mL chloroform in a round-bottomed flask and the solvent was removed *in vacuo* to form a thin lipid layer. The thin film was dried under high vacuum for at least 6 h and suspended on the internal solution (4 mL) and vortexed using a lab dancer to form large multilamellar vesicles, which was subjected to nine freeze-thaw cycles alternating between water (at room temperature) and liquid nitrogen. Further, the formed lipid was left to rest for 30 minutes and then subjected to extrusion through a 200 nm polycarbonate membranes 25 times to form the unilamellar vesicles. The formed vesicles were subjected to dialysis for 4 h in the desired external solution to remove any unencapsulated internal salts. Finally, using the required external solution, the

lipid was diluted to 1.0 mM. The pH of the internal and external solutions was maintained at 7.2 using phosphate buffer with a 500 mM total ionic strength. Test compound in DMSO (40 μ L) was added to start the experiment and chloride selective electrode was used to monitor the chloride efflux. Detergent (50 μ L) was added after 300 seconds to lyse the vesicles, while the 100% chloride efflux reading was taken at 420 seconds.

- Hill plots for Cl/NO₃:

Hill plots were performed for Cl/NO₃ exchange assay by conducting transport assay at different concentrations of tested compounds. Receptor concentration vs chloride efflux at 270 s (the endpoint of transport assay) were plotted and fitted to the Hill equation using Origin 2019b:

$$y = V_{max} \frac{x^n}{k^n + x^n} = 100\% \frac{x^n}{(EC_{50})^n + x^n}$$

Where y is the chloride efflux at 270 s (%) and x is the tested compound concentration (mol% relative to lipid concentration)

V_{max} is the maximum efflux possible and considered as 100% as this is experimentally the maximum chloride efflux possible.

k (EC_{50} value) is the carrier concentration needed to reach $V_{max}/2$.

Each data point on each Hill plot are an average of at least two repeated runs. Error bars represent standard deviation about the mean.

Hill plots for receptors **5.1** and **5.5** were not performed due to low potency and solubility issues of ionophore **5.1** and **5.5**, respectively.

b- KCl efflux – cationohore coupling:

In this assay, 300 mM total ionic strength of both K gluconate external solution and KCl internal solution were maintained. The vesicles were made in a similar way to Cl/NO₃ exchange assay except that gel filtration, using sephadex, replaced dialysis to allow exchange of any unencapsulated KCl for KGlu. External KGlu solution (10 mL) was used to dilute the lipid solution obtained after sephadex to obtain a lipid stock of known concentration. A cationohore, monensin or Valinomycin, (10 µL, 0.5 mM) was added first to the lipid solution at concentration 0.1 mol% with respect to lipid concentration. Receptor was added after 30 seconds of the cationohore addition to start the experiment.

5.4.4.2 General preparation for HPTS assays:

Base-pulse 8-hydroxypyrene-1,3,6-trisulfonic acid trisodium salt (HPTS) assays were conducted using unilamellar 1-palmitoyl-2-oleoylphosphatidylcholine vesicles (POPC) with a mean diameter of 200 nm loaded with the pH sensitive fluorescence dye HPTS (1 mM).⁵¹⁻⁵³ A chloroform solution of POPC (~ 30 mg/mL) was evaporated under vacuum and dried for at least 6 h. The thin film was hydrated by the internal solution containing HPTS (1 mM) and was subjected to nine freeze-thaw cycles followed by extrusion 25 times through a 200 nm polycarbonate membrane. Size exclusion chromatography using sephadex G-25 column and HPTS-free external solution as an eluent was conducted to remove untrapped HPTS from the vesicles` solution. The internal and external solutions used were identical salt solution potassium gluconate (KGlu) or KCl (100 mM) buffered with 10 mM HEPES at pH 7.0. Finally, for each measurement, external solution (KCl or KGlu) was used to dilute the lipid stock to obtain 2.5 mL lipid suspension

containing 0.1 mM lipid. A base pulse of KOH (25 μ L, 0.5 M) at a final concentration of 5 mM was added to generate a transmembrane pH gradient. After the tested receptors were added, HPTS fluorescence ratio ($\lambda_{\text{ex}} = 460$ nm, $\lambda_{\text{em}} = 510$ nm divided by $\lambda_{\text{ex}} = 403$ nm, $\lambda_{\text{em}} = 510$ nm) was recorded. Assisting ionophore (carbonyl cyanide phenylhydrazone (CCCP) or valinomycin) was used as a 5 μ L DMSO. Bovine serum albumins (BSA) was added to vesicles at 1 mol% (with respect to lipid) and allowed to stir for 30 minutes to test if the transport is fatty acid independent, while, oleic acid (1 mol% and 10 mol%) was used as a source of fatty acid to test if the transport is fatty acid dependent. Detergent (25 μ L) was added at 200 seconds to destroy the pH gradient to calibrate the assay.

Results are the average of at least three repeats and the fractional fluorescence intensity (I_f) was determined using the following formula:

$$I_f = \frac{R_t - R_0}{R_d - R_0}$$

Where

- R_t is the fluorescence ratio at time t.
- R_0 is the fluorescence ratio at time 0
- R_d is the fluorescence ratio after detergent addition.

Hill plots were determined for KCl and KGlu transport assays by conducting transport assays at different tested receptors concentrations. Receptor concentration vs fractional fluorescence intensity I_f at 200 s (the endpoint of transport assay) were plotted and fitted to the Hill equation using Origin 2019b:

The following formula was used to calculate hill coefficients (n) and EC_{50} (200 s) values by fitting the curves to the following equation:

$$y = y_0 + (y_{max} - y_0) \frac{x^n}{k^n + x^n}$$

Where:

- y is I_f (200 s) value of the ionophore at concentration x (receptors concentration is expressed as ionophore to lipid molar ratio).
- y_0 is I_f value at 200 s, without addition of the ionophore.
- y_{max} is the maximum I_f value.
- n is the Hill coefficient, and K is the EC_{50} (200 s) value.

5.4.4.3 Chloride vs anions selectivity assay:

Unilamellar vesicles were prepared in a similar pattern to KCl-KOH assay as reported in section 5.4.4.2. Internal solution of each experiment contained KCl (100 mM) and HPTS (1 mM) while five external solutions were used at 100 mM with different salts KCl, KBr, KI, KNO₃ and KClO₄. Both external and internal solutions are buffered with HEPES (10 mM) to pH 7.0. HPTS is a pH responsive probe that has two wavelengths corresponding to the acidic and basic forms, 403 nm and 460, respectively. Fluorescence ratio between acidic and basic forms was measured for the five receptors against chloride/anion (X^-) selectivity. If the anion X^- is being transported into the vesicles, it would transport as HX and so lowered the pH inside the vesicles, resulting in a negative Normalized HPTS value. However, if the chloride is being transported out along with the proton gradient, so the pH inside the vesicles would be decreased, causing a positive Normalized HPTS value.

5.4.4.4 Calcein leakage assays:

A chloroform solution of POPC was evaporated under vacuum and dried for at least 6 h as reported.⁴³ The thin film was hydrated by the internal solution containing calcein disodium salt (100 mM) and NaCl (100 mM) buffered to pH 7.4 with HEPES (10 mM). Then, the lipid suspension was subjected to nine freeze-thaw cycles followed by extrusion 25 times through a 200 nm polycarbonate membrane. Size exclusion chromatography using sephadex G-25 column and calcein-free external solution, containing NaCl (100 mM) and Na₂SO₄ (100 mM) buffered to pH 7.4 with HEPES (10 mM).

The resulting suspension of dye-encapsulated LUVs with a mean diameter of 200 nm was diluted with the external solution to obtain 2.5 mL lipid suspension containing a 0.1 mM lipid concentration. After the tested receptors **5.1-5.5** were added at 1 mol%, calcein fluorescence ($\lambda_{\text{ex}} = 490$ nm, $\lambda_{\text{em}} = 520$ nm) was recorded at 25 °C. Detergent (25 μ L) was added at 200 seconds to lyse the vesicle and to calibrate the assay.

The fractional calcein release (FR) was calculated as follows (with I_t = fluorescence intensity at time t, I_0 = fluorescence intensity at time 0 and I_{max} = fluorescence intensity after addition of detergent):

$$FR = \frac{I_t - I_0}{I_{\text{max}} - I_0}$$

5.4.5 Reduction kinetic studies

Three reducing agents were used in the current study, namely: the tripeptide glutathione (GSH), dithiothreitol (DTT) and HCl of tris(2-carboxyethyl)phosphine

(TCEP). The reduction kinetic study of complexes **5.13**, **5.14**, **5.16** and **5.17** has been done in organic solvent (DMSO), in liposomes with external addition of the reducing agent and in GSH encapsulated liposomes and was monitored by UV-Vis and fluorescence spectroscopies. Absorbance studies UV-Vis spectra were recorded on an Agilent Cary 100 UV-Vis spectrophotometer, equipped with a temperature-controlled multicell holder and a temperature control unit. Fluorescence spectra were conducted on an Agilent Cary Eclipse fluorescence spectrophotometer, equipped with a temperature control unit and a magnetic stirrer. In the current study GSH was used in 6:1, relative to tested compound, while DTT and TCEP were used in 3:1, relative to tested compound.

Reactivity with different thiols was quantified by measuring the increase in fluorescence at 365 nm (285 nm excitation) for probe **5.2** and complexes **5.13** and **5.16** and at 400 nm (350 nm excitation) for probe **5.3** and complexes **5.14** and **5.17** over time and the increase in absorbance at 325 nm for all tested compounds over time. Receptors **5.2** and **5.3** and complexes **5.13**, **5.14**, **5.16** and **5.17** were dissolved in DMSO at room temperature to afford the probe concentration at 0.5 mM. GSH, DTT and TCEP stock solutions (3.0 mM, 1.5 mM, 1.5 mM, respectively) were freshly prepared in deionized water for the DMSO experiments and in the external solution for the experiments conducted in liposomes. Generally, 5 μ L (0.5 mM, final concentration = 1 μ M) of tested compounds were used in fluorescence experiments, while low absorbance was detected for this concentration in UV-Vis, loading volume of tested compounds was changed to 25 μ L (0.5 mM, final concentration = 5 μ M). The absorbance or the emission spectra at a certain wavelength (noted for each compound above) was plotted against the wavelength using OriginPro 9.1.

Reduction kinetics in DMSO:

UV-Vis: In a quartz cuvette and at 25 °C, tested compound (25 µL, 0.5 mM) was added to DMSO 2450 µL. The reducing agent (25 µL) GSH (3.0 mM), DTT (1.5 mM) or TCEP (1.5 mM) was added with stirred for 30 seconds. A baseline absorbance was measured on 2475 µL DMSO and 25 µL of the reducing agent, and spectra were collected at 1 minute intervals over a period of 15 minutes. After 15 minutes, there was no significant change in the absorbance intensity. Results are the average of at least two repeats.

Fluorescence: DMSO (2490 µL) and tested compound (5 µL) were added to a disposable cuvette with stirring and at 25 °C. Reducing agent (5 µL) GSH (3.0 mM), DTT (1.5 mM) or TCEP (1.5 mM) was added and stirred for 30 seconds and spectra was collected every minute for 30 minutes. Results are the average of at least three repeats.

Reduction kinetics in liposomes:

Unilamellar KCl (100 mM) vesicles, buffered with 10 mM HEPES at pH 7.0, were prepared as mentioned earlier in section S6.1, however, without addition of HPTS probes. The and UV-Vis and fluorescence properties of receptors **5.2** and **5.3** were exploited to monitor the reduction kinetics of complexes **5.13**, **5.14**, **5.16** and **5.17**. It was noted that both transporters **5.2** and **5.3** retained their UV-Vis properties and had the same λ_{max} as in organic solvent experiment (DMSO, S7.1). Transporter **5.2** retained its fluorescence nature in the KCl-liposomes, while transporter **5.3** fluorescence diminished, when it was added to liposomes. Thus reduction kinetics of complexes **5.13** and **5.16** was monitored by UV-Vis and fluorescence, while

reduction complexes **5.14** and **5.17** to the free anion transporter **5.3** could be only monitored by UV-Vis.

UV-Vis: In a quartz cuvette and at 25 °C, tested compound (25 µL, 0.5 mM) was added to 2450 µL of the liposomal suspension. The reducing agent (25 µL) GSH (3.0 mM), DTT (1.5 mM) or TCEP (1.5 mM) was added with stirred for 30 seconds. A baseline absorbance was measured on 2450 µL liposomal suspension 25 µL of reducing agent, and 25 µL DMSO. Spectra were collected at 5 minutes intervals over a period of 3-4 h. Results are the average of at least two repeats.

Fluorescence: Fluorescence spectra were recorded on excitation wavelength 285 nm and emission wavelengths 300-500 ($\lambda_{\text{ex}} = 285 \text{ nm}$, $\lambda_{\text{em}} = 300\text{-}500 \text{ nm}$). Liposomal suspension (2490 µL) and tested compound (5 µL) were added to a standard disposable cuvette with stirring and at 25 °C. Reducing agent (5 µL) GSH (3.0 mM), DTT (1.5 mM) or TCEP (1.5 mM) was added and stirred for 30 seconds and spectra was collected every minute for 1.5-3.0 h. Results are the average of at least three repeats.

Reduction kinetics in encapsulated GSH Liposomes:

Assuming the fraction of the interior volume of 200 nm unilammellar vesicles was 0.059%, two different 10 mM (final concentration in 2.5 mL = 6 µM) and 50 mM (final concentration in 2.5 mL = 30 µM) GSH encapsulated KCl liposomes, buffered with 10 mM HEPES at pH 7.0, were made. A chloroform solution of POPC (~ 30 mg/mL) was evaporated under vacuum and dried for at least 6 h. The thin film was hydrated by the internal solution containing GSH (10 mM or 50 mM)

and was subjected to nine freeze-thaw cycles followed by extrusion 25 times through a 200 nm polycarbonate membrane. Size exclusion chromatography using sephadex G-25 column and HPTS-free external solution as an eluent was conducted to remove untrapped GSH from the vesicles` solution.

The internal and external solutions used were KCl (100 mM) buffered with 10 mM HEPES at pH 7.0. Finally, for each measurement, external solution (KCl) was used to dilute the lipid stock to obtain 2.5 mL lipid suspension containing 0.1 mM lipid. A base pulse of KOH (25 μ L, 0.5 M) at a final concentration 5 mM was added to generate a transmembrane pH gradient. After the tested receptors were added, compound **5.2** fluorescence spectra of excitation = 285 nm and emission = 300-500 nm were recorded. Compound **5.3** and its complexes **5.14** and **5.17** were excluded as receptor **5.3** fluorescence properties diminished fluorescence in liposomal solution.

UV-Vis and fluorescence reduction kinetic experiments were used as in the previous section where 50 mM GSH encapsulated vesicles used in UV-Vis study and 10 mM GSH encapsulated vesicles used in fluorescence studies, corresponding to 1:6 compound:GSH in each case.

5.4.6 Transport studies upon reduction of complexes 5.13, 5.14 5.16 and 5.17

Base-pulse 8-hydroxypyrene-1,3,6-trisulfonic acid trisodium salt (HPTS) assays were conducted using unilamellar 1-palmitoyl-2-oleoylphosphatidylcholine vesicles (POPC) with a mean diameter of 200 nm loaded with the pH sensitive fluorescence dye HPTS (1 mM).⁵¹⁻⁵³ A chloroform solution of POPC (~ 30 mg/mL) was evaporated under vacuum and dried for at least 6 h. The thin film was hydrated

by the internal solution containing HPTS (1 mM) and was subjected to nine freeze-thaw cycles followed by extrusion 25 times through a 200 nm polycarbonate membrane. Size exclusion chromatography using sephadex G-25 column and HPTS-free external solution as an eluent was conducted to remove untrapped HPTS from the vesicles' solution. The internal and external solutions used were identical salt solution potassium gluconate (KGlu) or KCl (100 mM) buffered with 10 mM HEPES at pH 7.0. Finally, for each measurement, external solution (KCl or KGlu) was used to dilute the lipid stock to obtain 2 mL lipid suspension containing 0.1 mM lipid. A base pulse of KOH (25 μ L, 0.5 M) at a final concentration 5 mM was added to generate a transmembrane pH gradient. After the tested receptors were added, HPTS fluorescence ratio ($\lambda_{\text{ex}} = 460$ nm, $\lambda_{\text{em}} = 510$ nm divided by $\lambda_{\text{ex}} = 403$ nm, $\lambda_{\text{em}} = 510$ nm) was recorded. Assisting ionophore (carbonyl cyanide phenylhydrazone (CCCP) or valinomycin) was used as a 5 μ L DMSO. Bovine serum albumins (BSA) was added to vesicles at 1 mol% (with respect to lipid) and allowed to stir for 30 minutes to test if the transport is fatty acid independent, while, oleic acid (1 mol% and 10 mol%) was used as a source of fatty acid to test if the transport is fatty acid dependent. Detergent (25 μ L) was added at 200 seconds to destroy the pH gradient to calibrate the assay.

5.5 References:

1. Hennig, A.; Gabriel, G. J.; Tew, G. N.; Matile, S. Stimuli-responsive polyguanidino-oxanorbornene membrane transporters as multicomponent sensors in complex matrices. *J. Am. Chem. Soc.* **2008**, 130, 10338-10344.
2. Vlatkovic, M.; Collins, B. S.; Feringa, B. L. Dynamic responsive systems for catalytic function. *Chemistry* **2016**, 22, 17080-17111.
3. Zhou, R.; Zhu, S.; Gong, L.; Fu, Y.; Gu, Z.; Zhao, Y. Recent advances of stimuli-responsive systems based on transition metal dichalcogenides for smart cancer therapy. *J. Mater. Chem. B* **2019**, 7, 2588-2607.
4. Wezenberg, S. J.; Feringa, B. L. Supramolecularly directed rotary motion in a photoresponsive receptor. *Nat. commun.* **2018**, 9, 1-7.
5. Rao, N. V.; Ko, H.; Lee, J.; Park, J. H. Recent progress and advances in stimuli-responsive polymers for cancer therapy. *Front. Bioeng. Biotechnol.* **2018**, 6, 1-15.

6. Lee, S.; Flood, A. H. Photoresponsive receptors for binding and releasing anions. *J. Phys. Org. Chem.* **2013**, *26*, 79-86.
7. Howe, E. N.; Busschaert, N.; Wu, X.; Berry, S. N.; Ho, J.; Light, M. E.; Czech, D. D.; Klein, H. A.; Kitchen, J. A.; Gale, P. A. Ph-regulated nonelectrogenic anion transport by phenylthiosemicarbazones. *J. Am. Chem. Soc.* **2016**, *138*, 8301-8308.
8. Vlatkovic, M.; Feringa, B. L.; Wezenberg, S. J. Dynamic inversion of stereoselective phosphate binding to a bisurea receptor controlled by light and heat. *Angew. Chem. Int. Ed. Engl.* **2016**, *55*, 1001-1004.
9. McNaughton, D. A.; Fu, X.; Lewis, W.; D'Alessandro, D. M.; Gale, P. A. Hydroquinone-based anion receptors for redox-switchable chloride binding. *Chemistry* **2019**, *1*, 80-88.
10. Saha, A.; Akhtar, N.; Kumar, V.; Kumar, S.; Srivastava, H. K.; Kumar, S.; Manna, D. Ph-regulated anion transport activities of bis(iminourea) derivatives across the cell and vesicle membrane. *Org. Biomol. Chem.* **2019**, *17*, 5779-5788.
11. Evans, N. H.; Beer, P. D. Advances in anion supramolecular chemistry: From recognition to chemical applications. *Angew. Chem. Int. Ed. Engl.* **2014**, *53*, 11716-11754.
12. Busschaert, N.; Caltagirone, C.; Van Rossom, W.; Gale, P. A. Applications of supramolecular anion recognition. *Chem. Rev.* **2015**, *115*, 8038-8155.
13. Busschaert, N.; Park, S. H.; Baek, K. H.; Choi, Y. P.; Park, J.; Howe, E. N. W.; Hiscock, J. R.; Karagiannidis, L. E.; Marques, I.; Felix, V.; Namkung, W.; Sessler, J. L.; Gale, P. A.; Shin, I. A synthetic ion transporter that disrupts autophagy and induces apoptosis by perturbing cellular chloride concentrations. *Nat. Chem.* **2017**, *9*, 667-675.
14. Gadsby, D. C. Ion channels versus ion pumps: The principal difference, in principle. *Nat. Rev. Mol. Cell. Biol.* **2009**, *10*, 344-352.
15. Ashcroft, F. M. *Ion channels and disease*. Academic press: Massachusetts, United States, 1999.
16. Li, H.; Valkenier, H.; Judd, L. W.; Brotherhood, P. R.; Hussain, S.; Cooper, J. A.; Jurcek, O.; Sparkes, H. A.; Sheppard, D. N.; Davis, A. P. Efficient, non-toxic anion transport by synthetic carriers in cells and epithelia. *Nat. Chem.* **2016**, *8*, 24-32.
17. Verkman, A. S.; Galletta, L. J. Chloride channels as drug targets. *Nat. Rev. Drug Discov.* **2009**, *8*, 153-171.
18. Van Rossom, W.; Asby, D. J.; Tavassoli, A.; Gale, P. A. Perenosins: A new class of anion transporter with anti-cancer activity. *Org. Biomol. Chem.* **2016**, *14*, 2645-2650.
19. Rodilla, A. M.; Korrodi-Gregorio, L.; Hernando, E.; Manuel-Manresa, P.; Quesada, R.; Perez-Tomas, R.; Soto-Cerrato, V. Synthetic tambjamine analogues induce mitochondrial swelling and lysosomal dysfunction leading to autophagy blockade and necrotic cell death in lung cancer. *Biochem. Pharmacol.* **2017**, *126*, 23-33.
20. Soto-Cerrato, V.; Manuel-Manresa, P.; Hernando, E.; Calabuig-Farinas, S.; Martinez-Romero, A.; Fernandez-Duenas, V.; Sahlholm, K.; Knopfel, T.; Garcia-Valverde, M.; Rodilla, A. M.; Jantus-Lewintre, E.; Farras, R.; Ciruela, F.; Perez-Tomas, R.; Quesada, R. Facilitated anion transport induces hyperpolarization of the cell membrane that triggers differentiation and cell death in cancer stem cells. *J. Am. Chem. Soc.* **2015**, *137*, 15892-15898.
21. Park, S.-H.; Park, S.-H.; Howe, E. N.; Hyun, J. Y.; Chen, L.-J.; Hwang, I.; Vargas-Zuñiga, G.; Busschaert, N.; Gale, P. A.; Sessler, J. L. Determinants of ion-transporter cancer cell death. *Chem* **2019**, *5*, 2079-2098.
22. Forman, H. J.; Zhang, H.; Rinna, A. Glutathione: Overview of its protective roles, measurement, and biosynthesis. *Mol. Asp. Med.* **2009**, *30*, 1-12.
23. Wu, G.; Fang, Y. Z.; Yang, S.; Lupton, J. R.; Turner, N. D. Glutathione metabolism and its implications for health. *J. Nutr.* **2004**, *134*, 489-492.
24. Hegedus, C.; Kovacs, K.; Polgar, Z.; Regdon, Z.; Szabo, E.; Robaszkiewicz, A.; Forman, H. J.; Martner, A.; Virag, L. Redox control of cancer cell destruction. *Redox Biol.* **2018**, *16*, 59-74.
25. Mura, S.; Nicolas, J.; Couvreur, P. Stimuli-responsive nanocarriers for drug delivery. *Nature Mater.* **2013**, *12*, 991-1003.
26. Meng, F.; Hennink, W. E.; Zhong, Z. Reduction-sensitive polymers and bioconjugates for biomedical applications. *Biomaterials* **2009**, *30*, 2180-2198.
27. Li, R.; Xie, Y. Nanodrug delivery systems for targeting the endogenous tumor microenvironment and simultaneously overcoming multidrug resistance properties. *J. Control. Release* **2017**, *251*, 49-67.
28. Chan, N.; Khorsand, B.; Aleksanian, S.; Oh, J. K. A dual location stimuli-responsive degradation strategy of block copolymer nanocarriers for accelerated release. *Chem. Commun.* **2013**, *49*, 7534-7536.

29. Jia, L.; Cui, D.; Bignon, J.; Di Cicco, A.; Wdzieczak-Bakala, J.; Liu, J.; Li, M. H. Reduction-responsive cholesterol-based block copolymer vesicles for drug delivery. *Biomacromolecules* **2014**, *15*, 2206-2217.
30. Li, Y.; Wu, Y.; Chen, J.; Wan, J.; Xiao, C.; Guan, J.; Song, X.; Li, S.; Zhang, M.; Cui, H. A simple glutathione-responsive turn-on theranostic nanoparticle for dual-modal imaging and chemo-photothermal combination therapy. *Nano Lett.* **2019**, *19*, 5806-5817.
31. Sharma, A.; Lee, M.-G.; Won, M.; Koo, S.; Arambula, J. F.; Sessler, J. L.; Chi, S.-G.; Kim, J. S. Targeting heterogeneous tumors using a multifunctional molecular prodrug. *J. Am. Chem. Soc.* **2019**, *141*, 15611-15618.
32. Hickey, J. L.; Ruhayel, R. A.; Barnard, P. J.; Baker, M. V.; Berners-Price, S. J.; Filipovska, A. Mitochondria-targeted chemotherapeutics: The rational design of gold(I) *N*-heterocyclic carbene complexes that are selectively toxic to cancer cells and target protein selenols in preference to thiols. *J. Am. Chem. Soc.* **2008**, *130*, 12570-12571.
33. Akhtar, N.; Pradhan, N.; Saha, A.; Kumar, V.; Biswas, O.; Dey, S.; Shah, M.; Kumar, S.; Manna, D. Tuning the solubility of the ionophores: Glutathione-mediated transport of chloride ion across the membranes. *Chem. Commun.* **2019**, *55*, 8482-8485.
34. Gao, L.; Kim, K. J.; Yankaskas, J. R.; Forman, H. J. Abnormal glutathione transport in cystic fibrosis airway epithelia. *Am. J. Physiol.* **1999**, *277*, L113-118.
35. Montoya, C.; Cervantes, R.; Tiburcio, J. Neutral bis(benzimidazole) λ -shaped anion receptor. *Tetrahedron Lett.* **2015**, *56*, 6177-6182.
36. Peng, C. C.; Zhang, M. J.; Sun, X. X.; Cai, X. J.; Chen, Y.; Chen, W. H. Highly efficient anion transport mediated by 1,3-bis(benzimidazol-2-yl)benzene derivatives bearing electron-withdrawing substituents. *Org. Biomol. Chem.* **2016**, *14*, 8232-8236.
37. Yu, X. H.; Hong, X. Q.; Chen, W. H. Fluorinated bisbenzimidazoles: A new class of drug-like anion transporters with chloride-mediated, cell apoptosis-inducing activity. *Org. Biomol. Chem.* **2019**, *17*, 1558-1571.
38. Zou, T.; Lum, C. T.; Chui, S. S.; Che, C. M. Gold(III) complexes containing *n*-heterocyclic carbene ligands: Thiol "switch-on" fluorescent probes and anti-cancer agents. *Angew. Chem. Int. Ed. Engl.* **2013**, *52*, 2930-2933.
39. Addison, A. W.; Burke, P. J. Synthesis of some imidazole- and pyrazole-derived chelating agents. *J. Heterocycl. Chem.* **1981**, *18*, 803-805.
40. Li, G.; Huang, J.; Zhang, M.; Zhou, Y.; Zhang, D.; Wu, Z.; Wang, S.; Weng, X.; Zhou, X.; Yang, G. Bis(benzimidazole)pyridine derivative as a new class of g-quadruplex inducing and stabilizing ligand. *Chem. Commun.* **2008**, 4564-4566.
41. Goeker, H.; Alp, M.; Ateş-Alagöz, Z.; Yıldız, S. Synthesis and potent antifungal activity against candida species of some novel 1*h*-benzimidazoles. *J. Heterocycl. Chem.* **2009**, *46*, 936-948.
42. Wu, X.; Howe, E. N. W.; Gale, P. A. Supramolecular transmembrane anion transport: New assays and insights. *Acc. Chem. Res.* **2018**, *51*, 1870-1879.
43. Howe, E. N. W.; Gale, P. A. Fatty acid fueled transmembrane chloride transport. *J. Am. Chem. Soc.* **2019**, *141*, 10654-10660.
44. Milano, D.; Benedetti, B.; Boccalon, M.; Brugnara, A.; Iengo, E.; Tecilla, P. Anion transport across phospholipid membranes mediated by a diphosphine-pd(II) complex. *Chem. Commun.* **2014**, *50*, 9157-9160.
45. Parnham, E. R.; Morris, R. E. 1-alkyl-3-methyl imidazolium bromide ionic liquids in the ionothermal synthesis of aluminium phosphate molecular sieves. *Chem. Mater.* **2006**, *18*, 4882-4887.
46. Wang, H. M.; Chen, C. Y.; Lin, I. J. Synthesis, structure, and spectroscopic properties of gold (I)-carbene complexes. *Organometallics* **1999**, *18*, 1216-1223.
47. Bourhis, L. J.; Dolomanov, O. V.; Gildea, R. J.; Howard, J. A.; Puschmann, H. The anatomy of a comprehensive constrained, restrained refinement program for the modern computing environment—olex2 dissected. *Acta Crystallogr. Sect. A: Found. Adv.* **2015**, *71*, 59-75.
48. Dolomanov, O. V.; Bourhis, L. J.; Gildea, R. J.; Howard, J. A.; Puschmann, H. Olex2: A complete structure solution, refinement and analysis program. *J. Appl. Crystallogr.* **2009**, *42*, 339-341.
49. Sheldrick, G. M. A short history of shelx. *Acta Crystallogr. Sect. A: Found. Crystallogr.* **2008**, *64*, 112-122.
50. Wu, X.; Wang, P.; Turner, P.; Lewis, W.; Catal, O.; Thomas, D. S.; Gale, P. A. Tetraurea macrocycles: Aggregation-driven binding of chloride in aqueous solutions. *Chem* **2019**, *5*, 1210-1222.
51. Berry, S. N.; Soto-Cerrato, V.; Howe, E. N.; Clarke, H. J.; Mistry, I.; Tavassoli, A.;

Chang, Y.-T.; Pérez-Tomás, R.; Gale, P. A. Fluorescent transmembrane anion transporters: Shedding light on anionophoric activity in cells. *Chem. Sci.* **2016**, *7*, 5069-5077.

52. Jowett, L. A.; Howe, E. N.; Wu, X.; Busschaert, N.; Gale, P. A. New insights into the anion transport selectivity and mechanism of tren-based tris-(thio)ureas. *Chem. Eur. J.* **2018**, *24*, 10475-10487.

53. Wu, X.; Judd, L. W.; Howe, E. N.; Withecombe, A. M.; Soto-Cerrato, V.; Li, H.; Busschaert, N.; Valkenier, H.; Pérez-Tomás, R.; Sheppard, D. N. Nonprotonophoric electrogenic Cl⁻ transport mediated by valinomycin-like carriers. *Chem* **2016**, *1*, 127-146.

Chapter 7:

Carbonic anhydrase inhibitors

FOREWORD TO CHAPTER 7

This chapter is accepted in the *J Med Chem* (doi: 10.1021/acs.jmedchem.9b02090, impact factor 6.054). This paper describes the design and synthesis of three dual-tailed sulfonamide series as potent carbonic anhydrase inhibitors. All compounds were evaluated for inhibitory action against pharmacologically relevant human (h) CAs isoforms I, II, IV, and VII and showed a significant selectivity to CA II, which is implicated in glaucoma. X-ray crystallographic analysis of three compounds bound to CA II showed the validity of the adopted drug design strategy as specific moieties within in the ligand structure interacted directly with the hydrophobic and hydrophilic halves of the CA II active site. Four compounds were evaluated for their intraocular pressure (IOP) lowering effects in a rabbit model of the glaucoma and two of them showed significant efficacy when compared to the clinically used drug dorzolamide. Supporting information to this chapter can be found in Appendix F (p. 343).

Contributions

Mohamed Fares	Compound design, performed the work and analysis, input into experimental design and prepared/edited the paper
Wagdy M. Eldehna	Compound design and proof reading
Hatem A. Abdel-Aziz	
Thomas S. Peat	Performed and solved the protein X-ray crystallization
Alessio Nocentini	Performed the <i>in vitro</i> enzyme assay.
Silvia Bua	
Cecilia Lanzi,	Performed the <i>in vivo</i> study
Laura Lucarini	
Emanuela Masini	
Claudiu T. Supuran	Oversight of the project prepared/edited the paper
Paul A. Keller	Oversight of the project, editing and proof-reading

7.1 Introduction

Glaucoma is an optic neuropathy disease that affects more than 64 million people worldwide and is implicated with 5 million instances of blindness which accounts for 12% of blindness, globally.^{1, 2} Despite profound advances in the area, the understanding of the primary causes of glaucoma is still not complete.¹ Glaucoma is categorized into two major classes according to the anatomic configuration of the aqueous humor, namely open angle glaucoma (OAG), which is prevalent in Europe and Africa and angle-closure glaucoma (CAG), which mainly affects Asian countries.² Risk factors of OAG are age-related and are associated with high intra ocular pressure (IOP) and thin central cornea.³

Current approaches used in the clinic to manage OAG mainly include IOP lowering drugs and surgery. There are fundamentally five drug classes used to lower IOP, namely, carbonic anhydrase inhibitors, cholinomimetics, sympathomimetic, β -blockers and prostaglandin analogues.⁴ Limitations in determining IOP reduction *in vitro* make common drug discovery approaches such as cell-based assay or high throughput screening not useful to assess the drop in IOP.¹ Whilst some promising candidates are under clinical trials as anti-glaucoma agents, the development of new, safe and effective glaucoma drugs is in high demand.¹

Carbonic anhydrases (CA, EC 4.2.1.1) constitute a superfamily of ubiquitous metalloenzymes which principally act as catalysts in the CO₂ hydration reaction. The 15 isoforms identified in human belong to the α -class of the 8 genetically diverse families of CA discovered to date (α -, β -, γ -, δ -, ζ -, η -, θ - and ι -CAs). These 15 isozymes differ in multiple factors including catalytic activity, structural fold,

tissue and subcellular localization and response to different kinds of modulators.⁵⁻

¹⁰ Abnormal expression of hCAs isoforms such as II and IV were detected in glaucoma.^{7, 10, 11}

Great effort has been made in the design and synthesis of selective CA inhibitors (CAI) with anti-glaucoma activity. Primary sulfonamides such as acetazolamide (**7.1, AAZ**) (Figure 7.1) have been clinically used for almost 70 years as systemic anti-glaucoma agents despite a range of side effects due to the lack of enzymatic selectivity.⁹ The second generation antiglaucoma drugs, such as dorzolamide (**7.2, DRZ**) and brinzolamide (**7.1, BRZ**) (Figure 7.1), act topically thus leading to a significant side effects reduction.¹² They contain an amino group which can be converted to a HCl salt, conferring better water solubility.

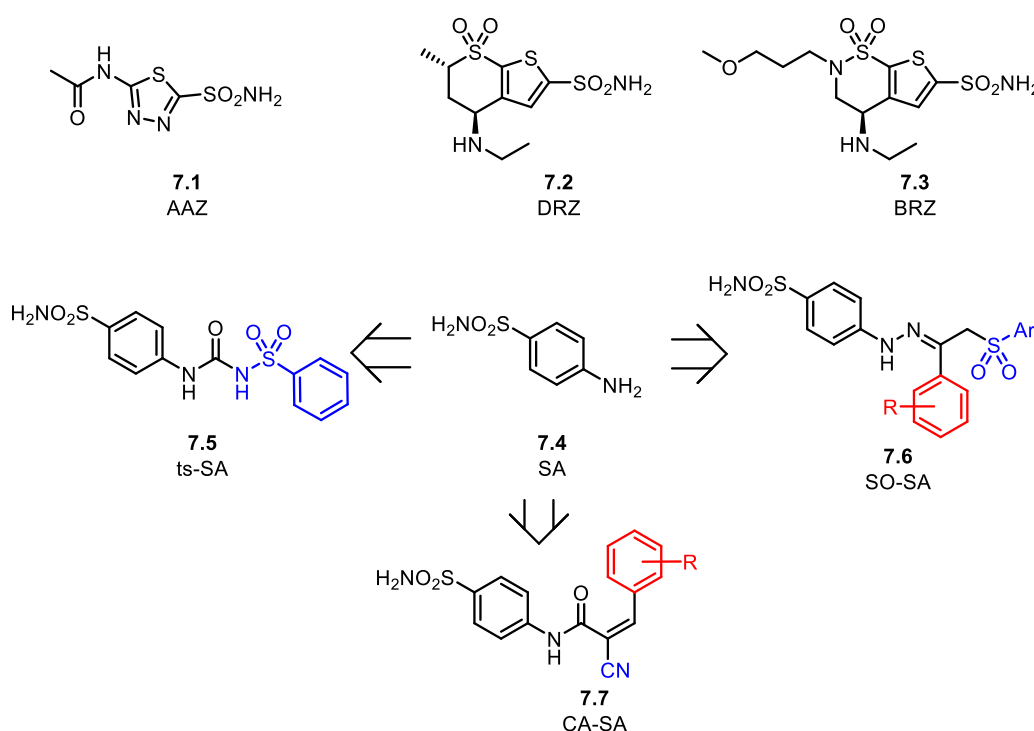


Figure 7.1: Structures of clinically used CAIs and other inhibitors derived from sulfanilamide (SA).

The design and development of selective CAI is challenging. Many strategies have been adopted including the widely used ring and tail approaches.¹²⁻¹⁴ CA inhibitors such as **AAZ (7.1)**, **DRZ (7.2)** and **BRZ (7.3)** are examples of the ring approach, in which a primary sulfonamide group is attached to varied types of main aromatic rings (Figure 7.1).¹² In the tail approach, a variety of molecular tails are attached to the scaffold bearing the zinc binding group to confer better physicochemical properties, such as increased water solubility, or to tune the inhibition profiles against the target CAs by interaction with the most diverse section of the CA active site, the medium-outer portion.¹⁶⁻¹⁹ Sulfanilamide (**7.4**, Figure 7.1), clinically used as an antibacterial, has been the lead CA inhibitor in many drug-design strategies whereby a variety of tail functionalities were used, such as tosylureido (**ts-SA, 7.5**), cyanoamide (**CA-SA, 7.7**), or dual-tailed arylsulfone (**SO-SA, 7.6**) (Figure 7.1).^{15,16}

7.2 Results and discussion

7.2.1 Drug design and chemistry

In the current study, a new class of 3-oxo-*N*-(4-sulfamoylphenyl)butanamides was proposed based on the dual tail approach (Figure 7.2). Considering the benzenesulfonamide as zinc-binding motif (orange in Figure 7.2), aryl groups were included in the derivatives tails to interact with the CA hydrophobic region (red in Figure 7.2), whereas H-bonds acceptor moieties were included for the interactions with Gln and Asn residues present in the hydrophilic half of the active site (blue in Figure 7.2).

The synthesized compounds were thus investigated for their inhibitory effect against the cytosolic isoforms hCA I, II and VII and the transmembrane hCA IV. The best inhibitors in terms of potency and selectivity against the CAs implicated

in glaucoma were assessed *in vivo* for their IOP lowering action using **DRZ** as a standard. Evidence for the mode of binding of these dual tailed sulfonamides to hCA II was achieved at the molecular level by X-ray crystallographic analysis with three of the most potent CA II inhibitors.

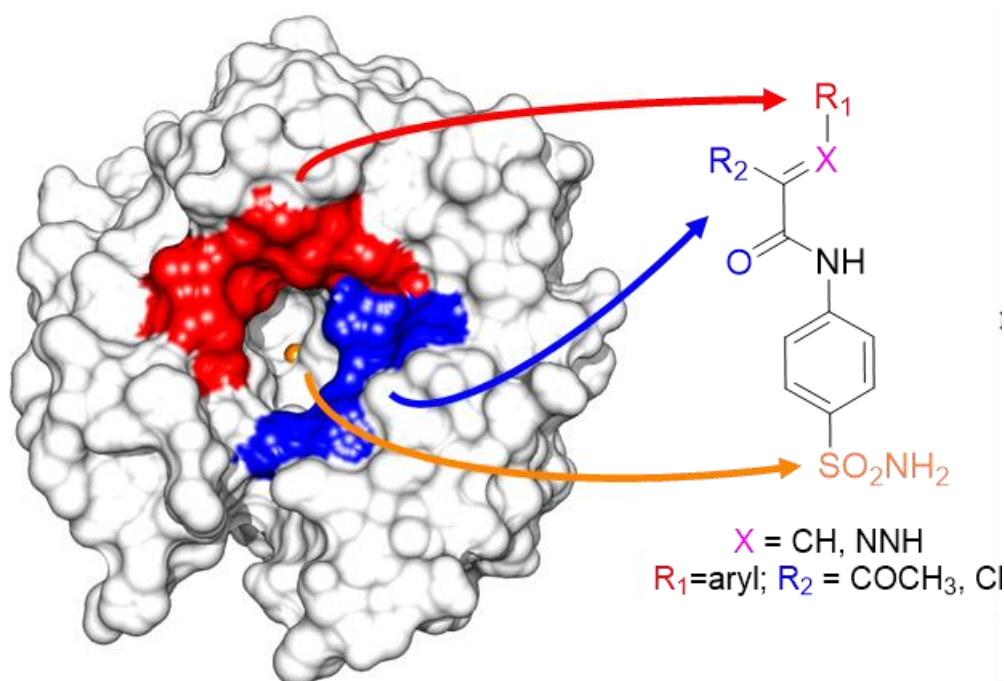
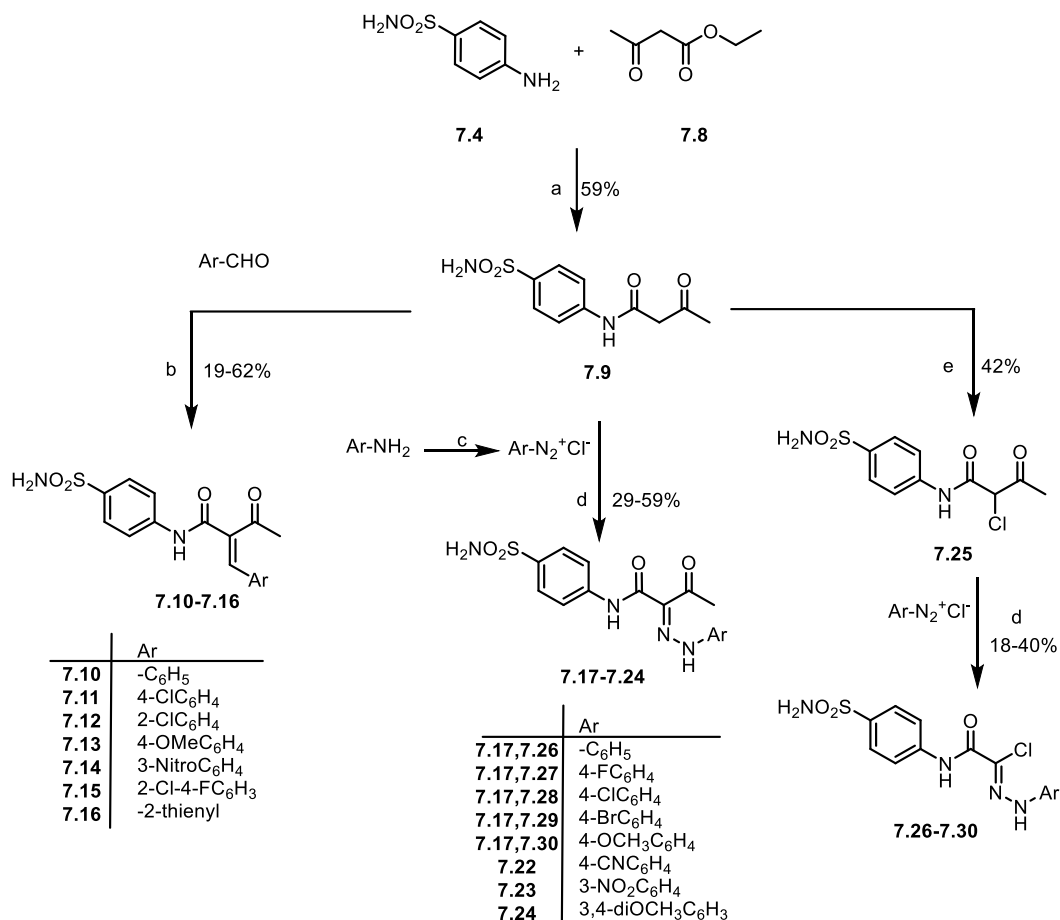


Figure 7.2: Design of dual-tailed sulfonamides targeting hCAs. The molecular surface of hydrophobic and hydrophilic halves of the CA active site are coloured in red and blue, respectively. The Zn(II) ion is represented as an orange sphere (pdb 1CA2).

The key intermediate **7.9** was synthesized by reacting sulfanilamide **7.4** with ethyl acetoacetate **7.8** (Scheme 7.1).¹⁷ Knoevenagel condensation of acetoacetanilide **7.9** with the aldehydes in the presence of catalytic piperidine and acetic acid afforded **7.10-7.16** derivatives in yields of 30-62% (Scheme 7.1).



Scheme 7.1: Reagents and conditions: a) neat reaction, reflux, 15 min; b) MS 4 Å, piperidine, acetic acid, ethanol, RT, 8 h; c) NaNO₂/HCl, 0 °C; d) sodium acetate trihydrate, ethanol, 0 °C; e) SO₂Cl₂, 0 °C, 1 h then RT for 4 h.

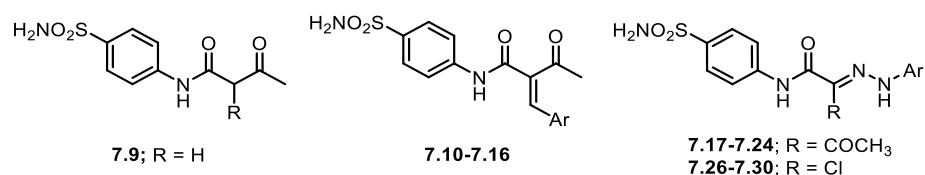
In a typical example, analysis of the ¹H NMR and ¹³C NMR spectra of **7.13** revealed the disappearance of the resonances at 3.60 ppm and 52.8 ppm, respectively, assigned to the methylene group in **7.9**, indicating the formation of arylidene **7.13**. The ¹H NMR spectrum showed two singlets at 2.37 and 3.70 ppm, assigned to CH₃ and OCH₃, respectively. The arylidene H was assigned to the singlet at δ 7.61. The protons *ortho* to the methoxy group in the aryl substituent were assigned the resonance at 6.83 ppm, while the protons *meta* to the methoxy group were assigned to the resonance at 7.49 ppm. The *p*-sulfamoyl aryl substituents were assigned to the two doublets at 7.70 ppm (*meta* to the sulfamoyl group) and 7.77 ppm (*ortho* to

the sulfamoyl group). The halogenated derivative **7.25** was synthesized by chlorination of the key intermediate **7.9** using sulfuryl chloride (Scheme 7.1).¹⁸ Access to derivatives of the type **7.17-7.24** and **7.26-7.30** was accomplished via classic Japp-Klingemann coupling reaction of 3-oxo-*N*-(4-sulfamoylphenyl)butanamide **7.9** and 2-chloro-3-oxo-*N*-(4-sulfamoylphenyl)butanamide **7.25**, respectively with diazonium salts in the presence of sodium acetate trihydrate and ethanol (Scheme 7.1).¹⁹ Analysis of the ¹H NMR spectra of **7.17-7.24** and **7.26-7.30** showed the disappearance of the resonances at ~3.60 and 5.42 ppm assigned to the methylene and methane in **7.9**, respectively. It should be mentioned that derivatives **7.26-7.30** may react non-specifically with nucleophiles present in biomolecules due to the presence of an activated chlorine atom, although we did not see this behavior with CAs.

7.2.2 Carbonic anhydrase inhibition

Compounds **7.9**, **7.10-7.16**, **7.17-7.24** and **7.26-7.30** were evaluated for their inhibition against the cytosolic CA I, II and VII and the membrane-bound CA IV using a stopped-flow CO₂ hydrase assay method.²⁰ The clinically used acetazolamide (**7.1**, **AAZ**) was used as the standard in the kinetic evaluation.

The ubiquitous CA I was inhibited efficiently by compounds **7.9** and **7.10-7.16** with inhibition constants (K_i values) spanning a narrow range between 7.3 and 75.5 nM with the 2-chlorophenyl derivative **7.12** showing the best activity with a K_i value of 7.3 nM against CA I. An inhibition decline was observed for compounds of subset **7.17-7.24** and **7.26-7.30**, with the exception of **7.17**, **7.24**, **7.28** and **7.30** whose K_i values spanned the range 44.1-86.1 nM (Table 7.1).

Table 7.1: Inhibition data of compounds **7.9**, **7.10-7.16**, **7.17-7.24** and **7.26-7.30** against isoforms hCA I, II, IV and VII by a stopped-flow CO₂ hydrase assay.²⁰

Cmp	R	Ar	K_i (nM) ^a			
			CA I	CA II	CA IV	CA VII
7.9	H	-	69.2±5.5	39.5±1.7	885.3±41	273.1±15
7.10	-	C ₆ H ₅	68.7±3.9	4.4±0.16	957.5±53	44.4±1.9
7.11	-	4-ClC ₆ H ₄	41.1±1.8	0.61±0.02	145.0±7.0	4.3±0.14
7.12	-	2-ClC ₆ H ₄	7.3±0.61	0.36±0.03	382.8±19	2.9±0.09
7.13	-	4-OCH ₃ C ₆ H ₄	15.3±1.2	0.45±0.02	608.5±26	3.1±0.12
7.14	-	3-NO ₂ C ₆ H ₄	75.5±5.0	6.9±0.11	387.0±24	46.3±3.0
7.15	-	2-Cl-4-F-C ₆ H ₄	52.7±3.9	5.6±0.25	222.5±15	23.5±1.6
7.16	-	2-thienyl	49.1±4.8	2.9±0.10	810.4±63	5.3±0.24
7.17	COCH ₃	C ₆ H ₅	82.2±6.4	4.3±.31	>10000	647.0±33
7.18	COCH ₃	4-FC ₆ H ₄	2669±231	8.1±0.65	>10000	3323±159
7.19	COCH ₃	4-ClC ₆ H ₄	2642±114	5.2±0.20	>10000	1690±73
7.20	COCH ₃	4-BrC ₆ H ₄	>10000	370.5±16	>10000	>10000
7.21	COCH ₃	4-CNC ₆ H ₄	512.9±38	52.2±1.4	>10000	761.5±54
7.22	COCH ₃	4-OCH ₃ C ₆ H ₄	703.7±49	273.1±13	>10000	3589.4±23
7.23	COCH ₃	3-NO ₂ C ₆ H ₄	750.6±62	71.4±3.9	>10000	792.4±55
7.24	COCH ₃	3,4-diOCH ₃ C ₆ H ₃	59.3±2.8	5.0±0.14	1477±96	4.4±0.31
7.26	Cl	C ₆ H ₅	227.1±11.6	40.6±2.1	7364±124	68.1±4.5
7.27	Cl	4-FC ₆ H ₄	295.6±14.5	34.8±1.1	7380±210	46.6±3.0
7.28	Cl	4-ClC ₆ H ₄	44.1±2.3	3.0±0.24	906.5±64	6.1±0.52
7.29	Cl	4-BrC ₆ H ₄	925.7±57	262.1±17	>10000	1034.1±76
7.30	Cl	4-OCH ₃ C ₆ H ₃	86.1±3.3	21.1±0.93	6415.6±320	55.2±3.1
AAZ	-	-	250±13	25.0±1.1	74.0±4.1	2.5±0.14
DRZ	-	-	>50000	9±0.51	8500±245	3.5±0.13
BRZ	-	-	730±24	3±0.12	3950±341	2.8±0.11

^a Mean ± SD, from three replicates, by a stopped flow technique.

In contrast, the other derivatives of the two subsets showed inhibition of CA I in the high nanomolar to low micromolar range (227.1-2669 nM) up to no inhibition observed below 10 μM for **7.20**. Thus, incorporation of halo-substituted phenyl moieties in the scaffolds **7.17-7.24** and **7.26-7.30** produced a detrimental effect on the inhibition of CA I.

The target CA II was potently inhibited by compounds **7.10-7.16** with low to subnanomolar K_i values (0.36-6.9 nM) whereas **7.9** showed a K_i of 39.5 nM. Of note is the subnanomolar CA II inhibition by **7.11-7.13**, significantly lower than that of **AAZ (7.1)**, which endow them with significant potential for the treatment of a wealth of diseases implicating CA II abnormal levels or activities. More complex SAR were instead produced with the inhibition data against CA II of compounds from subsets **7.17-7.24** and **7.26-7.30**. While the absence of, or presence of specific substituents certain substituents (*e.g.* *o*-chloro, *p*-chloro or *p*-methoxy) on the outer phenyl ring enabled the compounds to hold a low nanomolar efficacy (K_i values in the range 3.0-8.1 nM for **7.17-7.19**, **7.24** and **7.28**), some others led to a drop of inhibition effectiveness culminating with K_i values of 370.5 and 262.1 nM arising from the incorporation of a *para*-bromo substituent in the **7.17-7.24** and **7.26-7.30** scaffolds.

The membrane bound CA IV was the least inhibited isoform here screened by compounds **7.9**, **7.10-7.16**, **7.17-7.24** and **7.26-7.30**. Whereas compounds **7.9** and **7.10-7.16** retained a submicromolar inhibition with K_i values spanning 145.0 - 885.3 nM, derivatives from subsets **7.17-7.24** and **7.26-7.30** reported some micromolar K_i values against CA IV (0.91-7.38 μ M), but mostly did not produced inhibition below 10 μ M (**7.17-7.22**, **7.29**).

The cytosolic isoform CA VII, generally defined as a brain-associated isozyme, was efficiently inhibited by compounds **7.10-7.16**, though by an order of magnitude lower than CA II with K_i values spanning 2.9 - 46.6 nM, with **7.11-7.13** being again the most potent inhibitors (K_i values of 4.3, 2.9 and 3.1 nM, respectively). Again, a drop-in inhibition was observed with compounds from subset **7.17-7.24**, where K_i values were in the range 647.0 - >10000 nM, with the exception of the 3,4-

dimethoxyphenyl derivative **7.24**, which held 4.4 nM K_i . In contrast, most compounds bearing a chloro substituent in place of the acetyl group from subset **7.26-7.30** showed an effective CA VII inhibition in the range 6.1-68.1 nM, except **7.29**, the *p*-Br-phenyl derivative, that displayed a K_i of 1034.1 nM.

7.2.3 Protein X-ray crystallography

To gain insights into the ligand-target interactions driving such intense hCA II inhibition, the X-ray co-crystallographic analysis of the adducts of hCA II with **7.10**, **7.13** and **7.16** was achieved at resolutions of 1.67, 1.32 and 1.48 Å, respectively (Figure 7.3). The sulfonamide coordination to the Zn(II) is present in all adducts, as well as the two H-bond networks involving the SO₂NH⁻ group and Thr199. The phenyl ring bearing the sulfonamide moiety of **7.11**, **7.13** and **7.16** forms hydrophobic interactions with Val121, Val143 and Leu198. As originally designed, the carbonyl group of the amide and acetyl moieties are oriented towards the hydrophilic half of the hCA II active site where they establish H-bond networks. In detail, the amidic oxo group of **7.11**, **7.13** and **7.16** H-bonded to the Gln92 side chain NH₂. In contrast, the oxo-acetyl group of **7.11** and **7.16** are directly H-bonded to the Asn67 side chain NH₂ and by a water-bridge with Asn62, whereas the hCA II/**7.13** adduct possesses a sole water-bridged H-bond between the acetyl group and Asn67. The outer aromatic ring of **7.11**, **7.13** and **7.16** were bound within the hydrophobic pocket of the hCA II active site by π -alkyl interactions with Leu198, Pro202, Leu204, Val135 and Phe131, as hypothesized in the drug design phase.

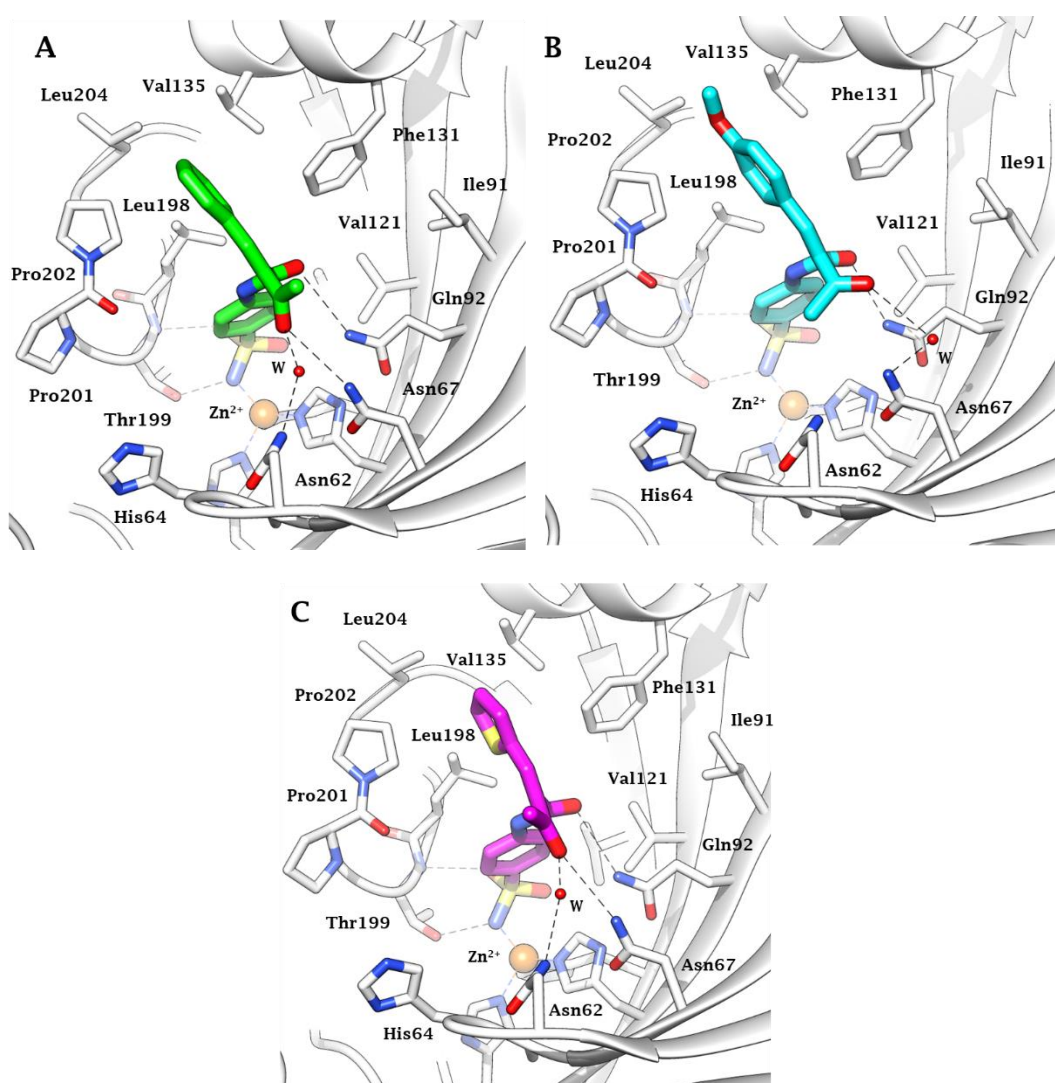


Figure 7.3: Active site view of the hCA II adduct with A) **7.10** (pdb 6UFB), B) **7.13** (pdb 6UFC) and C) **7.16** (pdb 6UFD). Hydrogen bonds are represented as black dashed lines.

7.2.4 Anti-glaucoma activity (IOP lowering activity)

The IOP lowering properties of the most potent CA II inhibitors, **7.11-7.13** and **7.16**, were assessed in a rabbit model of glaucoma (Figure 7.4). **DZA** hydrochloride 1% was used as the standard, and control experiments utilised the vehicle (0.9% NaCl + 0.1% DMSO + 0.1% EtOH). A 1% solution of the compounds were administered as eye drops to rabbits with high IOP, induced by the injection of 0.05 mL of hypertonic saline solution (5% NaCl in distilled water) into the vitreous of

both eyes. At 60 min post-instillation compounds **7.11** and **7.13** decreased IOP by 9.0 and 10.0 mmHg, while the standard **DRZ** was less effective with an IOP reduction of 8.5 mmHg (Figure 7.4). In contrast, **7.12** and **7.16** produced an IOP reduction of 6.4 and 7.5 mmHg, respectively. At the 120 min mark after the administration, **7.11** and **7.13** triggered an even more marked IOP drop to 12.8 and 12.3 mmHg. **DRZ** retained a comparable action, with the IOP reduction settling at 9.0 mmHg. Derivative **7.16** showed an enhanced efficacy after 120 min post-instillation, with a reduction of 8.9 mmHg, compared to **DRZ**. In contrast, **7.12** reported a rapid reduction of efficacy (only 3.6 mmHg reduction) 120 min after post-administration. Oddly, **7.12** uniquely protracted its action after 240 min post-instillation at 2.0 mmHg, whereas the IOP lowering activity of **7.11** and **7.13** settled at 1.3 and 1.5 mmHg, respectively.

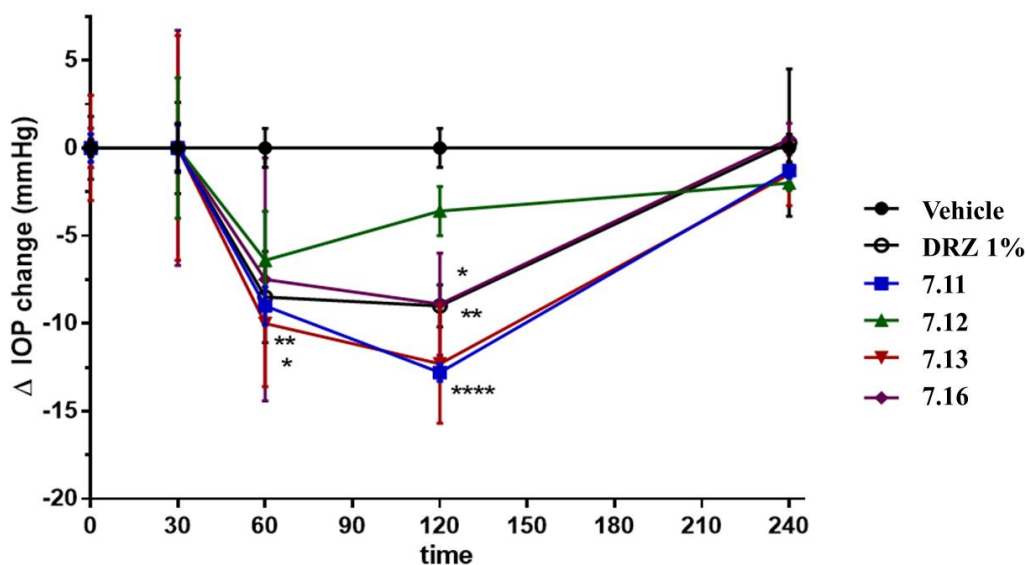


Figure 7.4. Drop of intraocular pressure (Δ IOP, mmHg) versus time (min) in hypertonic saline-induced ocular hypertension in rabbits, treated with 50 μ L of 1% solution of compounds **7.11-7.13** and **7.16** and **DRZ** as the standard. Data are analyzed with 2way Anova followed by Bonferroni multiple comparison test. * $p < 0.05$ **7.11**, **7.16**, **DRZ** vs vehicle at 60' and **DRZ** vs vehicle at 120'; ** $p < 0.01$ **7.13** and vs vehicle at 60' and **7.16** vs vehicle at 120'; **** $p < 0.001$ **7.11** and **7.13** vs vehicle at 120'.

7.3 Conclusions

Three series of dual-tailed sulfonamide CA inhibitors **7.10-7.16**, **7.17-7.24** and **7.26-7.30** were designed, synthesized and evaluated for their inhibitory profiles against four carbonic anhydrase isoforms: hCA I, II, IV, and VII. The tested compounds showed selectivity to CA II and compounds **7.10-7.16** emerged as the most potent CA II inhibitors with low to sub nanomolar K_i values (0.36-6.9 nM). To further understand and rationalize the strong inhibitory profile of the compounds against CA II, X-ray crystallographic studies were performed which showed defined moieties within the ligand structures specifically interact with the hydrophobic and hydrophilic halves of the CA II active site. As CA II up-regulation is implicated with glaucoma, the most active CA II inhibitors **7.11-7.13** and **7.16** (K_i values of 0.36-2.9 nM) were evaluated for their IOP lowering action against **DRZ** as the standard. Compound **7.16** showed a comparable IOP lowering effect to **DRZ** (IOP reduction = 8.5 mmHg), while compounds **7.11** and **7.13** were more potent than **DRZ** with IOP reduction of 12.8 and 12.3 mmHg, respectively. Therefore, this study presents compounds **7.11** and **7.13** as potential promising candidates for the development of therapeutic anti-glaucoma strategies.

7.4 Experimental Protocol

7.4.1 Chemistry

Melting points were measured with a Gallenkamp (Griffin) apparatus and are uncorrected. Reactions were monitored by TLC analysis using silica gel GF/UV 254 and visualized with UV light. Flash chromatography was performed using Merck silica gel 60 (70–230 mesh) under positive air pressure. Infrared (IR) spectra were obtained on a Shimadzu IRAfinity-1 FTIR spectrometer. NMR spectra were

recorded on Bruker 400 and 500 MHz FT-NMR spectrometers. ^1H spectra were run at 400 and 500 MHz, while ^{13}C spectra were run at 100 and 125 MHz. Chemical shifts (δ_{H}) are reported relative to TMS as the internal standard and coupling constant (J) values are reported in Hertz. The abbreviations used are as follows: s, singlet; d, doublet; t, triplet; m, multiplet. All reagents and solvents were purified and dried by standard techniques. The purity of tested compounds was greater than 95% as determined by HPLC analysis using a Shimadzu CLASS-VP LC10 analytical HPLC system equipped with a Photo Diode Array Detector and autosampler (see Supporting Information). Low resolution mass spectrometry (MS) was performed on a Shimadzu LC-2010 Electrospray ionization (ESI) Mass Spectrometer. Samples were prepared using HPLC grade methanol. The principal ion peaks m/z values are reported with their relative intensities in parentheses. High resolution mass spectra (HRMS) were obtained using a Waters Quadrupole-Time of Flight (Q-Tof) mass spectrometer *via* ESI with Leucine-Enkephalin as internal standard. All compounds were screened for PAINS alerts using the SwissADME server (www.swissadme.ch). Derivatives **7.17-7.24** showed alerts due to imine functionality, however, these compounds are not the major lead outcomes from this study and are not taken further. The activity results can still be used in the context of SAR as an enzyme assay was used, and thus binding results are still valid. It should be noted that drugs developed in this area are for topical use, and not systemic use.

3-Oxo-*N*-(4-sulfamoylphenyl)butanamide (7.9)^{17, 21}

Sulfanilamide **4** (3.44 g, 20 mmol) was added to a boiling ethyl acetoacetate **7.8** (7.77 mL, 61 mmol) and the mixture was heated at reflux for 20 minutes. After

cooling, HCl 10% (10 mL) was added and the mixture was stirred for 30 minutes, the solid material filtered out and crystallized from aqueous ethanol to give **7.9** (3.02 g, 59%) as white crystals; m.p. 180 °C (Lit. 183-186 °C).²² The product contains about 10% of enol form as analysed by ¹H NMR. ¹H NMR (500 MHz, DMSO-*d*₆) δ: 2.21 (s, 3H, CH₃), 3.60 (s, 2H, CH₂), 7.25 (br. s, 2H, NH₂), 7.71 (d, *J* = 9.0 Hz, 2H, ArH), 7.76 (d, *J* = 9.0 Hz, 2H, ArH), 10.43 (s, 1H, NH). Enol form signals: 1.93 (s, 3H, CH₃), 5.23 (s, 1H, =CH), 10.26 (s, 1H, NH), 13.59 (br. s, 1H, OH); ¹³C NMR (126 MHz, DMSO-*d*₆): 30.7 (CH₃), 52.8 (CH₂), 119.1, 127.2, 139.0, 142.2, 166.1, 203.1; MS (ESI-) 255 (100%, M-H)⁻, 291 (34%, M+Cl); HRMS (ESI-) calcd for C₁₀H₁₁N₂O₄S: 255.0440, found 255.0437.

General procedure A for preparation of 2-arylidene-3-oxo-*N*-(4-sulfamoylphenyl)butanamides 7.10-7.16: A suspension of 3-oxo-*N*-(4-sulfamoylphenyl)butanamide **7.9** (256 mg, 1 mmol), the appropriate aldehyde (1 mmol) piperidine (10 μL, 0.1 mmol) and acetic acid (6 μL, 0.1 mmol) in absolute ethanol (10 mL) and was stirred for 6-8 h at room temperature. The mixture was slowly poured into brine (20 mL) and extracted with dichloromethane (3 × 10 mL), dried (anhyd. MgSO₄), the solvent removed under reduced pressure, and the resulting residue purified *via* flash chromatography (petroleum ether: ethyl acetate = 5:5) to give **7.10-7.16**.

(*E*)-2-Benzylidene-3-oxo-*N*-(4-sulfamoylphenyl)butanamide (7.10): Using the general procedure A and benzaldehyde (106 mg, 1 mmol), compound **7.10** (153 mg, 45%) was isolated as a white solid, m.p. 172 °C. ¹H NMR (500 MHz, DMSO-*d*₆) δ: 2.47 (s, 3H, CH₃), 7.30 (br. s, 2H, NH₂), 7.39-7.41 (m, 3H, ArH), 7.42 (d, *J* =

7.0 Hz, 2H, ArH), 7.76 (s, 1H, arylideneH), 7.76-7.79 (m, 4H, ArH), 10.76 (s, 1H, NH); ^{13}C NMR (126 MHz, DMSO- d_6): 26.9 (CH₃), 119.6, 127.5, 129.7, 130.4, 131.4, 133.8, 138.1, 139.6, 140.9, 142.3, 166.8 (CONH), 197.1 (COCH₃); MS (ESI-) 343 (100%, M-H)⁻, 379 (25%, M+Cl); HRMS (ESI-) calcd for C₁₇H₁₅N₂O₄S: 343.0753, found 343.0757.

(*E*)-2-(4-Chlorobenzylidene)-3-oxo-*N*-(4-sulfamoylphenyl)butanamide 7.11:

Using the general procedure and 4-chlorobenzaldehyde (140 mg, 1 mmol), compound **7.11** (204 mg, 54%) was isolated as a white solid, m.p. 183 °C. ^1H NMR (500 MHz, CD₃OD) δ : 2.46 (s, 3H, CH₃), 7.31 (br. s, 2H, NH₂), 7.52 (d, J = 8.4 Hz, 2H, ArH), 7.64 (d, J = 8.4 Hz, 2H, ArH), 7.76-7.80 (m, 5H, 4ArH+arylideneH), 10.77 (s, 1H, NH); ^{13}C NMR (126 MHz, DMSO- d_6): 26.5 (CH₃), 119.2, 127.0, 129.3, 131.5, 132.3, 135.5, 138.1, 139.0, 139.2, 141.7, 166.0, 196.5; MS (ESI-) 377 (100%, M (^{35}Cl)-H)⁻, 379 (34%, M (^{37}Cl)-H)⁻; HRMS (ESI-) calcd for C₁₇H₁₄³⁵ClN₂O₄S: 377.0363, found 377.0367.

(*E*)-2-(2-Chlorobenzylidene)-3-oxo-*N*-(4-sulfamoylphenyl)butanamide 7.12:

Using the general procedure and 2-chlorobenzaldehyde (140 mg, 1 mmol), compound **7.12** (136 mg, 36%) was isolated as a white solid, m.p. 192 °C. ^1H NMR (500 MHz, CD₃OD) δ : 2.50 (s, 3H, CH₃), 7.24 (td, J = 7.7, 1.3 Hz, 1H, ArH), 7.37, (td, J = 7.8, 1.7 Hz, 1H, ArH), 7.51 (dd, J = 8.1, 1.3 Hz, 1H, ArH), 7.65 (dd, J = 7.9, 1.7 Hz, 1H, ArH), 7.69 (d, J = 8.8 Hz, 2H, ArH), 7.83 (d, J = 8.8 Hz, 2H, ArH), 8.01 (s, 1H, arylideneH); ^{13}C NMR (126 MHz, CD₃OD): 25.2 (CH₃), 119.4, 126.9, 127.0, 129.1, 129.8, 131.5, 131.6, 134.8, 136.9, 139.1, 141.5, 166.4, 196.1; MS (ESI-): 377 (100%, M (^{35}Cl)-H)⁻, 379 (35%, M (^{37}Cl)-H), (ESI+): 401 (M+Na);

HRMS (ESI-) calcd for C₁₇H₁₄³⁵ClN₂O₄S: 377.0363, found 377.0356.

(E)-2-(4-Methoxybenzylidene)-3-oxo-N-(4-sulfamoylphenyl)butanamide 7.13:

Using the general procedure and 4-methoxybenzaldehyde (136 mg, 1 mmol), compound **7.13** (217 mg, 58%) was isolated as a white solid, m.p. 162 °C. ¹H NMR (DMSO-*d*₆) δ: ¹H NMR (500 MHz, CD₃OD) δ 2.37 (s, 3H, CH₃), 3.70 (s, 3H, OCH₃), 6.83 (d, *J* = 9.0 Hz, 2H, ArH), 7.49 (d, *J* = 9.0 Hz, 2H, ArH), 7.61 (s, 1H, arylideneH), 7.70 (d, *J* = 9.0 Hz, 2H, ArH), 7.77 (d, *J* = 9.0 Hz, 2H, ArH); ¹³C NMR (126 MHz, CD₃OD): 24.8 (CH₃), 54.6 (OCH₃), 114.2, 119.3, 125.3, 126.9, 131.9, 134.8, 139.0, 141.4, 141.8, 162.2, 168.0, 196.8; MS (ESI-) 373 (100%, M-H)⁻, (ESI+): 397 (M+Na); HRMS (ESI-) calcd for C₁₈H₁₇N₂O₅S: 373.0858, found 373.0840.

(E)-2-(3-Nitrobenzylidene)-3-oxo-N-(4-sulfamoylphenyl)butanamide 7.14:

Using the general procedure and 3-nitrobenzaldehyde (151 mg, 1 mmol), compound **7.14** (74 mg, 19%) was isolated as a white solid, m.p. 196 °C. ¹H NMR (DMSO-*d*₆) δ: ¹H NMR (400 MHz, DMSO) δ 2.50 (s, CH₃, 3H), 7.30 (br. s, 2H, NH₂), 7.72-7.81 (m, 5H, ArH), 7.97 (s, 1H, arylideneH), 8.03 (d, *J* = 8.5 Hz, 1H, ArH), 8.26 (d, *J* = 8.5 Hz, 1H, ArH), 8.56 (s, 1H, ArH), 10.83 (s, 1H, NH); ¹³C NMR (101 MHz, DMSO) δ: 26.8 (CH₃), 119.7, 124.5, 125.3, 127.3, 131.1, 135.5, 135.9, 138.4, 139.7, 139.8, 141.7, 148.5, 165.8, 196.9; MS (ESI-) 388 (100%, M-H)⁻, (ESI+): 412 (M+Na); HRMS (ESI-) calcd for C₁₇H₁₄N₃O₆S: 388.0603, found 388.0605.

(E)-2-(2-Chloro-4-fluorobenzylidene)-3-oxo-N-(4-sulfamoylphenyl)

butanamide 7.15: Using the general procedure and 2-chloro-4-fluorobenzaldehyde (158 mg, 1 mmol), compound **7.15** (99 mg, 25%) was isolated as a yellow solid, m.p. 152 °C. ¹H NMR (400 MHz, CD₃OD) δ: 2.50 (s, 1H, CH₃), δ 7.06 (td, *J* = 8.5, 2.6 Hz, 1H, ArH), 7.37 (dd, *J* = 8.5, 2.6 Hz, 1H, ArH), 7.69-7.71 (m, 3H, ArH), 7.84 (d, *J* = 9.0 Hz, 2H, ArH), 7.95 (s, 1H, arylideneH); ¹³C NMR (101 MHz, CD₃OD) δ: 25.2 (CH₃), 114.3 (d, *J*_{C-F} 28), 117.0 (d, *J*_{C-F} 31), 119.4, 126.9, 130.7 (d, *J*_{C-F} 11), 135.8, 136.0 (d, *J*_{C-F} 14), 139.0, 139.0, 139.1, 141.4, 162.2 (d, *J*_{C-F} 315), 166.3, 195.9; MS (ESI⁻): 395 (100%, M-H)⁻, 397 (30%, M(³⁷Cl)-H), (ESI⁺): 319 (M+Na); HRMS (ESI⁻) calcd for C₁₇H₁₃³⁵ClFN₂O₄S: 359.0269, found 395.0271.

(E)-3-Oxo-N-(4-sulfamoylphenyl)-2-(thiophen-2-ylmethylene)butanamide

7.16: Using the general procedure and thiophene-2-carbaldehyde (112 mg, 1 mmol), compound **7.16** (217 mg, 62%) was isolated as a yellow solid, m.p. 185 °C. ¹H NMR (500 MHz, DMSO-*d*₆) δ: 2.43 (s, 1H, CH₃), 7.19 (dd, *J* = 5.0, 3.7 Hz, 1H, ArH), 7.30 (br. s, 2H, NH₂), 7.64 (dd, *J* = 3.7, 1.3 Hz, 1H, ArH), 7.83-7.85 (m, 5H, ArH), 8.01 (s, 1H, arylideneH), 10.84 (s, 1H, NH); ¹³C NMR (126 MHz, DMSO-*d*₆): 26.5 (CH₃), 119.5, 127.3, 128.6, 133.7, 133.9, 134.7, 136.0, 137.0, 139.4, 142.4, 166.0, 196.1; MS (ESI⁻) 349 (100%, M-H)⁻, (ESI⁺): 373 (M+Na); HRMS (ESI⁻) calcd for C₁₅H₁₃N₂O₄S₂: 349.0317, found 349.0311.

General procedure B for preparation of (E)-3-oxo-2-(2-arylhydrazineylidene)-N-(4-sulfamoylphenyl)butanamides 7.17-7.24: The diazonium salt was prepared by slowly adding a cold sodium nitrite solution (0.7 g, 10 mmol) in deionized water

(5 mL) to a cold solution of the appropriate arylamine (10 mmol) dissolved in 6 M hydrochloric acid (6 mL). To a cold solution of 3-oxo-*N*-(4-sulfamoylphenyl)butanamide **7.9** (256 mg, 1 mmol) and sodium acetate trihydrate (408 mg, 3 mmol) in ethanol (10 mL), the appropriate diazonium chloride solution (15 mmol) was slowly added over a period 30 min at 0-5 °C. The reaction mixture was stirred for further 3 h at 0-5 °C and 3 h at room temperature. The resulting solid was filtered, washed with water (2 x 10 mL), dried and recrystallized from EtOH/DMF to afford **7.17-7.24**.

(*E*)-3-Oxo-2-(2-phenylhydrazineylidene)-*N*-(4-sulfamoylphenyl)butanamide

7.17: Using general procedure B and aniline (93 mg, 1 mmol), compound **7.17** (165 mg, 46%) was isolated as yellow solid, m.p. 215 °C. ¹H NMR (500 MHz, DMSO-*d*₆) δ: 2.46 (s, 3H, CH₃), 7.16 (t, *J* = 7.5 Hz, 1H, ArH), 7.28 (br. s, 2H, NH₂), 7.41 (t, *J* = 7.5 Hz, 2H, ArH), 7.54 (d, *J* = 7.5 Hz, 2H, ArH), 7.80 (d, *J* = 9.0 Hz, 2H, ArH), 7.83 (d, *J* = 9.0 Hz, 2H, ArH), 11.44 (s, 1H, CONH), 13.77 (s, 1H, NNH); ¹³C NMR (126 MHz, DMSO-*d*₆): 26.3, 116.4, 120.3, 125.5, 127.3, 127.4, 130.0, 139.9, 140.7, 142.3, 162.5, 198.8; MS (ESI⁻): 359 (100%, M-H)⁻; HRMS (ESI⁻) calcd for C₁₆H₁₅N₄O₄S: 359.0809, found 359.0823.

(*E*)-2-(2-(4-Fluorophenyl)hydrazineylidene)-3-oxo-*N*-(4-sulfamoylphenyl)

butanamide 7.18: Using general procedure B and 4-fluoroaniline (111 mg, 1 mmol), compound **7.18** (185 mg, 49%) was isolated as a greenish solid, m.p. 248 °C. ¹H NMR (400 MHz, DMSO-*d*₆) δ: 2.50 (s, 3H, CH₃), 7.25-7.30 (m, 4H, NH₂ + 2ArH), 7.59-7.63 (m, 2H, ArH), 7.82 (d, *J* = 11.0 Hz, 2H, ArH), 7.85 (d, *J* = 11.0 Hz, 2H, ArH), 11.39 (s, 1H, CONH), 13.65 (s, 1H, NNH); ¹³C NMR (101 MHz,

DMSO-*d*₆): 26.3, 116.7 (d, J^2_{C-F} 29 Hz), 118.2 (d, J^3_{C-F} 10 Hz), 120.3, 127.3, 127.7, 139.0, 139.9, 140.7, 158.7 (d, J^1_{C-F} 240 Hz), 162.4, 198.7; MS (ESI-) 377 (100%, M-H⁻); HRMS (ESI-) calcd for C₁₆H₁₄FN₄O₄S: 377.0714, found 377.0729.

(*E*)-2-(2-(4-Chlorophenyl)hydrazineylidene)-3-oxo-*N*-(4-sulfamoylphenyl)

butanamide 7.19: Using general procedure B and 4-chloroaniline (127 mg, 1 mmol), compound **7.19** (217 mg, 55%) was isolated as a yellow solid, m.p. 260 °C. ¹H NMR (500 MHz, DMSO-*d*₆) δ : 2.49 (s, 3H, CH₃), 7.32 (br. s, 2H, NH₂), 7.44 (d, J = 8.5 Hz, 2H, ArH), 7.56 (d, J = 8.5 Hz, 2H, ArH), 7.80 (d, J = 9.0 Hz, 2H, ArH), 7.83 (d, J = 9.0 Hz, 2H, ArH), 11.34 (s, 1H, CONH), 13.51 (s, 1H, NNH); ¹³C NMR (126 MHz, DMSO-*d*₆): 26.2, 117.9, 120.3, 127.2, 128.8, 128.9, 129.8, 139.9, 140.7, 141.4, 162.1, 198.4; MS (ESI-) 393 (100%, M (³⁵Cl)-H⁻), 395 (30%, M (³⁷Cl)-H⁻); HRMS (ESI-) calcd for C₁₆H₁₄³⁵ClN₄O₄S: 393.0419, found 393.0435.

(*E*)-2-(2-(4-Bromophenyl)hydrazineylidene)-3-oxo-*N*-(4-sulfamoylphenyl)

butanamide 7.20: Using general procedure B and 4-bromoaniline (171 mg, 1 mmol), compound **7.20** (258 mg, 59%) was isolated as a yellow solid, m.p. >260 °C. ¹H NMR (500 MHz, DMSO-*d*₆) δ : 2.50 (s, 3H, CH₃), 7.52 (d, J = 9.0 Hz, 2H, ArH), 7.59 (d, J = 9.0 Hz, 2H, ArH), 7.82 (d, J = 9.0 Hz, 2H, ArH), 7.85 (d, J = 9.0 Hz, 2H, ArH), 11.32 (s, 1H, CONH), 13.39 (s, 1H, NNH); ¹³C NMR (126 MHz, DMSO-*d*₆): 26.4, 117.3, 118.5, 120.5, 127.5, 129.3, 133.0, 140.1, 141.0, 142.1, 162.4, 198.7; MS (ESI-) 437 (100%, M (⁷⁹Br)-H⁻), 339 (100%, M (⁸¹Br)-H⁻); HRMS (ESI-) calcd for C₁₆H₁₄⁷⁹BrN₄O₄S: 436.9919, found 436.9925.

(E)-2-(2-(4-Cyanophenyl)hydrazineylidene)-3-oxo-N-(4-sulfamoylphenyl)

butanamide 7.21: Using general procedure B and 4-aminobenzonitrile (118 mg, 1 mmol), compound **7.21** (119 mg, 31%) was isolated as a yellow solid, m.p. >260 °C. ¹H NMR (DMSO-*d*₆) δ: ¹H NMR (500 MHz, DMSO-*d*₆) δ: 2.50 (s, 3H, CH₃), 7.32 (br. s, 2H, NH₂), 7.65 (d, *J* = 9.0 Hz, 2H, ArH), 7.82 (d, *J* = 9.0 Hz, 2H, ArH), 7.85 (d, *J* = 9.0 Hz, 2H, ArH), 11.15 (s, 1H, CONH), 12.85 (s, 1H, NNH); ¹³C NMR (126 MHz, DMSO-*d*₆) δ: 26.3, 106.1, 116.6, 119.8, 120.5, 127.5, 133.2, 134.5, 140.2, 141.1, 146.6, 161.9, 198.1; MS (ESI⁻): 384 (100%, M-H)⁻; HRMS (ESI⁻) calcd for C₁₇H₁₄N₅O₄S: 384.0761, found 384.0776.

(E)-2-(2-(4-Methoxyphenyl)hydrazineylidene)-3-oxo-N-(4-sulfamoylphenyl)

butanamide 7.22: Using general procedure B and 4-methoxyaniline (123 mg, 1 mmol), compound **7.22** (168 mg, 43%) was isolated as a yellow solid, m.p. 255 °C. ¹H NMR (500 MHz, DMSO-*d*₆) δ: 2.50 (s, 3H, CH₃), 3.78 (s, 3H, OCH₃), 7.02 (d, *J* = 8.5 Hz, 2H, ArH), 7.34 (br. s, 2H, NH₂), 7.53 (d, *J* = 8.5 Hz, 2H, ArH), 7.83-7.88 (m, 4H, ArH), 11.57 (s, 1H, CONH), 14.07 (s, 1H, NNH); ¹³C NMR (126 MHz, DMSO-*d*₆) δ: 25.6, 55.2, 114.7, 117.4, 119.7, 125.1, 126.7, 135.1, 139.2, 140.1, 157.1, 162.2, 198.1; MS (ESI⁻): 389 (100%, M-H)⁻; HRMS (ESI⁻) calcd for C₁₇H₁₇N₄O₅S: 389.0914, found 389.0933.

(E)-2-(2-(3-Nitrophenyl)hydrazineylidene)-3-oxo-N-(4-sulfamoylphenyl)

butanamide 7.23: Using general procedure B and 3-nitroaniline (138 mg, 1 mmol), compound **7.23** (117 mg, 29%) was isolated as a yellow solid, m.p. 248 °C. ¹H NMR (500 MHz, DMSO-*d*₆) δ: 2.48 (s, 3H, CH₃), 7.31 (br. s, 2H, NH₂), 7.65 (t, 1H, *J* = 8.5 Hz, 1H, ArH), 7.81 (d, *J* = 8.5 Hz, 2H, ArH), 7.84 (d, *J* = 8.5 Hz, 2H,

ArH), 7.91 (d, $J = 8.0$ Hz, 1H, ArH), 7.95 (d, $J = 8.0$ Hz, 1H, ArH), 8.32 (s, 1H, ArH), 11.15 (s, 1H, CONH), 12.92 (s, 1H, NNH); ^{13}C NMR (126 MHz, DMSO- d_6) δ : 25.9, 110.4, 118.5, 120.1, 121.9, 127.2, 131.3, 132.1, 139.8, 140.8, 144.0, 149.0, 161.6, 197.7; MS (ESI-): 404 (100%, M-H) $^-$; HRMS (ESI-) calcd for C₁₆H₁₄N₅O₆S: 404.0659, found 404.0673.

(E)-2-(2-(3,4-Dimethoxyphenyl)hydrazineylidene)-3-oxo-N-(4-

sulfamoylphenyl) butanamide 7.24: Using general procedure B and 3,4-dimethoxyaniline (153 mg, 1 mmol), compound **7.24** (168 mg, 40%) was isolated as an orange solid, m.p. 247 °C. ^1H NMR (500 MHz, DMSO- d_6) δ : 2.52 (s, 3H, CH₃), 3.77 (s, 3H, OCH₃), 3.82 (s, 3H, OCH₃), 7.02 (d, $J = 9.0$ Hz, 1H, ArH), 7.12 (dd, $J = 9.0, 2.5$ Hz, 1H, ArH), 7.26 (d, $J = 2.5$ Hz, 1H, ArH), 7.31 (br. s, 2H, NH₂), 7.82 (d, $J = 9.0$ Hz, 2H, ArH), 7.85 (d, $J = 9.0$ Hz, 2H, ArH), 11.54 (s, 1H, CONH), 13.99 (s, 1H, NNH); ^{13}C NMR (126 MHz, DMSO- d_6) δ : 26.4, 56.2, 56.5, 101.4, 108.6, 113.1, 120.5, 126.1, 127.5, 136.1, 140.0, 140.9, 147.5, 150.3, 162.9, 198.8; MS (ESI-): 419 (100%, M-H) $^-$, HRMS (ESI-) calcd for C₁₈H₁₉N₄O₆S: 419.1020, found 419.1035.

2-Chloro-3-oxo-N-(4-sulfamoylphenyl)butanamide 7.25: To a stirred suspension of 3-oxo-N-(4-sulfamoylphenyl)butanamide **7.9** (2.56 g, 10 mmol) in toluene (30 mL) with ice cooling was added dropwise over 1 h sulfonyl chloride (1.50 g, 11 mmol) and the reaction warmed at 40-50 °C until completion as analysed by TLC. The toluene was evaporated, and the residue was crystallized from ethanol to afford **7.25** (1.22 g, 42%) as white crystals, m.p. 140 °C. The product contains about 32% of enol form as analysed by ^1H NMR. ^1H NMR (500

MHz, DMSO-*d*₆) δ : 2.32 (s, 3H, CH₃), 2.52 (s, 3H, CH₃), 5.42 (s, 1H, CH), 7.31 (br. s, 2H, NH₂), 7.34 (br. s, 2H, NH₂), 7.74-7.76 (m, 4H, ArH), 7.80-7.82 (m, 4H, ArH), 7.34 (br. s, 2H, NH₂), 10.98 (s, 1H, NH), 10.99 (s, 1H, NH); ¹³CNMR (126 MHz, DMSO-*d*₆) δ : 24.7, 27.5, 64.2, 84.0, 120.0, 121.3, 127.1, 127.3, 140.0, 140.6, 140.7, 141.3, 162.3, 163.9, 192.3, 197.3; MS (ESI-): 289 (100%, M(³⁵Cl)-H), 391 (30%, M (³⁷Cl)-H); HRMS (ESI-) calcd for C₁₀H₁₀³⁵ClN₂O₄S: 289.0044, found 289.0058.

General procedure C for preparation of (Z)-2-oxo-N-aryl-2-((4-sulfamoylphenyl)amino)acetohydrazonoyl chloride 7.26-7.30: To a cold solution of 2-chloro-3-oxo-N-(4-sulfamoylphenyl)butanamide **7.25** (290 mg, 1 mmol) and sodium acetate trihydrate (408 mg, 3 mmol) in ethanol (10 mL), the appropriate diazonium chloride solution (15 mmol) was slowly added over a period 30 min at 0-5 °C. The reaction mixture was stirred for further 3 h at 0-5 °C and 3 h at room temperature. The resulting solid was filtered, washed with water (2 x 10 mL), air dried and recrystallized from EtOH/DMF to afford **7.26-7.30**.

(Z)-2-Oxo-N-phenyl-2-((4-sulfamoylphenyl)amino)acetohydrazonoyl chloride 7.26: Using general procedure C and aniline (93 mg, 1 mmol), compound **7.26** (151 mg, 34%) was isolated as a white solid, m.p. 245 °C. ¹H NMR (500 MHz, DMSO-*d*₆) δ : 7.00 (t, *J* = 7.5 Hz, 1H, ArH), 7.29 (br. s, 2H, NH₂), 7.34 (t, *J* = 7.5, 8.5 Hz, 2H, ArH), 7.61 (d, *J* = 8.5 Hz, 2H, ArH), 7.82 (d, *J* = 9.0 Hz, 2H, ArH), 7.92 (d, *J* = 9.0 Hz, 2H, ArH), 10.34 (s, 1H, NH), 10.41 (s, 1H, NH); ¹³C NMR (126 MHz, DMSO-*d*₆) δ : 115.4, 118.2, 120.8, 122.6, 127.0, 129.5, 139.5, 141.8, 143.2, 158.1; MS (ESI-): 351 (100%, M (³⁵Cl)-H)⁻, 353 (33%, M (³⁷Cl)-H)⁻, HRMS (ESI-) calcd for C₁₄H₁₂³⁵ClN₄O₃S: 351.0319, found 351.0310.

(Z)-N-(4-Fluorophenyl)-2-oxo-2-((4-sulfamoylphenyl)amino)

acetohydrazonoyl chloride 7.27: Using general procedure C and 4-fluoroaniline (111 mg, 1 mmol), compound **7.27** (100 mg, 27%) was isolated as a buff solid, m.p. 250 °C. ¹H NMR (500 MHz, DMSO-*d*₆) δ: 7.16 (t, *J* = 8.8 Hz, 2H, ArH), 7.28 (br. s, 2H, NH₂), 7.61 (dd, *J* = 8.8, 5.0 Hz, 2H, ArH), 7.82 (d, *J* = 8.5 Hz, 2H, ArH), 7.91 (d, *J* = 8.5 Hz, 2H, ArH), 10.32 (s, 1H, NH), 10.42 (s, 1H, NH); ¹³C NMR (126 MHz, DMSO-*d*₆) δ: 116.0 (d, *J*²_{C-F} 23 Hz), 116.8 (d, *J*³_{C-F} 8 Hz), 118.2, 120.8, 126.9, 139.4, 139.7, 141.7, 157.3 (d, *J*¹_{C-F} 238 Hz), 158.0; MS (ESI⁻): 369 (100%, M (³⁵Cl)-H)⁻, 371 (33%, M (³⁷Cl)-H)⁻; HRMS (ESI⁻) calcd for C₁₄H₁₁F³⁵ClN₄O₃S: 369.0224, found 369.0232.

(Z)-N-(4-Chlorophenyl)-2-oxo-2-((4-sulfamoylphenyl)amino)

acetohydrazonoyl chloride 7.28: Using general procedure C and 4-chloroaniline (127 mg, 1 mmol), compound **7.28** (154 mg, 40%) was isolated as a yellow solid, m.p. 255 °C. ¹H NMR (500 MHz, DMSO-*d*₆) δ: 7.29 (br. s, 2H, NH₂), 7.37 (d, *J* = 8.3 Hz, 2H, ArH), 7.62 (d, *J* = 8.3 Hz, 2H, ArH), 7.82 (d, *J* = 8.5 Hz, 2H, ArH), 7.92 (d, *J* = 8.5 Hz, 2H, ArH), 10.36 (s, 1H, NH), 10.51 (s, 1H, NH); ¹³C NMR (126 MHz, (CD₃)₂CO) δ: 123.2, 129.5, 130.0, 131.1, 132.6, 137.0, 139.3, 143.6, 157.0, 163.2; MS (ESI⁻): 385 (100%, (³⁵Cl) M-H)⁻, HRMS (ESI⁻) calcd for C₁₄H₁₁³⁵Cl₂N₄O₃S: 384.9929, found 384.9935.

(Z)-N-(4-Bromophenyl)-2-oxo-2-((4-sulfamoylphenyl)amino)

acetohydrazonoyl chloride 7.29: Using general procedure C and 4-bromoaniline (171 mg, 1 mmol), compound **7.29** (137 mg, 32%) was isolated as a yellow solid, m.p. >260 °C. ¹H NMR (500 MHz, DMSO-*d*₆) δ: 7.29 (br. s, 2H, NH₂), 7.50 (d, *J*

= 9.0 Hz, 2H, ArH), 7.56 (d, $J = 9.0$ Hz, 2H, ArH), 7.81 (d, $J = 9.0$ Hz, 2H, ArH), 7.91 (d, $J = 9.0$ Hz, 2H, ArH), 10.37 (s, 1H, NH), 10.51 (s, 1H, NH); ^{13}C NMR (126 MHz, DMSO- d_6) δ : 113.5, 116.8, 118.5, 120.2, 126.3, 131.5, 138.9, 141.0, 142.0, 157.2; MS (ESI-): 429 (100%, M-H) $^-$, HRMS (ESI-) calcd for $\text{C}_{14}\text{H}_{11}^{79}\text{Br}^{35}\text{ClN}_4\text{O}_3\text{S}$: 428.9424, found 428.9428.

(Z)-N-(4-Methoxyphenyl)-2-oxo-2-((4-sulfamoylphenyl)amino)

acetohydrazonoyl chloride 7.30: Using general procedure C and 4-anisidine (123 mg, 1 mmol), compound **7.30** (69 mg, 18%) was isolated as a yellow solid, m.p. 250 °C. ^1H NMR (500 MHz, DMSO- d_6) δ : 3.72 (s, 3H, OCH $_3$), 7.26 (br. s, 2H, NH $_2$), 7.51 (d, $J = 9.0$ Hz, 2H, ArH), 7.78 (d, $J = 9.0$ Hz, 2H, ArH), 7.82 (d, $J = 9.0$ Hz, 2H, ArH), 7.89 (d, $J = 9.0$ Hz, 2H, ArH), 10.24 (s, 1H, NH), 10.27 (s, 1H, NH); ^{13}C NMR (126 MHz, DMSO- d_6) δ : 55.7, 114.8, 116.6, 118.2, 120.6, 126.4, 136.9, 139.9, 141.9, 155.3, 158.1; MS (ESI-): 381 (100%, (^{35}Cl) M-H) $^-$, HRMS (ESI-) calcd for $\text{C}_{15}\text{H}_{14}^{35}\text{ClN}_4\text{O}_4\text{S}$: 381.0424, found 381.0407.

7.4.2 Protein X-ray crystallography

CA II protein was concentrated to 7 mg/mL and set up in SD-2 plates (Molecular Dimensions) with 200 nL plus 200 nL drops (protein plus reservoir solution) over 50 μL reservoirs and incubated at 8° C. The reservoir conditions consisted of 2.5-2.8 M ammonium sulfate with 100 mM Tris pH 8.5-9.0. Compounds were soaked into the crystals for approximately 24 hours and subsequently glycerol (20% final concentration) was added to cryoprotect the crystals for cryo-cooling. Data were collected at the Australian Synchrotron MX1 beamline in Oct 2017 and at the MX2 beamline in Nov 2017. Data were auto-processed with XDS²³ and then Aimless²⁴

was used to scale the reflections, Phaser²⁵ was used with model 4cq0 to phase the data and Coot²⁶ was used to manually place the atoms in electron density. AFITT (OpenEye Scientific Software) was used to place the ligands into density and generate the dictionary files. REFMAC²⁷ was used to refine the structures. The **7.13** (high resolution at 1.32 Å) structure used anisotropic refinement whereas the other structures were refined using isotropic refinement. The models and structure factors have been deposited at the RCSB with PDB codes: 6UFB (ligand **7.10**), 6UFC (ligand **7.13**) and 6UFD (ligand **7.16**).

7.4.3 CA Inhibition

An Applied Photophysics stopped-flow instrument was used for assaying the CA catalyzed CO₂ hydration activity.²⁰ Phenol red (at a concentration of 0.2 mM) was used as indicator, working at the absorbance maximum of 557 nm, with 20 mM Hepes (pH 7.5) as buffer and 20 mM Na₂SO₄ (for maintaining constant the ionic strength), following the initial rates of the CA-catalyzed CO₂ hydration reaction for a period of 10–100 s. The CO₂ concentrations ranged from 1.7 to 17 mM for the determination of the kinetic parameters and inhibition constants. For each inhibitor, at least six traces of the initial 5–10% of the reaction have been used for determining the initial velocity. The uncatalyzed rates were determined in the same manner and subtracted from the total observed rates.

Stock solutions of inhibitor (0.1 mM) were prepared in distilled–deionized water, and dilutions up to 0.01 nM were carried out subsequently with the assay buffer. Inhibitor and enzyme solutions were preincubated together for 6 hours at room temperature prior to assay in order to allow for the formation of the E–I complex. The inhibition constants were obtained by nonlinear least-squares methods using

PRISM 3 and the Cheng–Prusoff equation, as reported earlier,^{28, 29} and represent the mean from at least three different determinations. All CA isoforms were recombinant ones obtained in-house as reported earlier.^{30, 31}

7.4.4 Hypertensive rabbit IOP lowering studies

The experimental procedures were carried out on New Zealand albino rabbits, following the Resolution of the Association for Research in Vision and Ophthalmology, the Good Laboratory Practice for the use of animals upon authorization of Italian Ministry of Health (number 1179/2015-PR), in agreement with the European Union Regulations (OJ of ECL 358/1, 12/12/1986).³² Male albino rabbits (body weight 2-2.5 kg) were kept in individual cages, food and water was provided *ad libitum*. The animals were maintained on a 12 h-12 h light/dark cycle in a temperature-controlled room (22-23 °C). Animals were identified with a tattoo in the ear, numbered consecutively and examined before the beginning of the study to verify the good general and ophthalmic health condition. All the compounds were dissolved in pyrogen free sterile 0.9% NaCl solution (i.e. physiologic solution) and 0.1% DMSO, 0.1% EtOH at 1 mM concentration. Vehicle was 0.9% NaCl + 0.1% DMSO + 0.1% EtOH. The viability of compounds was evaluated after repeated administration using the Draize Eye Test (Wilhelmus, 2001). Topical delivery into the conjunctival cul-de-sac is the most common route of ocular drug delivery.

All compounds were given prior to saline injection and the IOP was measured at the very beginning of the experimental session to establish basal IOP. Ocular hypertension was induced by the injection of 0.05 mL of sterile hypertonic saline (5%) into the vitreous bilaterally with local anaesthesia provided by one drop of

0.2% oxybuprocaine hydrochloride in each eye one minute prior. IOP was measured using a Pneumotonometer (Reichert Inc. Depew, NY) after hypertonic saline injection after stabilization (normally 10 minutes) to verify the rise of IOP into the suitable experimental range (IOP >30 and < 40 mmHg) and after 60, 90, 120, 240 minutes in all groups after drug or vehicle treatment. One drop of 0.2% oxybuprocaine hydrochloride was instilled in each eye immediately before each set of pressure measurements

7.5 References

1. Donegan, R. K.; Lieberman, R. L. Discovery of molecular therapeutics for glaucoma: Challenges, successes, and promising directions. *J. Med. Chem.* **2016**, *59*, 788-809.
2. Weinreb, R. N.; Leung, C. K.; Crowston, J. G.; Medeiros, F. A.; Friedman, D. S.; Wiggs, J. L.; Martin, K. R. Primary open-angle glaucoma. *Nat. Rev. Dis. Primers.* **2016**, *2*, 1-19.
3. Quigley, H. A.; Broman, A. T. The number of people with glaucoma worldwide in 2010 and 2020. *Br. J. Ophthalmol.* **2006**, *90*, 262-267.
4. Weinreb, R. N.; Aung, T.; Medeiros, F. A. The pathophysiology and treatment of glaucoma: A review. *JAMA.* **2014**, *311*, 1901-1911.
5. Eldehna, W. M.; Fares, M.; Ceruso, M.; Ghabbour, H. A.; Abou-Seri, S. M.; Abdel-Aziz, H. A.; Abou El Ella, D. A.; Supuran, C. T. Amido/ureidosubstituted benzenesulfonamides-isatin conjugates as low nanomolar/subnanomolar inhibitors of the tumor-associated carbonic anhydrase isoform xii. *Eur. J. Med. Chem.* **2016**, *110*, 259-266.
6. Supuran, C. T. Carbonic anhydrases: Novel therapeutic applications for inhibitors and activators. *Nat. Rev. Drug Discov.* **2008**, *7*, 168-181.
7. Supuran, C. T. Structure-based drug discovery of carbonic anhydrase inhibitors. *J. Enzyme Inhib. Med. Chem.* **2012**, *27*, 759-772.
8. Eldehna, W. M.; Abo-Ashour, M. F.; Nocentini, A.; Gratteri, P.; Eissa, I. H.; Fares, M.; Ismael, O. E.; Ghabbour, H. A.; Elaasser, M. M.; Abdel-Aziz, H. A.; Supuran, C. T. Novel 4/3-((4-oxo-5-(2-oxoindolin-3-ylidene)thiazolidin-2-ylidene)amino) benzenesulfonamides: Synthesis, carbonic anhydrase inhibitory activity, anticancer activity and molecular modelling studies. *Eur. J. Med. Chem.* **2017**, *139*, 250-262.
9. Bozdog, M.; Pinard, M.; Carta, F.; Masini, E.; Scozzafava, A.; McKenna, R.; Supuran, C. T. A class of 4-sulfamoylphenyl- ω -aminoalkyl ethers with effective carbonic anhydrase inhibitory action and antiglaucoma effects. *J. Med. Chem.* **2014**, *57*, 9673-9686.
10. Nocentini, A.; Ferraroni, M.; Carta, F.; Ceruso, M.; Gratteri, P.; Lanzi, C.; Masini, E.; Supuran, C. T. Benzenesulfonamides incorporating flexible triazole moieties are highly effective carbonic anhydrase inhibitors: Synthesis and kinetic, crystallographic, computational, and intraocular pressure lowering investigations. *J. Med. Chem.* **2016**, *59*, 10692-10704.
11. Eldehna, W. M.; Abo-Ashour, M. F.; Berrino, E.; Vullo, D.; Ghabbour, H. A.; Al-Rashood, S. T.; Hassan, G. S.; Alkahtani, H. M.; Almehizia, A. A.; Alharbi, A.; Abdel-Aziz, H. A.; Supuran, C. T. Slc-0111 enamionone analogs, 3/4-(3-aryl-3-oxopropenyl) aminobenzenesulfonamides, as novel selective subnanomolar inhibitors of the tumor-associated carbonic anhydrase isoform ix. *Bioorg. Chem.* **2019**, *83*, 549-558.
12. Tanpure, R. P.; Ren, B.; Peat, T. S.; Bornaghi, L. F.; Vullo, D.; Supuran, C. T.; Poulsen, S. A. Carbonic anhydrase inhibitors with dual-tail moieties to match the hydrophobic and hydrophilic halves of the carbonic anhydrase active site. *J. Med. Chem.* **2015**, *58*, 1494-1501.
13. Ibrahim, H. S.; Allam, H. A.; Mahmoud, W. R.; Bonardi, A.; Nocentini, A.; Gratteri, P.; Ibrahim, E. S.; Abdel-Aziz, H. A.; Supuran, C. T. Dual-tail arylsulfone-based benzenesulfonamides differently match the hydrophobic and hydrophilic halves of human carbonic anhydrases active

- sites: Selective inhibitors for the tumor-associated hca ix isoform. *Eur. J. Med. Chem.* **2018**, 152, 1-9.
14. Fares, M.; Eladwy, R. A.; Nocentini, A.; El Hadi, S. R. A.; Ghabbour, H. A.; Abdel-Megeed, A.; Eldehna, W. M.; Abdel-Aziz, H. A.; Supuran, C. T. Synthesis of bulky-tailed sulfonamides incorporating pyrido[2,3-*d*][1,2,4]triazolo[4,3-*a*]pyrimidin-1(5*H*)-yl moieties and evaluation of their carbonic anhydrases i, ii, iv and ix inhibitory effects. *Bioorg. Med. Chem.* **2017**, 25, 2210-2217.
 15. Bozdag, M.; Ferraroni, M.; Nuti, E.; Vullo, D.; Rossello, A.; Carta, F.; Scozzafava, A.; Supuran, C. T. Combining the tail and the ring approaches for obtaining potent and isoform-selective carbonic anhydrase inhibitors: Solution and x-ray crystallographic studies. *Bioorg. Med. Chem.* **2014**, 22, 334-340.
 16. Alafeefy, A. M.; Isik, S.; Abdel-Aziz, H. A.; Ashour, A. E.; Vullo, D.; Al-Jaber, N. A.; Supuran, C. T. Carbonic anhydrase inhibitors: Benzenesulfonamides incorporating cyanoacrylamide moieties are low nanomolar/subnanomolar inhibitors of the tumor-associated isoforms ix and xii. *Bioorg. Med. Chem.* **2013**, 21, 1396-1403.
 17. Hodgkinson, A.; Staskun, B. Conversion of 2, 2-dichloroacetoacetanilides into 4-(hydroxymethyl)-2(1*H*)-quinolones. *J. Org. Chem.* **1969**, 34, 1709-1713.
 18. Frohberg, P.; Drutkowski, G.; Wagner, C. Synthesis and structural assignment of oxanilone-*n*-arylhydrazonoyl chlorides. *Eur. J. Org. Chem.* **2002**, 2002, 1654-1663.
 19. Fares, M.; Said, M. A.; Alsherbiny, M. A.; Eladwy, R. A.; Almahli, H.; Abdel-Aziz, M. M.; Ghabbour, H. A.; Eldehna, W. M.; Abdel-Aziz, H. A. Synthesis, biological evaluation and molecular docking of certain sulfones as potential nonazole antifungal agents. *Molecules* **2016**, 21, E114.
 20. Khalifah, R. G. The carbon dioxide hydration activity of carbonic anhydrase. I. Stop-flow kinetic studies on the native human isoenzymes b and c. *J. Biol. Chem.* **1971**, 246, 2561-2573.
 21. Fedenko, V.; Avramenko, V.; Khmel', M.; Solomko, Z. Reaction of *o*-aminobenzenesulfonamides with β - keto esters. *Zh. Org. Khim. (Abst.)* **1978**, 8, 1673-1676.
 22. Osolodkin, D. I.; Kozlovskaya, L. I.; Dueva, E. V.; Dotsenko, V. V.; Rogova, Y. V.; Frolov, K. A.; Krivokolysko, S. G.; Romanova, E. G.; Morozov, A. S.; Karganova, G. G.; Palyulin, V. A.; Pentkovski, V. M.; Zefirov, N. S. Inhibitors of tick-borne flavivirus reproduction from structure-based virtual screening. *ACS. Med. Chem. Lett.* **2013**, 4, 869-874.
 23. Kabsch, W. Xds. *Acta Crystallogr. Sect. D. Biol. Crystallogr.* **2010**, 66, 125-132.
 24. Evans, P. R. An introduction to data reduction: Space-group determination, scaling and intensity statistics. *Acta Crystallogr. D Biol. Crystallogr.* **2011**, 67, 282-292.
 25. McCoy, A. J.; Grosse-Kunstleve, R. W.; Adams, P. D.; Winn, M. D.; Storoni, L. C.; Read, R. J. Phaser crystallographic software. *J. Appl. Crystallogr.* **2007**, 40, 658-674.
 26. Emsley, P.; Lohkamp, B.; Scott, W. G.; Cowtan, K. Features and development of coot. *Acta Crystallogr. D Biol. Crystallogr.* **2010**, 66, 486-501.
 27. Murshudov, G. N.; Skubak, P.; Lebedev, A. A.; Pannu, N. S.; Steiner, R. A.; Nicholls, R. A.; Winn, M. D.; Long, F.; Vagin, A. A. Refmac5 for the refinement of macromolecular crystal structures. *Acta Crystallogr. D Biol. Crystallogr.* **2011**, 67, 355-367.
 28. Nocentini, A.; Carta, F.; Tanc, M.; Selleri, S.; Supuran, C. T.; Bazzicalupi, C.; Gratteri, P. Deciphering the mechanism of human carbonic anhydrases inhibition with sulfocoumarins: Computational and experimental studies. *Chemistry* **2018**, 24, 7840-7844.
 29. Nocentini, A.; Moi, D.; Balboni, G.; Salvadori, S.; Onnis, V.; Supuran, C. T. Synthesis and biological evaluation of novel pyrazoline-based aromatic sulfamates with potent carbonic anhydrase isoforms ii, iv and ix inhibitory efficacy. *Bioorg. Chem.* **2018**, 77, 633-639.
 30. Nocentini, A.; Gratteri, P.; Supuran, C. T. Phosphorus versus sulfur: Discovery of benzenephosphonamidates as versatile sulfonamide-mimic chemotypes acting as carbonic anhydrase inhibitors. *Chemistry* **2019**, 25, 1188-1192.
 31. Nocentini, A.; Bonardi, A.; Gratteri, P.; Cerra, B.; Gioiello, A.; Supuran, C. T. Steroids interfere with human carbonic anhydrase activity by using alternative binding mechanisms. *J. Enzyme Inhib. Med. Chem.* **2018**, 33, 1453-1459.
 32. Kilkenny, C.; Browne, W. J.; Cuthill, I. C.; Emerson, M.; Altman, D. G. Improving bioscience research reporting: The arrive guidelines for reporting animal research. *J. Pharmacol. Pharmacother.* **2010**, 1, 94-99.

Chapter 8.

Conclusions and Future Directions

8.1 The search for anti-CHIKV lead compounds (Chapters 2-4)

8.1.1 Conclusions

Using a multi-disciplinary approach, considerable efforts have been made towards the development of potential anti-CHIKV. The key findings from this study can be summarised into two main sections:

a) application of medicinal chemistry concepts to existing inhibitors:

By applying robust medicinal chemistry strategies such as hybridization, bioisosteric substitution and simplification of existing anti-CHIKV agents, we devised three series of analogue scaffolds, thiazolopyrimidine, triazolopyrimidine and 2-anilinopyrimidine, respectively, as shown in Figure 8.1 (Chapter 2 and 3).

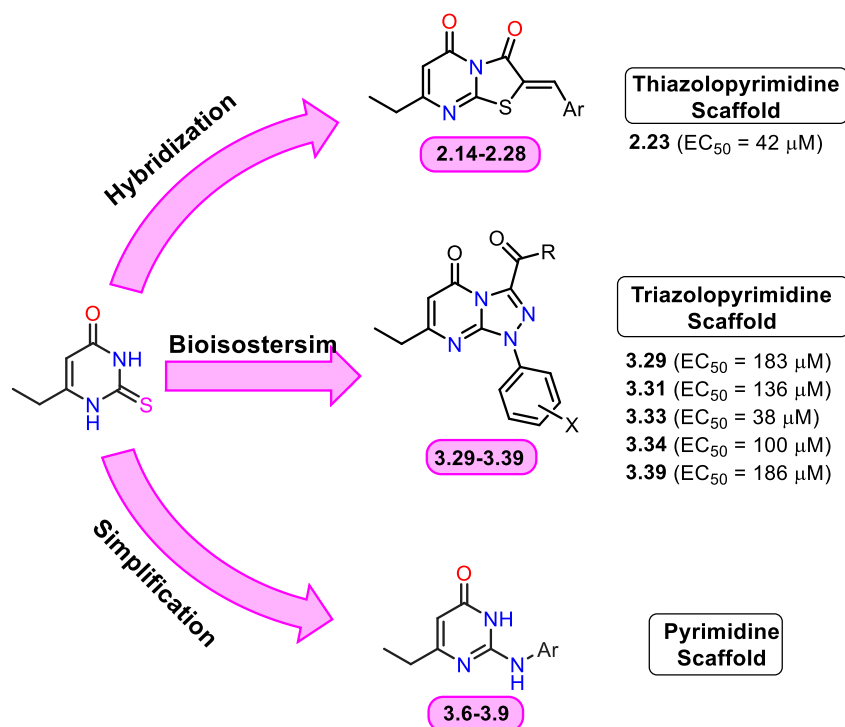


Figure 8.1: Summary of the application to medicinal chemistry concepts

Starting from 6-ethyl thiouracil, target compounds **2.14-2.28**, **3.29-3.39** and **3.6-3.9** were synthesized using the state-of-art organic chemistry. The first series of (*Z*)-7-ethyl-2-arylidine-5*H*-thiazolo[3,2-*a*]pyrimidine-3,5(2*H*)-diones **2.14-2.28** was

synthesized by optimization of the multi-component reaction conditions *via* replacing chloroacetic acid with the more regioselective bromoacetic acid, lowering reaction temperature and changing the mode of addition. X-ray crystal structure and computational studies showed that only one regioselective isomer formed with the *Z* configuration that is potentially stabilized by two intramolecular hydrogen bonds. Anti-CHIKV activity evaluation showed the tailed thiazolopyrimidine **2.23** (Figure 8.1) as a promising lead compound for future development with $EC_{50} = 42 \mu\text{M}$, with $IC_{50} > 250 \mu\text{M}$ against the breast cancer cell line MCF-7 and the endothelial human sapiens cell line EA.hy926.

The triazolopyrimidines **3.29-3.39** and anilinopyrimidines **3.6-3.9**, were designed, synthesised and bioassayed for anti-CHIKV activity and cytotoxicity. Five derivatives of triazolopyrimidine scaffold **3.29**, **3.31**, **3.33**, **3.34** and **3.39** showed anti-CHIKV activity spanning from 38-186 μM and compound **3.33** emerged as the most active and least toxic ($EC_{50} = 42 \mu\text{M}$, with $IC_{50} > 300 \mu\text{M}$) against the breast cancer cell lines MCF-7 and MDA-MB-231 and the endothelial human sapiens cell line EA.hy926). Compound **3.33** showed considerable advantages over the parent compound **3.1**, including the ability of the 3 position in **3.33** to accommodate substituents and accessibility, low cost and diversities of the hydrazonoyl chlorides starting materials. Derivative **3.33** may provide new and promising scope for improved drug design utilising this inexpensive scaffold. Series **3.6-3.9** proved to only exhibit weak anti-CHIKV activity. Comparisons of the geometries and Electrostatic Potential-mapped surfaces of minimal pharmacophore models **3.53-3.56** of anti-CHIKV agents has allowed for a consensus model for effective target binding. These results place future research into anti-CHIKV agents in better standing.

b) Structure-guided drug design (**Chapter 4**):

In a previous study, eleven potential inhibitors of the CHIKV proteins were identified by virtual screening of NCI Diversity set II database (1541 compounds) against three CHIKV proteins (nsP2, nsP3 and envelope glycoprotein) (Figure 8.2).^{1,2} Herein, we requested these compounds and sent them to be bioassayed for their anti-CHIKV activity. Three CHIKV inhibitors were identified out of the 1541 *in silico* screened database (Figure 8.2).

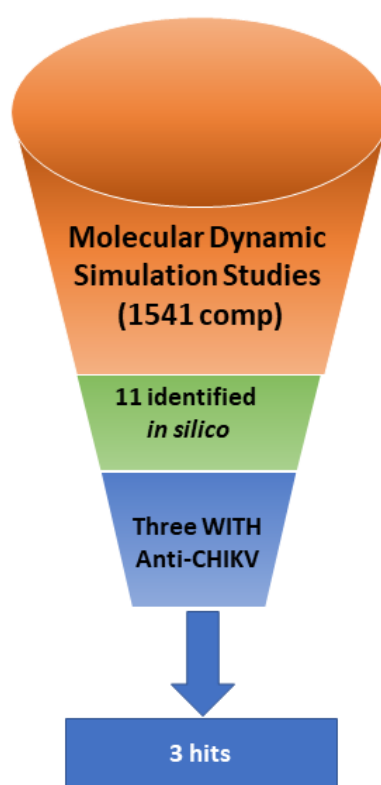


Figure 8.2: Structure-guided drug design workflow in this dissertation.

Synthesis of a small library of NCI-37168 (**4.5** (Figure 8.3) $EC_{50} < 0.8$ $\mu\text{g/mL}$) was achieved by applying amide coupling conditions to 2-naphthoic acid or 3-hydroxy-2-naphthoic acid with different anilines to afford **4.14-4.19**. These compounds were investigated for their anti-CHIKV activity at 20 $\mu\text{g/mL}$ and showed that the hydroxyl group at position 2 of the naphthalene scaffold and the *m*-nitro group are

203

important for the anti-viral activity.

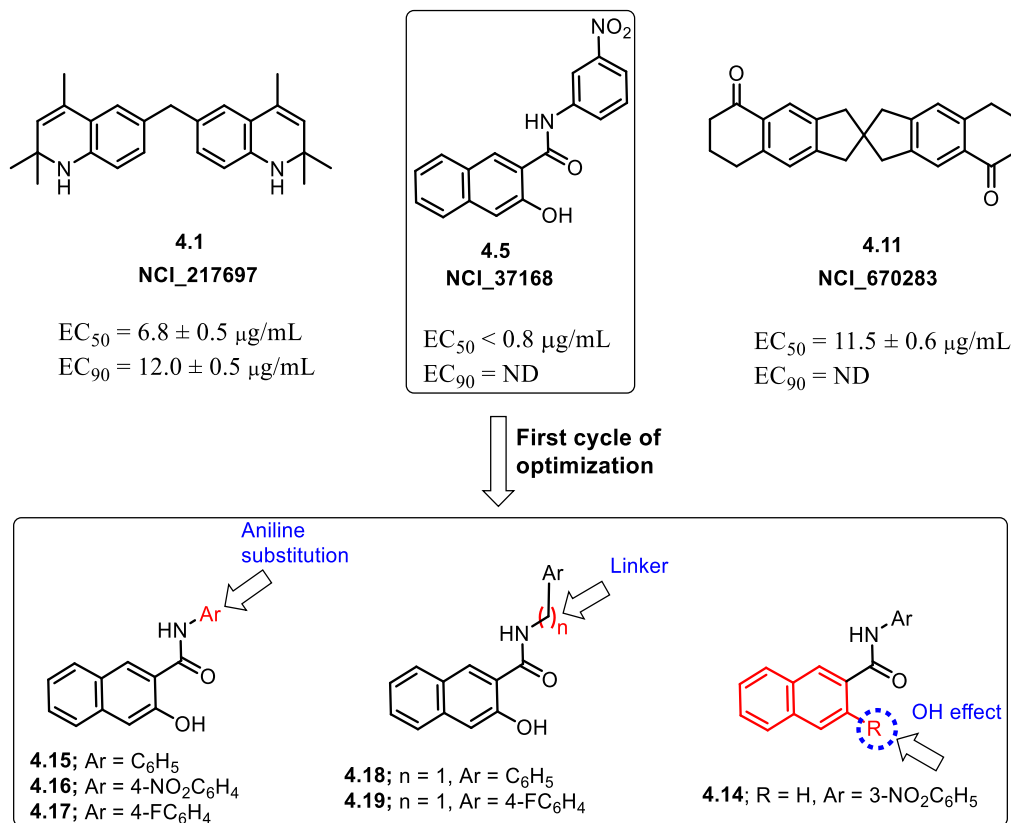


Figure 8.3: Structure of the active potential leads **4.1**, **4.5** and **4.11** and optimization of **4.5**.

8.1.2 Future directions

a) application to medicinal chemistry concepts to existing inhibitors:

Antiviral activity evaluation demonstrated the tailed thiazolopyrimidine **2.23** as a candidate for future development. The rest of the compounds among thiazolopyrimidines **2.14-2.28**, except **2.23**, showed no or weak anti-CHIKV, which indicate that the thiazolo[3,2-*a*]pyrimidine scaffold is not important for the antiviral activity (Figure 8.4). Further medicinal chemistry optimization could be achieved by retaining the tail, while replacing thiazolo[3,2-*a*]pyrimidine bicyclic system with thiazolidine scaffold **8.1** (Figure 8.4).

The most active anti-CHIKV compound **3.33** among the tested 1-aryl-[1,2,4]triazolo[4,3-*a*]pyrimidines **3.29-3.39**, could be subjected to another cycle of optimization by varying R_1 and R_2 to further explore the structure activity relationship of this scaffold (Figure 8.4).

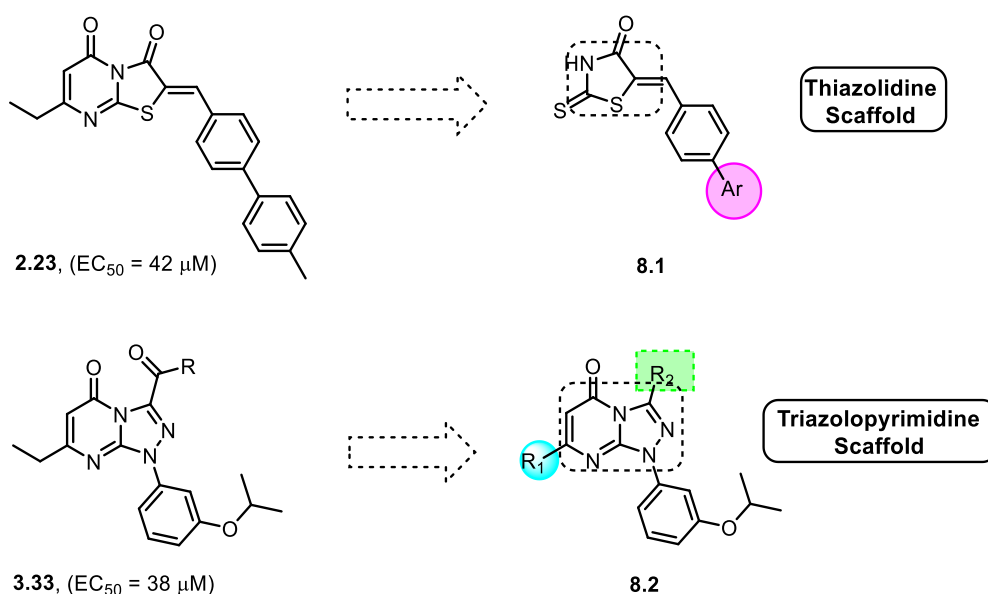


Figure 8.4: Future development of the thiazolopyrimidine **2.23** and triazolopyrimidine **3.33**.

b) Structure-guided drug design (**Chapter 4**):

Compounds **4.14-4.19** will be tested for their antiviral activity at lower concentration to investigate their antiviral activity, while lowering their toxic effect. Inhibition profile of these derivatives against the protein target nsP3 could be performed and iterative cycles of optimization could be achieved to decrease their cytotoxic effect, while retaining the anti-CHIKV activity. The quinoline derivative **4.1** (Figure 8.3) showed a strong inhibitory effect against CHIKV (EC₅₀ = 6.8 ± 0.5 mg/mL, EC₉₀ = 12.0 ± 0.5 mg/mL) and could be considered as a promising hit for future development. further work will be performed in our lab on compounds 4.1 and 4.11.

8.2 Fluorescent anion transporters (Chapters 5-6)

8.2.1 Conclusions

An investigation into the design and synthesis of two new classes of fluorescent anion transporters for pharmacological applications has been undertaken (Chapters 5-6). The first anion transporters study (Chapter 5) aimed to find switchable anion reporters that are switched on in the presence of the reducing agents GSH, DTT and TCEP. We have developed five new anion transporters 5.1-5.5 and four putative anionophores 5.13, 5.14, 5.16 and 5.17 that are ‘switched on’ in the presence of the reducing agent GSH which is found in higher concentrations in tumours than in healthy tissue. Biological testing of these compound is currently undergoing.

A new class of bisurea anion transporters bearing the fluorescent 4-methyl coumarin has been developed (Chapter 6, 6.1-6.4). The fluorescent anion receptors elicited a relatively strong chloride binding affinity in DMSO-*d*₆/0.5% H₂O with $K_a = 81 - 177 \text{ M}^{-1}$ and superior Cl⁻/NO₃⁻ exchange ability in ISE-based affinity and H⁺/Cl⁻ cotransport activity. Transporters 6.1-6.4 showed efficient anion binding and transport properties than the previously reported fluorescent anion transporters.^{3,4} In terms of the biological component of this project the four coumarin-bisurea compounds 6.1-6.4 synthesised during this work are currently under evaluation in cell-based assays and cellular fluorescent imaging.

8.2.2 Future directions

Based on the biological evaluation and if the switchable abilities of the gold complexes 5.13, 5.14, 5.16 and 5.17 could be replicated in a cellular environment, it would be beneficial to create a larger library of NHC-based bisbenzimidazole-pyridine (8.3, Figure 8.5) and investigate their biological properties (Figure 8.5).

The designed receptors **8.3** could be with a wide variety of substitutions at the R₁, R₂ and R₃ positions and modifying the coordination metal (gold III) with other metals such as ruthenium (with anticancer property) whilst retaining the basic bisbenzimidazole pyridine scaffold present in **5.1-5.5** (Figure 8.5).

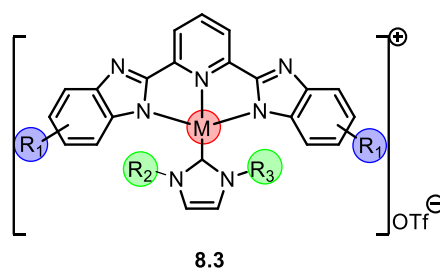


Figure 8.5: Future development of the switchable anion transporters **5.13**, **5.14**, **5.16** and **5.17**.

The synthesized coumarin-bisurea conjugates **6.1-6.4** are currently under biological evaluation, and based on the derived structure activity relationship, further medicinal chemistry derivatisation could be achieved such as formation of macrocycle fluorescent probes based on these receptors for fluorescent imaging of subcellular organelles application.

8.3 Carbonic anhydrase inhibitors (Chapter 7):

8.3.1 Conclusions:

Based on the dual-tailed approach of the CA inhibitors, we designed and synthesized three series of dual-tailed sulfonamide CA inhibitors **7.10-7.16**, **7.17-7.24** and **7.26-7.30**.⁵ They were tested for their inhibitory profiles against four carbonic anhydrase isoforms: hCA I, II, IV, and VII. Series **7.10-7.16** emerged as the most potent CA II inhibitors with low to sub nanomolar K_i values (0.36-6.9 nM) (Figure 8.6). X-ray crystallographic studies of **7.10**, **7.13** and **7.16** against CA II were conducted to further understand and rationalize the strong CA II inhibitory profile of the compounds. As per our design, the X-ray crystallographic studies

showed defined moieties within the ligand structures specifically interact with the hydrophobic and hydrophilic halves of the CA II active site (Figure 8.6). The most active CA II inhibitors **7.11-7.13** and **7.16** (K_i values of 0.36-2.9 nM) were evaluated for their IOP lowering action against DRZ as the standard. Compounds **7.11** and **7.13**, with IOP reduction of 12.8 and 12.3 mmHg, respectively, emerged as more potent than the clinically used drug **DRZ** (IOP reduction = 8.5 mmHg).

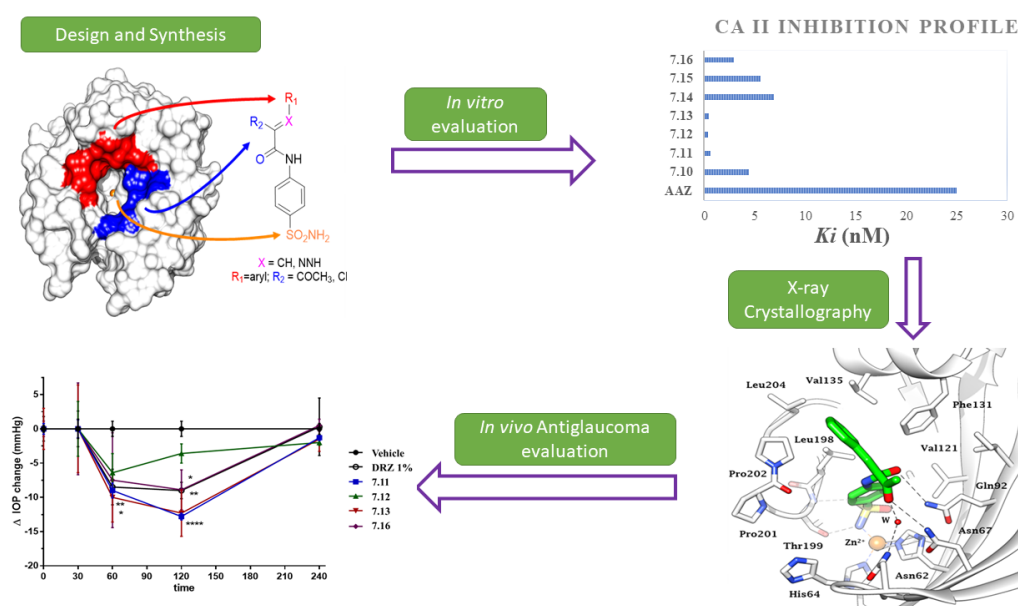


Figure 8.6: Drug design of the potent anti-glaucoma derivatives studied in the current thesis.

8.3.2 Future directions

This study presents compounds **7.11** and **7.13** as potential promising candidates for the development of therapeutic anti-glaucoma strategies. For further development on this scaffold, rigidification of the amide group could be done, with a wide variety of substitutions at the R_2 position, whilst retaining the 4-chloro or 4-methoxy substitutions at R_1 (**8.4**, Figure 8.7).

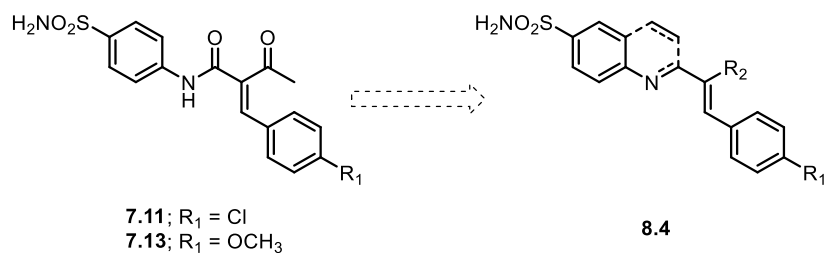


Figure 8.7: possible derivatization and development of the CA inhibitors

8.4 References

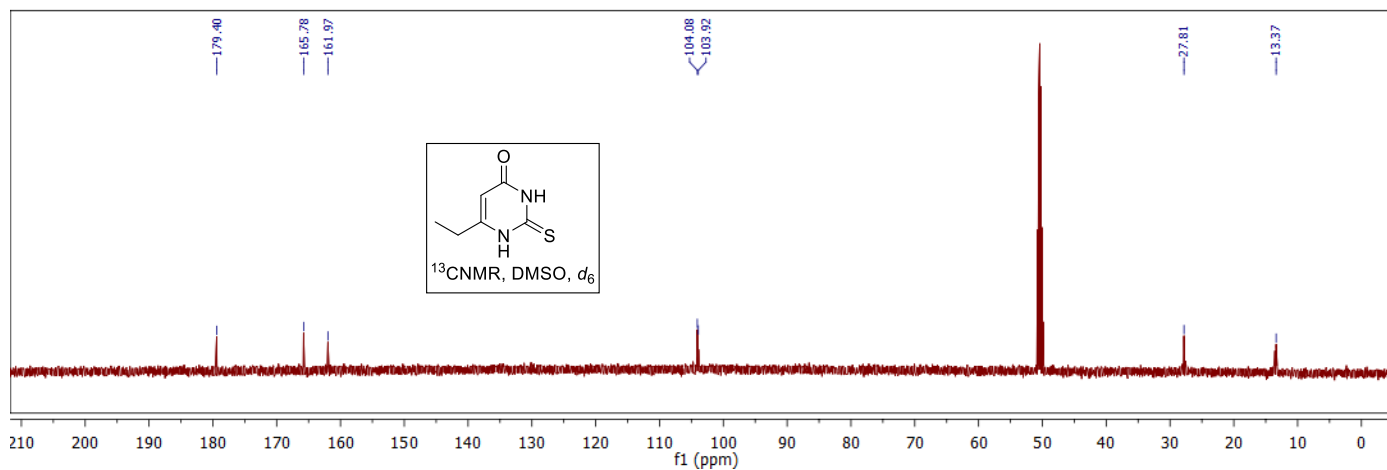
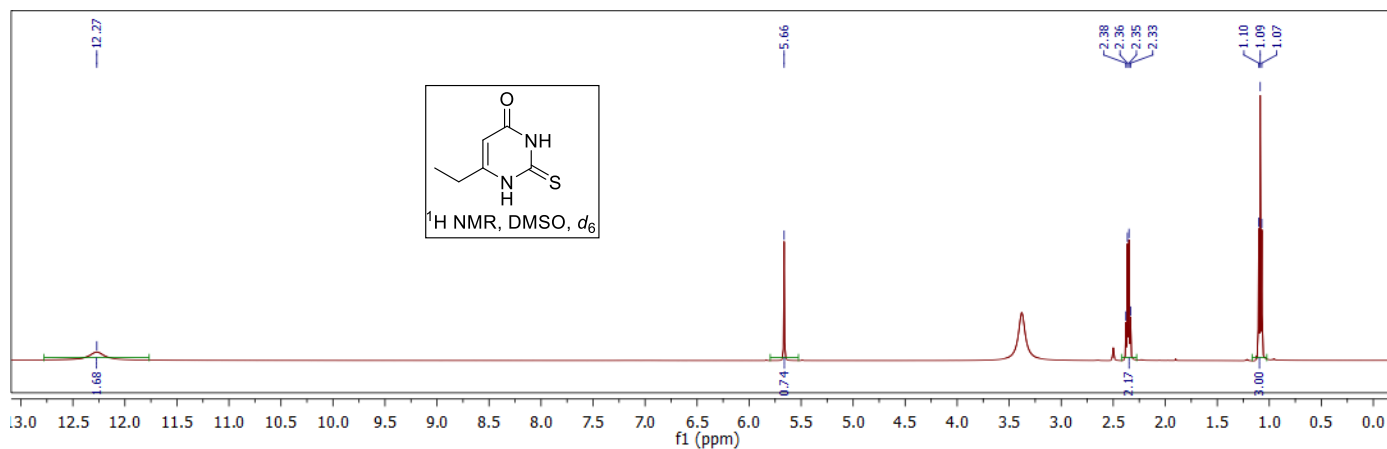
1. Nguyen, P. T.; Yu, H.; Keller, P. A. Discovery of in silico hits targeting the nsp3 macro domain of chikungunya virus. *J. Mol. Model.* **2014**, *20*, 1-12.
2. Nguyen, P. T.; Yu, H.; Keller, P. A. Identification of chikungunya virus nsp2 protease inhibitors using structure-base approaches. *J. Mol. Graphics Modell.* **2015**, *57*, 1-8.
3. Berry, S. N.; Soto-Cerrato, V.; Howe, E. N.; Clarke, H. J.; Mistry, I.; Tavassoli, A.; Chang, Y.-T.; Pérez-Tomás, R.; Gale, P. A. Fluorescent transmembrane anion transporters: Shedding light on anionophoric activity in cells. *Chem. Sci.* **2016**, *7*, 5069-5077.
4. Bao, X.; Wu, X.; Berry, S. N.; Howe, E. N. W.; Chang, Y. T.; Gale, P. A. Fluorescent squaramides as anion receptors and transmembrane anion transporters. *Chem. Commun.* **2018**, *54*, 1363-1366.
5. Tanpure, R. P.; Ren, B.; Peat, T. S.; Bornaghi, L. F.; Vullo, D.; Supuran, C. T.; Poulsen, S. A. Carbonic anhydrase inhibitors with dual-tail moieties to match the hydrophobic and hydrophilic halves of the carbonic anhydrase active site. *J. Med. Chem.* **2015**, *58*, 1494-1501.

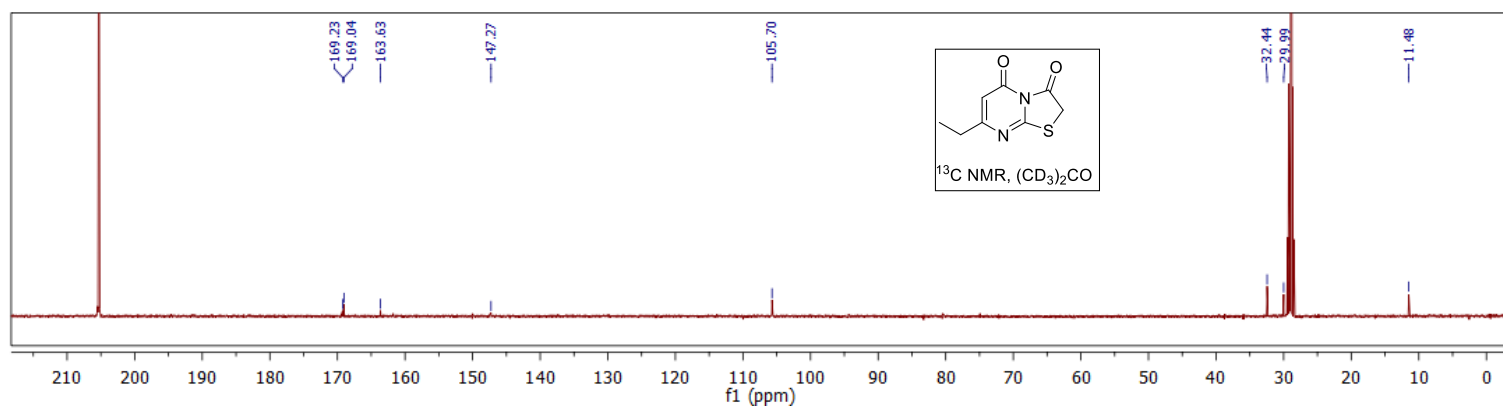
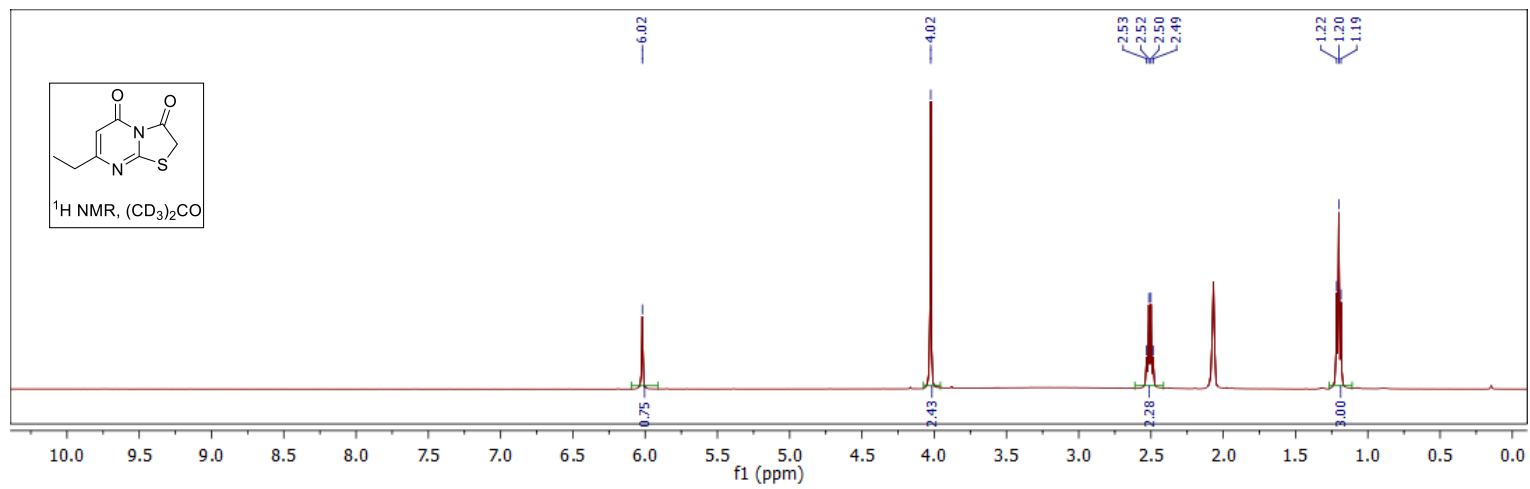
Appendices Table of Contents

Appendix A: <i>Supplementary Information to Chapter 2</i>	211
NMR spectra of compounds from chapter 2	211
Appendix B: <i>Supplementary Information to Chapter 3</i>	228
NMR spectra of compounds from chapter 3	228
Appendix C: <i>Supplementary Information to Chapter 4</i>	257
NMR spectra of compounds from chapter 4	257
Appendix D: <i>Supplementary Information to Chapter 5</i>	264
A) NMR spectra of compounds from chapter 5	264
B) Binding studies	279
C) Transport studies	287
D) Transport studies upon reduction of complexes	310
Appendix E: <i>Supplementary Information to Chapter 6</i>	315
A) NMR spectra of compounds from chapter 6	315
B) Binding studies	327
C) Transport studies	331
Appendix F: <i>Supplementary Information to Chapter 7</i>	343
A) NMR spectra of compounds from chapter 7	343
B) HPLC purity	376
C) Protein X-ray Crystallography	377

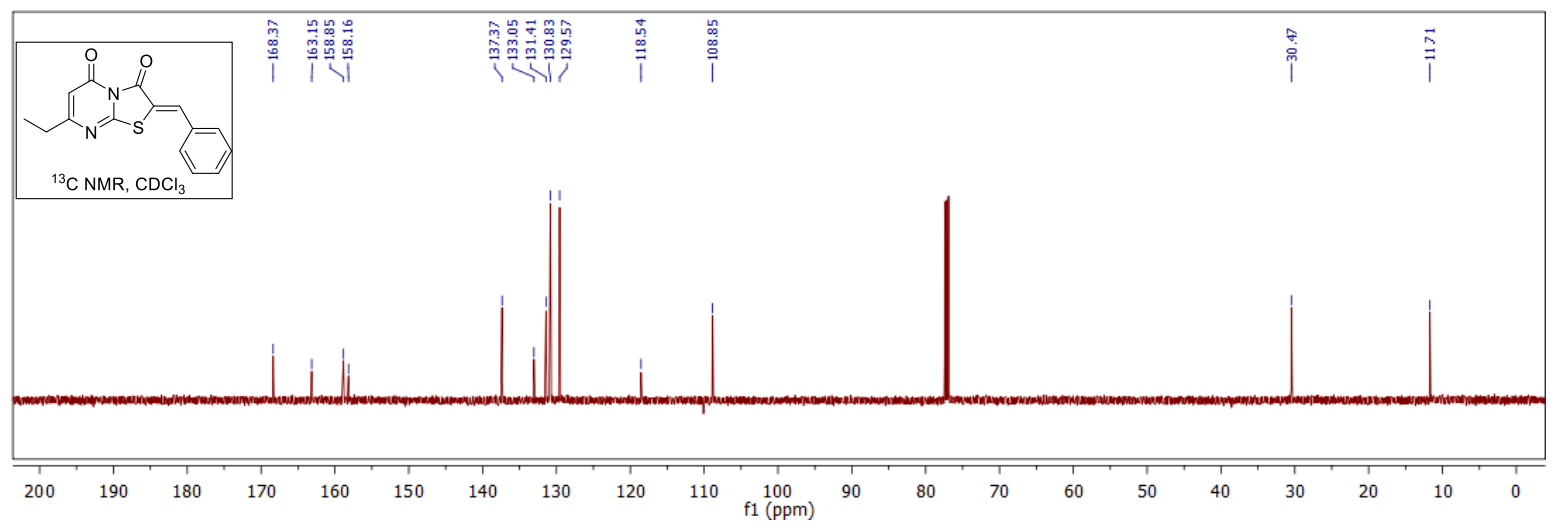
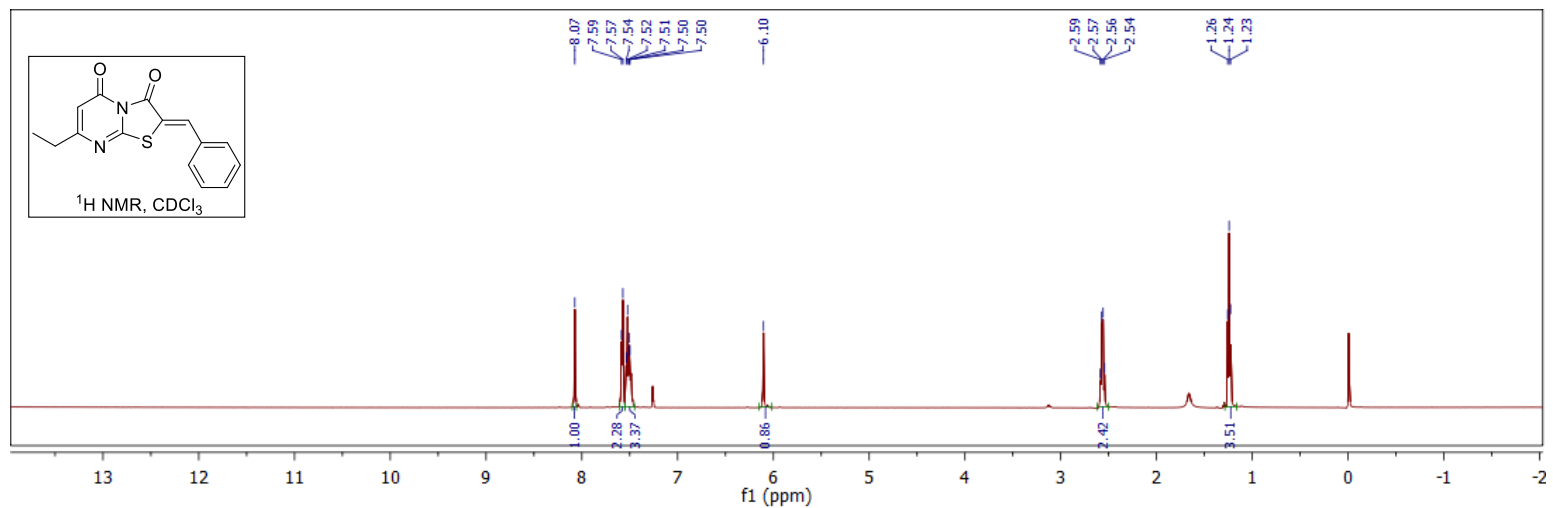
Appendix A: Supplementary Information to Chapter 2

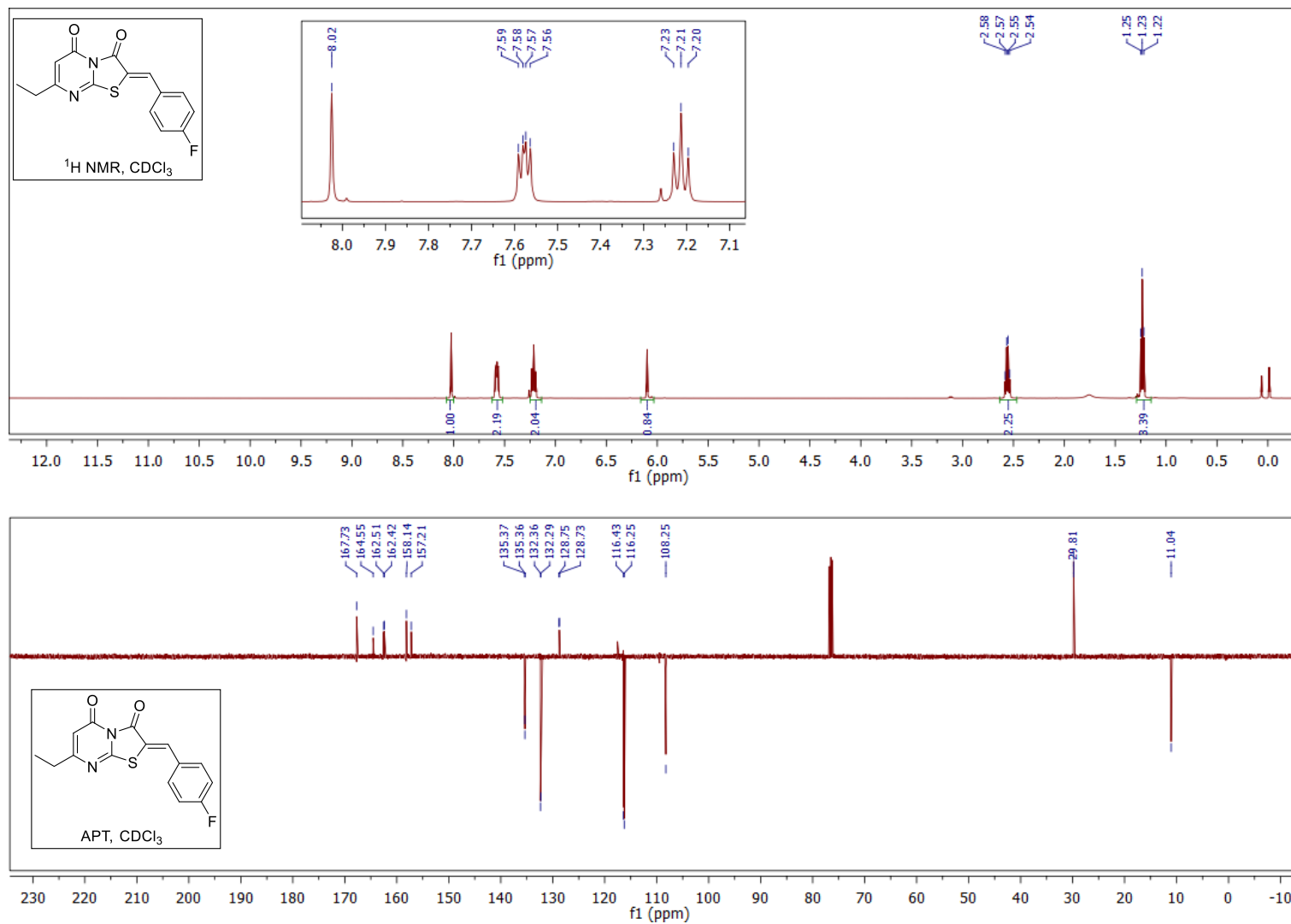
NMR spectra of compounds from chapter 2



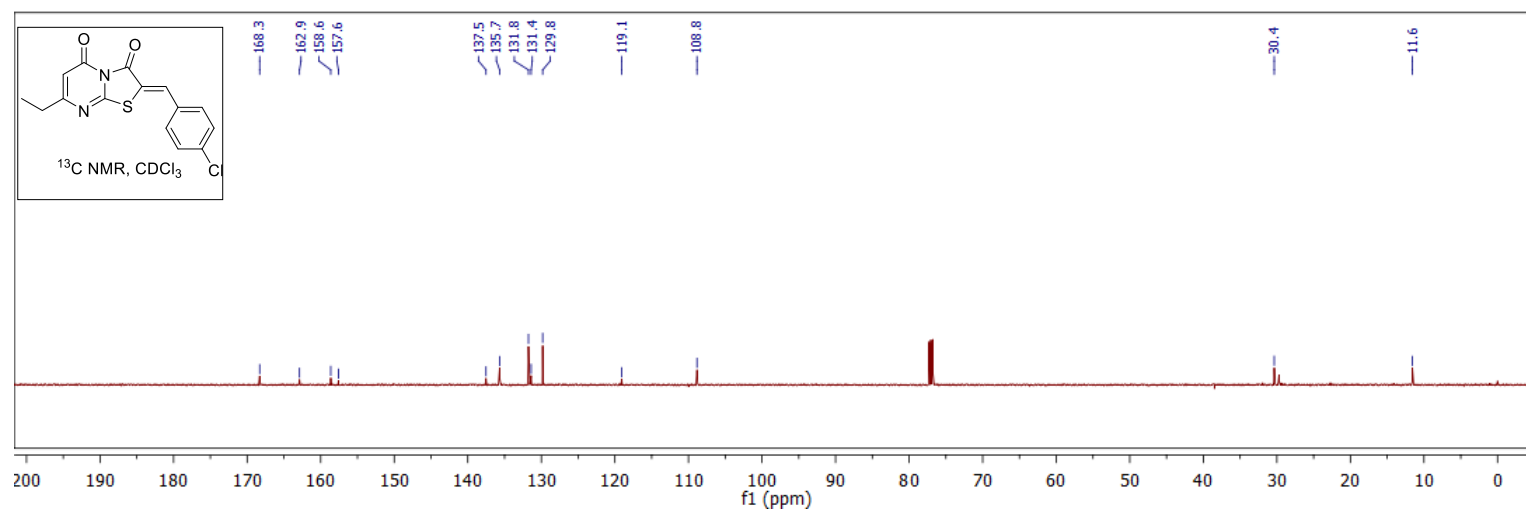
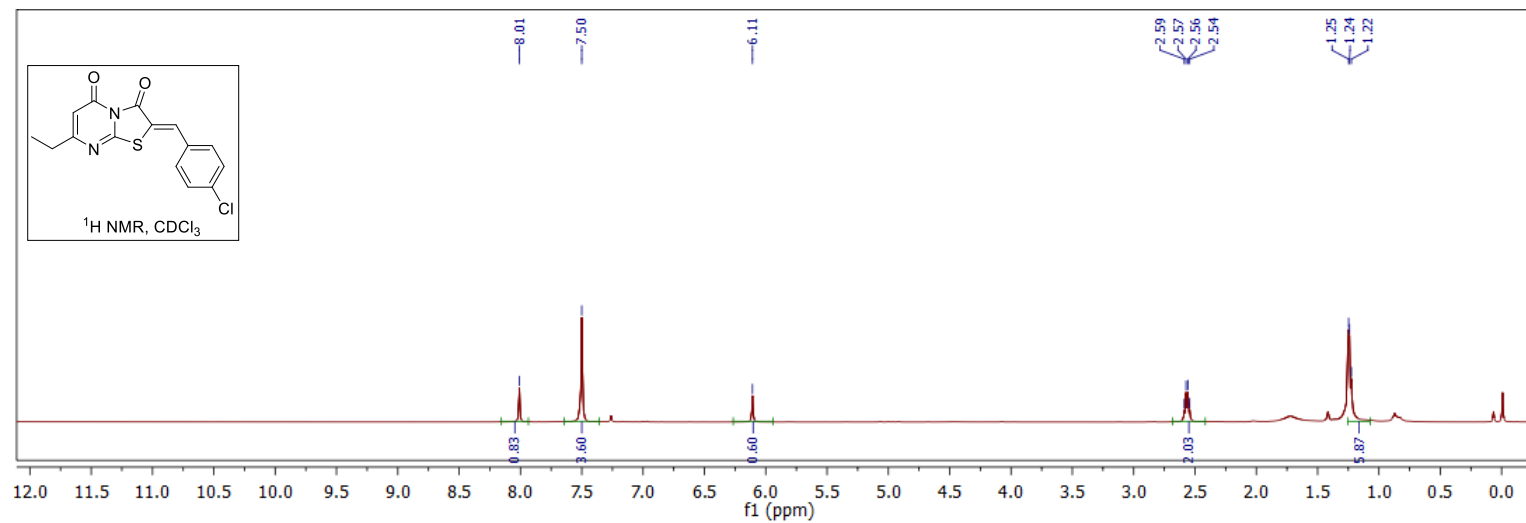


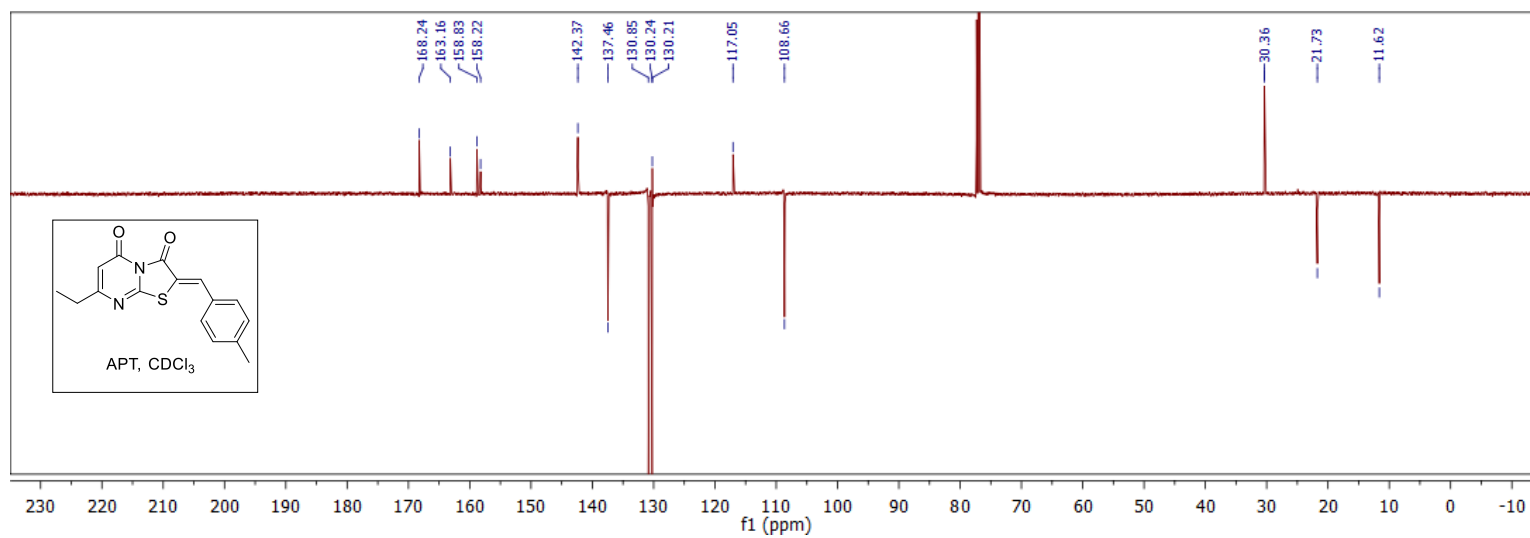
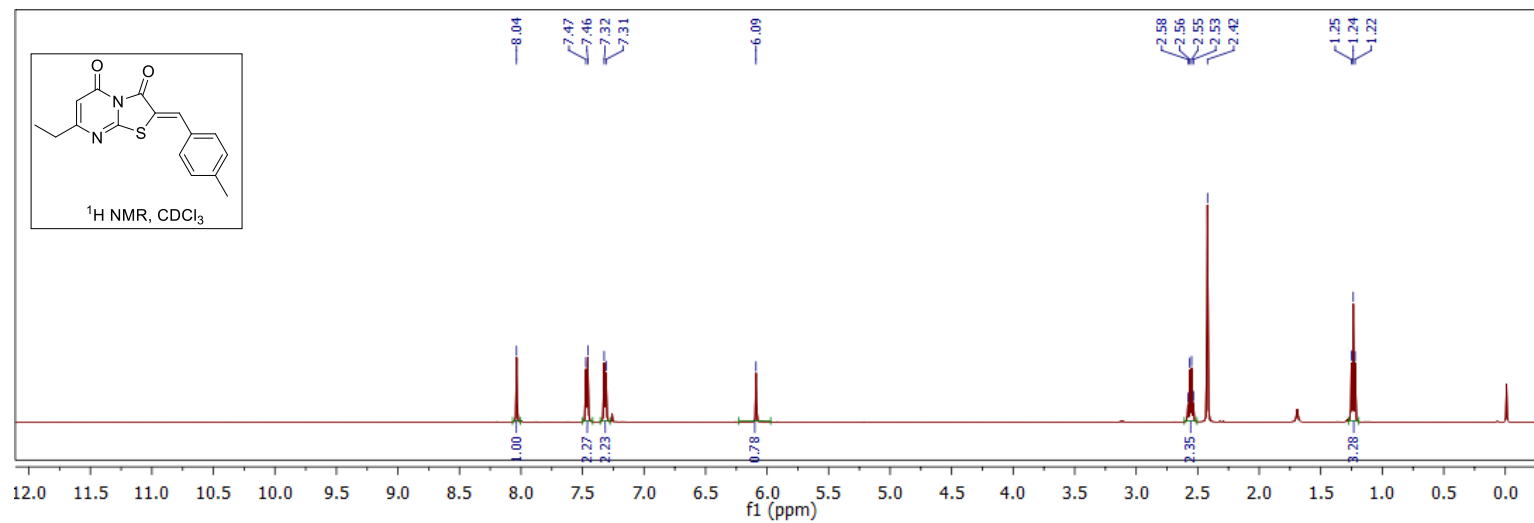
Appendix A for Chapter 2



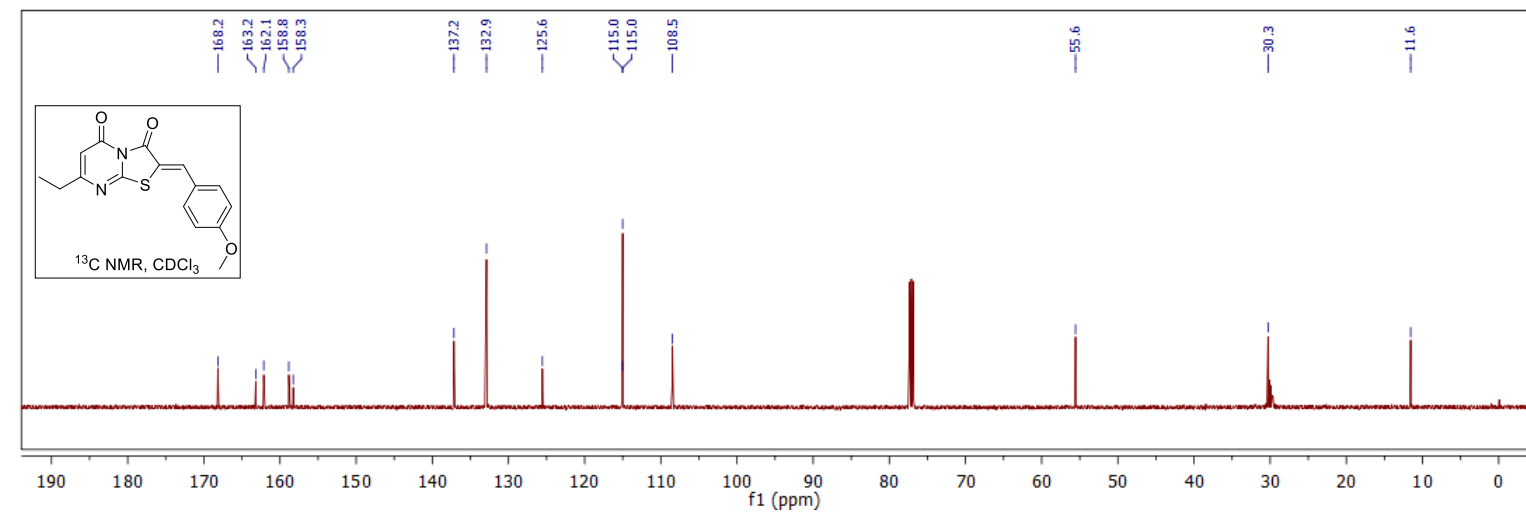
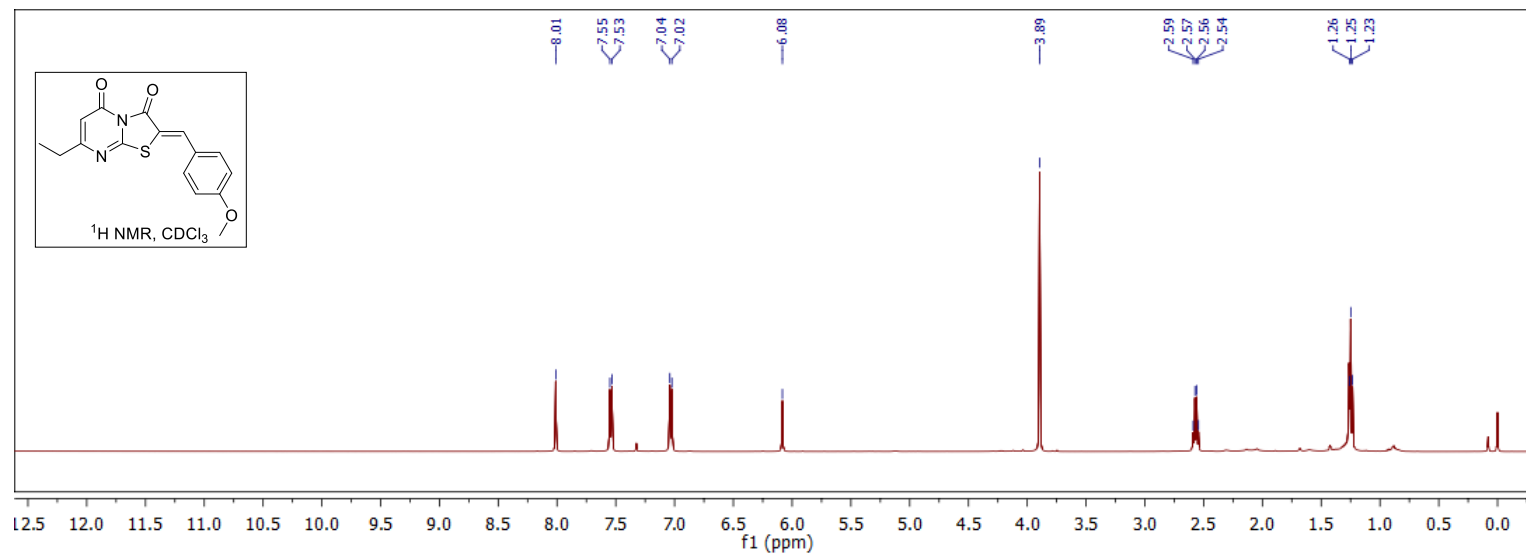


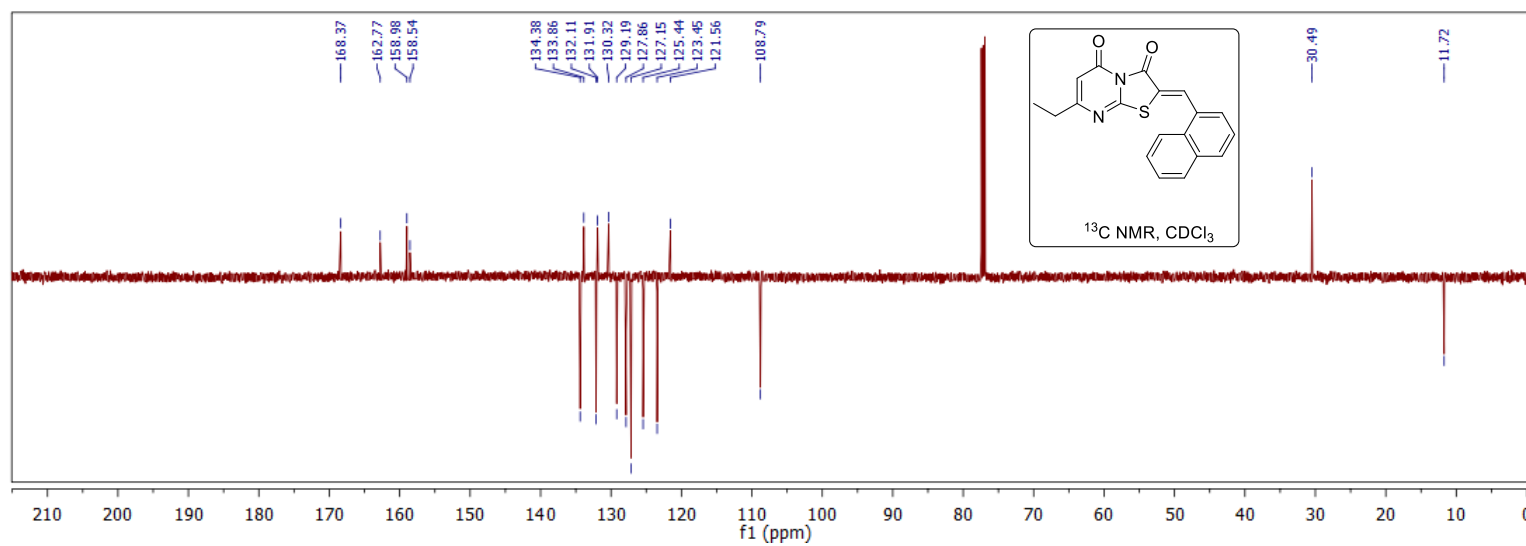
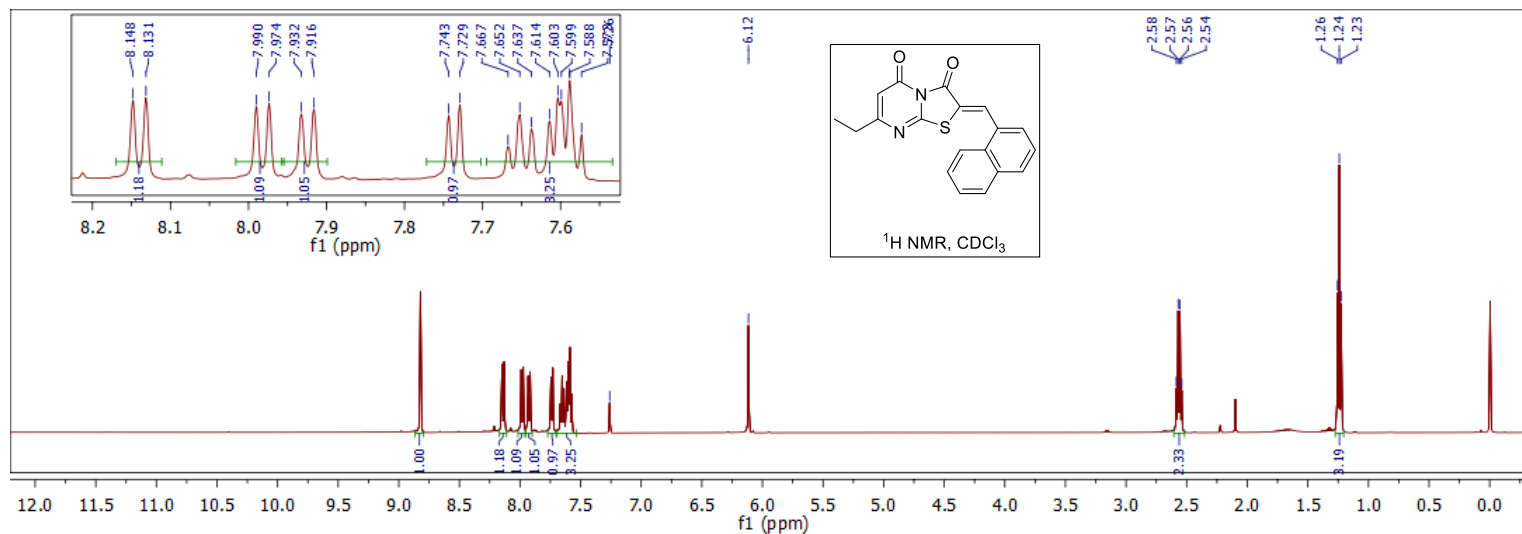
Appendix A for Chapter 2



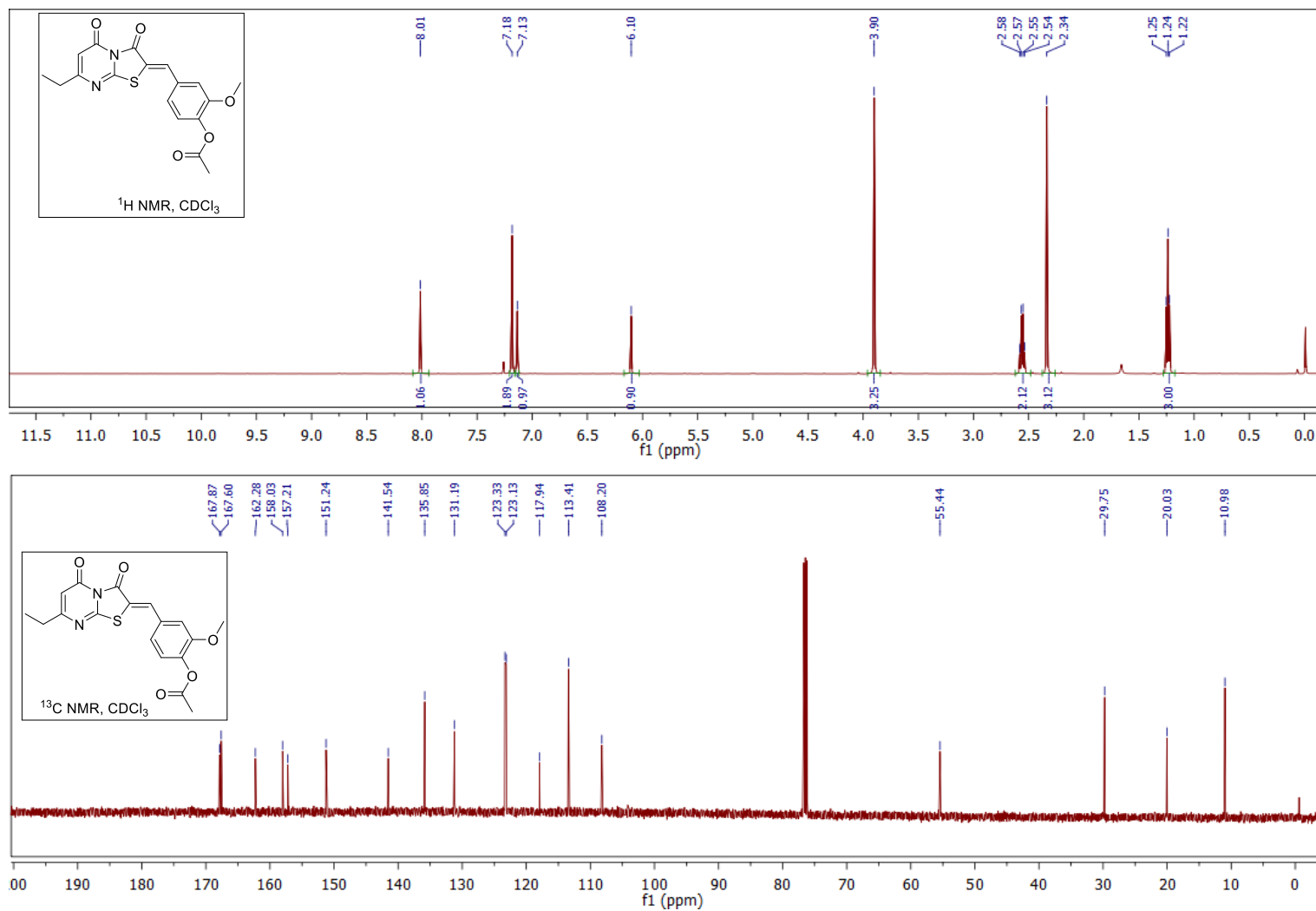


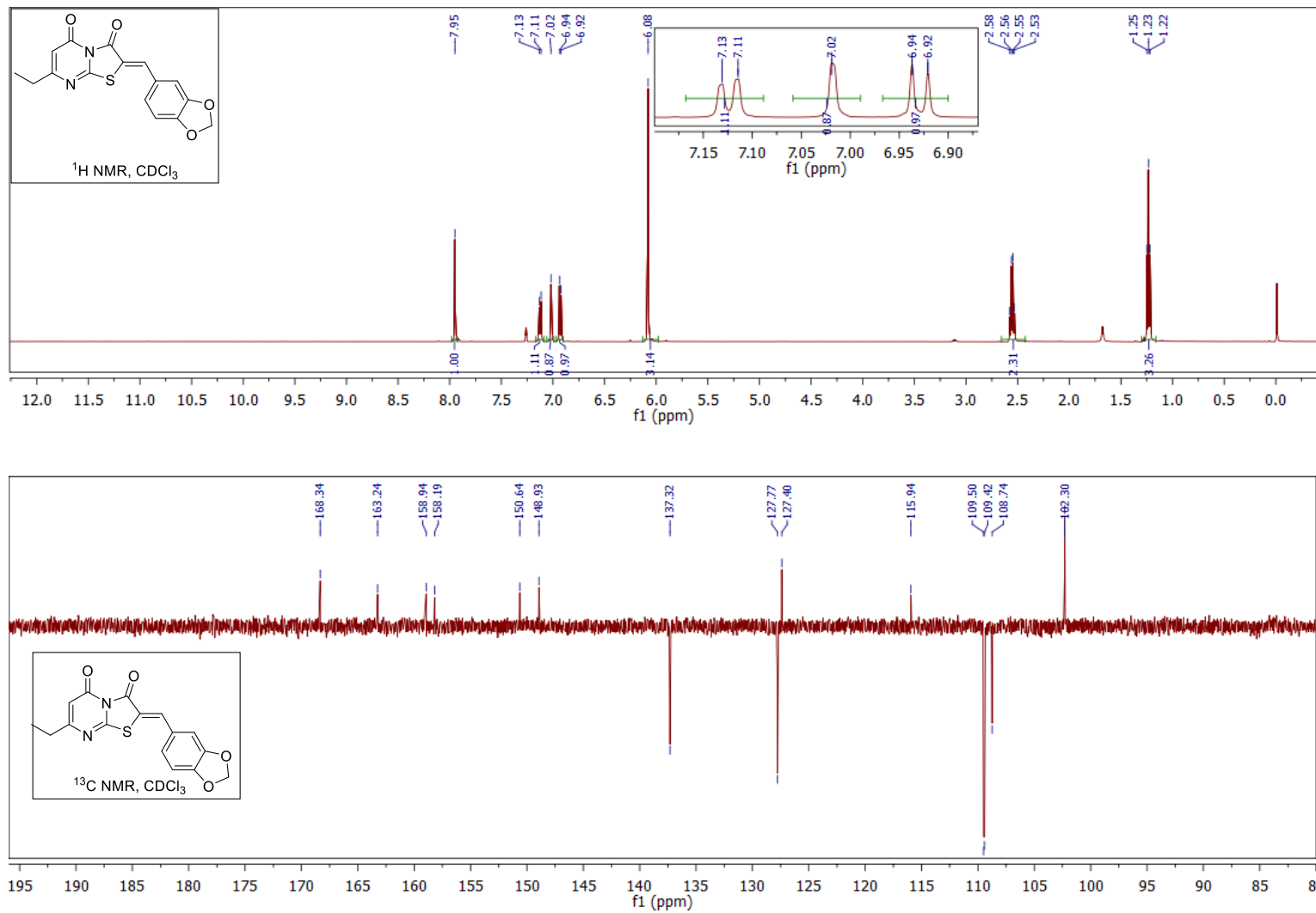
Appendix A for Chapter 2



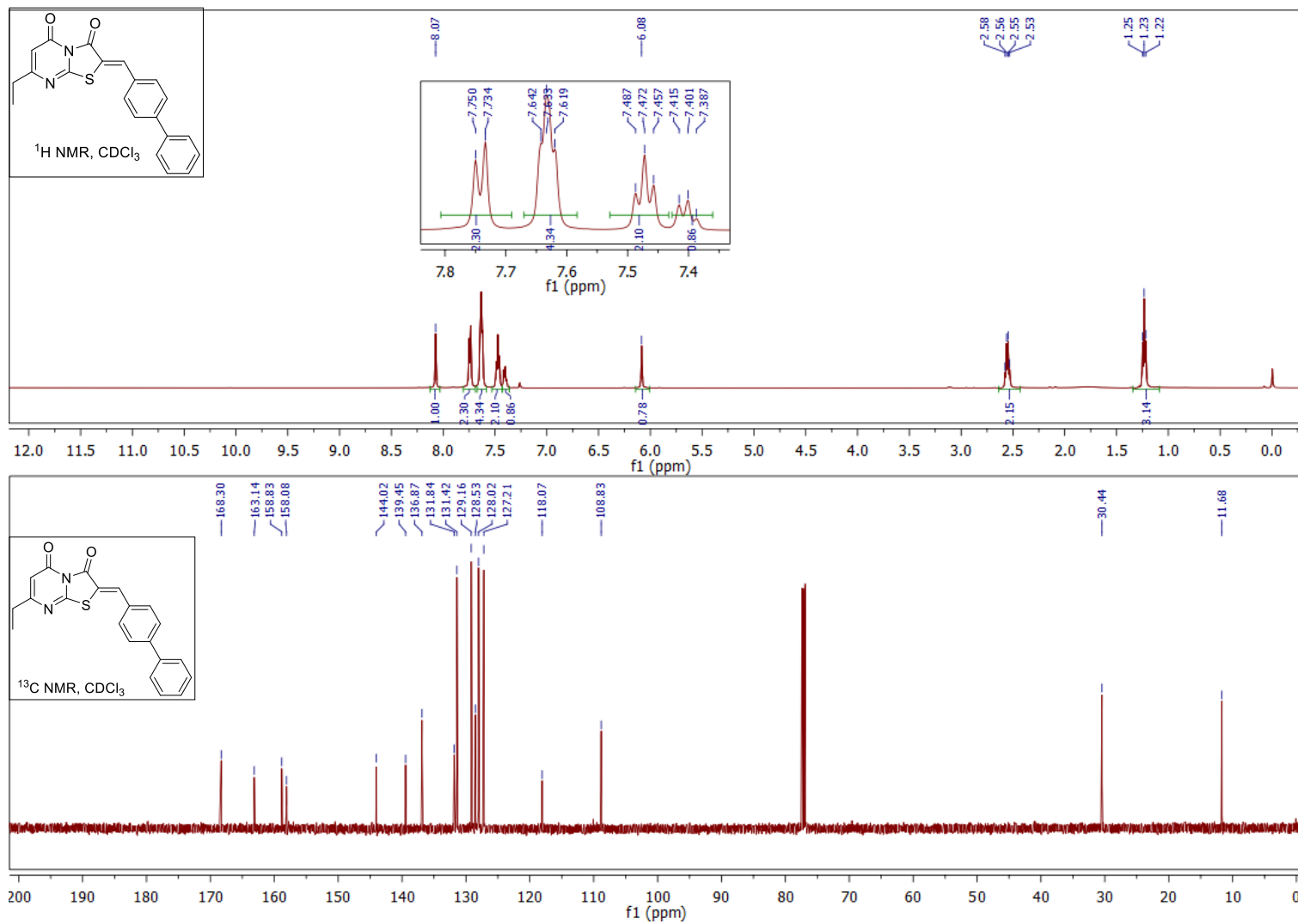


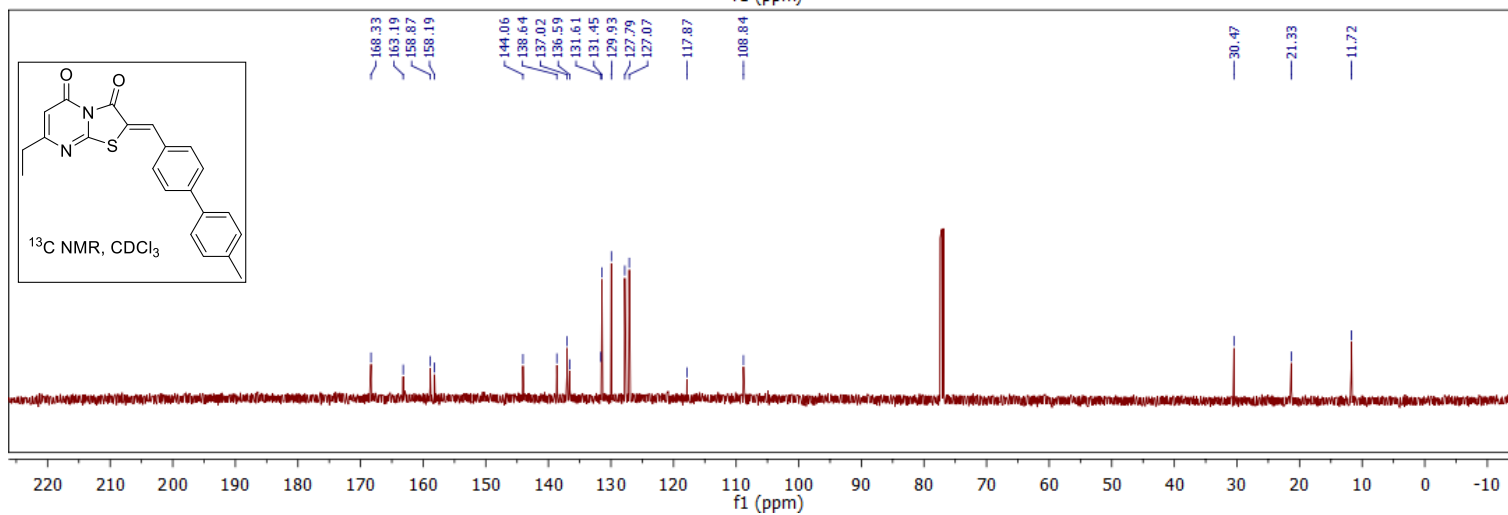
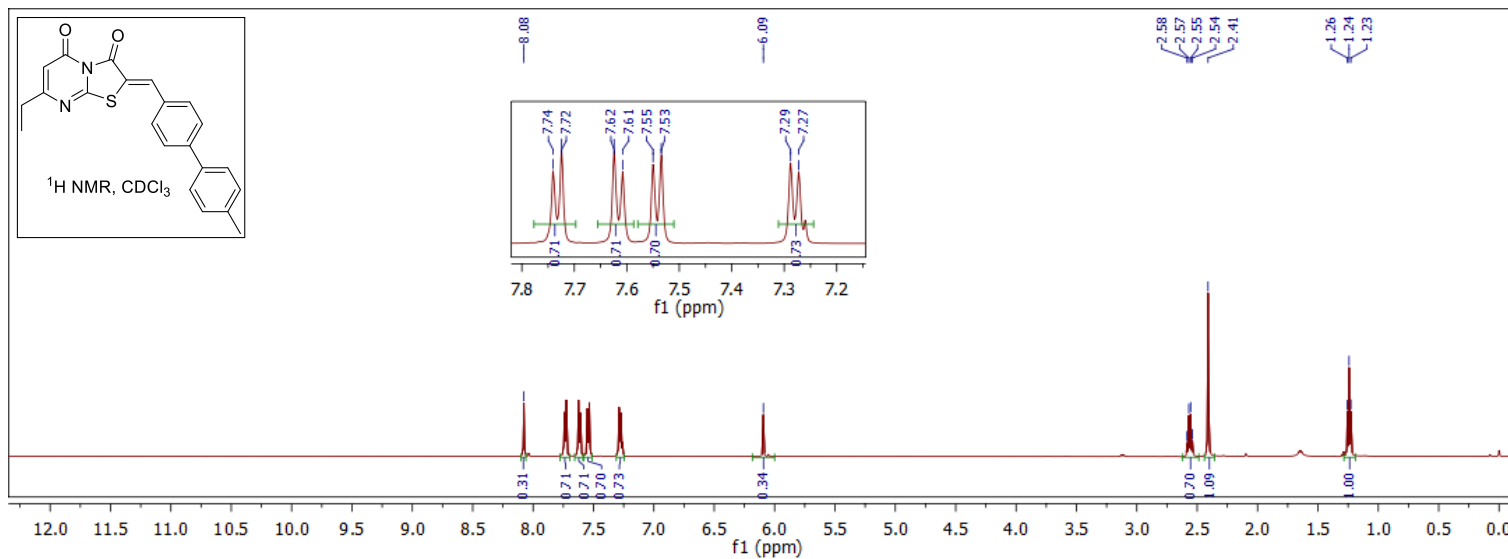
Appendix A for Chapter 2

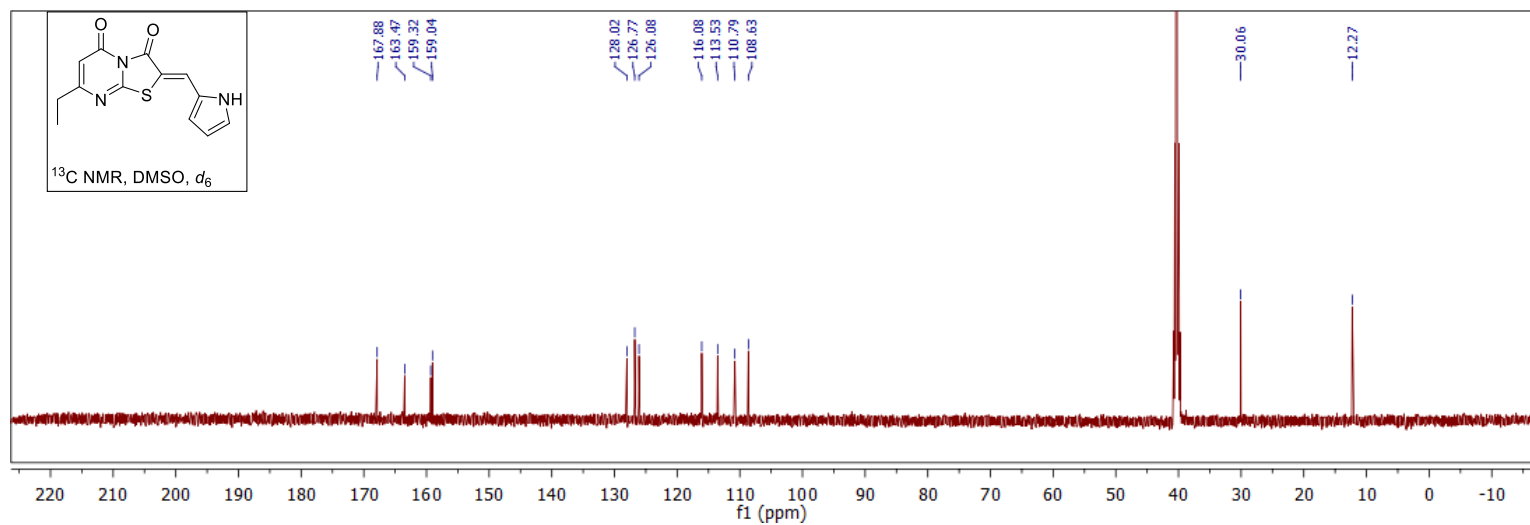
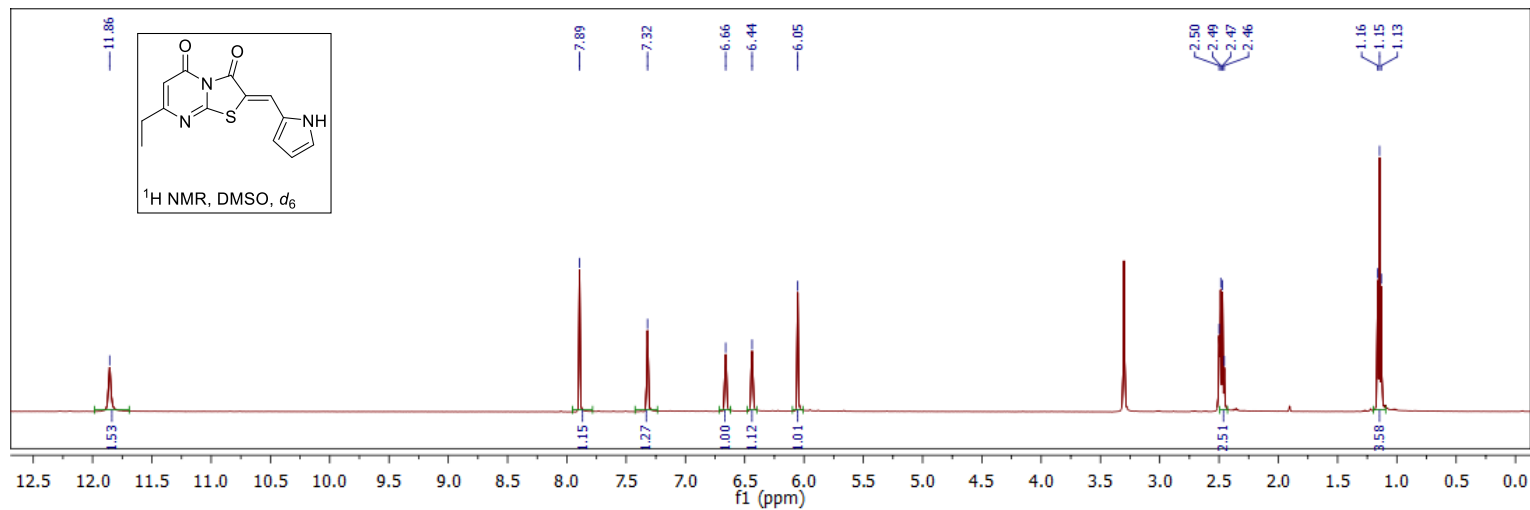


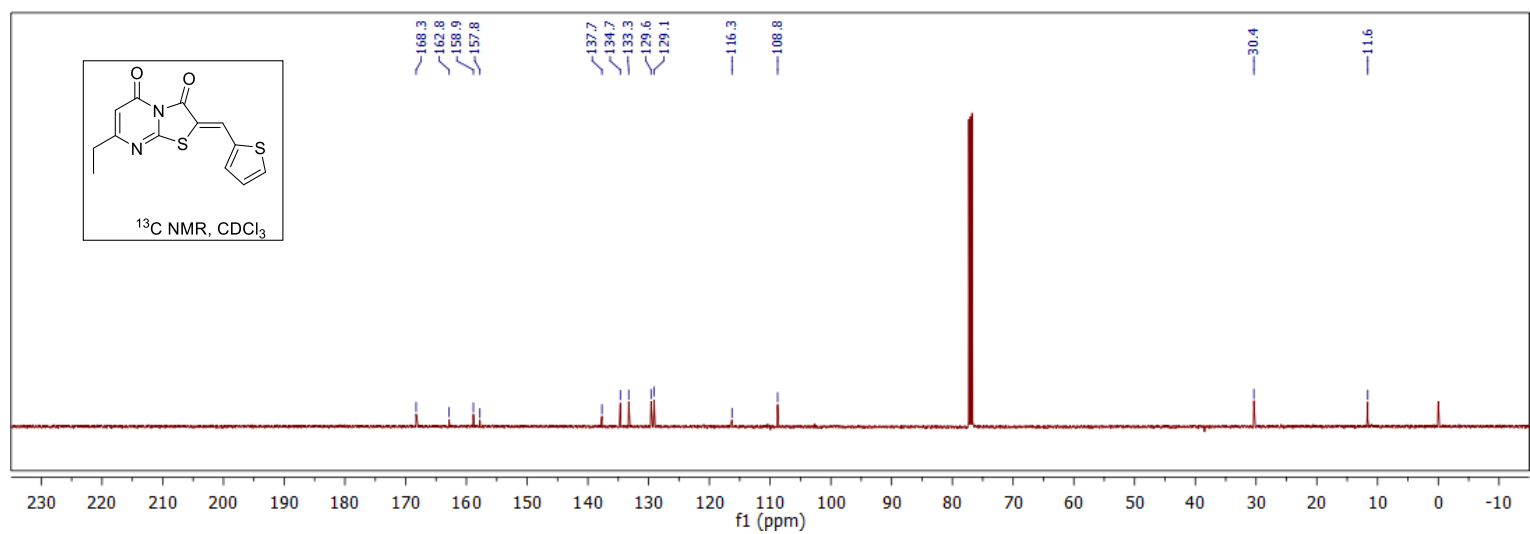
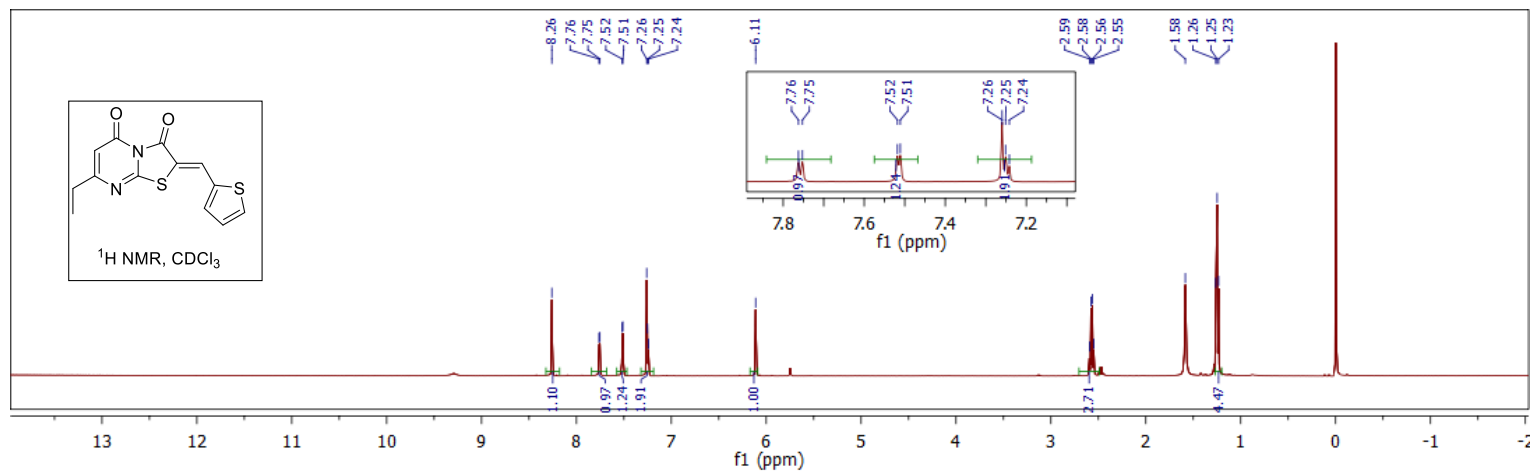


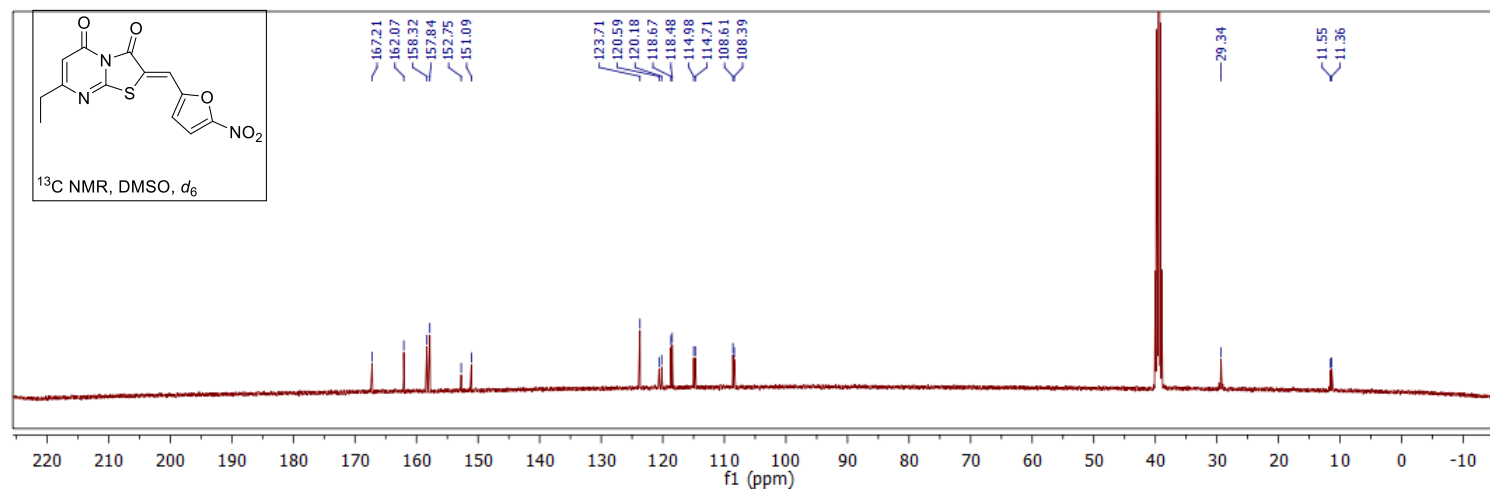
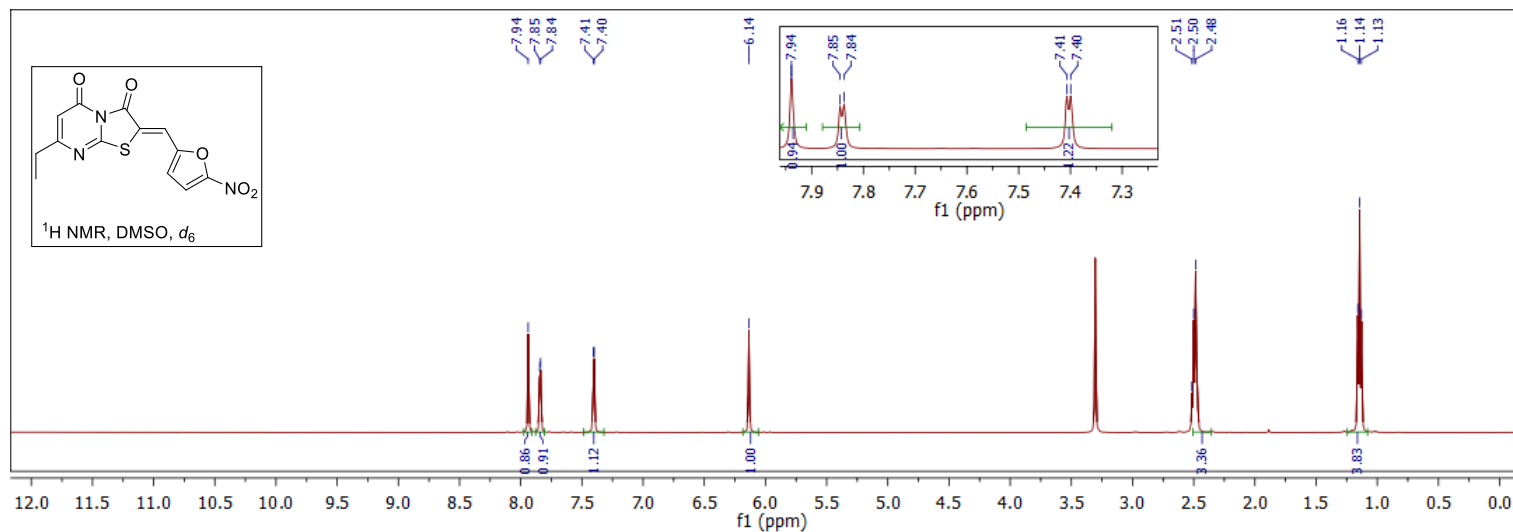
Appendix A for Chapter 2

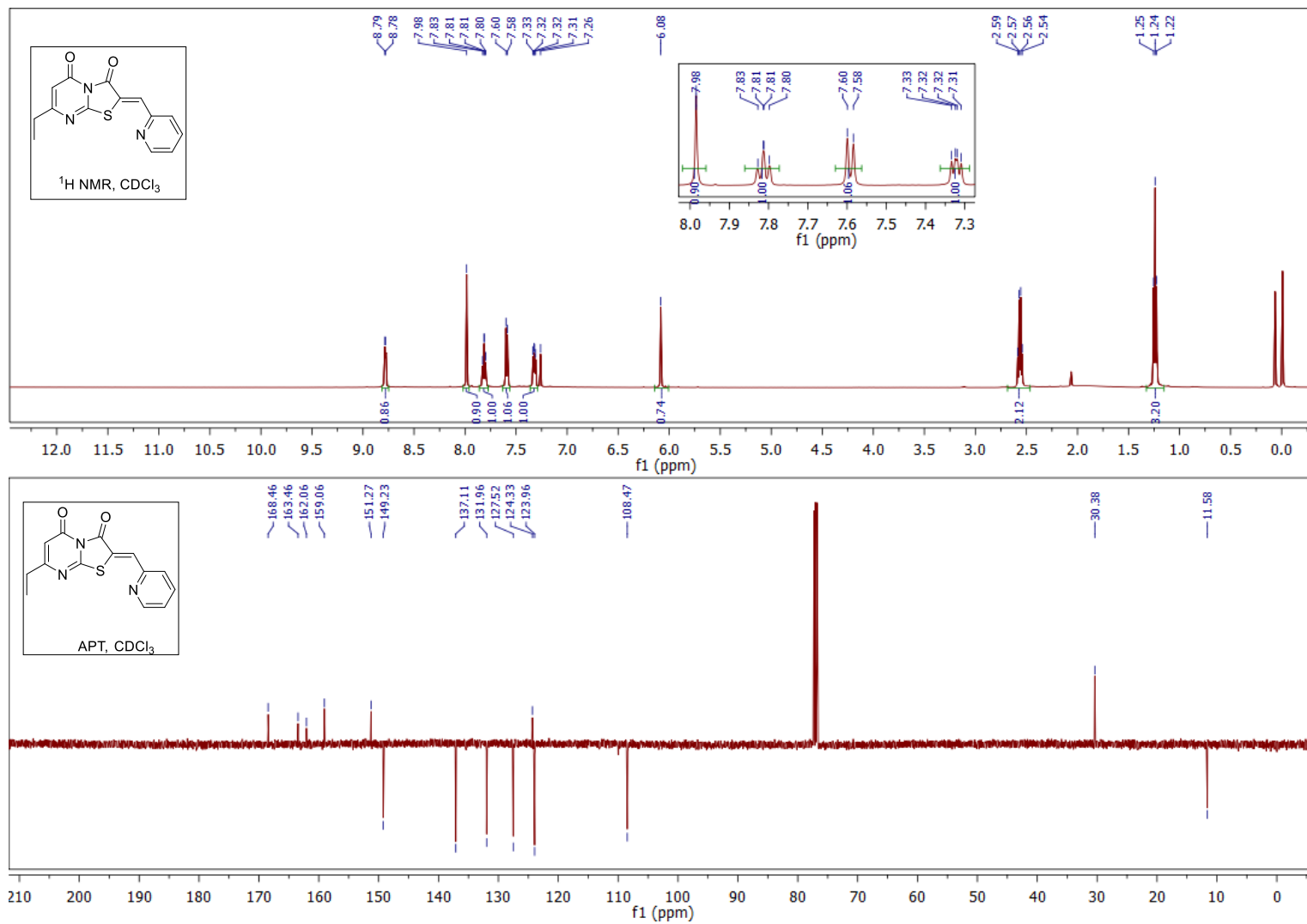




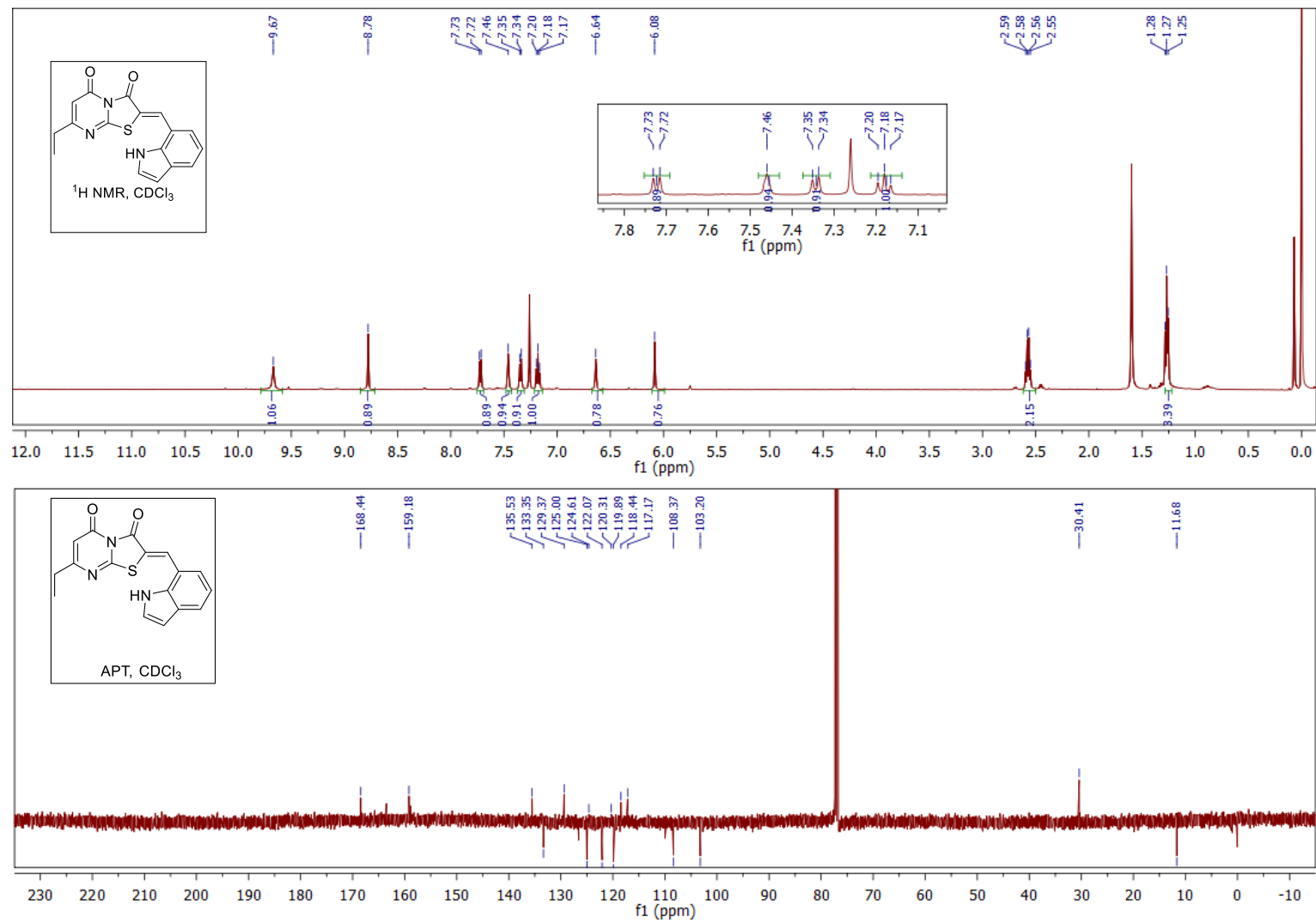






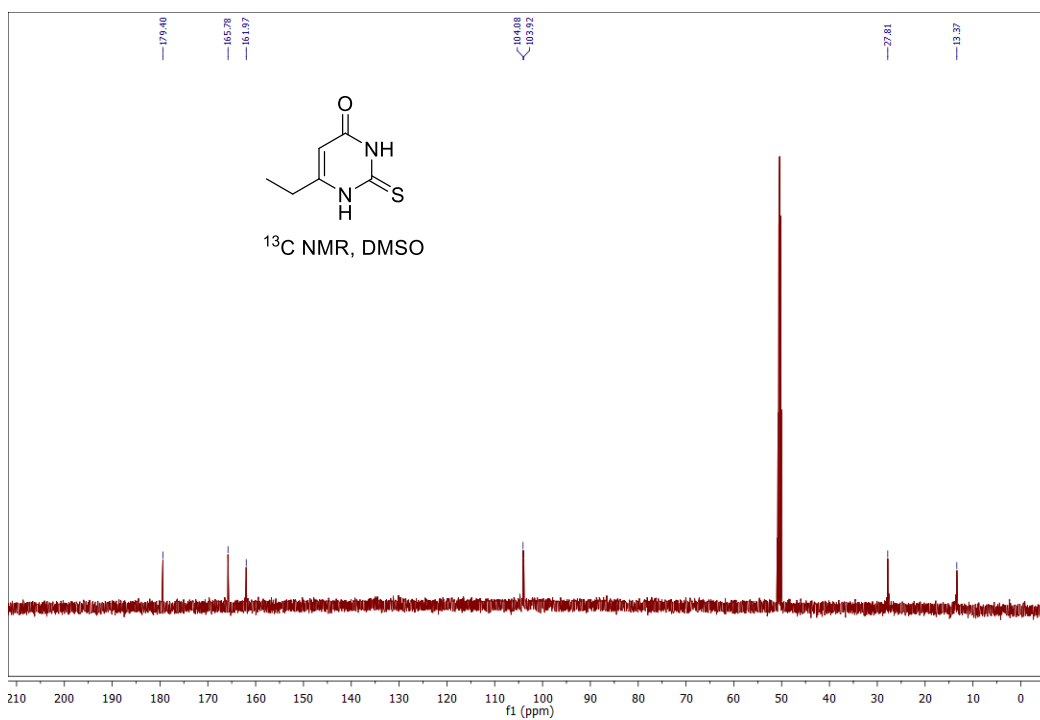
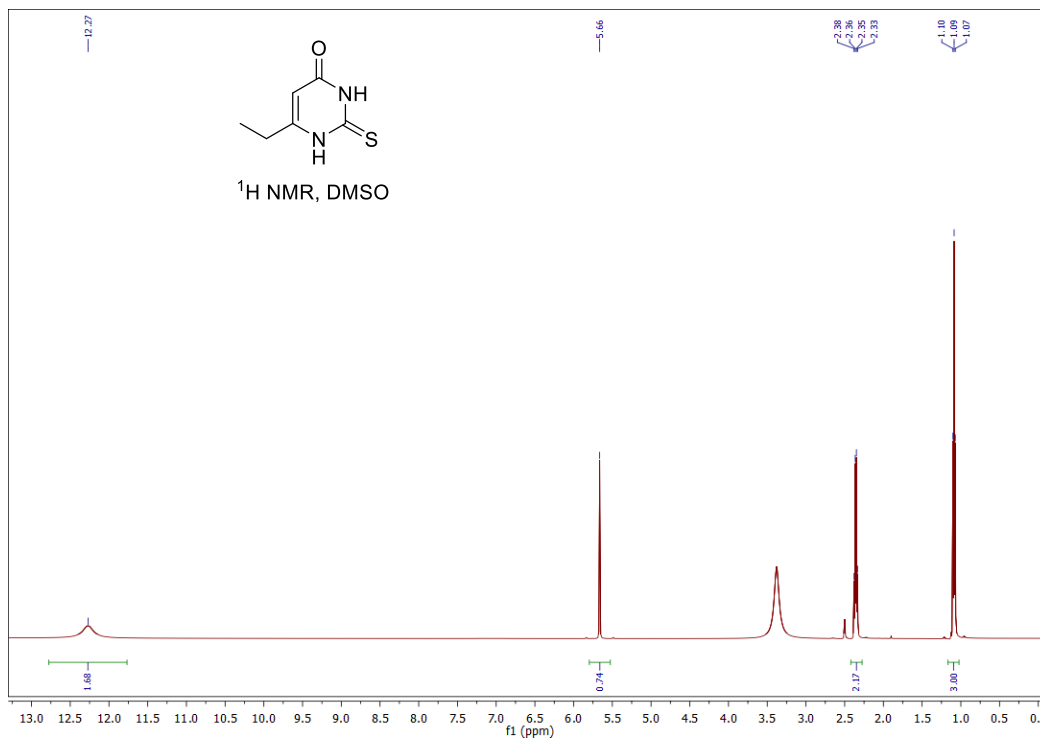


Appendix A for Chapter 2

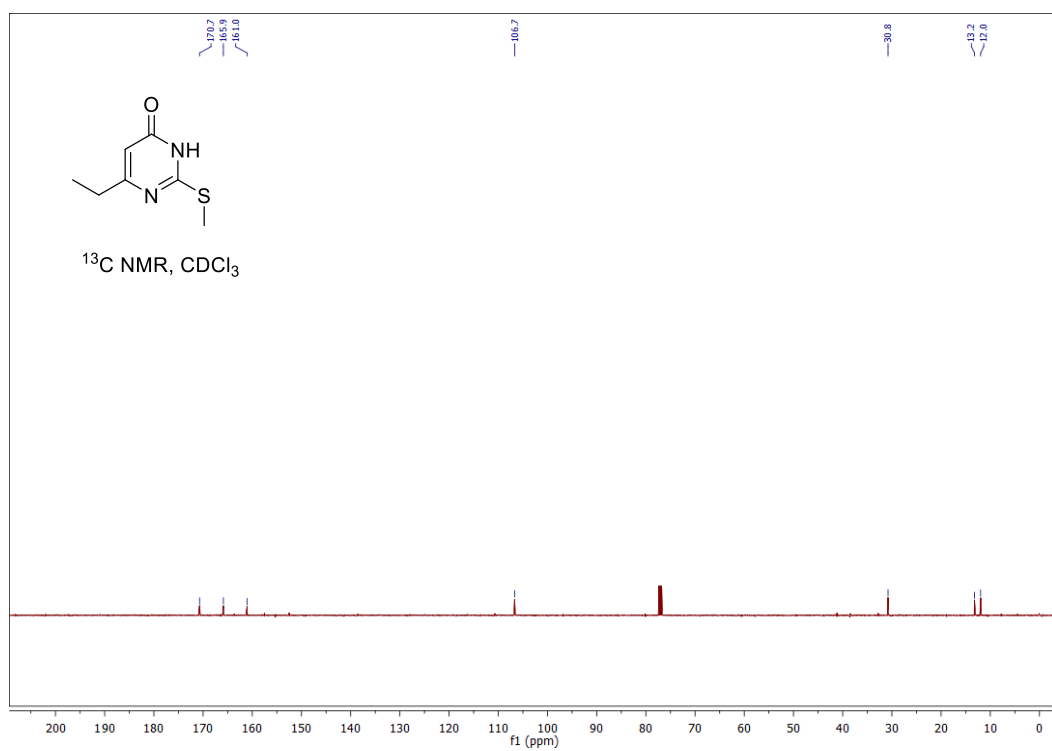
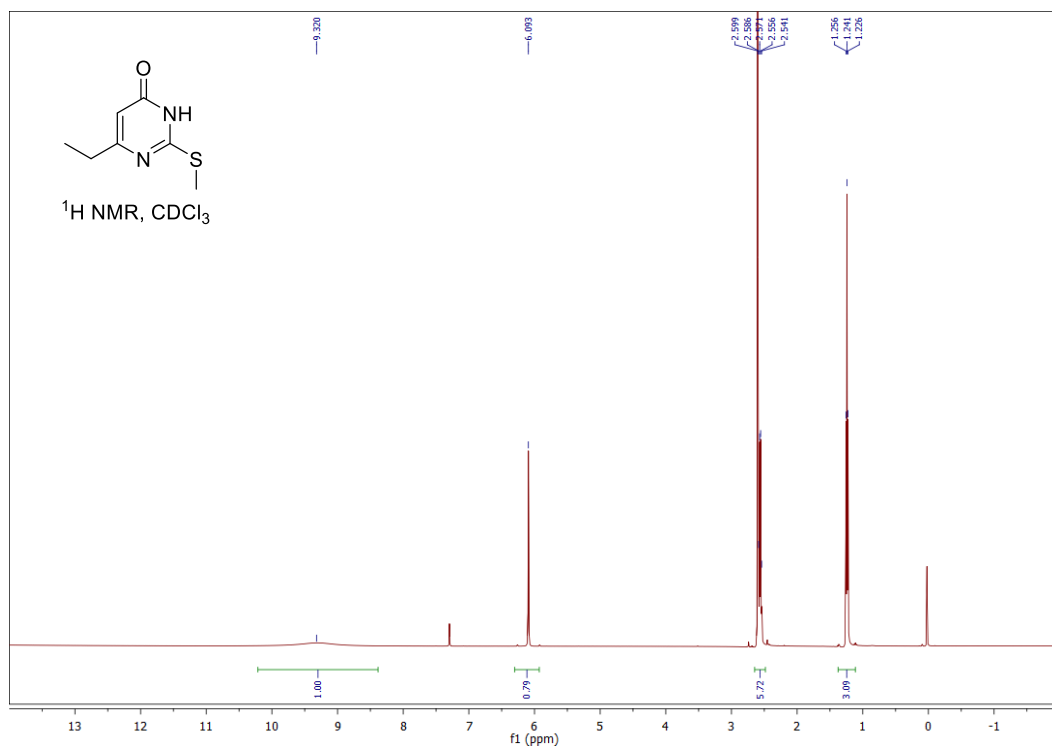


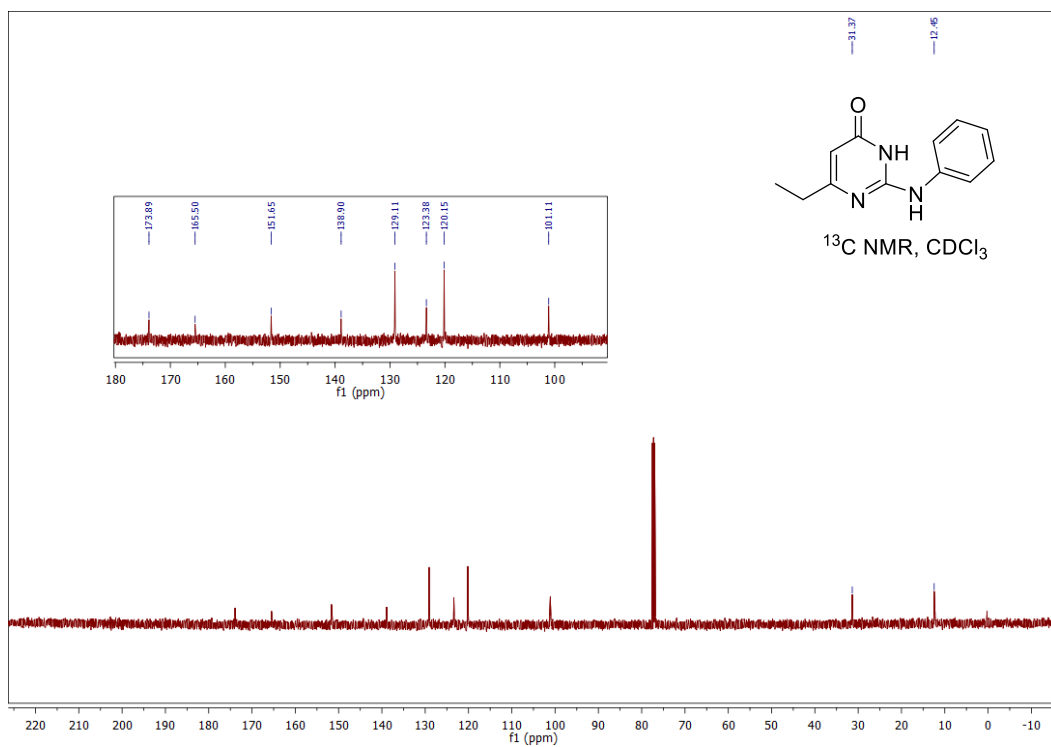
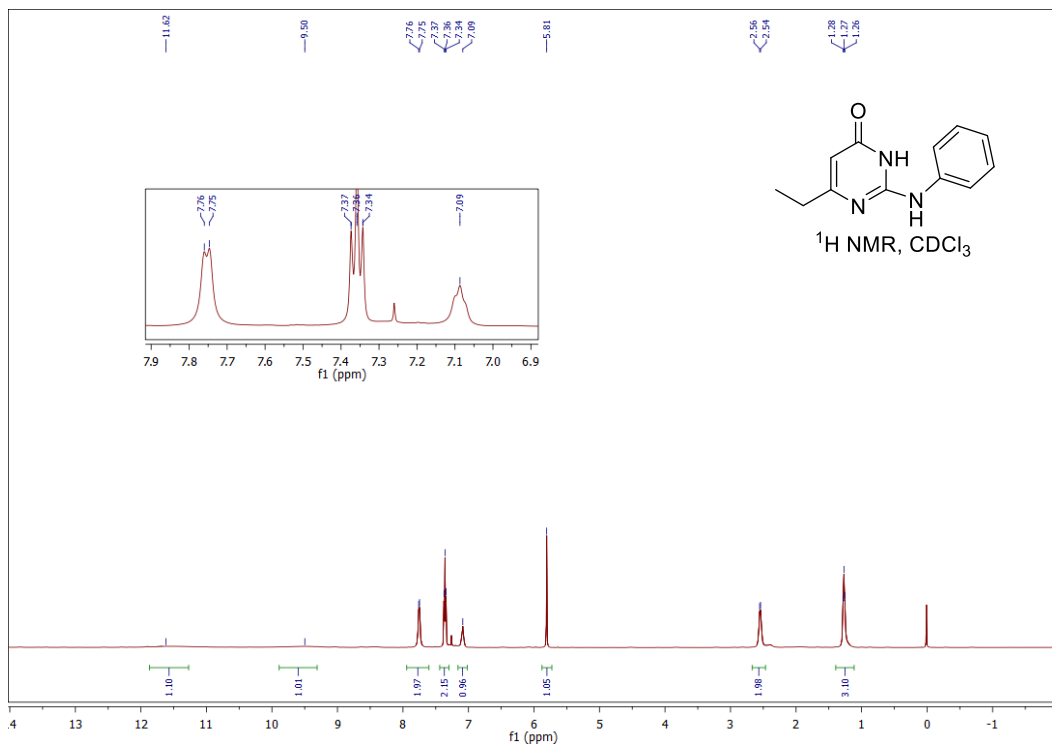
Appendix B: Supplementary Information to Chapter 3

NMR spectra of compounds from chapter 3

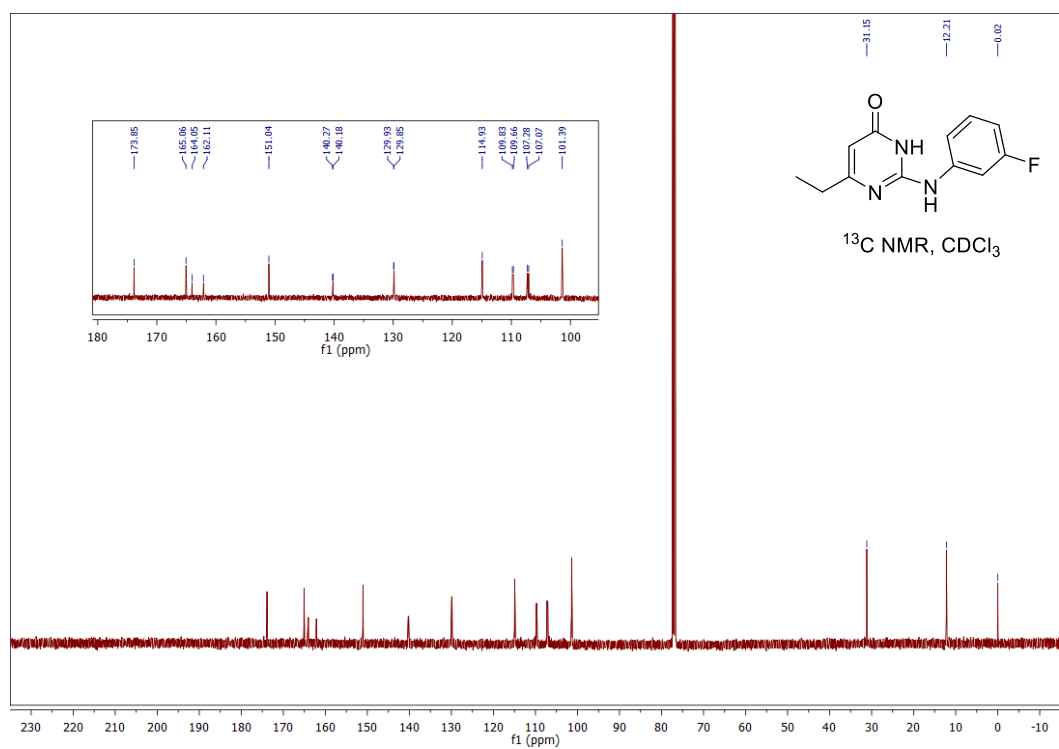
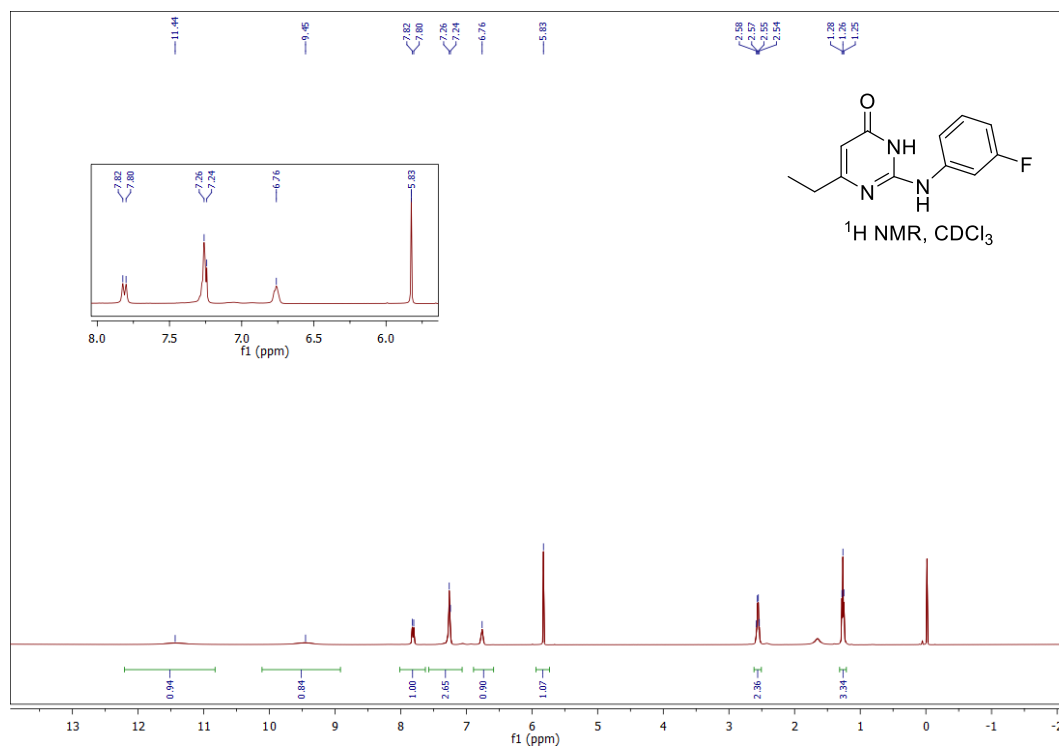


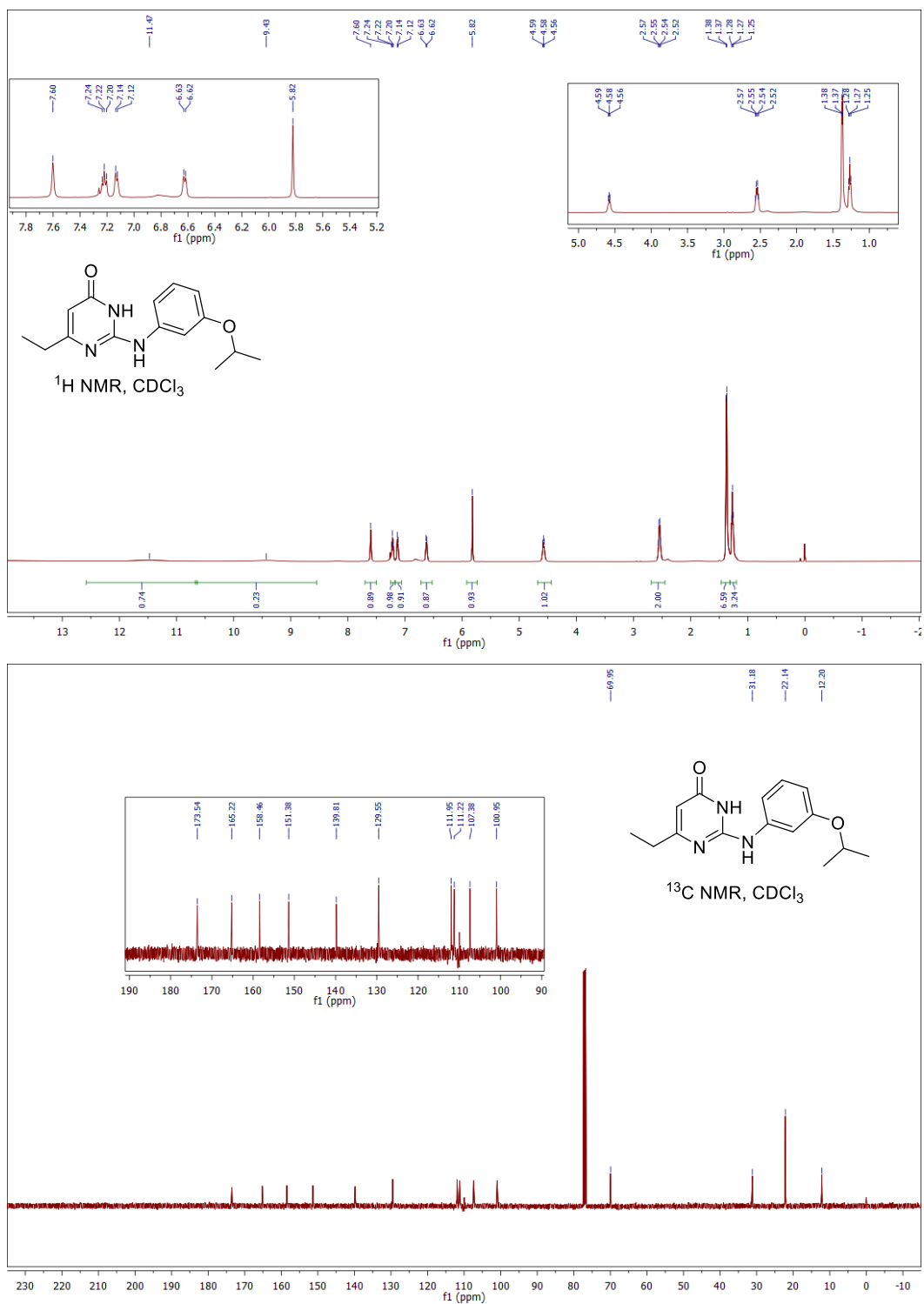
Appendix B for Chapter 3



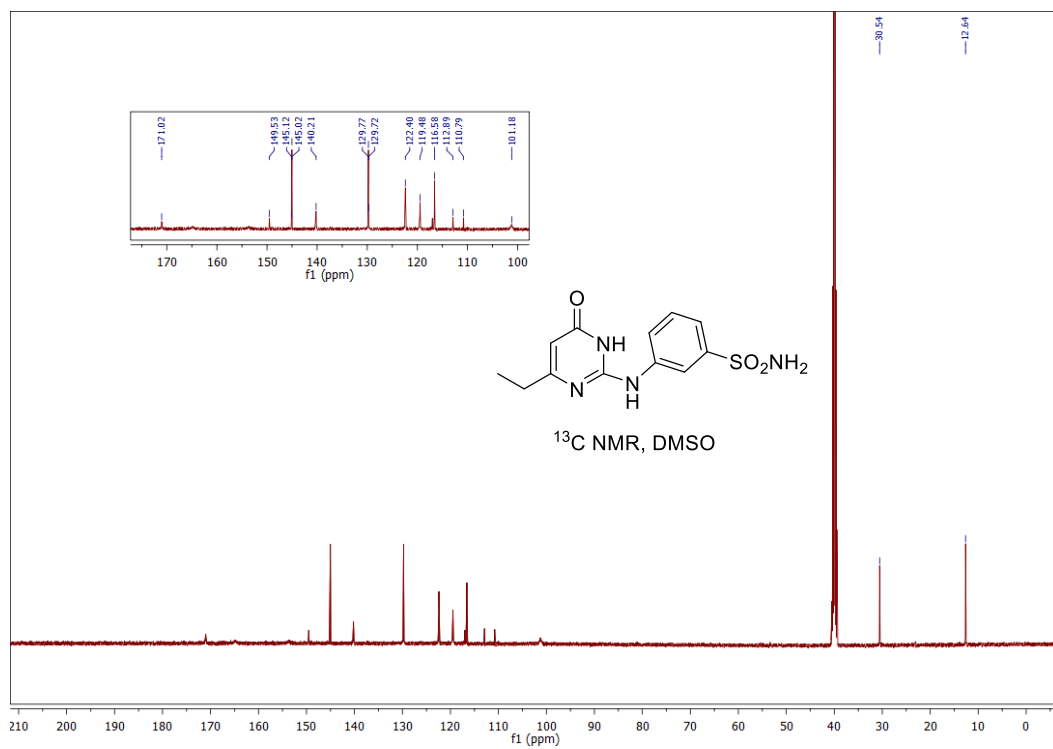
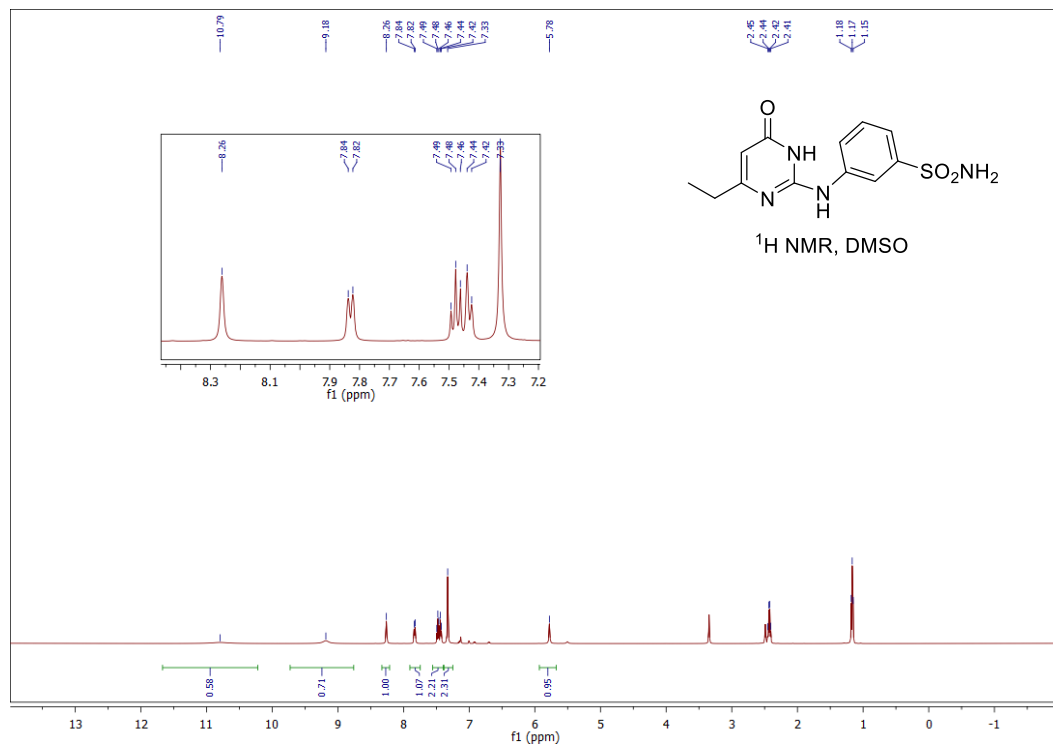


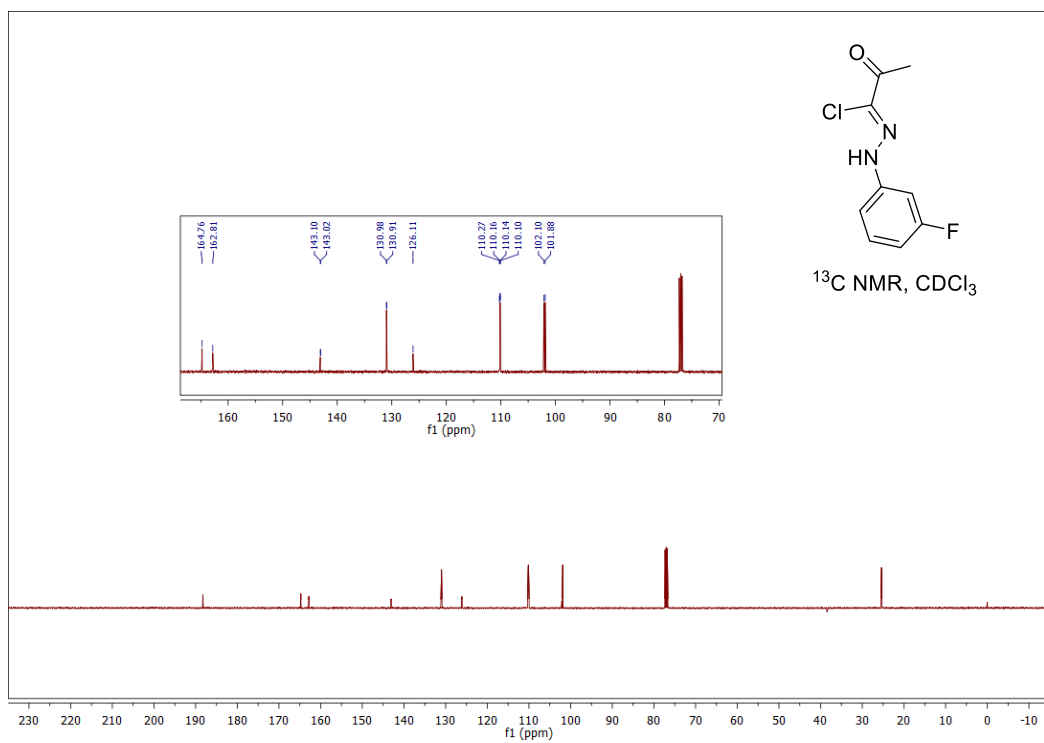
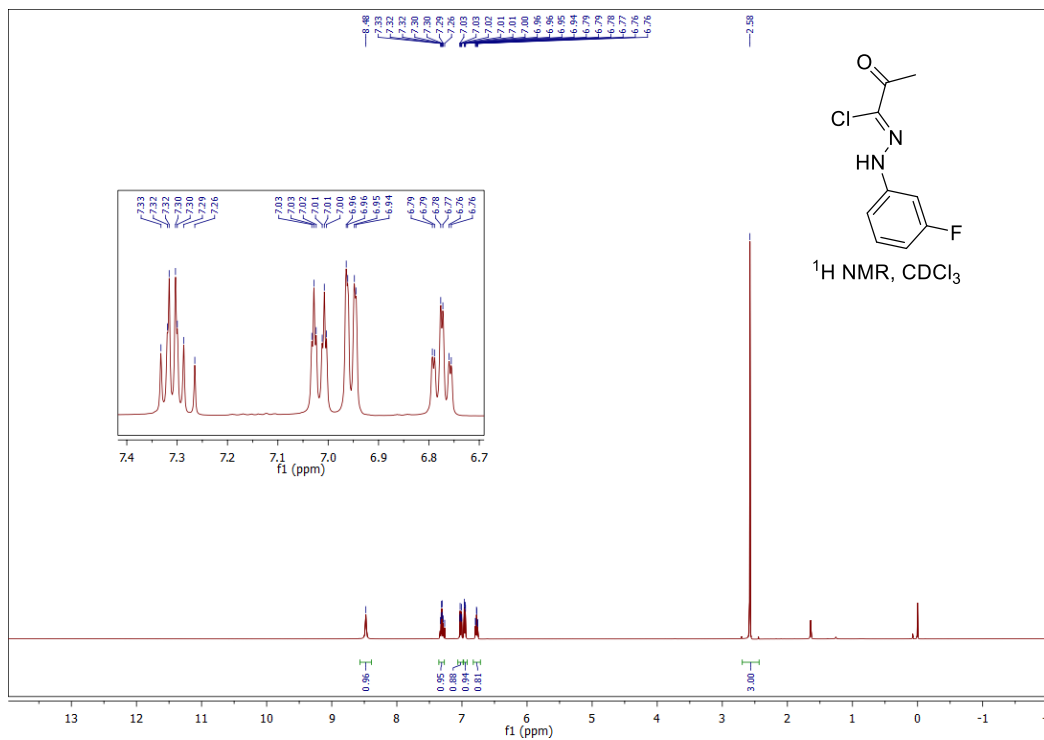
Appendix B for Chapter 3



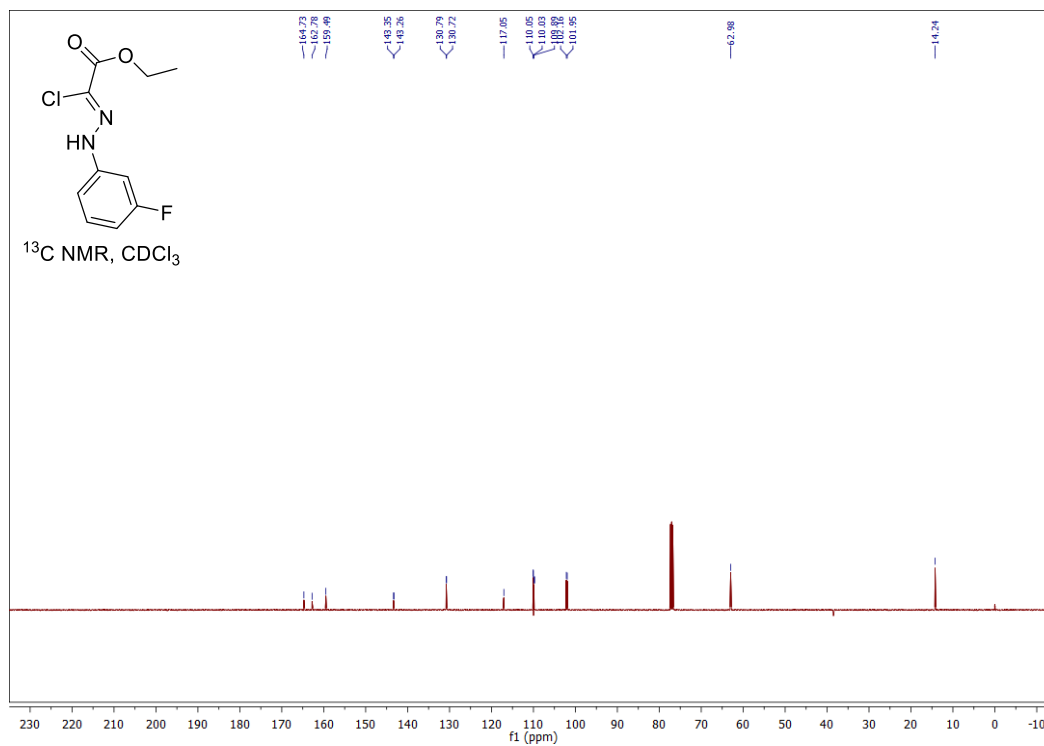
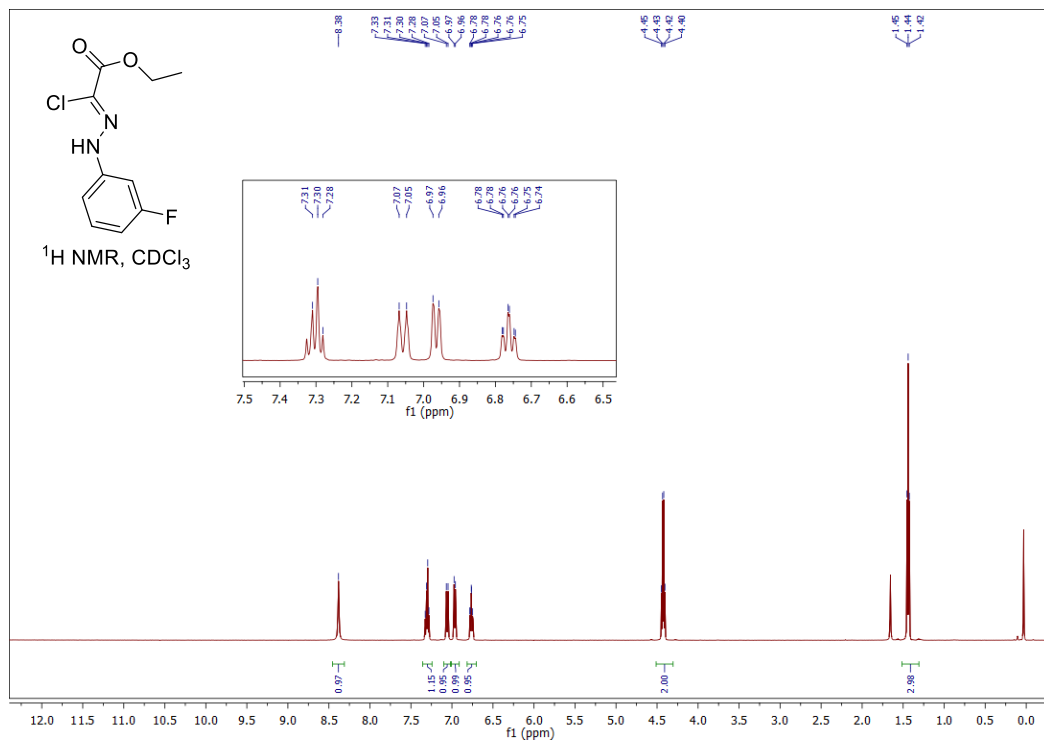


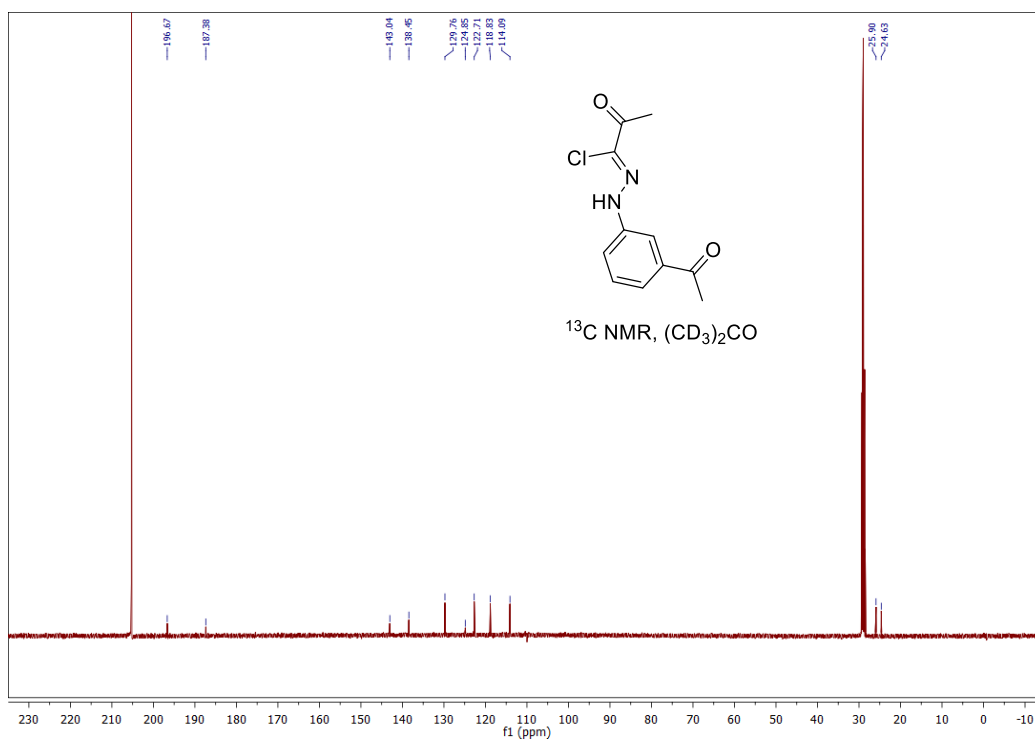
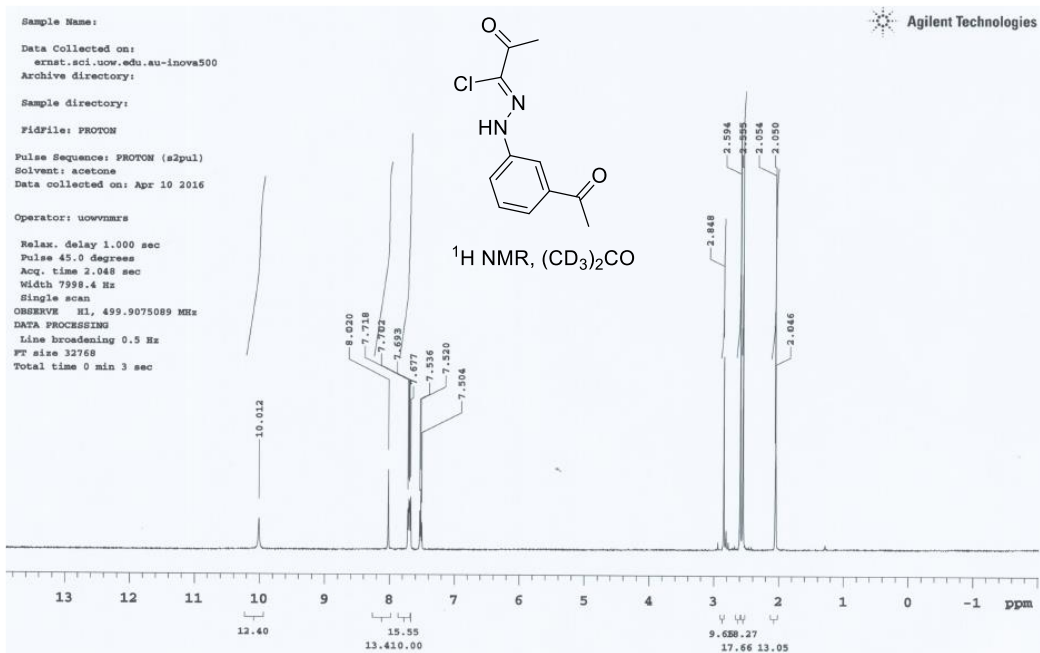
Appendix B for Chapter 3



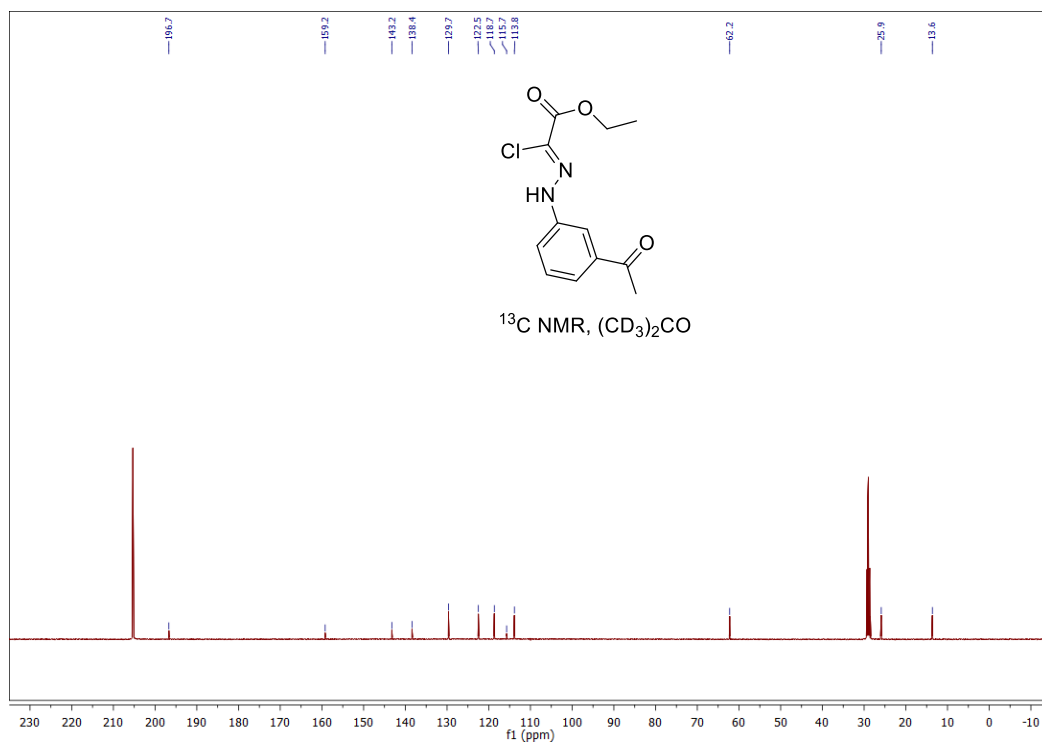
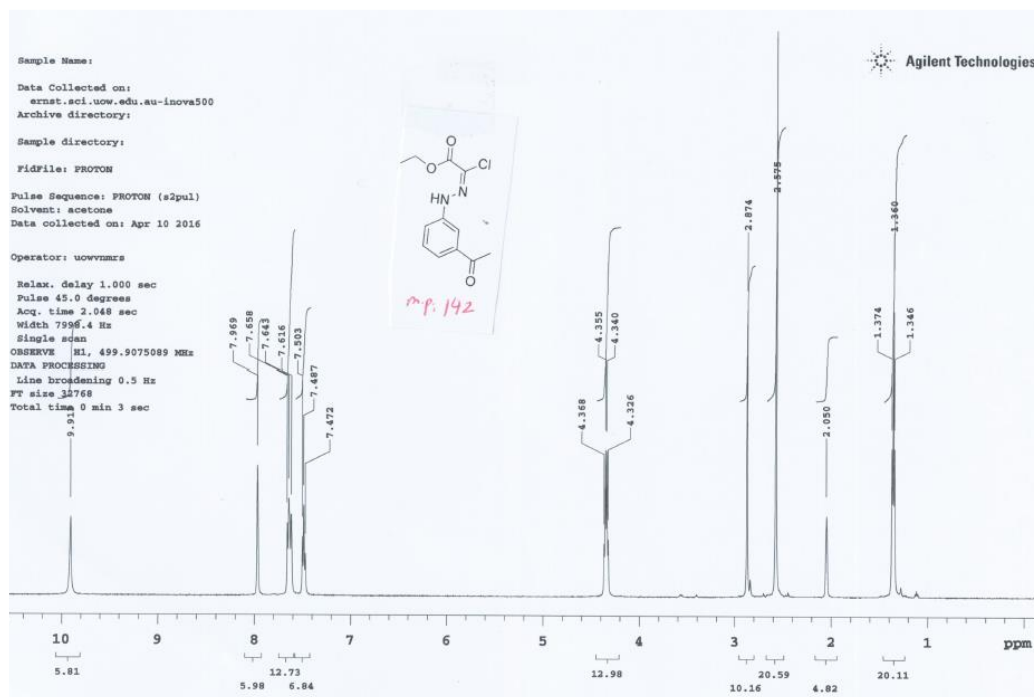


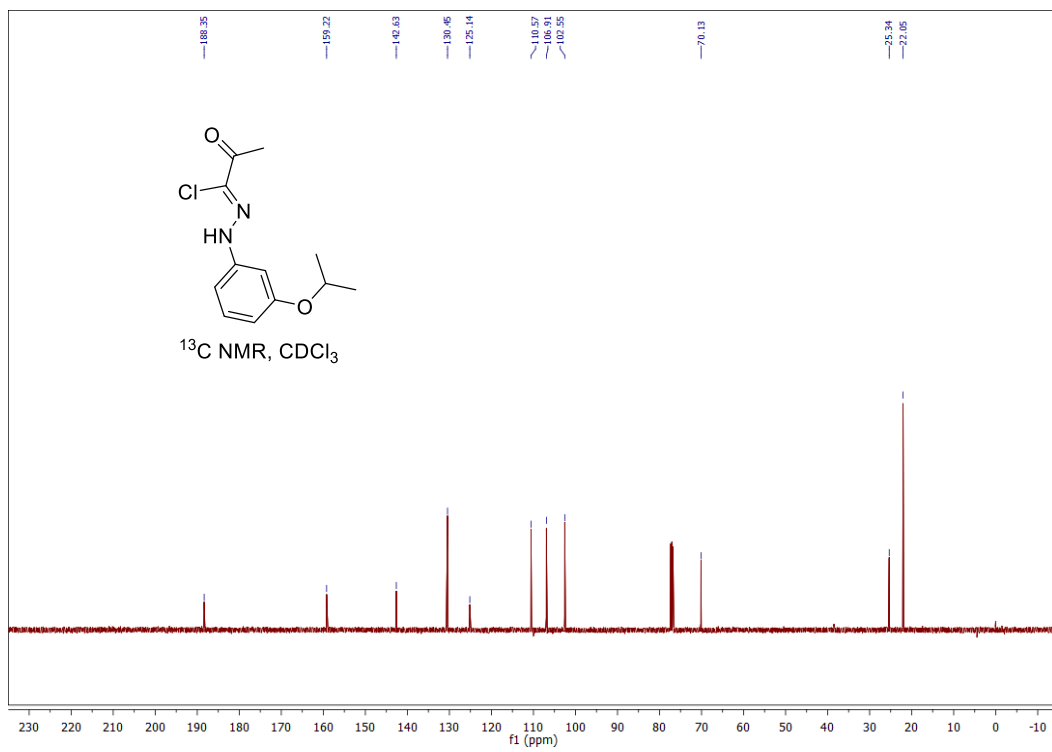
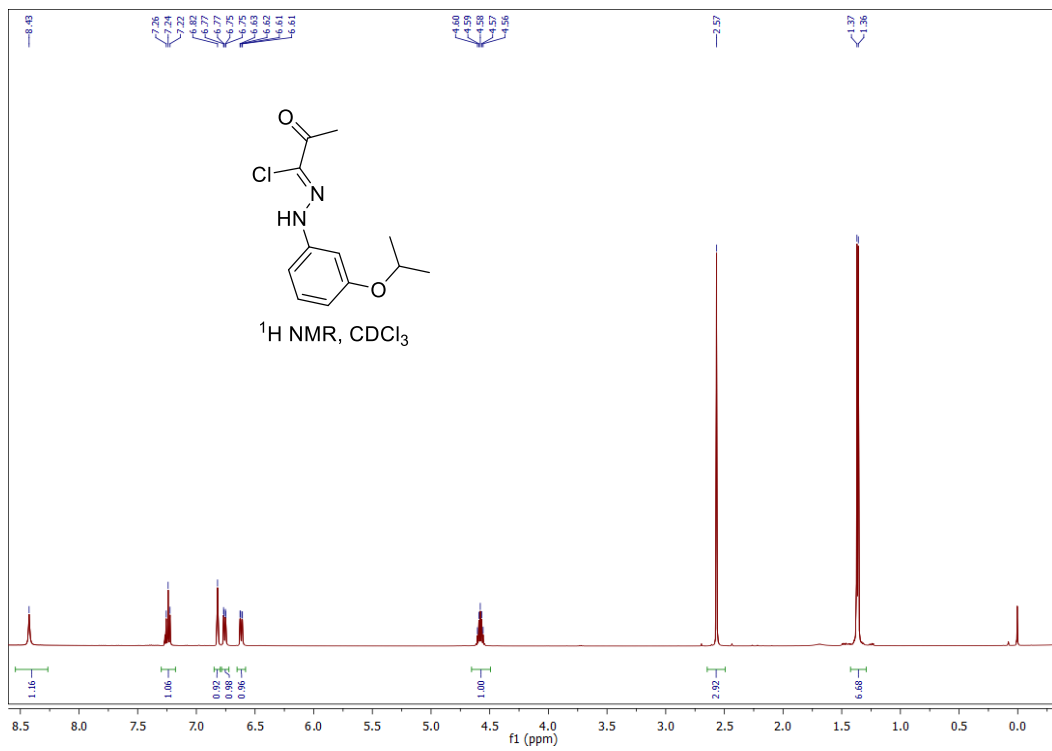
Appendix B for Chapter 3

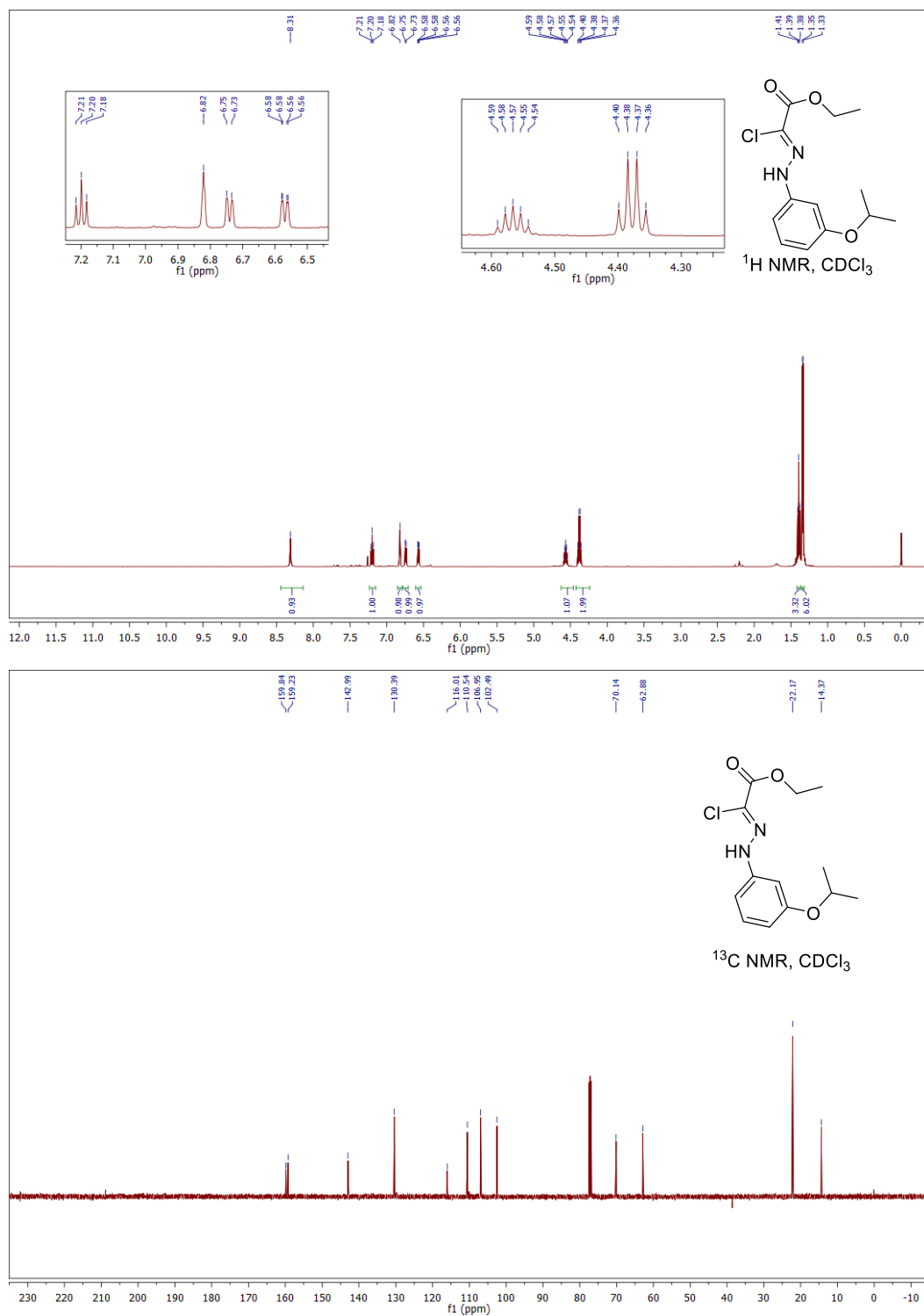


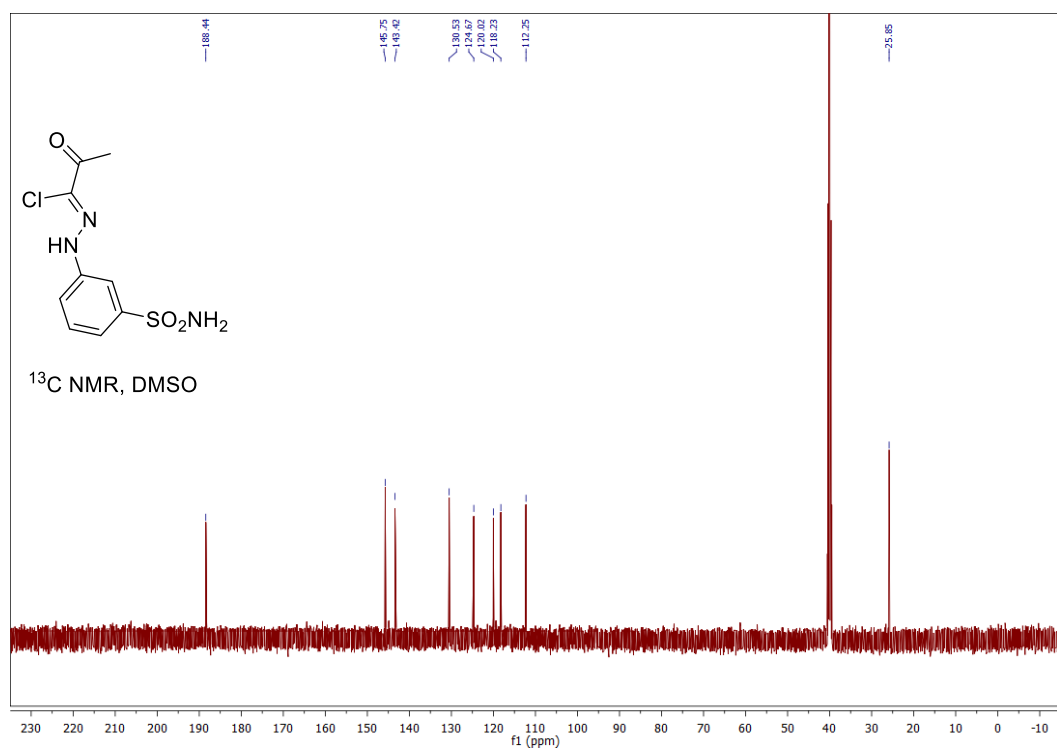
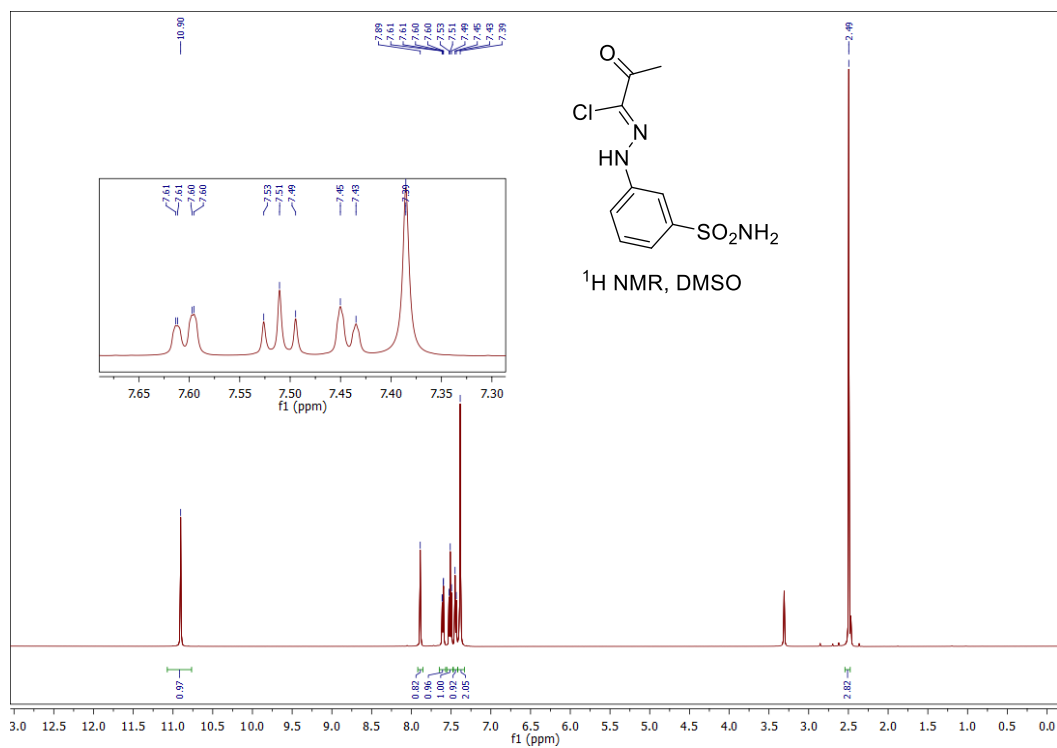


Appendix B for Chapter 3

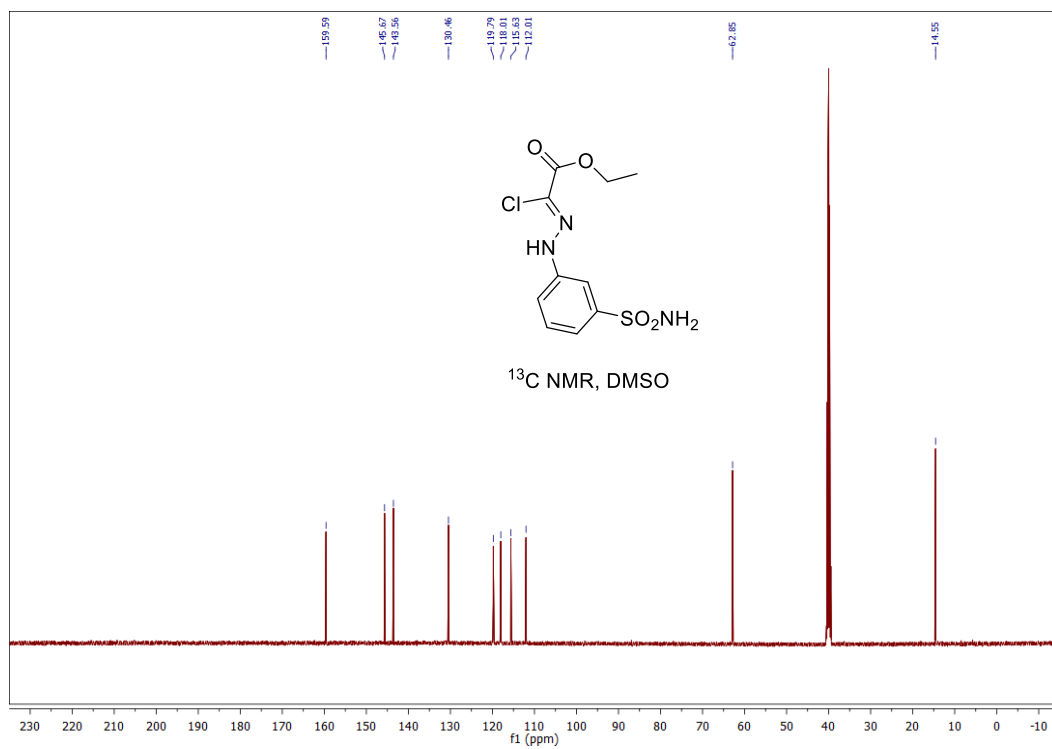
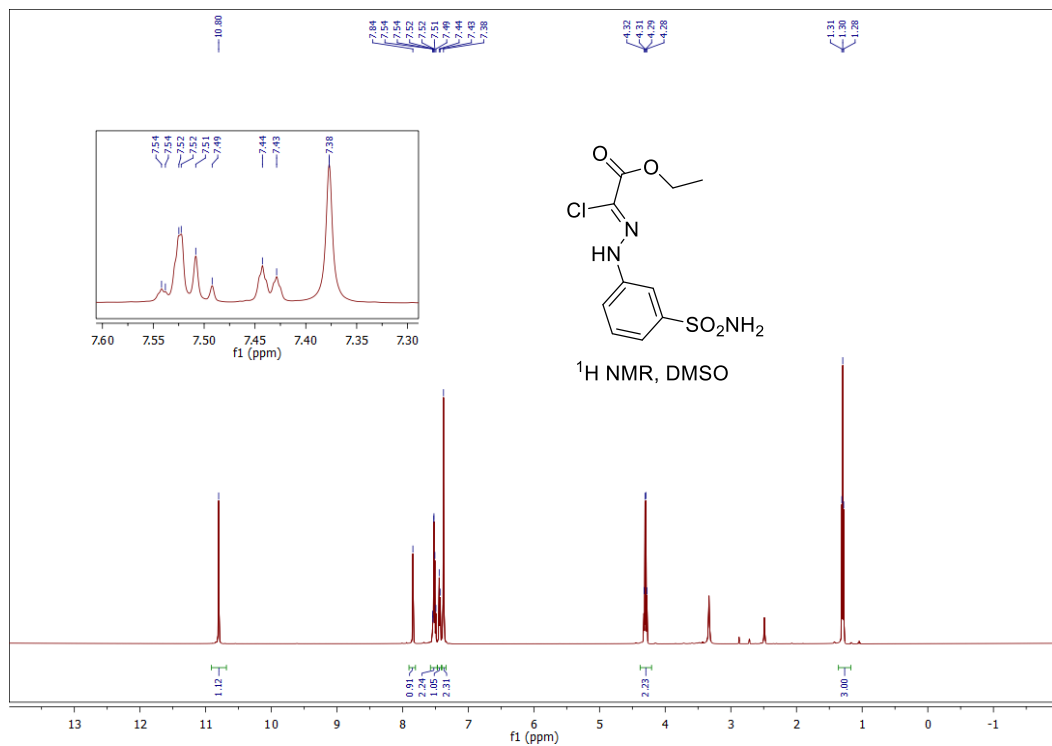


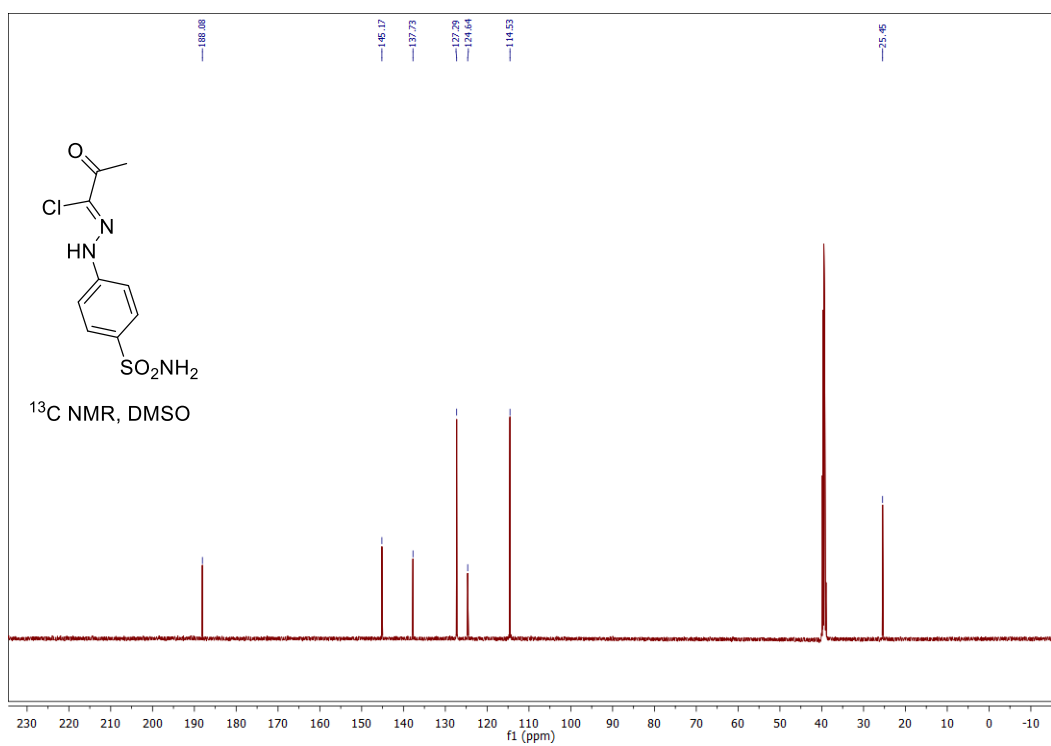
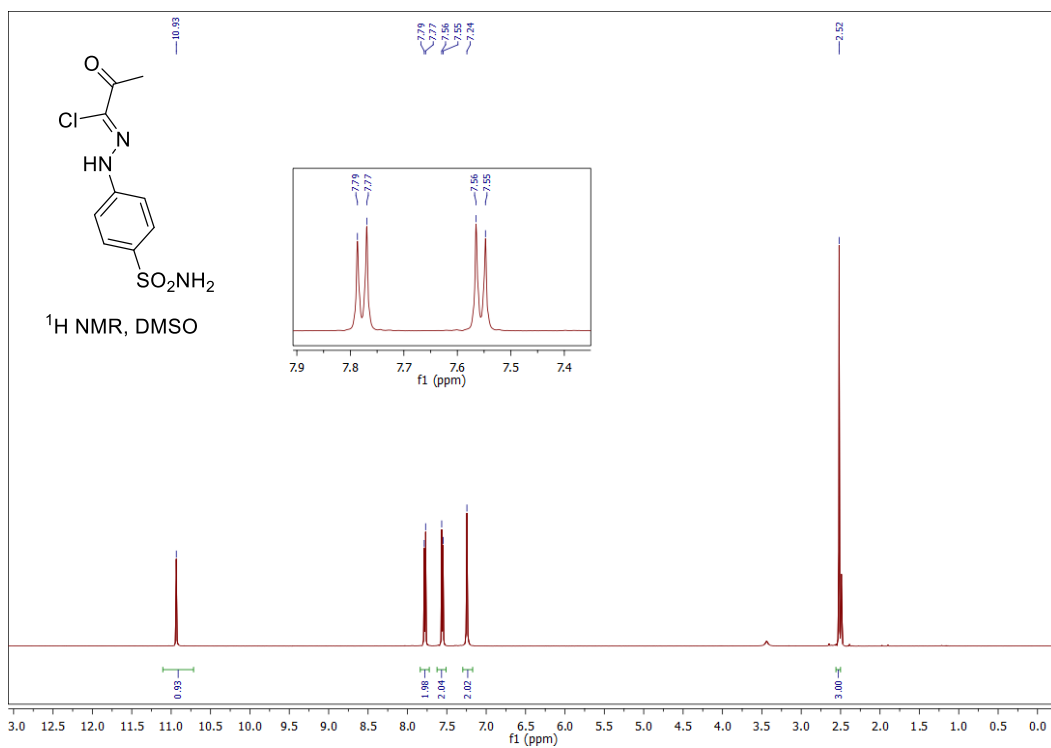




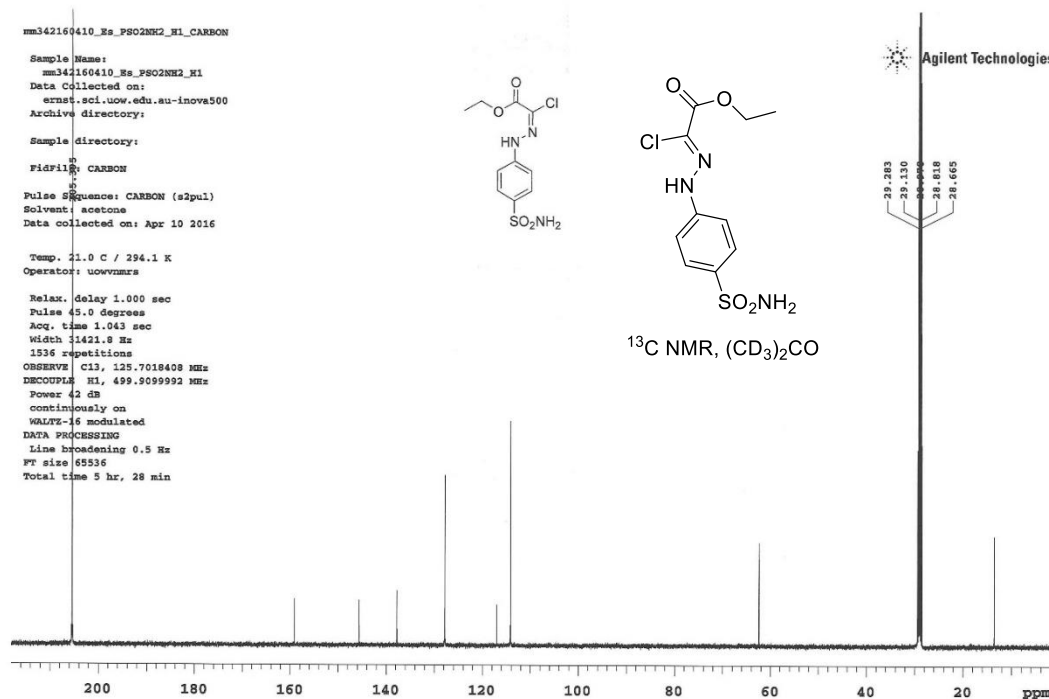
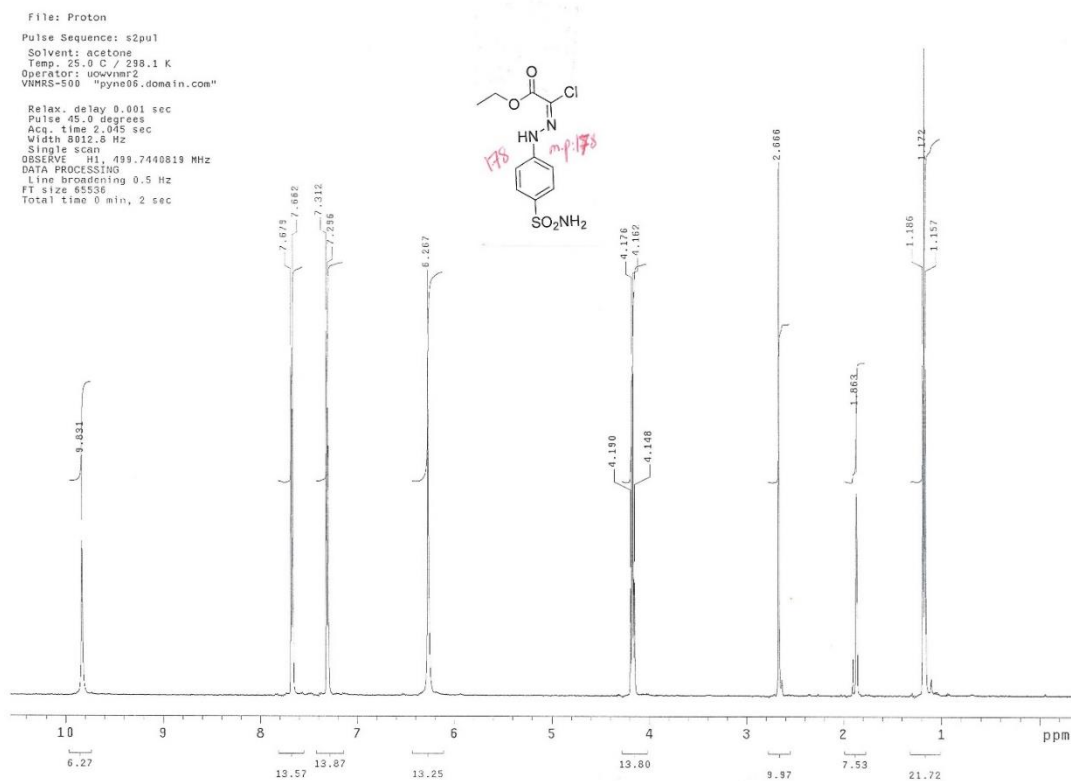


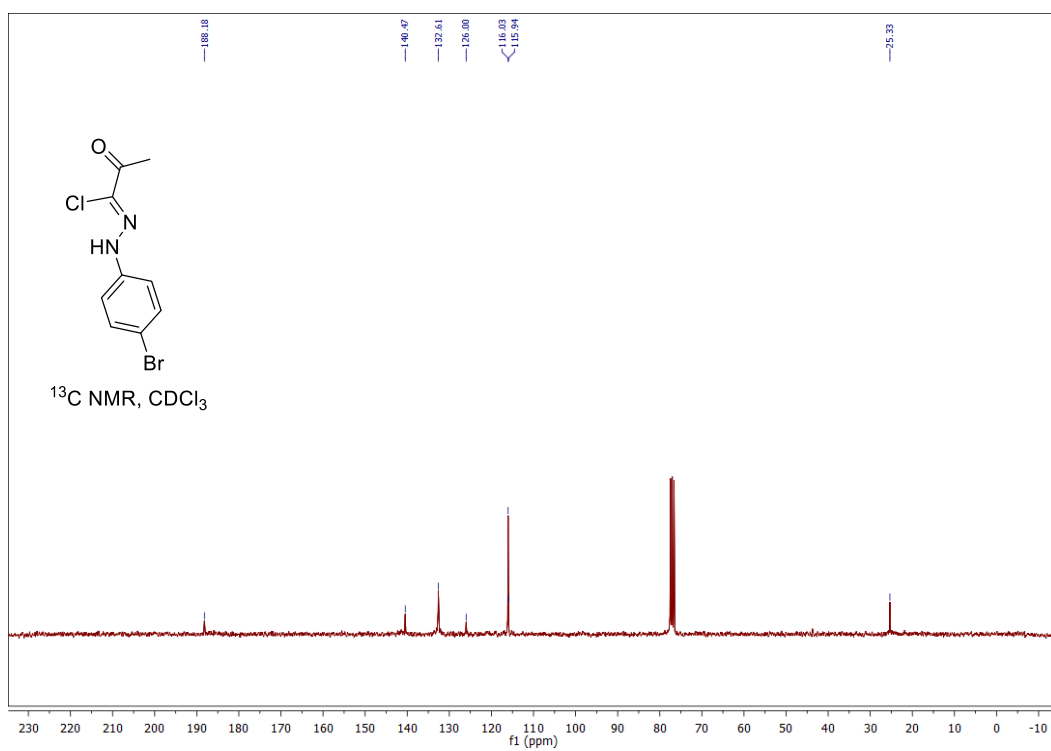
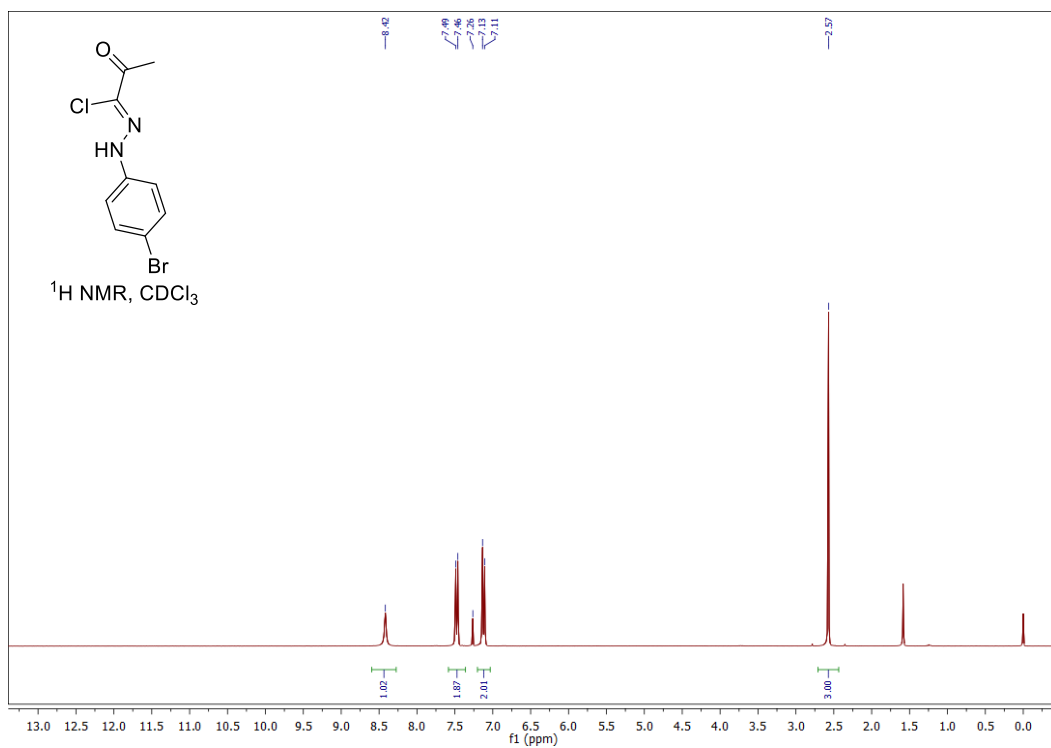
Appendix B for Chapter 3



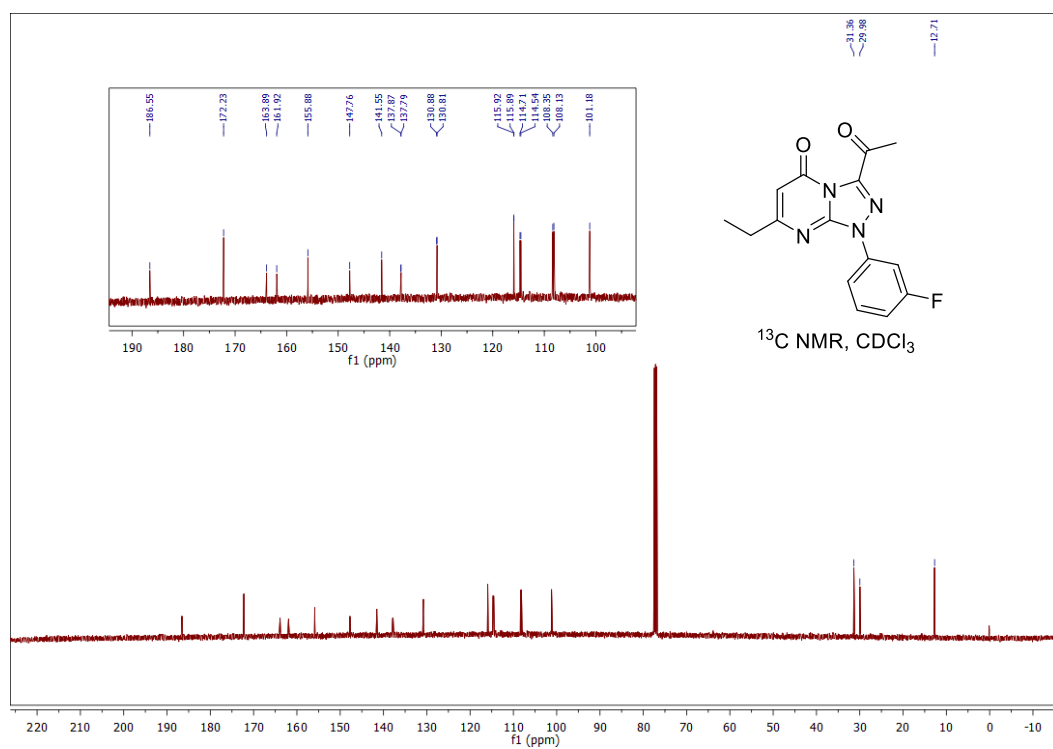
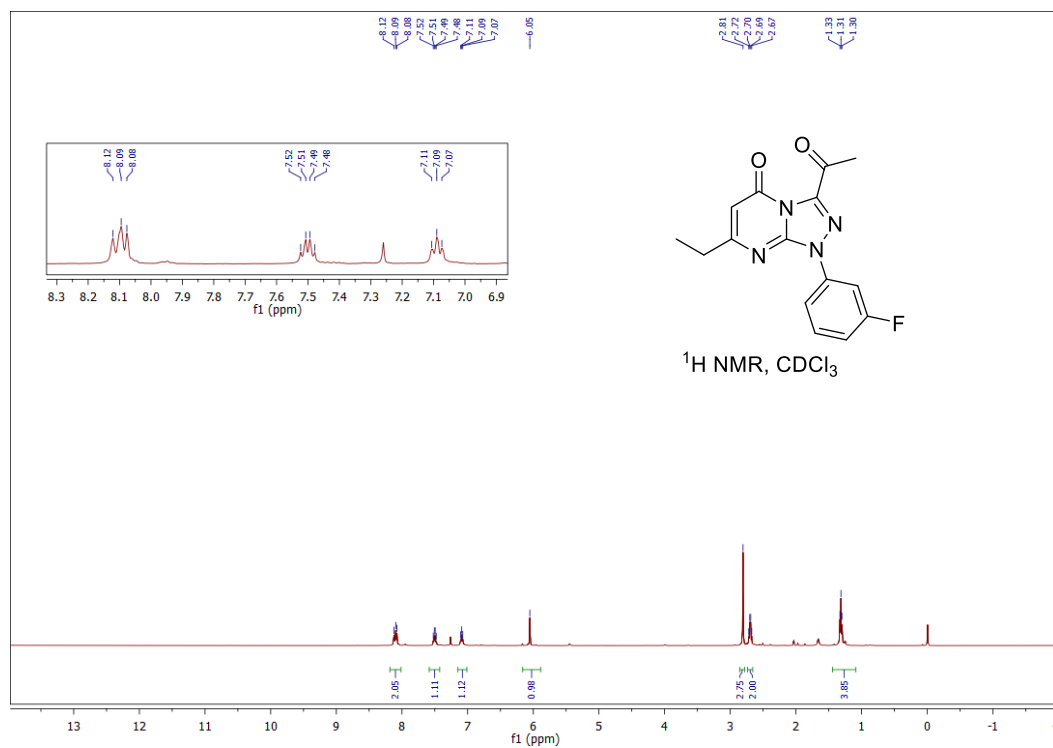


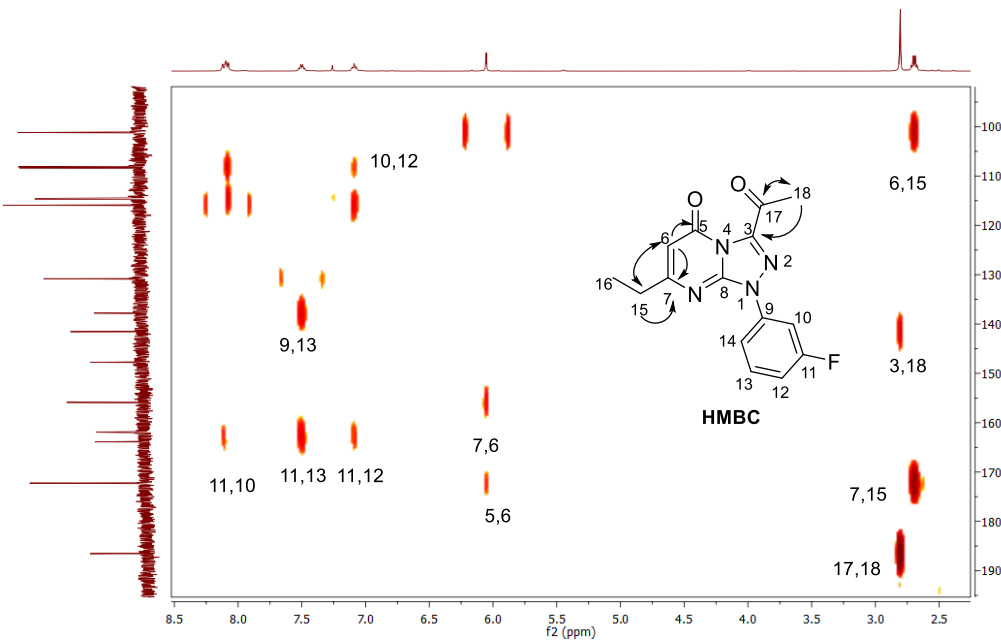
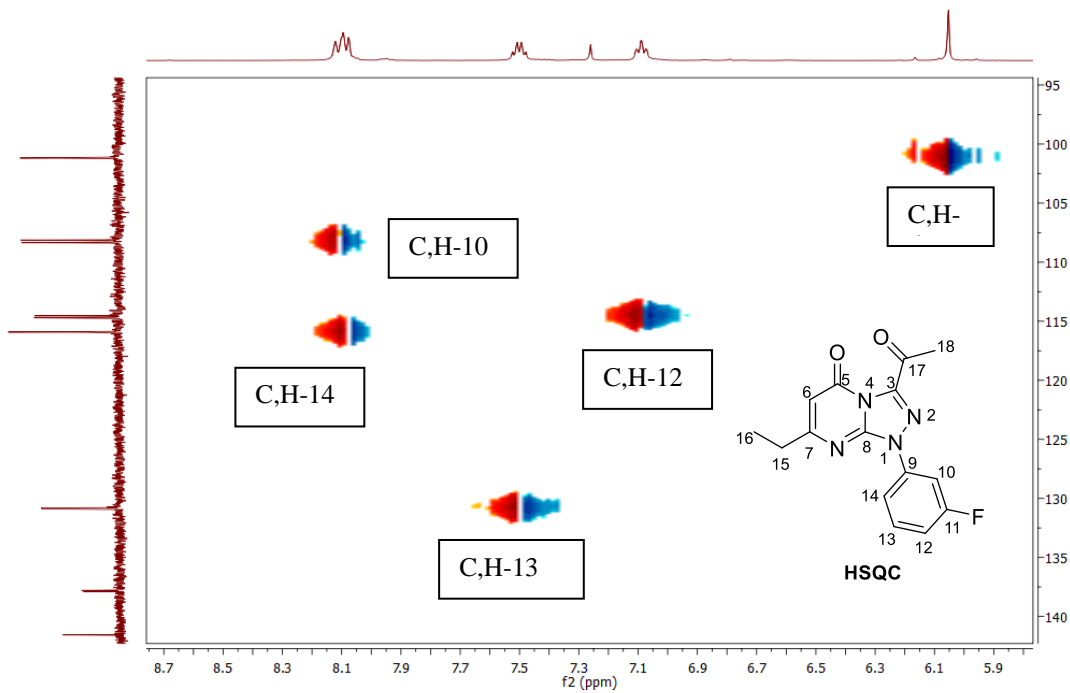
Appendix B for Chapter 3

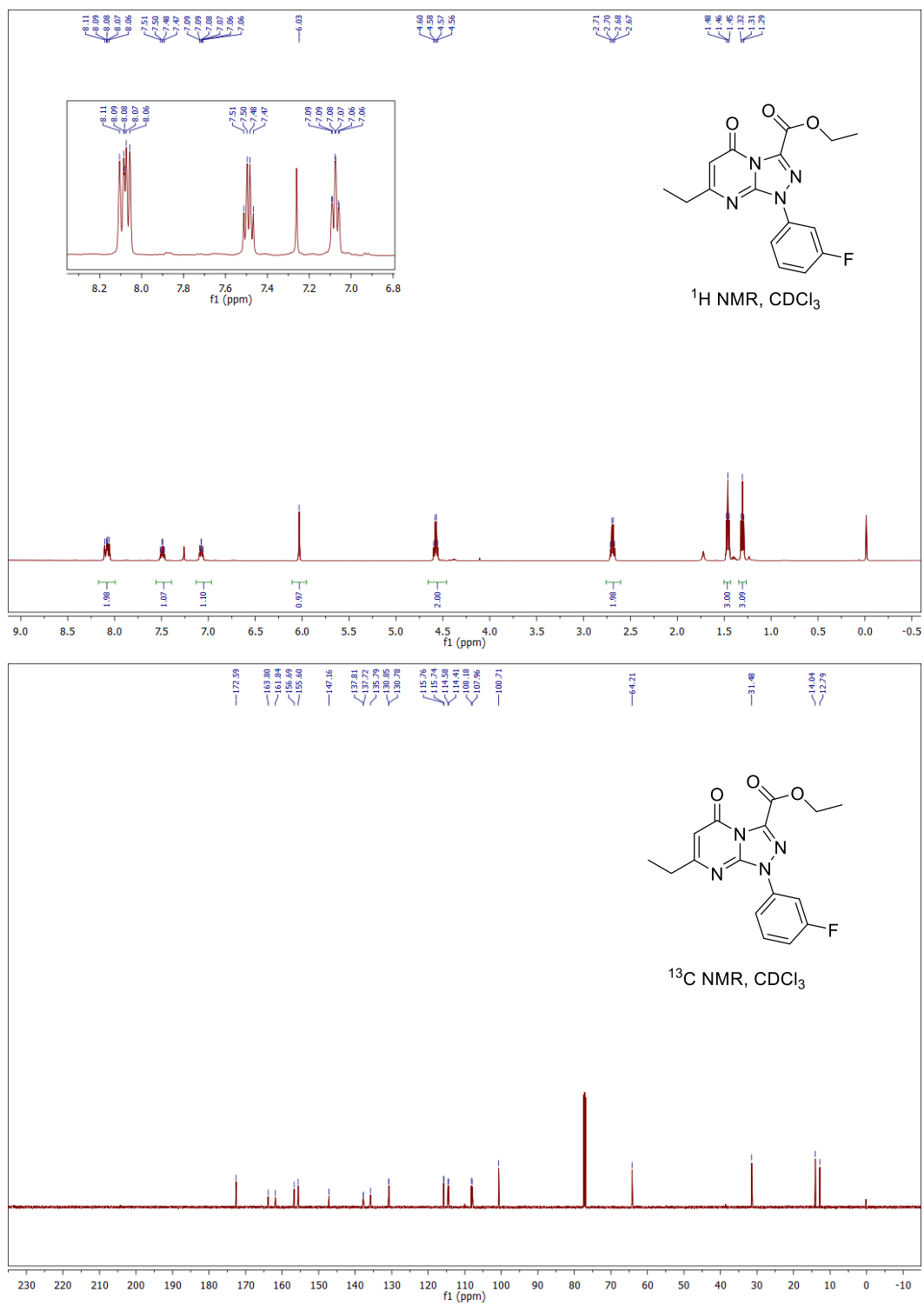


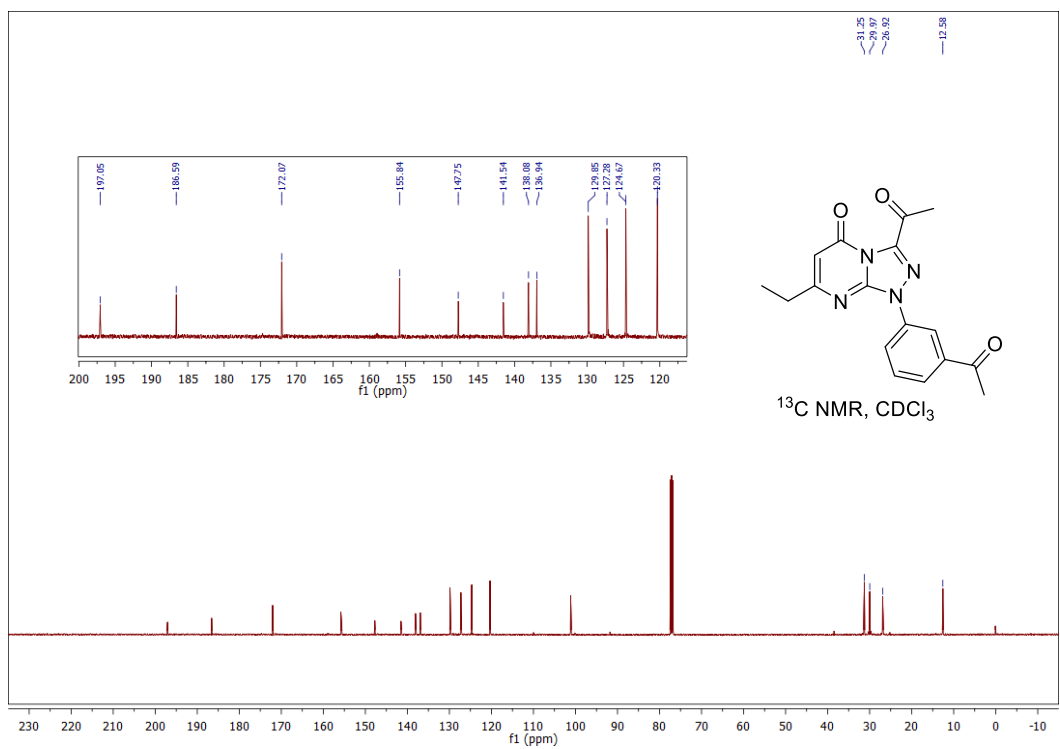
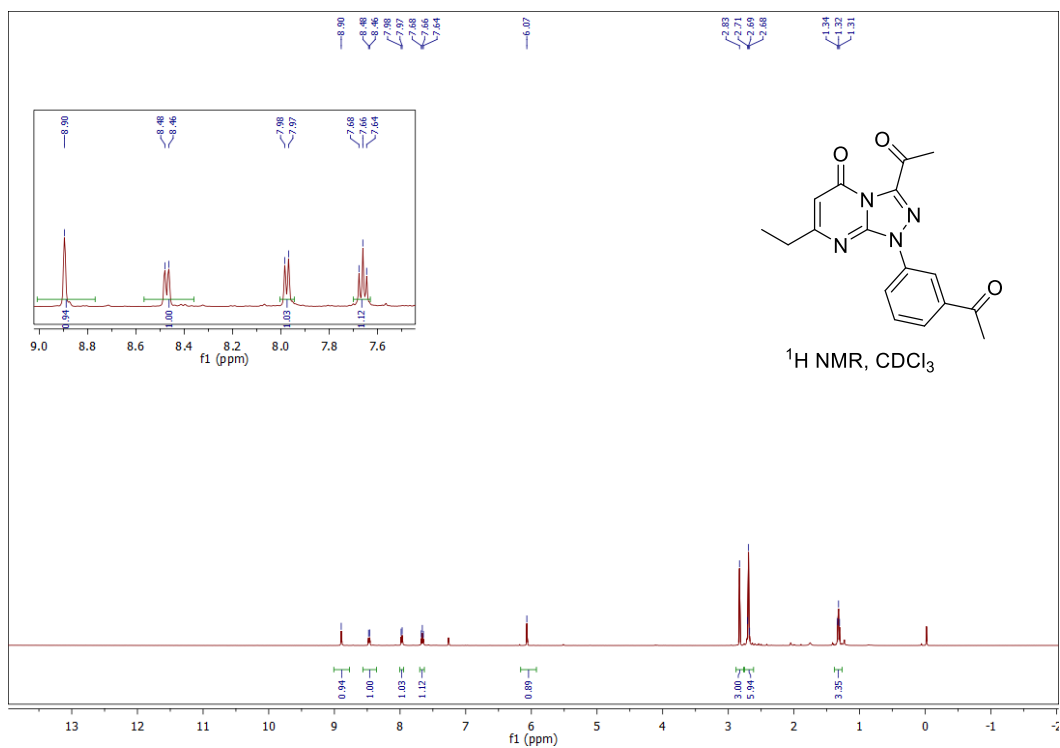


Appendix B for Chapter 3

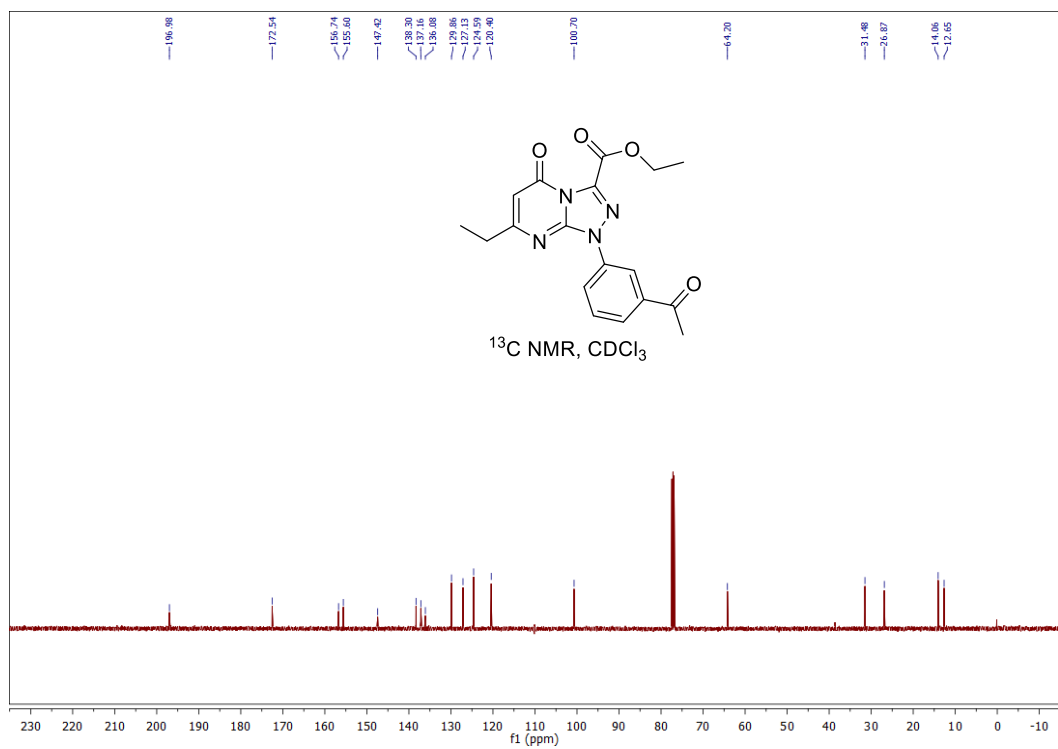
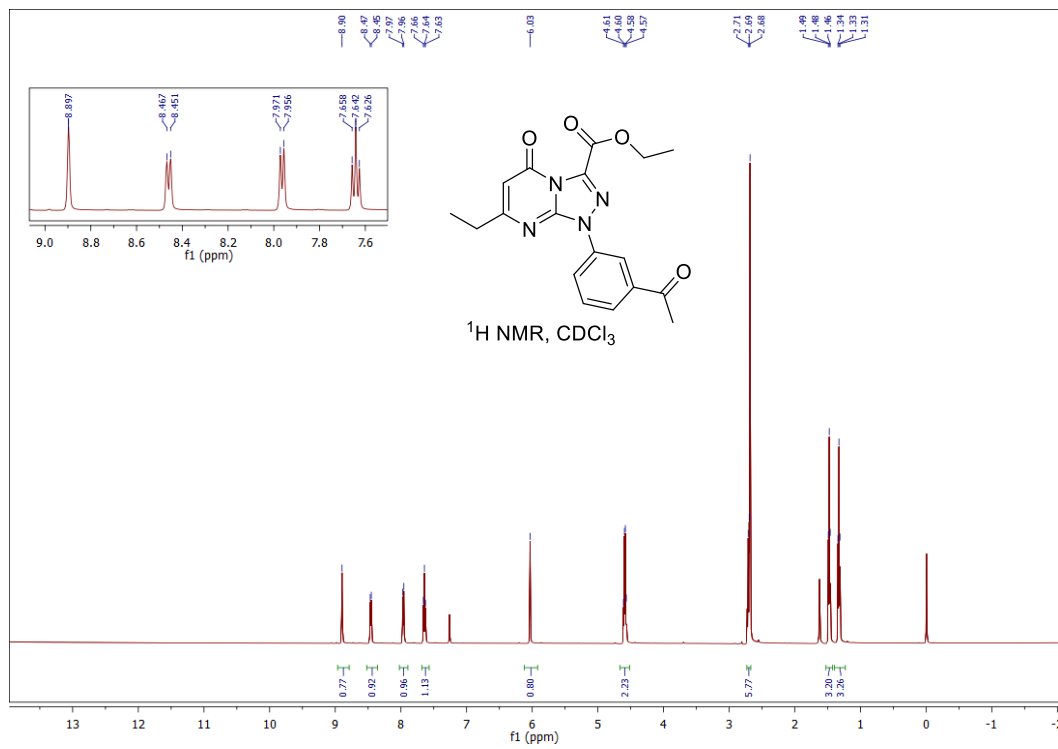


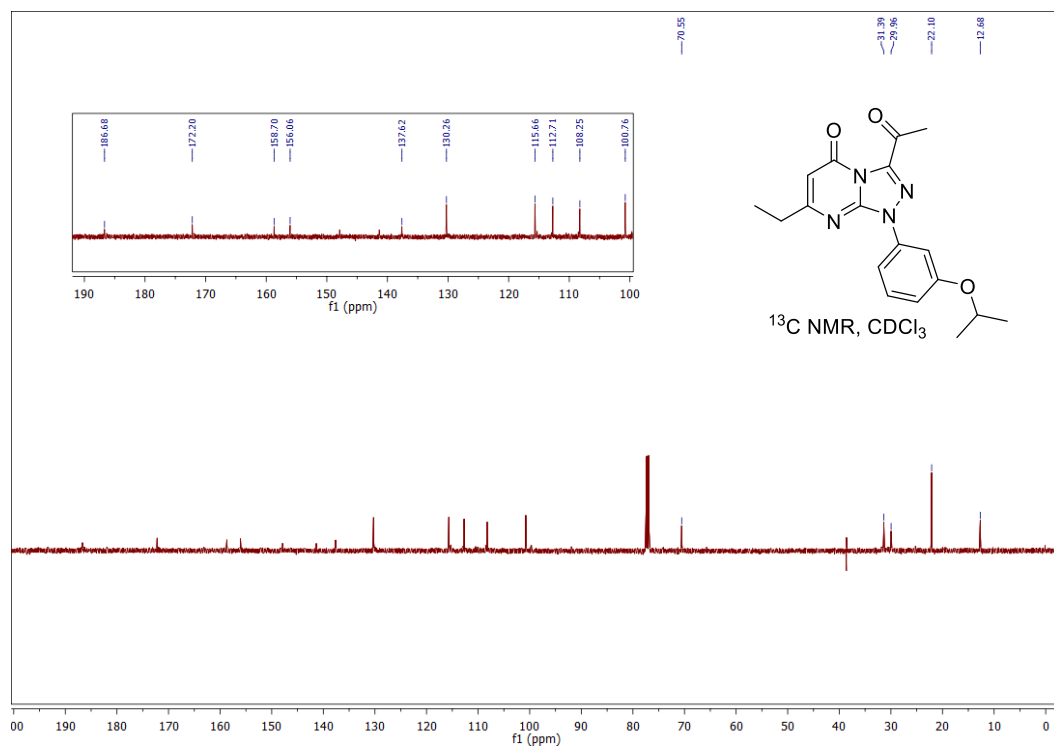
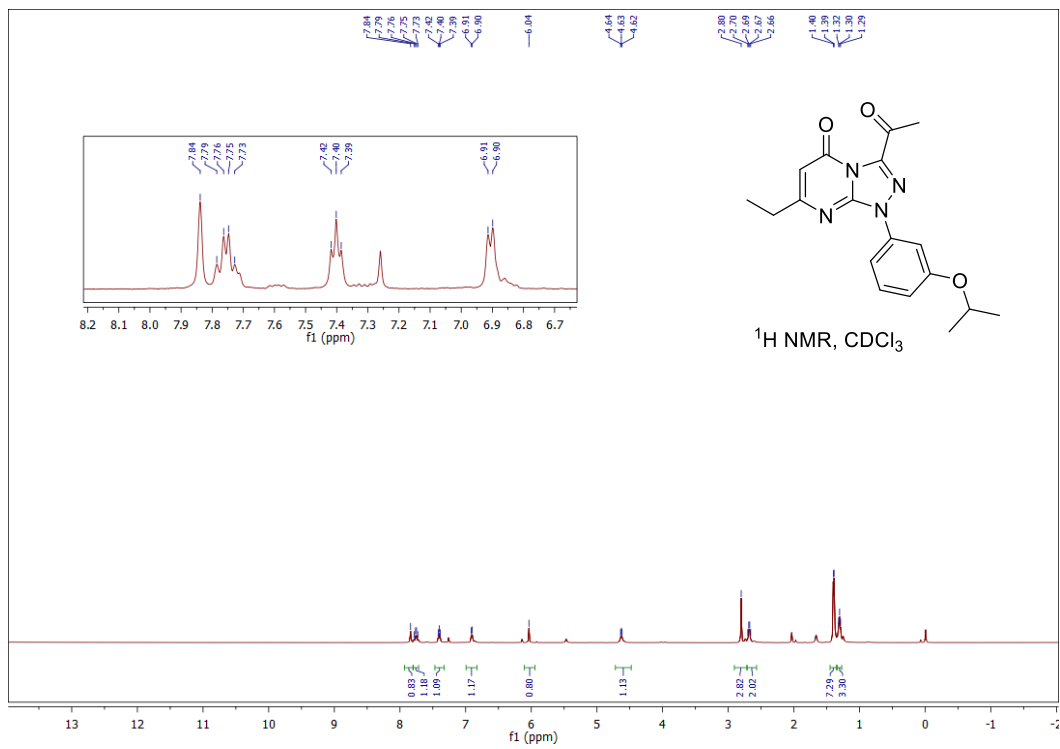




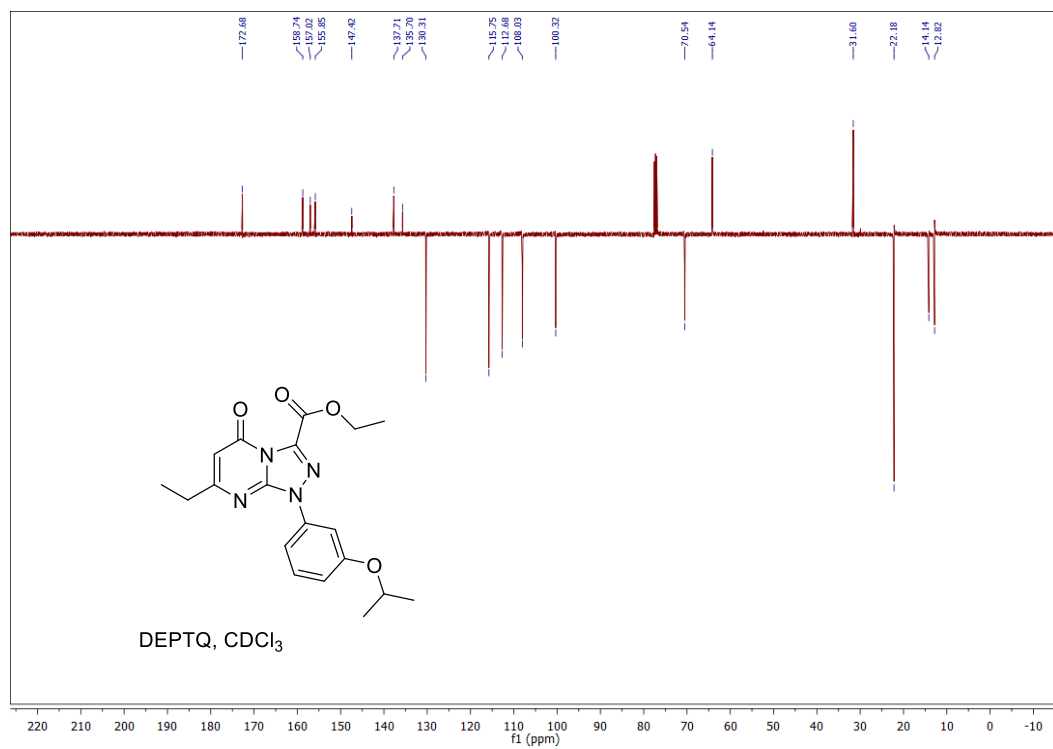
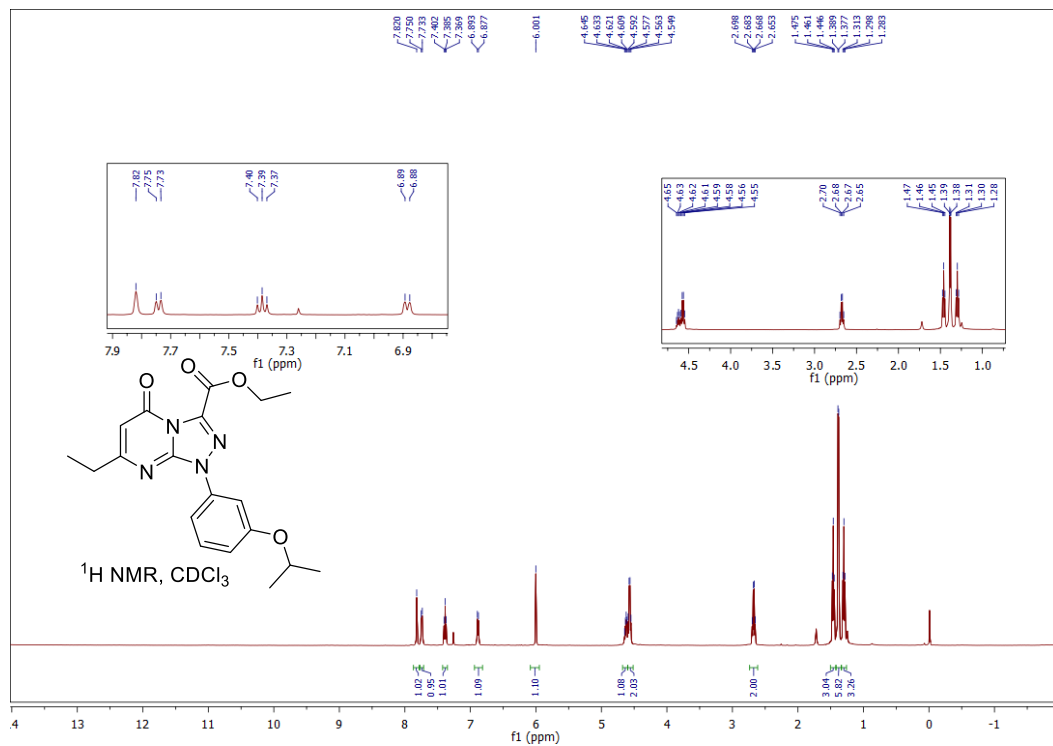


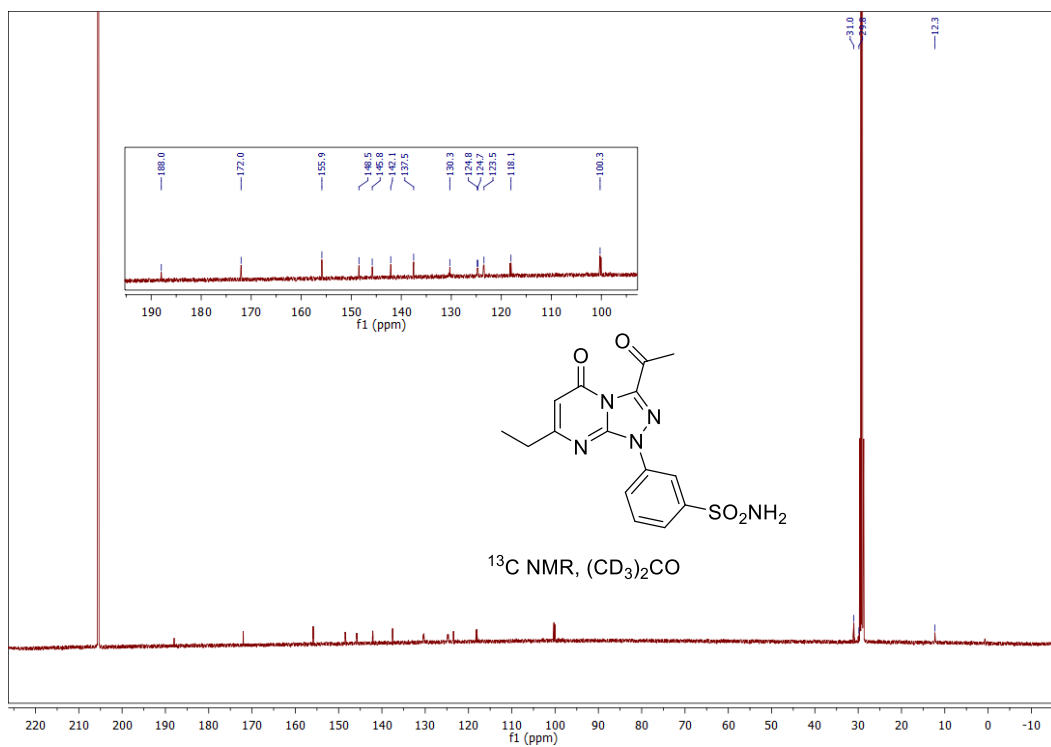
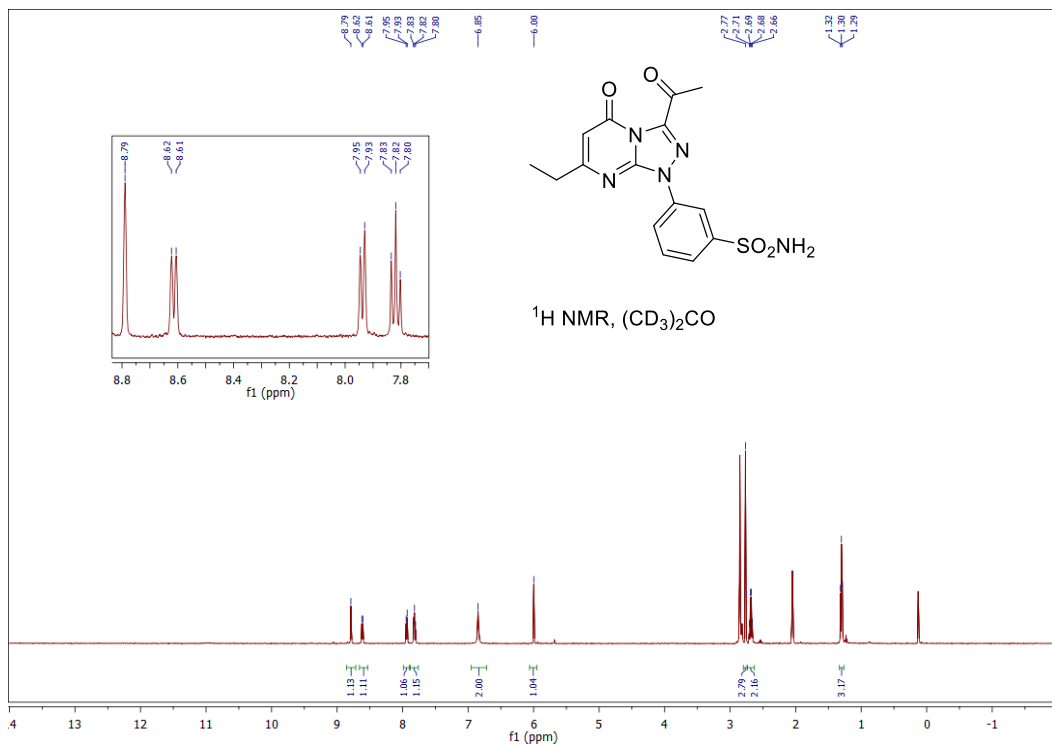
Appendix B for Chapter 3



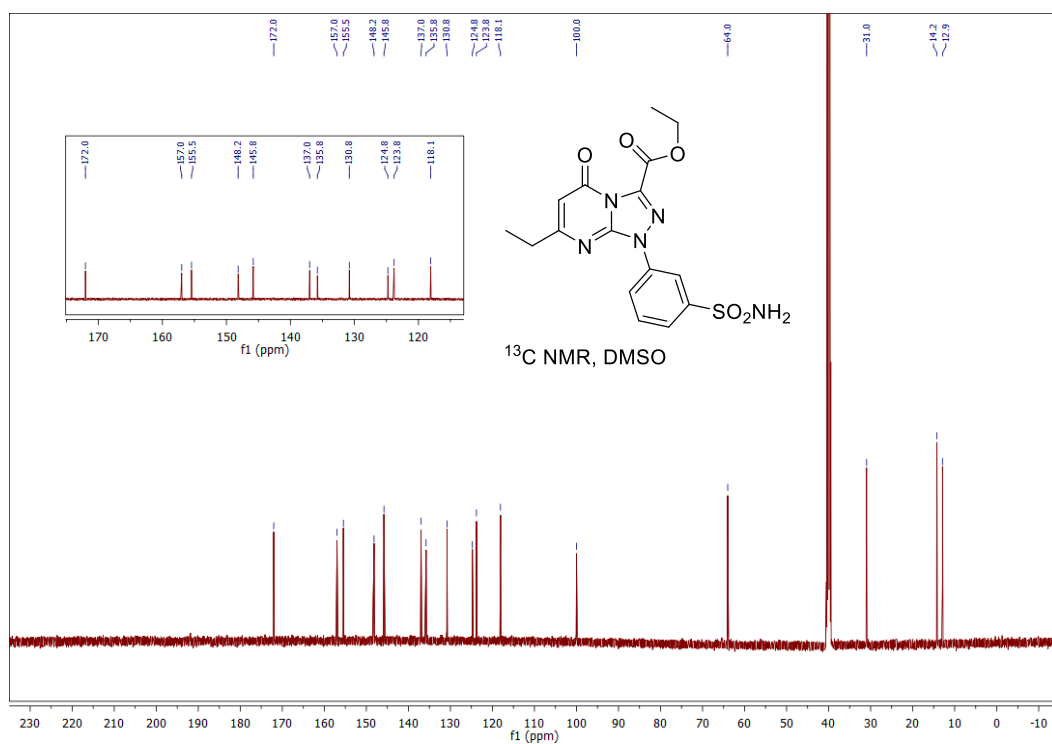
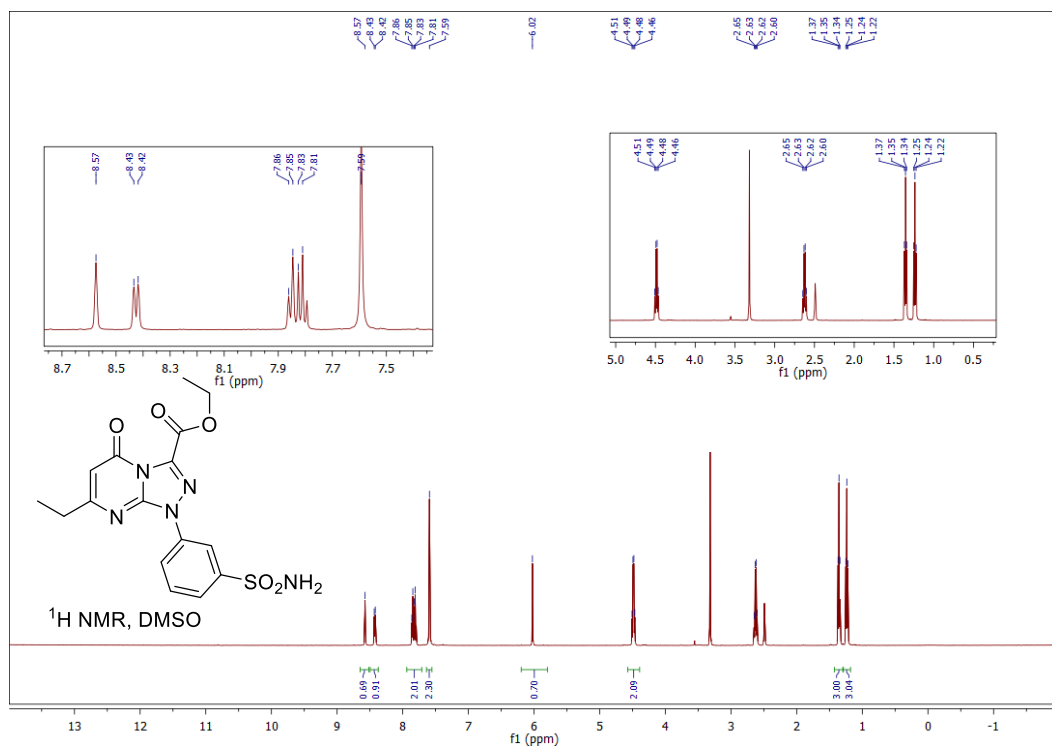


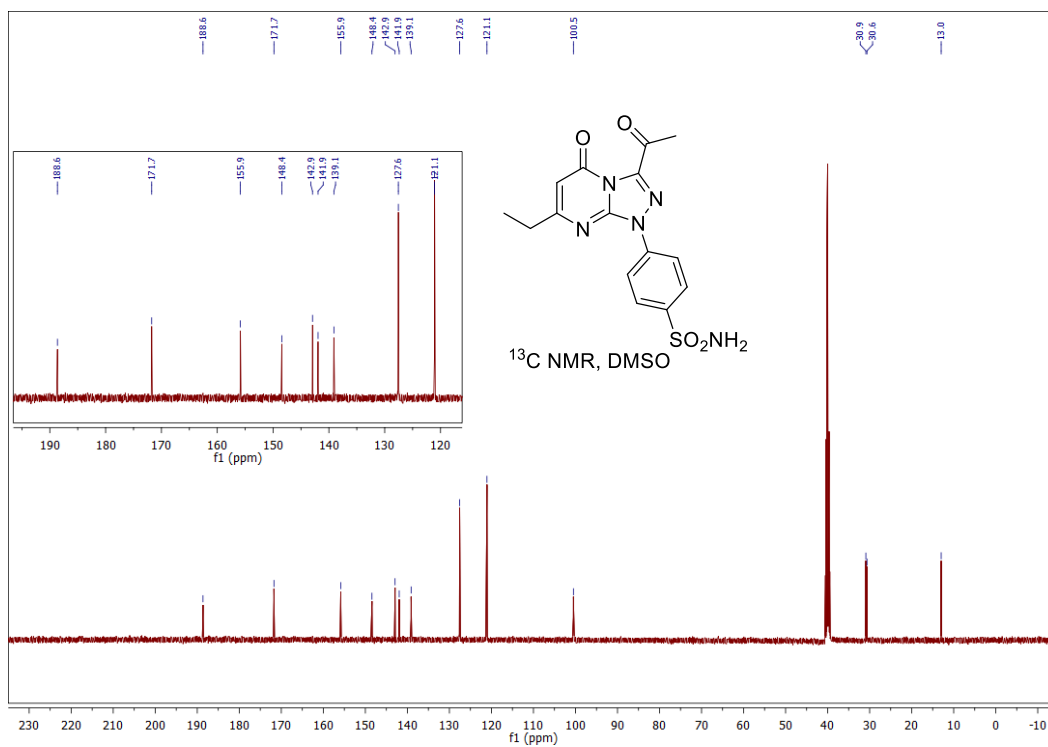
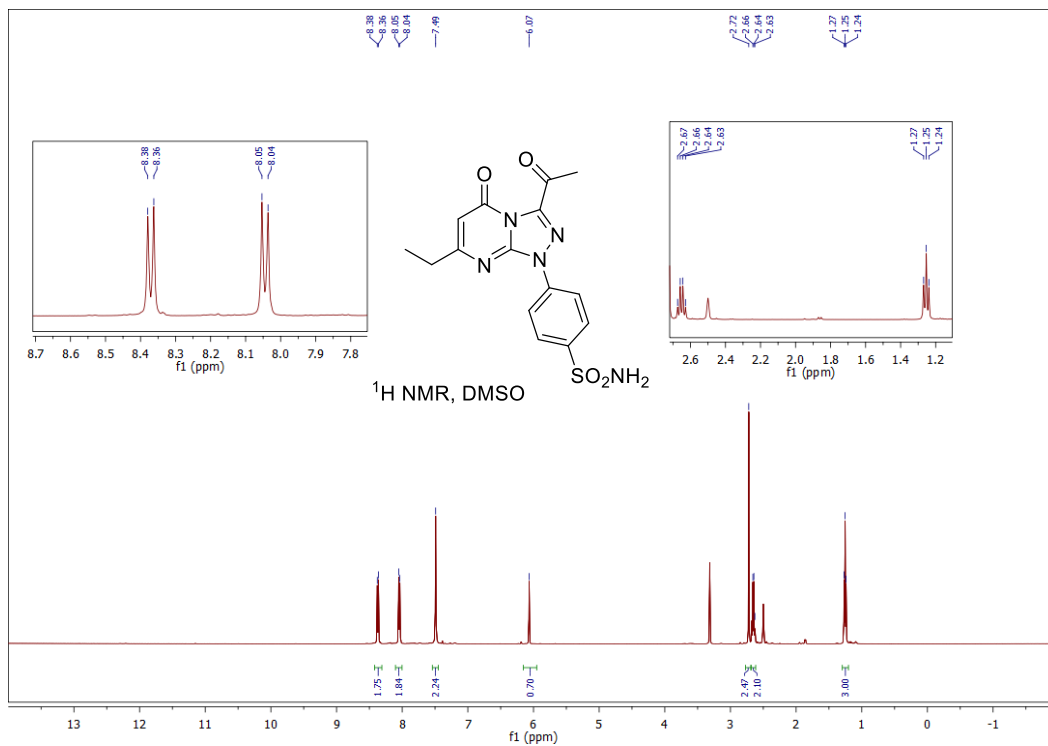
Appendix B for Chapter 3



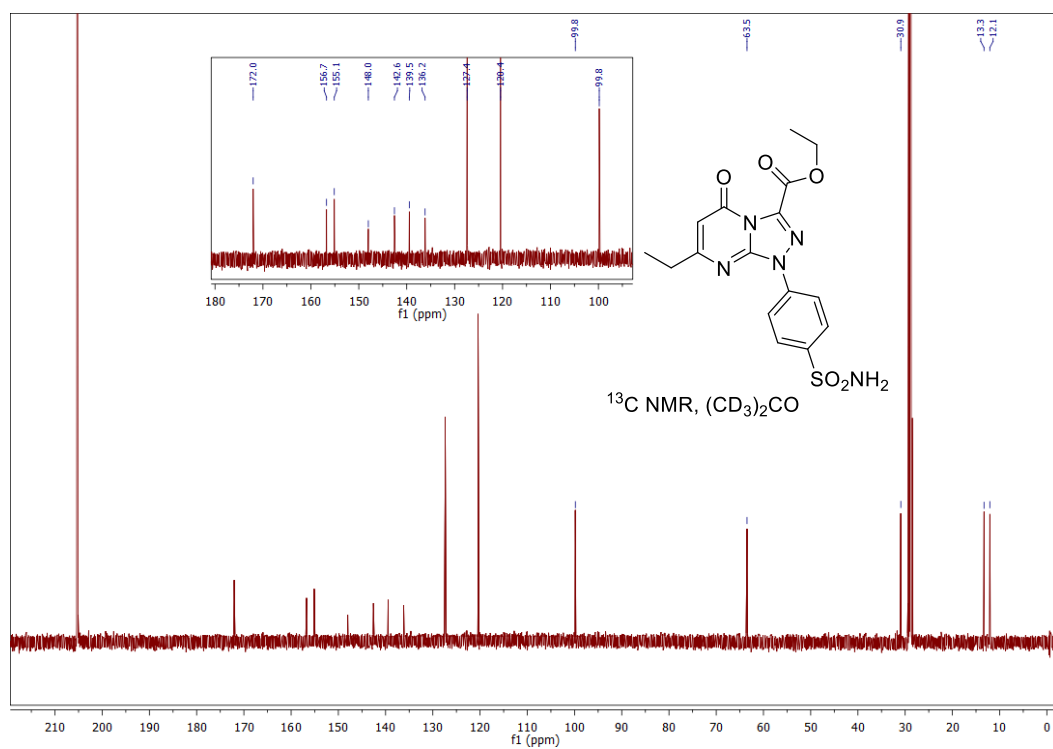
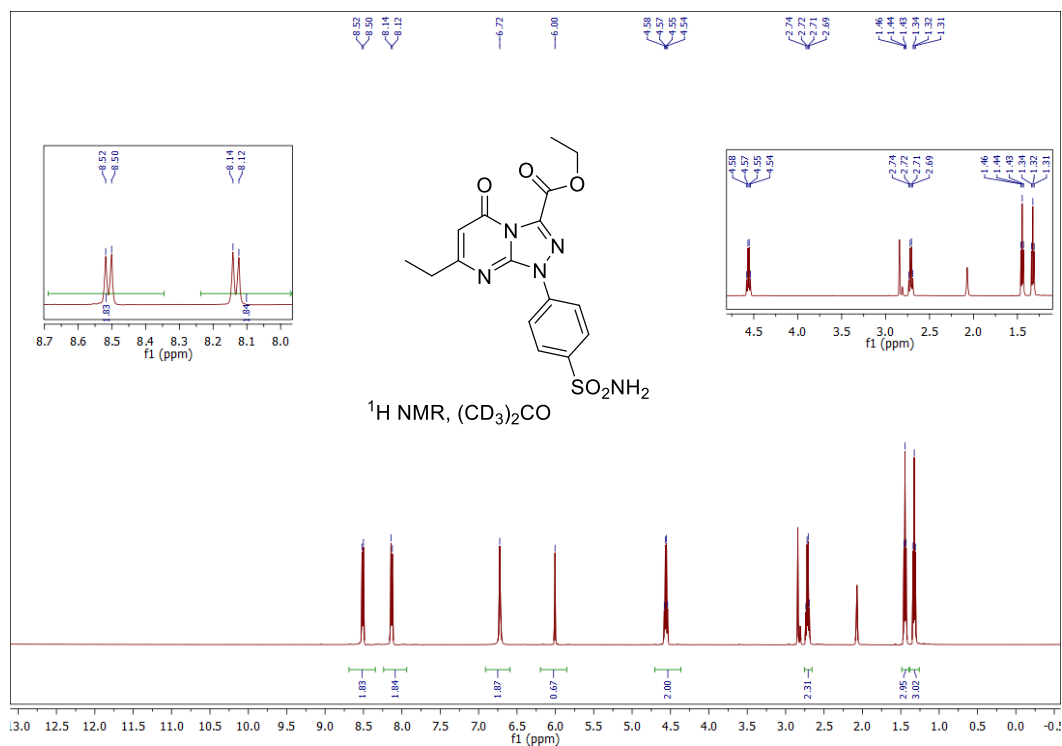


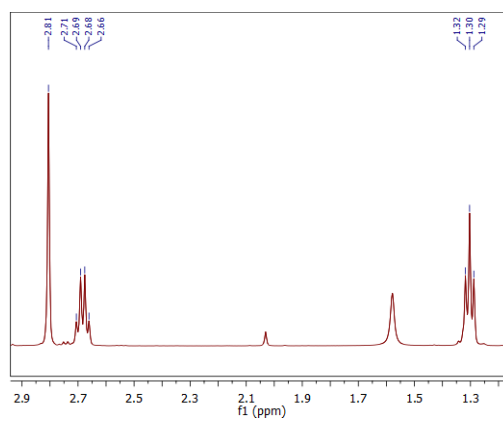
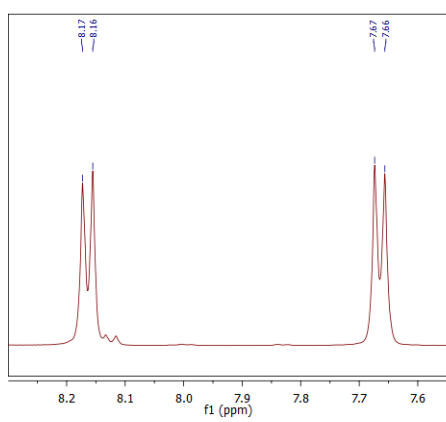
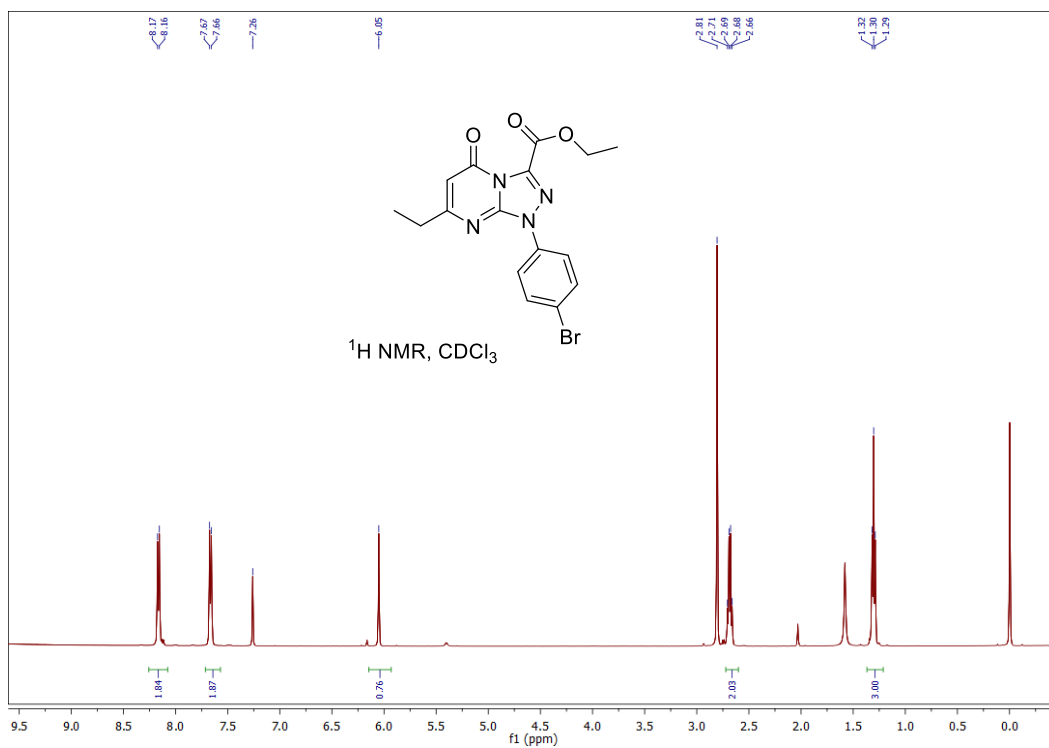
Appendix B for Chapter 3





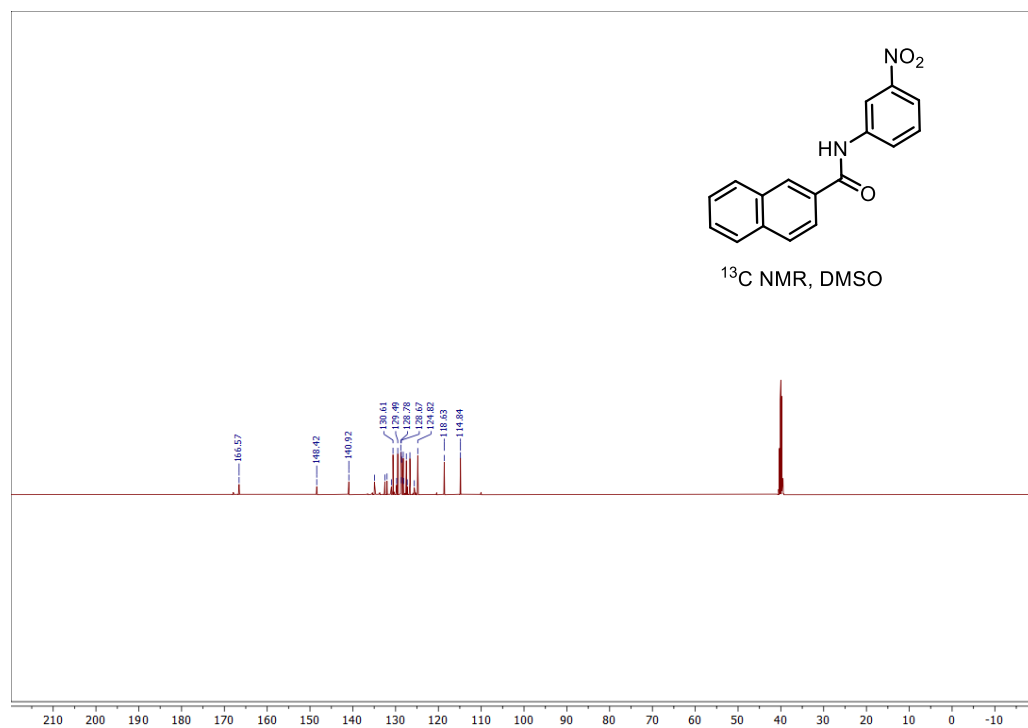
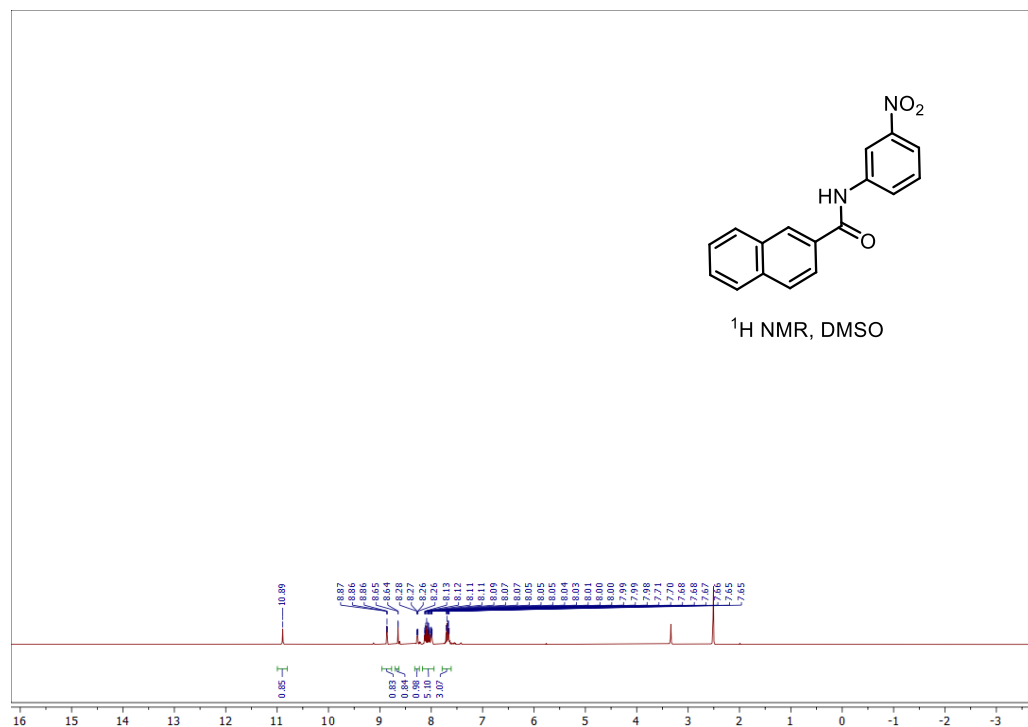
Appendix B for Chapter 3

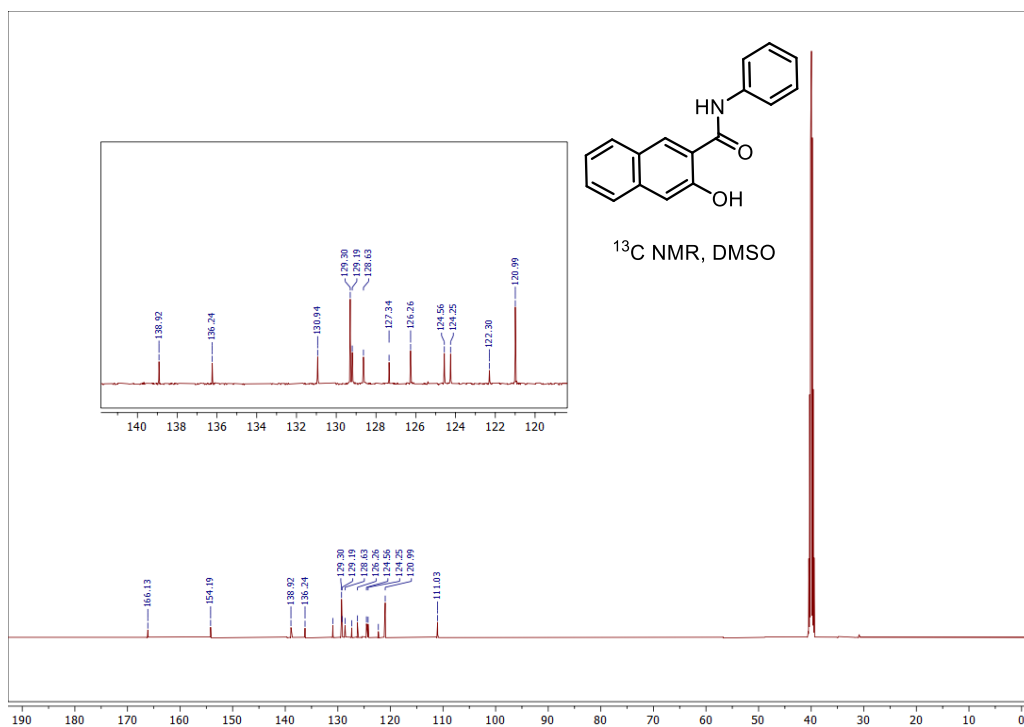
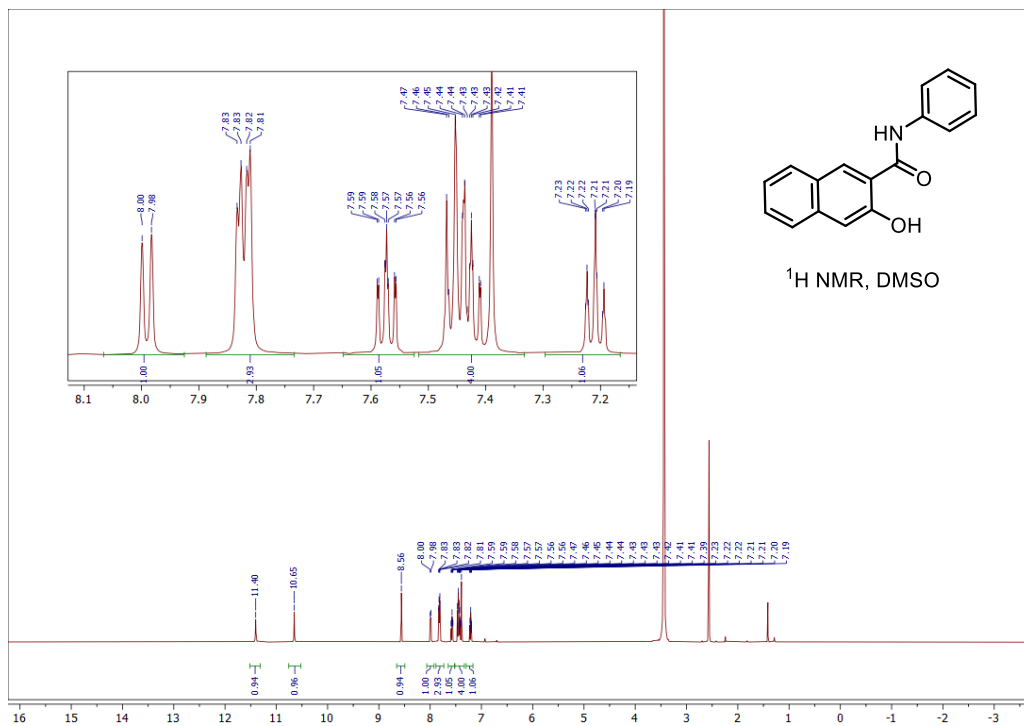


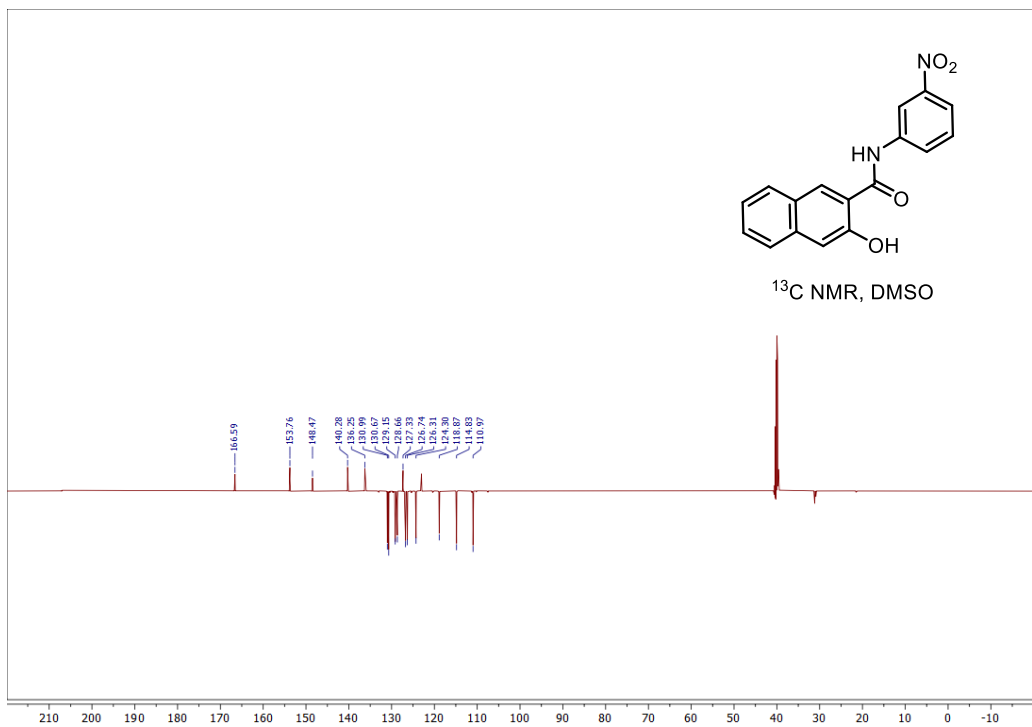
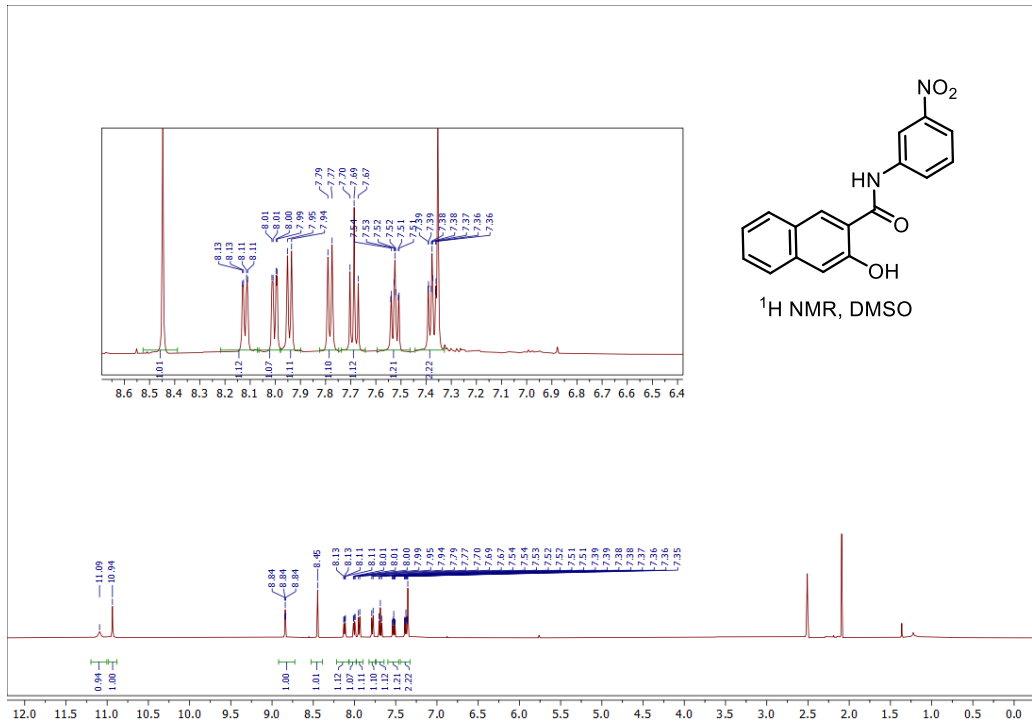


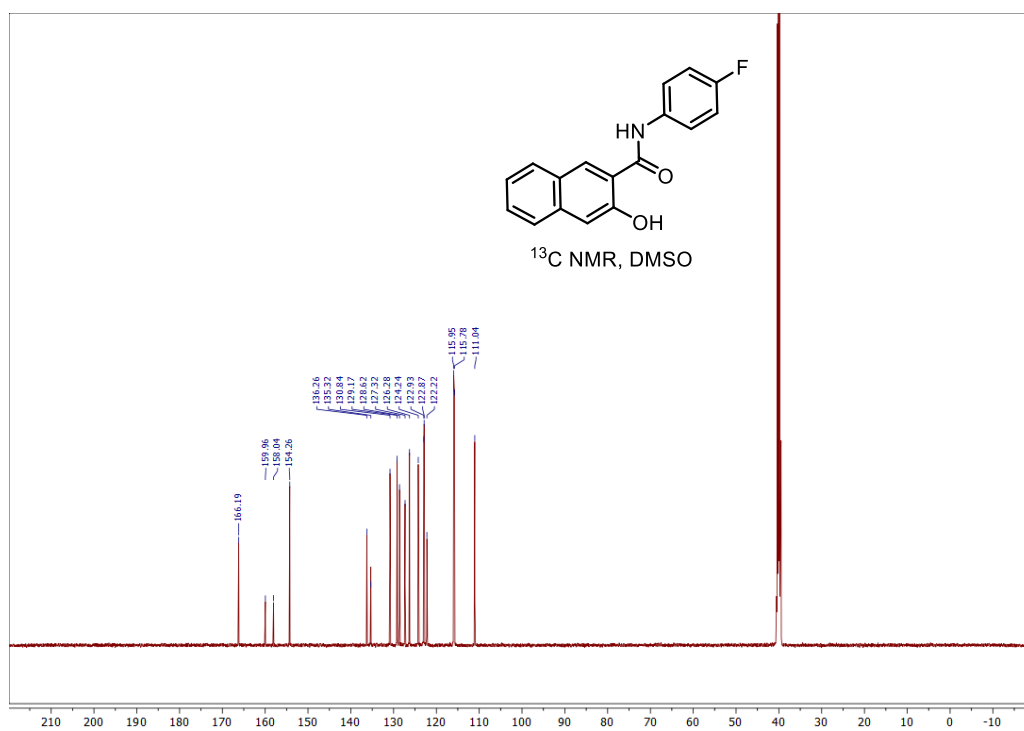
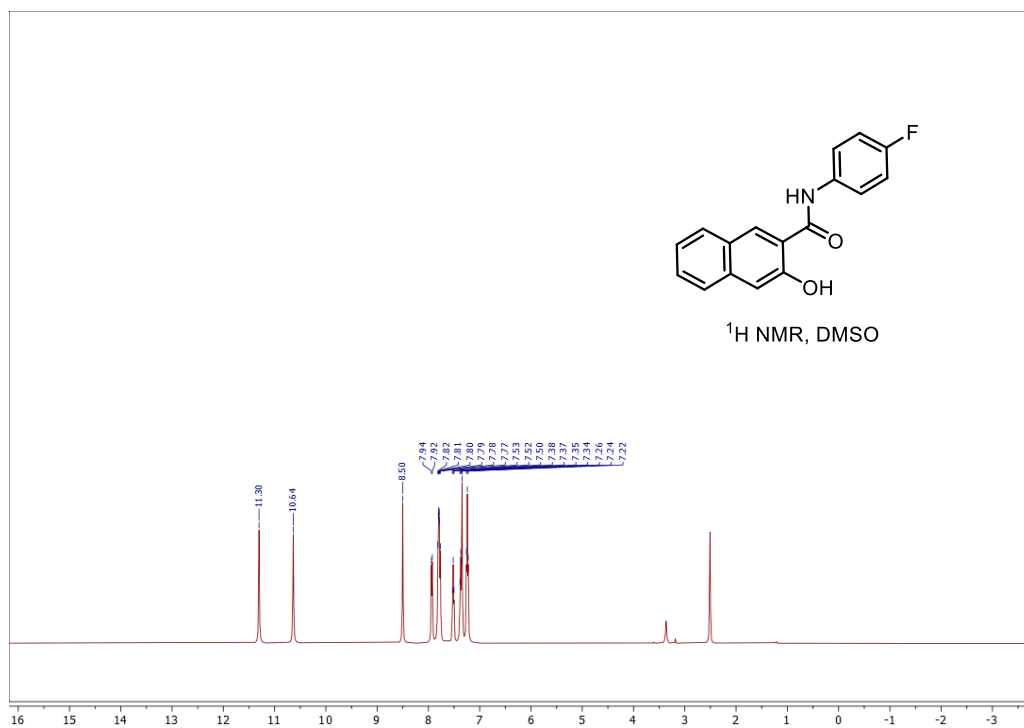
Appendix C: Supplementary Information to Chapter 4

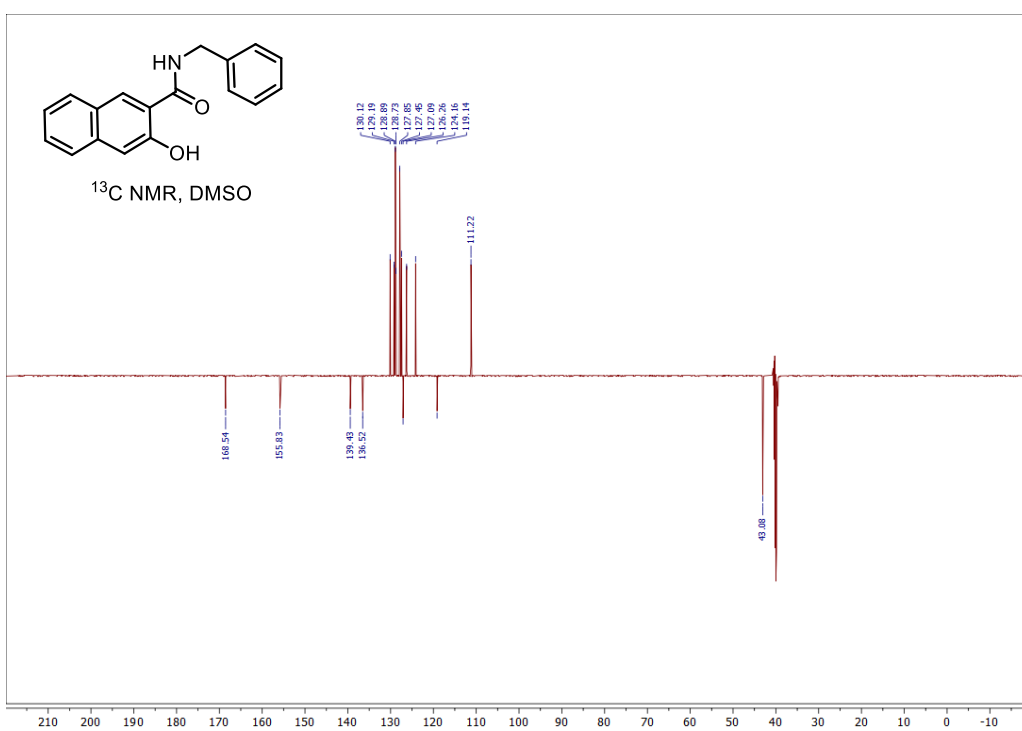
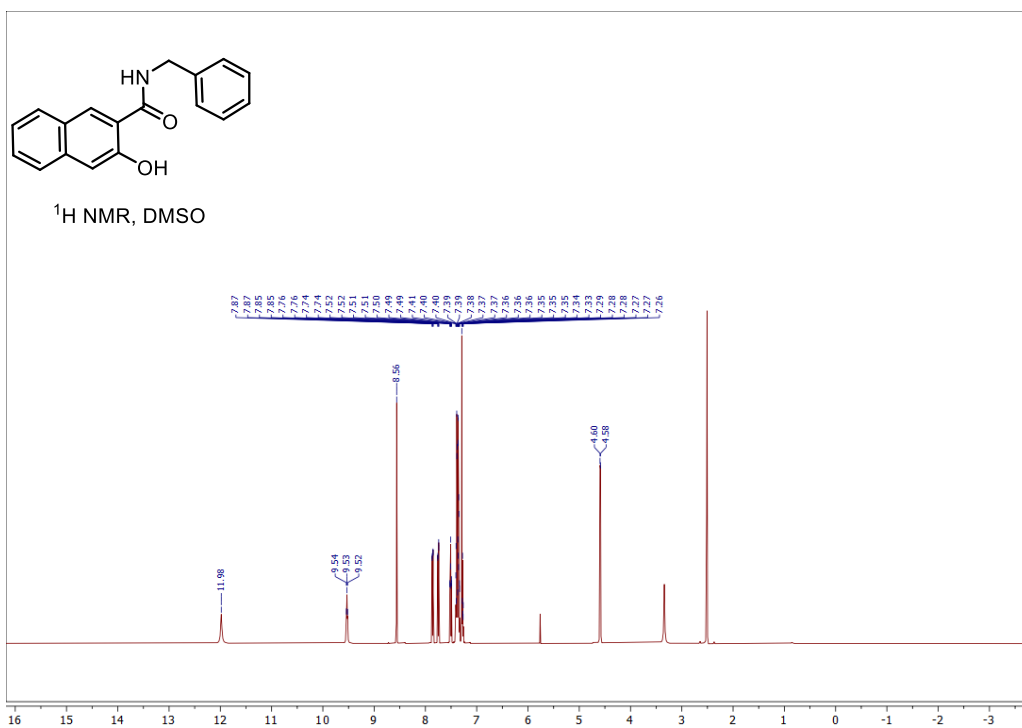
NMR spectra of compounds from chapter 4



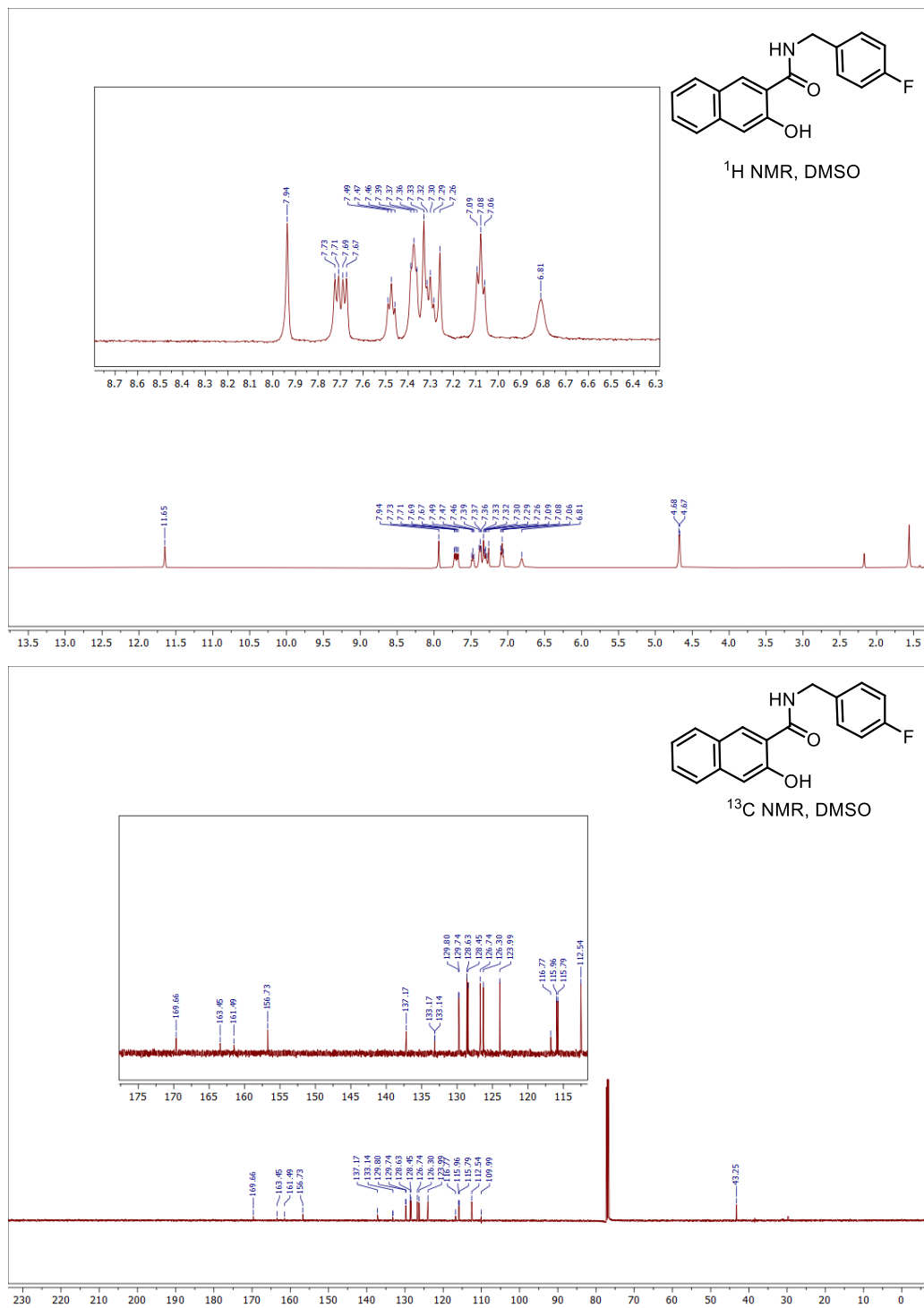






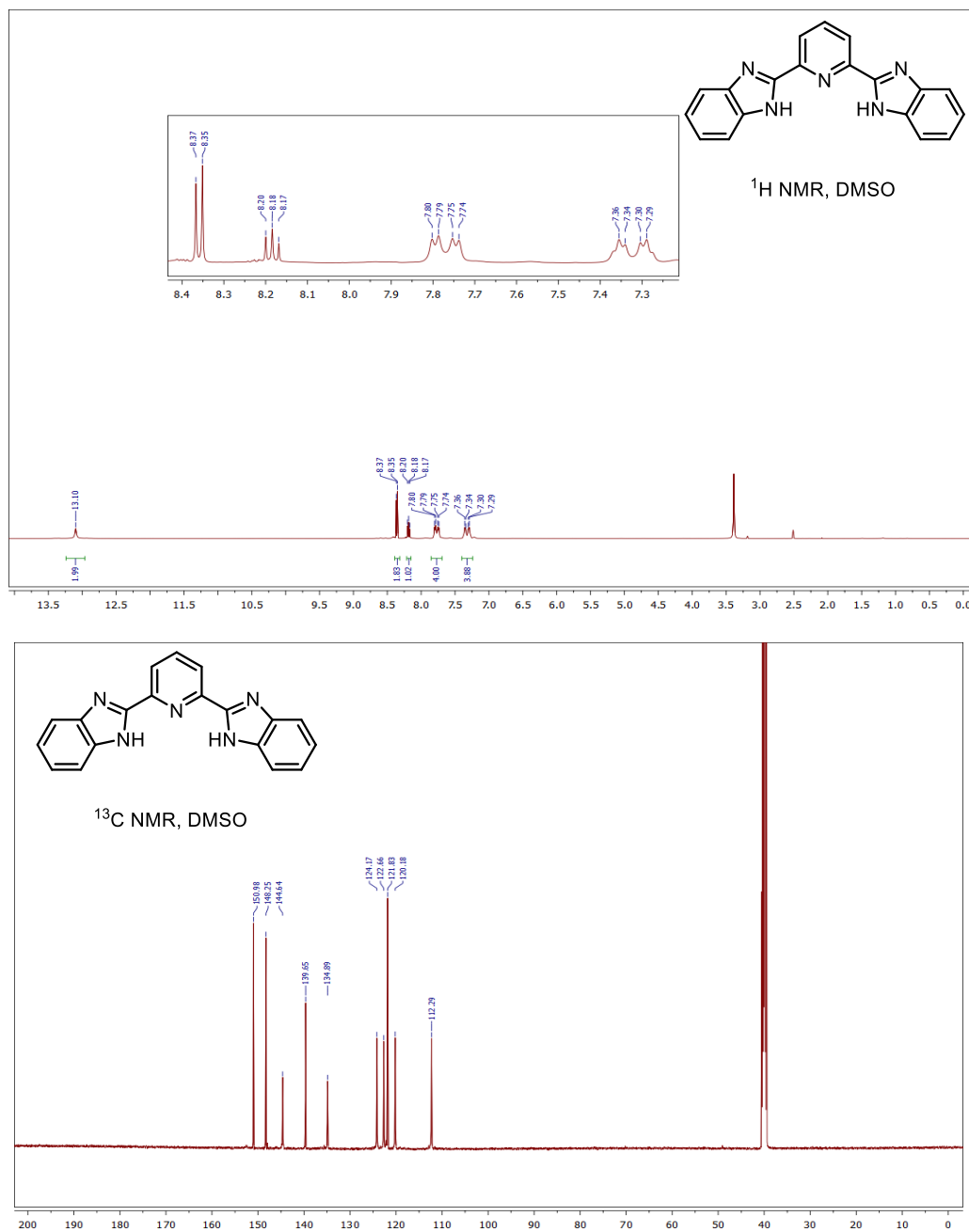


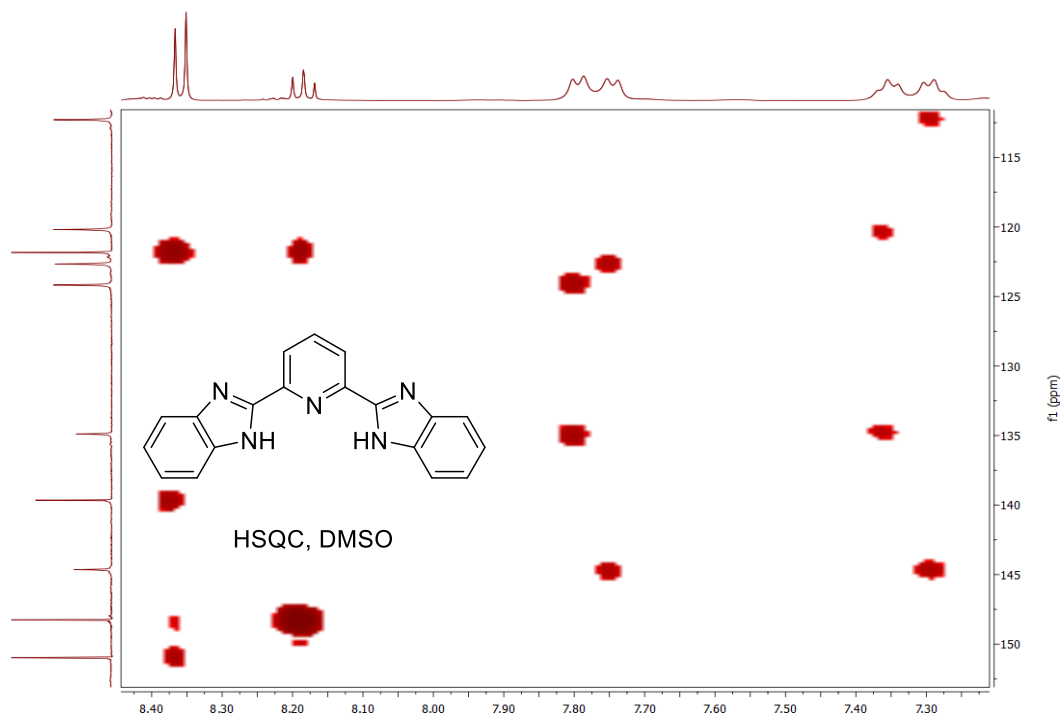
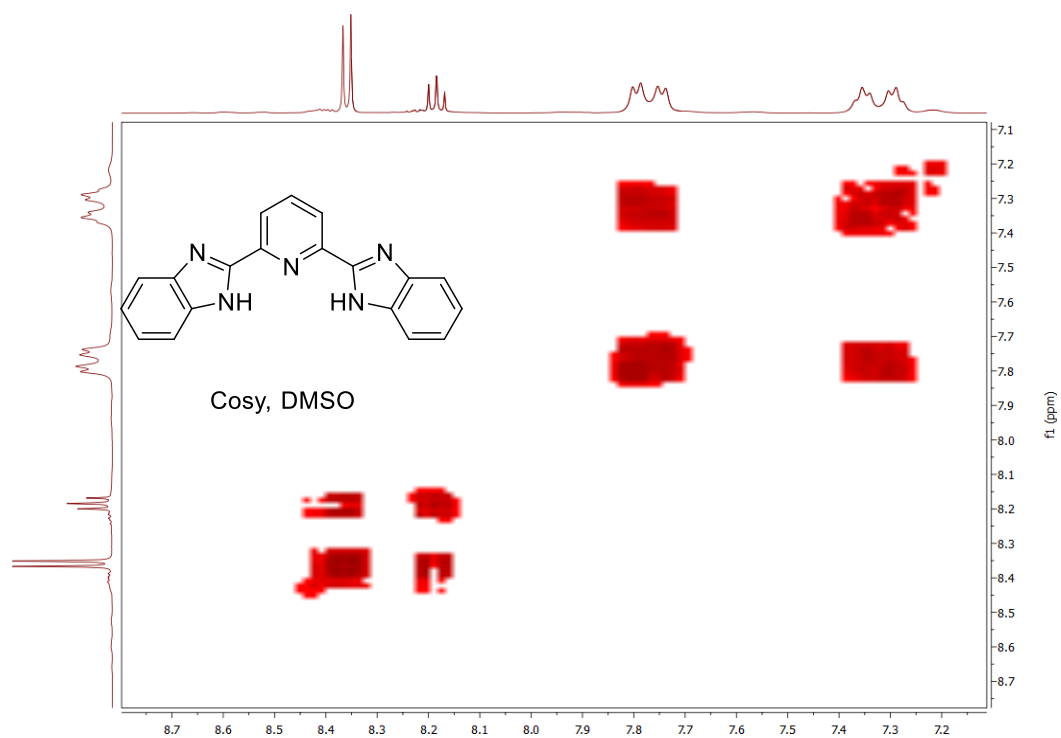
Appendix C for Chapter 4

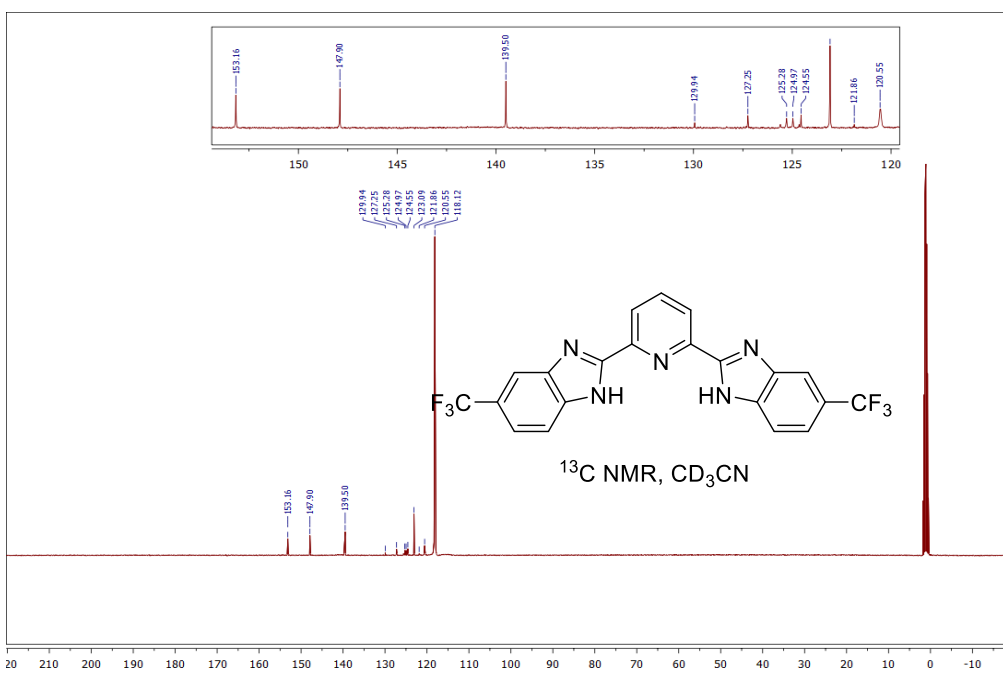
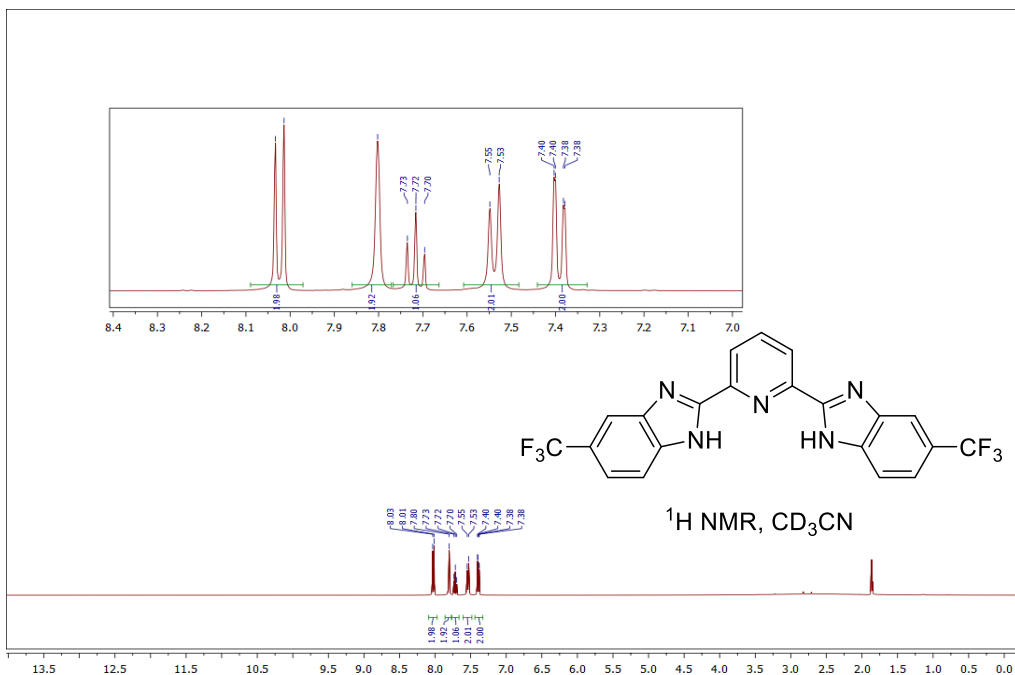


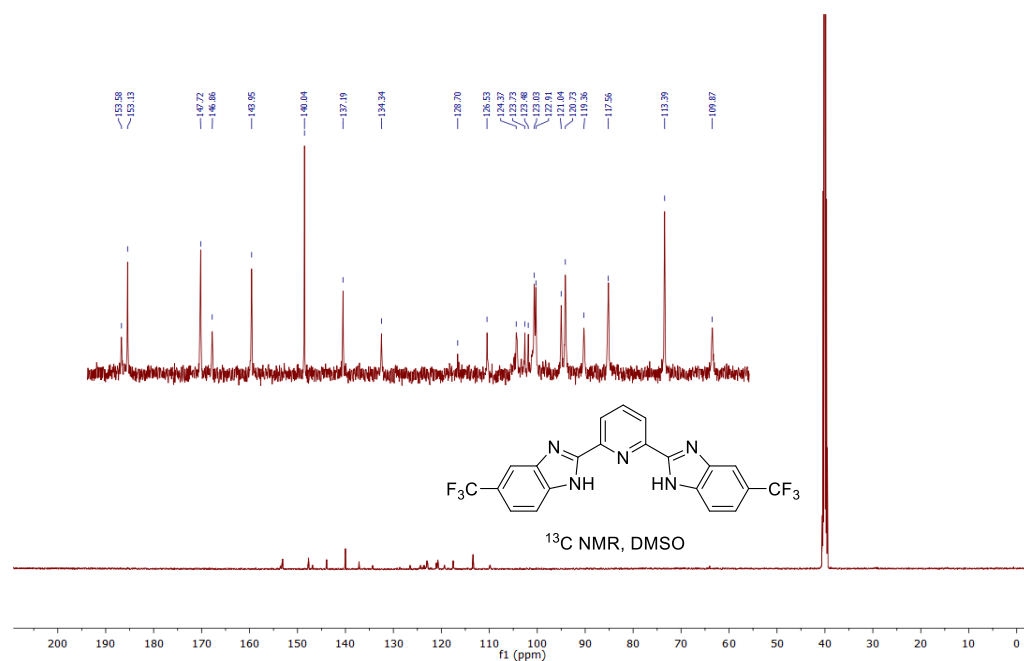
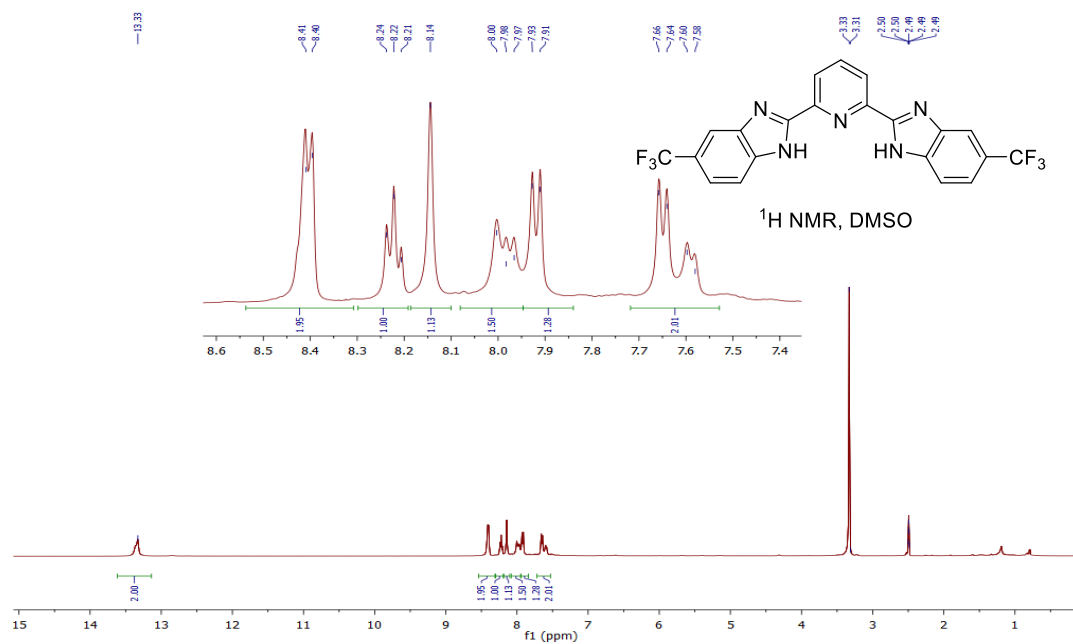
Appendix D: Supplementary Information to Chapter 5

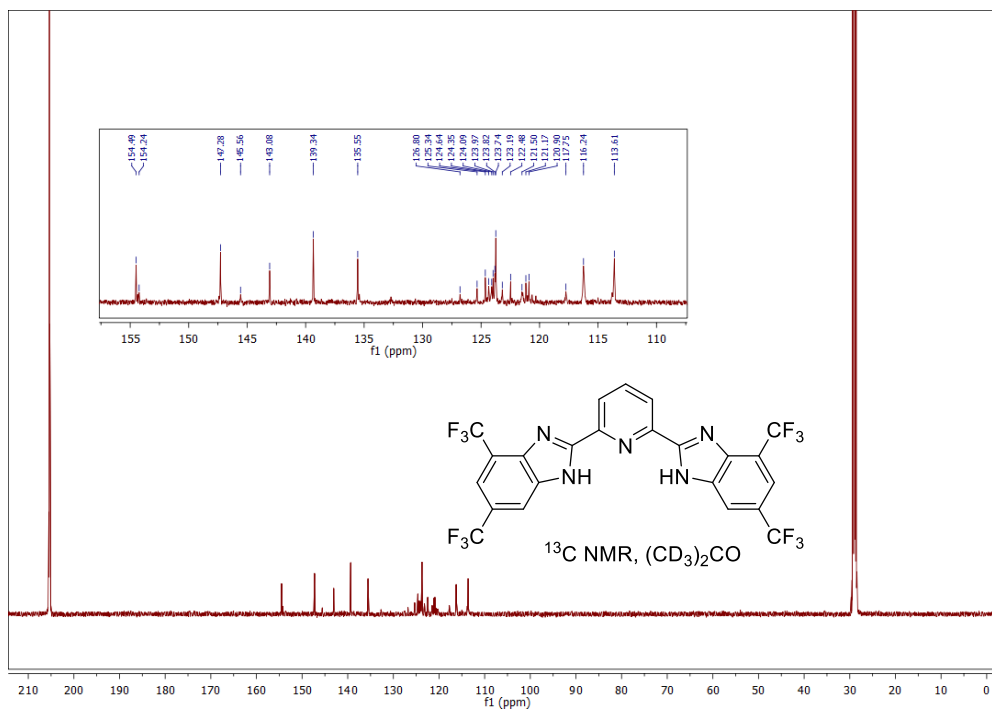
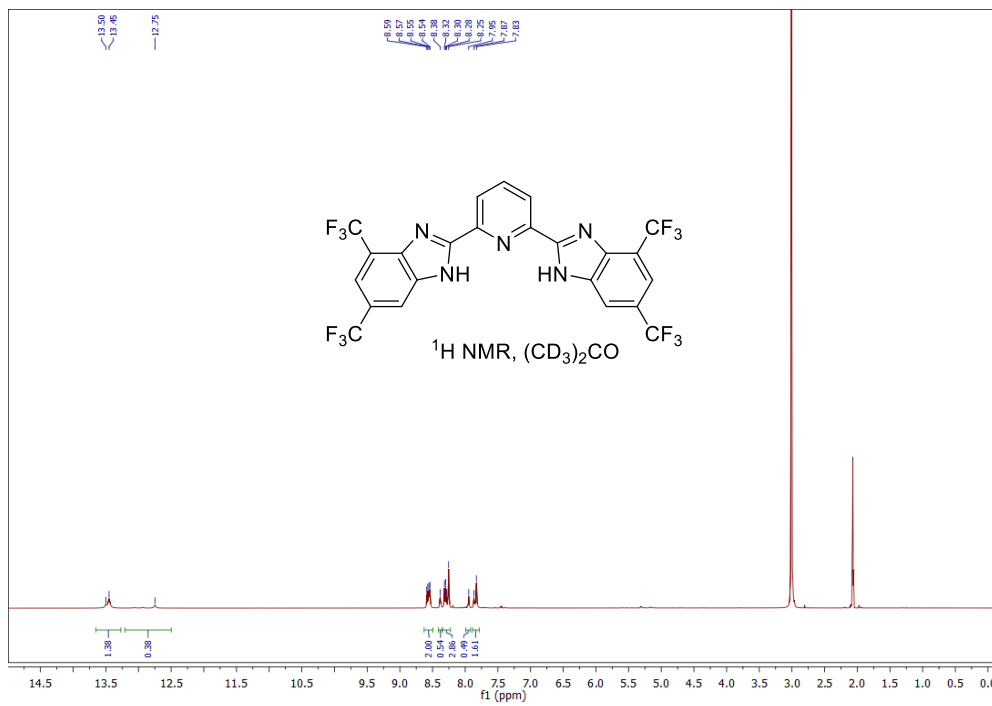
A) NMR spectra of compounds from chapter 5



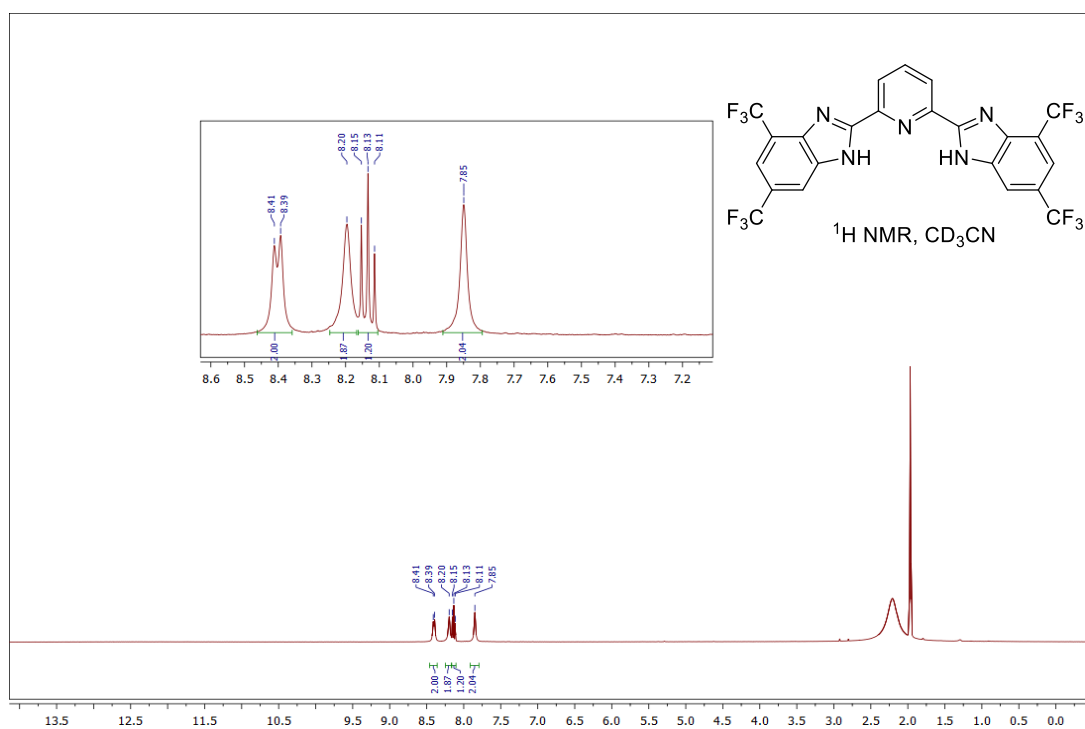
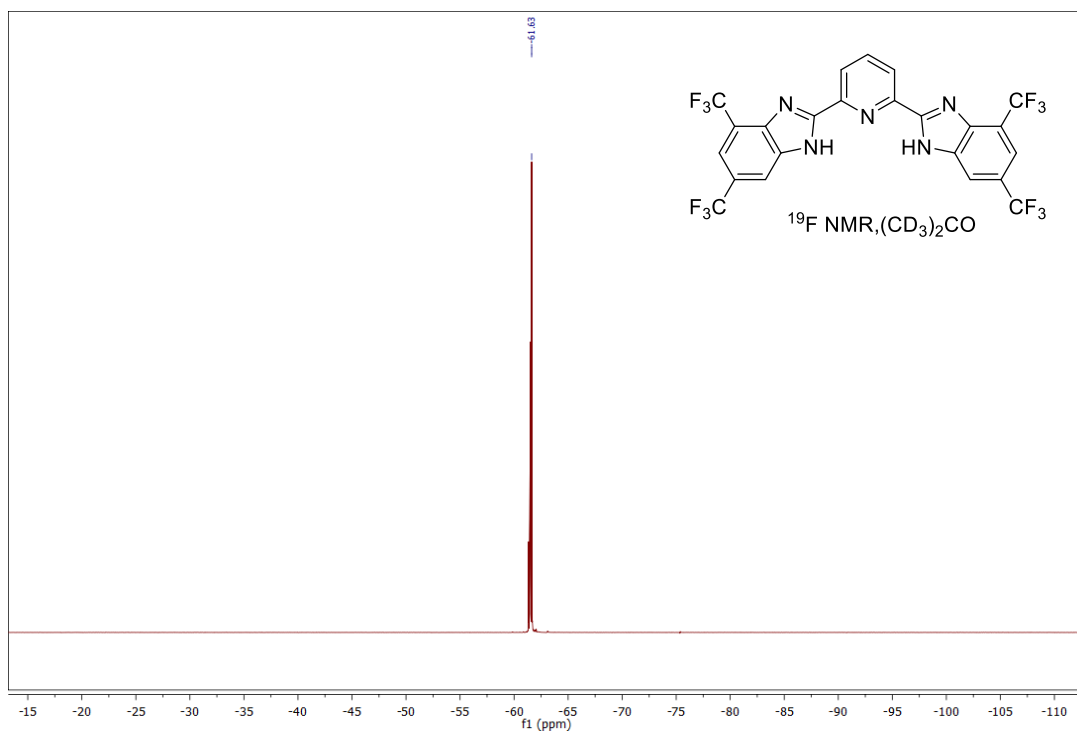


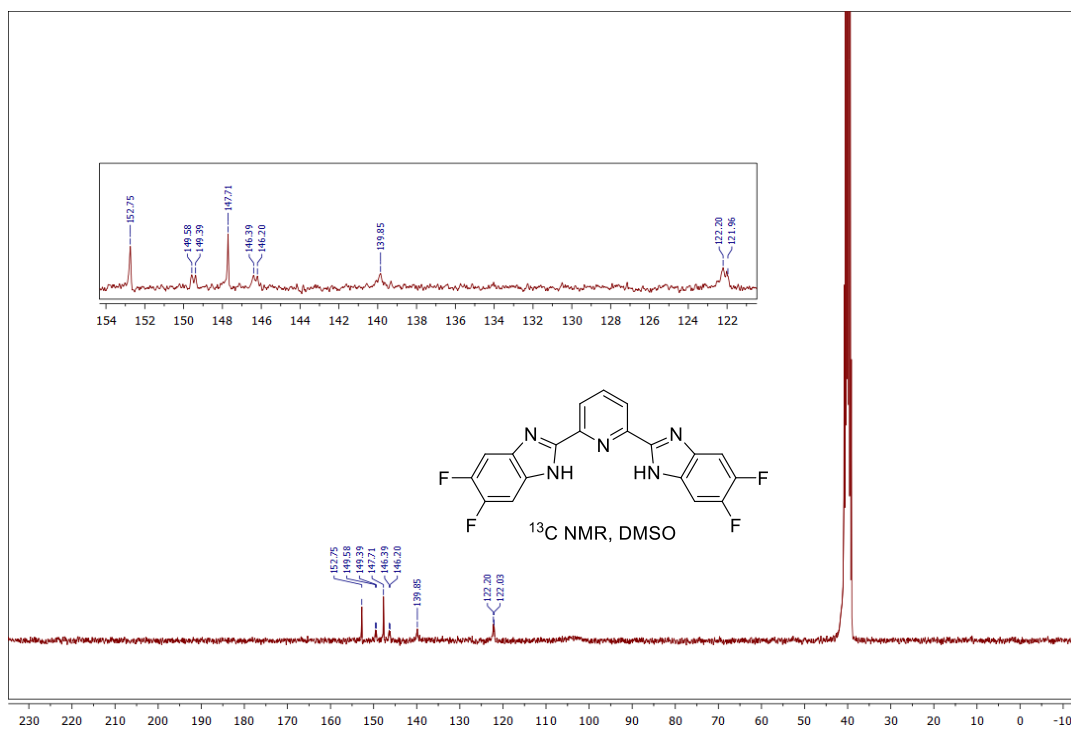
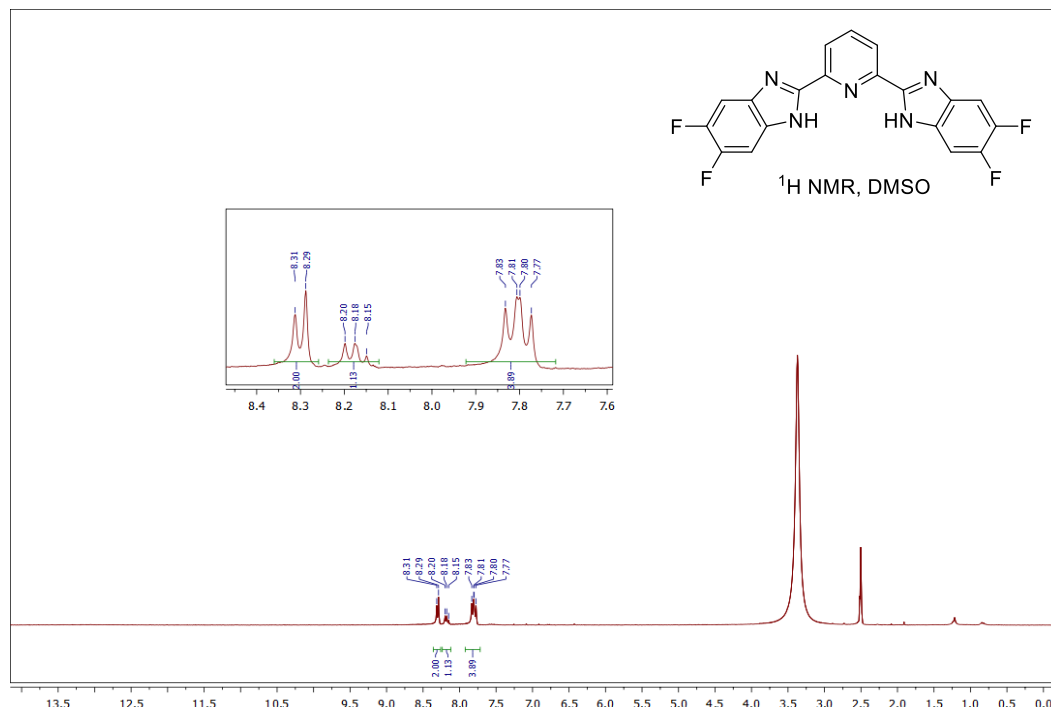


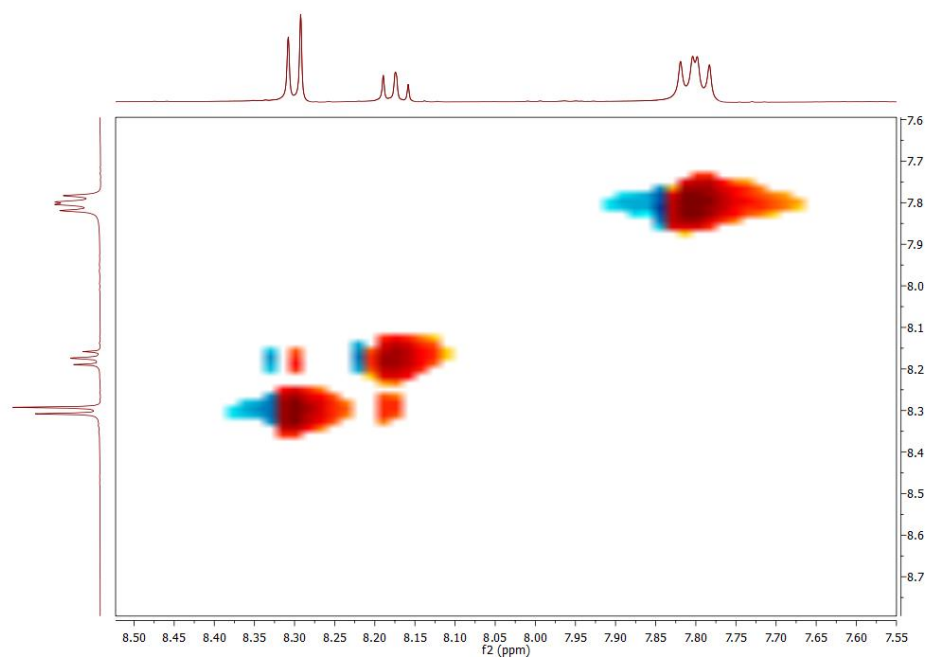
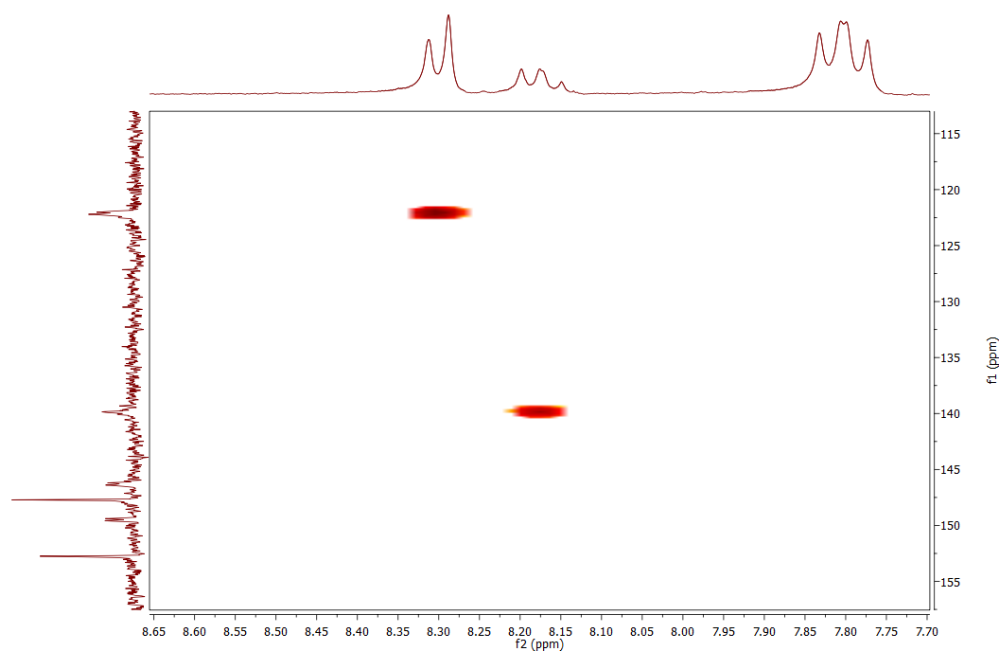


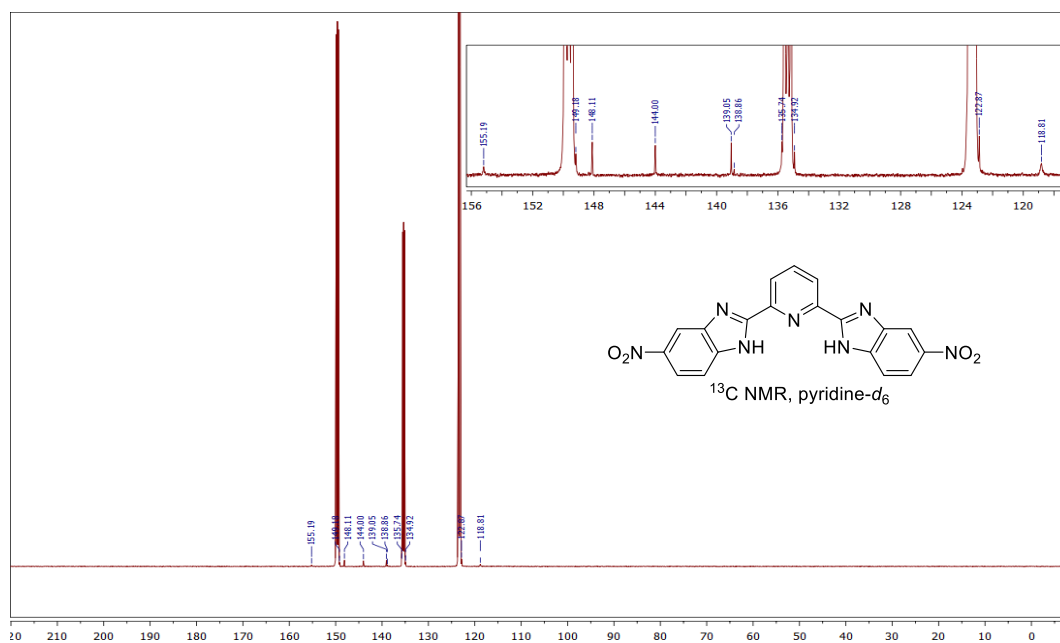
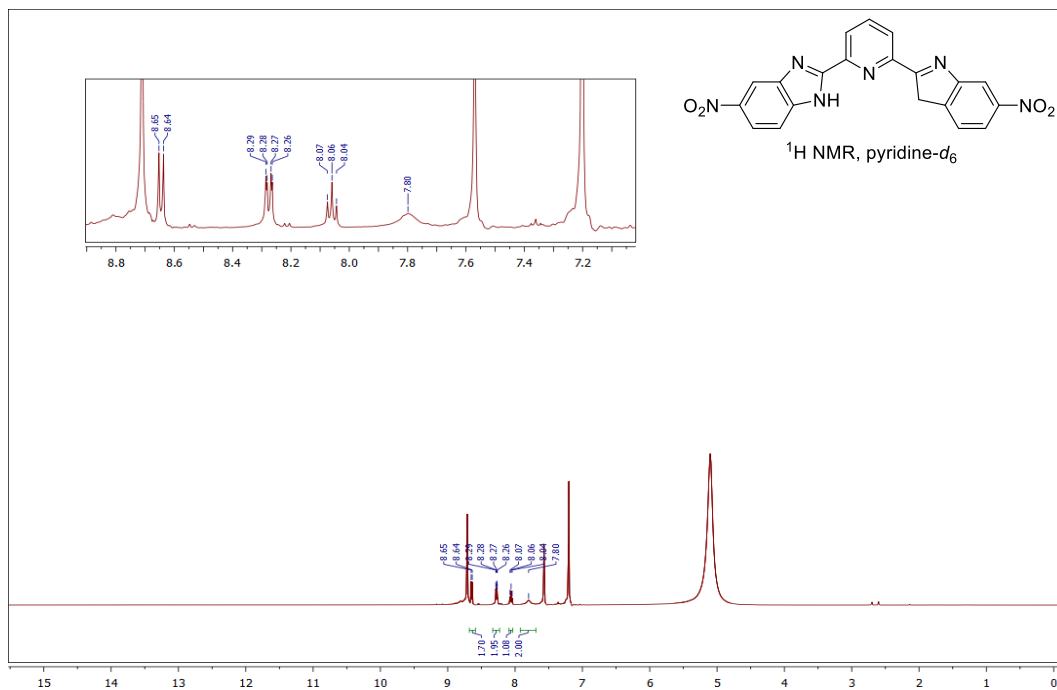


Appendix D for Chapter 5

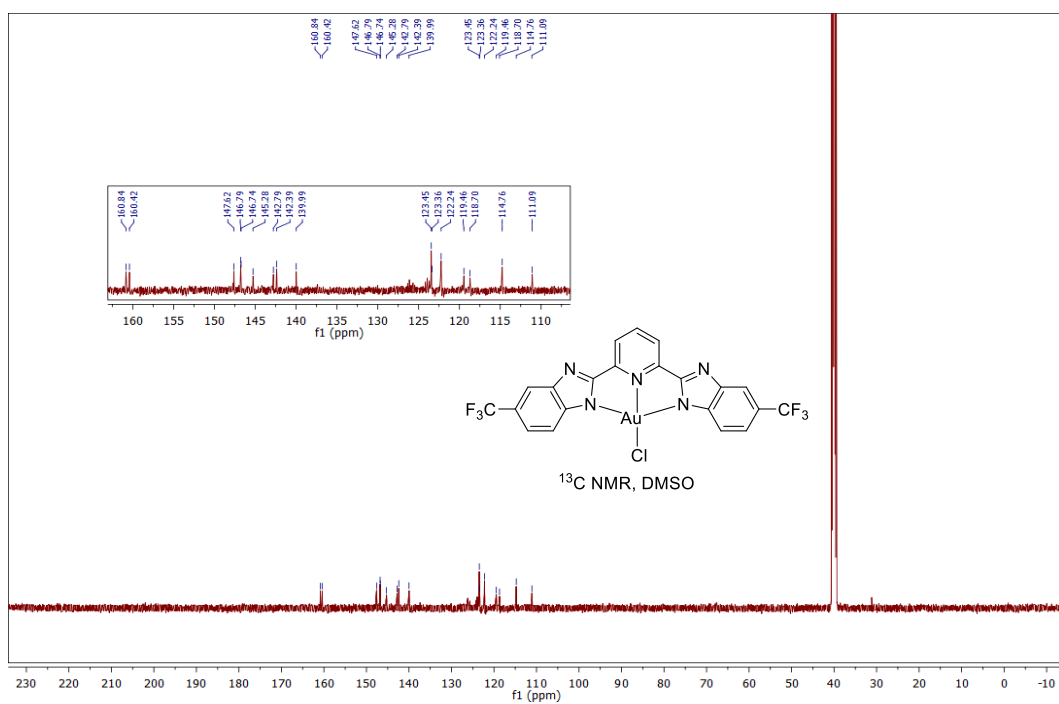
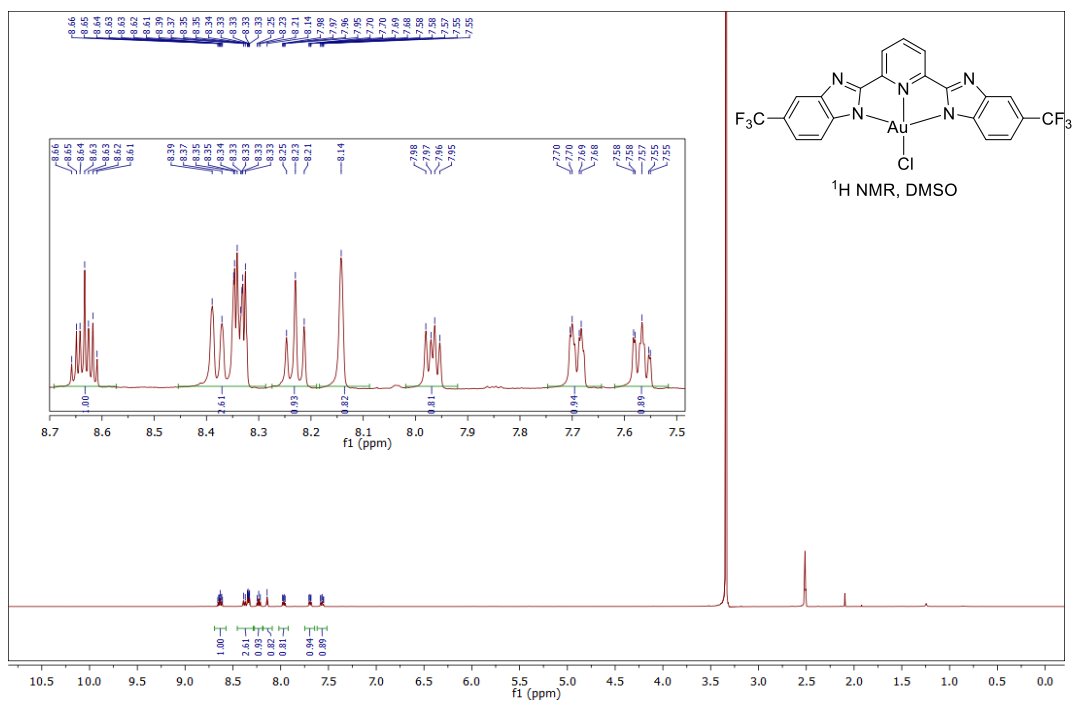


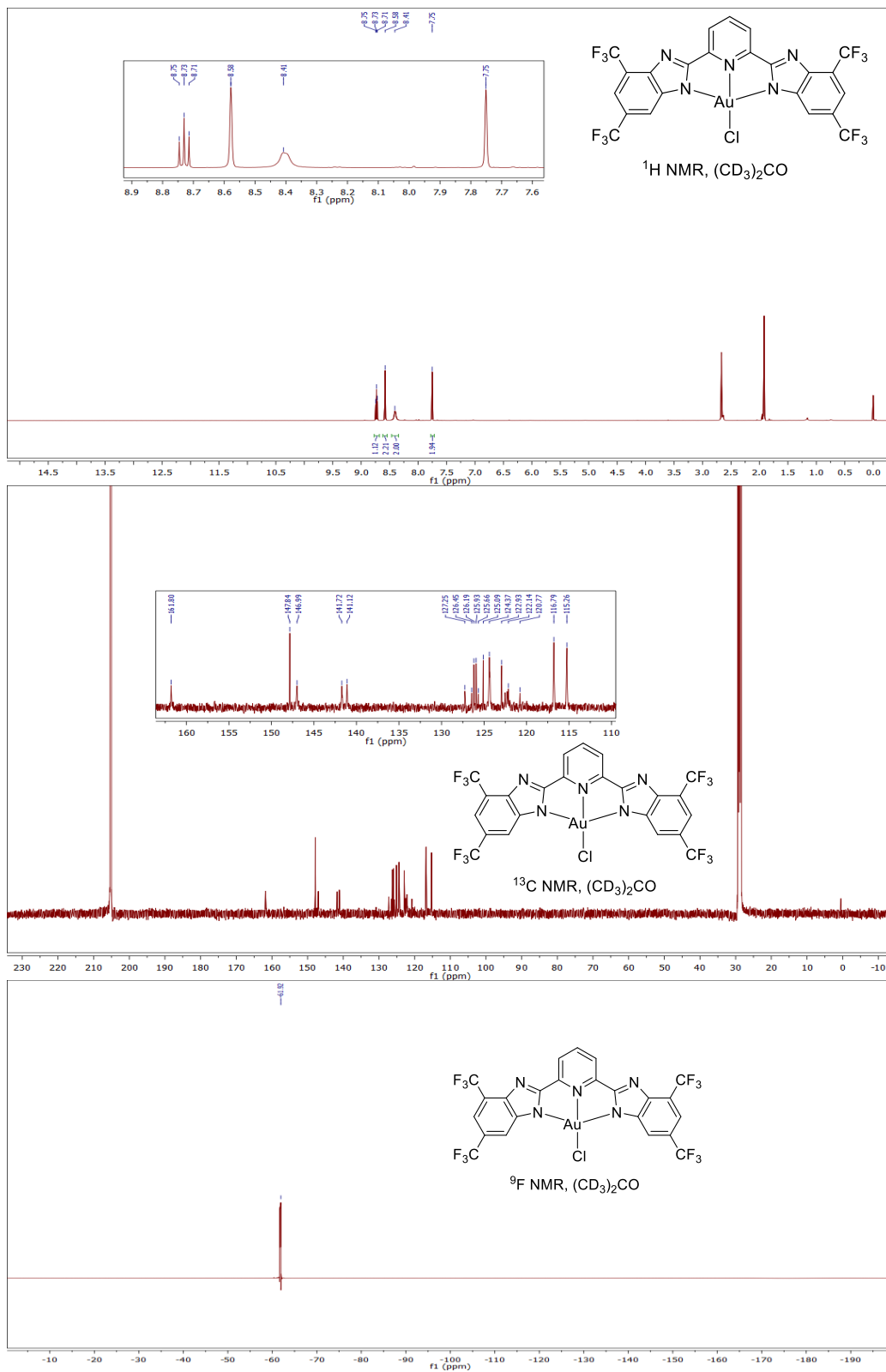


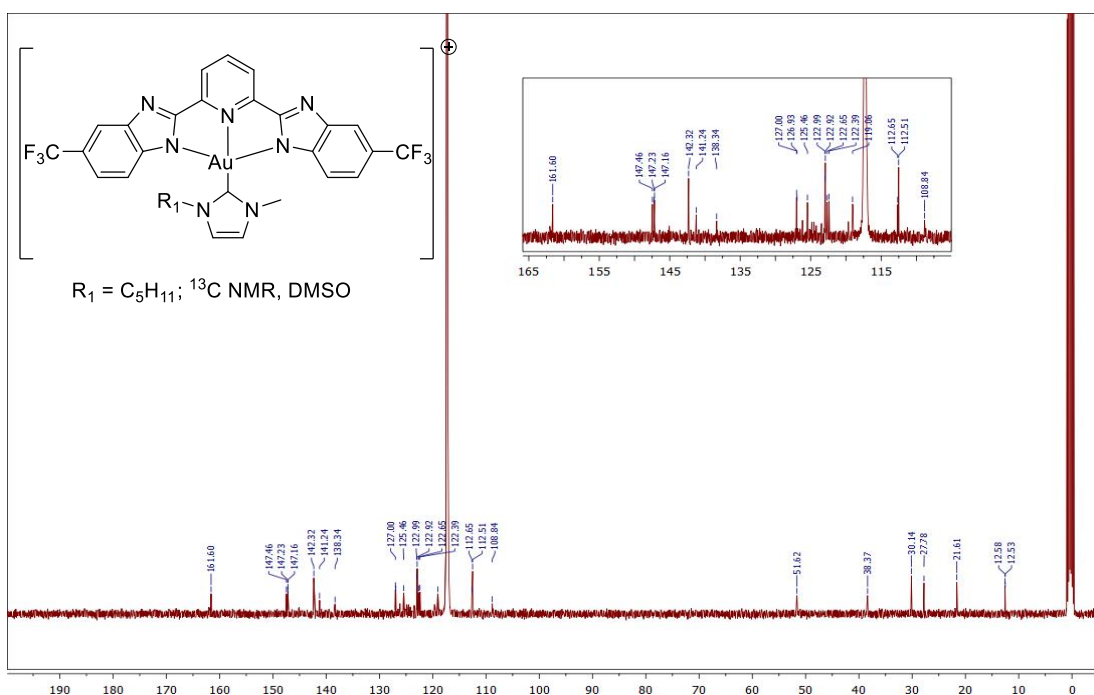
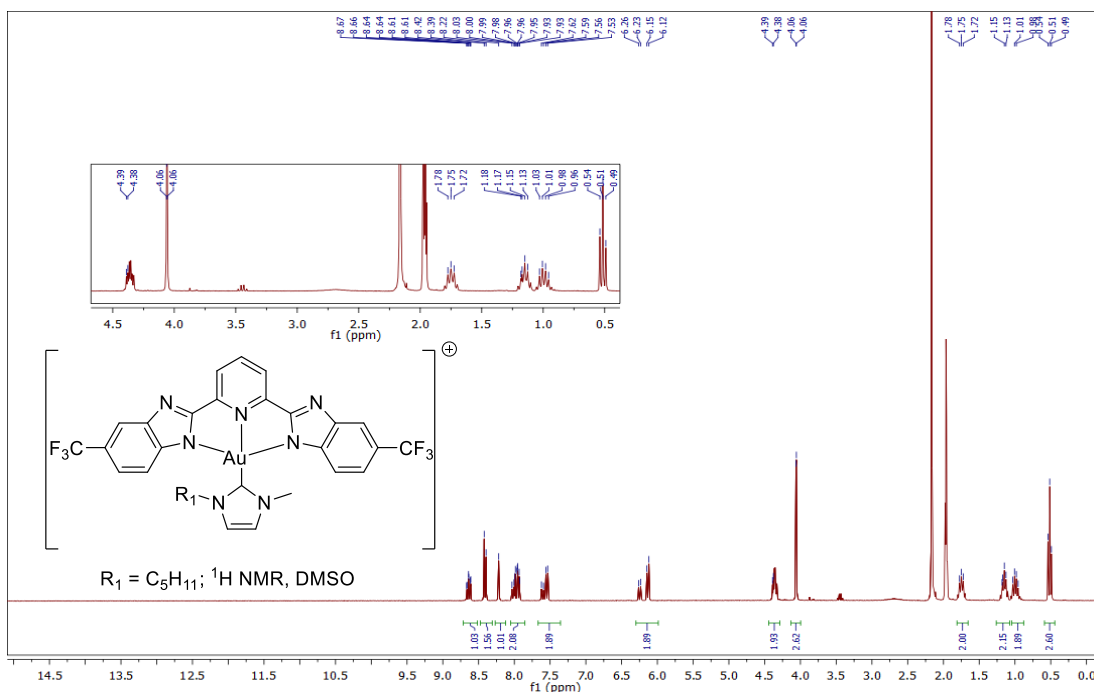


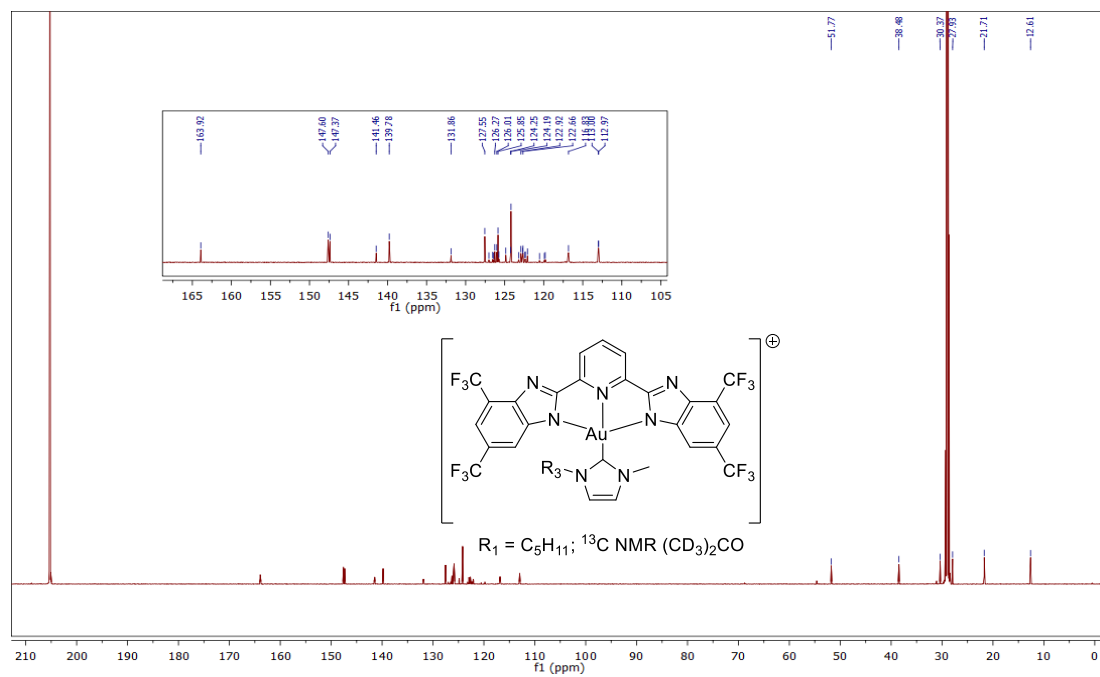
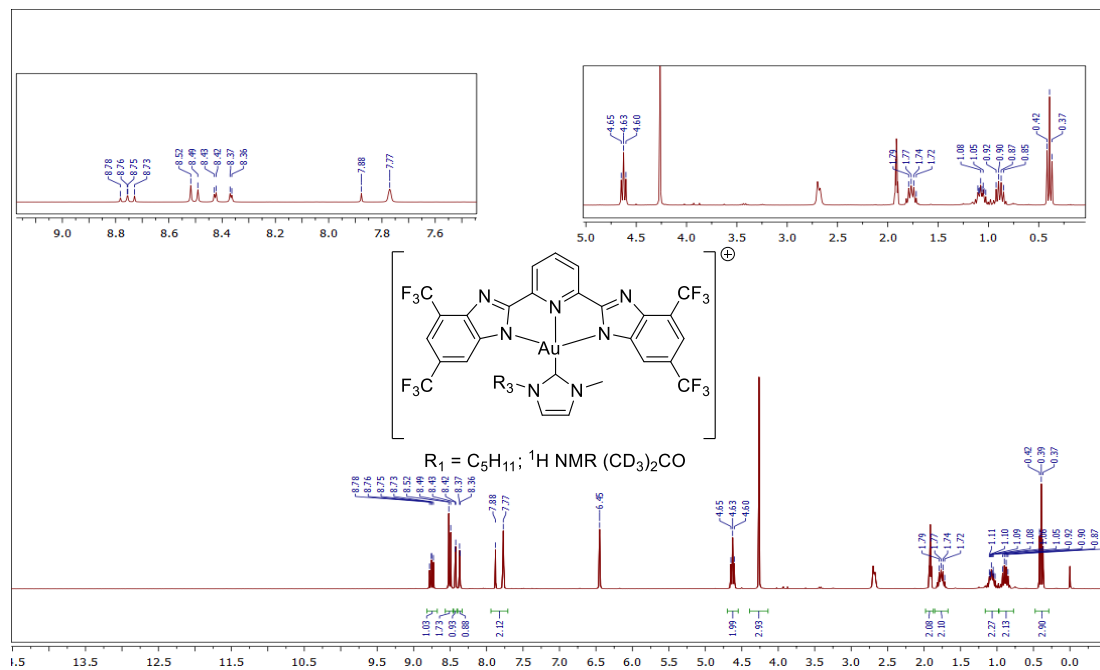


Appendix D for Chapter 5

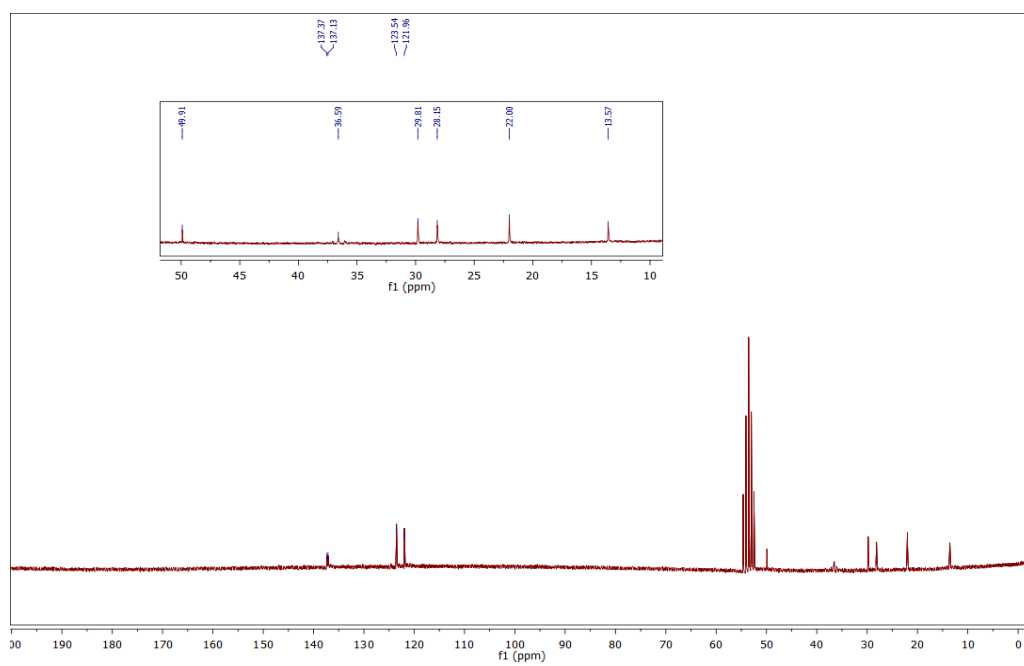
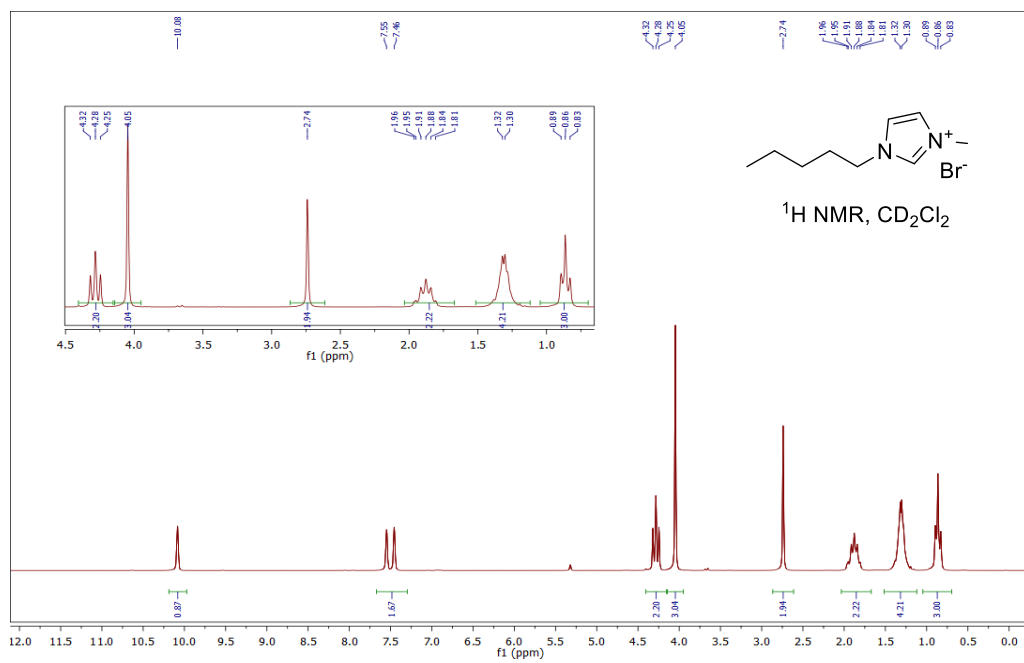


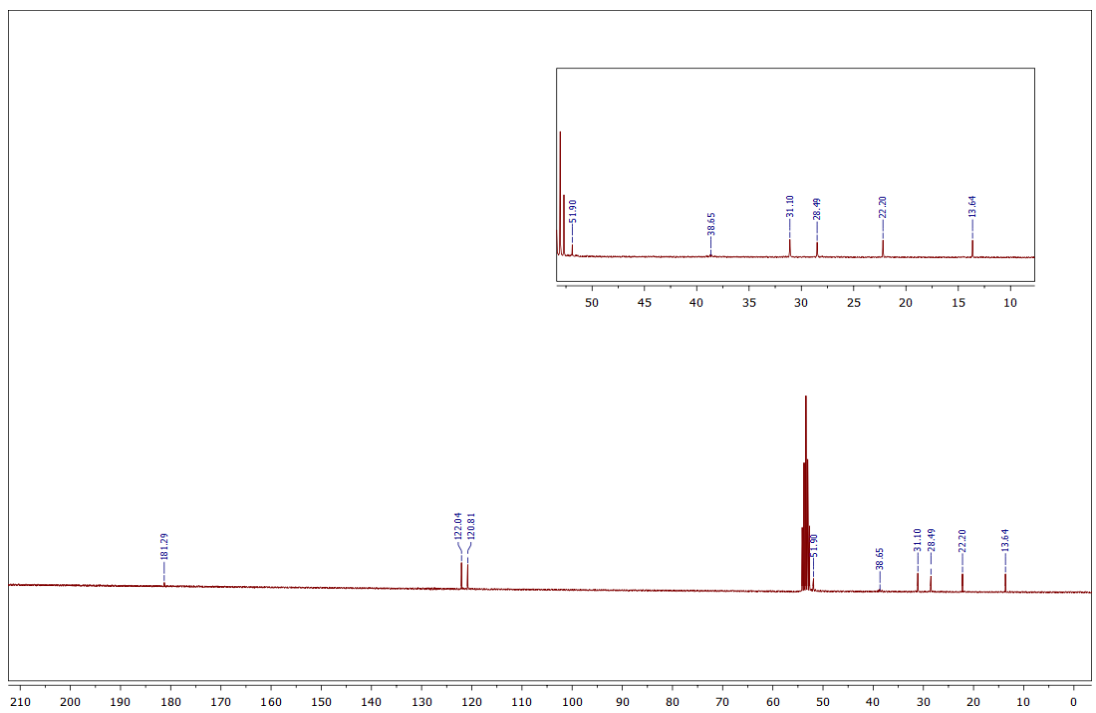
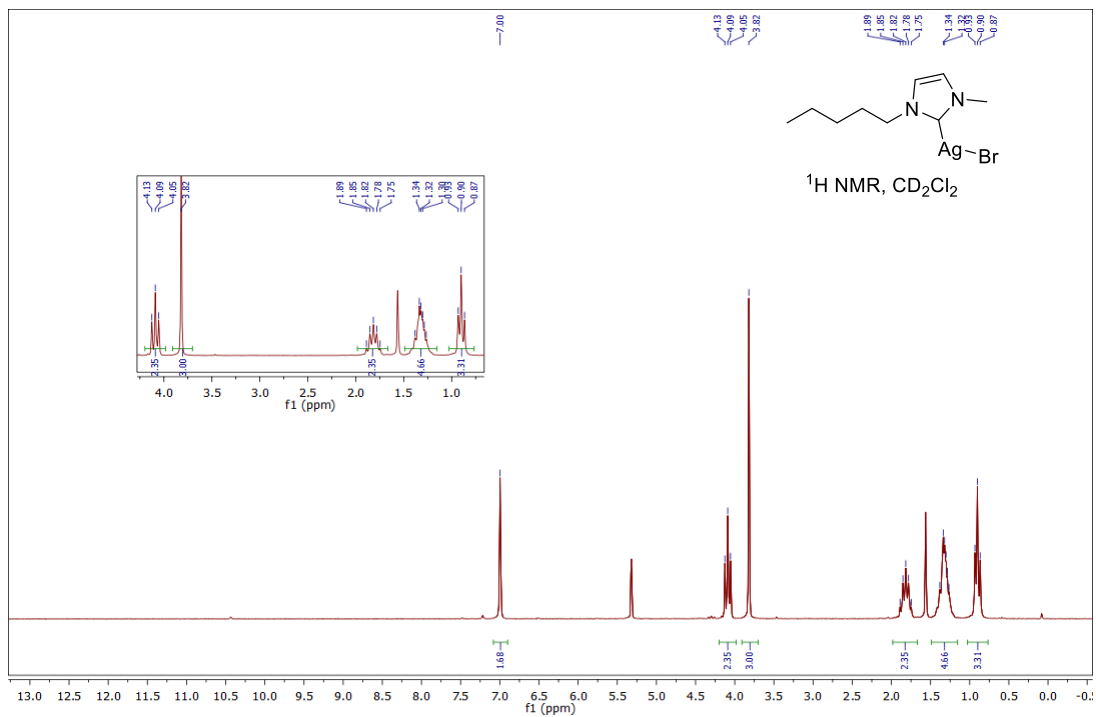






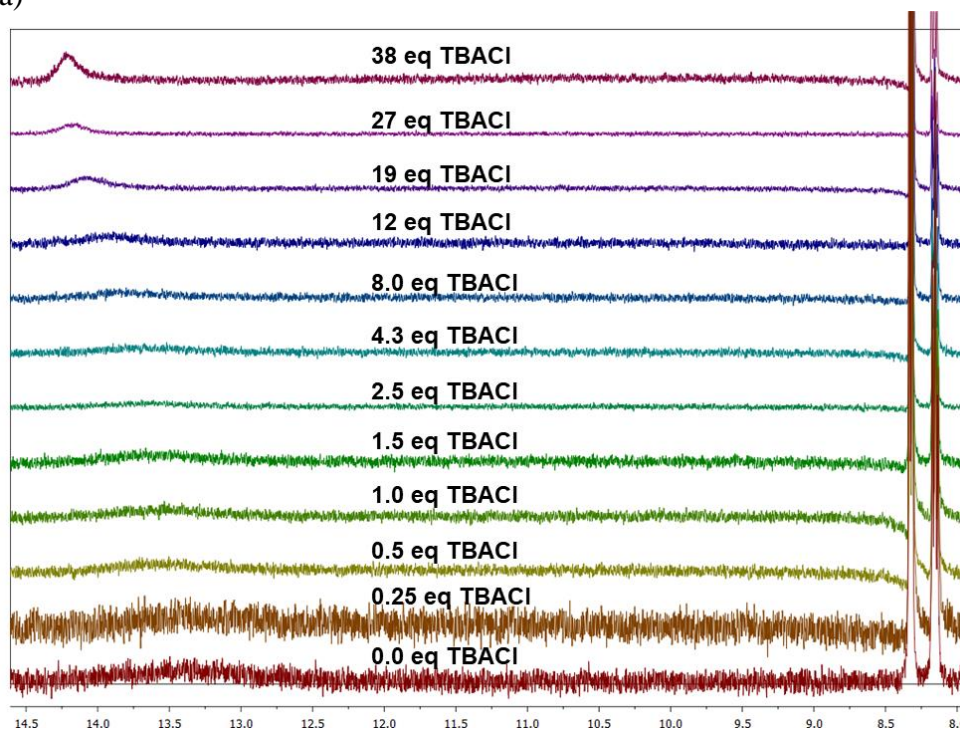
Appendix D for Chapter 5



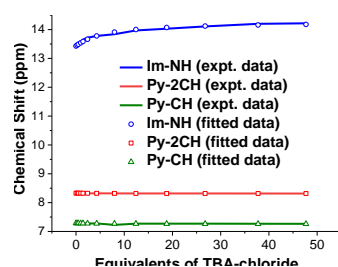


B) Binding studies:

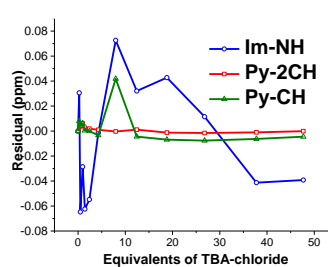
a)



b)



c)



d)

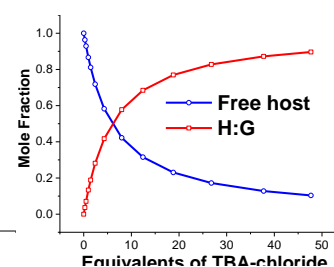
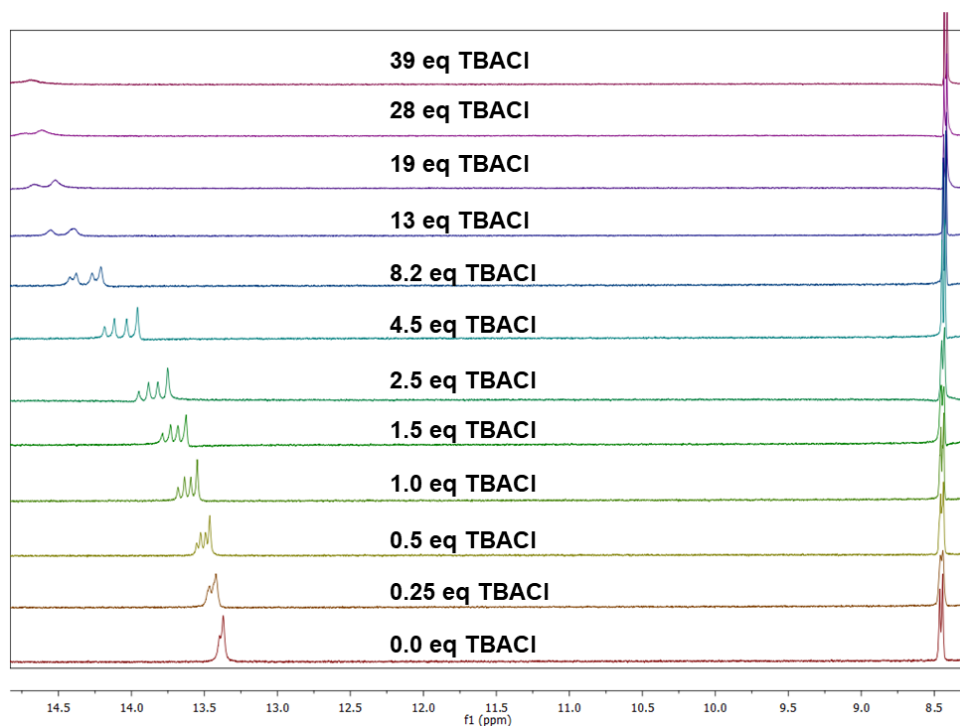
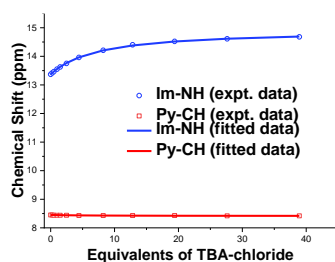


Figure D1: ^1H NMR spectroscopic titration of receptor 1 (2 mM) with TBACl in $\text{DMSO-}d_6$ with 0.5% water at 298 K. a) Stack plot. b) Fitplot for NH proton at $\delta = 13.43$ ppm (proton1, Im-NH) and CH protons at $\delta = 8.33$ ppm (proton2, Py-2CH) and $\delta = 7.29$ ppm (proton3, Py-CH), using global analysis with 1:1 ($K_a = 92 \text{ M}^{-1}$, error: 13%) and 2:1 host:guest stoichiometry ($K_{11} = 40$; $K_{12} = 2514 \text{ M}^{-1}$, error 11 and 21%). c) Plot of the residuals for $\delta = 13.43$ ppm (proton1), $\delta = 8.33$ ppm (proton2) and $\delta = 7.29$ ppm (proton3) using global analysis. d) Calculated mole fractions.

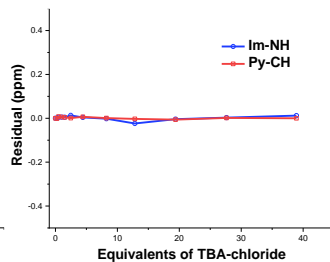
a)



b)



c)



d)

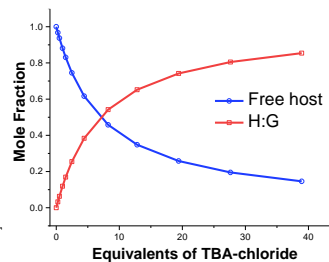


Figure D2: ^1H NMR spectroscopic titration of receptor **2** (2 mM) with TBACl in $\text{DMSO-}d_6$ with 0.5% water at 298 K. a) Stack plot. b) Fitplot for NH proton at $\delta = 13.37$ ppm (proton1, Im-NH) and CH proton at $\delta = 8.45$ ppm (proton2, Py-CH) using global analysis with 1:1 host:guest stoichiometry ($K_a = 77 \text{ M}^{-1}$, error: 2%). c) Plot of the residuals for $\delta = 13.37$ ppm (proton1) and $\delta = 8.45$ ppm (proton2) using global analysis. d) Calculated mole fractions.

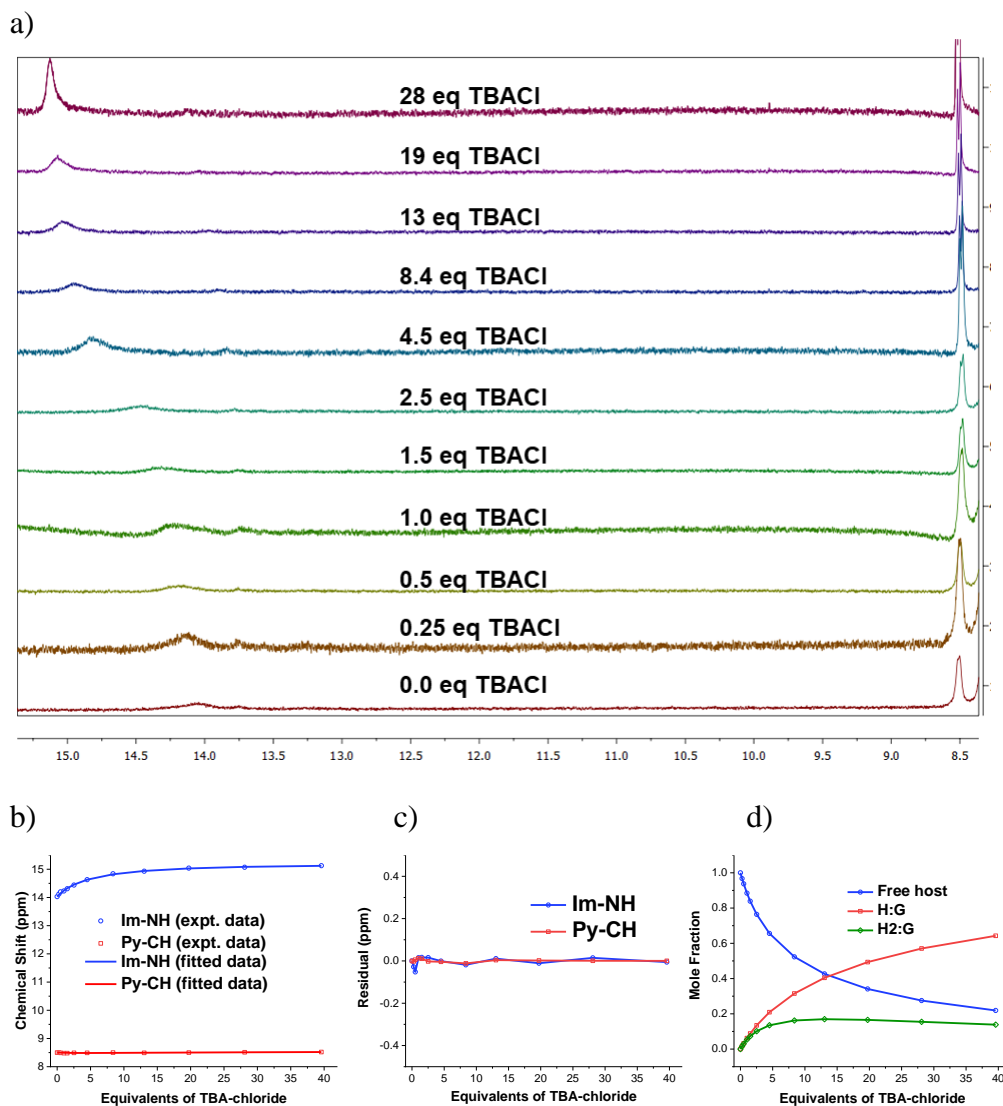


Figure D3: ^1H NMR spectroscopic titration of receptor 3 (2 mM) with TBACl in $\text{DMSO-}d_6$ with 0.5% water at 298 K. a) Stack plot. b) Fitplot for NH proton at $\delta = 14.03$ ppm (proton1, Im-NH) and CH proton at $\delta = 8.50$ ppm (proton2, Py-CH), using global analysis with 1:1 ($K_a = 133 \text{ M}^{-1}$, error: 6%) and 2:1 host:guest stoichiometry ($K_{11} = 40$; $K_{12} = 259 \text{ M}^{-1}$, error 17% for both of them). c) Plot of the residuals for $\delta = 14.03$ ppm (proton1) and $\delta = 8.50$ ppm (proton2) using global analysis. d) Calculated mole fractions.

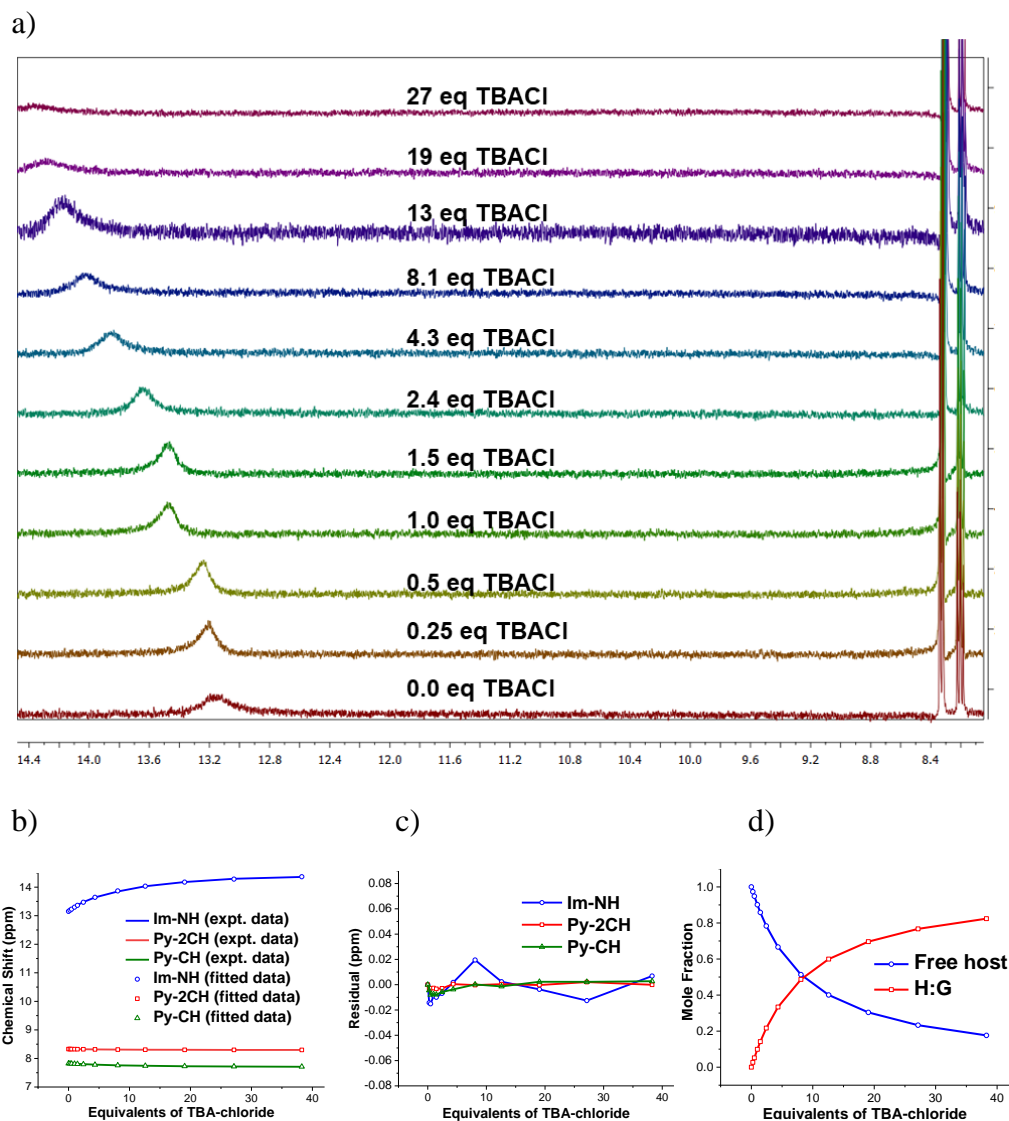


Figure D4: ^1H NMR spectroscopic titration of receptor 1 (2 mM) with TBACl in $\text{DMSO-}d_6$ with 0.5% water at 298 K. a) Stack plot. b) Fitplot for NH proton at $\delta = 13.15$ ppm (proton1, Im-NH) and CH protons at $\delta = 8.33$ ppm (proton2, Py-2CH) and $\delta = 7.83$ ppm (proton3, Py-CH), using global analysis with 1:1 host:guest stoichiometry ($K_a = 63 \text{ M}^{-1}$, error: 2%). c) Plot of the residuals for $\delta = 13.15$ ppm (proton1), $\delta = 8.33$ ppm (proton2) and $\delta = 7.83$ ppm (proton3) using global analysis. d) Calculated mole fractions.

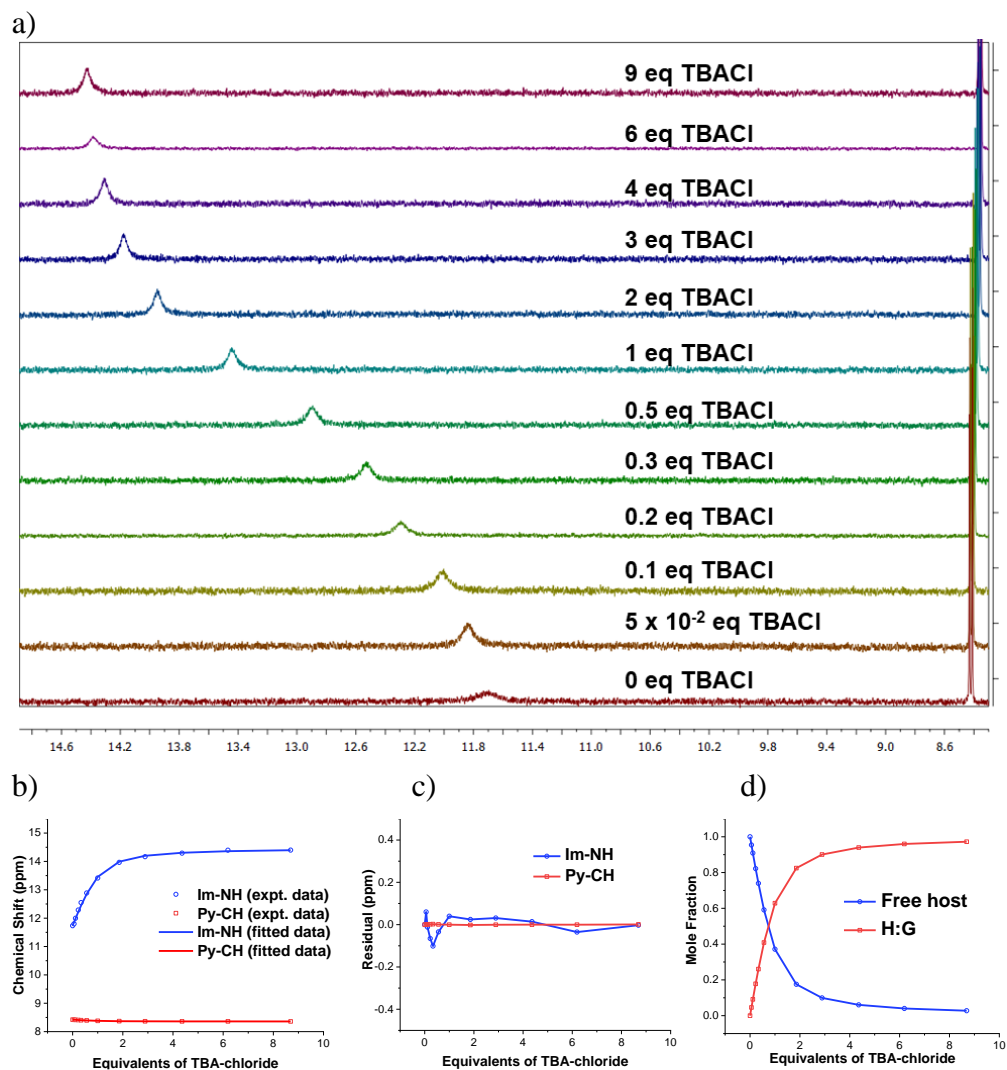


Figure D5: ^1H NMR spectroscopic titration of receptor 1 (1 mM) with TBACl in CD_3CN at 298 K. a) Stack plot. b) Fitplot for NH proton at $\delta = 11.73$ ppm (proton1, Im-NH) and CH proton at $\delta = 8.42$ ppm (proton2, Py-CH), using global analysis with 1:1 host:guest stoichiometry ($K_a = 4586 \text{ M}^{-1}$, error: 11%). c) Plot of the residuals for $\delta = 11.73$ ppm (proton1) and $\delta = 8.42$ ppm (proton2) using global analysis. d) Calculated mole fractions.

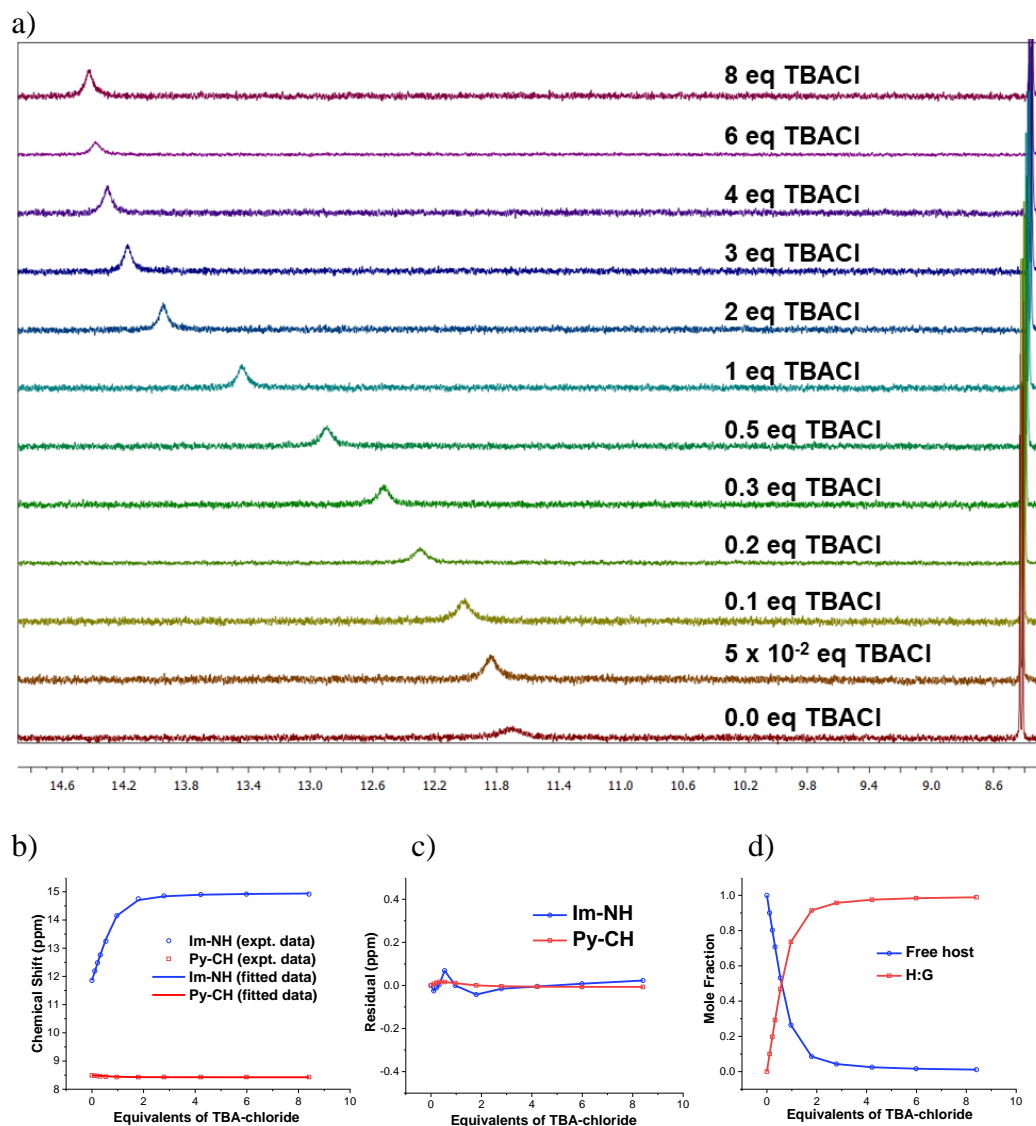


Figure D6: ^1H NMR spectroscopic titration of receptor 2 (1 mM) with TBACl in CD_3CN at 298 K. a) Stack plot. b) Fitplot for NH proton at $\delta = 11.85$ ppm (proton1, Im-NH) and CH proton at $\delta = 8.49$ ppm (proton2, Py-CH), using global analysis with 1:1 host:guest stoichiometry ($K_a = 12051 \text{ M}^{-1}$, error: 10%). c) Plot of the residuals for $\delta = 11.85$ ppm (proton1) and $\delta = 8.49$ ppm (proton2) using global analysis. d) Calculated mole fractions.

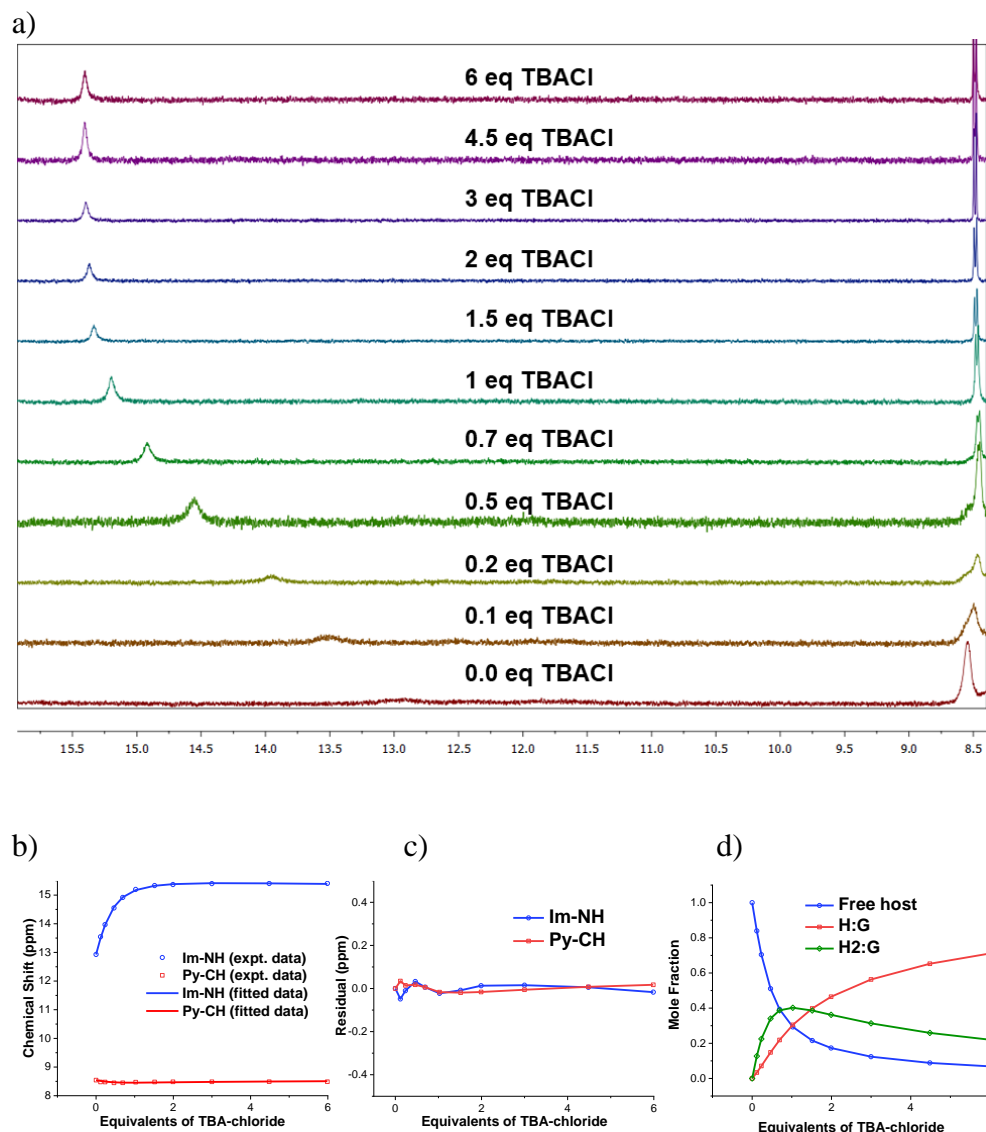


Figure D7: ^1H NMR spectroscopic titration of receptor **3** (1 mM) with TBACl in CD_3CN at 298 K. a) Stack plot. b) Fitplot for NH proton at $\delta = 12.93$ ppm (proton1, Im-NH) and CH proton at $\delta = 8.54$ ppm (proton2, Py-CH), using global analysis with 2:1 host:guest stoichiometry ($K_{11} = 1987$; $K_{12}: 2238 \text{ M}^{-1}$, error 15 and 7%, respectively). c) Plot of the residuals for $\delta = 12.93$ ppm (proton1) and $\delta = 8.54$ ppm (proton2) using global analysis. d) Calculated mole fractions.

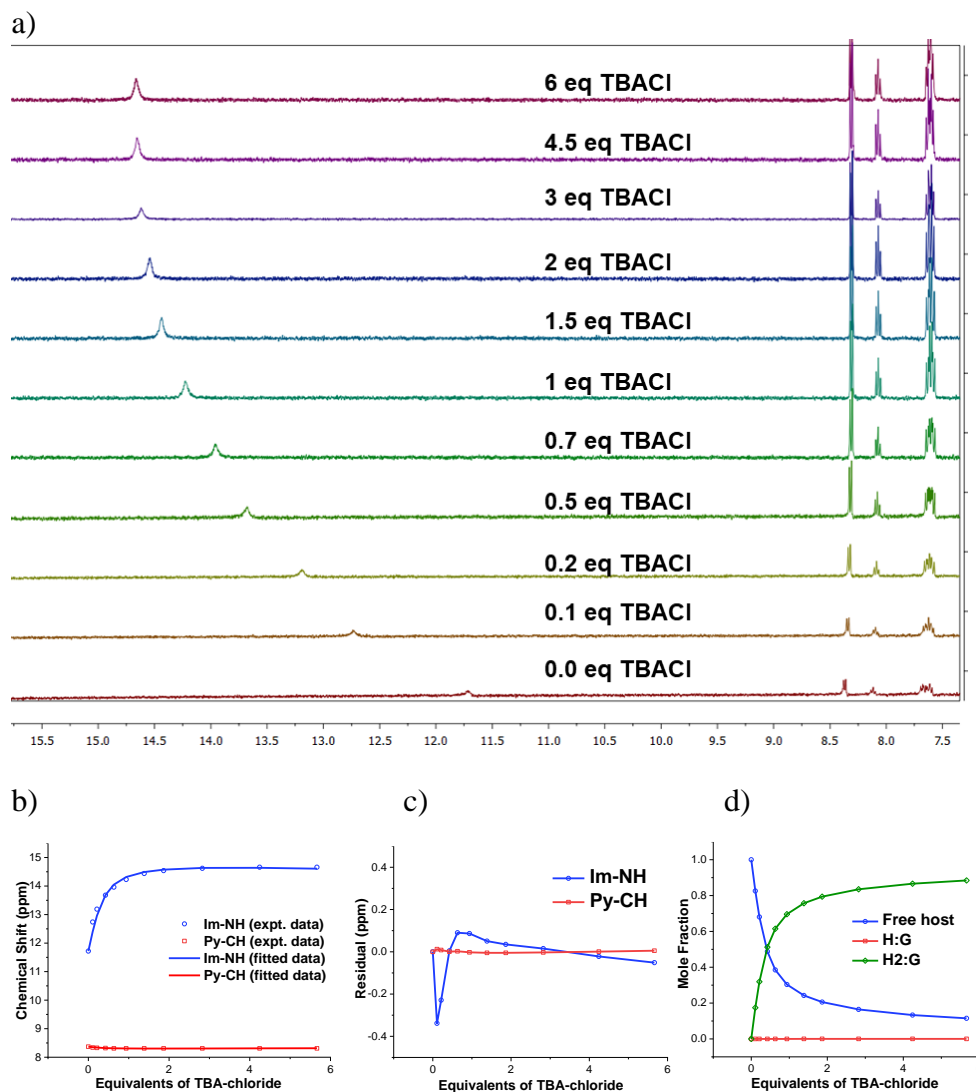


Figure D8: ^1H NMR spectroscopic titration of receptor **4** (1 mM) with TBACl in CD_3CN at 298 K. a) Stack plot. b) Fitplot for NH proton at $\delta = 11.72$ ppm (proton1, Im-NH) and CH proton at $\delta = 8.37$ ppm (proton2, Py-CH), using global analysis with 2:1 host:guest stoichiometry ($K_{11} = 0.69$; $K_{12} = 8.2 \times 10^6 \text{ M}^{-1}$). c) Plot of the residuals for $\delta = 11.72$ ppm (proton1) and $\delta = 8.37$ ppm (proton2) using global analysis. d) Calculated mole fractions.

C) Transport studies:

1) HPTS

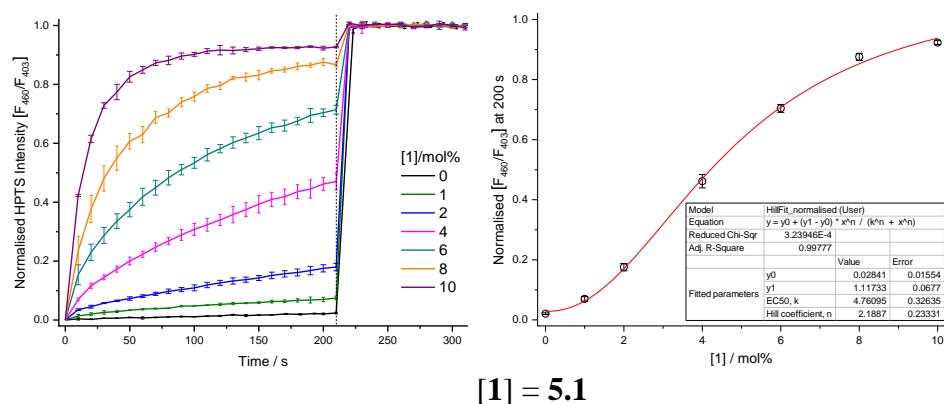


Figure D9: Hill plot analysis of H^+/Cl^- symport or Cl^-/OH^- antiport facilitated by compound **5.1** using KCl-KOH assay from POPC vesicles loaded with KCl (100 mM), buffered to pH 7.0 with HEPES (10 mM). The test compound was added at 0 s and detergent was added at 200 s. Ionophore concentrations are shown as ionophore to lipid molar ratios. Error bars represent SD from at least three repeats.

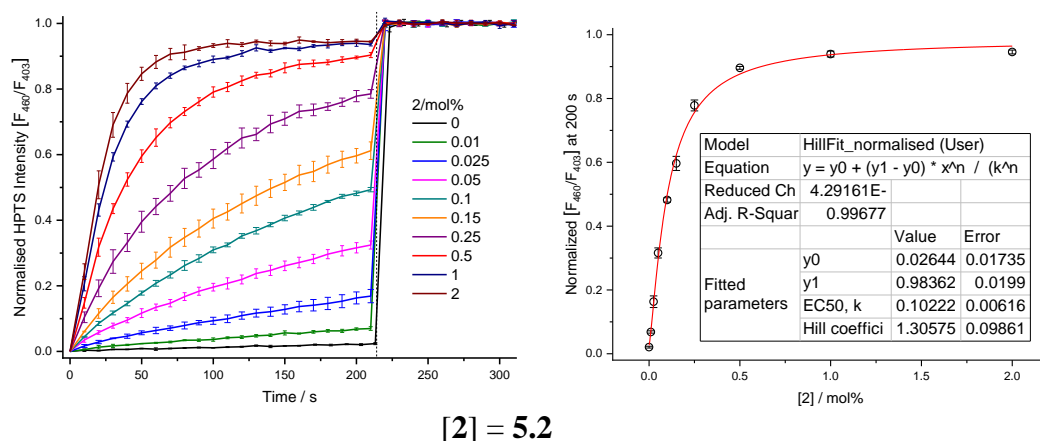
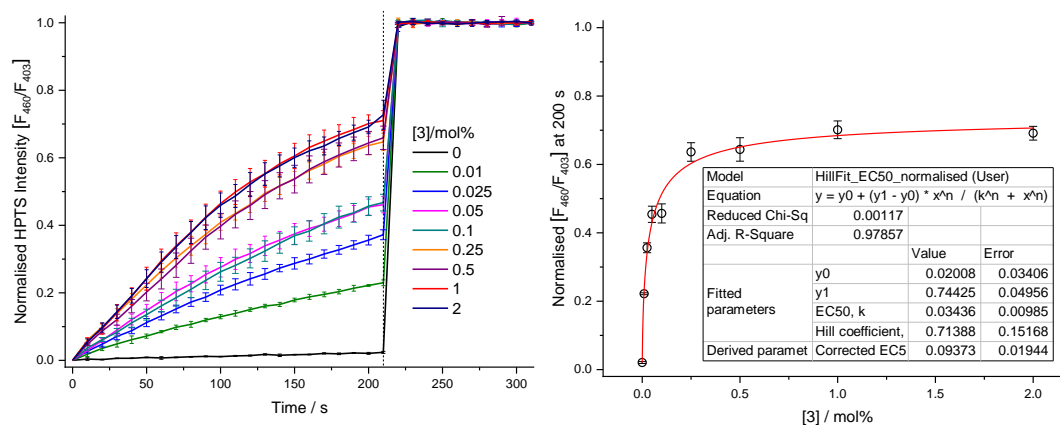
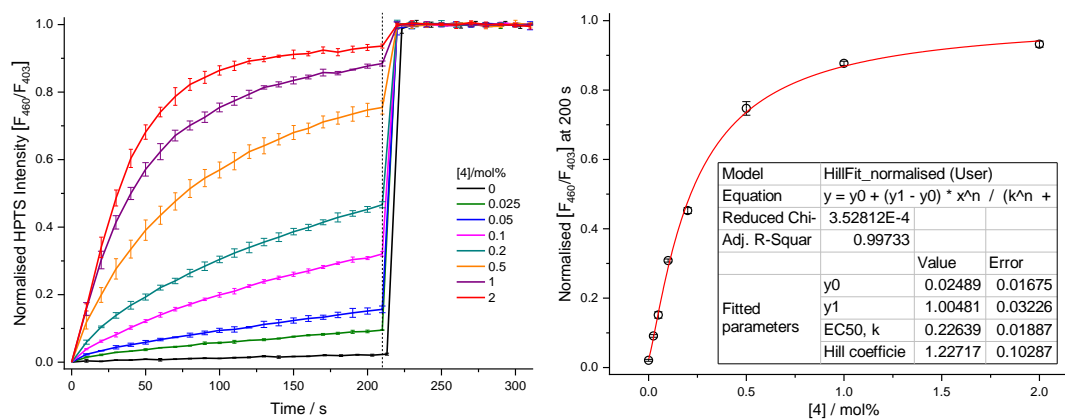


Figure D10: Hill plot analysis of H^+/Cl^- symport or Cl^-/OH^- antiport facilitated by compound **5.2** using KCl-KOH assay from POPC vesicles loaded with KCl (100 mM), buffered to pH 7.0 with HEPES (10 mM). The test compound was added at 0 s and detergent was added at 200 s. Ionophore concentrations are shown as ionophore to lipid molar ratios. Error bars represent SD from at least three repeats.



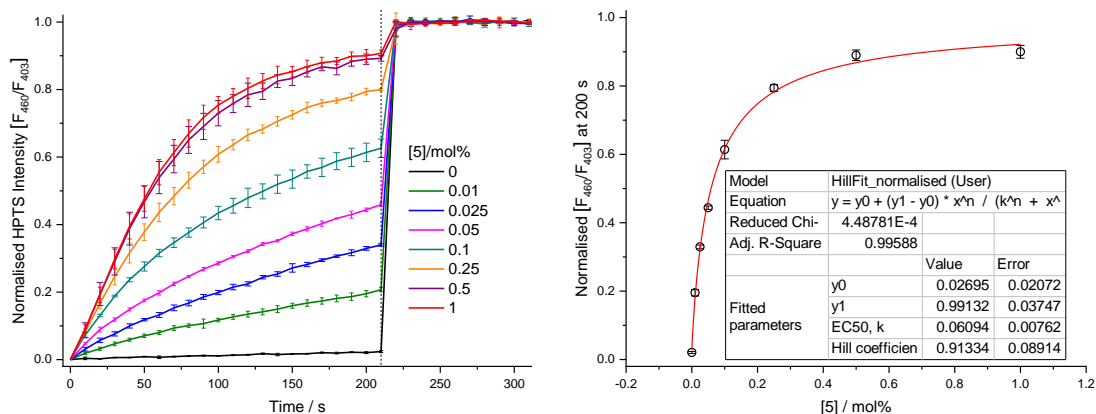
[3] = 5.3

Figure D11: Hill plot analysis of H^+/Cl^- symport or Cl^-/OH^- antiport facilitated by compound **5.3** using KCl-KOH assay from POPC vesicles loaded with KCl (100 mM), buffered to pH 7.0 with HEPES (10 mM). The test compound was added at 0 s and detergent was added at 200 s. Ionophore concentrations are shown as ionophore to lipid molar ratios. Error bars represent SD from at least three repeats.



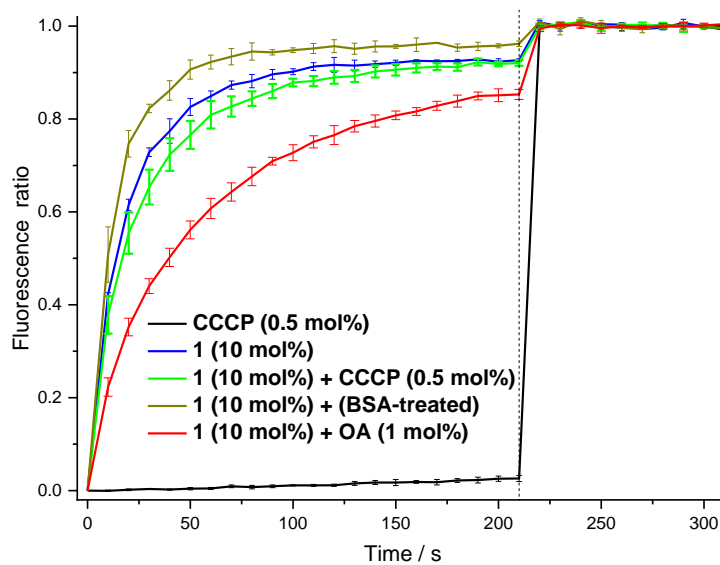
[4] = 5.4

Figure D12: Hill plot analysis of H^+/Cl^- symport or Cl^-/OH^- antiport facilitated by compound **5.4** using KCl-KOH assay from POPC vesicles loaded with KCl (100 mM), buffered to pH 7.0 with HEPES (10 mM). The test compound was added at 0 s and detergent was added at 200 s. Ionophore concentrations are shown as ionophore to lipid molar ratios. Error bars represent SD from at least three repeats.



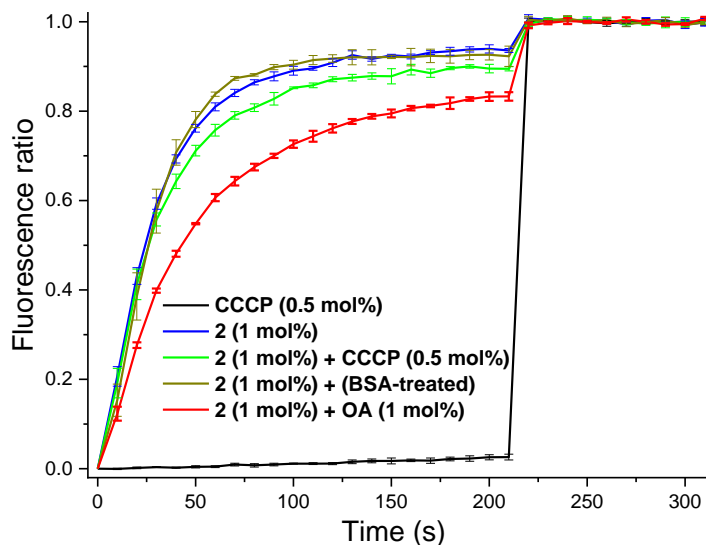
5 = 5.5

Figure D13: Hill plot analysis of H⁺/Cl⁻ symport or Cl⁻/OH⁻ antiport facilitated by compound **5.5** using KCl-KOH assay from POPC vesicles loaded with KCl (100 mM), buffered to pH 7.0 with HEPES (10 mM). The test compound was added at 0 s and detergent was added at 200 s. Ionophore concentrations are shown as ionophore to lipid molar ratios. Error bars represent SD from at least three repeats.



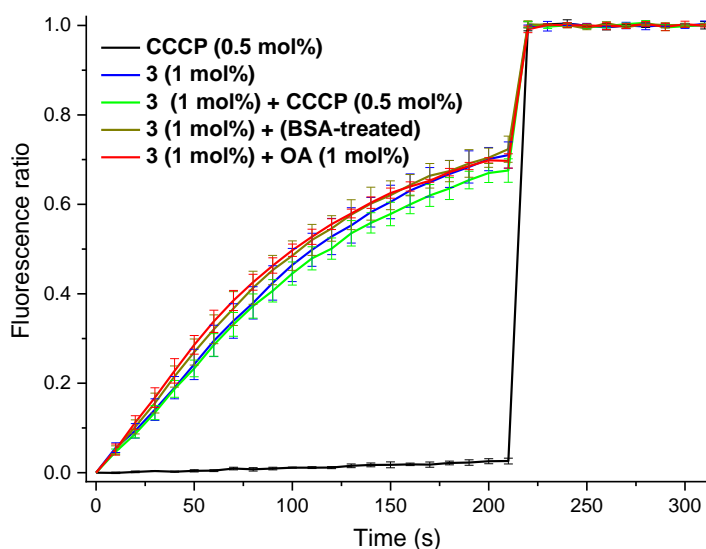
1 = 5.1

Figure D14: Using KCl-KOH assay from POPC vesicles loaded with KCl (100 mM), buffered to pH 7.0 with HEPES (10 mM), different conditions were applied to determine the effect of addition of the protonophore cccp at 0.5 mol% (to measure of chloride uniport solely), oleic acid at 1 mol% (as a source of fatty acid) and BSA-treated lipid (to test if the transport is fatty acid dependent) on the rate of chloride transport of receptor **5.1** (10 mol%).



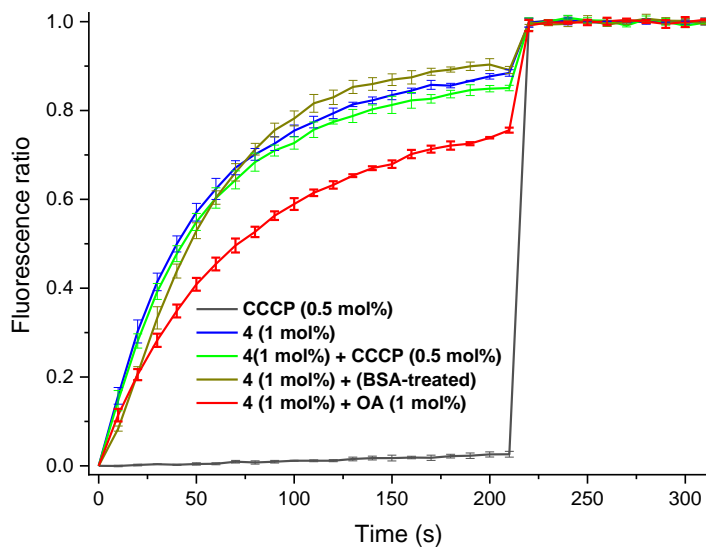
2 = 5.2

Figure D15: Using KCl-KOH assay from POPC vesicles loaded with KCl (100 mM), buffered to pH 7.0 with HEPES (10 mM), different conditions were applied to determine the effect of addition of the protonophore cccp at 0.5 mol% (as a measure of chloride uniport), oleic acid at 1 mol% (as a source of fatty acid) and BSA-treated lipid (to test if the transport is fatty acid dependent) on the rate of chloride transport of receptor **5.2** (1 mol%).



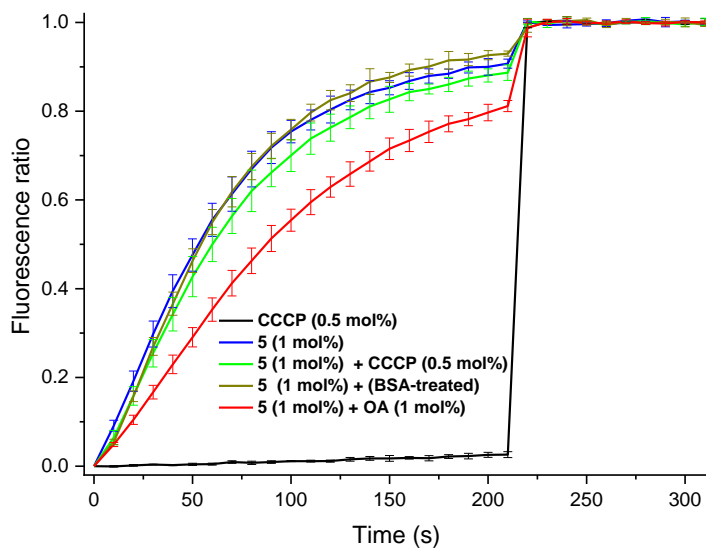
3 = 5.3

Figure D16: Using KCl-KOH assay from POPC vesicles loaded with KCl (100 mM), buffered to pH 7.0 with HEPES (10 mM), different conditions were applied to determine the effect of addition of the protonophore cccp at 0.5 mol% (as a measure of chloride uniport), oleic acid at 1 mol% (as a source of fatty acid) and BSA-treated lipid (to test if the transport is fatty acid dependent) on the rate of chloride transport of receptor **5.3** (1 mol%).



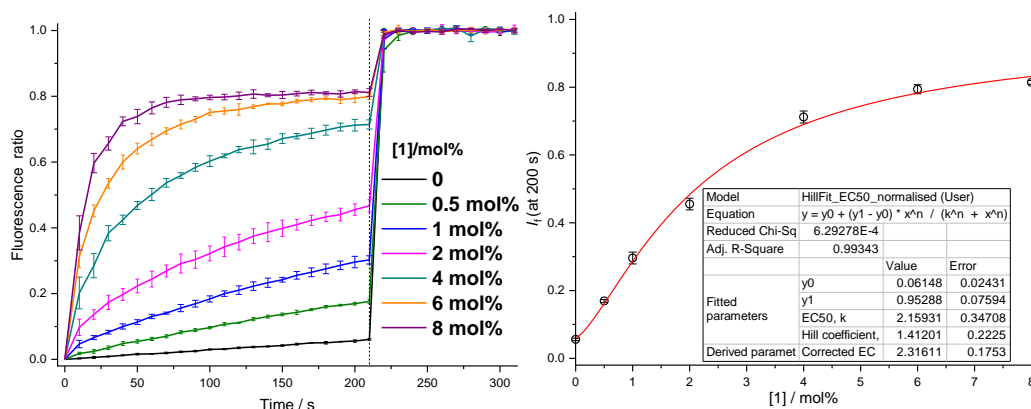
4 = [5.4]

Figure D17: Using KCl-KOH assay from POPC vesicles loaded with KCl (100 mM), buffered to pH 7.0 with HEPES (10 mM), different conditions were applied to determine the effect of addition of the protonophore cccp at 0.5 mol% (as a measure of chloride uniport), oleic acid at 1 mol% (as a source of fatty acid) and BSA-treated lipid (to test if the transport is fatty acid dependent) on the rate of chloride transport of receptor **5.4** (1 mol%).



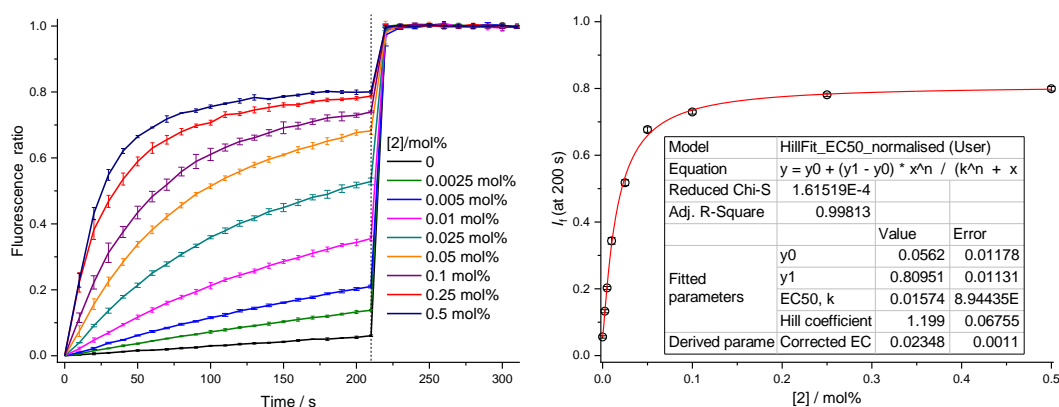
5 = [5.5]

Figure D18: Using KCl-KOH assay from POPC vesicles loaded with KCl (100 mM), buffered to pH 7.0 with HEPES (10 mM), different conditions were applied to determine the effect of addition of the protonophore cccp at 0.5 mol% (as a measure of chloride uniport), oleic acid at 1 mol% (as a source of fatty acid) and BSA-treated lipid (to test if the transport is fatty acid dependent) on the rate of chloride transport of receptor **5.5** (1 mol%).



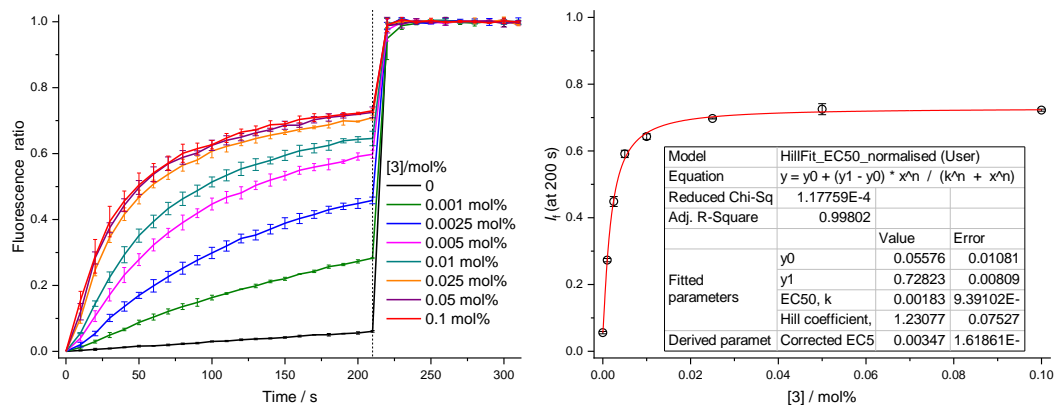
[1] = 5.1

Figure D19: Hill plot analysis of H^+ flux facilitated by compound 5.1 using K₂Glu-KOH assay from POPC vesicles loaded with K₂Glu (100 mM), buffered to pH 7.0 with HEPES (10 mM). The test compound was added at 0 s and detergent was added at 200 s. Ionophore concentrations are shown as ionophore to lipid molar ratios. Error bars represent SD from at least three repeats.



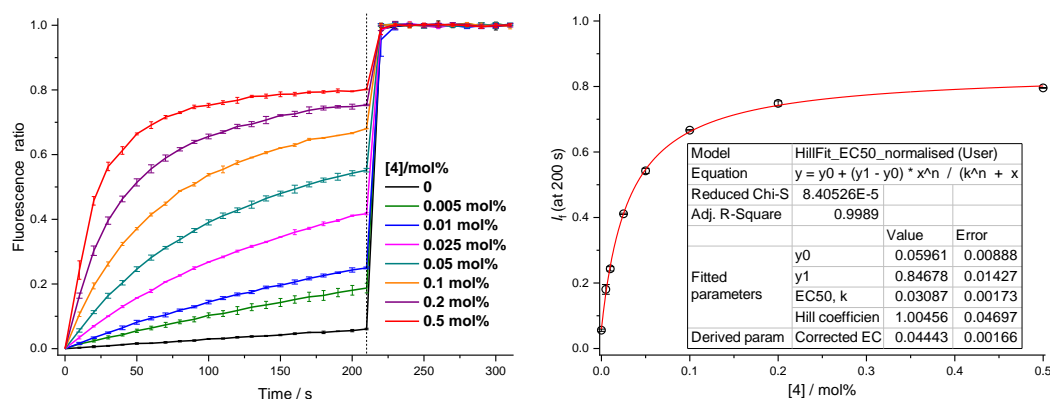
[2] = 5.2

Figure D20: Hill plot analysis of H^+ flux facilitated by compound 5.2 using K₂Glu-KOH assay from POPC vesicles loaded with K₂Glu (100 mM), buffered to pH 7.0 with HEPES (10 mM). The test compound was added at 0 s and detergent was added at 200 s. Ionophore concentrations are shown as ionophore to lipid molar ratios. Error bars represent SD from at least three repeats.



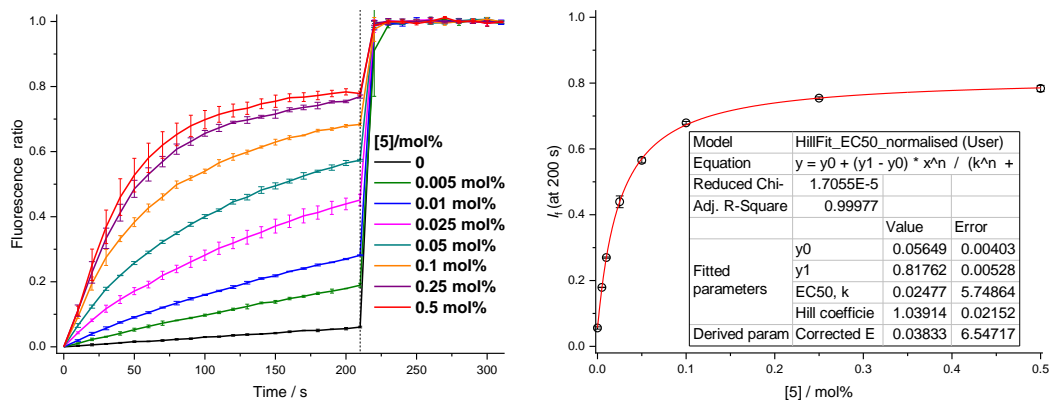
[3] = 5.3

Figure D21: Hill plot analysis of H⁺ flux facilitated by compound **5.3** using KGlu-KOH assay from POPC vesicles loaded with KGlu (100 mM), buffered to pH 7.0 with HEPES (10 mM). The test compound was added at 0 s and detergent was added at 200 s. Ionophore concentrations are shown as ionophore to lipid molar ratios. Error bars represent SD from at least three repeats.



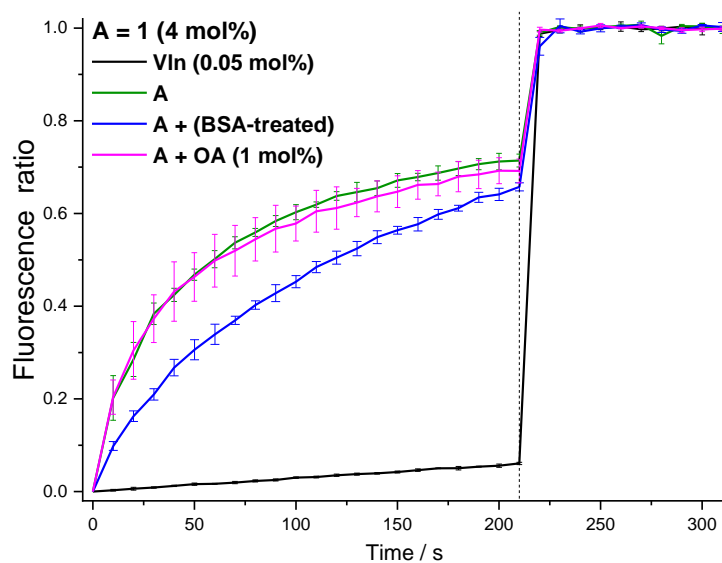
[4] = 5.4

Figure D22: Hill plot analysis of H⁺ flux facilitated by compound **5.4** using KGlu-KOH assay from POPC vesicles loaded with KGlu (100 mM), buffered to pH 7.0 with HEPES (10 mM). The test compound was added at 0 s and detergent was added at 200 s. Ionophore concentrations are shown as ionophore to lipid molar ratios. Error bars represent SD from at least three repeats.



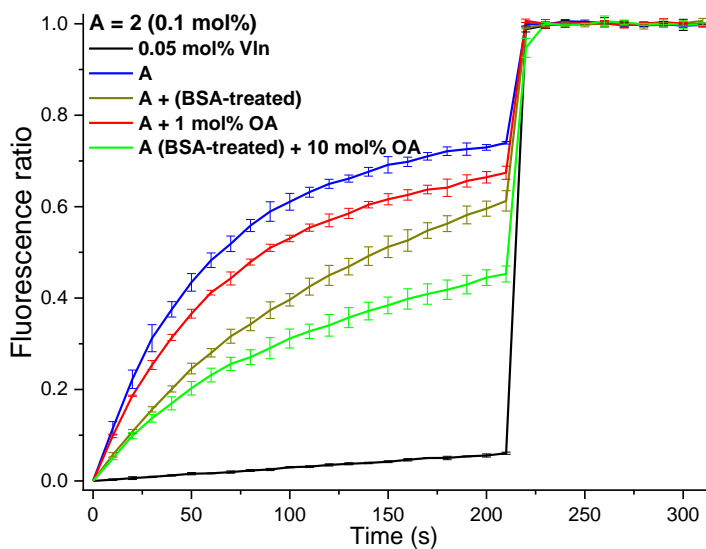
5 = 5.5

Figure D23: Hill plot analysis of H^+ flux facilitated by compound **5.5** using KGlu-KOH assay from POPC vesicles loaded with KGlu (100 mM), buffered to pH 7.0 with HEPES (10 mM). The test compound was added at 0 s and detergent was added at 200 s. Ionophore concentrations are shown as ionophore to lipid molar ratios. Error bars represent SD from at least three repeats.



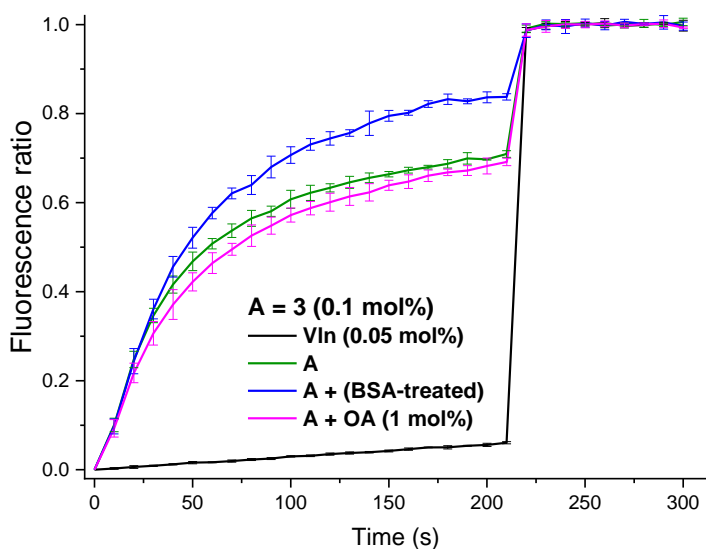
1 = 5.1

Figure D24: Using KGlu-KOH assay from POPC vesicles loaded with KGlu (100 mM), buffered to pH 7.0 with HEPES (10 mM), different conditions were applied to determine the effect of addition of the ionophore valinomycin at 0.05 mol% (as a measure of H^+ flux), oleic acid at 1 mol% (as a source of fatty acid) and BSA-treated lipid (to test if the transport is fatty acid dependent) on the rate of chloride transport of receptor **5.1** (4 mol%).



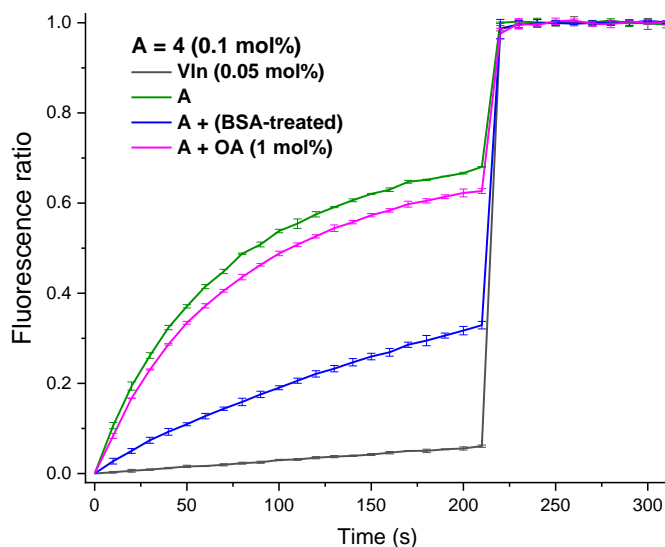
2 = 5.2

Figure D25: Using KGlu-KOH assay from POPC vesicles loaded with KGlu (100 mM), buffered to pH 7.0 with HEPES (10 mM), different conditions were applied to determine the effect of addition of the ionophore valinomycin at 0.05 mol% (as a measure of H^+ flux), oleic acid at 1 mol% AND 10 mol% (as a source of fatty acid) and BSA-treated lipid (to test if the transport is fatty acid dependent) on the rate of chloride transport of receptor **5.2** (0.1 mol%).



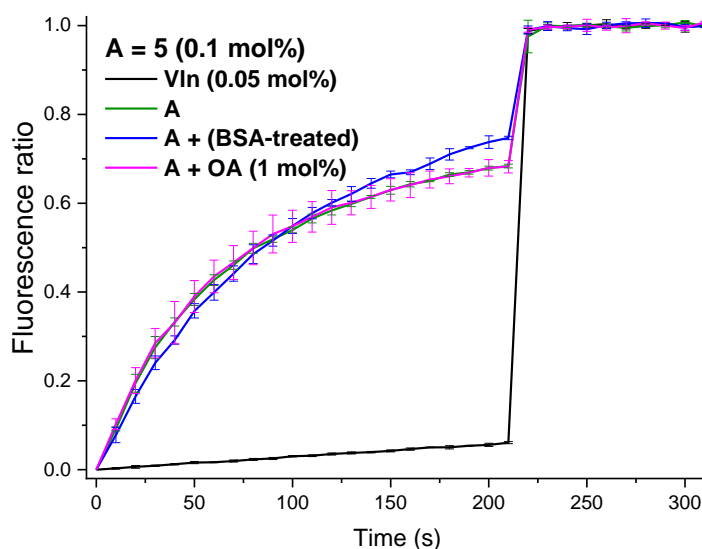
3 = 5.3

Figure D26: Using KGlu-KOH assay from POPC vesicles loaded with KGlu (100 mM), buffered to pH 7.0 with HEPES (10 mM), different conditions were applied to determine the effect of addition of the ionophore valinomycin at 0.05 mol% (as a measure of H^+ flux), oleic acid at 1 mol% (as a source of fatty acid) and BSA-treated lipid (to test if the transport is fatty acid dependent) on the rate of chloride transport of receptor **5.3** (0.1 mol%).



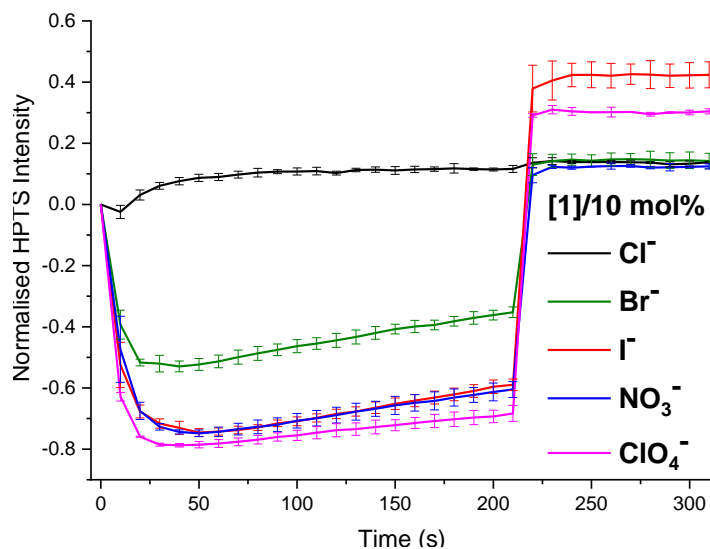
4 = 5.4

Figure D27: Using KGlu-KOH assay from POPC vesicles loaded with KGlu (100 mM), buffered to pH 7.0 with HEPES (10 mM), different conditions were applied to determine the effect of addition of the ionophore valinomycin at 0.05 mol% (as a measure of H^+ flux), oleic acid at 1 mol% (as a source of fatty acid) and BSA-treated lipid (to test if the transport is fatty acid dependent) on the rate of chloride transport of receptor **5.4** (0.1 mol%).



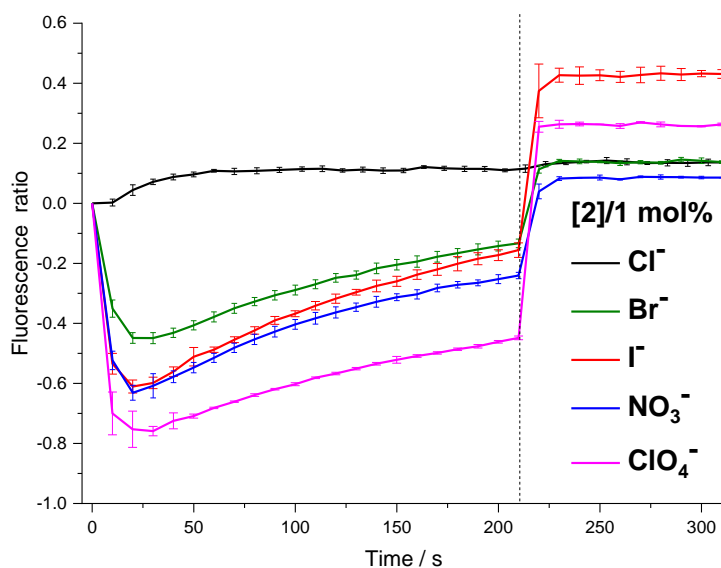
5 = 5.5

Figure D28: Using KGlu-KOH assay from POPC vesicles loaded with KGlu (100 mM), buffered to pH 7.0 with HEPES (10 mM), different conditions were applied to determine the effect of addition of the ionophore valinomycin at 0.05 mol% (as a measure of H^+ flux), oleic acid at 1 mol% (as a source of fatty acid) and BSA-treated lipid (to test if the transport is fatty acid dependent) on the rate of chloride transport of receptor **5.5** (0.1 mol%).



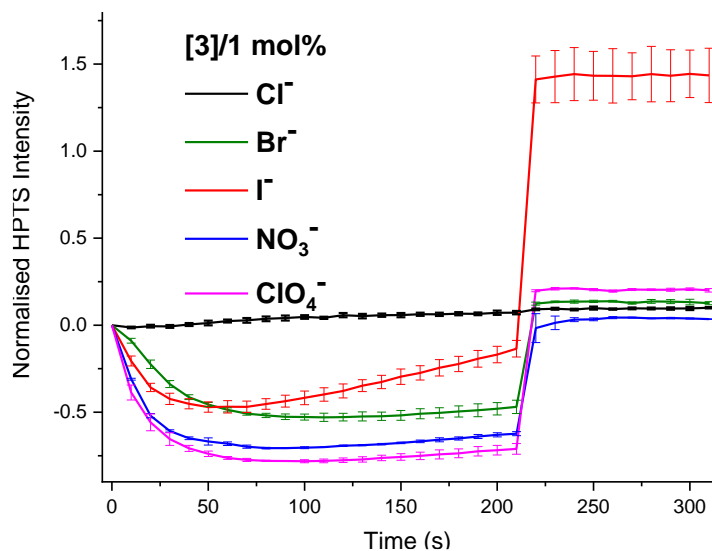
[1] = 5.1

Figure D29: Observed fluorescence ratio response due to HCl influx in the presence of compounds **5.1** (10 mol%) into vesicles loaded with KCl (100 mM) and suspended in KCl, KBr, KI, KNO₃ and KClO₄ (100 mM). All external and internal solutions were buffered to pH 7 with HEPES (10 mM).



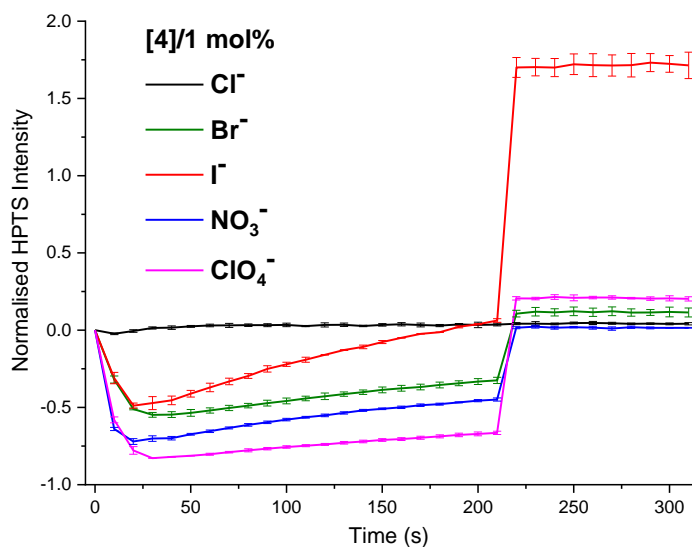
[2] = 5.2

Figure D30: Observed fluorescence ratio response due to HCl influx in the presence of compounds **5.2** (1 mol%) into vesicles loaded with KCl (100 mM) and suspended in KCl, KBr, KI, KNO₃ and KClO₄ (100 mM). All external and internal solutions were buffered to pH 7 with HEPES (10 mM).



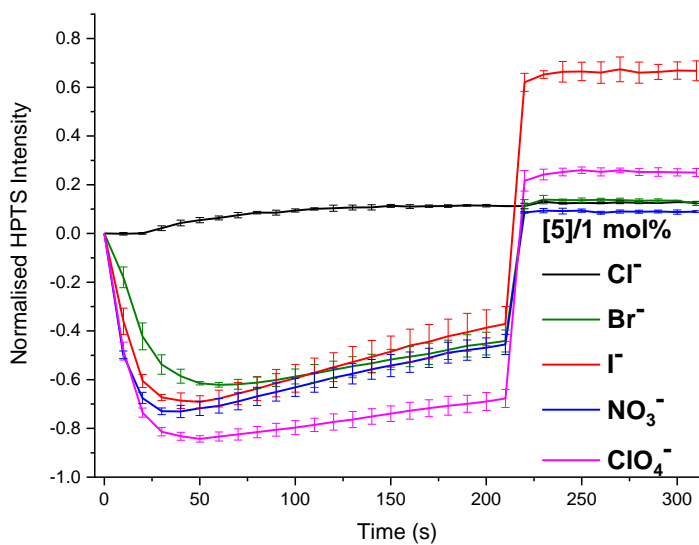
[3] = 5.3

Figure D31: Observed fluorescence ratio response due to HCl influx in the presence of compounds **5.3** (1 mol%) into vesicles loaded with KCl (100 mM) and suspended in KCl, KBr, KI, KNO_3 and KClO_4 (100 mM). All external and internal solutions were buffered to pH 7 with HEPES (10 mM).



[4] = 5.4

Figure D32: Observed fluorescence ratio response due to HCl influx in the presence of compounds **5.4** (1 mol%) into vesicles loaded with KCl (100 mM) and suspended in KCl, KBr, KI, KNO_3 and KClO_4 (100 mM). All external and internal solutions were buffered to pH 7 with HEPES (10 mM).



[5] = 5.5

Figure D33: Observed fluorescence ratio response due to HCl influx in the presence of compounds **5.5** (1 mol%) into vesicles loaded with KCl (100 mM) and suspended in KCl, KBr, KI, KNO₃ and KClO₄ (100 mM). All external and internal solutions were buffered to pH 7 with HEPES (10 mM).

2) Potassium over sodium selectivity:

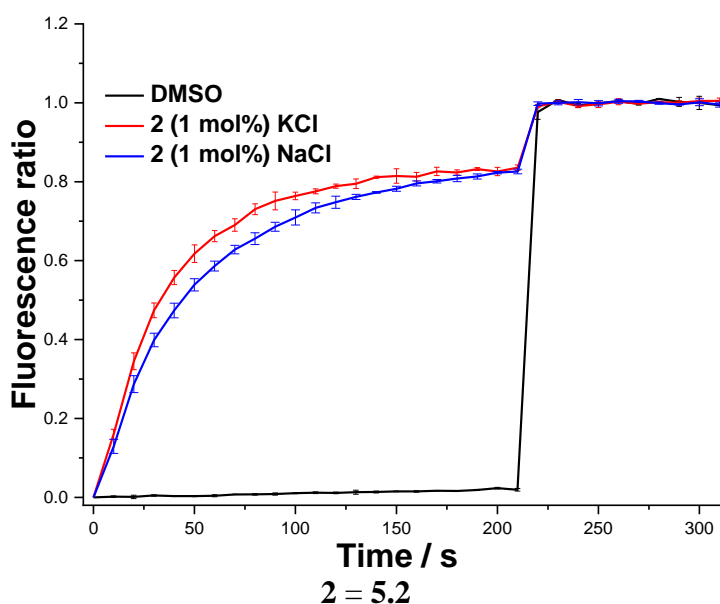


Figure D34: Observed fluorescence ratio response due to HCl influx or Cl⁻/OH⁻ antiport facilitated by compound **5.2** (1 mol%) using KCl-KOH and NaCl-KOH assays from POPC vesicles loaded with KCl (100 mM) or NaCl, respectively. All external and internal solutions were buffered to pH 7.0 with HEPES (10 mM). The test compound was added at 0 s and detergent was added at 200 s. Ionophore concentrations are shown as ionophore to lipid molar ratios. Error bars represent SD from at least three repeats.

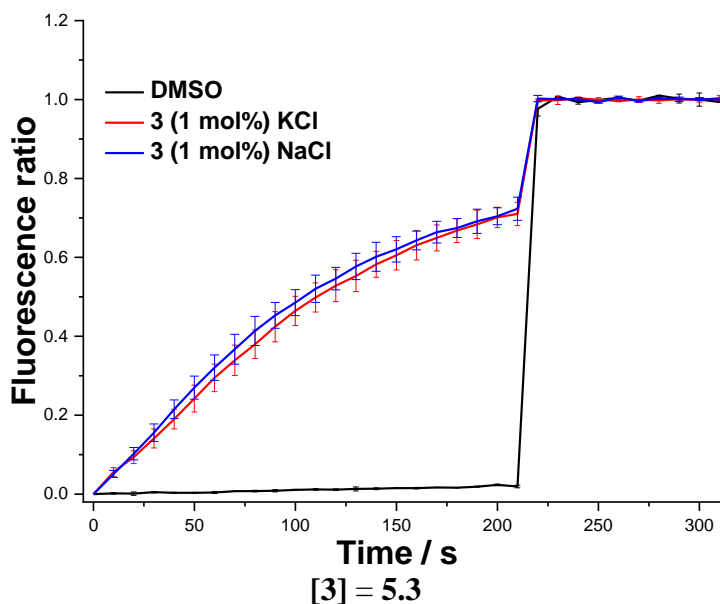


Figure D35: Observed fluorescence ratio response due to HCl influx or Cl⁻/OH⁻ antiport facilitated by compound **5.3** (1 mol%) using KCl-KOH and NaCl-KOH assays from POPC vesicles loaded with KCl (100 mM) or NaCl, respectively. All external and internal solutions were buffered to pH 7.0 with HEPES (10 mM). The test compound was added at 0 s and detergent was added at 200 s. Ionophore concentrations are shown as ionophore to lipid molar ratios.

3) Calcein leakage assays:

A chloroform solution of POPC was evaporated under vacuum and dried for at least 6 h as reported.¹ The thin film was hydrated by the internal solution containing calcein disodium salt (100 mM) and NaCl (100 mM) buffered to pH 7.4 with HEPES (10 mM). Then, the lipid suspension was subjected to nine freeze-thaw cycles followed by extrusion 25 times through a 200 nm polycarbonate membrane. Size exclusion chromatography using sephadex G-25 column and calcein-free external solution, containing NaCl (100 mM) and Na₂SO₄ (100 mM) buffered to pH 7.4 with HEPES (10 mM).

The resulting suspension of dye-encapsulated LUVs with a mean diameter of 200 nm was diluted with the external solution to obtain 2.5 mL lipid suspension containing a 0.1 mM lipid concentration. After the tested receptors **5.1-5.5** were added at 1 mol%, calcein fluorescence ($\lambda_{\text{ex}} = 490 \text{ nm}$, $\lambda_{\text{em}} = 520 \text{ nm}$) was recorded at 25 °C. Detergent (25 μL) was added at 200 seconds to lyse the vesicle and to calibrate the assay.

The fractional calcein release (FR) was calculated as follows (with I_t = fluorescence intensity at time t, I_0 = fluorescence intensity at time 0 and I_{max} = fluorescence intensity after addition of detergent):

$$FR = \frac{I_t - I_0}{I_{\text{max}} - I_0}$$

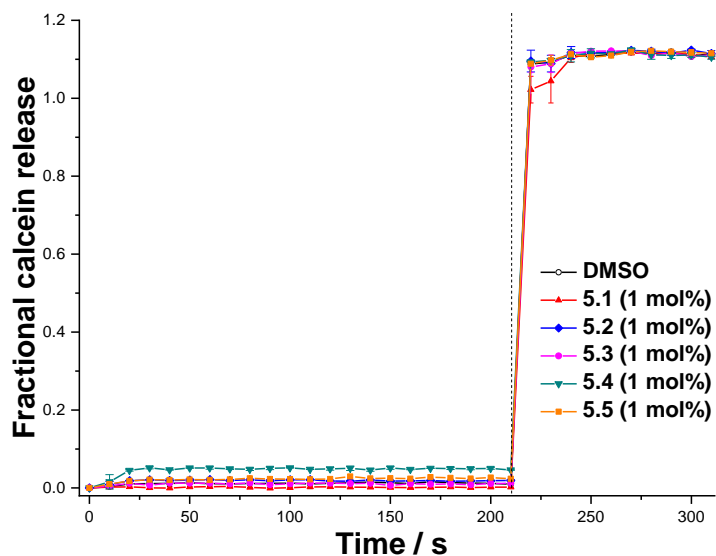


Figure D36: Calcein leakage by 5.1-5.5 (1 mol% carrier-to-lipid) from unilamellar POPC vesicles loaded with calcein disodium salt (100 mM) and NaCl (100 mM) buffered to pH 7.4 with HEPES (10 mM). At $t = 10$ s, a DMSO solution of the transporter was added to start the experiment. At the end of the experiment, detergent was added to lyse the vesicles. The results are shown as the fraction of calcein leaked from the vesicles.

4) Ion selective electrode (ISE) assays:

Cl/NO₃ exchange assay:

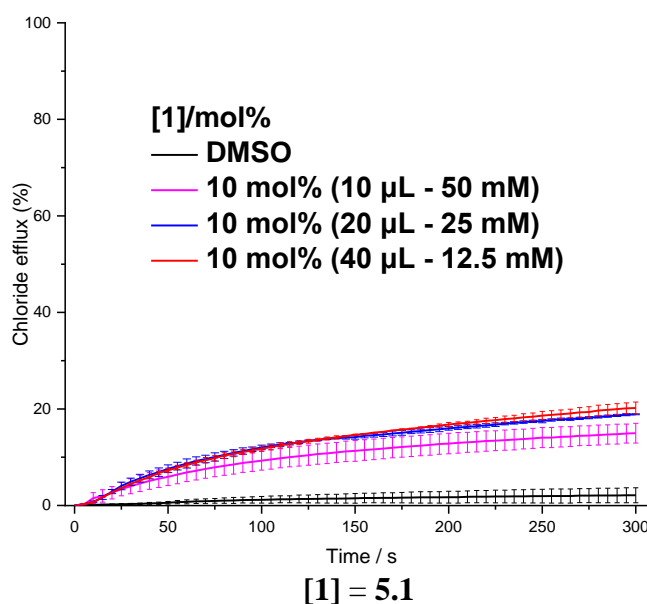


Figure D37: Chloride efflux mediated by receptor **5.1** (10 mol% w.r.t. lipid), added from stock DMSO solutions of the receptor at varying concentration with different loading volume. The compound was added to POPC vesicles containing 489 mM KCl and suspended in 489 mM KNO₃, both buffered to pH 7.2 with phosphate buffer. At the end of the experiment the vesicles were lysed with detergent to achieve 100% chloride efflux. Each point represents the average of 3 trials.

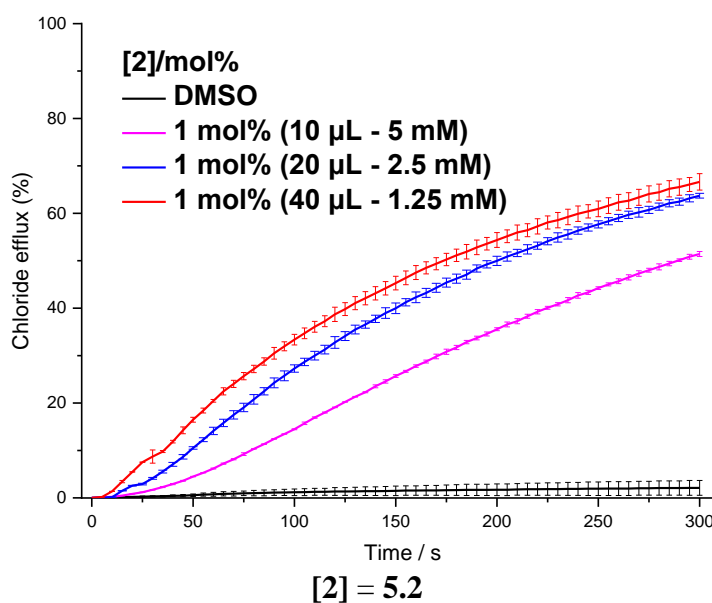


Figure D38: Chloride efflux mediated by receptor **5.2** (1 mol%), added from stock DMSO solutions of the receptor at varying concentration with different loading volume. The compound was added to POPC vesicles containing 489 mM KCl and suspended in 489 mM KNO₃, both buffered to pH 7.2 with phosphate buffer. At the end of the experiment the vesicles were lysed with detergent to achieve 100% chloride efflux. Each point represents the average of 3 trials.

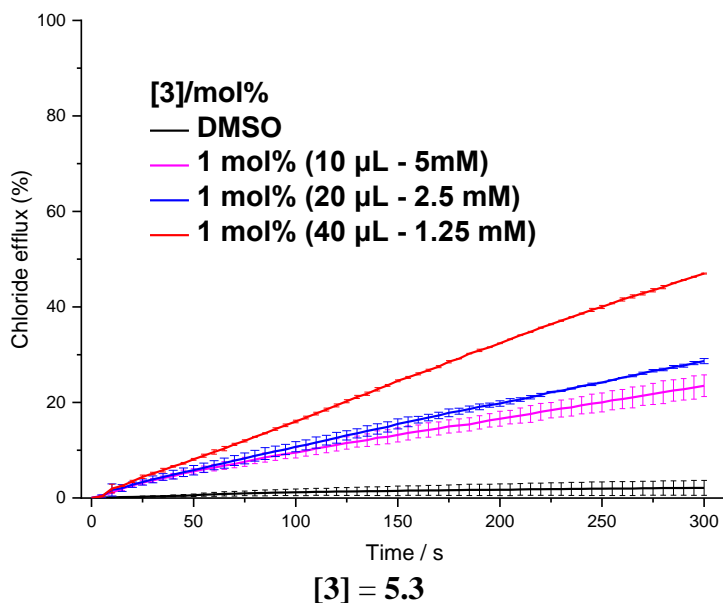


Figure D39: Chloride efflux mediated by receptor 5.3 (1 mol%), added from stock DMSO solutions of the receptor at varying concentration with different loading volume. The compound was added to POPC vesicles containing 489 mM KCl and suspended in 489 mM KNO₃, both buffered to pH 7.2 with phosphate buffer. At the end of the experiment the vesicles were lysed with detergent to achieve 100% chloride efflux. Each point represents the average of 3 trials.

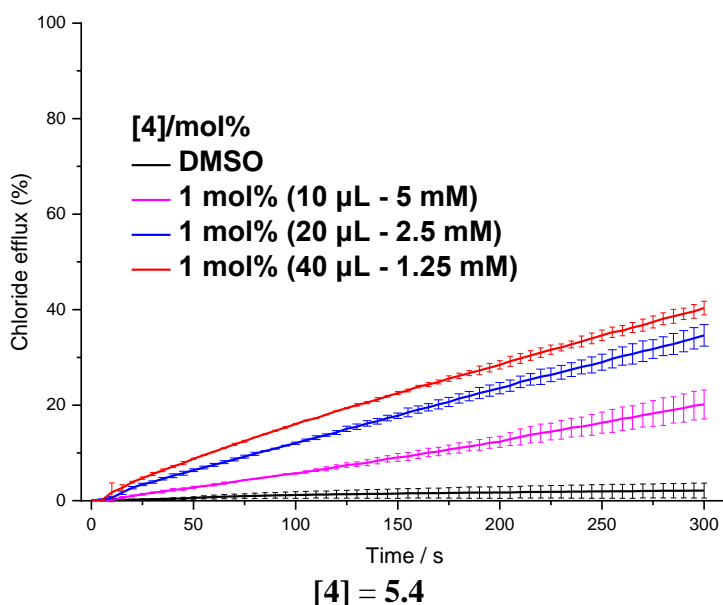
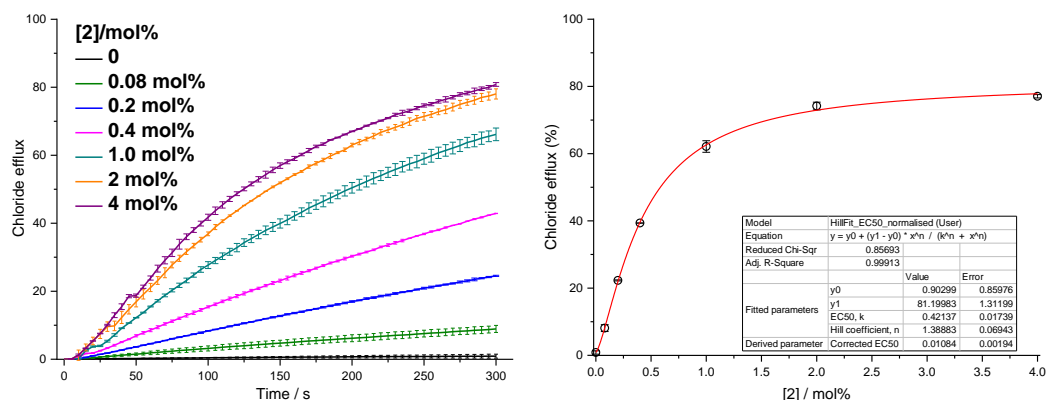
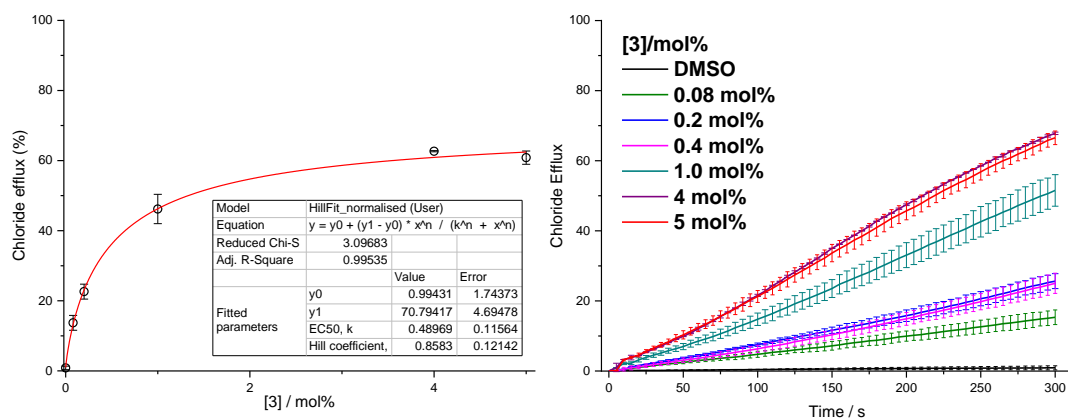


Figure D40: Chloride efflux mediated by receptor 5.4 (1 mol%), added from stock DMSO solutions of the receptor at varying concentration with different loading volume. The compound was added to POPC vesicles containing 489 mM KCl and suspended in 489 mM KNO₃, both buffered to pH 7.2 with phosphate buffer. At the end of the experiment the vesicles were lysed with detergent to achieve 100% chloride efflux. Each point represents the average of 3 trials.



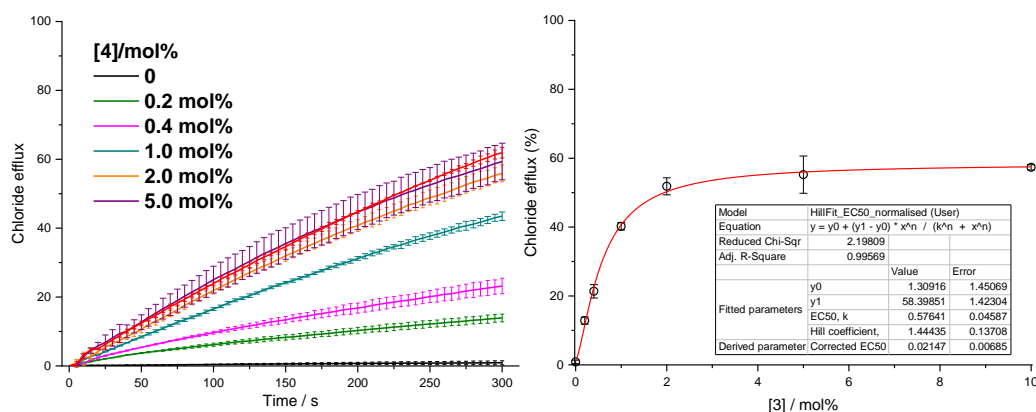
[2] = 5.2

Figure D41: Hill plot analysis of chloride efflux facilitated by compound **5.2** from unilamellar POPC vesicles that were loaded with a 489 mM KCl solution buffered to pH 7.2 with 5 mM phosphate, and were suspended in a 489 mM KNO₃ solution buffered to pH 7.2 with 5 mM phosphate salts. DMSO was used as a control. Each point is the average of three repeats.



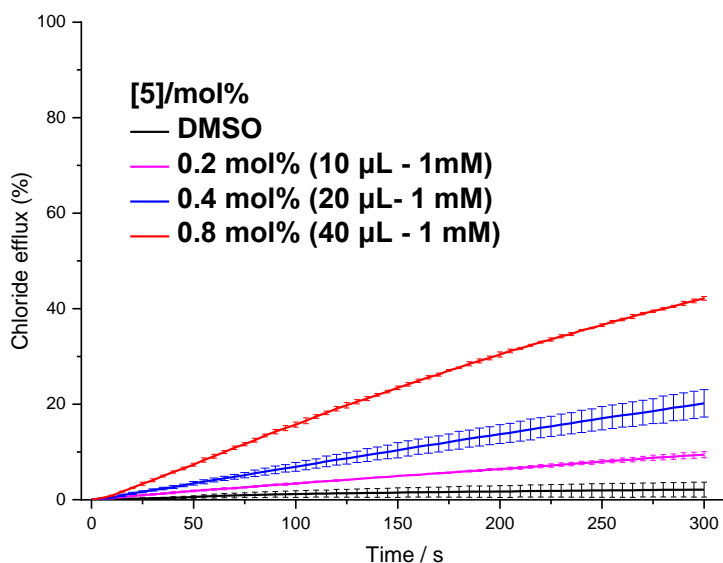
[3] = 5.3

Figure D42: Hill plot analysis of chloride efflux facilitated by compound **5.3** from unilamellar POPC vesicles that were loaded with a 489 mM KCl solution buffered to pH 7.2 with 5 mM phosphate, and were suspended in a 489 mM KNO₃ solution buffered to pH 7.2 with 5 mM phosphate salts. DMSO was used as a control. Each point is the average of three repeats.



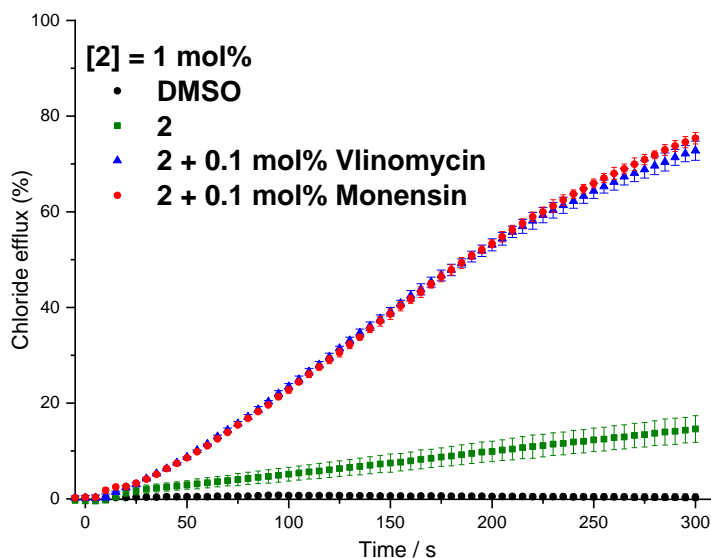
[4] = 5.4

Figure D43: Hill plot analysis of chloride efflux facilitated by compound **5.4** from unilamellar POPC vesicles that were loaded with a 489 mM KCl solution buffered to pH 7.2 with 5 mM phosphate, and were suspended in a 489 mM KNO₃ solution buffered to pH 7.2 with 5 mM phosphate salts. DMSO was used as a control. Each point is the average of three repeats.



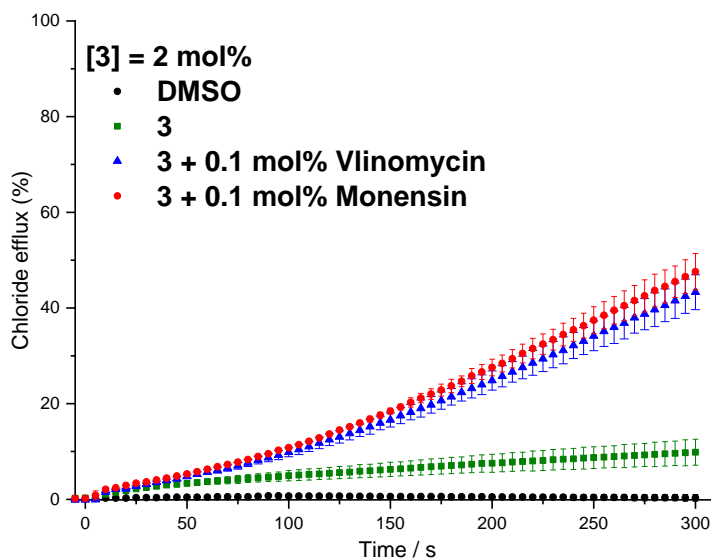
[5] = 5.5

Figure D44: Chloride efflux mediated by different mol% of transporter **5.5**, from unilamellar POPC vesicles that were loaded with a 489 mM KCl solution buffered to pH 7.2 with 5 mM phosphate, and were suspended in a 489 mM KNO₃ solution buffered to pH 7.2 with 5 mM phosphate salts. DMSO was used as a control. Each point is the average of three repeats. The maximum observed solubility of compound 5 in DMSO was 1 mM, so higher concentration could not be performed to get hill plot.



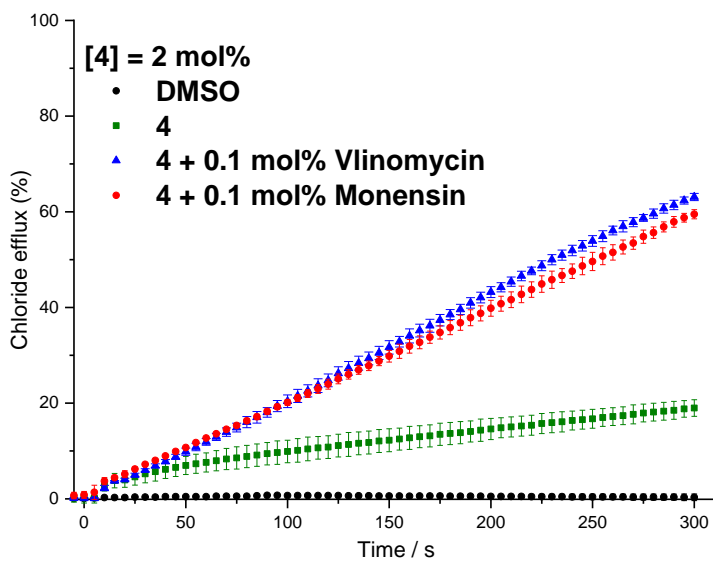
[2] = 5.2

Figure D45: Electrogenic or electroneutral transport mediated by compound **5.2** (1 mol% with respect to lipid) in the presence of monensin or valinomycin (0.1 mol% with respect to lipid). Unilamellar POPC vesicles were loaded with a 300 mM KCl solution buffered to pH 7.2 with 5 mM phosphate and were suspended in a 300 mM KGlu solution buffered to pH 7.2 with 5 mM phosphate salts. DMSO was used as a control. Each point is the average of three repeats.



[3] = 5.3

Figure D46: Electrogenic or electroneutral transport mediated by compound **5.3** (1 mol% with respect to lipid) in the presence of monensin or valinomycin (0.1 mol% with respect to lipid). Unilamellar POPC vesicles were loaded with a 300 mM KCl solution buffered to pH 7.2 with 5 mM phosphate and were suspended in a 300 mM KGlu solution buffered to pH 7.2 with 5 mM phosphate salts. DMSO was used as a control. Each point is the average of three repeats.



[4] = 5.4

Figure D47: Electrogenic or electroneutral transport mediated by compound **5.4** (1 mol% with respect to lipid) in the presence of monensin or valinomycin (0.1 mol% with respect to lipid). Unilamellar POPC vesicles were loaded with a 300 mM KCl solution buffered to pH 7.2 with 5 mM phosphate and were suspended in a 300 mM KGlu solution buffered to pH 7.2 with 5 mM phosphate salts. DMSO was used as a control. Each point is the average of three repeats.

5) Fluorescence titration studies with TBACl

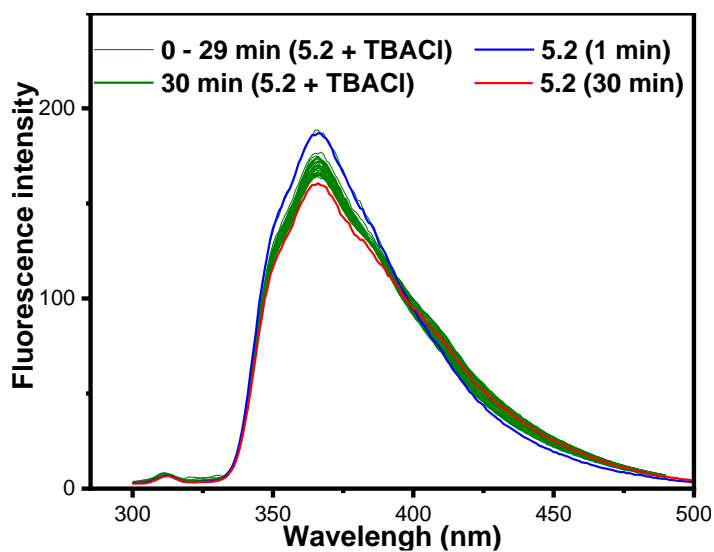


Figure D48: Fluorescent changes over 30 minutes (Ex = 285 nm) of compound **5.2** (1.0 μM) upon addition of 100 equivalents of TBACl (100 μM) in DMSO.

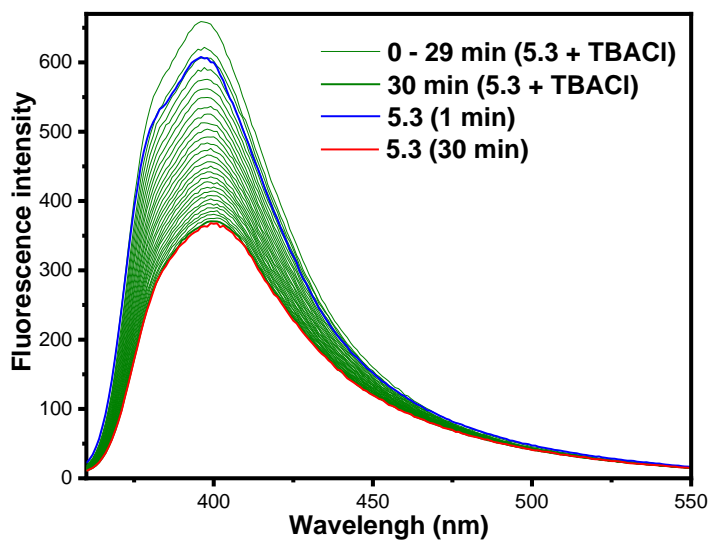


Figure D49: Fluorescent changes over 30 minutes (Ex = 350 nm) of compound **5.3** (1.0 μM) upon addition of 100 equivalents of TBACl (100 μM) in DMSO.

D) Transport studies upon reduction of complexes **5.13**, **5.14**, **5.16** and **5.17**.

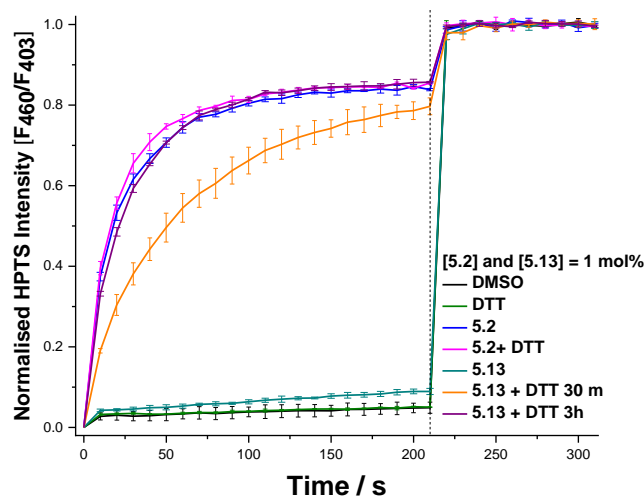


Figure D50: Observed fluorescence ratio response due to H^+/Cl^- symport or Cl^-/OH^- antiport upon reduction of complex **5.13** ($1\ \mu\text{M}$) by dithiothreitol DTT ($3\ \mu\text{M}$) using KCl-KOH assay from POPC vesicles loaded with KCl ($100\ \text{mM}$), buffered to pH 7.0 with HEPES ($10\ \text{mM}$) after 30 minutes and 3 hours. The test complex **6** ($1\ \text{mol}\%$) and KOH were added firstly, then DTT was added at 0 s. DMSO, DTT ($3\ \text{mol}\%$), parent anion transporter **5.2** and complex **5.13** (without addition of DTT) were used as controls. Detergent was added at 200 s. Ionophore concentrations are shown as ionophore to lipid molar ratios. Error bars represent SD from at least three repeats.

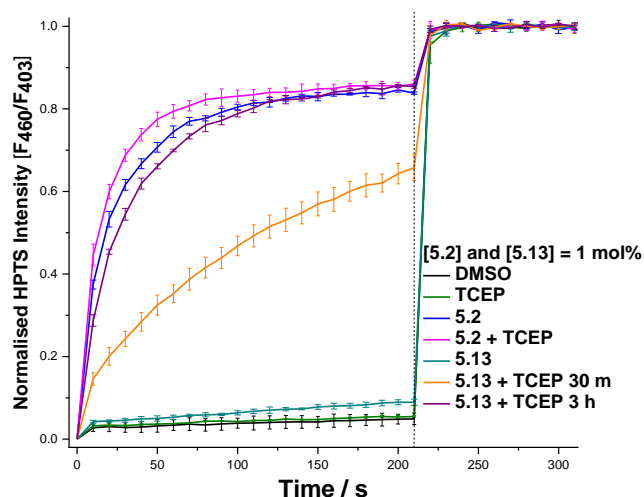


Figure D51: Observed fluorescence ratio response due to H^+/Cl^- symport or Cl^-/OH^- antiport upon reduction of complex **5.13** ($1\ \mu\text{M}$) by TCEP ($3\ \text{mM}$) using KCl-KOH assay from POPC vesicles loaded with KCl ($100\ \text{mM}$), buffered to pH 7.0 with HEPES ($10\ \text{mM}$) after 30 minutes and 3 hours. The test complex **5.13** ($1\ \text{mol}\%$) and KOH were added firstly, then TCEP was added at 0 s. DMSO, TCEP ($3\ \text{mol}\%$), parent anion transporter **5.2** and complex **5.13** (without addition of TCEP) were used as controls. Detergent was added at 200 s. Ionophore concentrations are shown as ionophore to lipid molar ratios. Error bars represent SD from at least three repeats.

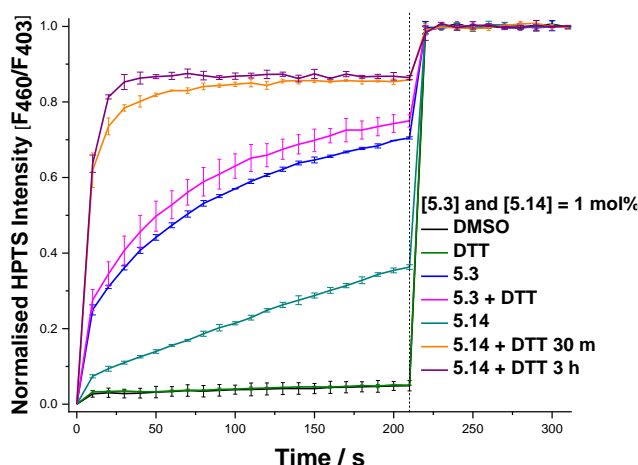


Figure D52: Observed fluorescence ratio response due to H^+/Cl^- symport or Cl^-/OH^- antiport upon reduction of complex **5.14** ($1 \mu\text{M}$) by dithiothreitol DTT (3 mM) using KCl-KOH assay from POPC vesicles loaded with KCl (100 mM), buffered to pH 7.0 with HEPES (10 mM) after 30 minutes and 3 hours. The test complex **5.14** (1 mol%) and KOH were added firstly, then DTT was added at 0 s. DMSO, DTT (3 mol%), parent anion transporter **5.3** and complex **5.14** (without addition of DTT) were used as controls. Detergent was added at 200 s. Ionophore concentrations are shown as ionophore to lipid molar ratios. Error bars represent SD from at least three repeats.

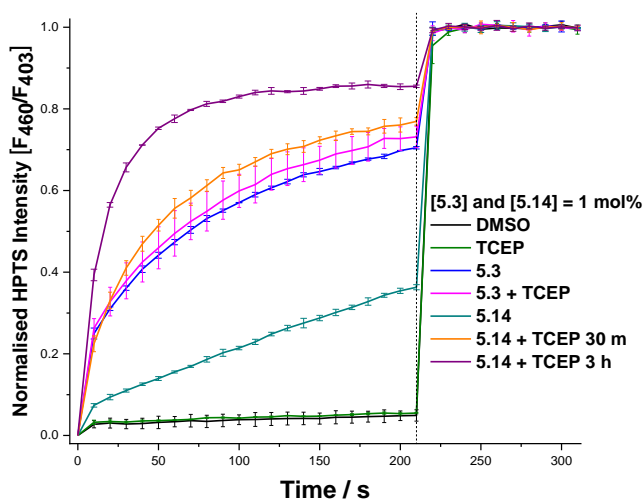


Figure D53: Observed fluorescence ratio response due to H^+/Cl^- symport or Cl^-/OH^- antiport upon reduction of complex **5.14** ($1 \mu\text{M}$) by TCEP (3 mM) using KCl-KOH assay from POPC vesicles loaded with KCl (100 mM), buffered to pH 7.0 with HEPES (10 mM) after 30 minutes and 3 hours. The test complex **5.14** (1 mol%) and KOH were added firstly, then TCEP was added at 0 s. DMSO, TCEP (3 mol%), parent anion transporter **5.3** and complex **5.14** (without addition of TCEP) were used as controls. Detergent was added at 200 s. Ionophore concentrations are shown as ionophore to lipid molar ratios. Error bars represent SD from at least three repeats.

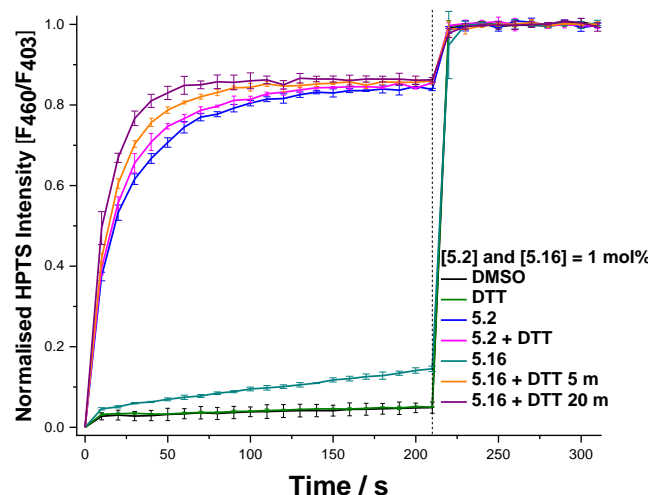


Figure D54: Observed fluorescence ratio response due to H^+/Cl^- symport or Cl^-/OH^- antiport upon reduction of complex **5.16** ($1\ \mu\text{M}$) by dithiothreitol DTT ($3\ \text{mM}$) using KCl-KOH assay from POPC vesicles loaded with KCl ($100\ \text{mM}$), buffered to pH 7.0 with HEPES ($10\ \text{mM}$) after 5 minutes and 20 minutes. The test complex **5.16** ($1\ \text{mol}\%$) and KOH were added firstly, then DTT was added at 0 s. DMSO, DTT ($3\ \text{mol}\%$), parent anion transporter **5.2** and complex **5.16** (without addition of DTT) were used as controls. Detergent was added at 200 s. Ionophore concentrations are shown as ionophore to lipid molar ratios. Error bars represent SD from at least three repeats.

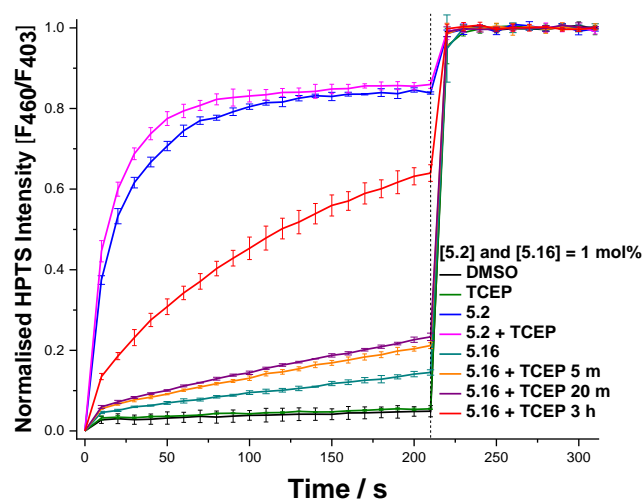


Figure D55: Observed fluorescence ratio response due to H^+/Cl^- symport or Cl^-/OH^- antiport upon reduction of complex **5.16** ($1\ \mu\text{M}$) by TCEP ($3\ \text{mM}$) using KCl-KOH assay from POPC vesicles loaded with KCl ($100\ \text{mM}$), buffered to pH 7.0 with HEPES ($10\ \text{mM}$) after 5 minutes, 20 minutes and 3 hours. The test complex **5.16** ($1\ \text{mol}\%$) and KOH were added firstly, then TCEP was added at 0 s. DMSO, TCEP ($3\ \text{mol}\%$), parent anion transporter **5.2** and complex **5.16** (without addition of TCEP) were used as controls. Detergent was added at 200 s. Ionophore concentrations are shown as ionophore to lipid molar ratios. Error bars represent SD from at least three repeats.

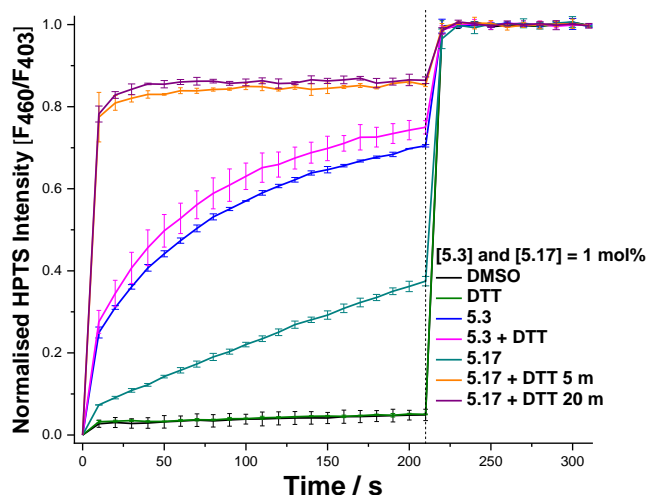


Figure D56: Observed fluorescence ratio response due to H^+/Cl^- symport or Cl^-/OH^- antiport upon reduction of complex **5.17** ($1\ \mu\text{M}$) by dithiothreitol DTT ($3\ \text{mM}$) using KCl-KOH assay from POPC vesicles loaded with KCl ($100\ \text{mM}$), buffered to pH 7.0 with HEPES ($10\ \text{mM}$) after 5 minutes and 20 minutes. The test complex ($1\ \text{mol}\%$) and KOH were added firstly, then DTT was added at 0 s. DMSO, DTT ($3\ \text{mol}\%$), parent anion transporter **5.2** and complex **5.17** (without addition of DTT) were used as controls. Detergent was added at 200 s. Ionophore concentrations are shown as ionophore to lipid molar ratios. Error bars represent SD from at least three repeats.

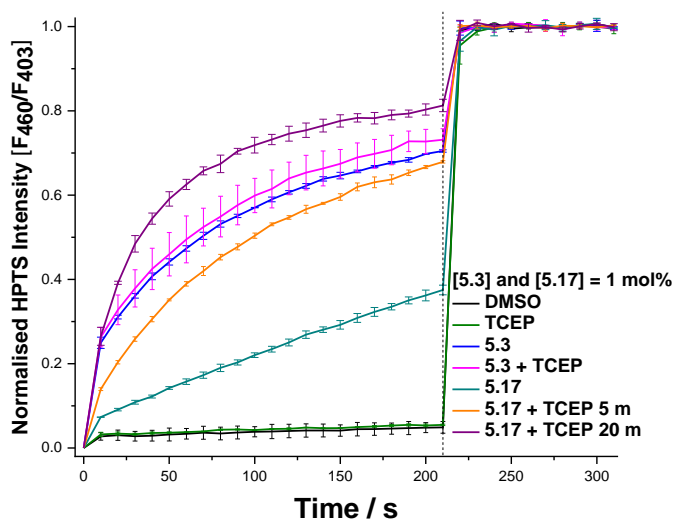


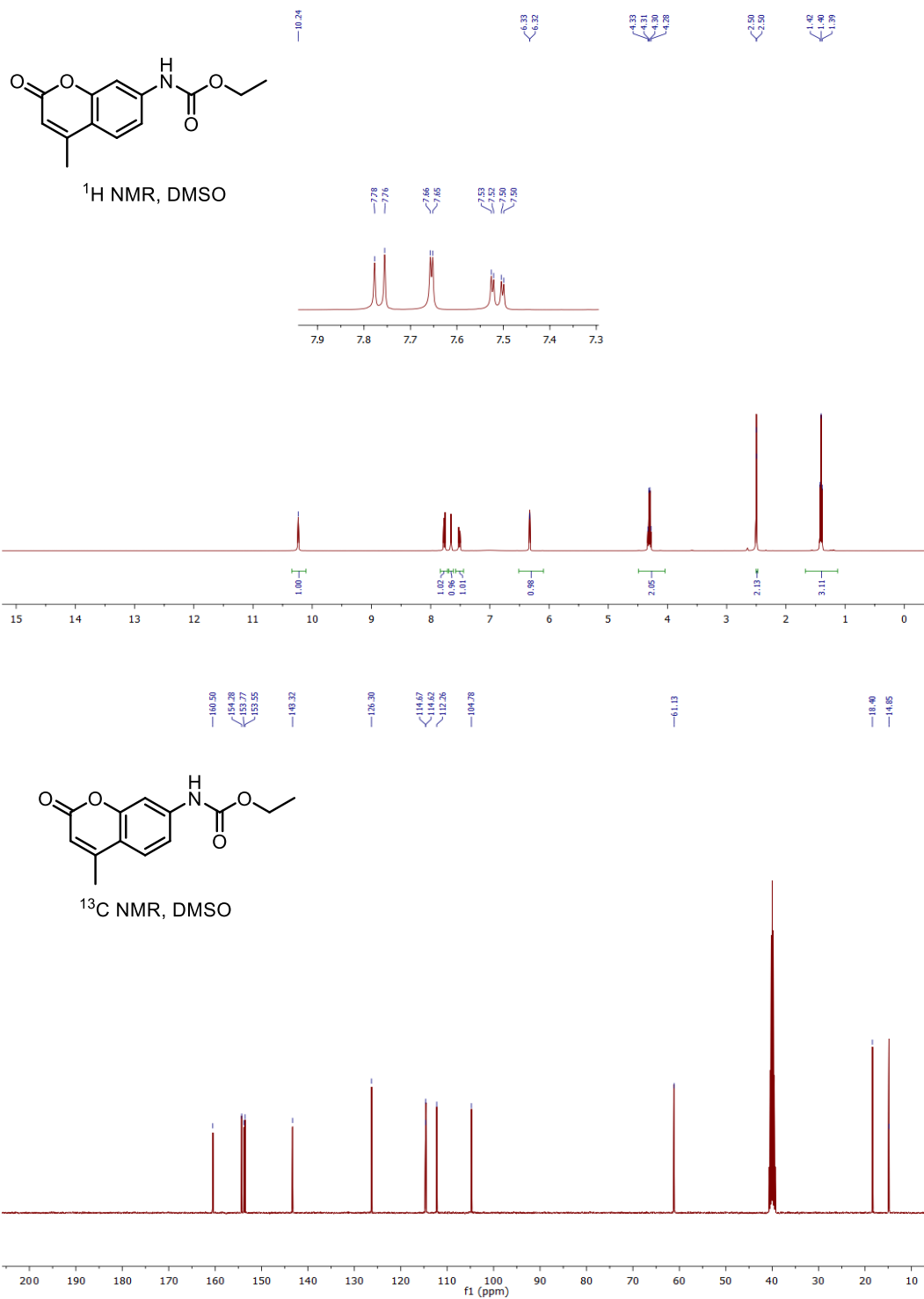
Figure D57: Observed fluorescence ratio response due to H^+/Cl^- symport or Cl^-/OH^- antiport upon reduction of complex **5.17** ($1\ \mu\text{M}$) by TCEP ($3\ \text{mM}$) using KCl-KOH assay from POPC vesicles loaded with KCl ($100\ \text{mM}$), buffered to pH 7.0 with HEPES ($10\ \text{mM}$) after 5 minutes and 20 minutes. The test complex **5.17** ($1\ \text{mol}\%$) and KOH were added firstly, then TCEP was added at 0 s. DMSO, TCEP ($3\ \text{mol}\%$), parent anion transporter **5.3** and complex **5.17** (without addition of TCEP) were used as controls. Detergent was added at 200 s. Ionophore concentrations are shown as ionophore to lipid molar ratios. Error bars represent SD from at least three repeats.

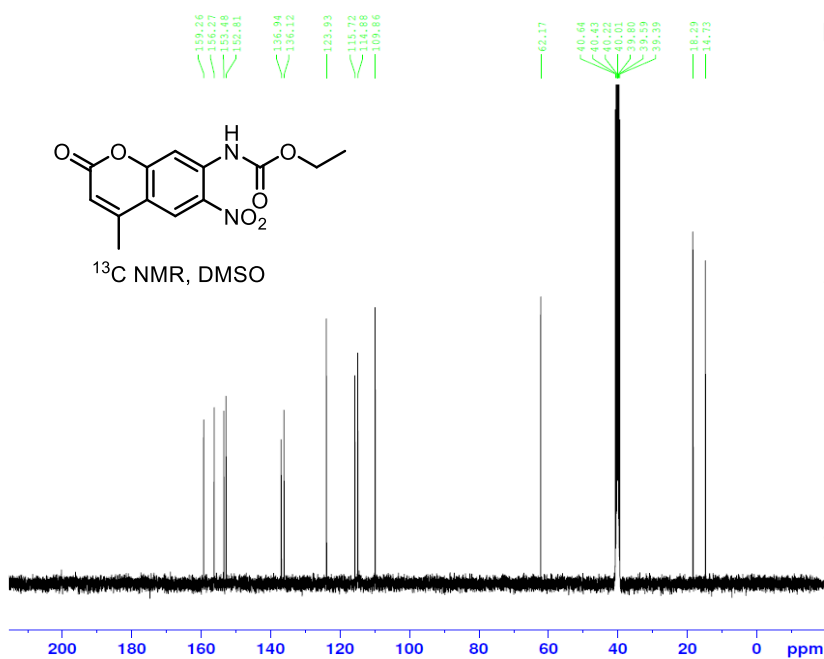
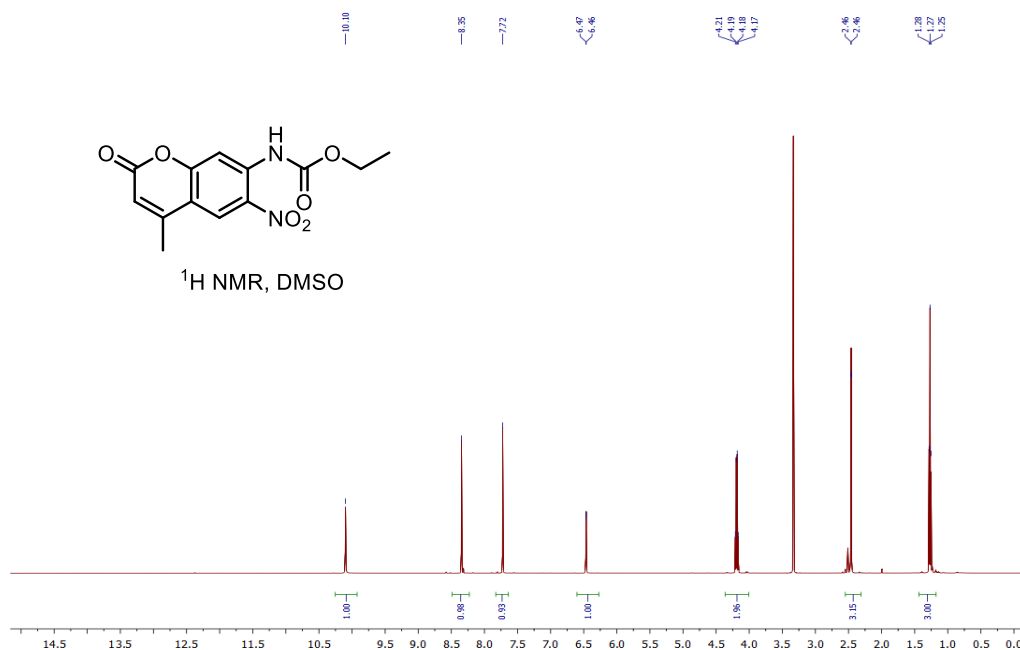
References:

1. Howe, E. N. W.; Gale, P. A. Fatty acid fueled transmembrane chloride transport. *J. Am. Chem. Soc.* **2019**, 141, 10654-10660.

Appendix E: Supplementary Information to Chapter 6

A) NMR spectra of compounds from chapter 6

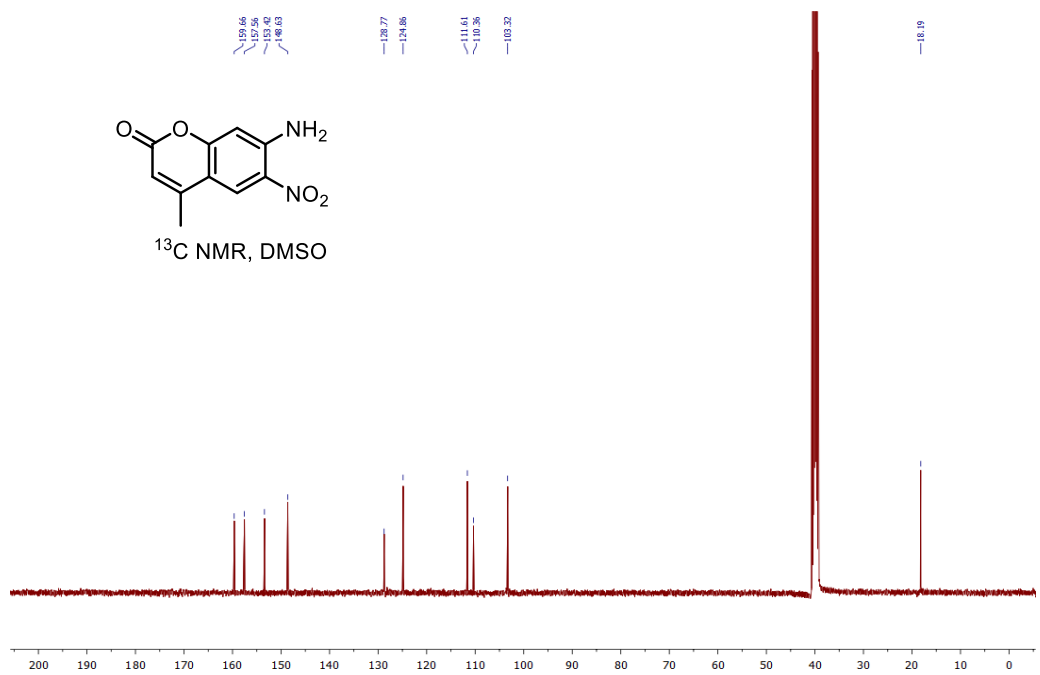
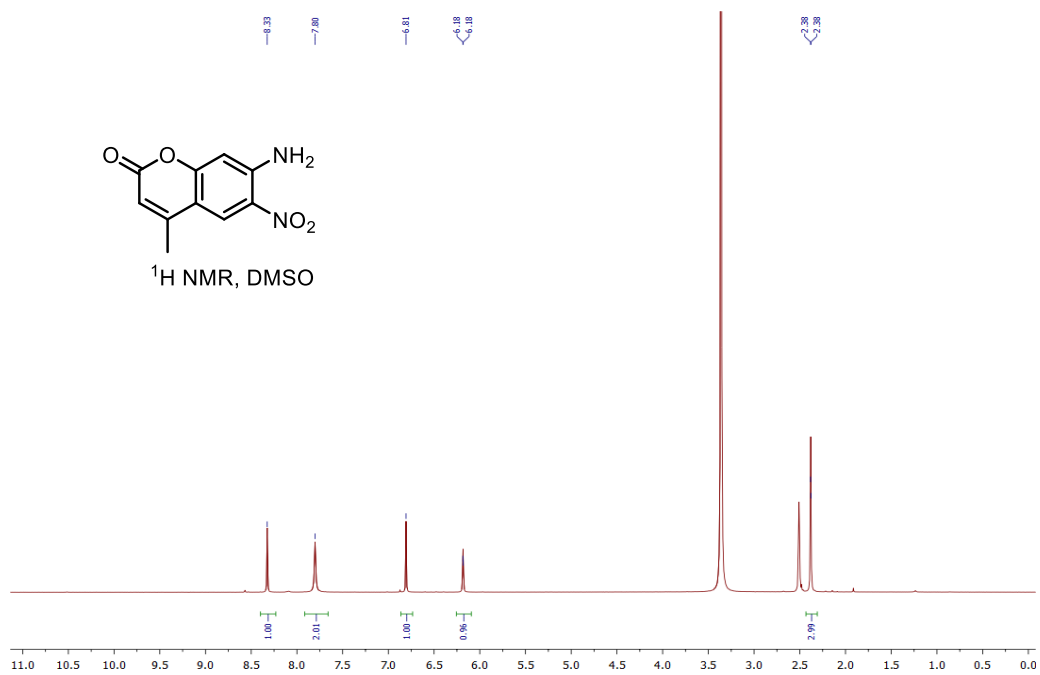


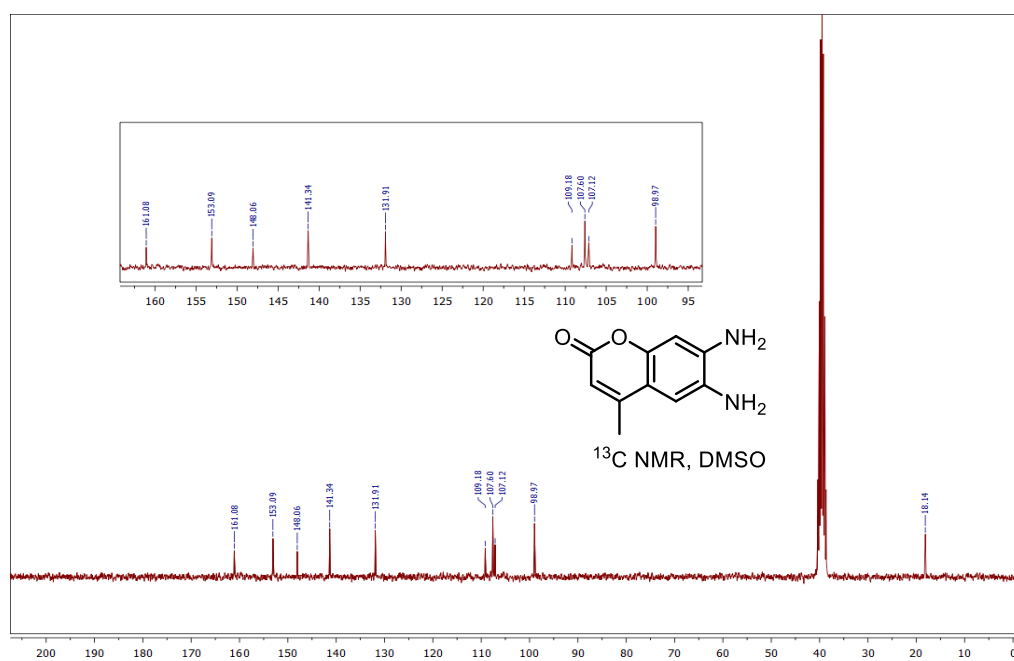
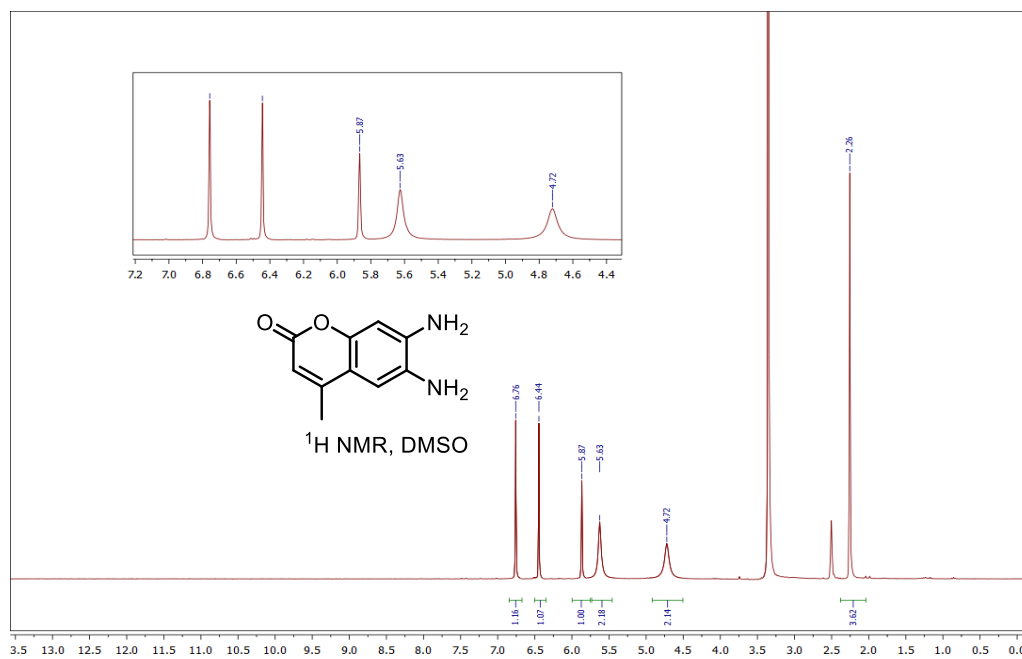


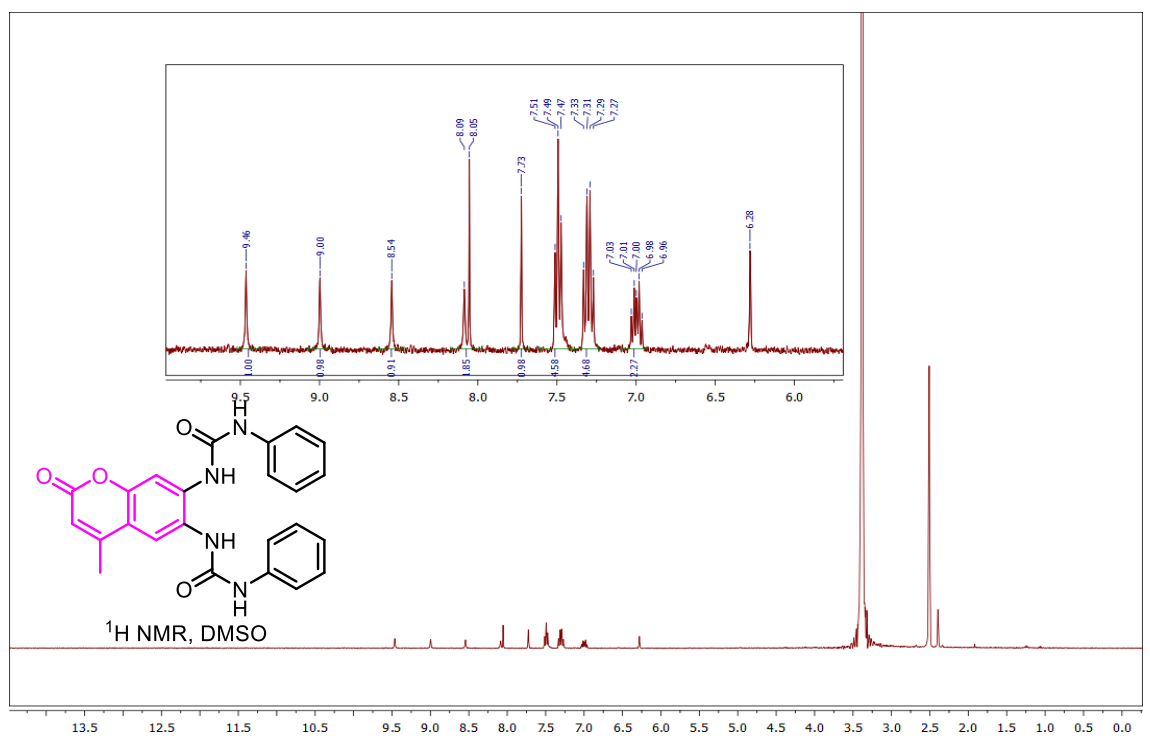
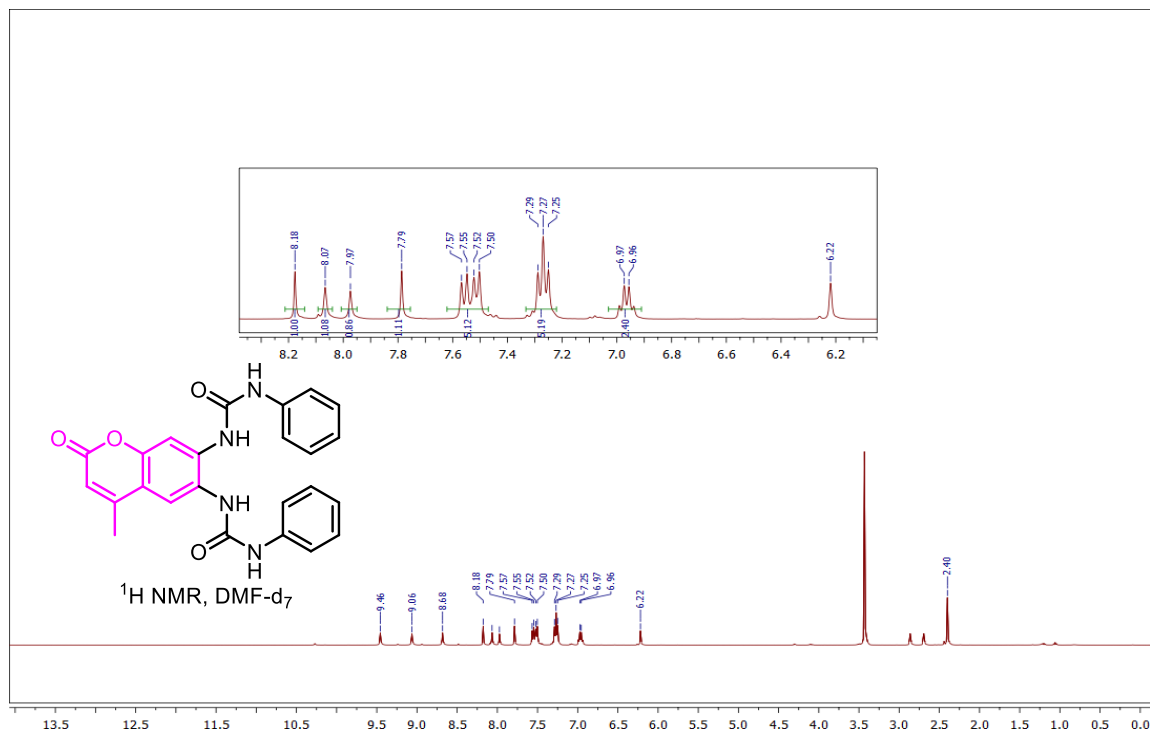
Current Data Parameters
 NAME mEm_181017_34
 EXPNO 2
 PROCNO 1

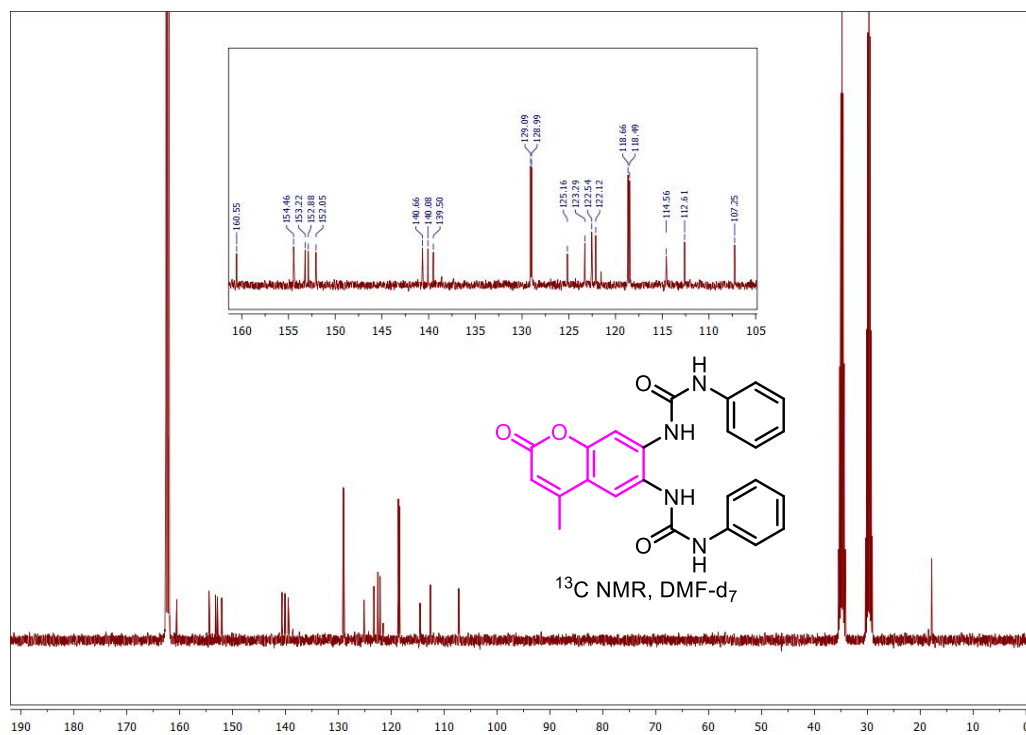
F2 - Acquisition Parameters
 Date_ 20181018
 Time 3.02 h
 INSTRUM spect
 PROBHD Z108618_0921 ()
 PULPROG zgpg30
 TD 65536
 SOLVENT DMSO
 NS 1024
 DS 4
 SWH 24038.461 Hz
 FIDRES 0.733596 Hz
 AQ 1.3631488 sec
 RC 196.38
 DW 20.800 usec
 DE 6.50 usec
 TE 299.1 K
 D1 2.00000000 sec
 D11 0.03000000 sec
 TD0 1
 SFO1 100.6303741 MHz
 NUC1 13C
 P1 10.00 usec
 PLW1 55.50099945 W
 SFO2 400.1616006 MHz
 NUC2 1H
 CPDPRG2 waltz16
 PCD02 90.00 usec
 PLW2 11.52400017 W
 PLW12 0.27886000 W
 PLW13 0.14026000 W

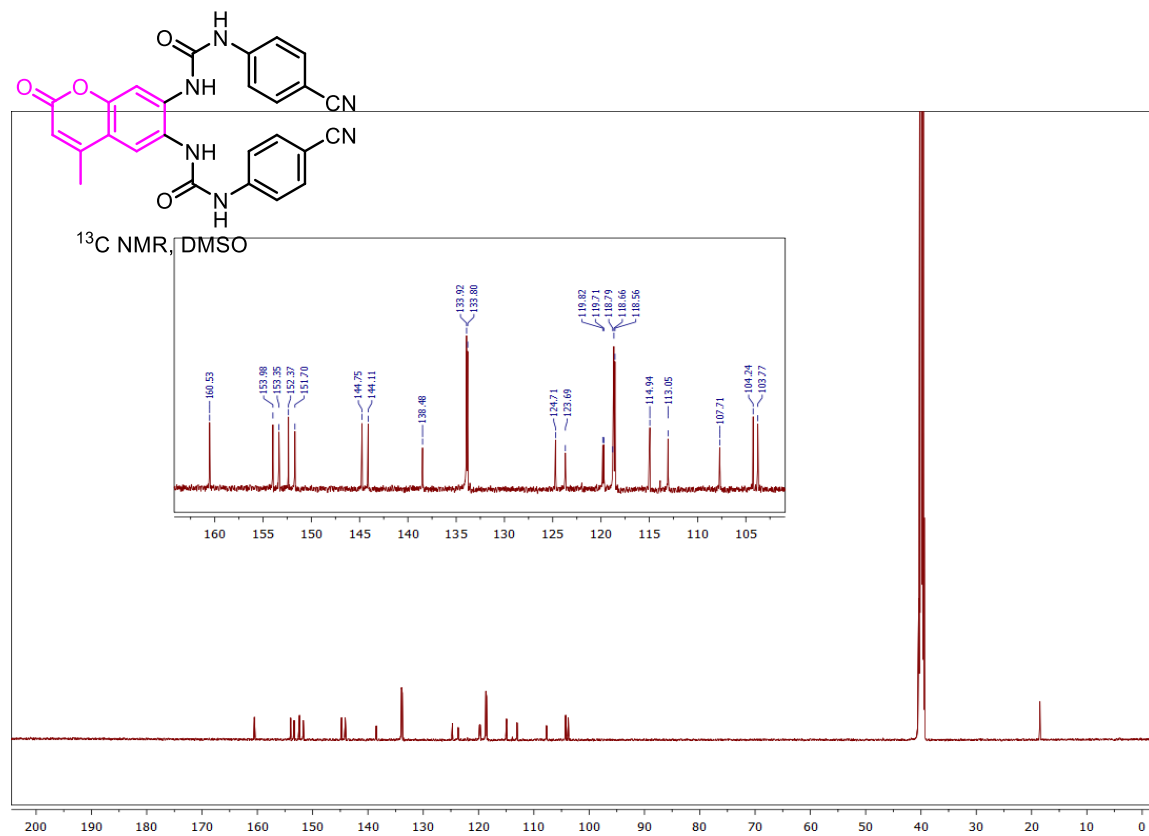
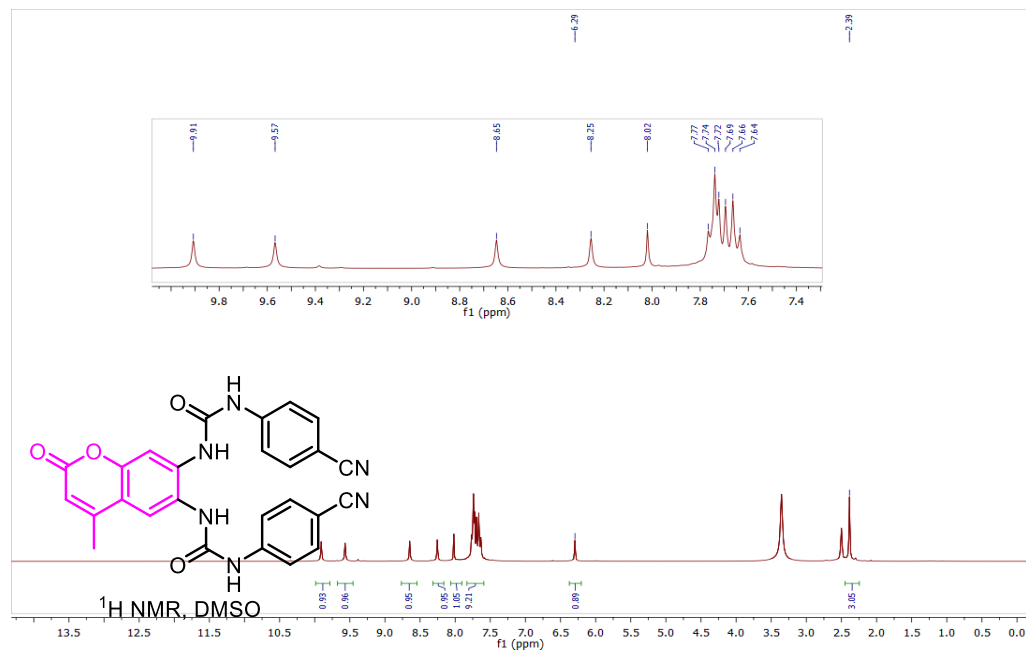
F2 - Processing parameters
 SI 32768
 SF 100.6203120 MHz
 WDW EM
 SSB 0
 LB 1.00 Hz
 GB 0
 PC 1.40

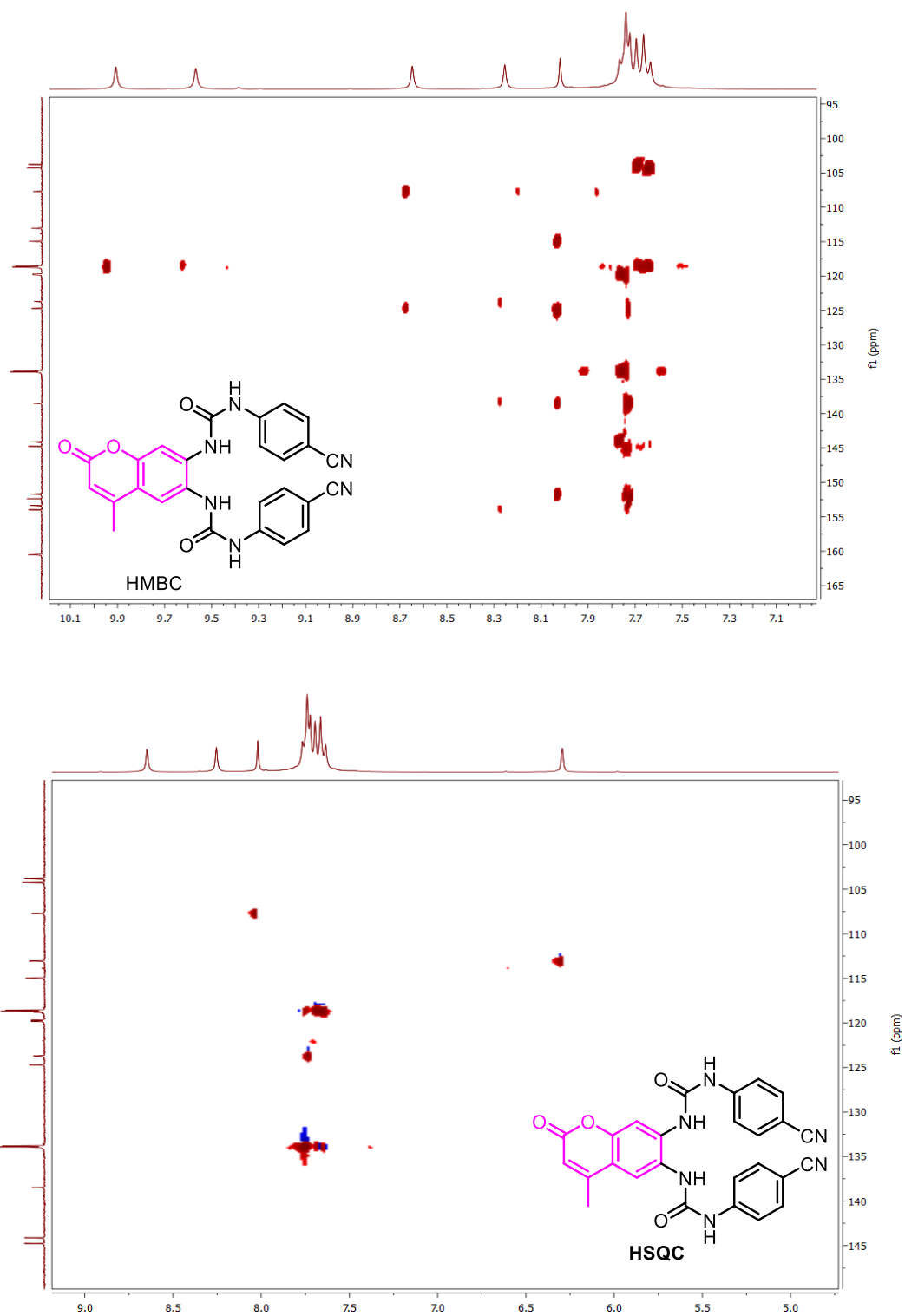


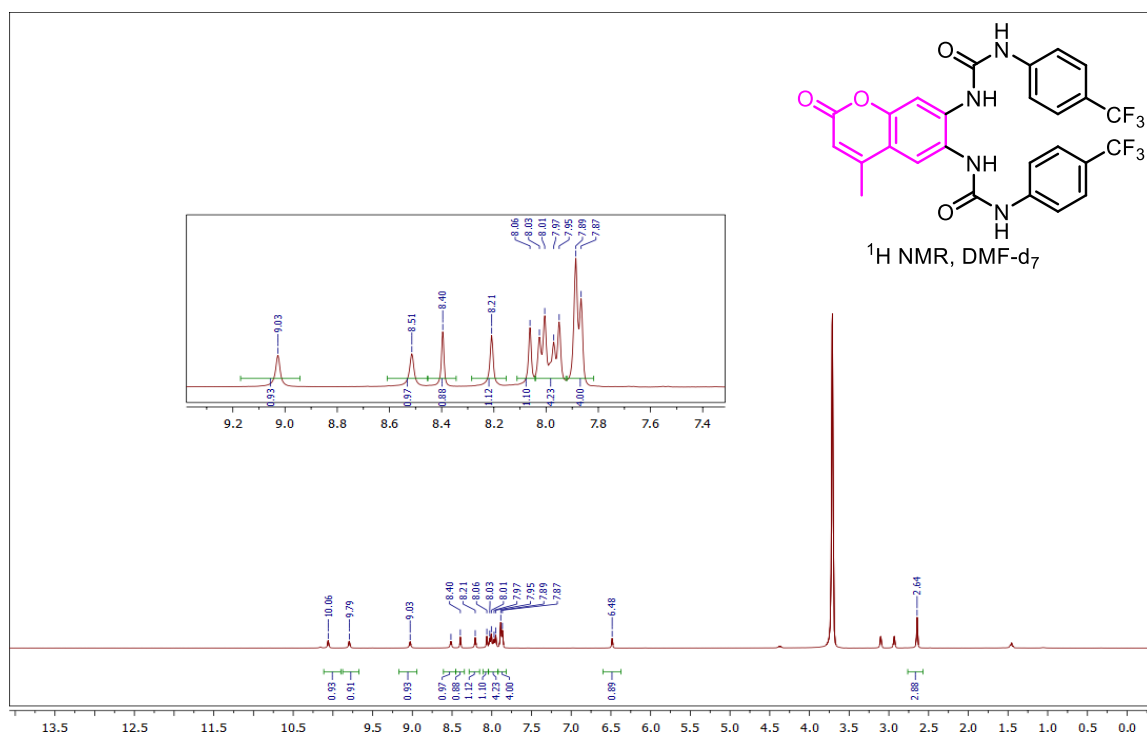
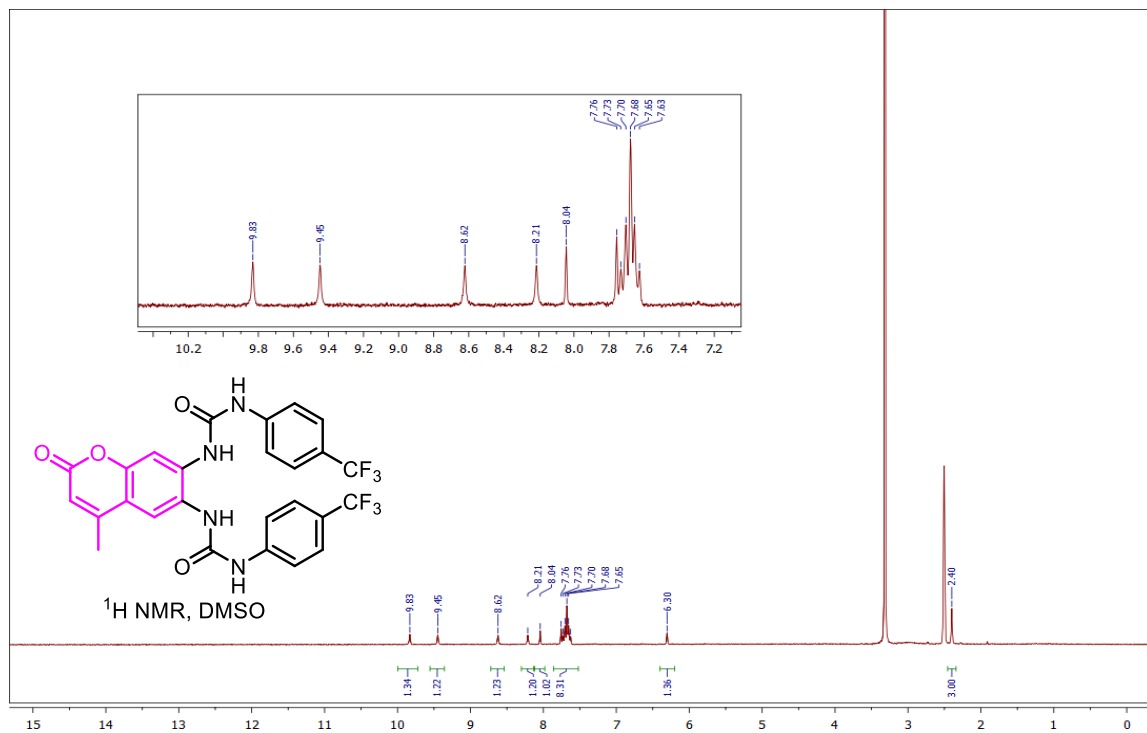


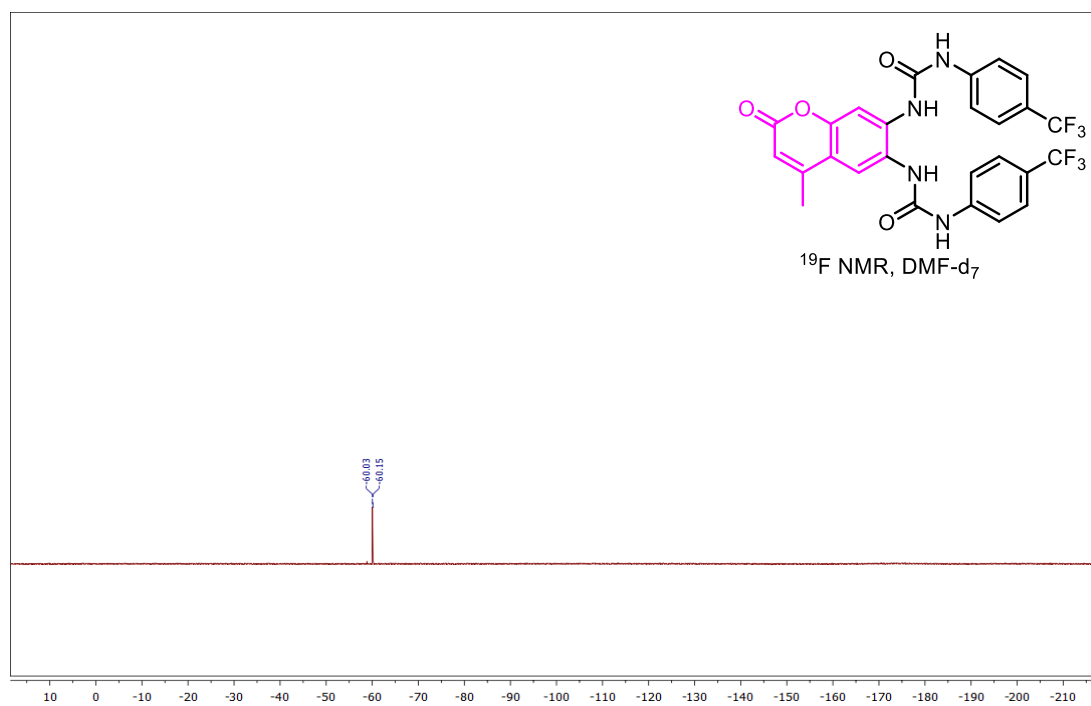
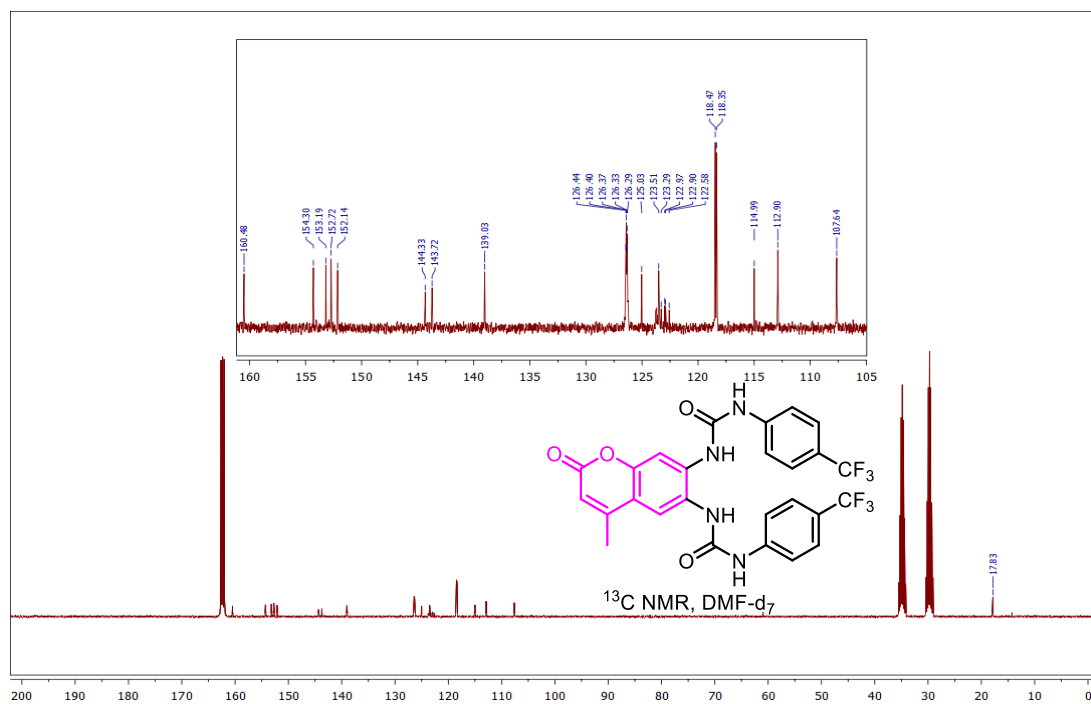




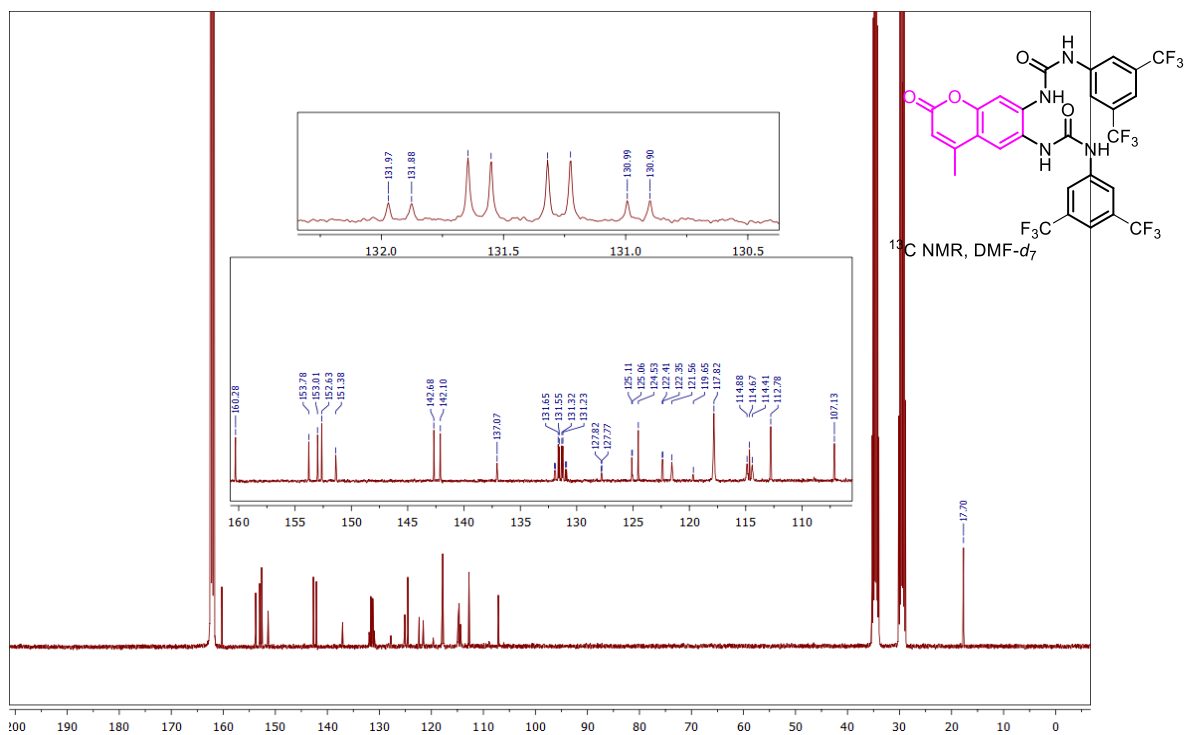
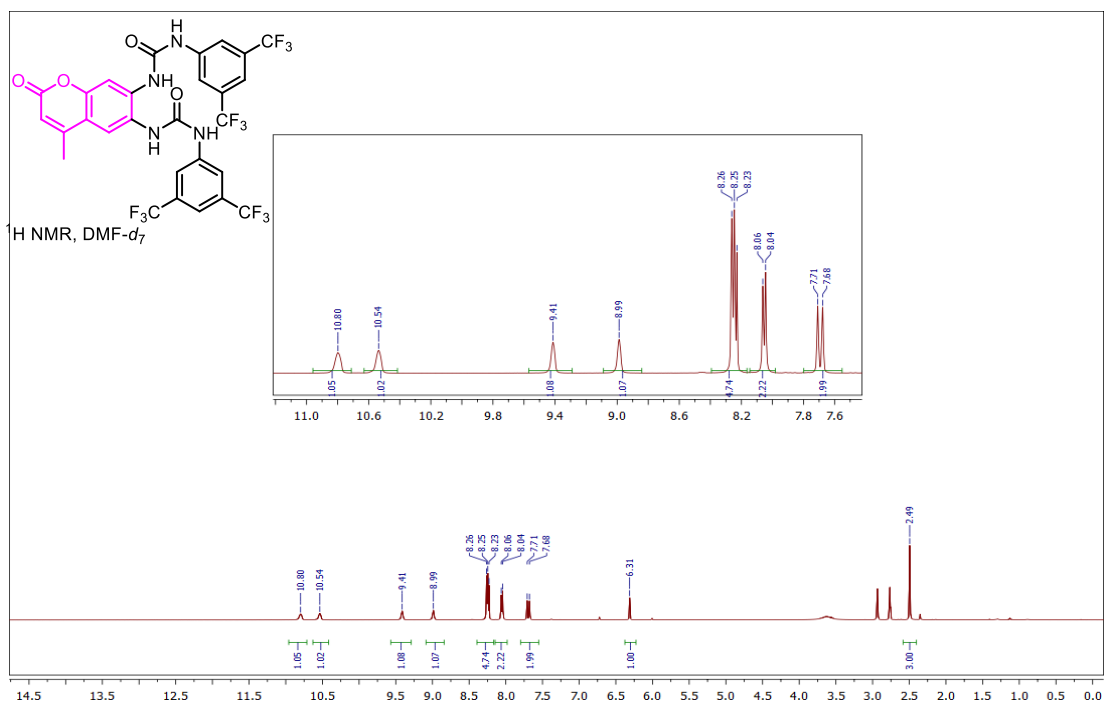


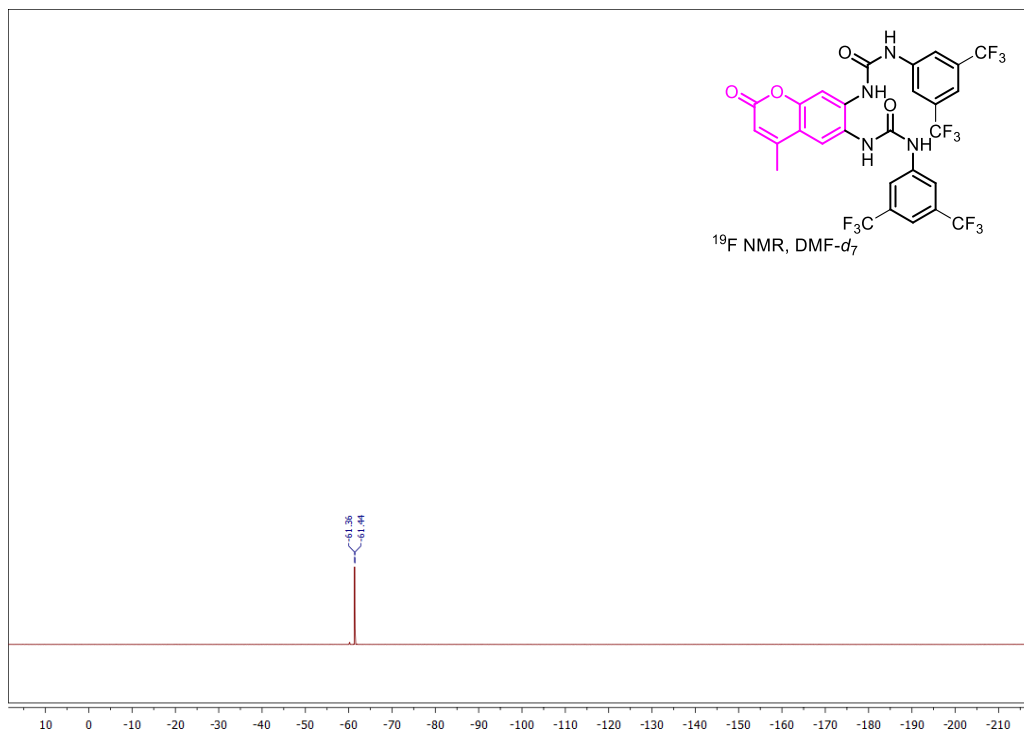






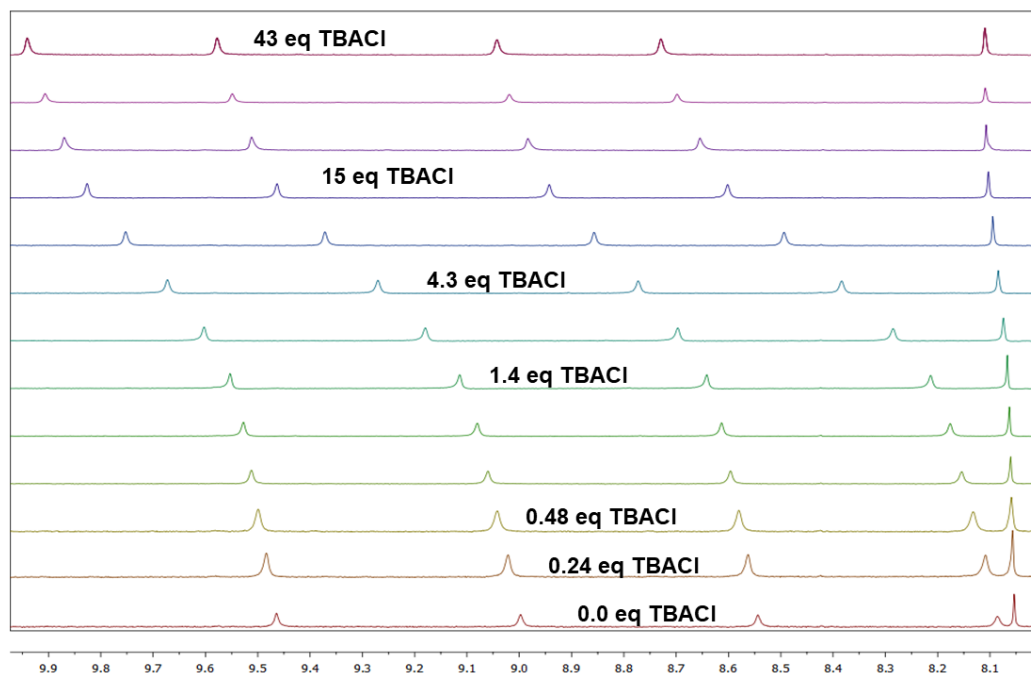
Appendix E for Chapter 6



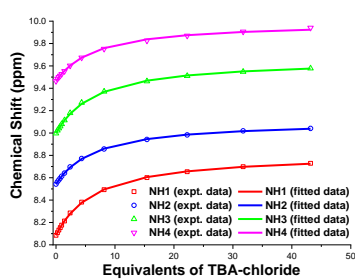


B) Binding studies:

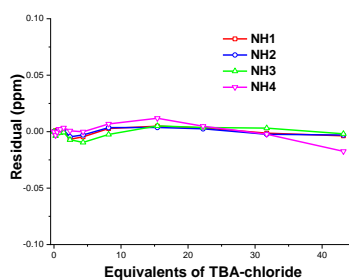
a)



b)



c)



d)

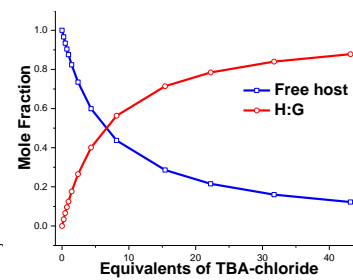
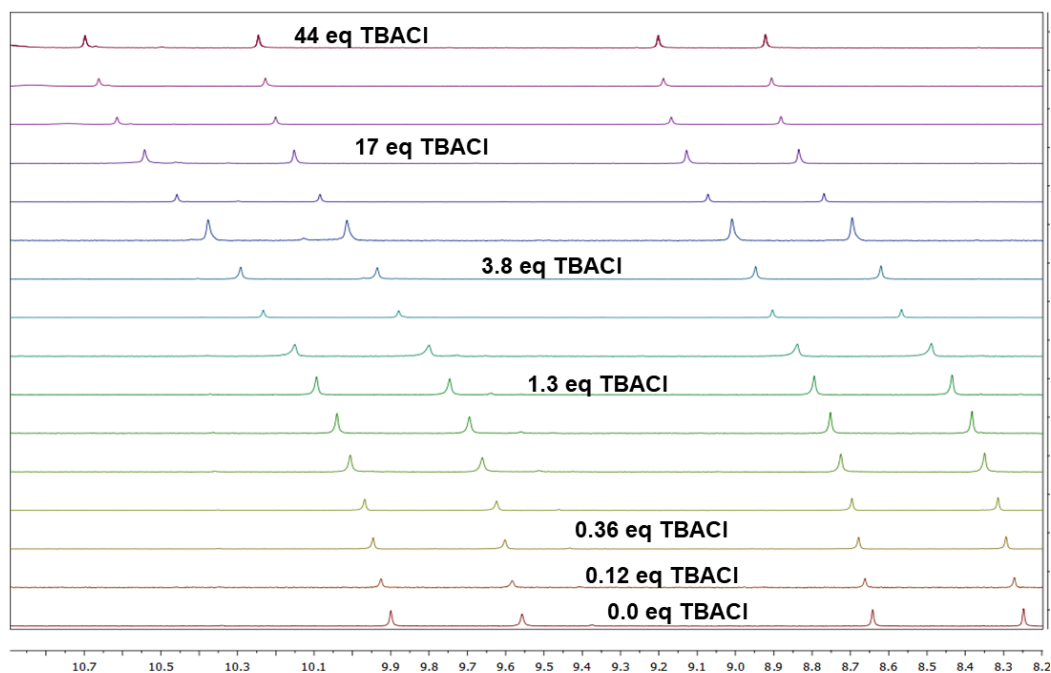
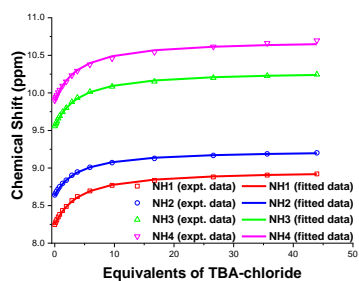


Figure E1: ^1H NMR spectroscopic titration of receptor **6.1** (2 mM) with TBACl in $\text{DMSO-}d_6$ with 0.5% water at 298 K. a) Stack plot. b) Fitplot for 4 NH protons at $\delta = 8.09, 8.54, 9.00$ and 9.46 using global analysis with 1:1 ($K_a = 81 \text{ M}^{-1}$, error: 1%). c) Plot of the residuals for using global analysis. d) Calculated mole fractions.

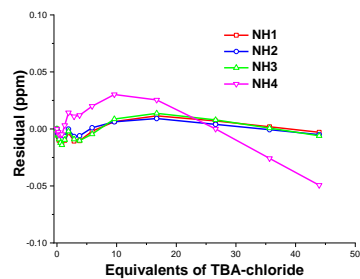
a)



b)



c)



d)

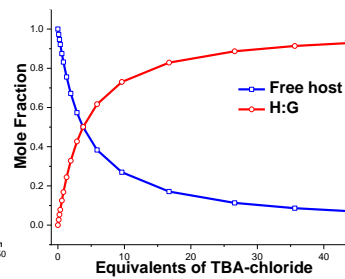
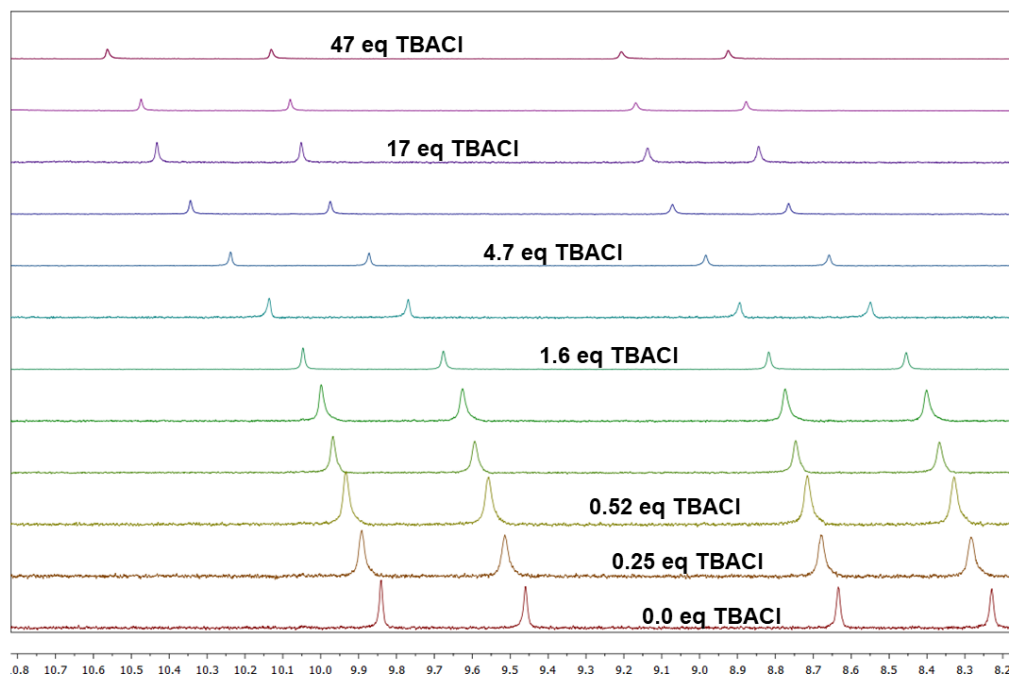
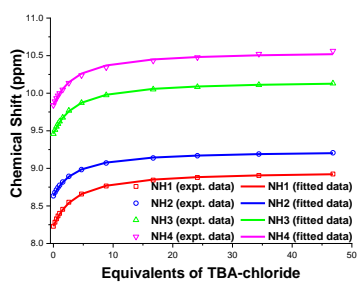


Figure E2: ^1H NMR spectroscopic titration of receptor **6.2** (2 mM) with TBACl in $\text{DMSO-}d_6$ with 0.5% water at 298 K. a) Stack plot. b) Fitplot for 4 NH protons at $\delta = 8.25, 8.64, 9.56$ and 9.90 using global analysis with 1:1 ($K_a = 146 \text{ M}^{-1}$, error: 3%). c) Plot of the residuals for using global analysis. d) Calculated mole fractions.

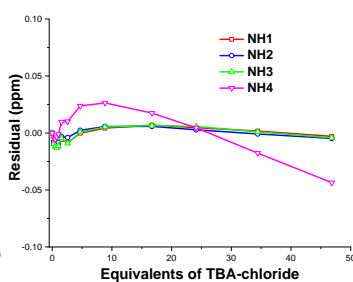
a)



b)



c)



d)

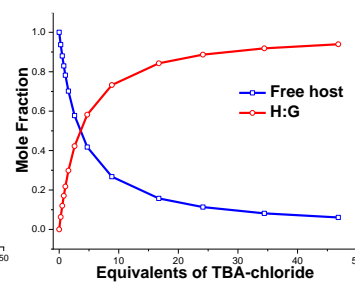


Figure E3: ^1H NMR spectroscopic titration of receptor **6.3** (2 mM) with TBACl in $\text{DMSO-}d_6$ with 0.5% water at 298 K. a) Stack plot. b) Fitplot for 4 NH protons at $\delta = 8.23, 8.63, 9.46$ and 9.84 using global analysis with 1:1 ($K_a = 177 \text{ M}^{-1}$, error: 3%). c) Plot of the residuals for using global analysis. d) Calculated mole fractions.

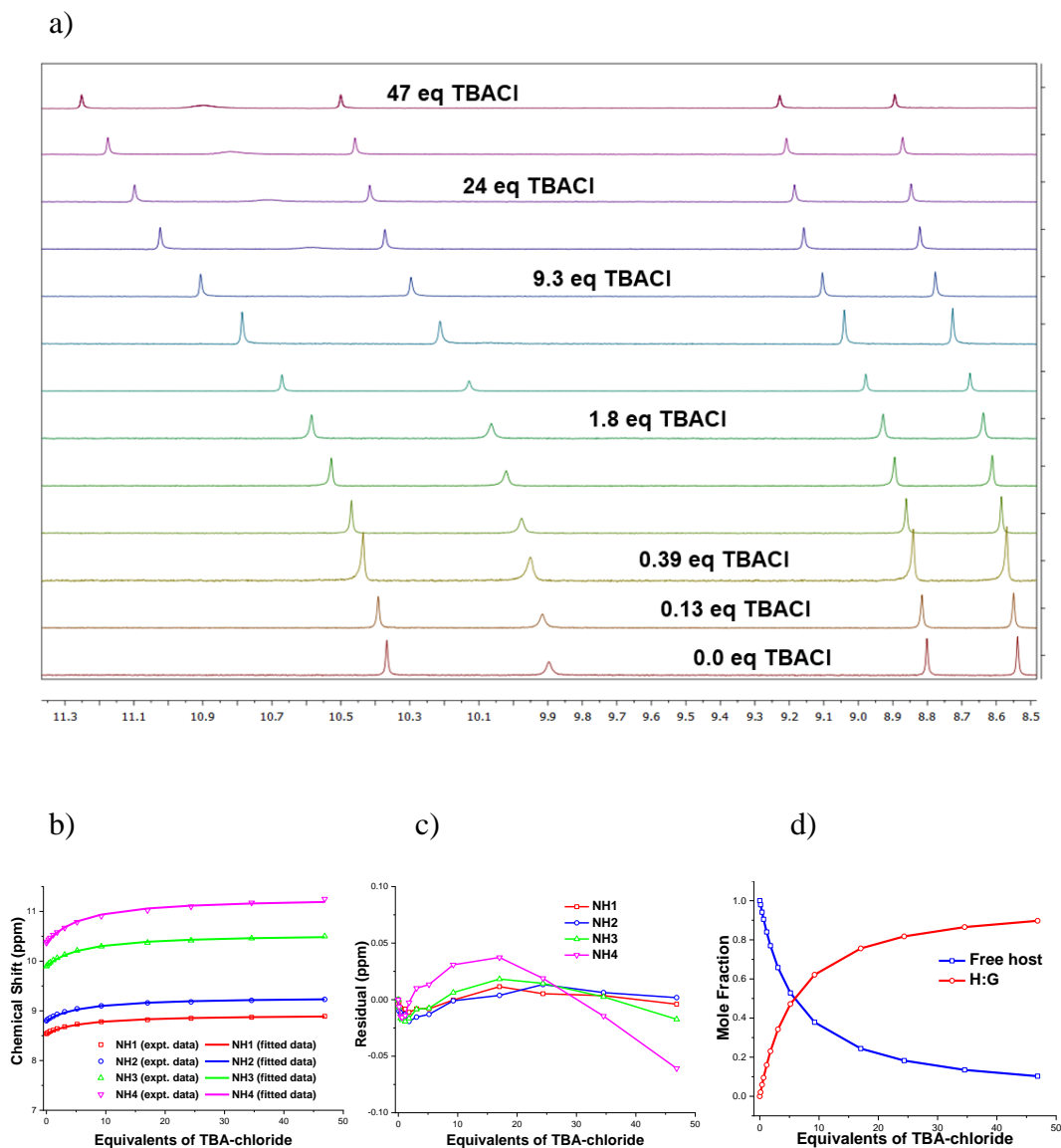


Figure E4: ^1H NMR spectroscopic titration of receptor **6.4** (2 mM) with TBACl in $\text{DMSO-}d_6$ with 0.5% water at 298 K. a) Stack plot. b) Fitplot for 4 NH protons at $\delta = 8.54, 8.80, 9.90$ and 10.37 using global analysis with 1:1 ($K_a = 96 \text{ M}^{-1}$, error: 5%). c) Plot of the residuals for using global analysis. d) Calculated mole fractions.

C) Transport studies:

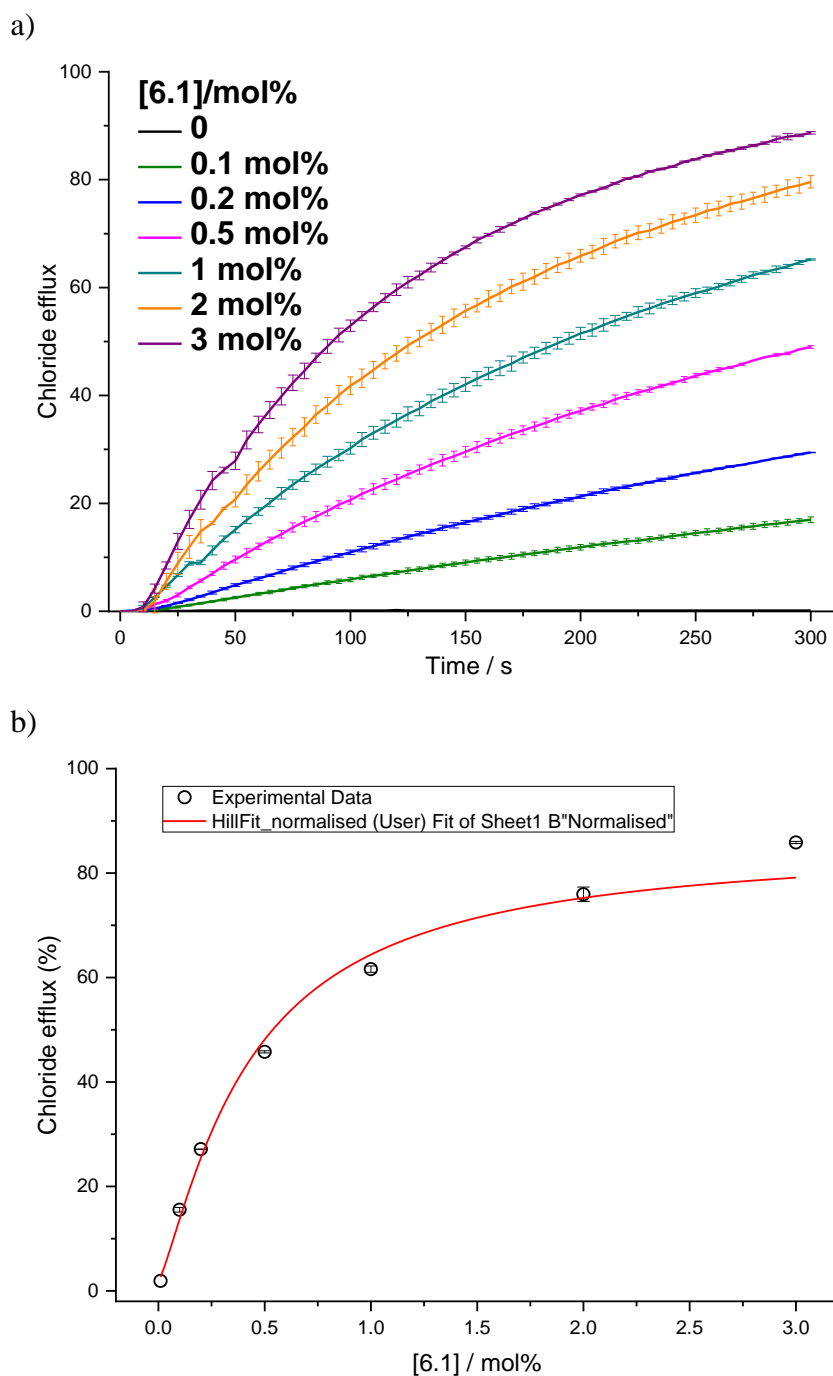


Figure E5: a) Dose response curve and b) Hill plot analysis of chloride efflux facilitated by compound **6.1** from unilamellar POPC vesicles that were loaded with a 489 mM KCl solution buffered to pH 7.2 with 5 mM phosphate, and were suspended in a 489 mM KNO₃ solution buffered to pH 7.2 with 5 mM phosphate salts. DMSO was used as a control. Each point is the average of at least two repeats.

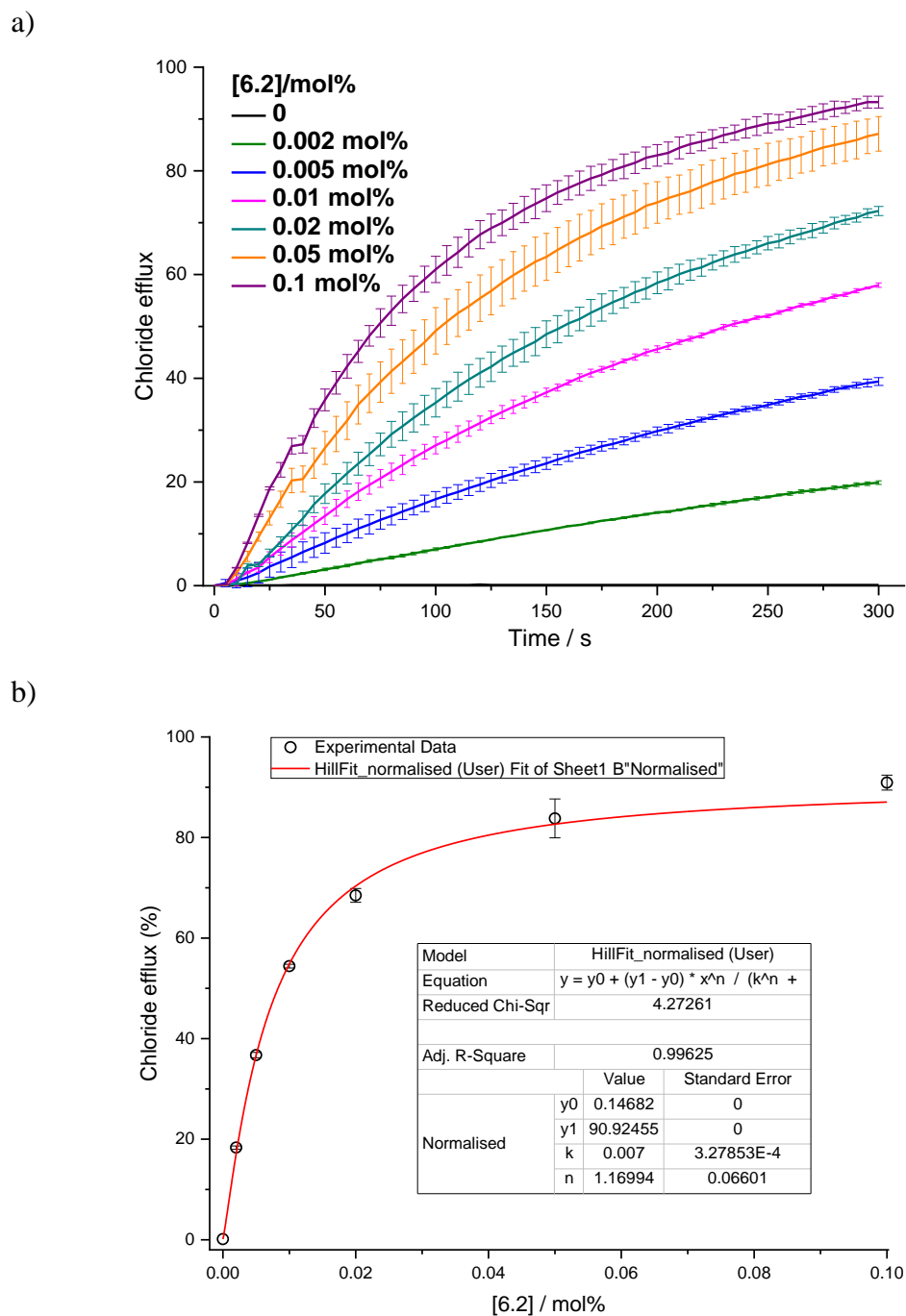


Figure E6: a) Dose response curve and b) Hill plot analysis of chloride efflux facilitated by compound **6.2** from unilamellar POPC vesicles that were loaded with a 489 mM KCl solution buffered to pH 7.2 with 5 mM phosphate, and were suspended in a 489 mM KNO₃ solution buffered to pH 7.2 with 5 mM phosphate salts. DMSO was used as a control. Each point is the average of at least two repeats.

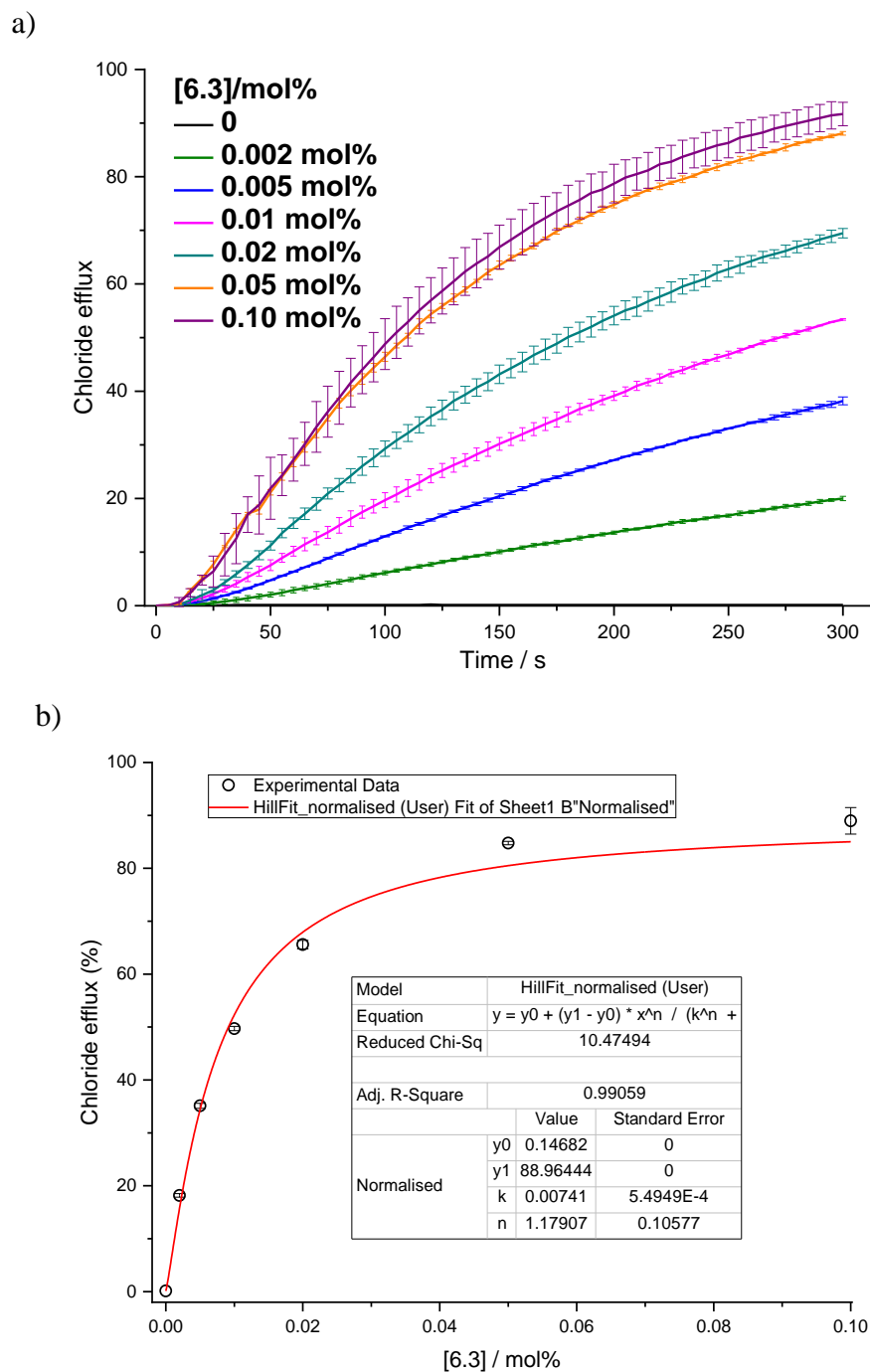
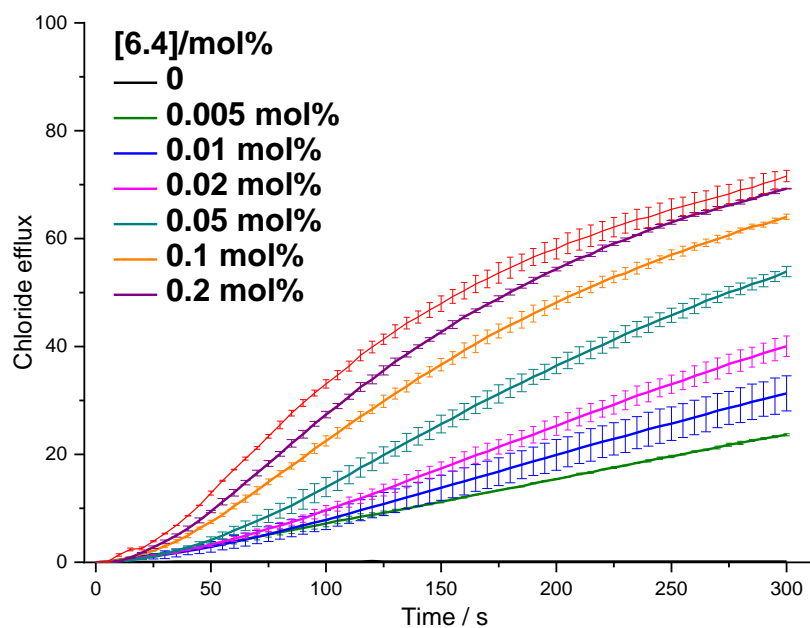


Figure E7: a) Dose response curve and b) Hill plot analysis of chloride efflux facilitated by compound **6.3** from unilamellar POPC vesicles that were loaded with a 489 mM KCl solution buffered to pH 7.2 with 5 mM phosphate, and were suspended in a 489 mM KNO₃ solution buffered to pH 7.2 with 5 mM phosphate salts. DMSO was used as a control. Each point is the average of at least two repeats.

a)



b)

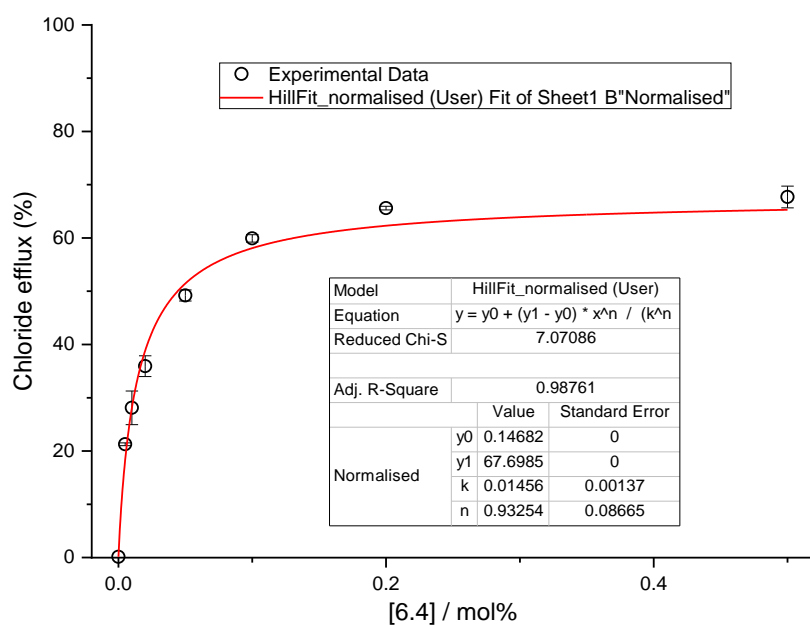


Figure E8: a) Dose response curve and b) Hill plot analysis of chloride efflux facilitated by compound **6.4** from unilamellar POPC vesicles that were loaded with a 489 mM KCl solution buffered to pH 7.2 with 5 mM phosphate, and were suspended in a 489 mM KNO₃ solution buffered to pH 7.2 with 5 mM phosphate salts. DMSO was used as a control. Each point is the average of at least two repeats.

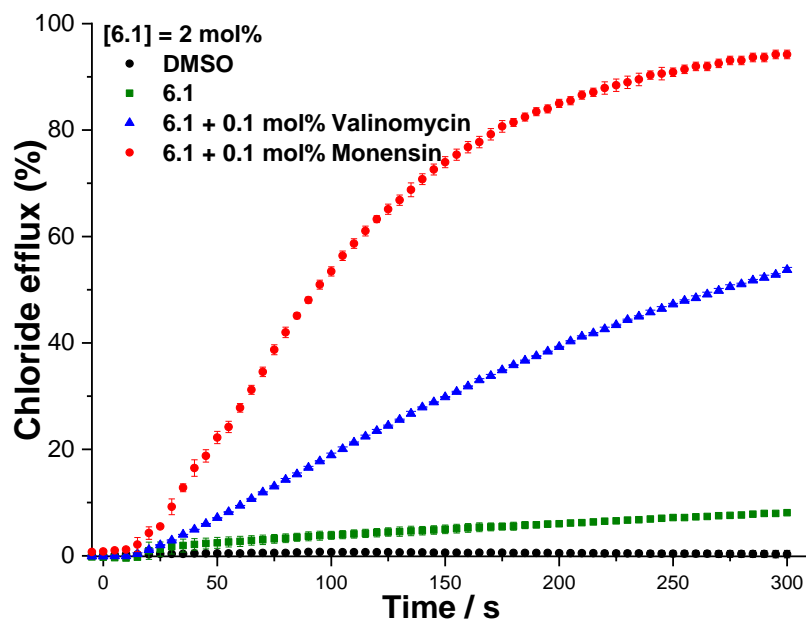


Figure E9: Electrogenic or electroneutral transport mediated by compound **6.1** (2 mol% with respect to lipid) in the presence of monensin or valinomycin (0.1 mol% with respect to lipid). Unilamellar POPC vesicles were loaded with a 300 mM KCl solution buffered to pH 7.2 with 5 mM phosphate and were suspended in a 300 mM KGlu solution buffered to pH 7.2 with 5 mM phosphate salts. DMSO was used as a control. Each point is the average of at least two repeats.

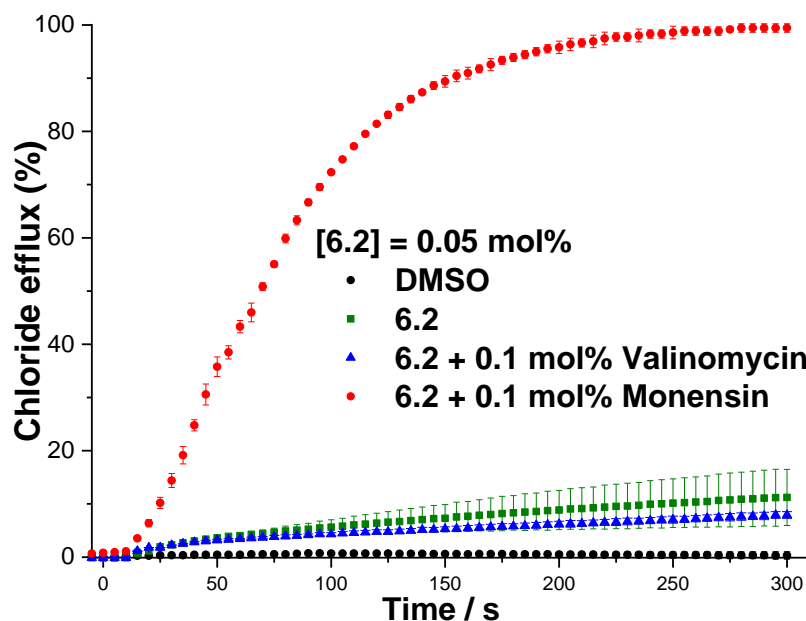


Figure E10: Electrogenic or electroneutral transport mediated by compound **6.2** (0.05 mol% with respect to lipid) in the presence of monensin or valinomycin (0.1 mol% with respect to lipid). Unilamellar POPC vesicles were loaded with a 300 mM KCl solution buffered to pH 7.2 with 5 mM phosphate and were suspended in a 300 mM KGlu solution buffered to pH 7.2 with 5 mM phosphate salts. DMSO was used as a control. Each point is the average of at least two repeats.

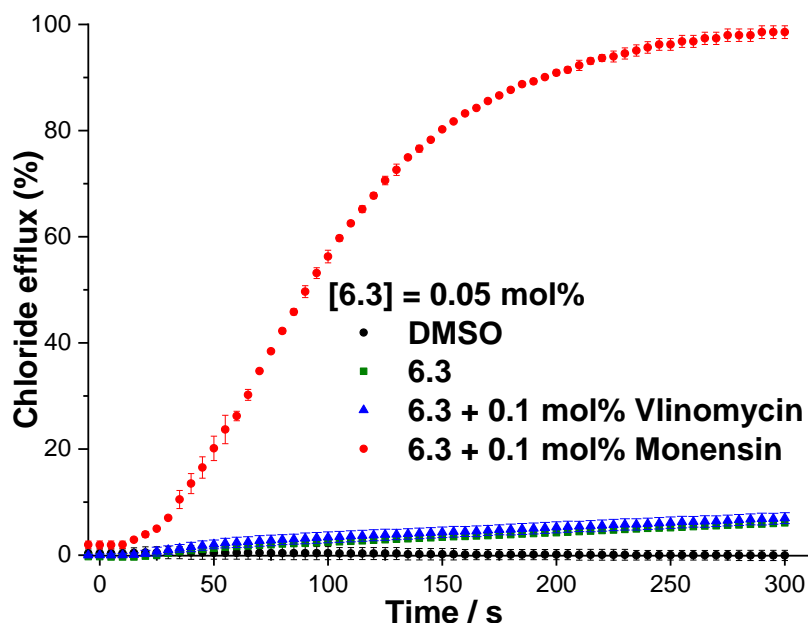


Figure E11: Electrogenic or electroneutral transport mediated by compound **6.3** (0.05 mol% with respect to lipid) in the presence of monensin or valinomycin (0.1 mol% with respect to lipid). Unilamellar POPC vesicles were loaded with a 300 mM KCl solution buffered to pH 7.2 with 5 mM phosphate and were suspended in a 300 mM KGlu solution buffered to pH 7.2 with 5 mM phosphate salts. DMSO was used as a control. Each point is the average of at least two repeats.

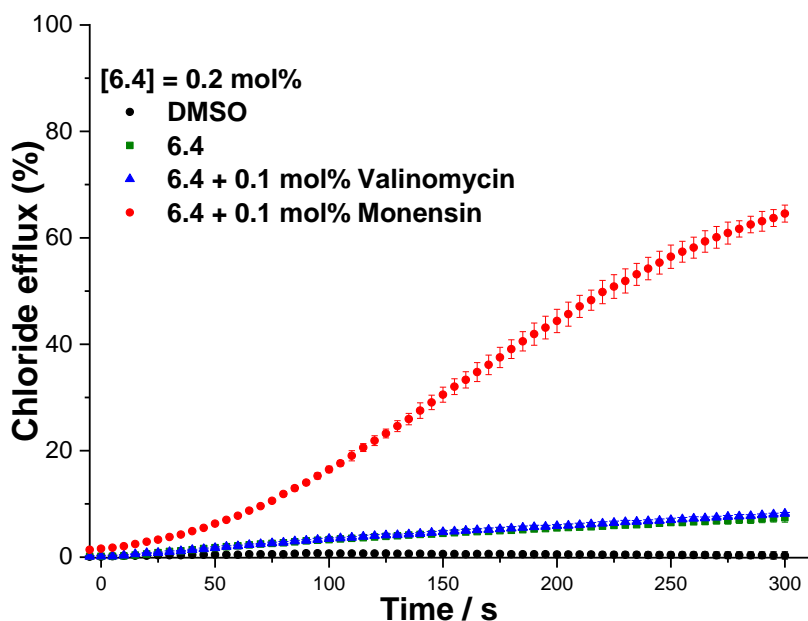


Figure E12: Electrogenic or electroneutral transport mediated by compound **6.4** (0.2 mol% with respect to lipid) in the presence of monensin or valinomycin (0.1 mol% with respect to lipid). Unilamellar POPC vesicles were loaded with a 300 mM KCl solution buffered to pH 7.2 with 5 mM phosphate and were suspended in a 300 mM KGlu solution buffered to pH 7.2 with 5 mM phosphate salts. DMSO was used as a control. Each point is the average of at least two repeats.

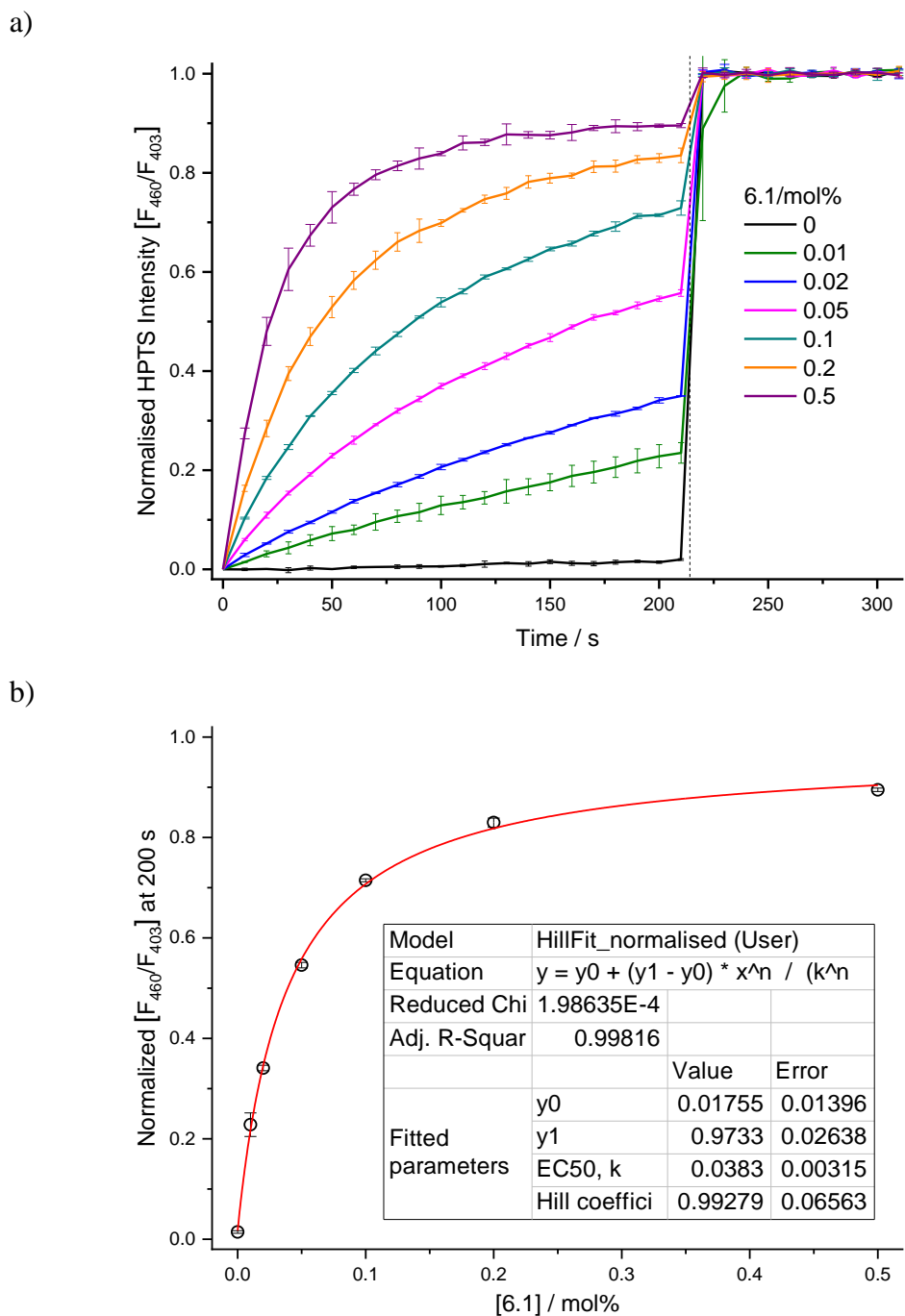


Figure E13: a) Dose response curve, b) Hill plot analysis of H^+/Cl^- symport or Cl^-/OH^- antiport facilitated by compound **6.1** using KCl-KOH assay from POPC vesicles loaded with KCl (100 mM), buffered to pH 7.0 with HEPES (10 mM). The test compound was added at 0 s and detergent was added at 200 s. Ionophore concentrations are shown as ionophore to lipid molar ratios. Error bars represent SD from at least three repeats.

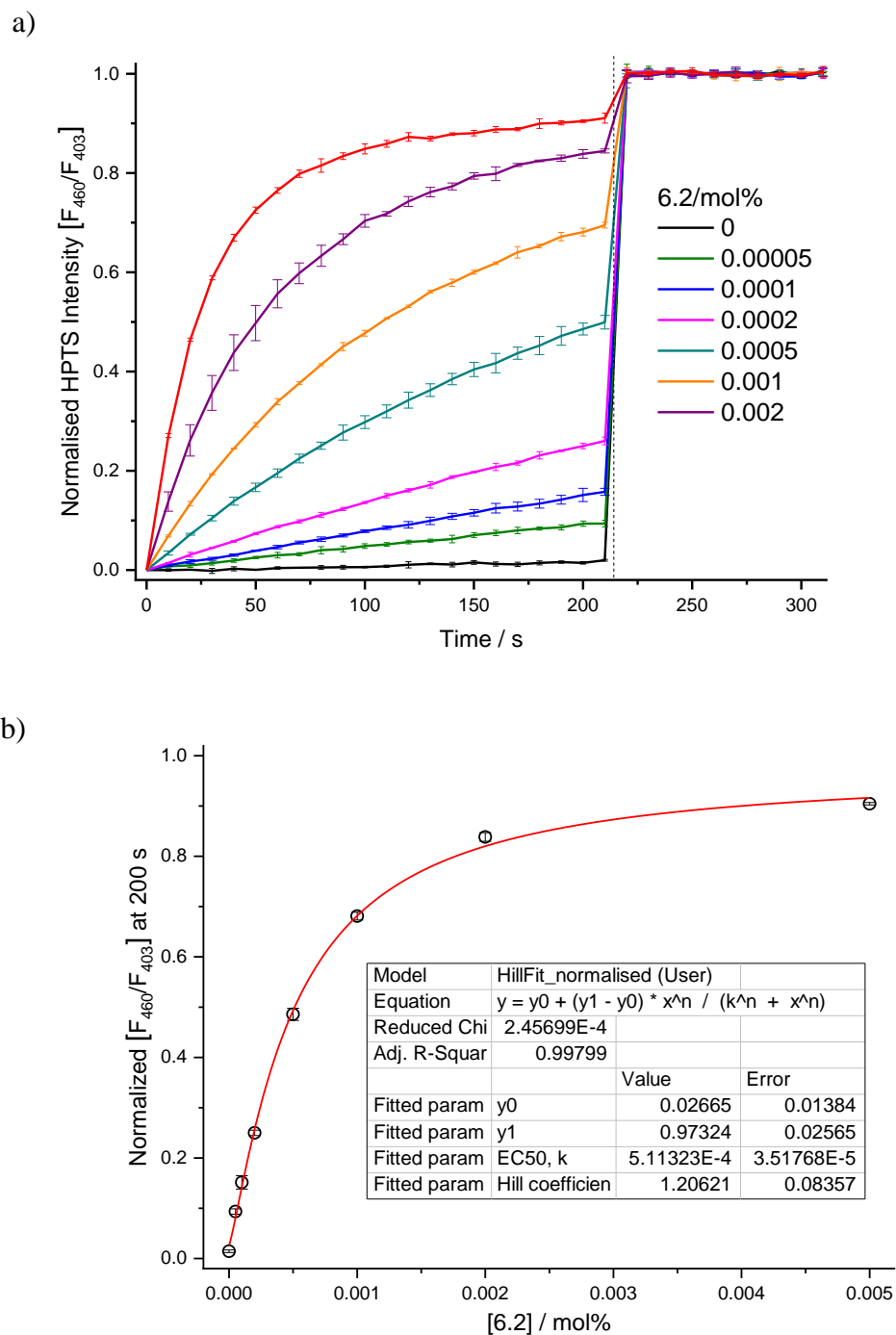


Figure E14: a) Dose response curve, b) Hill plot analysis of H^+/Cl^- symport or Cl^-/OH^- antiport facilitated by compound **6.2** using KCl-KOH assay from POPC vesicles loaded with KCl (100 mM), buffered to pH 7.0 with HEPES (10 mM). The test compound was added at 0 s and detergent was added at 200 s. Ionophore concentrations are shown as ionophore to lipid molar ratios. Error bars represent SD from at least three repeats.

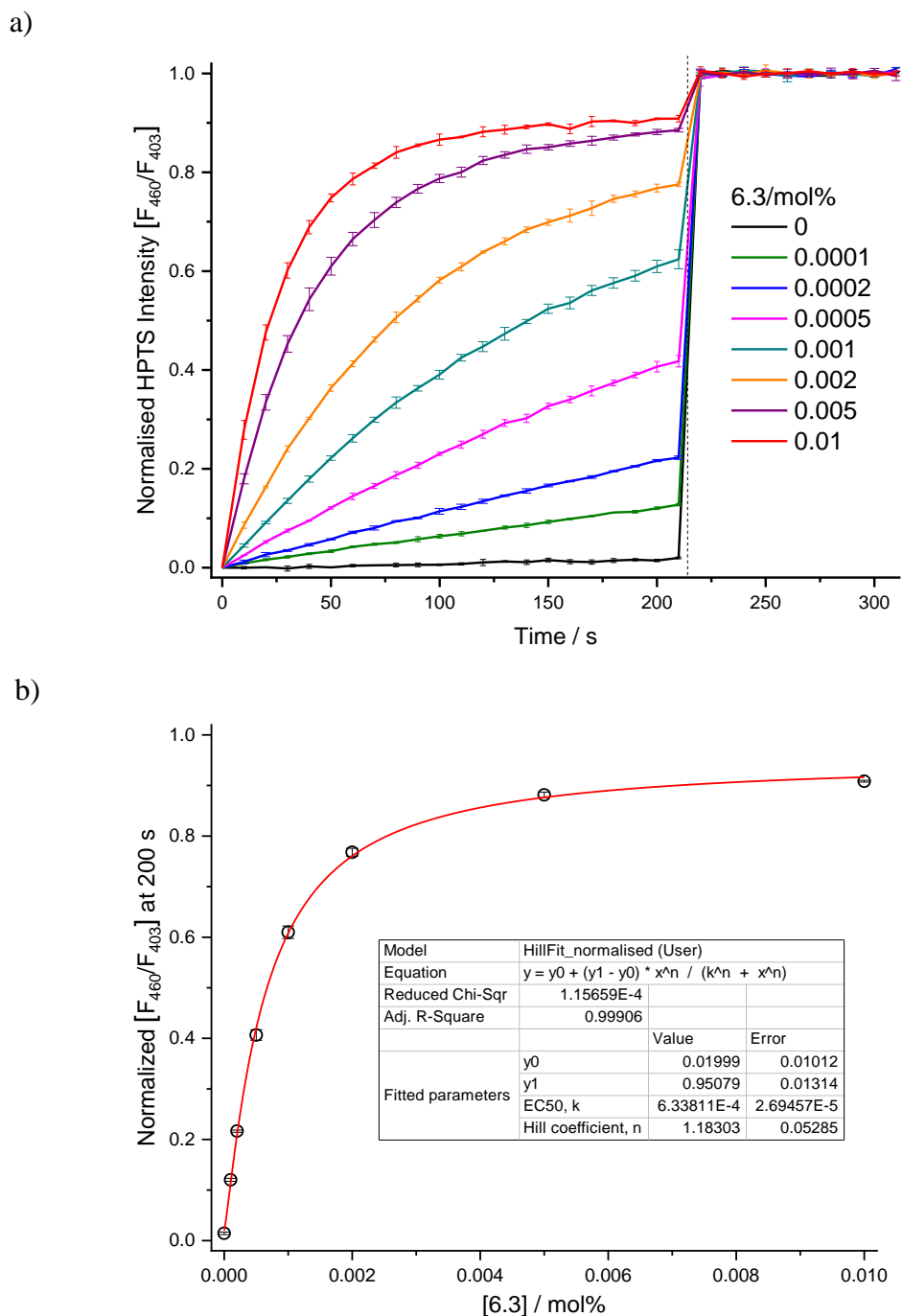
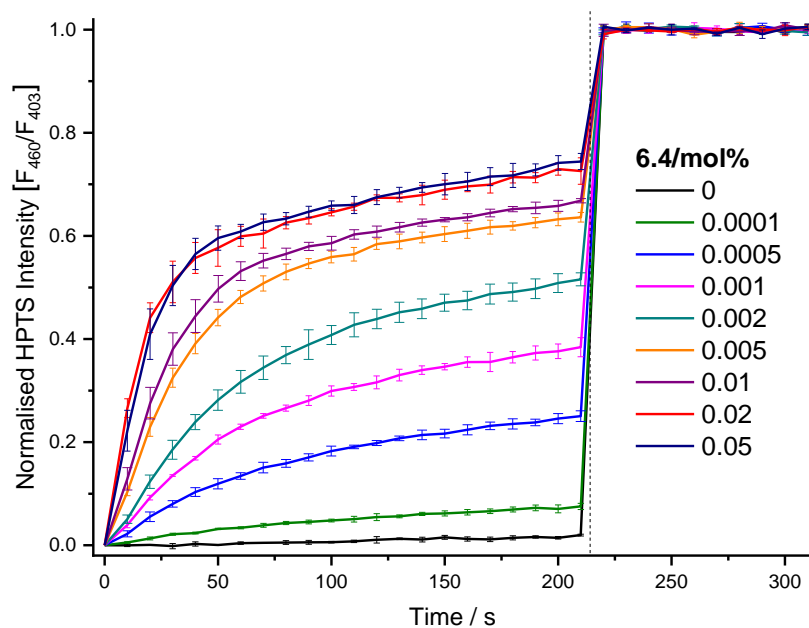


Figure E15: a) Dose response curve, b) Hill plot analysis of H^+/Cl^- symport or Cl^-/OH^- antiport facilitated by compound **6.3** using KCl-KOH assay from POPC vesicles loaded with KCl (100 mM), buffered to pH 7.0 with HEPES (10 mM). The test compound was added at 0 s and detergent was added at 200 s. Ionophore concentrations are shown as ionophore to lipid molar ratios. Error bars represent SD from at least three repeats.

a)



b)

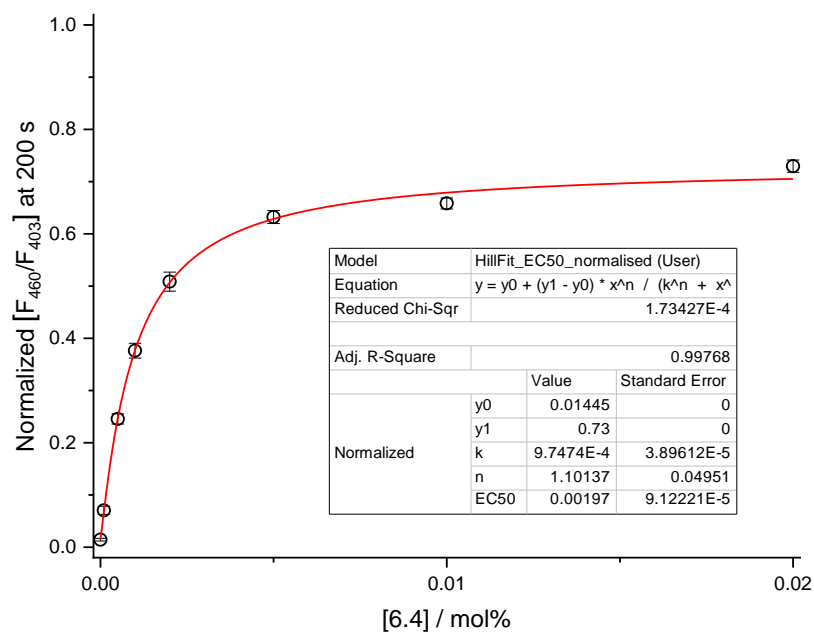


Figure E16: a) Dose response curve, b) Hill plot analysis of H^+/Cl^- symport or Cl^-/OH^- antiport facilitated by compound **6.4** using KCl-KOH assay from POPC vesicles loaded with KCl (100 mM), buffered to pH 7.0 with HEPES (10 mM). The test compound was added at 0 s and detergent was added at 200 s. Ionophore concentrations are shown as ionophore to lipid molar ratios. Error bars represent SD from at least three repeats.

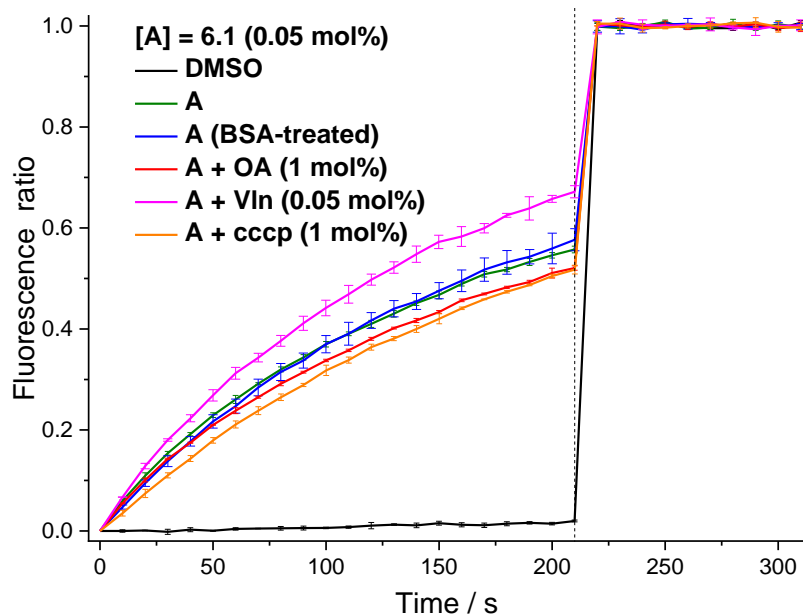


Figure E17: Using KCl-KOH assay from POPC vesicles loaded with KCl (100 mM), buffered to pH 7.0 with HEPES (10 mM), different conditions were applied including using BSA-treated lipid (to test if the transport is fatty acid dependent) addition of oleic acid at 1 mol% (as a source of fatty acid), addition of the protonophore cccp at 1 mol% (to measure of chloride uniport solely), or addition of valinomycin at 0.05 mol% (as a measure of H^+ flux), on the rate of chloride transport of receptor **6.1** (0.05 mol%).

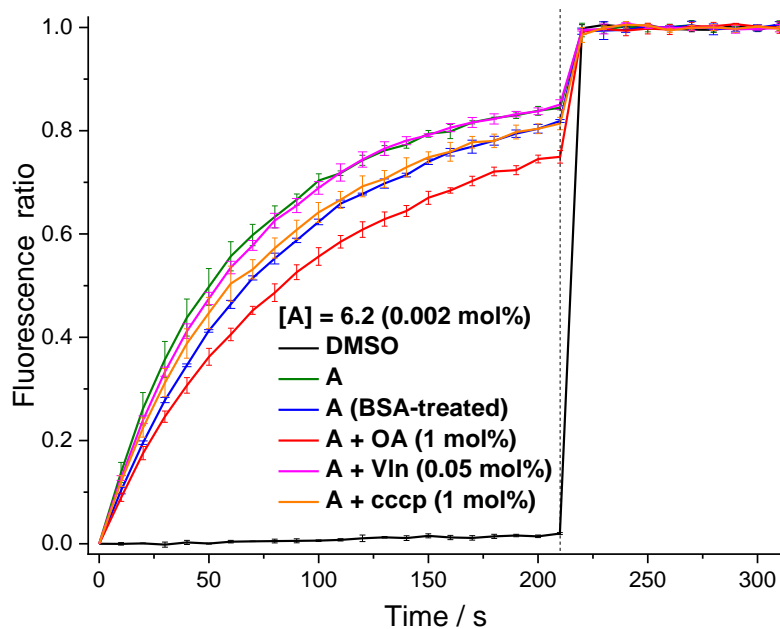


Figure E18: Using KCl-KOH assay from POPC vesicles loaded with KCl (100 mM), buffered to pH 7.0 with HEPES (10 mM), different conditions were applied including using BSA-treated lipid (to test if the transport is fatty acid dependent) addition of oleic acid at 1 mol% (as a source of fatty acid), addition of the protonophore cccp at 1 mol% (to measure of chloride uniport solely), or addition of valinomycin at 0.05 mol% (as a measure of H^+ flux), on the rate of chloride transport of receptor **6.2** (0.002 mol%).

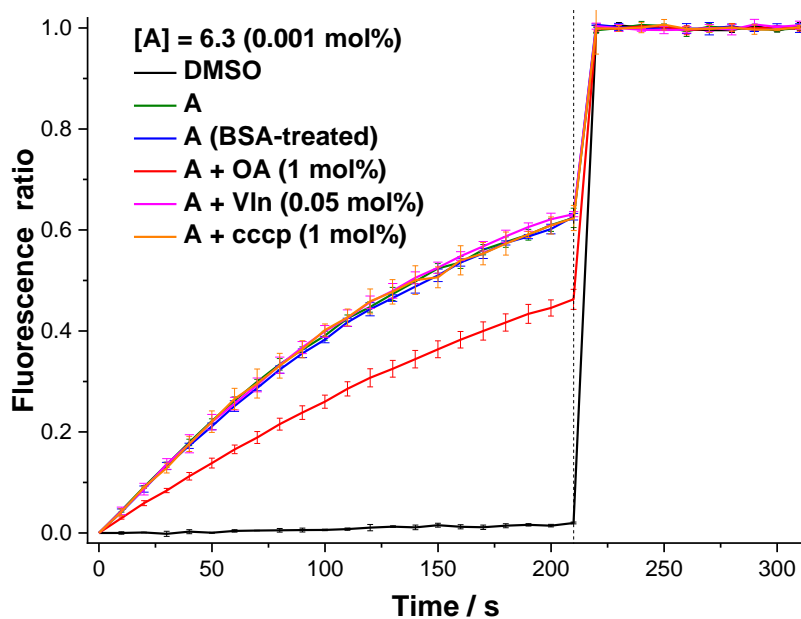


Figure E19: Using KCl-KOH assay from POPC vesicles loaded with KCl (100 mM), buffered to pH 7.0 with HEPES (10 mM), different conditions were applied including using BSA-treated lipid (to test if the transport is fatty acid dependent) addition of oleic acid at 1 mol% (as a source of fatty acid), addition of the protonophore cccp at 1 mol% (to measure of chloride uniport solely), or addition of valinomycin at 0.05 mol% (as a measure of H^+ flux), on the rate of chloride transport of receptor **6.3** (0.001 mol%).

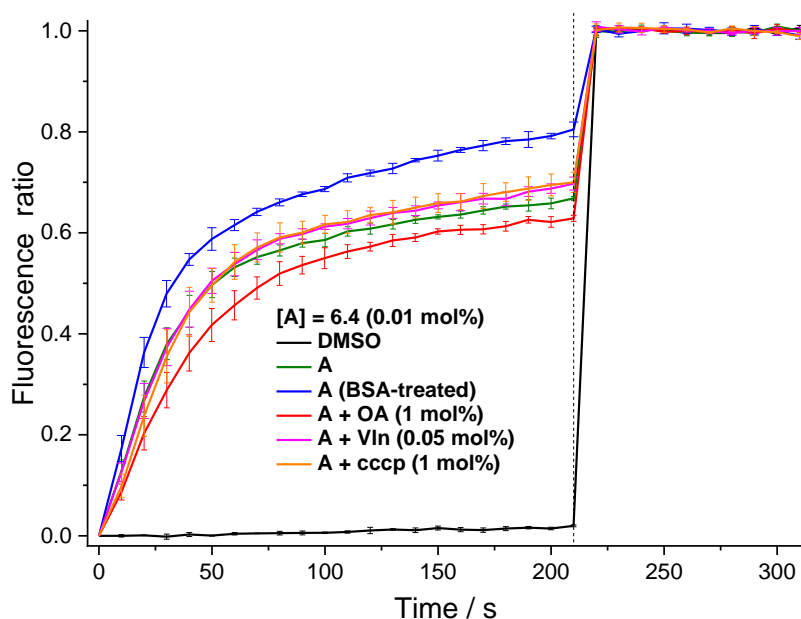
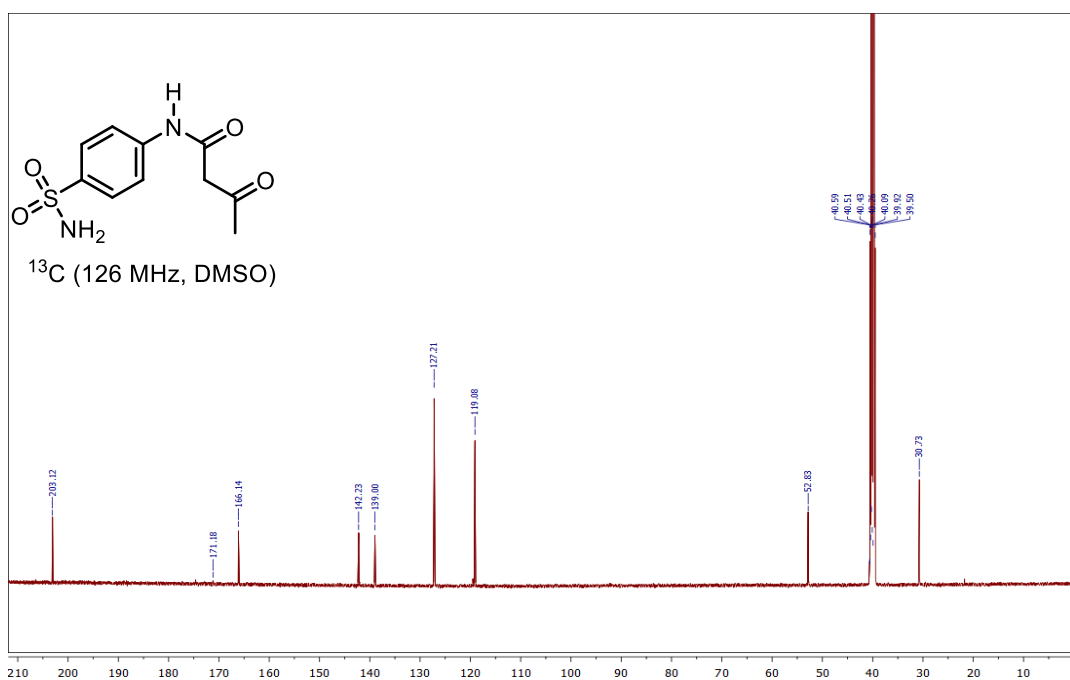
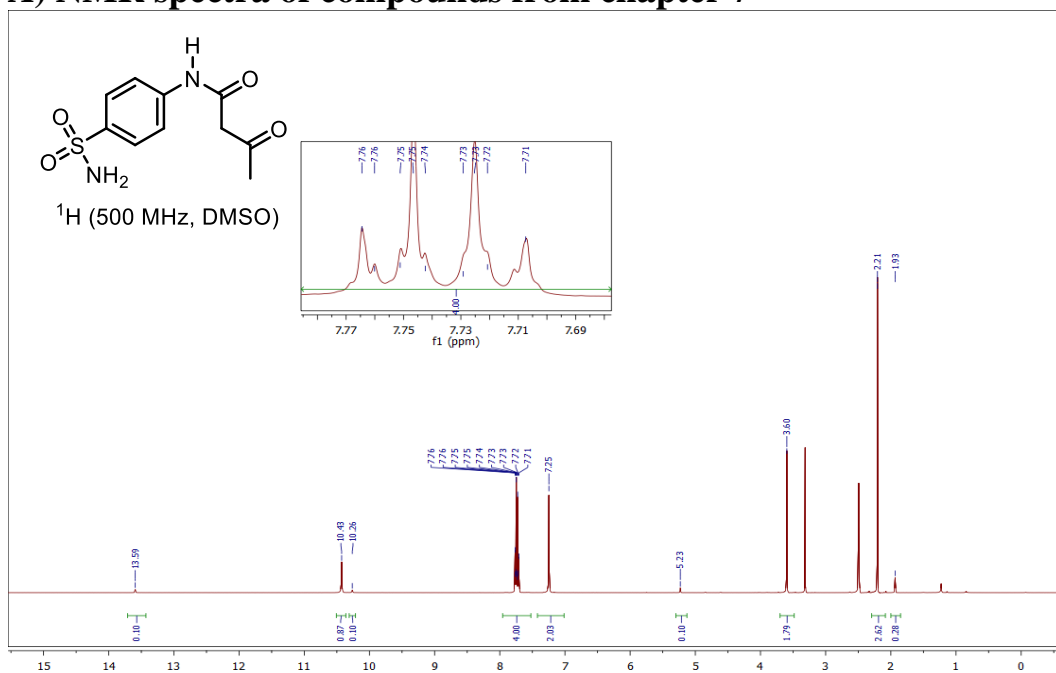
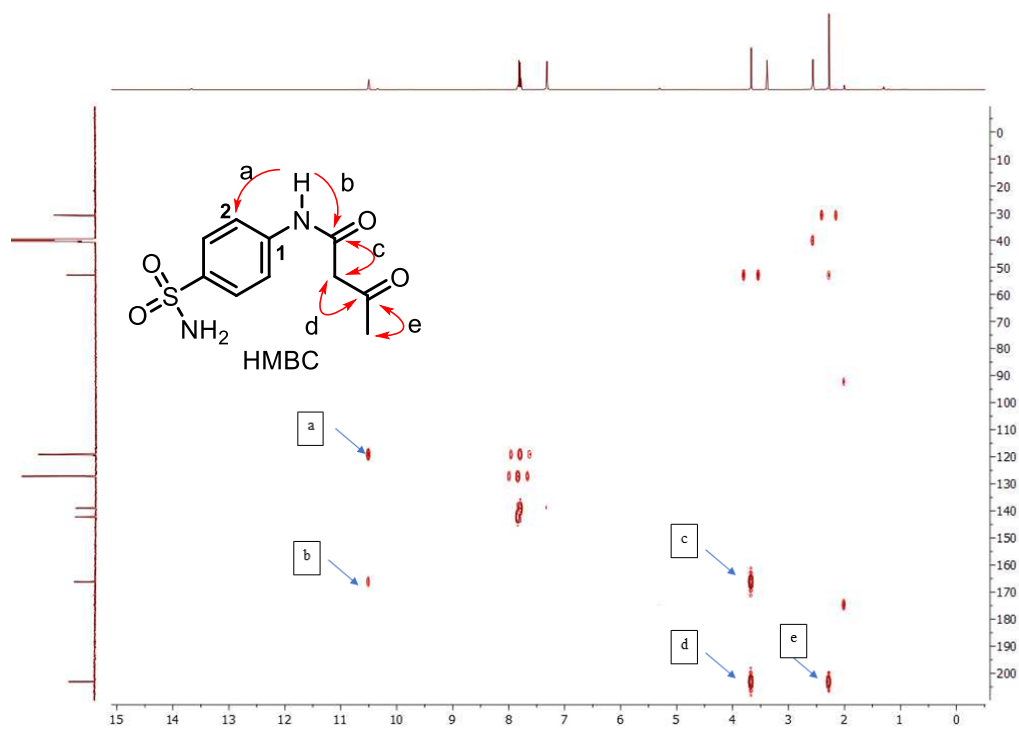


Figure E20: Using KCl-KOH assay from POPC vesicles loaded with KCl (100 mM), buffered to pH 7.0 with HEPES (10 mM), different conditions were applied including using BSA-treated lipid (to test if the transport is fatty acid dependent) addition of oleic acid at 1 mol% (as a source of fatty acid), addition of the protonophore cccp at 1 mol% (to measure of chloride uniport solely), or addition of valinomycin at 0.05 mol% (as a measure of H^+ flux), on the rate of chloride transport of receptor **6.4** (0.01 mol%).

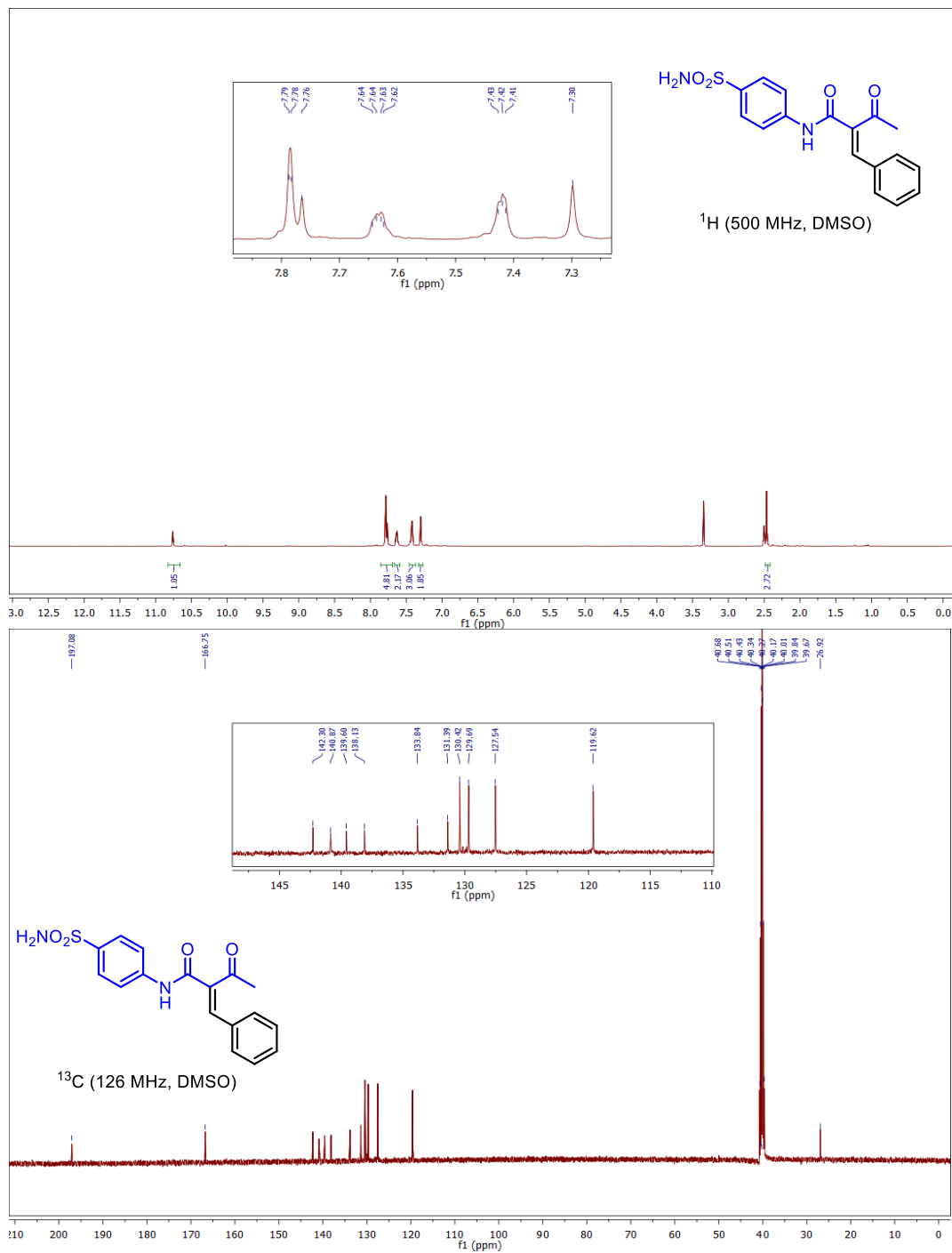
Appendix F: Supplementary Information to Chapter 7

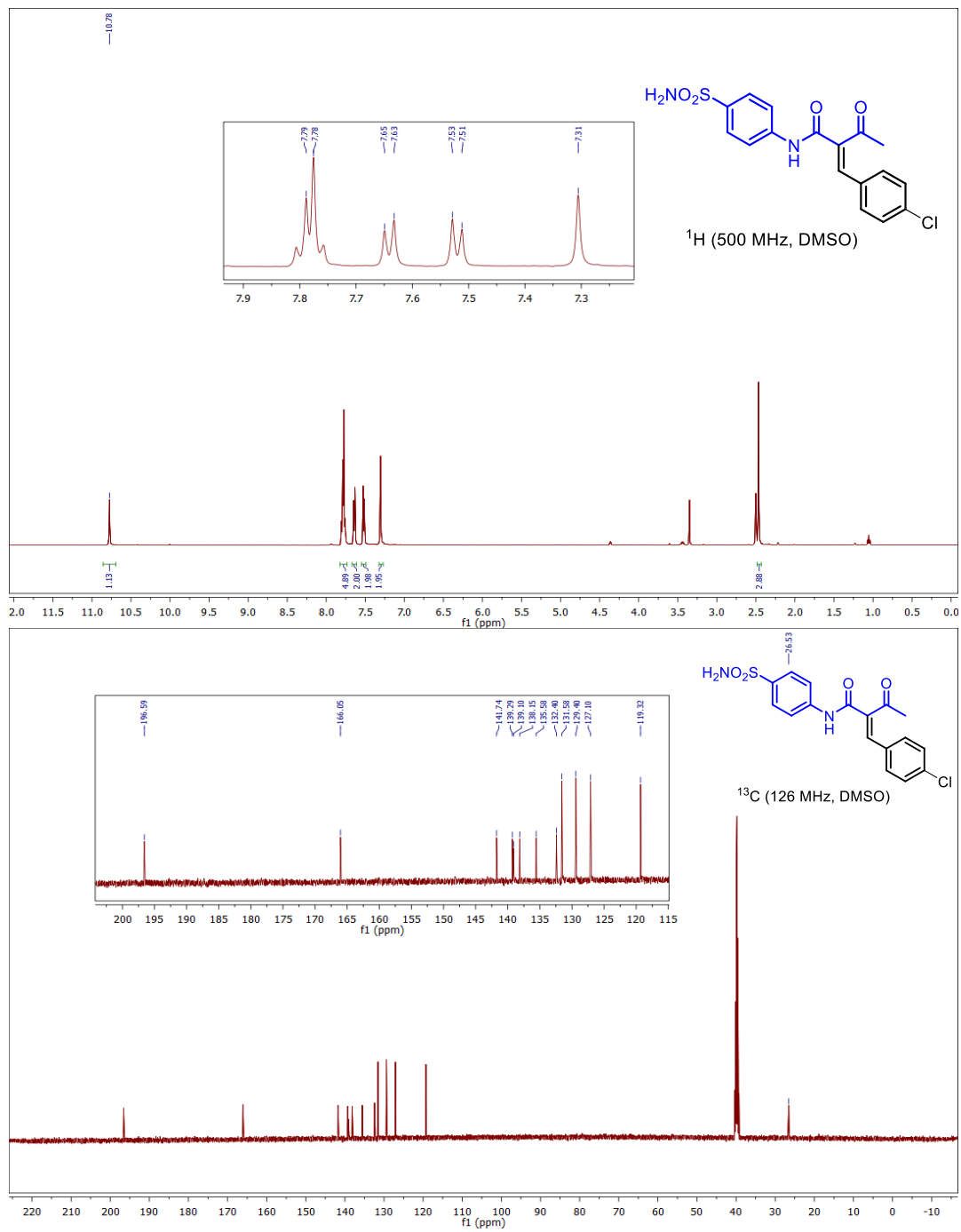
A) NMR spectra of compounds from chapter 7



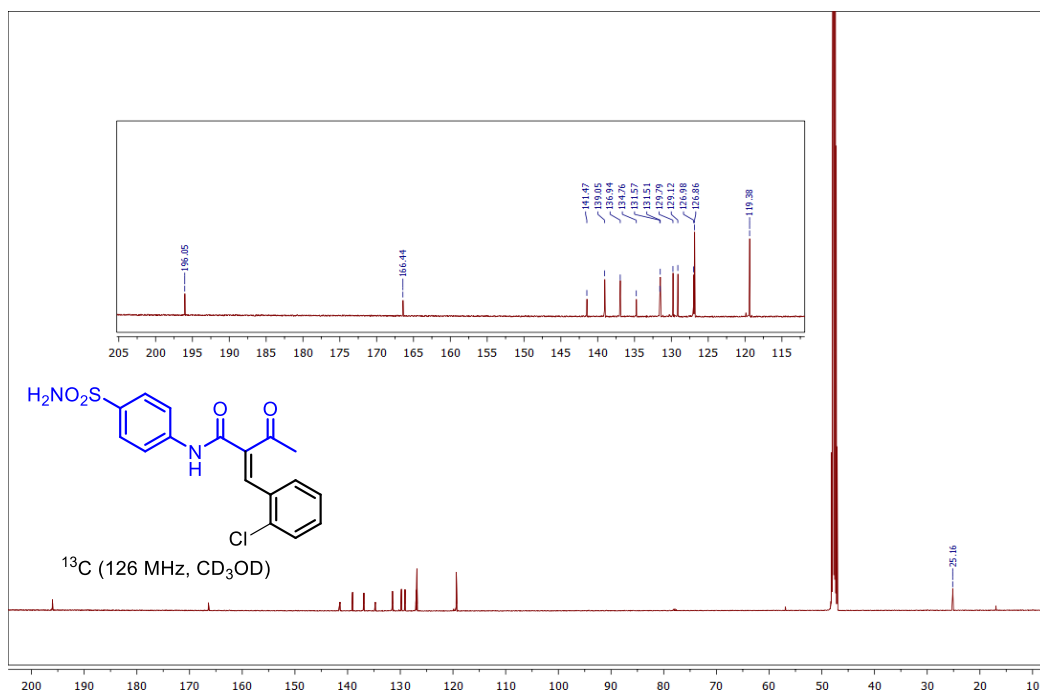
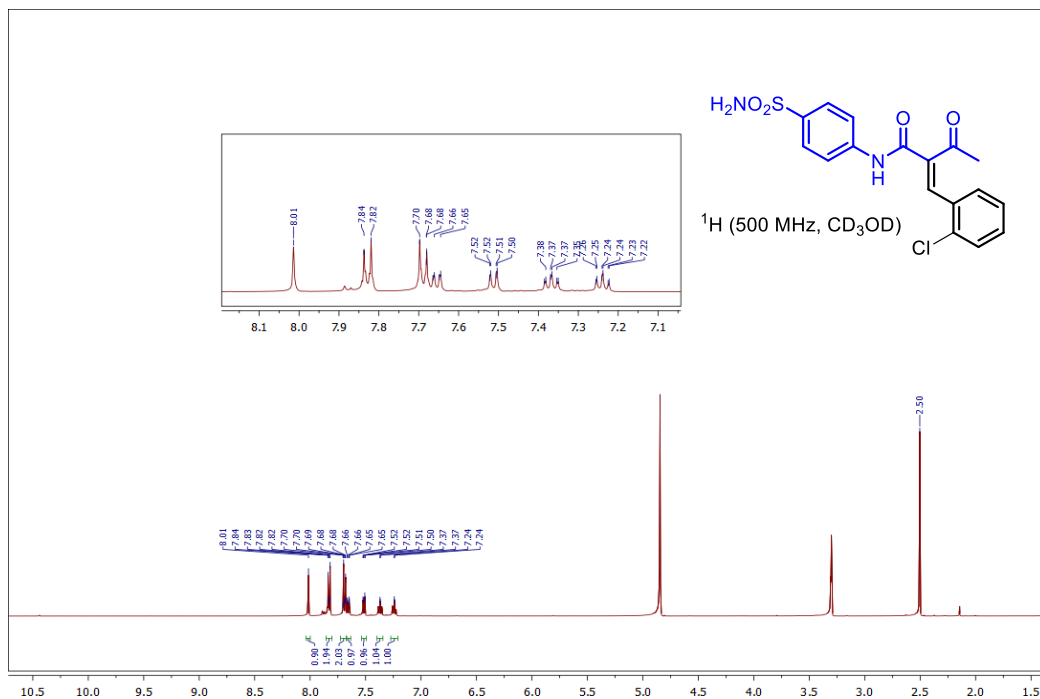


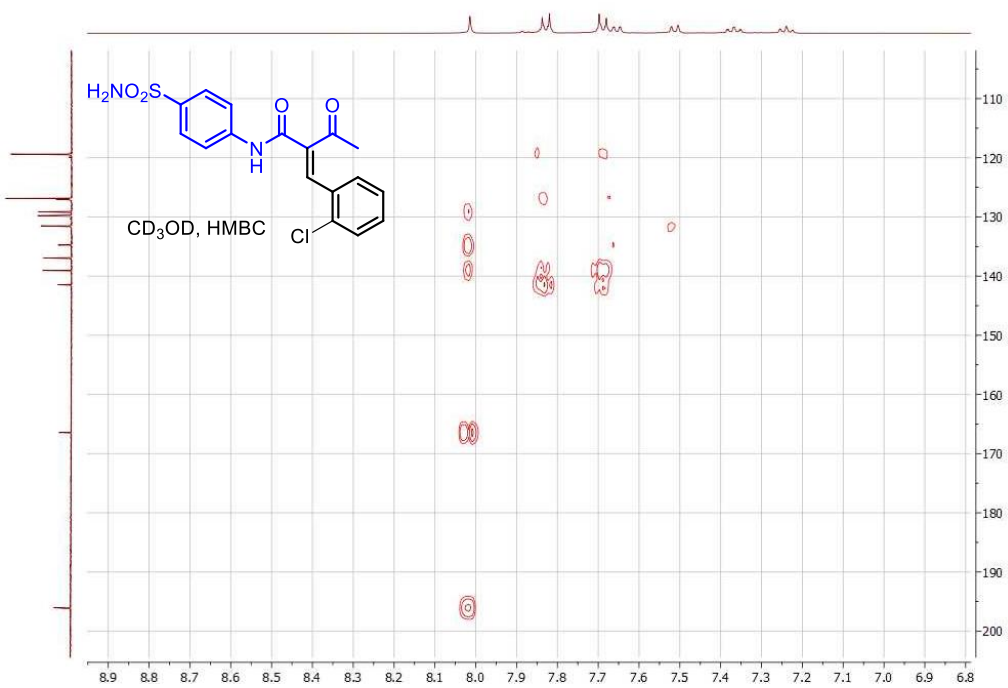
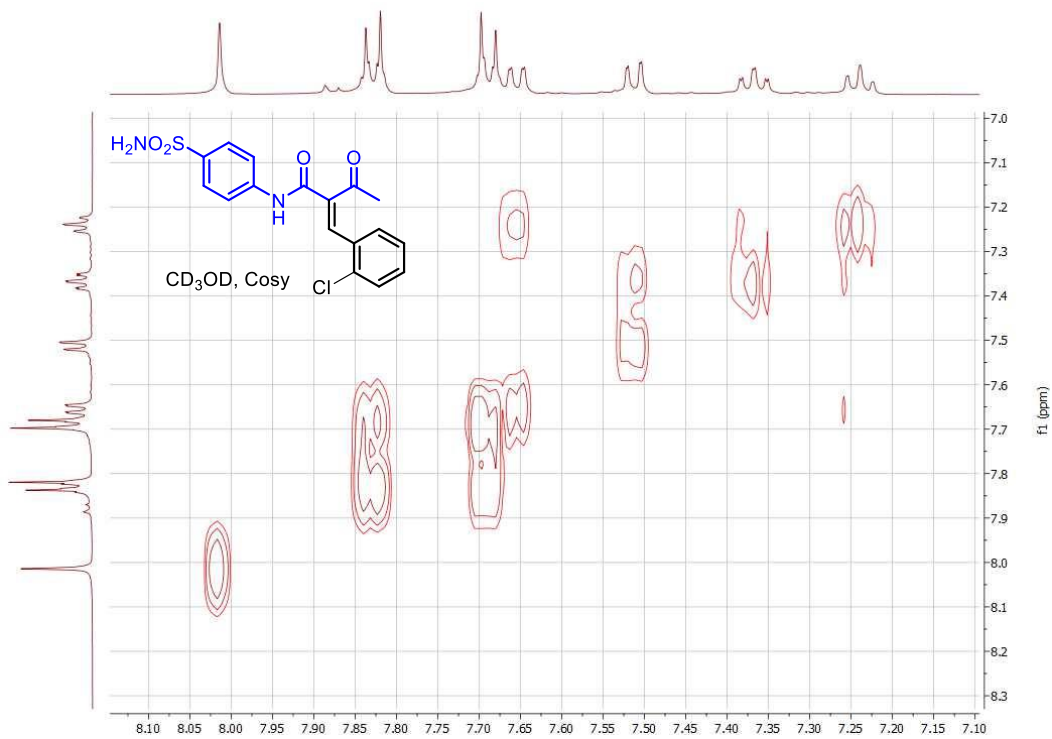
Appendix F for Chapter 7



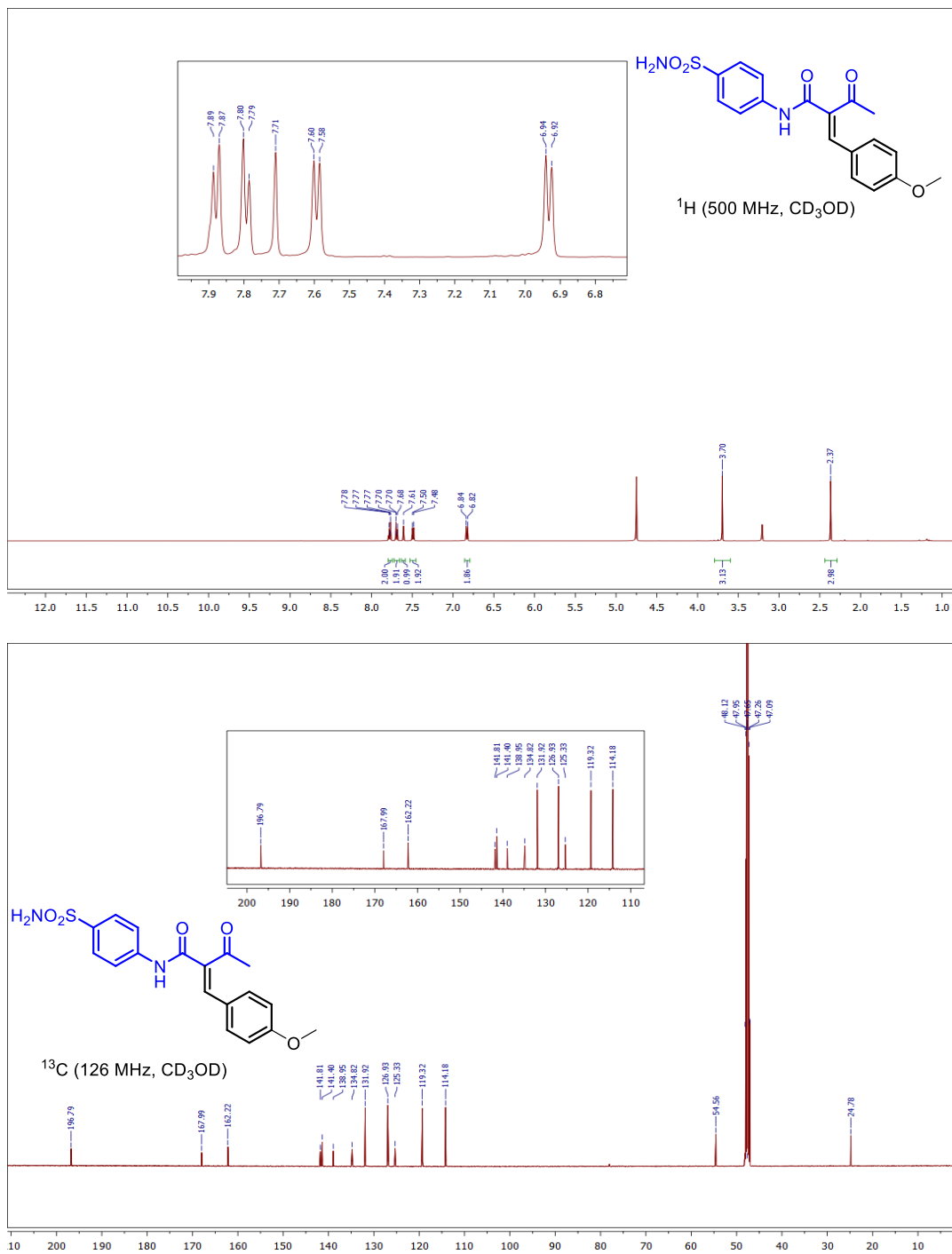


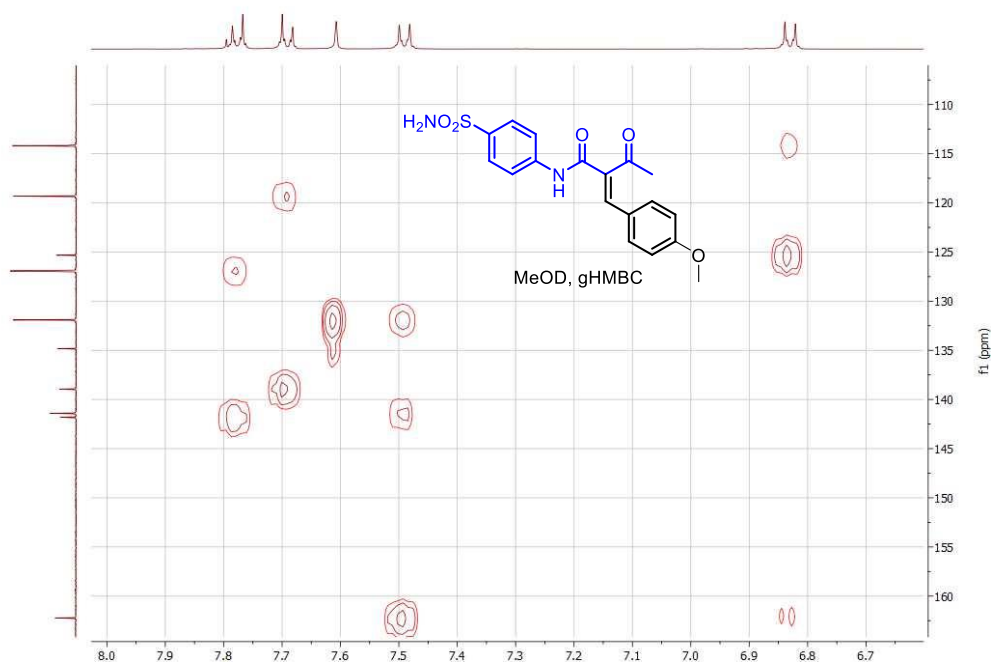
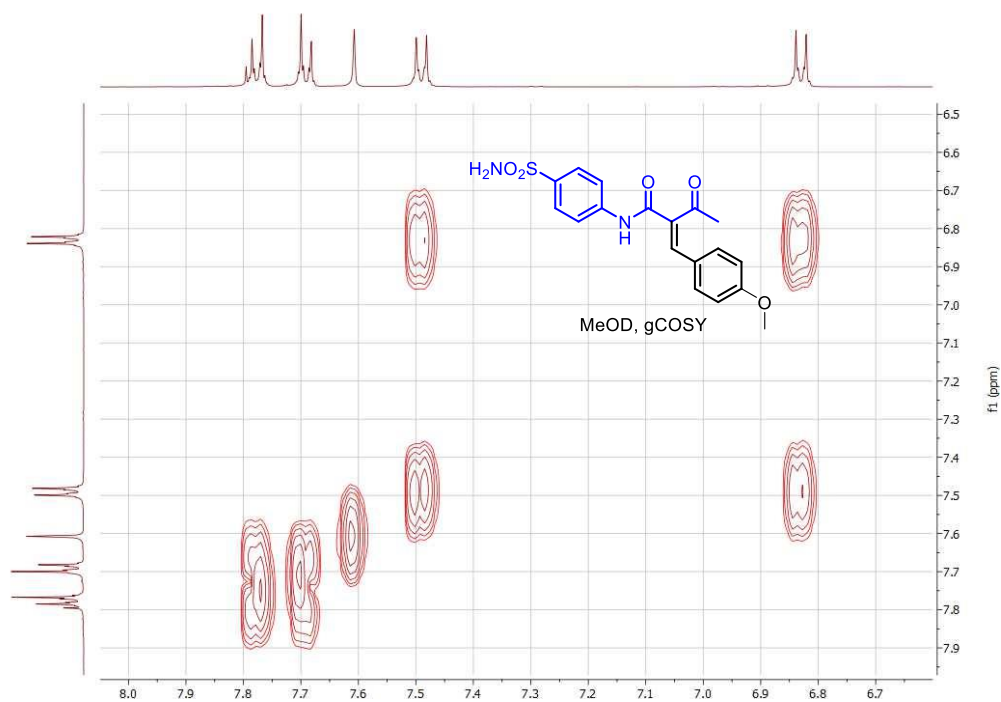
Appendix F for Chapter 7

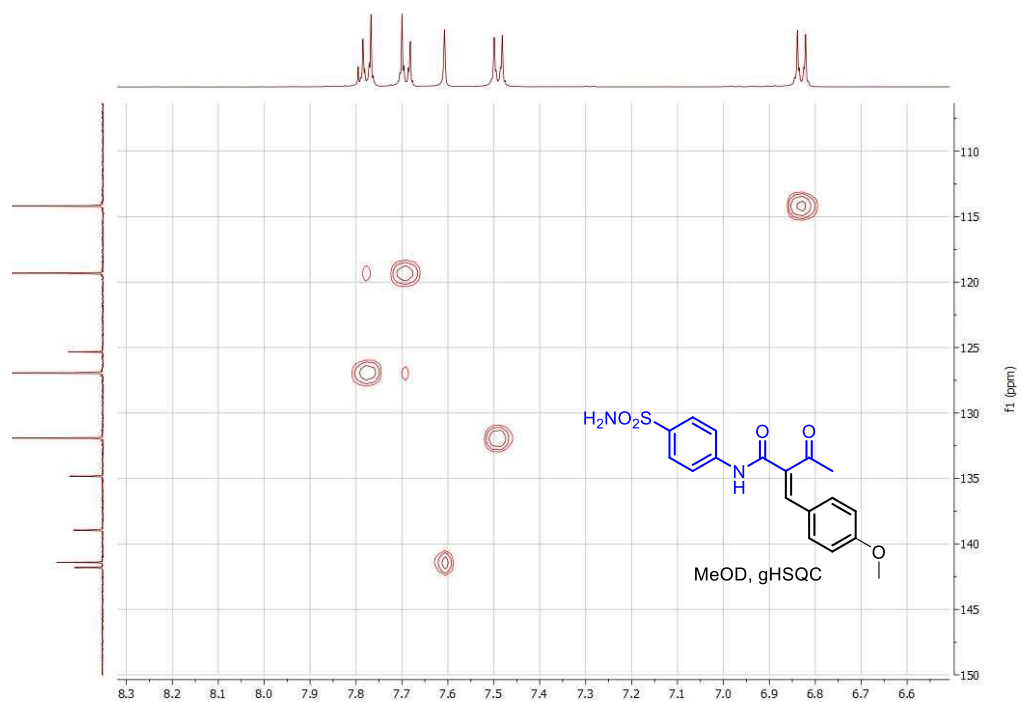


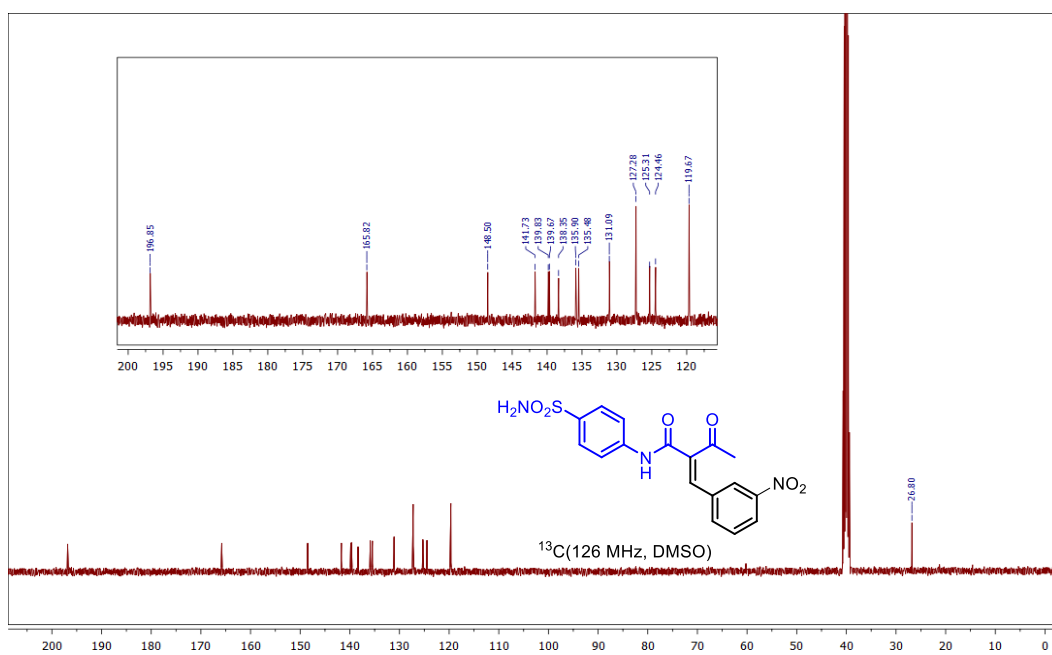
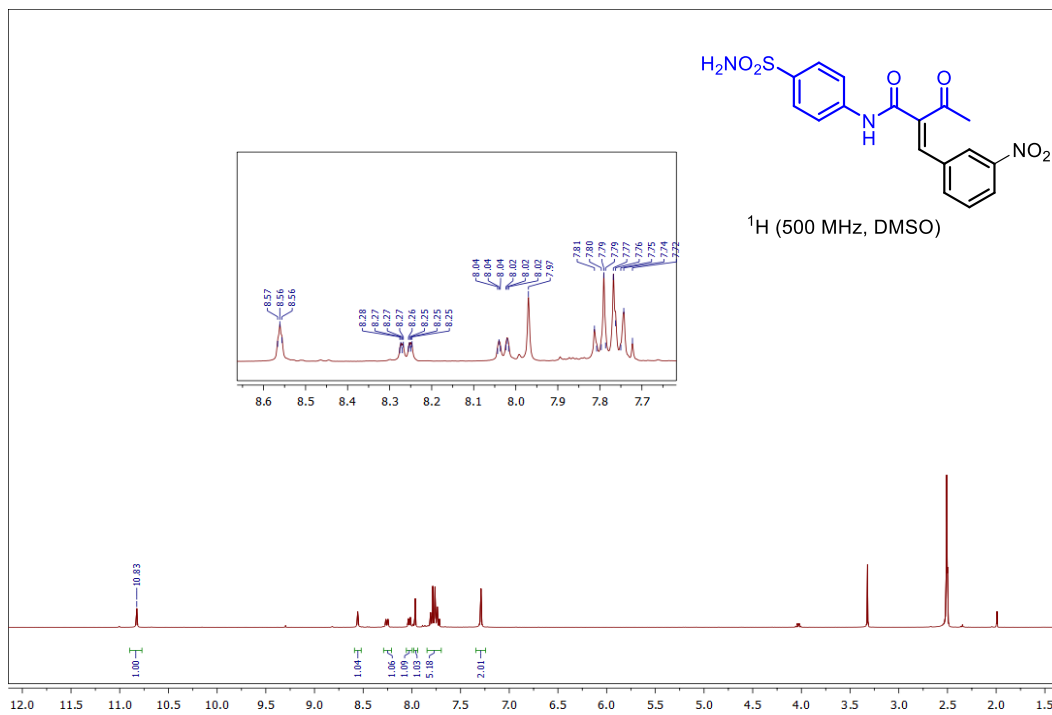


Appendix F for Chapter 7

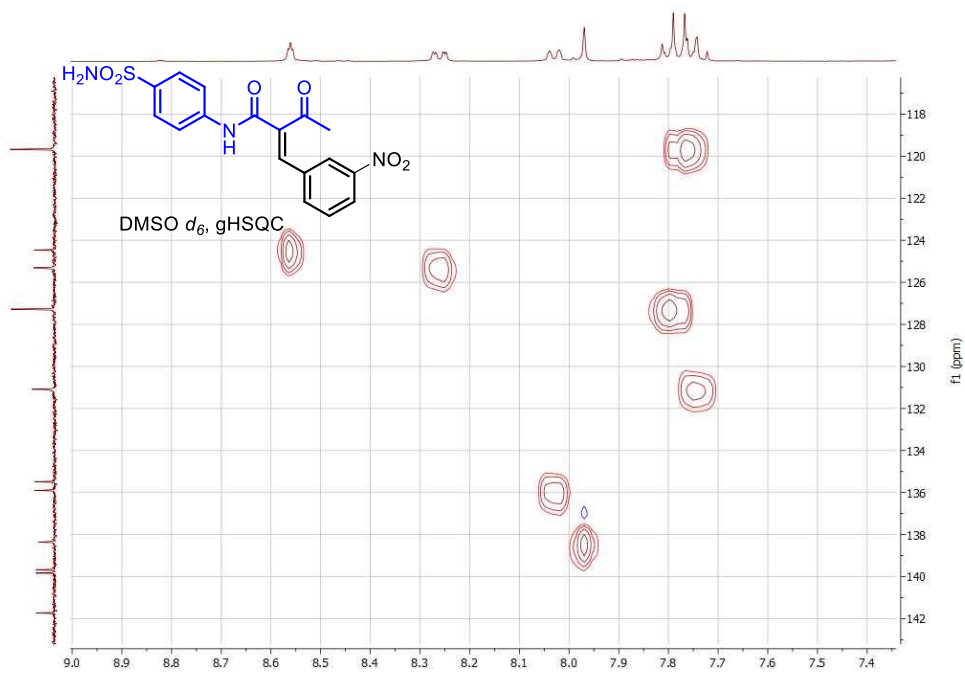
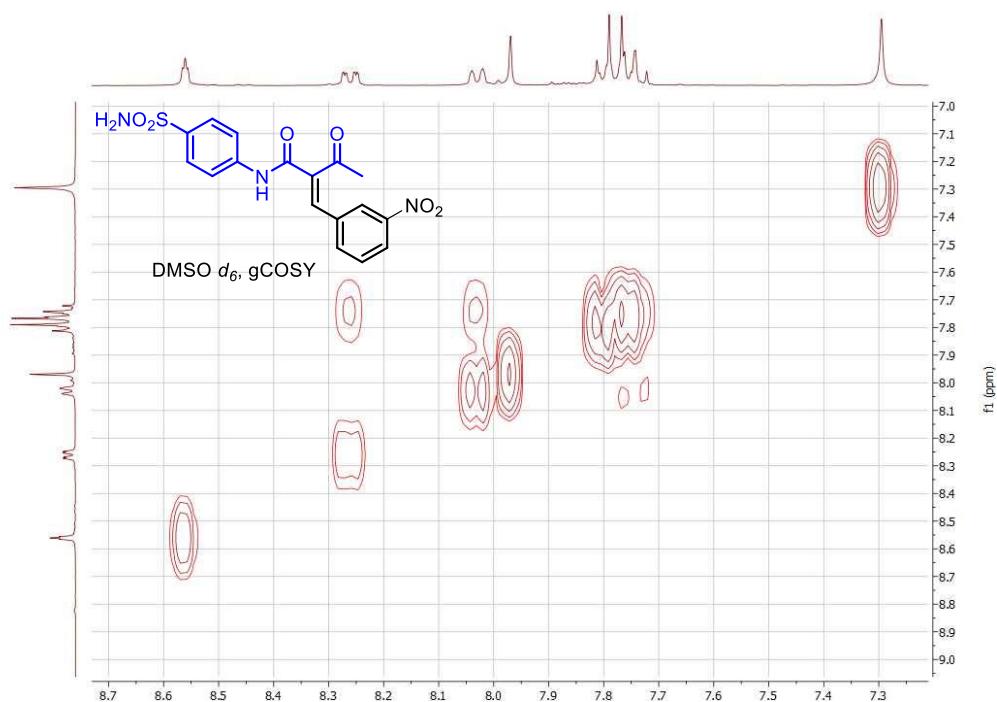


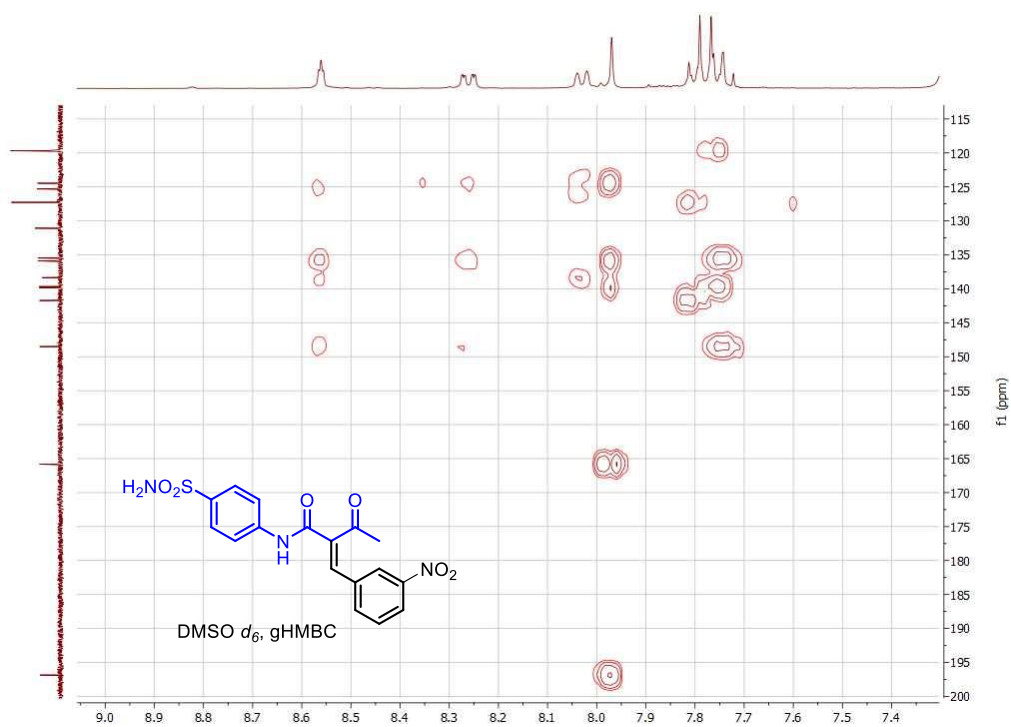




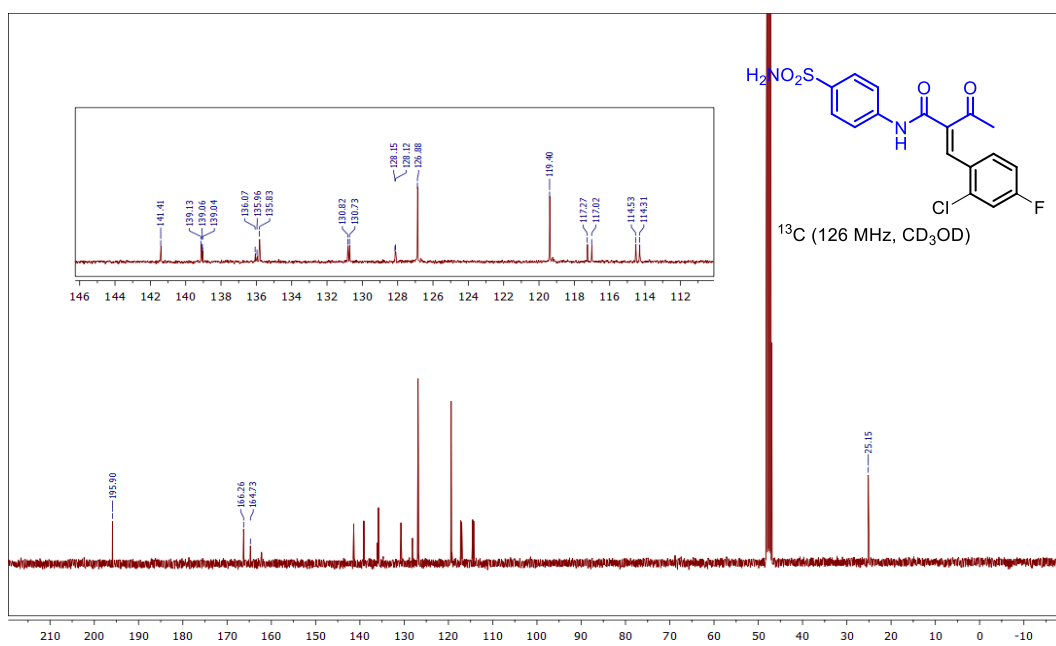
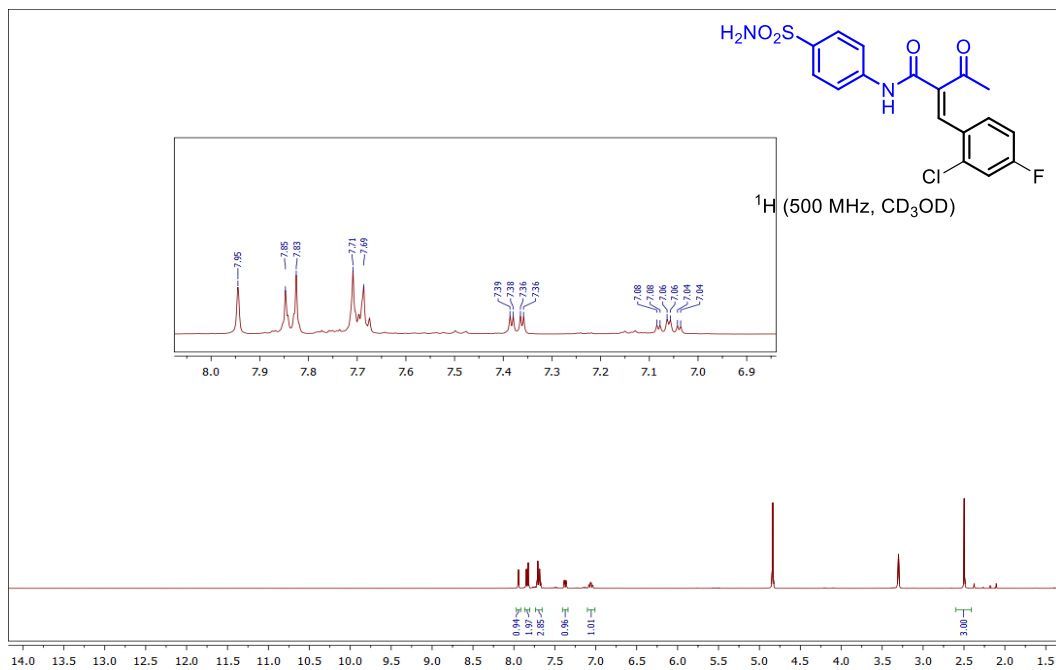


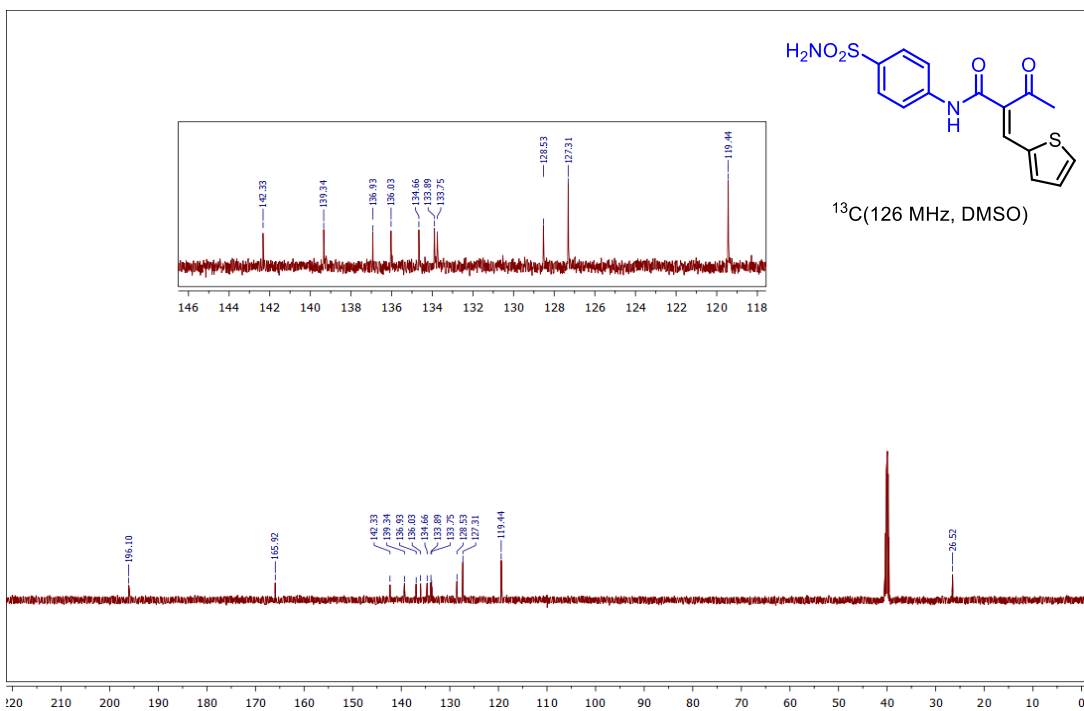
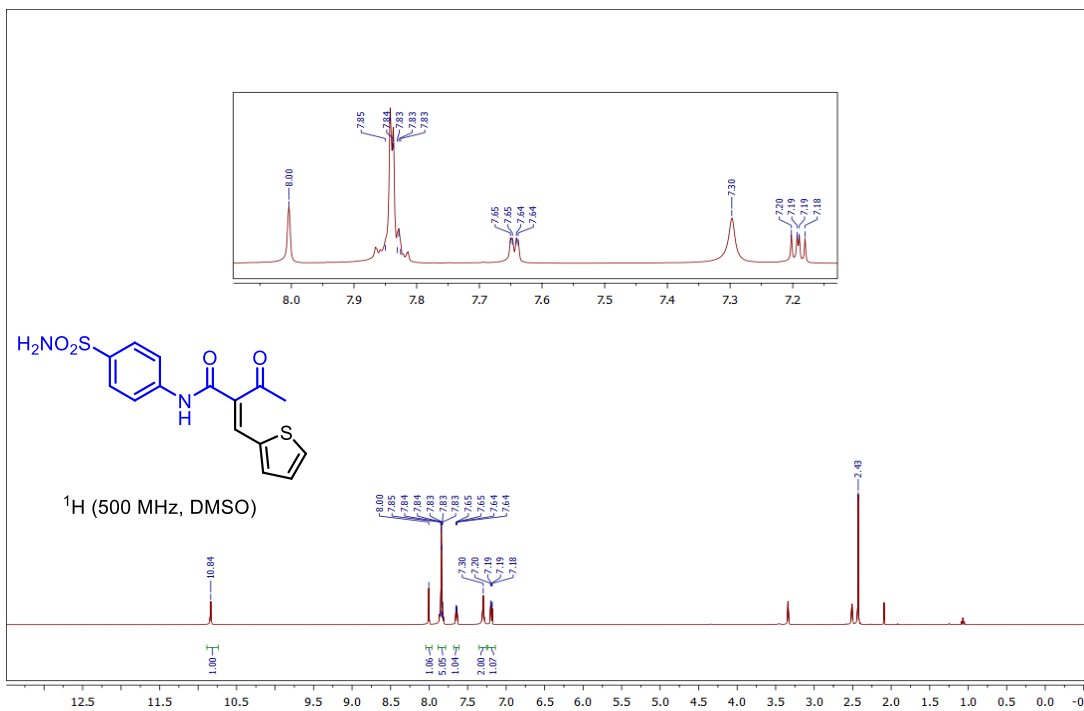
Appendix F for Chapter 7



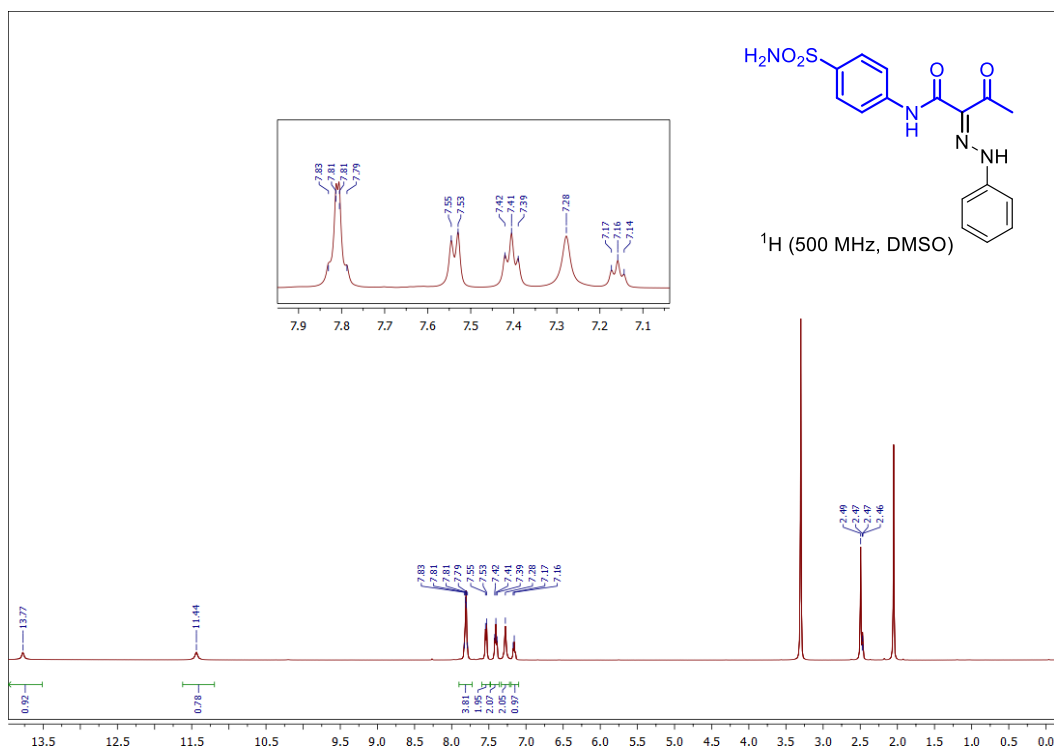


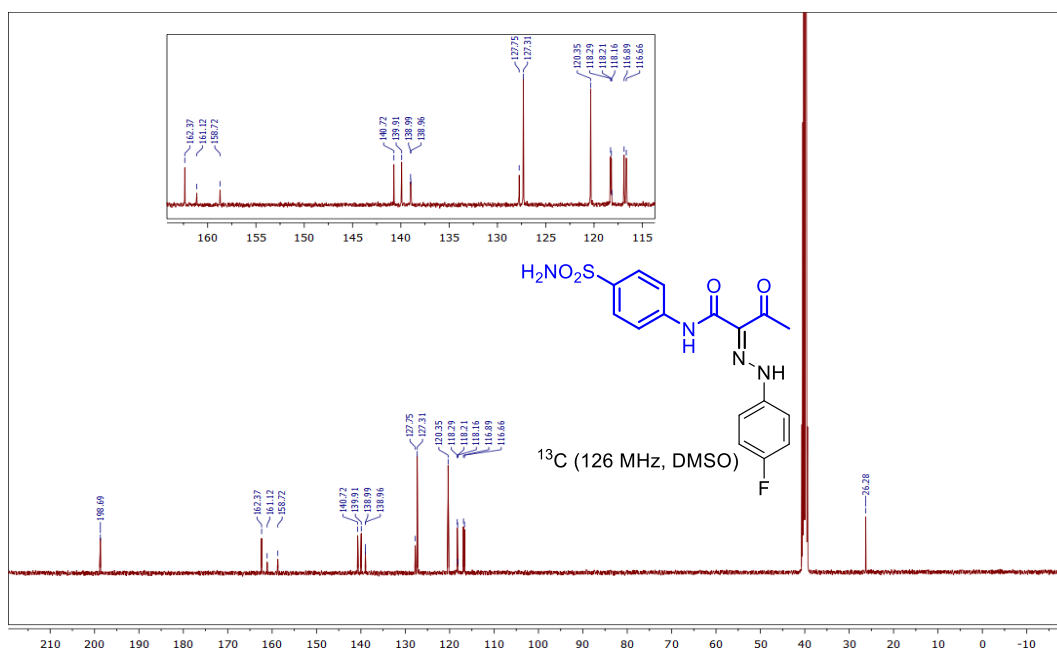
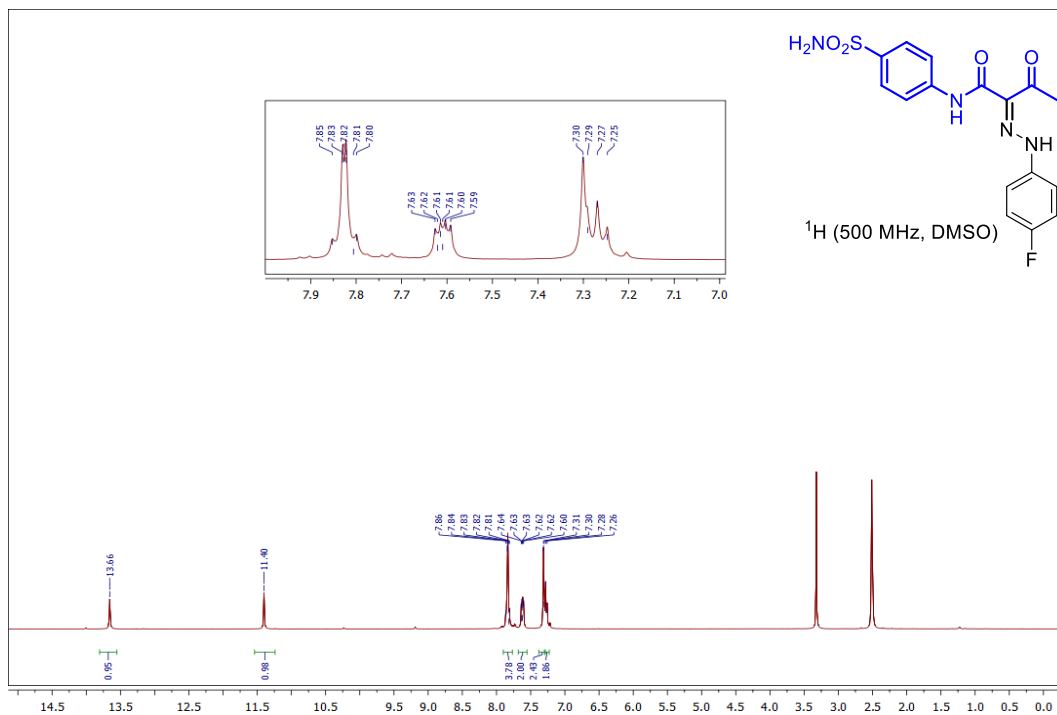
Appendix F for Chapter 7



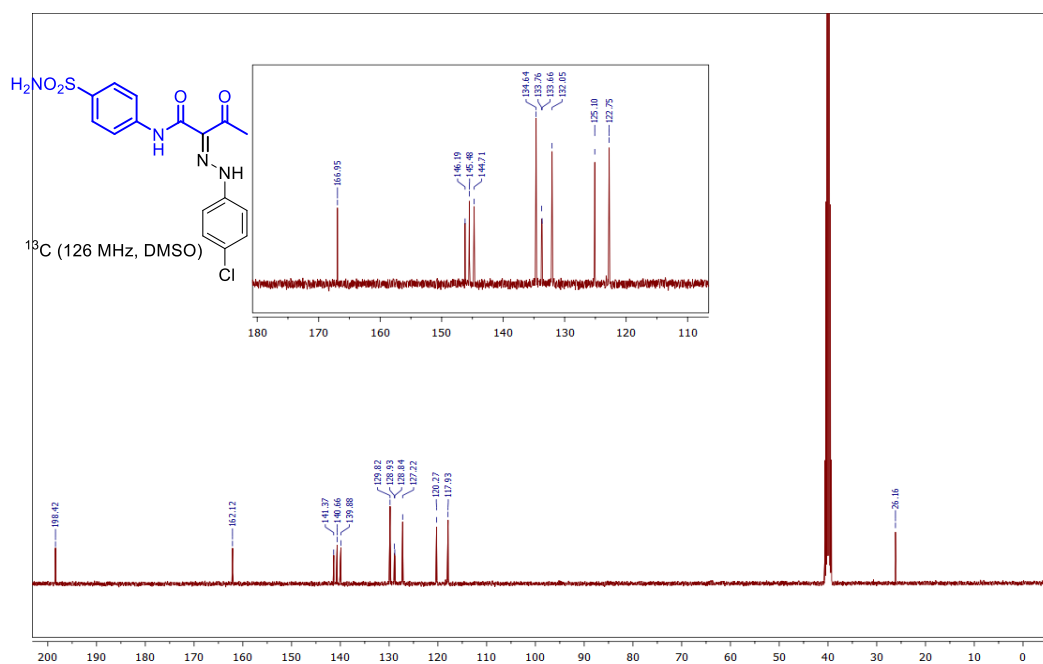
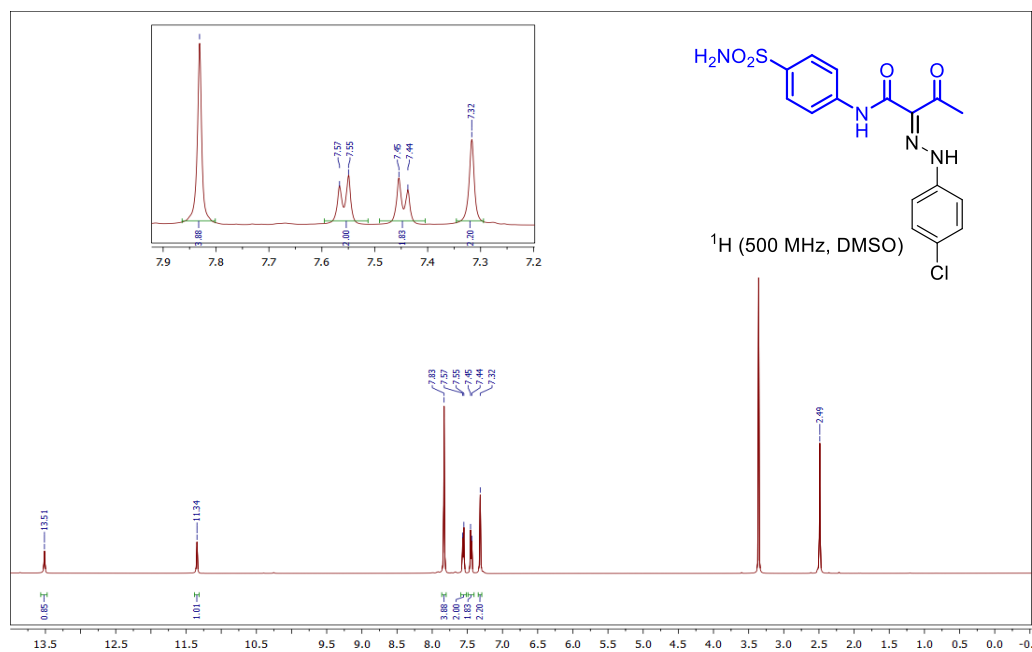


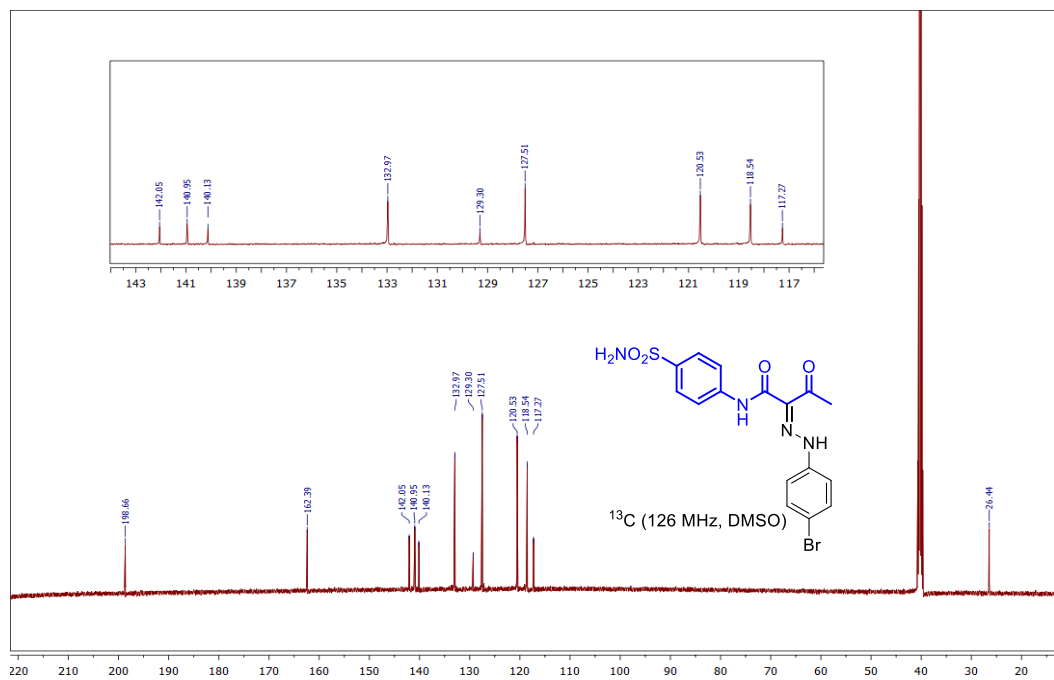
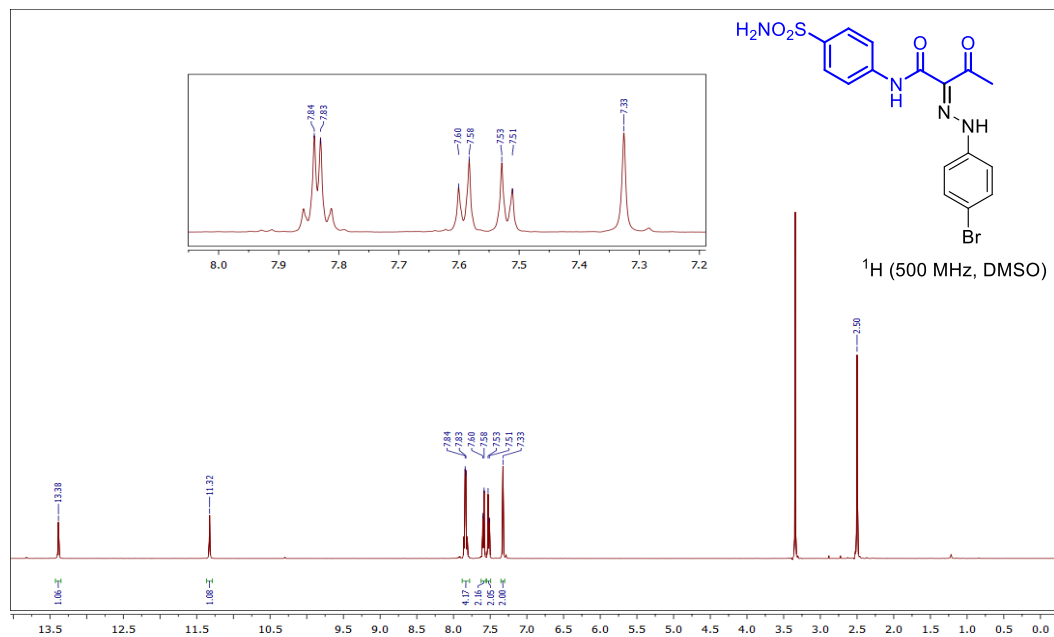
Appendix F for Chapter 7



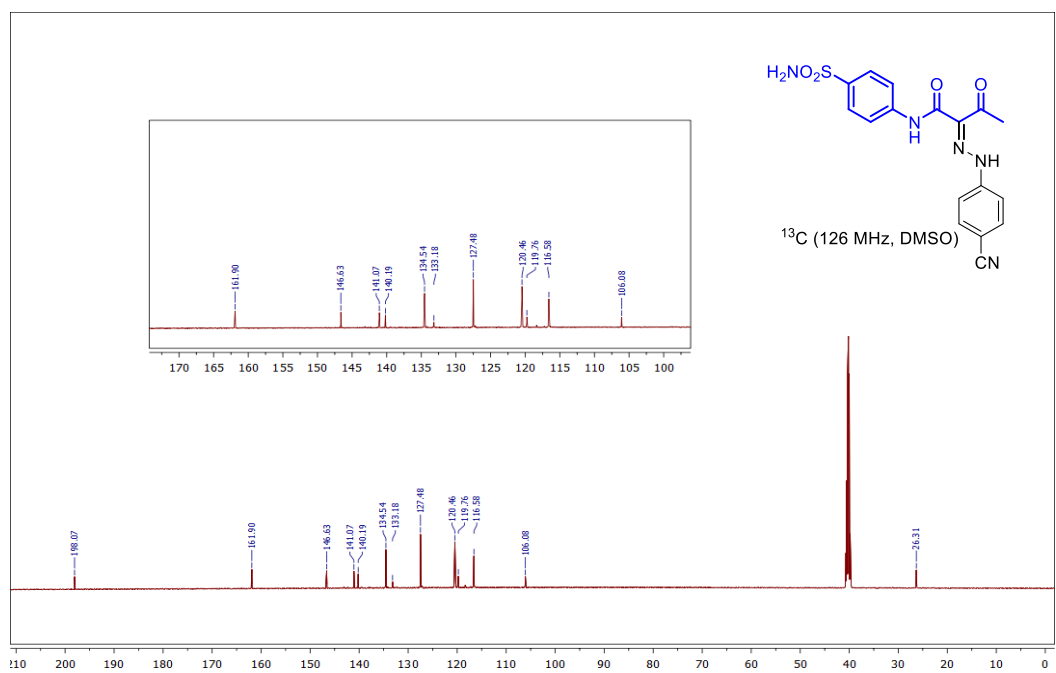
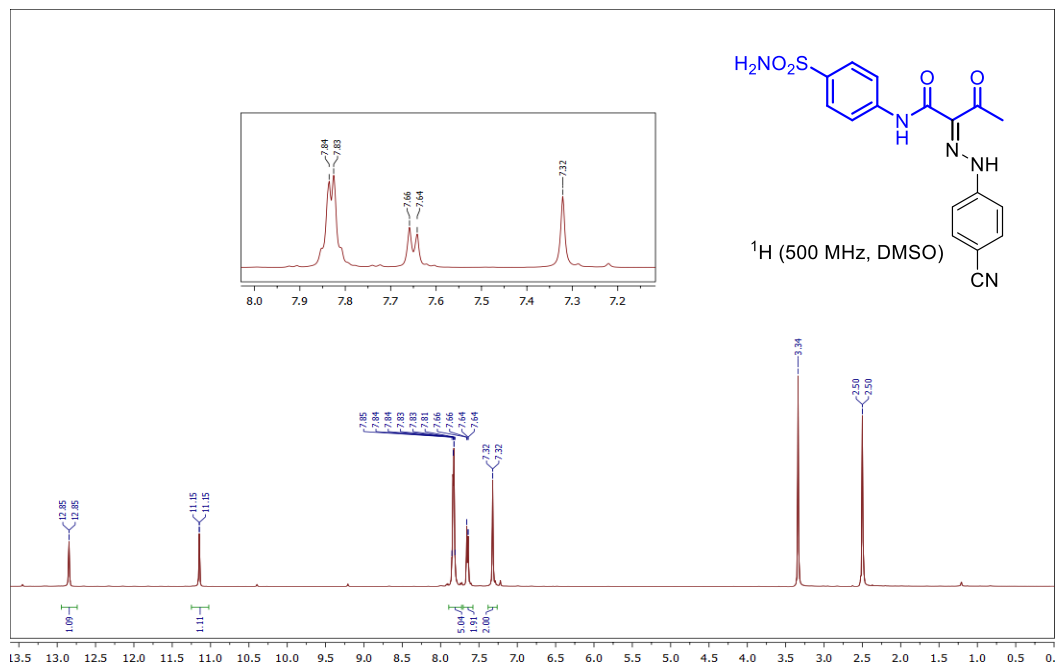


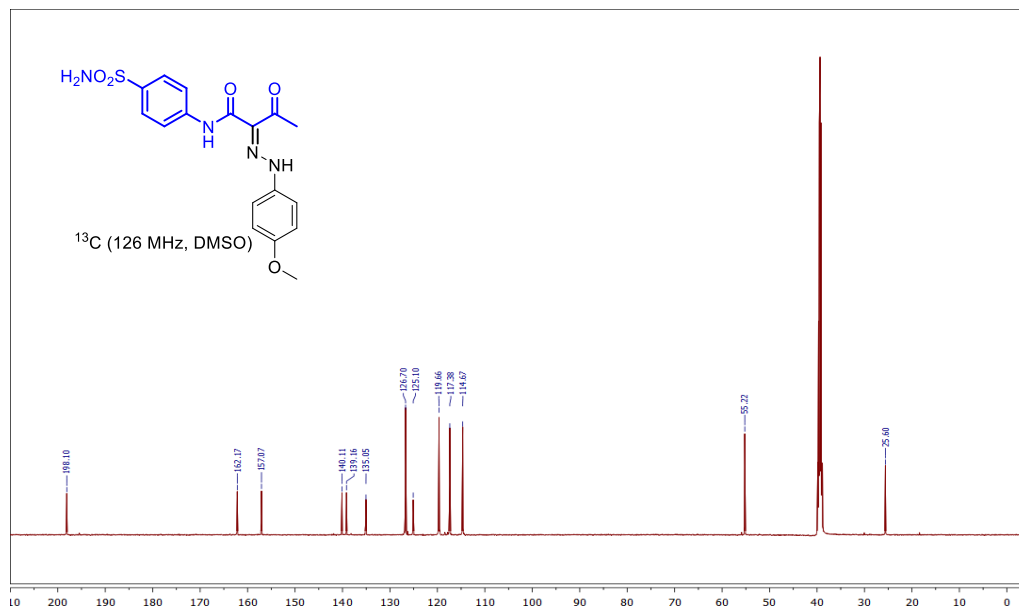
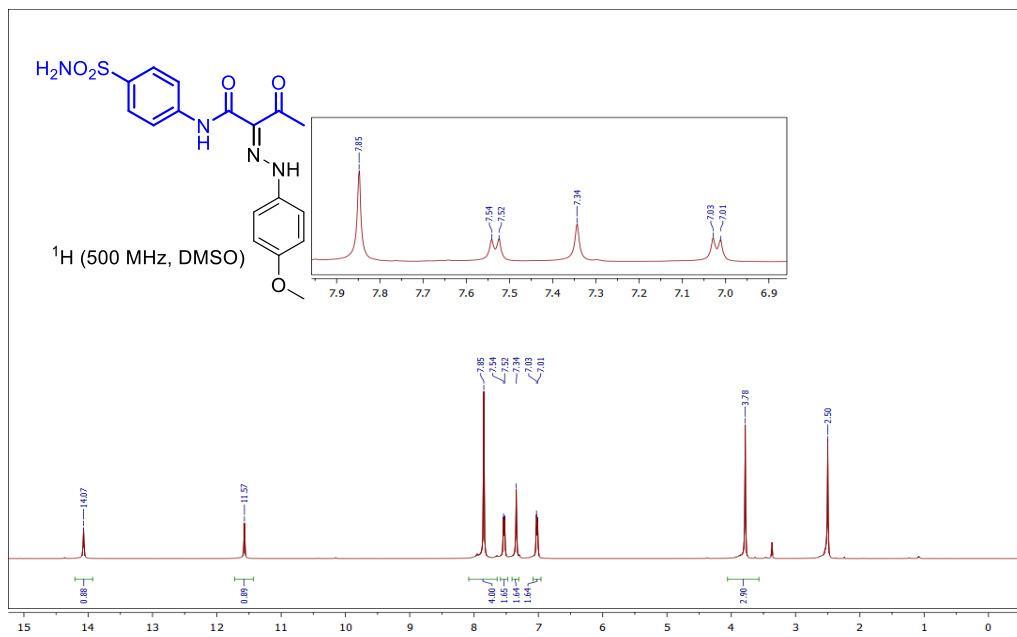
Appendix F for Chapter 7

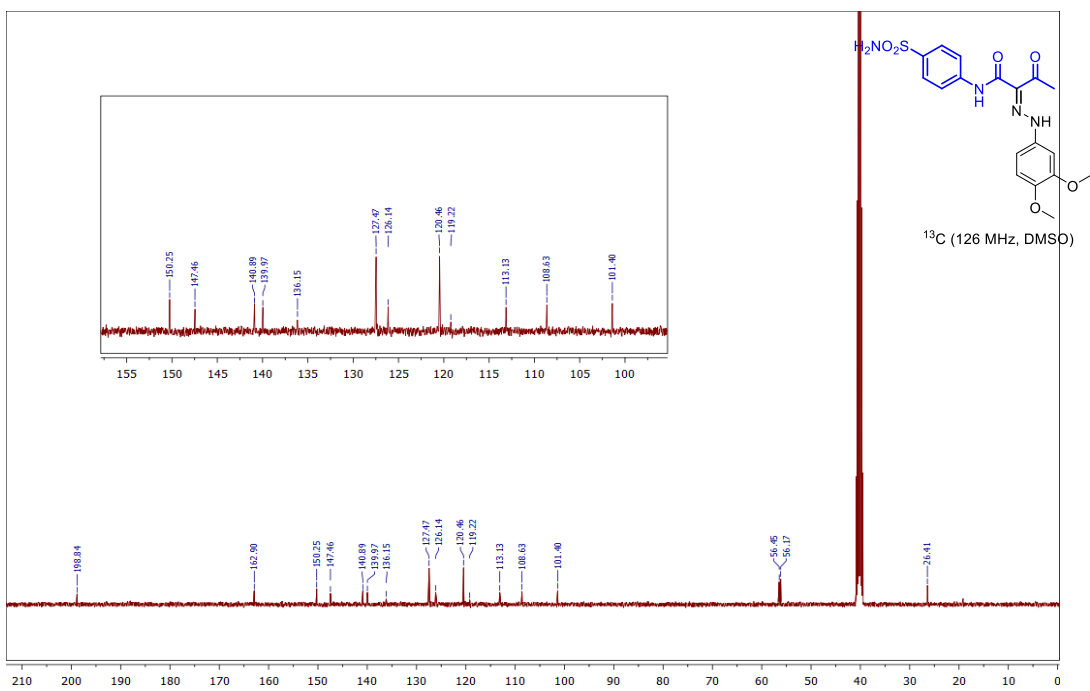
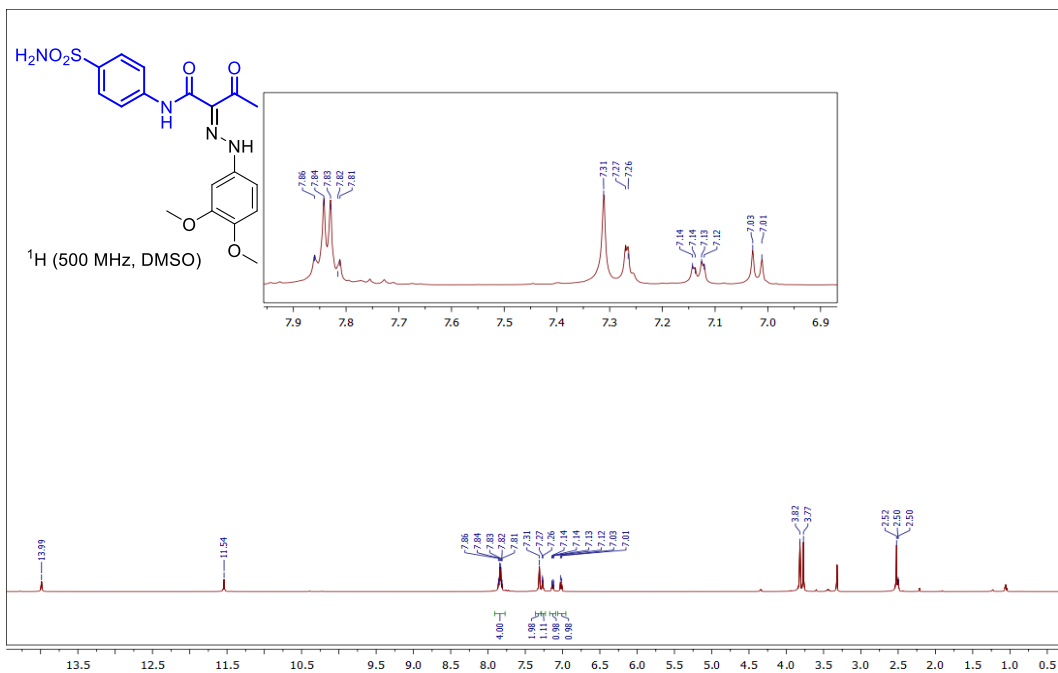




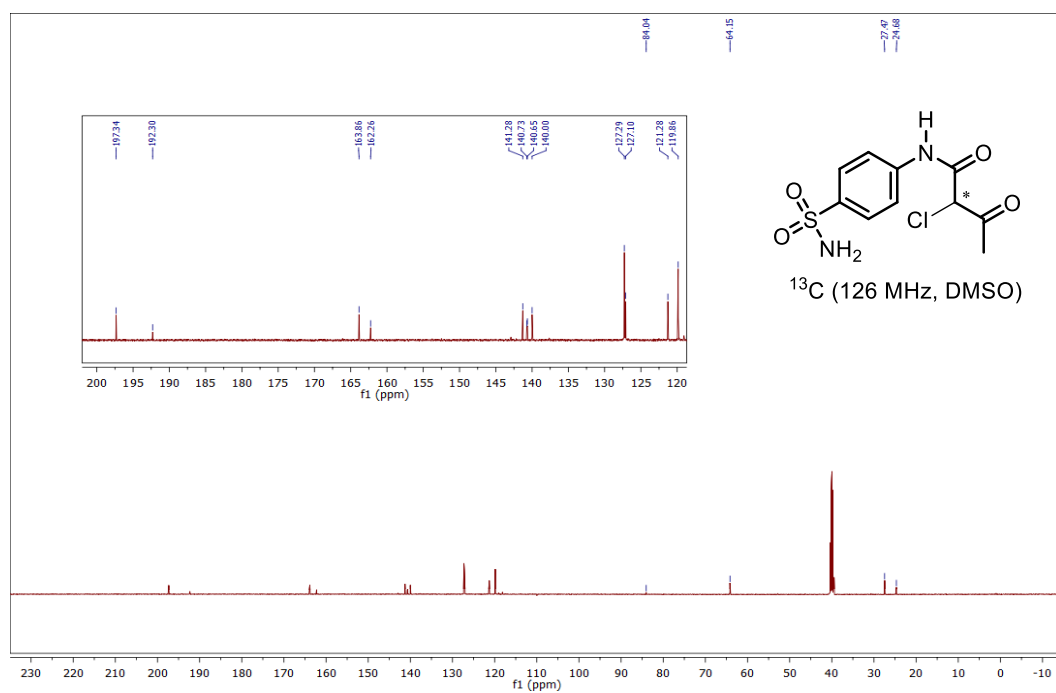
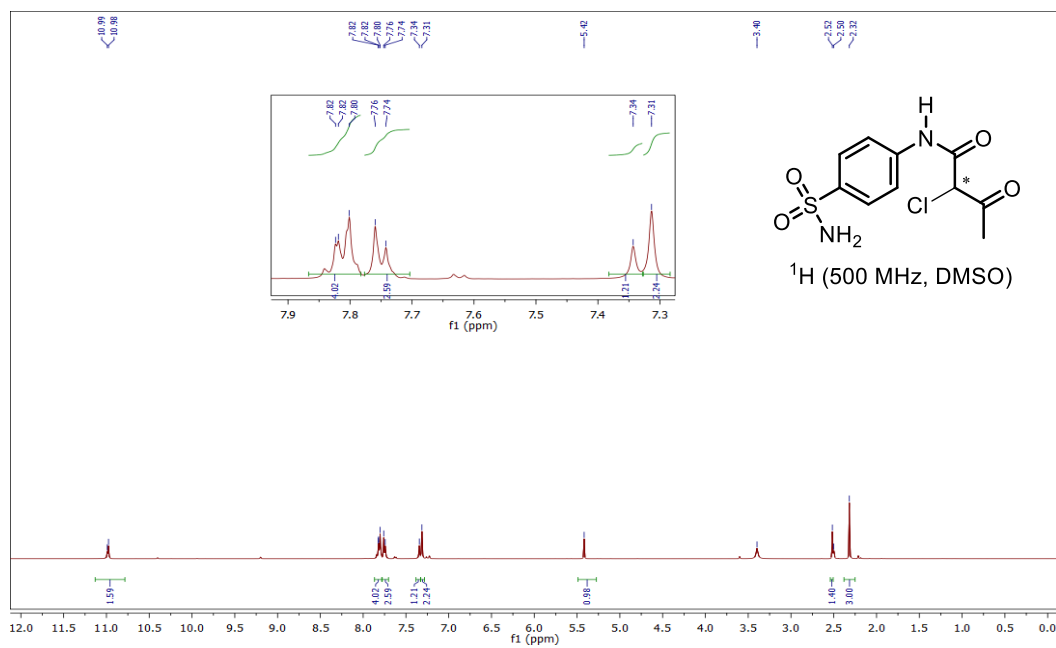
Appendix F for Chapter 7

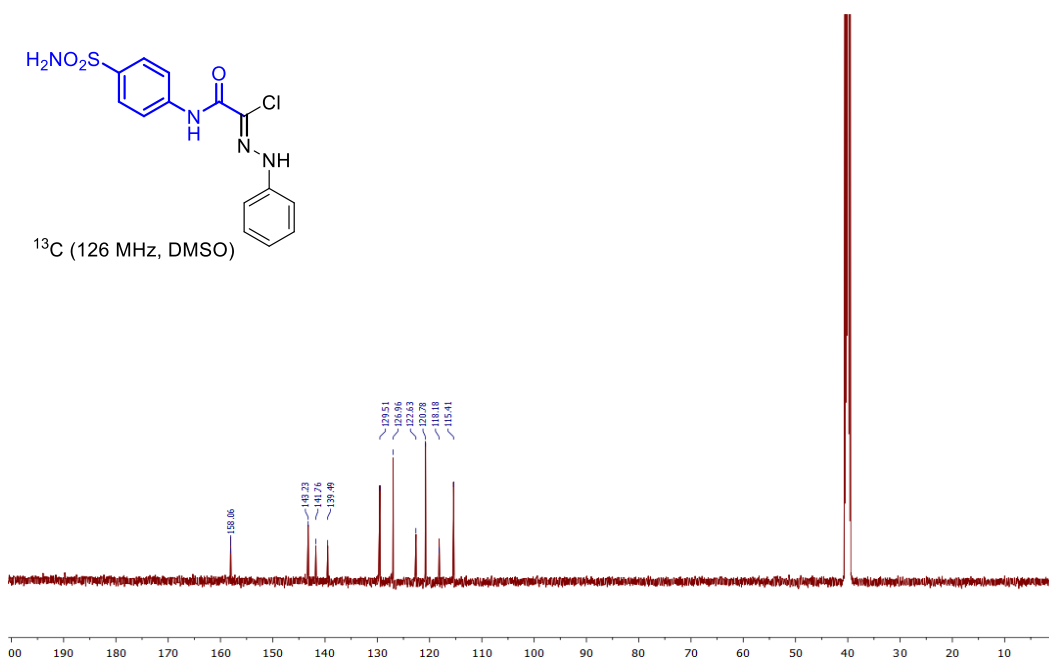
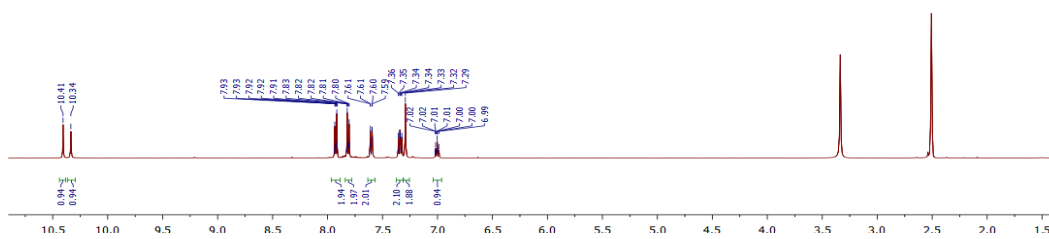
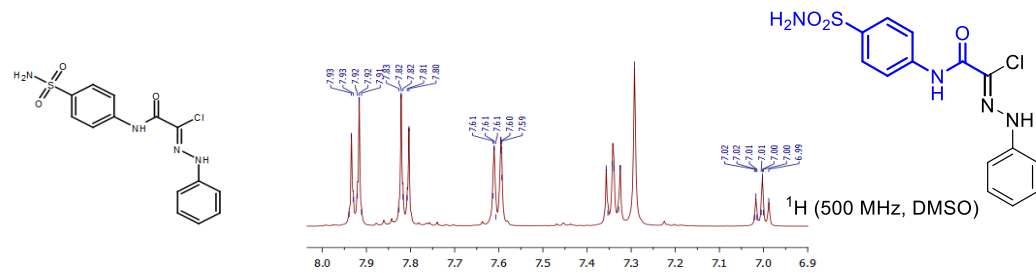




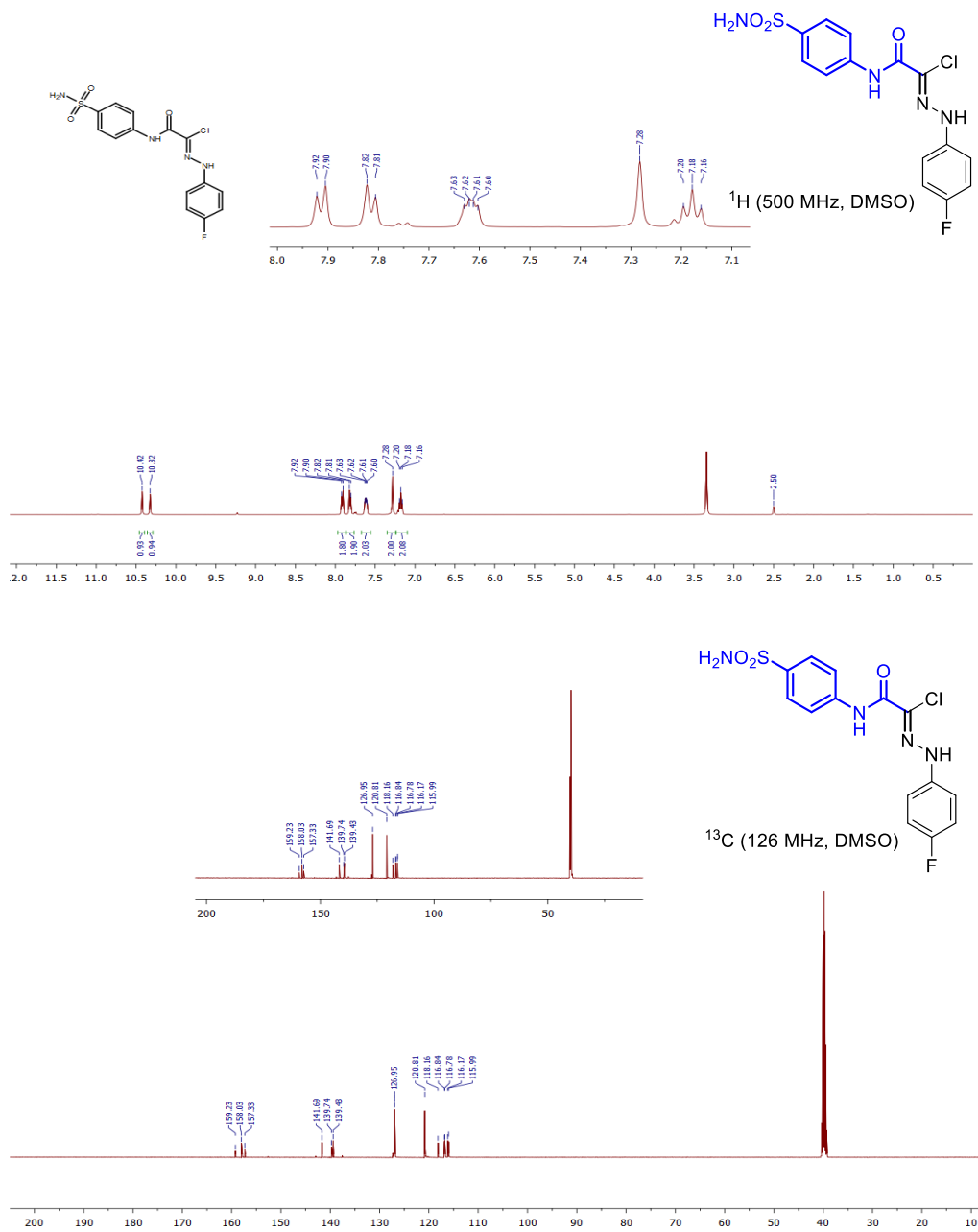


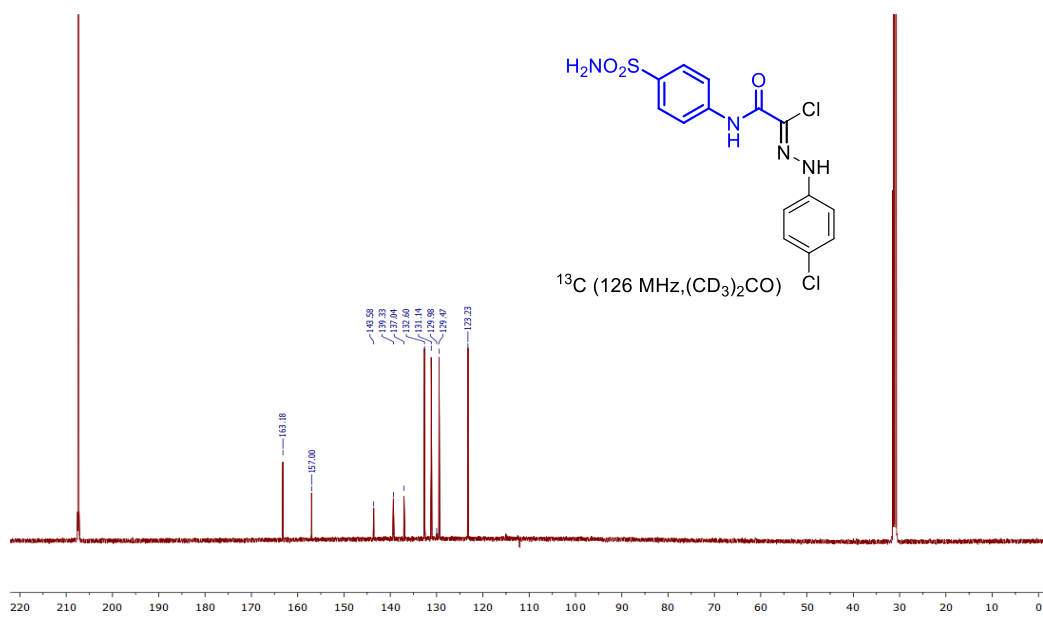
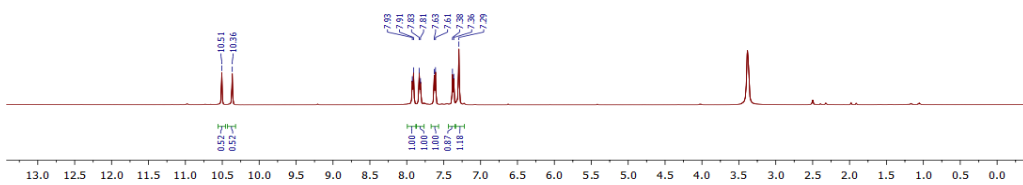
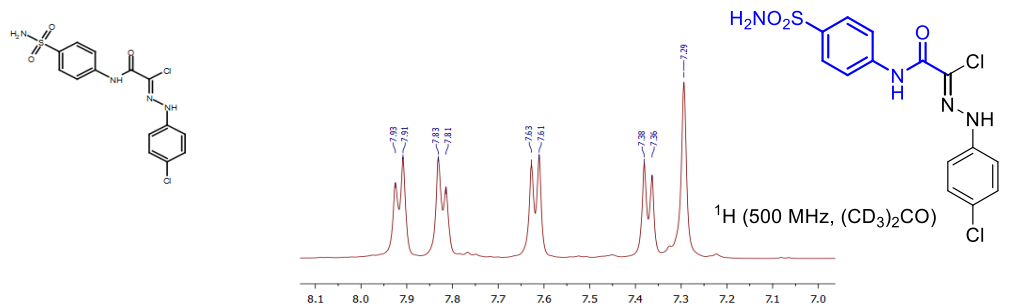
Appendix F for Chapter 7



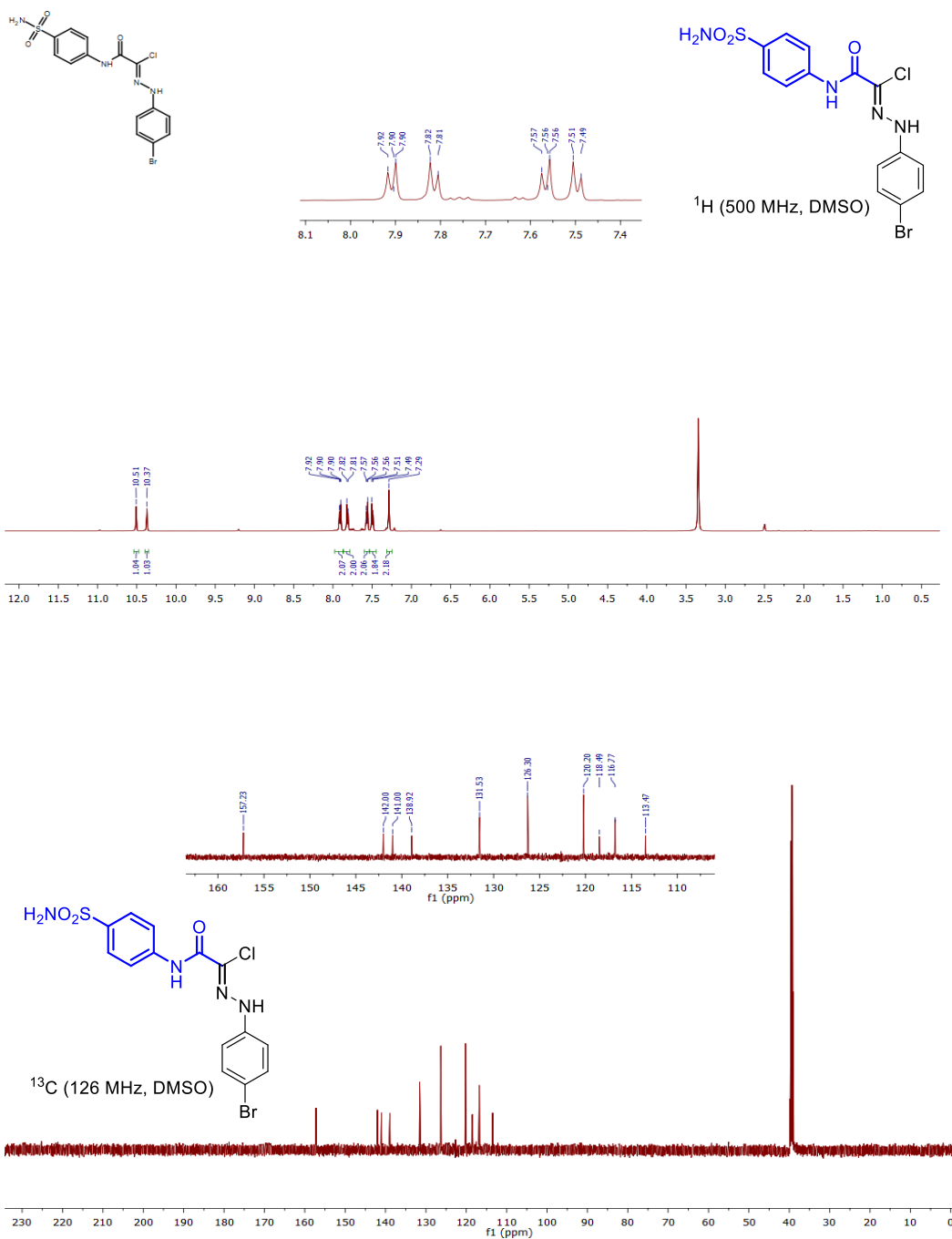


Appendix F for Chapter 7



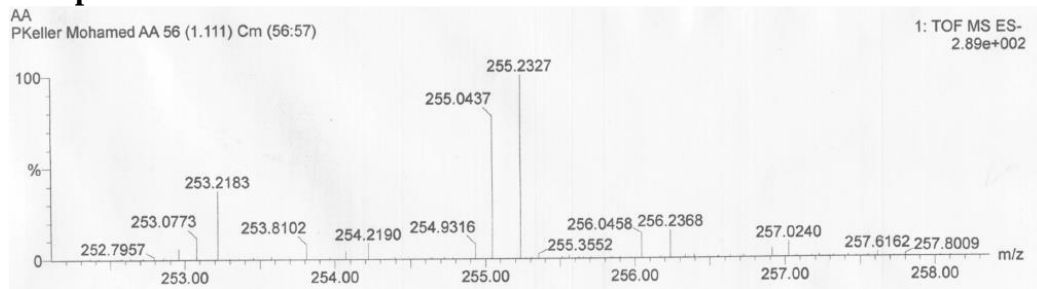


Appendix F for Chapter 7

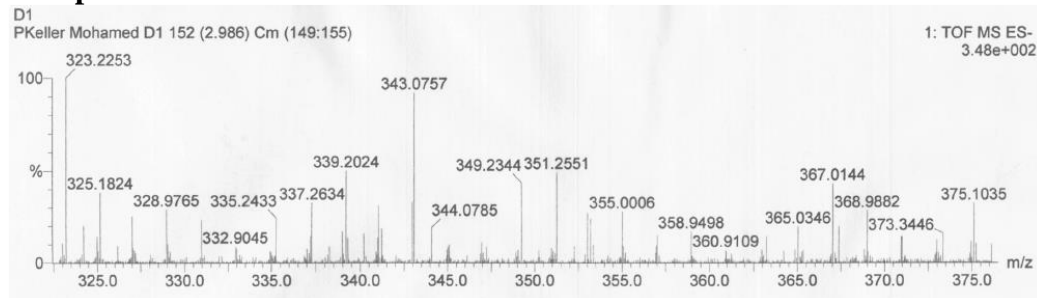


Selected high-resolution mass spectra:

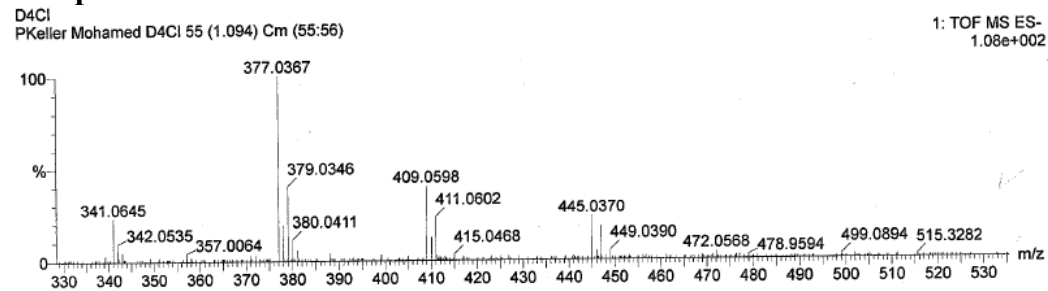
Compound 7.9:



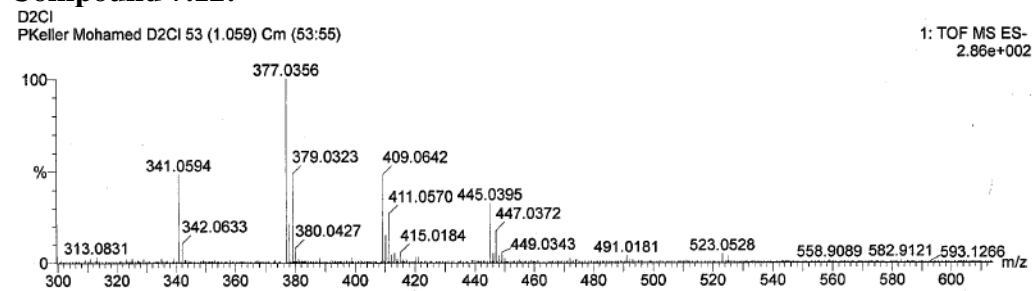
Compound 7.10:



Compound 7.11:



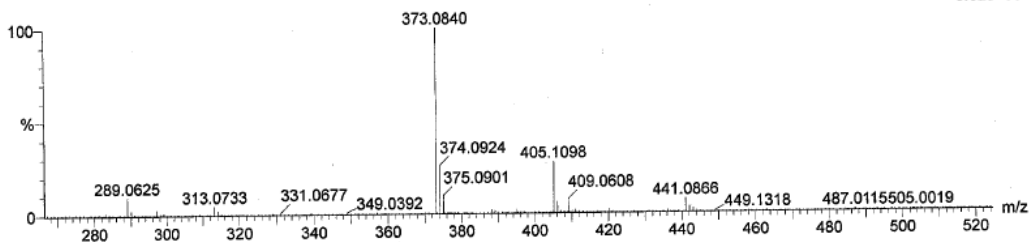
Compound 7.12:



Compound 7.13:

DOME
PKeller Mohamed DOME 33 (0.679) Cm (31:35)

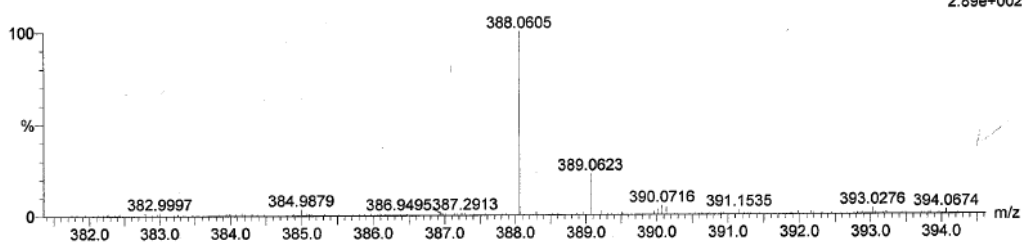
1: TOF MS ES-
8.62e+002



Compound 7.14:

DNO2
PKeller Mohamed DNO2 151 (2.969) Cm (151:152)

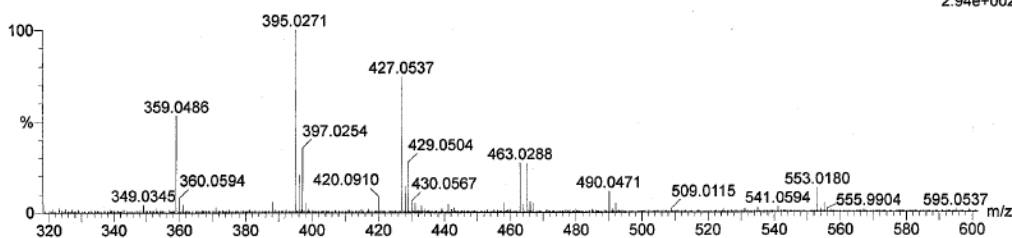
1: TOF MS ES-
2.89e+002



Compound 7.15:

DFC1
PKeller Mohamed DFC1 73 (1.460) Cm (71:77)

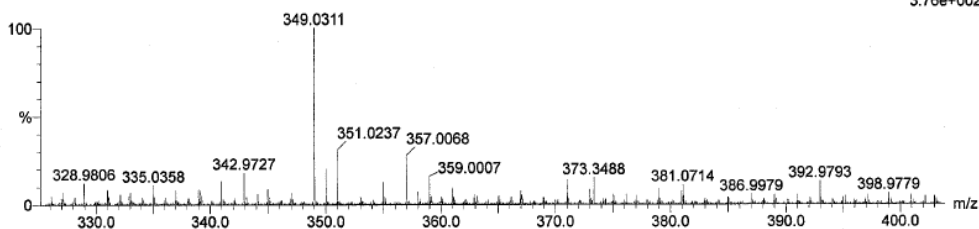
1: TOF MS ES-
2.94e+002



Compound 7.16:

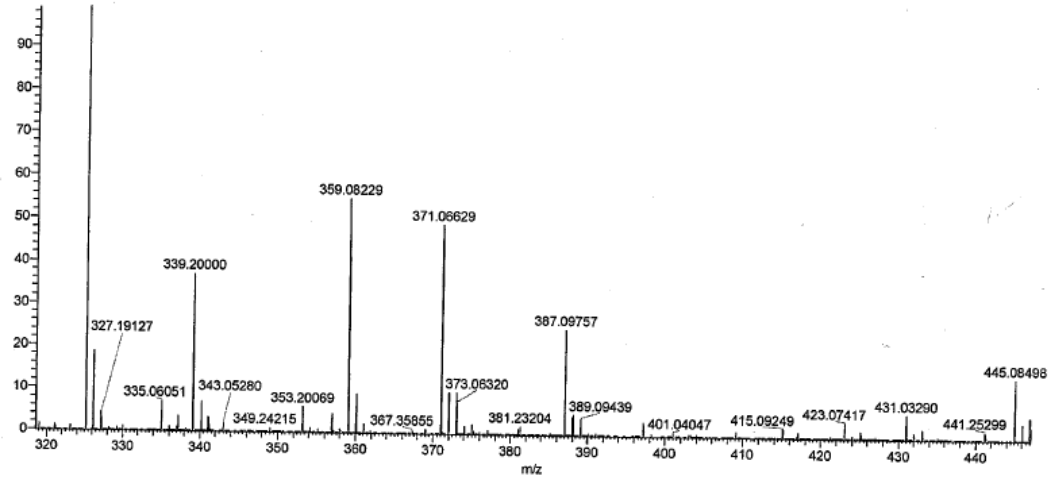
D7
PKeller Mohamed D7 165 (3.247) Cm (162:167)

1: TOF MS ES-
3.76e+002



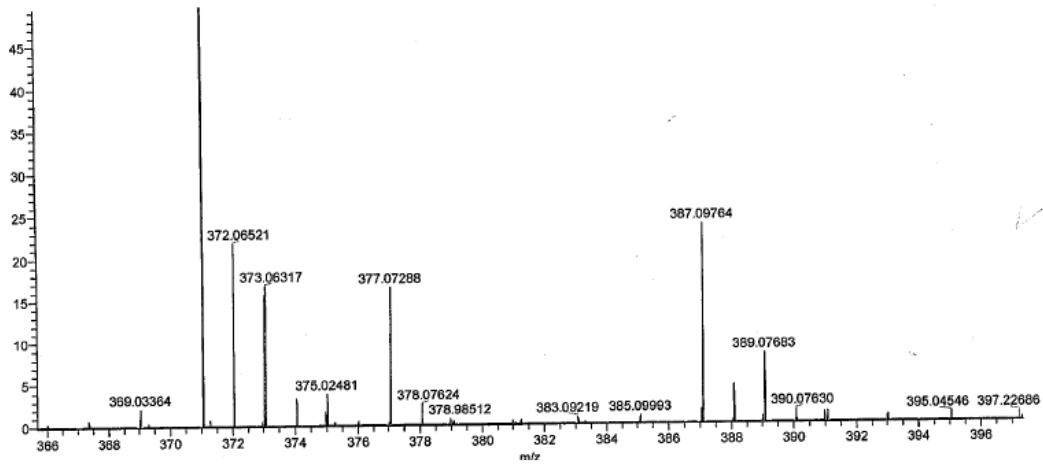
Compound 7.17:

PK_MMetwaly_N1H#9-88 RT: 0.05-0.47 AV: 80 NL: 1.12E6
T: FTMS - p ESI Full ms [100.0000-1000.0000]



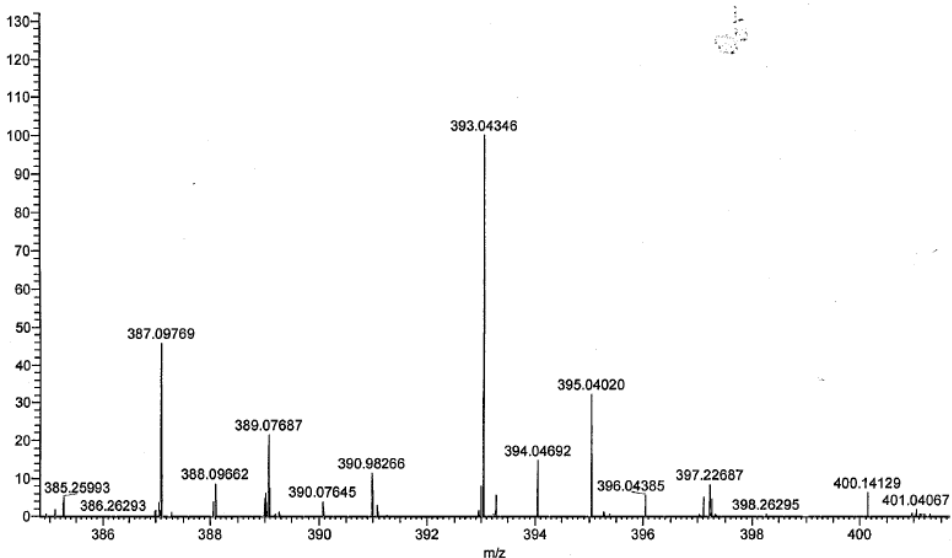
Compound 7.18

PK_MMetwaly_N2_F2#9-78 RT: 0.05-0.42 AV: 70 NL: 1.40E6
T: FTMS - p ESI Full ms [100.0000-1000.0000]



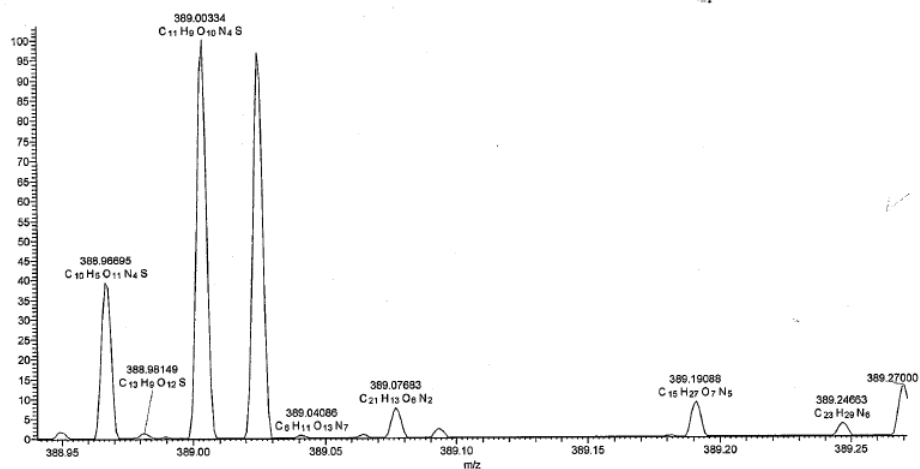
Compound 7.19:

PK_MMetwaly_N8_4_Cib_20180806143137 #9-26 RT: 0.05-0.16 AV: 18 NL: 3.36E5
T: FTMS - p ESI Full ms [100.0000-1000.0000]



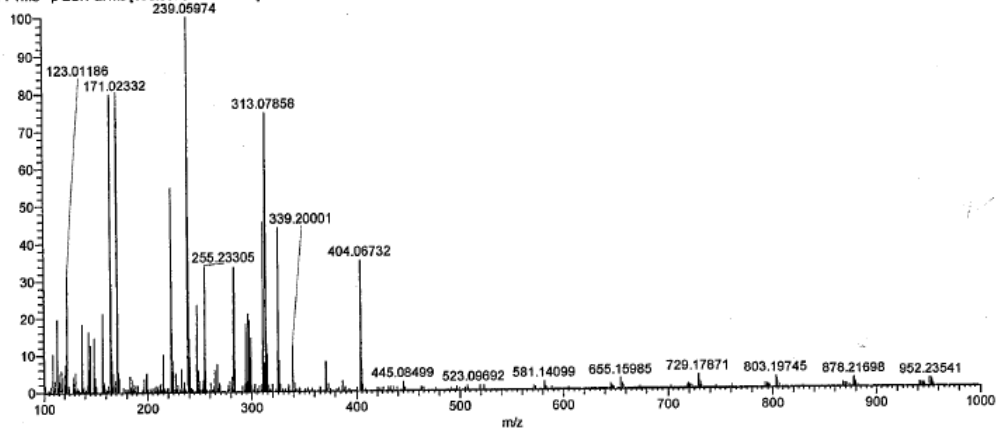
Compound 7.22:

PK_MMetwaly_N5_40Me_20180602122532 #9-99 RT: 0.05-0.50 AV: 91 NL: 2.06E4
T: FTMS - p ESI Full ms [100.0000-1000.0000]



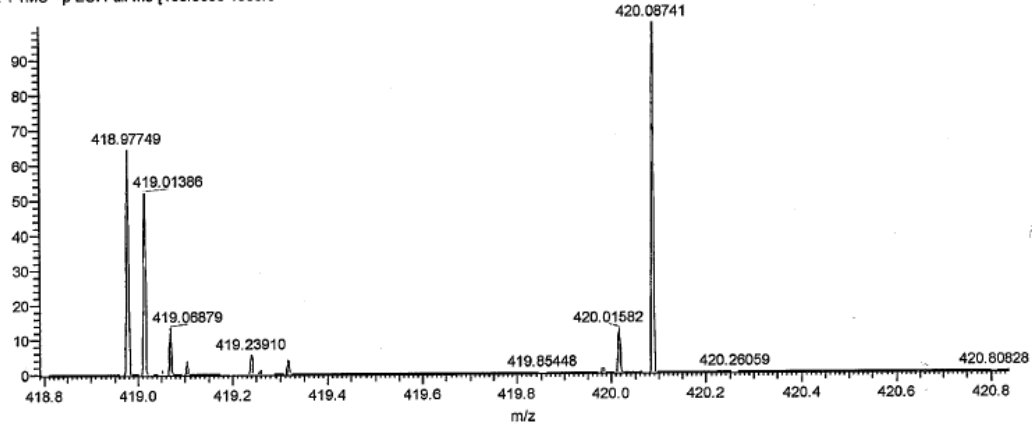
Compound 7.23:

PK_MMetwaly_N6_3NO2A #12 RT: 0.06 AV: 1 NL: 8.95E6
 T: FTMS - p ESI Full ms [100.0000-1000.0000]



Compound 7.24:

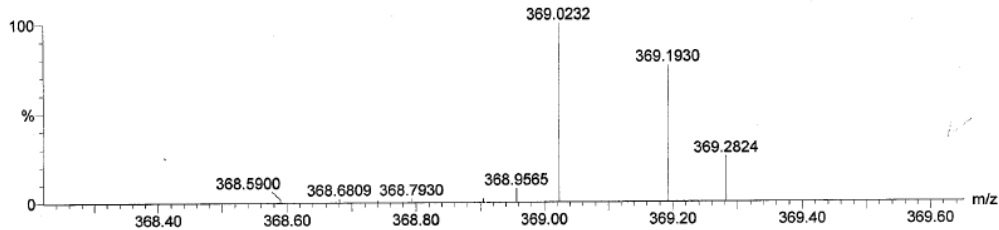
PK_MMetwaly_N7_DioMe_20180802115938 #9-99 RT: 0.05-0.50 AV: 91 NL: 7.75E4
 T: FTMS - p ESI Full ms [100.0000-1000.0]



Compound 7.27:

C2-4F
 PK_MMetwaly C2-4F 231 (4.531) Cm (228:231)

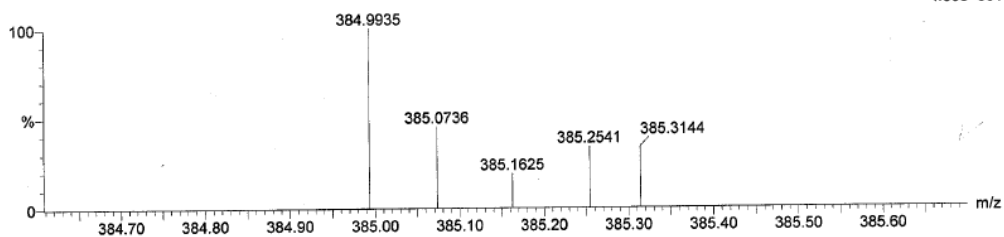
1: TOF MS ES-
 5.18e+002



Compound 7.28:

C3
PK MMetwaly C3 43 (0.869) Cm (43)

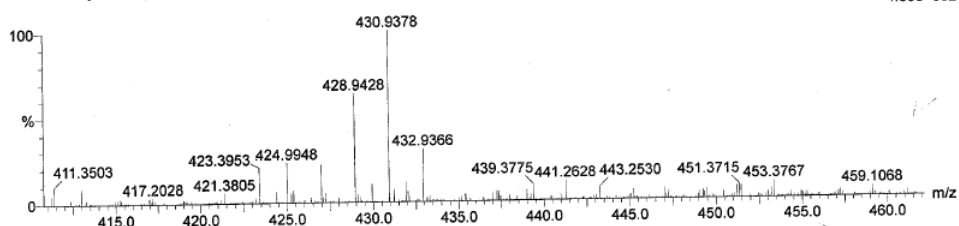
1: TOF MS ES-
4.00e+001



Compound 7.29:

C4
PK MMetwaly C4 33 (0.679) Cm (33)

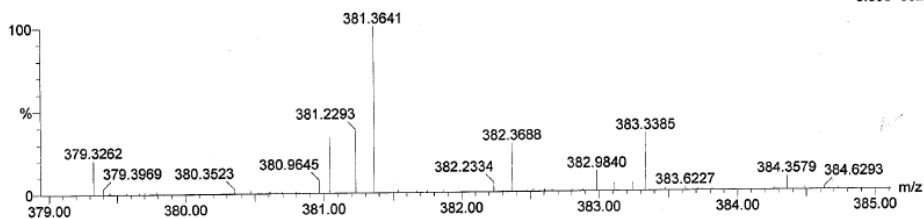
1: TOF MS ES-
4.38e+002



Compound 7.30:

C5
PK MMetwaly C5 58 (1.164) Cm (58:59)

1: TOF MS ES-
3.55e+002



B) HPLC purity:

The purity of all tested compounds was determined by High Performance Liquid Chromatography (HPLC) analysis and was greater than 95%. HPLC was performed with a Shimadzu CLASS-VP LC10 analytical HPLC system (Shimadzu Corporation, Kyoto, Japan) equipped with a diode array detector and an auto-sampler with detection at 254 nm and at a flow rate of 0.5 mL/min. The column used in HPLC analysis was Luna C18 column (250 × 4.6 mm; 5 μm particle size; Phenomenex, Australia). Column temperature was not controlled during the experiment. The mobile phase consisted of (A) water/TFA (99.9:0.1, v/v) and (B) acetonitrile/TFA (99.9:0.1, v/v).

Table F1: HPLC purity of the synthesized compounds

Compound	Formula	Retention time	Purity
7.9	C ₁₀ H ₁₂ N ₂ O ₄ S	5.58	98.4%
7.10	C ₁₇ H ₁₆ N ₂ O ₄ S	5.56	98.6%
7.11	C ₁₇ H ₁₅ ClN ₂ O ₄ S	5.79	96.1%
7.12	C ₁₇ H ₁₅ ClN ₂ O ₄ S	5.80	97.2%
7.13	C ₁₈ H ₁₈ N ₂ O ₅ S	5.54	95.5%
7.14	C ₁₇ H ₁₅ N ₃ O ₆ S	5.90	98.0%
7.15	C ₁₇ H ₁₄ ClFN ₂ O ₄ S	5.85	95.2%
7.16	C ₁₅ H ₁₄ N ₂ O ₄ S ₂	5.48	98.0%
7.17	C ₁₆ H ₁₆ N ₄ O ₄ S	6.74	98.0%
7.18	C ₁₆ H ₁₅ FN ₄ O ₄ S	6.75	95.2%
7.19	C ₁₆ H ₁₅ ClN ₄ O ₄ S	6.75	95.9%
7.20	C ₁₆ H ₁₅ BrN ₄ O ₄ S	6.72	95.6%
7.21	C ₁₇ H ₁₅ N ₅ O ₄ S	6.62	98.2%
7.22	C ₁₇ H ₁₈ N ₄ O ₅ S	6.63	99.4%
7.23	C ₁₆ H ₁₅ N ₅ O ₆ S	6.65	98.7%
7.24	C ₁₈ H ₂₀ N ₄ O ₆ S	6.66	97.4%
7.26	C ₁₄ H ₁₃ ClN ₄ O ₃ S	4.98	99.5%
7.27	C ₁₄ H ₁₂ FCIN ₄ O ₃ S	5.63	99.5%
7.28	C ₁₄ H ₁₂ Cl ₂ N ₄ O ₃ S	5.62	97.9%
7.29	C ₁₄ H ₁₂ BrClN ₄ O ₃ S	5.02	99.6%
7.30	C ₁₅ H ₁₅ ClN ₄ O ₄ S	5.02	99.4%

C) Protein X-ray crystallography data:

Table F2: Summary of Data Collection and Atomic Model Refinement Statistics

PDB	6UFB	6UFC	6UFD
compound	7.10	7.13	7.16
Space group	P21	P21	P21
Cell dimensions			
a, b, c	42.4, 41.5, 72.0	42.6, 41.5, 72.4	42.6, 41.7, 72.3
alpha, beta, gamma	90, 104.5, 90	90, 104.7, 90	90, 104.6, 90
Resolution (Å)	41.5 - 1.67	41.5 - 1.32	41.7 - 1.48
Resolution- high (Å)	1.70 - 1.67	1.35 - 1.32	1.50 - 1.48
Rmerge	0.091 (0.772)	0.083 (0.536)	0.127 (0.790)
Rpim	0.036 (0.302)	0.035 (0.235)	0.053 (0.370)
CC ½	0.999 (0.800)	0.998 (0.810)	0.995 (0.625)
I/sigI	17.2 (2.6)	12.2 (3.2)	10.1 (2.6)
Completeness (%)	97.3 (94.0)	97.7 (88.2)	97.7 (69.4)
Redundancy	7.5 (7.3)	6.7 (6.0)	6.7 (5.3)
Refinement			
resolution (Å)	41.0 - 1.67	40.3 - 1.32	41.3 - 1.48
unique reflections	26,243	52,867	38,441
Rwork/Rfree	15.1 / 18.6	11.7 / 14.4	14.9 / 16.7

(%)			
# atoms	2466	2510	2496
Protein	2164	2206	2203
metal (Zn)	1	1	1
ligand	24	26	23
water	258	270	250
B-factors	14.9	9.3	13.8
(Å ²)			
protein	15.1	14.4	14.0
metal (Zn)	7.9	7.0	6.4
ligand	19.6	20.4	16.5
water	26.0	27.7	25.4
r.m.s. deviations			
Bond length (Å)	0.010	0.008	0.009
Bond angle (°)	1.628	1.753	1.646

*** values in parenthesis are values in the high-resolution bin**

Figure F1: Graphical depiction of the model fit to experimental electron density of all instances of **7.10** in hCA II active site (pdb 6UFB). Each fit is shown from different orientation to approximate a three-dimensional view. 2mFo-DFc (at 0.7 rmsd) in gray mFo-DFc (at 3 Å rmsd) in purple (negative) and green (positive).

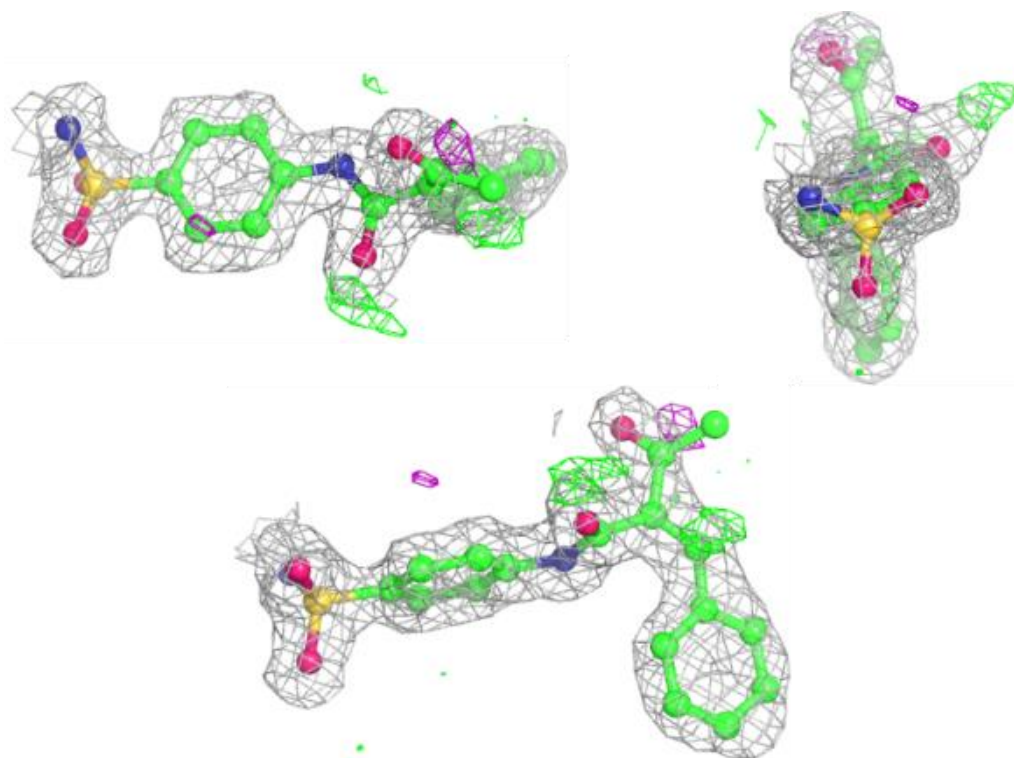


Figure F2: Graphical depiction of the model fit to experimental electron density of all instances of **7.13** in hCA II active site (pdb 6UFC). Each fit is shown from different orientation to approximate a three-dimensional view. 2mFo-DFc (at 0.7 rmsd) in gray mFo-DFc (at 3 Å rmsd) in purple (negative) and green (positive).

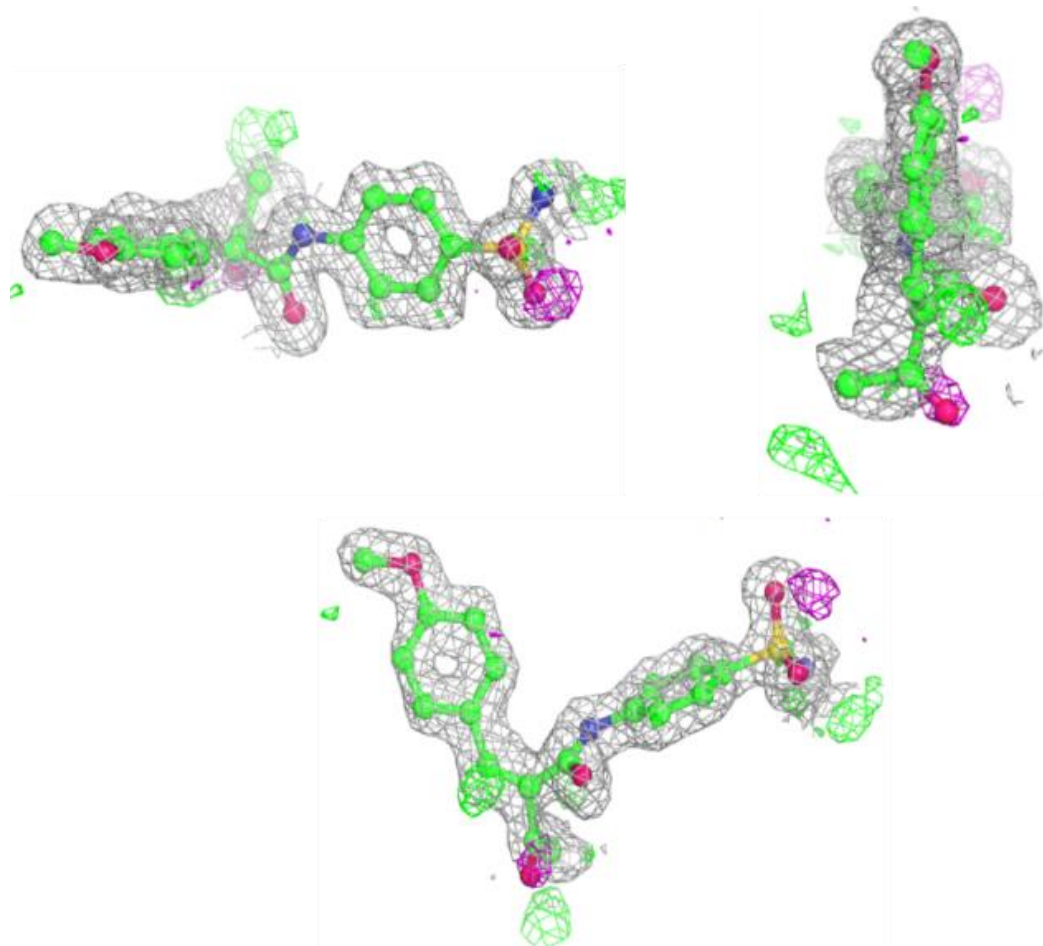


Figure F3: Graphical depiction of the model fit to experimental electron density of all instances of **7.16** in hCA II active site (pdb 6UFD). Each fit is shown from different orientation to approximate a three-dimensional view. 2mFo-DFc (at 0.7 rmsd) in gray mFo-DFc (at 3 Å rmsd) in purple (negative) and green (positive).

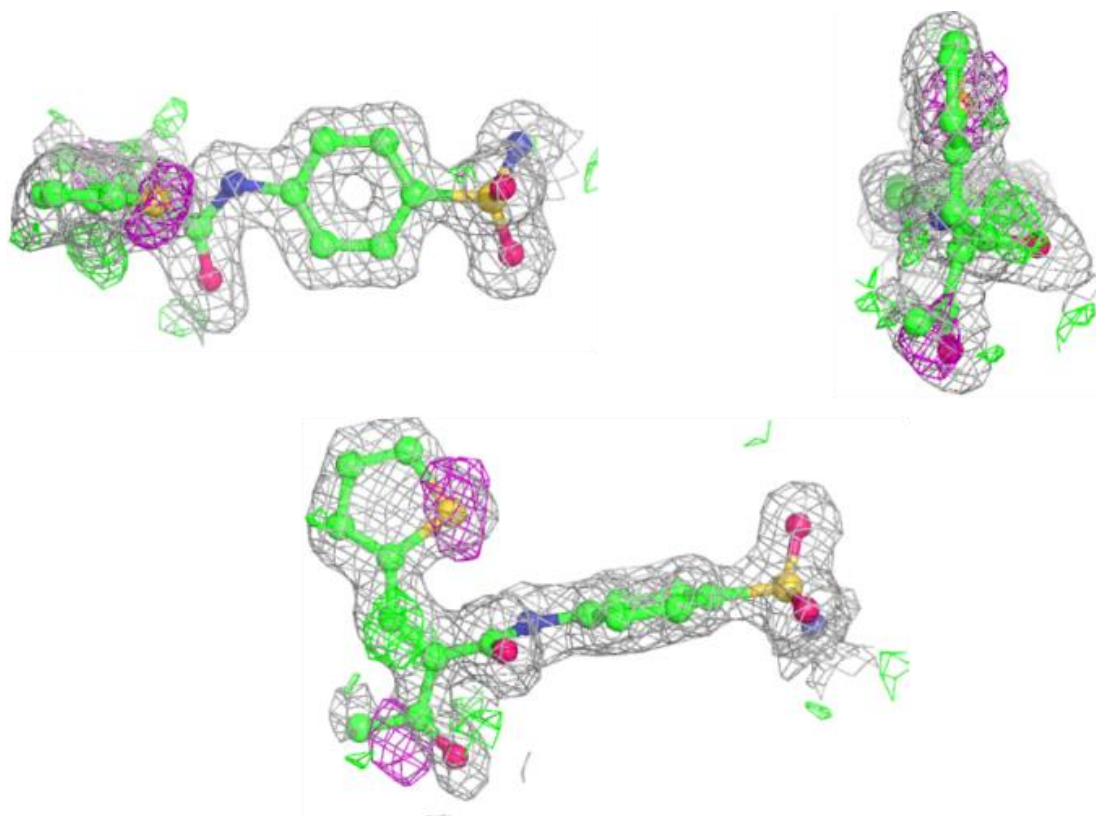


Figure F4: Protein X-ray structure of **7.10** bound to the active site in CA II (pdb 6UFB). The molecular surface of the active site is coloured in blue for the hydrophilic half and in red for the hydrophobic area.

